

UNITED STATES AIR FORCE

ADA248768

SUMMER RESEARCH PROGRAM -- 1991

SUMMER FACULTY RESEARCH PROGRAM (SFRP) REPORTS

VOLUME 5B

WRIGHT LABORATORY

RESEARCH & DEVELOPMENT LABORATORIES

5800 Uplander Way

Culver City, CA 90230-6608

Program Director, RDL
Gary Moore

Program Manager, AFOSR
Lt. Col. Claude Cavender

Program Manager, RDL
Claude Baum

Program Administrator, RDL
Gwendolyn Smith

Submitted to:

AIR FORCE OFFICE OF SCIENTIFIC RESEARCH

Bolling Air Force Base

Washington, D.C.

December 1991

Accession For	
NTIS	ORAG
DTIC	TAB
U. S. AIR FORCE	
Justification	
By	
Distribution	
Availability	
Dist	Avail
A-1	



AEOSR-TR- 92 0172

Approved for public release,
distribution unlimited

AFR 190-12 SCIENTIFIC RESEARCH (AFSC)
NOTICE OF TRANSMITTAL TO DTIC
This technical report has been reviewed and is
approved for public release IAW AFR 190-12
Distribution unlimited.
Glenn Miller
STINFO Program Manager

92 4 08 002

92-09029



REPORT DOCUMENTATION PAGE

Form Approved
OMB No 0704-0188

Public reporting burden for this collection of information is estimated to average 1 hour per response, including the time for reviewing instructions, searching existing data sources, gathering and maintaining the data needed, and completing and reviewing the collection of information. Send comments regarding this burden estimate or any other aspect of this collection of information, including suggestions for reducing this burden, to Washington Headquarters Services, Directorate for Information Operations and Reports, 1215 Jefferson Davis Highway, Suite 1204, Arlington, VA 22202-4302, and to the Office of Management and Budget, Paperwork Reduction Project (0704-0188), Washington, DC 20503.

1. AGENCY USE ONLY (Leave blank)		2. REPORT DATE 9 January 1992	3. REPORT TYPE AND DATES COVERED 21 Sep 90-30 Sep 91	
4. TITLE AND SUBTITLE 1991 Summer Faculty Research Program (SFRP) Volumes 2-5b Vol. 5B			5. FUNDING NUMBERS F49620-90-C-0076	
6. AUTHOR(S) Mr Gary Moore				
7. PERFORMING ORGANIZATION NAME(S) AND ADDRESS(ES) Research Development Laboratories (RDL) 5800 Uplander Way Culver City CA 90230-6608			8. PERFORMING ORGANIZATION REPORT NUMBER AFOSR-TR- 92 0172	
9. SPONSORING/MONITORING AGENCY NAME(S) AND ADDRESS(ES) AFOSR/I Bldg 410 Dolling AFB DC 20332-6448 Lt Col V. Claude Cavender			10. SPONSORING/MONITORING AGENCY REPORT NUMBER	
11. SUPPLEMENTARY NOTES				
12a. DISTRIBUTION/AVAILABILITY STATEMENT UNLIMITED			12b. DISTRIBUTION CODE	
13. ABSTRACT (Maximum 200 words) The purpose of this program is to develop the basis for continuing research of interest to the Air Force at the institution of the faculty member; to stimulate continuing relations among faculty members and professional peers in the Air Force, to enhance the research interests and capabilities of scientific and engineering educators; and to provide follow-on funding for research of particular promise that was started at an Air Force laboratory under the Summer Faculty Research Program. During the summer of 1991 170 university faculty conducted research at Air Force laboratories for a period of 10 weeks. Each participant provided a report of their research, and these reports are consolidated into this annual report.				
14. SUBJECT TERMS			15. NUMBER OF PAGES	
			16. PRICE CODE	
17. SECURITY CLASSIFICATION OF REPORT UNCLASSIFIED	18. SECURITY CLASSIFICATION OF THIS PAGE UNCLASSIFIED	19. SECURITY CLASSIFICATION OF ABSTRACT UNCLASSIFIED	20. LIMITATION OF ABSTRACT UL	

PREFACE

Reports in this volume are numbered consecutively beginning with number 1. Each report is paginated with the report number followed by consecutive page numbers, e.g., 1-1, 1-2, 1-3; 2-1, 2-2, 2-3.

Due to its length, Volume 5 is bound in two parts, 5A and 5B. Volume 5A contains reports #1-30. Volume 5B contains reports #31-55. The Table of Contents for Volume 5 is included in both parts.

This document is one of a set of 13 volumes describing the 1991 AFOSR Summer Research Program. The following volumes comprise the set:

<u>VOLUME</u>	<u>TITLE</u>
1	Program Management Report
	<i>Summer Faculty Research Program (SFRP) Reports</i>
2	Armstrong Laboratory, Wilford Hall Medical Center
3	Phillips Laboratory, Civil Engineering Laboratory
4	Rome Laboratory, Arnold Engineering Development Center, Frank J. Seiler Research Laboratory
5A&B	Wright Laboratory
	<i>Graduate Student Research Program (GSRP) Reports</i>
6	Armstrong Laboratory, Wilford Hall Medical Center
7	Phillips Laboratory, Civil Engineering Laboratory
8	Rome Laboratory, Arnold Engineering Development Center, Frank J. Seiler Research Laboratory
9	Wright Laboratory
	<i>High School Apprenticeship Program (HSA[®]) Reports</i>
10	Armstrong Laboratory
11	Phillips Laboratory, Civil Engineering Laboratory
12	Rome Laboratory, Arnold Engineering Development Center
13	Wright Laboratory

1991 FACULTY RESEARCH REPORTS

Wright Laboratory

<u>Report Number</u>	<u>Report Title</u>	<u>Author</u>
<u>VOLUME 5A</u>		
Aero Propulsion & Power Laboratory (PROP)		
1	Influence of Operating Temperature and Quench and Stability of Oxide High-T _c Superconductors	Dr. Mingking Chyu
2	Turbulent Length Scale Measurements in Axisymmetric Sudden Expansion Using LDV	Dr. Richard Gould
3	Electrical Field Effects on Propane/Air Flames	Dr. Harold Harris
4	Investigation of the Combustion Characteristics of Swirled Injectors in a Confined Coannular System with a Sudden Expansion	Dr. Paul Hedman
5	Critical Assessment of Research in Elastohydrodynamic Lubrication	Dr. Michael Khonsari
6	Effects of Riblets on Turbine Blade Heat Transfer and Velocity and Heat Transfer Measurements in a Ribbed Channel	Dr. Paul Maciejewski
7	Electron Density Measurements in Thermionically-Assisted Discharges in Cesium-Argon Plasmas	Dr. Douglas Marcum
8	A Numerical Method for Time-Dependent Incompressible and Compressible Navier-Stokes Flows	Dr. Tien-Mo Shih
9	Experimental and Analytical Investigation of Effects of Noncondensable Gases on On-Axis Rotating Heat Pipes	Dr. Kaveh Tagavi
10	Measurements of Droplet Velocities and Size Distributions in Pressure/Air Blast Atomizer	Dr. Richard Tankin
11	Transient Effects in Glow Discharges Using the GEC Reference Reactor	Dr. Fred Wells
Armament Laboratory (ATL)		
12	Signal Processing for High Speed Video Technology	Dr. Eugene Chenette
13	Light-Gas Gun Firing-Cycle Design for High Velocity and Low Projectile Loading	Dr. Rober Courter
14	Two Dimensional Simulation of Railgun Plasma Arcs	Dr. Manual Huerta
15	Nonlinear Estimation for Exoatmospheric Trajectories: The Daum-Based Filter	Dr. Antonio Magliaro
16	Practical Considerations for a First Cut Multi-Sensor Fusion Seeker	Dr. Charlesworth Martin

<u>Report Number</u>	<u>Report Title</u>	<u>Author</u>
17	Newton's Method Solvers for the Navier-Stokes Equations	Dr. Paul Orkwis
18	Analysis and Design of Nonlinear Missile Autopilots	Dr. Jeff Shamma
19	Qualitative Effects of KKV Impact Locations on Hydraulic RAM in Fuel Tanks at Fifty Percent Ullage (Hydrocode Analysis)	Dr. Steven Trogdon
20	Mounting Techniques for High G Impact Sensors	Dr. Wayne Zimmermann
Avionics Laboratory (AVION)		
21	Multiresolution FLIR Image Analysis	Dr. Raj Acharya
22	Automatic Segmentation of Infrared Images	Dr. Satish Chandra
23	Performance Evaluation of Rule Grouping Algorithm Running on the Activation Framework Architecture	Dr. Ing-Ray Chen
24	A Note on Prony's Method	Dr. David Choate
25	Correlation Dimension of Chaotic Attractors	Dr. Thomas Gearhart
26	Fiber Laser Preamplifier for Laser Radar Detectors	Dr. Richard Miers
27	A Methodology for Employing Modulation Quality Factors in the Analysis of LPI Waveforms	Dr. Glenn Prescott
28	Evaluating the Reusable Ada Avionics Software Packages (RAASP)	Dr. Brian Shelburne
29	Filtering by Similarity	Dr. Thomas Sudkamp
30	Aspects of Pattern Theory	Dr. James Wolper

VOLUME 5B

Electronic Technology Laboratory (ETL)

31	Velocity Distribution in a Degenerately-Doped Submicron-Length Field Effect Transistor	Dr. Vijay Arora
32	Sol-Gel Waveguide Laser Fabrication	Dr. Raymond Zanon

Flight Dynamics Laboratory (FDL)

33	Hypersonic Vehicle Control Strategies: Preliminary Consideration	Dr. Daniel Biezad
34	A Study on Interferometric Tomographic Application of the Aerodynamic Experimental Facilities at Wright Laboratory	Dr. Soyoung Cha

<u>Report Number</u>	<u>Report Title</u>	<u>Author</u>
<i><u>Wright Laboratory (cont.)</u></i>		
35	(Not Used)	
36	Evaluation of the Analytical Design Package (ADP) for Frameless Transparency Program	Dr. Joe Chow
37	A Massively Parallel Algorithm for Large-Scale Nonlinear Computation	Dr. Shurit Dey
38	Decentralized Control of Flexible Structures with Uncertain Interconnections	Dr. George Flowers
39	Computational Prediction of Static and Rolling of an Aircraft Tire on a Rigid Surface as Prelude to Wear Studies	Dr. Manjriker Gunaratne
40	De ply of Laminated Panels with Perforation Due to Impact	Dr. David Hui
41	Monitoring of Damage Accumulation for the Prediction of Fatigue Lifetime of Cord-Rubber Composites	Dr. Byung-Lip Lee
42	In-Flight Structural Combat Damage Detection and Evaluation for Enhanced Survivability of Military Aircraft	Dr. Vernon Matzen
43	A Report on Robust Control Design for Structured Uncertainties	Dr. Jenny Rawson
44	Experimental Investigation of the Influence of Constrained-Layer Damping Treatment on Parametric and Autoparametric Resonances in Nonlinear Structural Systems	Dr. Lawrence Zavodney
Materials Laboratory (MAT)		
45	Semi-Empirical Self-Consistent Calculations of GAAS Surface Restructuring	Dr. Shashikala Das
46	X-ray Crystallographic Studies of Model Systems for Rigid Rod Polymers and Molecules with Potential Nonlinear Optical Properties	Dr. Albert Fratini
47	Computer-Aided Process Planning for Grinding Operations	Dr. Rakesh Govind
48	Transmission Electron Microscopy of Deformation at the Interface of Ti-6-4//SCS6 SiC Fiber Composites	Dr. Warren Moberly
49	Ultrasonic Beam Propagation: Diffractionless Beams and Beams in Anisotropic Media	Dr. Byron Newberry
50	Geometric Reasoning for Process Planning	Dr. Joseph Nurre
51	Synthesis and Characterization of Chiral Mesogens for Use in Cyclic Siloxane Liquid Crystalline Materials	Dr. Steven Pollack

**Report
Number**

Report Title

Author

Wright Laboratory (cont.)

- | | | |
|----|--|-------------------------|
| 52 | Ab Initio Computational and NMR Relaxation Time Investigations of Rotational Barriers and Chain Dynamics in Perfluoropolyalkylethers | Dr. Martin Schwartz |
| 53 | On Photoreflectance Spectra from Two Dimensional Electron Gas in GaAs/AlGaAs Heterojunctions | Dr. Michael Sydor |
| 54 | Creep Behavior of a Fine-Grained $Y_3Al_5O_{12} + YAlO_3$ (18 Vol. %) Material | Dr. Jeffrey Wolfenstine |
| 55 | Elastic Moduli of Fiber Reinforced Brittle Matrix Composites with Interfacial Debonding | Dr. Fuh-Gwo Yuan |

ASPECTS OF PATTERN THEORY

James S. Woiper
Summer Faculty Research Fellow
WL/AART-2
Wright-Patterson AFB, OH 45431

and

Department of Mathematics
Idaho State University
Pocatello, ID 83209

Abstract. *Pattern Theory* (PT) is an attempt to create an engineering theory of algorithm design, analagous to control theory. The basic idea of PT is that binary functions which are "patterned" should decompose nicely. PT uses *Decomposed Function Cardinality* (DFC) of a function as a measure of its patterned-ness. This report details applications of PT to Signal Processing and Theoretical Computer Science, as well as attempts to improve the algorithms for computing DFC.

I. General Introduction

Pattern Theory (PT) is an attempt to create an engineering theory of algorithm design, analagous to control theory. The basic idea of PT is that binary functions which are "patterned" should decompose nicely. PT uses *Decomposed Function Cardinality* (DFC) of a function as a measure of its patterned-ness. Ordinarily, a binary function f of n variables has a 'cost' (ie, cardinality) of 2^n . But, for example, one can sometimes partition the variables into three or more disjoint subsets, eg, $\{x_1, x_2\}$, $\{x_3\}$ and $\{x_4\}$, and find functions F , ϕ , and g such that $f(x_1, x_2, x_3, x_4) = F(\phi(g(x_1, x_2), x_3), x_4)$. When this occurs, the sum of the cardinalities of the component functions may be less than that of f . The minimum of these costs is $DFC(f)$. DFC is related to other measures of complexity such as Kolmogorov complexity (program length) and time complexity.

There were several aspects to this Summer's SFRP effort. The first of these was the application of PT to problems in Signal Processing. An extended abstract detailing the results of this effort was submitted to the upcoming SIAM Symposium on Discrete Algorithms; a slightly modified version of this abstract is the first part of this report.

The second aspect was an attempt to find improved algorithms for computing DFC. Two new methods were tried, and memos were written describing the effectiveness of these methods. These two memos constitute the second and third parts of this report.

The third aspect was a successful attempt to simplify some results in Computational Complexity which were originally derived using the more traditional methods of Turing machines; we obtained these results using PT instead. The memo describing this effort is the fourth part of this report.

The author gratefully acknowledges the support of the T-2 group in this effort.

Function Decomposition as a Noise Filter

I. Introduction

This paper reports on the first uses of DFC in a real-world problem, namely, noise filtering. In this context "noise" means that each bit of the signal is changed with a fixed probability p . There are at least two important instances of this problem. In the first, imagine a binary signal being transmitted along a noisy channel; in the second, imagine a binary image. One needs to perform the usual signal processing functions on these.

II. DFC and noise

We analyze the effect of noise on DFC. The basic philosophy of PT, based on extensive experimental evidence, is that 'real-world' functions tend to be patterned in some way, and hence tend to decompose nicely. Thus, they have low DFC. On the other hand, 'random' functions (ie, noise) tend to be unpatterned and hence do not decompose. We have modelled this by considering the effect of probability p channel noise on a sequence of zeroes. Suppose we have a function of n variables (or, equivalently, a binary string of length 2^n) of which k are '1'. Let $C(k, n)$ denote the expected value of the DFC of such a function.

Empirical Observation.

$$C(k, n) = 2^n(1 - \exp(-12.8k/2^n)).$$

Notice that $C(k, n)$ is virtually 2^n when $k/n \geq 0.15$, ie, a 15% noise rate wipes out most decompositions.

Now, imagine that we have a function f which has been corrupted by a noise process. For convenience, let n be the observed output of the noise process. Then, the received signal is $f + n$. Now, we invoke the following proposition (which is really more of an observation).

Proposition (Asymptotic Semilinearity of DFC). Suppose that f and g are binary functions of n binary variables. Then $\text{DFC}(f + g) \leq \text{DFC}(f) + \text{DFC}(g) + O(1)$.

Proof. The cardinality of adding two binary variables — in this case the outputs of f and g — is 4. Thus, we can trivially decompose $f + g$ into a module for f , one for g , and one for addition, with total cost $\text{DFC}(f) + \text{DFC}(g) + 4$. However, it may be the case that interactions between f and g allow for smaller decompositions (eg, consider the case $f = g$). QED

We conclude that the effect of noise on DFC is roughly additive, ie, the difference between the noisy signal and the pure signal is roughly the DFC of the noise alone, which is predictable.

III. Using DFC as a Filter

We have identified two methods for using DFC as a noise filter. Computer experimentation has just begun on them.

DFC as Energy Function. We propose using DFC as a kind of energy function in a analogy with a Hopfield neural network. One can do noise reduction in a Hopfield network because the energy of a noisy pattern is generally higher than that of a nearby pattern on which the network has been trained. In the operation of the network, each node can asynchronously determine which of its possible states it should be in in order to reduce the global energy. Since the network evolves from its current position to one of lower energy, it probably settles at the correct pattern in the memory.

In our implementation, the network, which is fully interconnected, would be initialized to the noisy pattern. Each node is given a value equal to one of the values of the function in question. At each stage of processing, nodes would asynchronously change their values in order to decrease global DFC. Since DFC of a pattern is lower than DFC of a noisy pattern, the energy surface defined by DFC should have a local minimum at the noise-free pattern. Notice that no training of the network is required.

One possible application of this is in Coding. Codewords from a deterministic Error Correcting Code have a high degree of structure, hence low DFC. Corrupted codewords have higher DFC. If the initial state of the network corresponds to a corrupted codeword, then the network should reach an equilibrium at the nearest correct codeword.

Detecting Areas of Interest. Imagine listening for a weak thin (ie, relatively low bandwidth) signal over a noisy line. In these conditions it is sometimes difficult to determine whether a signal is present. However, under certain circumstances, the DFC of the portion where there is signal may be significantly lower than the DFC of noise alone, because of patterns within the signal.

IV. Conclusions

This abstract has discussed the use of Decomposed Function Decomposition as a theoretical and practical measure of the "pattern-ness" of a signal or function, and suggested several possible approaches to using DFC to solve real-world problems.

VI. Bibliography

- [H] Hopfield, J. J. ,*Proc. National Acad. Sci. USA*, 79 (1982), pp. 2554ff.
- [PT1] Ross, Timothy, M. Noviskey, T. Taylor, D. Gadd, *Pattern Theory: an engineering paradigm for algorithm design*, USAF Wright Laboratory Technical Report WL - TR - 91 - 1060.
- [PT2] Ross et al, submitted to Symposium on Discrete Algorithms.

Combinatorics of Partitions (an unsuccessful search heuristic)

I. Introduction

WL is very interested in improving the time it takes to compute Decomposed Function Cardinality (DFC). (The reference for this concept is WL Tech Report 91-1060.) This report details an unsuccessful attempt to apply results from the combinatorics of partitions to the problem. It is written with the hope that those who read it will not duplicate either our efforts or our mistakes.

II. Computing DFC

This section outlines, without much detail, the algorithm for finding a good decomposition of a function f . Let f be a function of n variables x_1, x_2, \dots, x_n . For each partition of n into two subsets of size (say) m and $n - m$, there is a partition matrix and a column multiplicity ν . Suppose that the partition is into $C = \{x_{i_1}, \dots, x_{i_m}\}$ and $R = \{x_{j_1}, \dots, x_{j_{n-m}}\}$, where C indicates the column variables and R indicates the row variables. The matrix has one row for each possible value of the row variables (ie, there are 2^{n-m} rows) and one column for each possible value of the column variables (so there are 2^m columns); the matrix entry is the value of the function when the variables have the corresponding values.

The idea is to choose the partition so that the column multiplicity ν is as small as possible. This indicates that the function can be simplified. (See the Tech Report for more details.)

III. Combinatorics of Partitions

For a fixed m , the partitions of n into two subsets of size m and $n - m$ are parametrized by the words formed from the alphabet $\{a, b\}$ which have m occurrences of the letter a and $n - m$ of b . Thus, for example, when $n = 5$ and $m = 3$ the possible words are $aaabb$, $aabab$, $abaab$, $baaab$, $aabba$, $ababa$, $baaba$, $babaa$, $bbaaa$, and $abbaa$. The positions of the 'a's indicates the column variables.

There is a partial order on the set of these words, and hence on the set of partitions of this size, defined as follows: the basic relation is that $w_1 b a w_2 > w_1 a b w_2$, where w_1 and w_2 are arbitrary subwords. The relation is completed by demanding that it be transitive, ie, if $w_1 > w_2$ and $w_2 > w_3$ then $w_1 > w_3$. The largest word is $bb \dots b a a \dots a$, and the smallest is $a a \dots a b b \dots b$.

The partially ordered set so defined (some people call these "posets") can be arranged on a graph. The largest element is at the top, there is one node for each word, and two words w_1 and w_2 are linked if the basic relation $w_1 > w_2$ is satisfied.

When these words are interpreted as partitions, the basic relation corresponds to exchanging a column variable and a row variable. This corresponds to moving through one link along the surface of the graph.

IV. Relations with Column Decomposition

The graph defined in III can be labelled as follows: on each node, label the graph with the value of ν for the corresponding partition matrix. It was hoped that ν would behave well as one moves along the graph. If this were the case, then one could start with an arbitrary partition and move towards better partitions by moving toward lower ν values.

But this is not the case. Here is the key result:

PROPOSITION. A basic move changes a partition matrix with column multiplicity ν to one with column multiplicity less than $4\nu^2$; this bound is sharp.

The following Lemma is useful in the proof of the above.

LEMMA. ν is invariant under permutations of the order of either the row or the column variables.

PROOF OF LEMMA. Permutation of the row variables applies the same permutation to the elements of each column. If two columns are equal before applying this permutation, they will remain so; and, if they are unequal before, they remain unequal.

Permutation of the column variables moves whole columns around in the table, so no change of multiplicity can occur. QED

PROOF OF PROPOSITION. By the Lemma, we can re-arrange the row and column variables (if necessary) so that the first row variable is being exchanged with the last column variable. The original partition matrix then has the following form, where each A_i , B_i is a semi-column, ie, column vector of length 2^{m-1} :

$$\begin{array}{cccc} A_1 & A_2 & \dots & A_{2^{n-m}} \\ B_1 & B_2 & \dots & B_{2^{n-m}} \end{array}$$

After the permutation of the indicated variables, the partition matrix has the following form:

$$\begin{array}{cccccc} A_1 & A_3 & \dots & A_{2^{n-m}-1} & B_1 & B_3 & \dots & B_{2^{n-m}-1} \\ A_2 & A_4 & \dots & A_{2^{n-m}} & B_2 & B_4 & \dots & B_{2^{n-m}} \end{array}$$

There are ν distinct A_i and ν distinct B_i , corresponding to the distinct columns in the original matrix. In the transformed matrix, the 2ν possible semi-columns may be placed virtually anywhere, depending on their locations in the original matrix. Since the columns of the new matrix are made up of two semi-columns from the original, there are $2\nu \cdot 2\nu$ or $4\nu^2$ possible columns in the transform.

It is easy to construct examples in which this bound occurs. QED

V. Conclusion

This memo has discussed the changes in the column multiplicity ν as one moves along the graph defined by partitions of the row and column variables into two subsets of size m and $n - m$. Since the value of ν can change dramatically with a single move, this cannot lead to an effective strategy for searching for partitions with minimal ν .

Discrete Fourier Transform as a Function Decomposition Search Heuristic

I. Introduction

[see Introduction to the memo above.]

II. Computing DFC

[See "An unsuccessful search heuristic", PT Task Order Report of 15-July- 1991.]

III. Fourier Transforms

The Fourier Transform is a well-known and widely-used tool in many areas of Mathematics, Science, and Engineering. Here is a brief description of the Discrete Fourier Transform [DFT]. Suppose that $f(i)$, $i = 0, \dots, n-1$ is some function of interest. Then its DFT is

$$\hat{f}(j) = \sum_{k=0}^{n-1} f(k) \exp(-ij\Omega k)$$

where $\Omega = 2\pi/n$ and $i^2 = -1$.

The DFT is useful for detecting periodic components of f because of the periodic nature of the complex exponential function. In particular, if f has period p then \hat{f} will have "spikes" at $\pm n\Omega/p$ (as well as at other places corresponding to "harmonics").

IV. DFC and periodicity

Let f be a binary function of n variables, and let $N = 2^n$. Think of f as function of integers i by taking binary equivalents. That is, if f is a function of (say) 3 binary variables x_1 , x_2 , and x_3 , consider the function \tilde{f} given by $\tilde{f}(i) = f(a_2, a_1, a_0)$, where $i = \sum a_i 2^i$ is the binary equivalent of i . Thus, for example, $\tilde{f}(3) = f(0, 1, 1)$ and $\tilde{f}(7) = f(1, 1, 1)$. Since f and \tilde{f} are uniquely paired, we do not make any distinction between them in what follows.

A function which decomposes well will naturally have some periodicity when expressed in this way. For example, imagine the function of 4 variables given by the table below, where the column variables are x_2 and x_4 .

	00	01	10	11
00	1	1	0	1
01	0	0	0	0
10	1	0	1	1
11	1	1	1	1

Columns 1 and 4 are the same, so for all x_1 and x_3 , $f(x_1, 0, x_3, 0) = f(x_1, 1, x_3, 1)$, ie, $f(8x_1 + 2x_3 + 4 + 1) = f(8x_1 + 2x_3)$. Thus one can expect that the DFT of f has indications of a period of 5 (even though f is not actually periodic).

V. So why doesn't it work?

The basic idea of this effort was to look at all of the local maxima of \hat{f} and use those to determine likely partitions for good decomposition. One imagines that \hat{f} might have lots of local maxima, but the number would be less than the number of partitions. This number depends only on the partition (not the function). Experimental procedure was to decompose all of the "benchmark" functions and compare with their DFTs. (These computations were made but the comparison was not done.)

FACT. Finding a given periodicity does not identify a unique partition of the variables.

Thus, in the example above, one can find other partitions for which the column differences are also 5. Here is what happens in the case of $n = 4$.

partition	column number decimal equivalents							
12, 34	0	4	8	12				
13, 24	0	2	8	10				
14, 23	0	1	8	9				
23, 14	0	2	4	6				
24, 13	0	1	4	5				
34, 12	0	1	2	3				
123, 4	0	2	4	6	8	10	12	14
124, 3	0	1	4	5	8	9	12	13
134, 2	0	1	2	3	8	9	10	11
234, 1	0	1	2	3	4	5	6	7

For example, the period '5' can occur for at least four of the partitions. In the case when the column variables are $\{2, 4\}$ it occurs if columns 1 (decimal equivalent 0) and 4 (decimal equivalent 5) are equal. For column variables $\{1, 2, 4\}$, it occurs if either column 1 equals column 4 or column 2 equals column 5 or column 5 equals column 8. If the column variables are $\{1, 3, 4\}$ then 5 occurs if column 4 equals column 5. When the column variables are $\{2, 3, 4\}$ then it occurs if column 1 equals column 6, column 2 equals column 7, or column 3 equals column 8.

Worse, suppose that you could determine 2 periodicities, say 2 and 6. This combination occurs for 3 possible partitions.

One possibility would be to try to locate the periodicity (this might be possible using a wavelet transform). However, this will also fail. There are too many partitions for which the same periodicity occurs at the same location. For example, columns with decimal equivalents of 2 and 8 occur for three partitions of 4 variables. If the corresponding columns are equal for some partition, then there is a periodicity of 6. Knowing that it "starts" at 2 doesn't help determine the partition.

There are other difficulties. For example, the "periodic-ness" due to two columns which almost match is almost the same as that of two columns which match perfectly; thus, this method would pick out lots of irrelevant partitions. Finally, it is not clear how to implement it for partial functions.

VI. Conclusion

This memo has discussed the possible application of certain transform techniques to the problem of determining function decompositions. These included the Fourier and wavelet transforms. While it was determined that these techniques were unlikely to be helpful, this is a positive result. The effort was part of a general plan to thoroughly explore the practical and theoretical aspects of Pattern Theory, and we have acquired more insight into the properties of partitions of the variables of binary functions.

Symmetry and Complexity of Languages: Pattern Theory as a Theoretical Tool

I. Introduction

PT provides new insights into various aspects of computing. In this note we apply PT to a theoretical problem in computational complexity, and rederive some results of Clote and Kranakis from the 1989 ACM Conference on Structure in Complexity Theory.

II. Statement of the Problem

Clote and Kranakis (henceforth [CK]) in their paper "Boolean functions, invariance groups, and parallel complexity" consider the relationship between symmetry and complexity.

DEFINITION. Let f be a boolean function on the n variables x_1, \dots, x_n . The Symmetry Group of f consists of those permutations σ of $\{1, \dots, n\}$ such that for all x_1, \dots, x_n one has $f(x_{\sigma(1)}, x_{\sigma(2)}, \dots, x_{\sigma(n)}) = f(x_1, \dots, x_n)$.

[CK]'s results have two aspects. In the first (which does not concern us here) they have a given symmetry group G and desire a function f with G as symmetry group. In the second, they are given a family of functions and some information about the symmetry groups of these functions; they then derive results about the circuit complexity of the functions.

They use two standard measures of complexity. A circuit is non-uniform NC^k if it has a polynomial number of elements and maximum depth $O(\log n)^k$. (Circuits are made of and, or and not gates.) A circuit is non-uniform NC if it is NC^k for some positive integer k .

The functions of interest are language acceptors. Thus $L \subset \{0, 1\}^*$ is some language, and f_n as the characteristic function for strings of length n from L , ie, f has value 1 if and only if its input is a possible string from L . Define $S_n(L)$ to be the symmetry group of f_n .

Here are some notions from group theory which are useful in this context. The Symmetric group Σ_n consists of all permutations of $\{1, \dots, n\}$ with composition as group operation. It has $n!$ elements. The Alternating Group A_n is the subgroup consisting of so-called even permutations, ie, those which can be written as a product of an even number of transpositions; it has size $n!/2$. If H is a subgroup of G then the order of H divides the order of G (Lagrange's Theorem); this quotient is denoted $[G : H]$, and is sometimes called the index of H in G . Thus, for example, $[\Sigma_n : A_n] = 2$.

The result from [CK] which we would like to prove using PT is:

THEOREM 2.1. Let L be a language such that there exists a polynomial $p(n)$ such that, for all $n > 0$, $[\Sigma_n : S_n(L)] \leq p(n)$. Then L can be realized by a non-uniform NC^1 circuit.

III. Group Theory and Complexity

The results in [CK] depend very heavily on the following deep lemmas from Group Theory. Their use cannot be avoided by the application of PT.

LEMMA 3.1 (O'Nan-Scott). Every subgroup of Σ_n not containing A_n is a member of one of five well-defined families of subgroups.

COROLLARY 3.2 ([CK], p. 64). Suppose that G_n is a family of permutation groups such that there exists k such that $[\Sigma_n : G_n] \leq n^k$. Then there exists an integer N such that for all $n > N$ there exists $i_n \leq k$ for which $G_n = U_n \times V_n$, where U_n and V_n are groups with disjoint support and, further, $U_n \subset \Sigma_{i_n}$ and $V_n \subset \Sigma_{n-i_n}$.

LEMMA 3.3 ([CK], p. 58). A_n cannot be the symmetry group of a boolean function.

There is also one deep theorem of complexity theory which we cannot avoid using yet.

LEMMA 3.4 (Babai, Luks, Seress). Let $G \subset \Sigma_n$ be a permutation group and suppose $\sigma \in \Sigma_n$. Then there exists an NC^1 circuit which determines if $\sigma \in G$.

NOTE. In this theorem G is specified by a set of generators.

IV. Results from PT

The following PT result, which relates DFC to circuit complexity, is useful in the sequel.

LEMMA 4.1 (Theorem 4.14 of PT-1 Report). Let $C(f)$ be the circuit complexity of f relative to the basis $\{AND, OR, NOT\}$. Then $DFC(f) \leq C(f) \leq nDFC(f)$.

V. The Key Lemma

[CK] use the following lemma, which they attribute to Buss.

LEMMA 5.1. Let $E_k(w)$ be the predicate "the binary word w has exactly k ones". Then $E_k(w)$ is NC^1 .

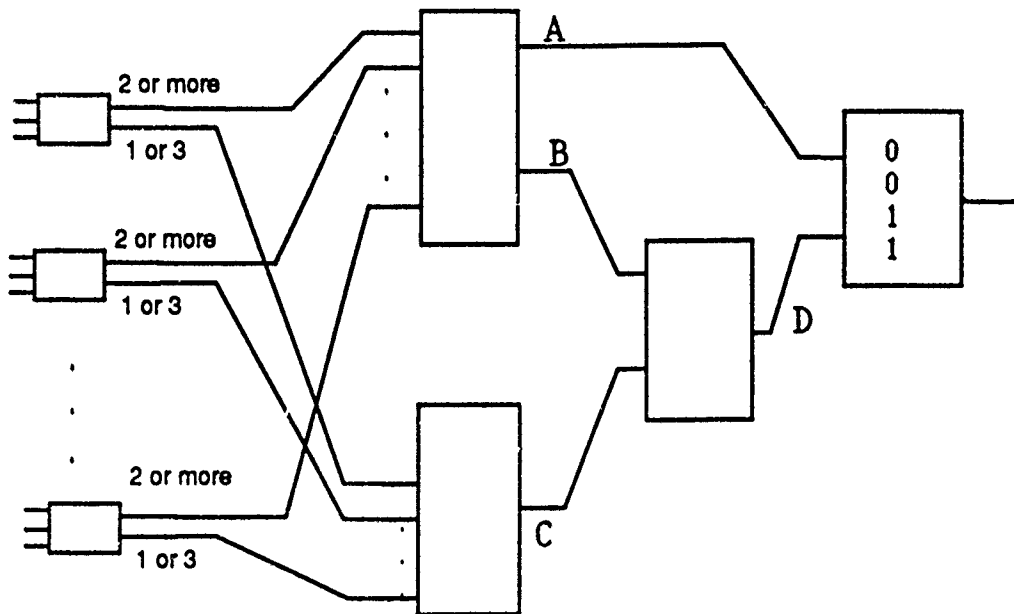
Buss's proof of this seems rather difficult and abstract (in particular, it uses Turing machines). We will prove it using PT.

First, notice that the Lemma reduces to the following:

LEMMA 5.2. Majority gate is NC^1 .

PROOF THAT 5.2 IMPLIES 5.1. First, notice that we can calculate E_k using the predicates $ATLEAST_k$ and $ATLEAST_{k+1}$: if the former is true and the latter is false, then E_k is true. Thus, we are reduced to showing that $ATLEAST$ is NC^1 . Now, imagine r bits of ones in parallel with the n bits of w . Let $w11\dots1$ denote the concatenation of w with r ones. If $r > n - 2k$ and $MAJGATE(w11\dots1)$ is true, then w had at least k ones. QED.

PROOF OF 5.2. This proof is by induction. Consider the following function decomposition:



The leftmost functions of 3 variables have two outputs: "at least 2 ones" and "1 or 3 ones". There are $O(n/3)$ of these, each with cardinality 16. If $n/4$ "at least 2 ones" are true, then *MAJGATE* is true; this is *A* above. *B* is true when at least $n/6$ "at least 2 ones" are true. *C* is true if at least $n/6$ "1 or 3 ones" is true. *D* is *B* and *C*; its negation is not *B* or not *C*. If not *B*, then fewer than $n/6$ of the 3 variable packets have "2 or more ones", which means that it is impossible to have " $n/2$ or more ones". If not *C*, then fewer than $n/6$ of the 3 variable packets have "1 or 3 ones"; this implies that there are fewer than $n/2$ ones.

By the induction assumption, the component functions have polynomial complexity, so the aggregate has polynomial complexity. Further, let $D(n)$ be the depth for n variables. Then evidently $D(n) = D(n/3) + 2$; by induction, this equals $D(n/3^2) + 4$, etc; thus, $D(n) = D(n/3^r) + 2r$. Eventually this leads to $D(n) = O(\log_3(n))$. QED

Overall Conclusions and Recommendations

The work detailed in this report confirms that Pattern Theory shows great promise as a tool in Signal Processing, Computer Science, and Mathematics (another effort over the summer used Pattern Theory to identify chaotic behavior in iterated functions). It is a subject which should be vigorously pursued.

One of the major limitations in the use of PT now is the time it takes to compute DFC, and there are several efforts underway to improve this. One recommendation is that the use of parallel algorithms should be investigated; so far there has been little work done in this direction, mostly due to hardware access difficulties. Another recommendation is that asymptotic results, like those in the fourth section of this report, should be obtained. These results may lead to procedures for effectively estimating DFC or, at least, to aids in branch-and-bound style search algorithms. Finally, the relationship between DFC and symmetry should be explored more carefully. The fourth section of this report indicates some possible lines of investigation. It is interesting to note that functions with non-trivial symmetry groups need not have low DFC, ie, a little symmetry need not make a function simple.

VELOCITY DISTRIBUTION IN A DEGENERATELY-DOPED SUBMICRON-LENGTH FIELD EFFECT TRANSISTOR

Final Report

by

**Vijay K. Arora
Professor of Electrical Engineering
Wilkes University, Wilkes-Barre, PA 18766**

on

**Research Completed at Research Division,
Solid State Electronics Directorate, Wright Laboratory,
Wright-Patterson Air Force Base, Ohio 45433-6543
(Focal Point: Dr. Chern Huang)**

Dates: April 29, 1991- July 5, 1991

under

**1991 Summer Research Program for Faculty and Graduate
Students of the Air Force Office of Scientific Research**

conducted by

**Research and Development Laboratories, 5800 Uplander Way,
Culver City, CA 90230-6608**

Abstract

Quantum-well microstructures for the design of submicron-length field effect transistors are investigated. As the electric field in the channel can become very high, an understanding of the velocity-limiting mechanism, a primary motivation behind this project, is achieved. It is shown that there is a poor correlation between the saturation velocity and the ohmic mobility. For nondegenerate semiconductors, the saturation velocity is limited by the appropriate average of the random thermal velocity. For degenerately-doped semiconductors, especially at low temperatures, the saturation velocity is found to be limited by the Fermi velocity which arises due to transfer of electrons from the parallel to the antiparallel direction of the electric field. The emission of an optical phonon was included by defining an inelastic scattering length at which point the energy absorbed by an electron equals the energy of an optical phonon. In order to study the validity of the theoretical ideas proposed, a comparison with the experimental data on bulk Si and GaAs quantum well was made, and excellent agreement obtained. The room-temperature velocity-field profiles obtained are used to evaluate the electric-field distribution, the velocity distribution, and carrier distribution in the channel of an 0.25- μm High Electron Mobility Transistors (HEMT). The long-channel limit of the theoretical results indicates that the *pinchoff* behavior is absent when velocity saturation is considered even in the long-channel FET's. These results have advanced our thinking of the mechanism behind velocity saturation and will have an impact on the design of transistors with material structures of various dimensionalities. In the concluding section, the possible applications of these ideas in designing new experiments are suggested. Two papers, one each on 2-D and 1-D quantum wells, based on this report are in the process of preparation. An oral presentation of this report was given at WPAFB on 24 June, 1991.

1. INTRODUCTION

The advances in the crystal growth, device concepts, and fabrication of electronic and optical devices in GaAs and other III- V semiconductors have inspired the scientists in several laboratories around the world to work on combining both types of devices to create a new, powerful class of high speed optoelectronic integrated circuits for optical communications and many other high speed applications like digital optical computers. For example, at Research Division of the Solid State Electronics Directorate of Wright-Patterson Air Force Base (WPAFB), interest in these devices exists in order to develop Microwave Monolithic Integrated Circuits (MMIC's). Several structures in 0.25- μm HEMT project are being evaluated.

GaAs has a direct band gap necessary for microwave sources. In addition, it has better electron transport properties than the industry's device vehicle, Si. Electrons in GaAs are about five times more mobile than in Si. GaAs is also available in semi-insulating form and, when used as a substrate, substantially reduces the parasitic capacitances. GaAs combined with lattice-matched alloy AlGaAs, has lead to the fabrication of very efficient lasers and many unique heterojunction devices which are not possible in Si. These include modulation-doped field effect transistors (MODFETs), metal-semiconductor field effect transistors (MESFETs), heterojunction bipolar transistors (HBTs), resonant tunneling devices (RTDs) and several variations of hot electron transistors (HETs) and High Electron Mobility Transistors (HEMTs). This new range of laterally patterned nanometer scale devices which are based on MODFET geometries provides many challenges to quantum transport theory. In such devices the quasi-two-dimensional (QTD) electron gas set up in a MODFET is reconfigured by surface patterning of the gate region to produce a variety of structures in the varying low dimensionality and coherence. With the ever increasing need for high-speed device applications, researchers at WPAFB are looking for breakthroughs on the conventional design of transistors.

One of the essential factors in the operational design of these microwave devices is the proper understanding of the relationship between velocity and electric field in the channel. A typical velocity-field (v - E) relationship for Γ -valley of the GaAs is shown in Figure 1. At lower electric fields, the relationship is linear. But, at high electric field, the velocity becomes saturated at 4.2×10^7 cm/s (as shown by flat dashed line).

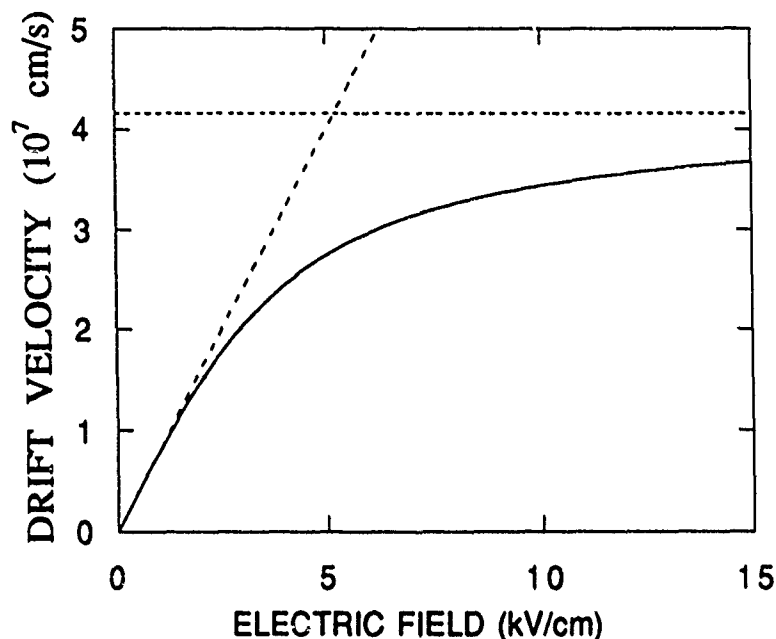


Figure 1. Room temperature velocity-field characteristics of the Γ -valley of nondegenerate bulk GaAs (after V. Arora, D. Mui, and H. Morkoc, IEEE Trans on Electron Devices, ED-34, 1231(1987)).

The primary motivation behind this study is to understand fully the v - E characteristics and the role these characteristics play in modelling of submicron channels of FET's. Recent developments in VLSI and VHSIC programs have indicated an ever-increasing importance of high-field effects which limit the velocity of carriers and hence impose an intrinsic limit on device speed. There have been numerous attempts to identify the mechanism responsible for this saturation of the carrier velocity in high electric field (See Ref. 1 for a review). Often a high mobility is cited in the published literature to give higher saturation velocity. But, recent experiments tend to indicate a poor correlation between saturation velocity and mobility.^{2,3} This absence of correlation was predicted, several years ago, in scaling theory arguments of Thornber.⁴ Saturation velocity was found to be invariant under scaling of the magnitude of scattering rates which alters mobility, while mobility was found to be invariant under scaling of the magnitude of momentum which alters saturation velocity, consistent with the predictions of Arora.¹

2. DISTRIBUTION FUNCTION

The understanding of the distribution function is essential in any carrier transport study. The equilibrium distribution function is well known to be the Fermi-Dirac distribution function. In equilibrium, the bands are flat unless there is a built-in electric field. The electrons are moving at random with the average velocity in each of the three cartesian directions equal to zero.

In low electric field \mathcal{E} , collisions can be considered point collisions as the energy $|q| \mathcal{E} \lambda_D$ (field broadening) absorbed by a carrier of charge q ($q = \pm e$ for holes(electrons)) in the de Broglie wavelength λ_D is negligible compared to collision broadening. But, as the electric field becomes larger, the field broadening tends to mask the collision broadening, and hence makes carrier transport virtually independent of scattering. The onset of nonlinear behavior thus takes place when field broadening is comparable to the collision broadening. This condition is equivalent to the condition that the momentum gained by the carrier from the field $e \mathcal{E} \tau$ in the mean free time τ is comparable to its thermal momentum $m^* v$. In terms of energy, this condition is equivalent to the condition that the energy gained by an electron in a mean free path $e \mathcal{E} \ell$ is comparable to the thermal energy $k_B T$. This condition was originally considered by Shockley,⁵ but was discarded in favor of the energy balance theories which dominated the high-field arena in those days.

Recently, due to the availability of supercomputers, Monte Carlo simulations of carrier trajectory have become very popular. In a simulation, the carrier is subjected to the classical laws of motion followed by a scattering event generated by a set of random numbers. The use of complicated energy-balance equations, which are generally difficult to solve for all possible scattering interactions thus can be avoided. Instead at each scattering event, the electron is allowed to keep a portion of energy gained from the field which accumulates as collisions proceed and could be emitted in the form of an optical phonon in an inelastic scattering. If this emission is disregarded, the accumulated energy can become very high, necessitating the use of high-energy scattering times, which are central to any successful simulation. The high collision broadening present in these

simulations can easily mask the semiclassical behavior of a carrier, as pointed out by Capasso et al.⁶ Dresden⁷ has reviewed assumptions, implicit and explicit, which are to be satisfied in treating electron as a classical particle. One such assumption is that the collision broadening \hbar/τ is much smaller than the thermal energy $k_B T$ ($\hbar/\tau \ll k_B T$), which is easily satisfied in low-field transport of carriers. But, if high collision broadening is present, this condition can be easily violated. In spite of these conceptual difficulties, the understanding of the physical mechanism responsible for velocity saturation and its interdependence on the ohmic mobility is missing in simulation experiments. As the mean free time τ is inversely proportional to the velocity v of a carrier for deformation potential scattering, a dominant mechanism in simulation experiments, a description of the carrier transport in terms of a constant mean free path $\ell = v \tau$ appears more appropriate.

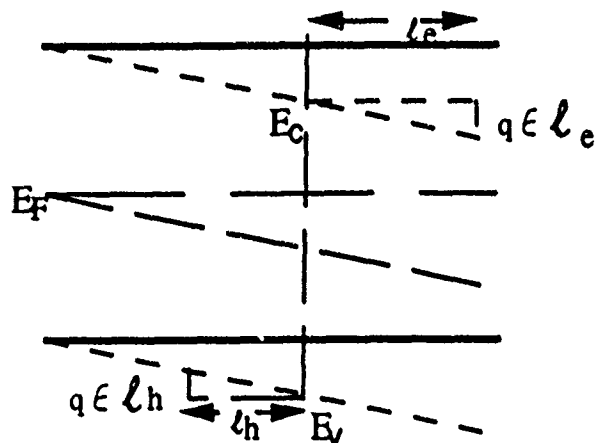


Figure 2. Energy band diagram of an intrinsic semiconductor in an electric field applied in the direction from right to left.

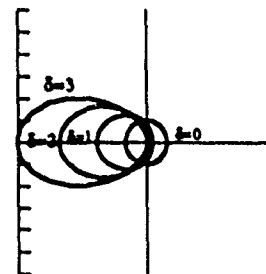


Figure 3. Polar Plot of the normalized distribution function $f(\epsilon, \epsilon, \theta) / f(\epsilon, 0, \theta)$ for holes. The electron distribution is the mirror image about the vertical axis.

In external fields, the Fermi energy (electrochemical potential) and bands are tilted parallel to each other⁸, as shown in Figure 2. An excellent description of the carrier transport with tilted band diagram is given by Böer,⁸ who examines the effect of built-in as well as the applied electric field on the distribution of carriers. The carrier distribution is determined

relative to the Fermi level. In zero bias, the distribution is independent of position and the Fermi level (chemical potential) is constant. In an external field, however, Fermi level and bands are tilted. The carrier distribution is now a function of spatial coordinates. When electrons are accelerated in the field, they move from a region of higher density $n(\epsilon - \zeta)$ to that of lower density $n(\epsilon - (\zeta \pm e \mathcal{E} \ell))$. These electrons can dissipate their net additional energy to the lattice by emitting phonons, thereby causing lattice heating. The carriers drop close to the conduction band edge and the motion is repeated. From intuitive arguments, as suggested by Böer,⁸ a limiting velocity comparable to the random thermal velocity at lattice temperature is expected. The carrier motion in an external field is, therefore, not random. It has a finite component in the field direction. This makes distribution of carriers asymmetric in the direction of applied electric field. The electrons will roll down the energy hill and holes will bubble up the energy hill. The electric field thus tries to organize the otherwise completely random motion. Understandably, the Fermi level will be affected by the applied electric field.

The distribution function for electrons rolling on a tilted band diagram, following the proposal of Zukotynski and Howlett,⁹ is obtained as follows:

$$f(\epsilon_k, \mathcal{E}, \theta) = \frac{1}{e^{(\epsilon_k - \zeta + e \mathcal{E} \cdot \ell(\epsilon_k))/k_B T} + 1} \quad (2.1)$$

For holes e in Equation (2.1) should be replaced by $-e$. $\ell(\epsilon_k) = \tau v$ is the energy-dependent mean free path. This distribution function thus has a very simple interpretation. The electrochemical potential ζ during the free flight of carriers changes by $\pm e \mathcal{E} \cdot \ell$ as electrons tend to sink and holes tend to float on the tilted energy band diagram. This observation may suggest that the applied electric field tends to organize the otherwise completely random motion. Electric dipoles $e \ell$ due to quasi-free motion of the carriers tend to organize in the direction of electric field for holes and in the opposite direction for electrons. The high-field effects thus become important when the dipole energy $e \mathcal{E} \cdot \ell$ is comparable to the thermal energy for nondegenerate electrons or the Fermi energy for degenerate electrons. The collisions tend to bring the electron closer to the conduction band edge. If the electric field is strong, this unidirectional motion will give carrier drift comparable to the thermal velocity which is average of

the magnitude of electron velocity v . A quasi-ballistic behavior of the carriers thus follows in strong electric field.

3. BULK CARRIER TRANSPORT

In order to show the validity of the ideas proposed in the previous section, we apply the distribution function to calculate the velocity-field characteristics for Silicon which has been extensively studied experimentally. As said earlier, for deformation potential scattering in bulk samples, a dominant scattering mechanism in silicon, the collision time is inversely proportional to the velocity of the carriers. Therefore, ℓ is constant. In this description, even if the scattering rates increase with the carrier velocity, the mean free path is essentially constant. This is the distinct advantage of using the mean free path over mean free time. The distribution function so obtained is strongly protruded in the direction of electric field and is central to the understanding of velocity-field characteristics. In the non-degenerate approximation (carrier concentration $n \ll \lambda_D^{-3}$, where $\lambda_D = h/(2m^*k_B T)^{1/2}$ is the thermal de Broglie wavelength of the electron), the distribution function can be written as

$$f(\epsilon_k, \ell, \theta) = e^{-(\epsilon_k - \delta)/k_B T} \cdot \delta \cos(\theta) \quad (3.1)$$

with

$$\delta = \frac{e \mathcal{E} \ell}{k_B T} \quad (3.2)$$

In Equation (3.1), we assume that the electric field is along the z -axis. A polar plot of $f(\epsilon_k, \ell, \theta)/f(\epsilon_k, 0, \theta)$ for electrons is shown in Figure 3. When $\delta \ll 1$, the distribution function is spherically symmetric. When $\delta > 1$, however, the distribution function deviates considerably from this spherical character and protrudes in the direction opposite to that of the applied electric field.

For a bulk parabolic semiconductor, the energy as a function of the momentum $\hbar k$ is given by

$$\epsilon_k = \frac{\hbar^2 (k_x^2 + k_y^2 + k_z^2)}{2m^*} \quad (3.3)$$

The drift velocity is obtained from the relationship

$$v_d = \frac{\sum_{k,d} f(\epsilon_k) (\hbar k / m^*)}{\sum_{k,d} f(\epsilon_k)} \quad (3.4)$$

Here d stands for spin. Converting \sum_k to integration using the factor $\Omega / (2\pi)^3$ (where Ω is the volume of the crystal), the drift velocity in response to an electric field applied in the polar z -direction is obtained as

$$v_d = \frac{2}{\sqrt{\pi}} v_{th} \frac{\int_0^\pi \sin(2\theta) \mathcal{F}_1(H(\theta)) d\theta}{\int_0^\pi \sin(\theta) \mathcal{F}_{1/2}(H(\theta)) d\theta} \quad (3.5)$$

where

$$\mathcal{F}_j(\eta) = \frac{1}{\Gamma(j+1)} \int_0^\infty \frac{x^j}{e^{(x-\eta)} + 1} dx \quad (3.6)$$

is the Fermi-dirac integral. $H(\theta)$, the quasi Fermi level of carrier, is defined as

$$H(\theta) = \eta - \delta \cos(\theta) = \frac{\zeta}{k_B T} - \delta \cos(\theta) \quad (3.7)$$

and

$$v_{th} = (2k_B T / m^*)^{1/2} \quad (3.8)$$

The normalized Fermi energy (electrochemical potential) η is obtained from carrier conservation by numerically solving the normalization equation

$$n_v = (\sqrt{\pi} / \lambda_D)^3 \int_0^\pi \sin(\theta) \mathcal{F}_{1/2}(H(\theta)) d\theta \quad (3.9)$$

where n_v is the carrier concentration per unit volume. Carriers in silicon are nondegenerate if carrier concentration is $0.1N_{c(v)}$, where $N_{c(v)}$ is the effective density of states for electrons(holes). At room temperature, $N_c = 2.86 \times 10^{19} \text{ cm}^{-3}$ and $N_v = 3.10 \times 10^{19} \text{ cm}^{-3}$, as recently evaluated by Green¹¹. Thus, nondegenerate approximation can easily be applied for carrier concentrations less than 10^{18} cm^{-3} . In the nondegenerate limit, Equation (3.5) can be considerably simplified, and the drift velocity is given by

$$v_d = \frac{2}{\sqrt{\pi}} v_{th} L(\delta) \quad (3.10)$$

where

$$L(\delta) = \coth(\delta) - 1/\delta \quad (3.11)$$

Thus if carrier mean free path is known, velocity-field characteristics can be obtained from Equation (3.10). The carrier mean free path can easily be obtained from ohmic mobility for which reliable experimental data is available. The electrochemical potential ζ , in nondegenerate approximation, does not play an active role in the expression of drift velocity. However, for degenerate case, the drift velocity depends on carrier concentration through ζ . Expanding Eq. (3.8) for low electric field and writing $v_d = \mu \epsilon$, the mobility expression is obtained as

$$\mu_{e(h)} = 4 e \ell_{e(h)} / 3 (2 \pi m^* k_B T)^{1/2}. \quad (3.12)$$

$\mu_{e(h)}$, the mobility of electrons(holes), a function of impurity concentration N , is given by the empirical relation in References 9,10.

With the values of $\ell_{e(h)}$ obtained from Equations. (3.12), the velocity-field characteristics of electrons and holes, as obtained from Equation (3.10) are shown by solid lines in Figures 4 and 5. The dashed lines show the experimentally observed velocity-field characteristics which are well-represented by the equation, originally suggested by Scharfetter and Gummel.⁹

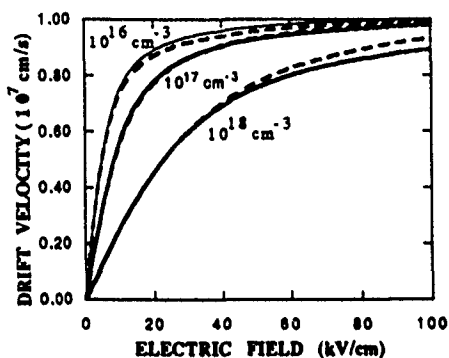


Figure 4. Velocity-field characteristics of electrons in silicon. The number on each curve is the impurity concentration in the sample.

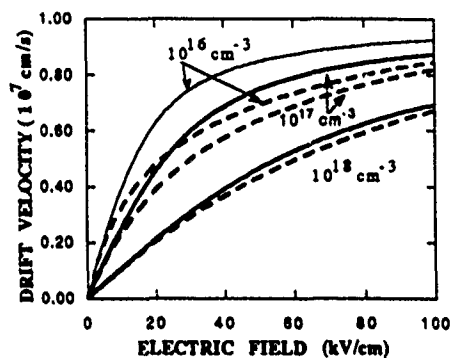


Figure 5. Velocity-field characteristics of holes in silicon. The number on each curve is the impurity concentration in the sample.

The agreement with the experimental data is as good as is possible within the experimental uncertainty, the scatter of data taken by different experimental techniques, and assumption of a parabolic model. Even though the ohmic mobilities are different for various impurity concentrations, the saturation velocity tends to a common value, although the approach towards saturation is much faster for high mobility materials. Because of the low ohmic mobility of holes, the approach towards saturation is much slower. The experimental hole mobility is lower than the theoretical mobility which considers hole bands to be parabolic with a single effective mass. At high electric fields, electron may transfer to split-off band which may give lower theoretical velocity and hence explain the discrepancy. As transport properties of this split-off band are not known, this inclusion is excluded in the present analysis. Room-temperature saturation values of 1.03×10^7 cm/s (electrons) and 1.00×10^7 cm/s (holes) are obtained. This indicates that high mobility does not necessarily lead to high saturation velocity. Only at moderate electric fields, the velocity of a high-mobility materials is higher than that of a low-mobility material. Experimental data on quantum-well heterostructures also support this observation. The mobility in quantum well heterostructure is much higher than that of bulk materials, but saturation velocity is lower¹⁴. Velocity measurements on a variety of samples lead to the same saturation velocity at a given temperature^{2,3}.

4. QTD Quantum Wells

For a quasi-two dimensional (QTD) quantum well, the energy is given by

$$\epsilon_{n,k_x,k_y} = n^2 \epsilon_0 + \frac{\hbar^2}{2m^*} (k_x^2 + k_y^2) \quad n=1,2,3,\dots \quad (4.1)$$

The drift velocity is calculated from Eq. (3.4) with k replaced by n, k_x, k_y , and we obtain (in the quantum limit)

$$v_d = \frac{\sqrt{\pi}}{2} v_{th} \frac{\int_0^{2\pi} \cos(\theta) \mathcal{F}_{1/2}(H(\theta)) d\theta}{\int_0^{2\pi} \ln(1+e^{H(\theta)}) d\theta} \quad (4.2)$$

where

$$H(\theta) = \eta - \delta \cos(\theta) \quad (4.3)$$

and η is now given by

$$\eta = \frac{\zeta - \epsilon_0}{k_B T} \quad (4.4)$$

η is now evaluated from the normalization condition

$$n = \lambda_D^{-2} \int_0^{2\pi} \ln(1+e^{H(\theta)}) d\theta \quad (4.5)$$

In the nondegenerate limit, Equation (4.2) simplifies to

$$v_d = \frac{\sqrt{\pi}}{2} v_{th} \frac{I_1(\delta)}{I_0(\delta)} \quad (4.6)$$

where $I_n(\delta)$ is the modified Bessel function of order n . Taking the limit of Equation (4.6) as $\delta \rightarrow \infty$, the saturation velocity in the nondegenerate case is

$$v_{dsat} = \frac{\sqrt{\pi}}{2} v_{th} \quad (4.7)$$

The drift velocity v_d given by Eq. (4.2) is evaluated for several values of the degeneracy parameter $N=n\lambda_D^2$ in Figure 6. It is clear from the figure that as N changes from unity to a small fraction, the simplified results of Equation (4.6) can be used. Observe also that for the moderate ($N=.1$) to highly ($N=1$) degenerate samples, the drift velocity at high fields clearly exceeds v_{dsat} as given by Eq. (4.7). These results are in conformity with the published results of experiments performed using a variety of sample preparations.

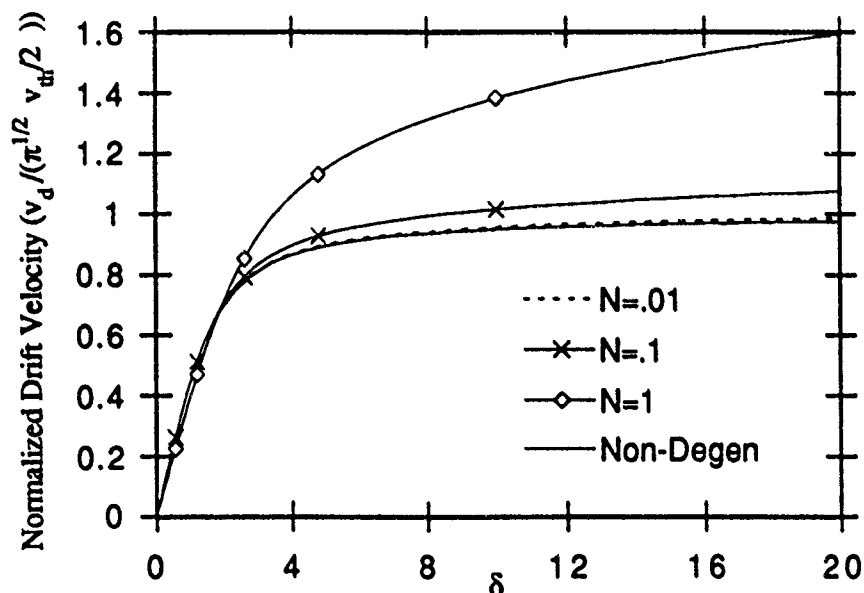


Figure 6. Velocity-field curves obtained from Eq. (4.2) at several values of N . The velocity-field curve obtained in the non-degenerate approximation (Eq. 4.6) is included for comparison.

All scattering events change the carrier momentum. However, only some of them, the inelastic scattering events change the energy of the carriers. Usually several scattering events are followed by one inelastic scattering usually by generating a phonon. The scattering length ℓ_{op} can be obtained by equating the energy gained by an electron in a mean free path to that of an optical phonon $\hbar\omega_0$:

$$\ell_{op} = \hbar \omega_0 / e \mathcal{E} \quad (4.8)$$

The total scattering length is then given by

$$\ell^{-1} = \ell_o^{-1} + \ell_{op}^{-1} \quad (4.9)$$

where ℓ_o is the zero-field scattering length obtained from the ohmic mobility. Figure 7 shows the comparison of theoretical results obtained from Eq. (4.2) with the experimental data of Hirakawa and Sakaki.² These experimental results could not be interpreted by a Monte Carlo theory.²

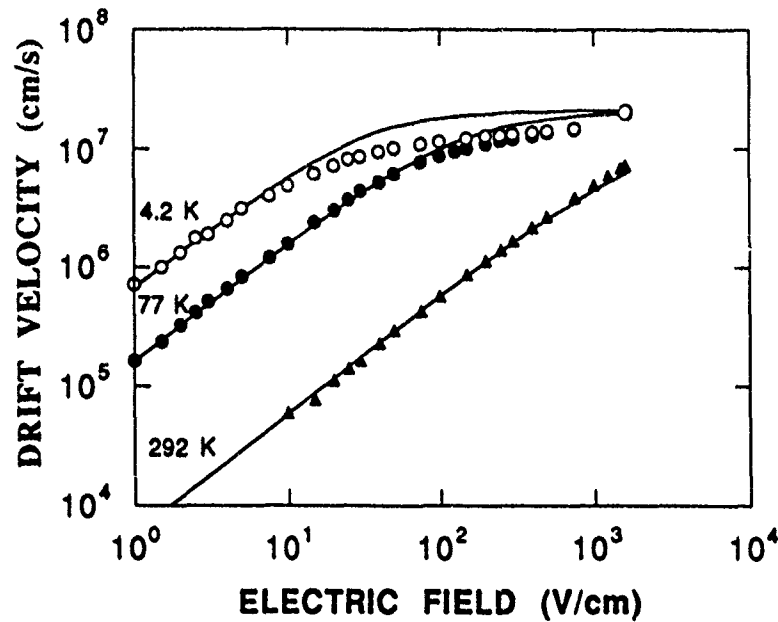


Figure 7. Comparison of velocity-field characteristics obtained from theory and experiment.² Solid lines are theoretical curves and scattered points are taken from K. Hirakawa and H. Sakaki, J. Appl. Phys. 63, 803(1985).

The multi-valley case of QTD quantum wells is much more complicated since not only the valleys in the GaAs, but also those in the neighboring AlGaAs layer play a critical role. Thus, velocity field characteristics depend strongly on the composition of the neighboring layer. If all valleys are assumed to be quantum-confined, the velocity field characteristics are given by the equation

$$v_d = \left(\frac{\pi k_B T}{2m_0} \right)^{1/2} \frac{\sum_{n,i} e^{-n^2 \epsilon_{\alpha,i}/k_B T} (m_i^*/m_0)^{1/2} I_1(\delta_{n,i}) e^{-\Delta_i/k_B T}}{\sum_{n,i} e^{-n^2 \epsilon_{\alpha,i}/k_B T} (m_i^*/m_0) I_0(\delta_{n,i}) e^{-\Delta_i/k_B T}} \quad (4.8)$$

with $\delta_{ni} = eE\ell_{ni}/k_B T$, where n,i stands for the n th subband in the i th valley. $I_n(x)$ is a Bessel function of order n . If the mean free path decreases with electron energy, as is the case for phonon scattering, the contribution from higher subbands can be neglected. Intervalley transfer will be affected by the change in energy separation between the valleys because of different effective masses.

Under the condition that the bandgap discontinuity for the higher subband is small, there will be a transition of Γ -valley electrons from 2D quantum-confined states to 3D propagating states in one of the higher valleys. In this case, the velocity-field characteristics are described by

$$v_d = \left(\frac{\pi k_B T}{2m_\Gamma} \right)^{1/2} \frac{I_1(\delta_\Gamma) + e^{-(\Delta_H - \epsilon_{\alpha\Gamma})/k_B T} \frac{2\pi L_z}{\lambda_{DH}} \frac{m_H^*}{m_\Gamma} \frac{2}{\pi^{3/2}} (\cosh(\delta_H) - \sinh(\delta_H)/\delta_H)}{I_0(\delta_\Gamma) + e^{-(\Delta_H - \epsilon_{\alpha\Gamma})/k_B T} \frac{2\pi L_z}{\lambda_{DH}} \frac{m_H^*}{m_\Gamma} \frac{1}{2\pi^{1/2}} \sinh(\delta_H)/\delta_H} \quad (4.9)$$

Here H stands for a higher valley. If growth conditions are such that $L_z \ll \lambda_{DH}/2\pi$, the contributions of the higher valleys can be neglected. In that case an electron will follow the velocity-field characteristics appropriate for the Γ -valley. Otherwise, it will exhibit a 3D behavior at sufficiently high electric fields.

5. Quantum-Well Wires

In the simplest model, the energy levels of a QWW are given by

$$\epsilon_{n,m,k_x} = n^2 \epsilon_{oz} + m^2 \epsilon_{oy} + \frac{\hbar^2 k_x^2}{2m^*}, \quad \text{where } n,m=1,2,3,\dots \quad (5.1)$$

By using Eq. (4.2), the velocity-field characteristics of a quantum-well wire can be described as

$$v_d = \frac{v_{th}}{\sqrt{\pi} \lambda_D n_f} \ln \left(\frac{1 + e^{\eta + \delta}}{1 + e^{\eta - \delta}} \right) \quad (5.2)$$

with

$$\eta = \frac{\zeta - \epsilon_{oz} - \epsilon_{oy}}{k_B T} \quad (5.3)$$

where η is obtained from the normalization condition

$$n_f = \lambda_D^{-1} \int_0^\infty x^{-1/2} dx \left(\frac{1}{e^{x - \eta - \delta}} + \frac{1}{e^{x - \eta + \delta}} \right) \quad (5.4)$$

Here, n_f is the number of carriers per unit length in the wire.

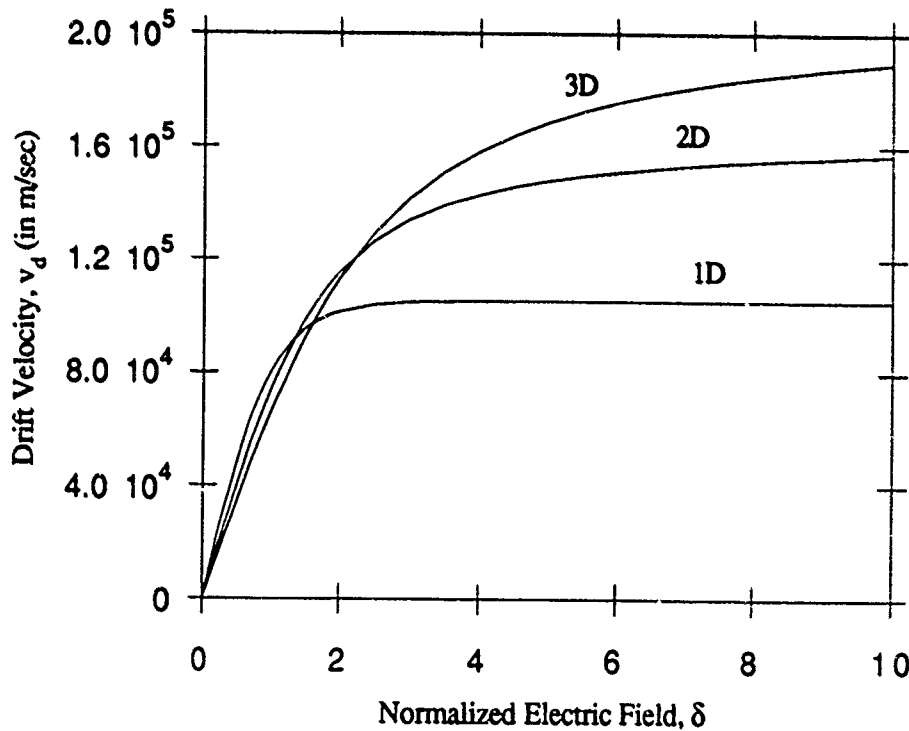


Figure 8. Comparison of GaAs velocity field characteristics for nondegenerate one, two, and three dimensional structures at 77 K.

In the nondegenerate limit, Eq. (5.2) simplifies to give

$$v_d = \frac{v_{th}}{\sqrt{\pi}} \tanh(\delta) \quad (5.5)$$

For Γ -valley transport in GaAs ($m^* = 0.067 m_0$) at $T = 77K$, the velocity-field characteristics under nondegenerate conditions, which are independent of carrier concentration, are compared in Figure 8. As can be seen from this comparison, even though mobilities may be higher in low-dimensional nanostructures, the saturation velocity tends to be lower. Thus, for the design of any high-speed transistor, the complete velocity-field profile is needed.

6. MODELLING OF FIELD EFFECT TRANSISTOR

Using the standard procedure,²⁰ velocity distribution in a $0.25\text{-}\mu\text{m}$ gate-length transistor was calculated at room-temperature. The velocity distribution is given by Figure 9.

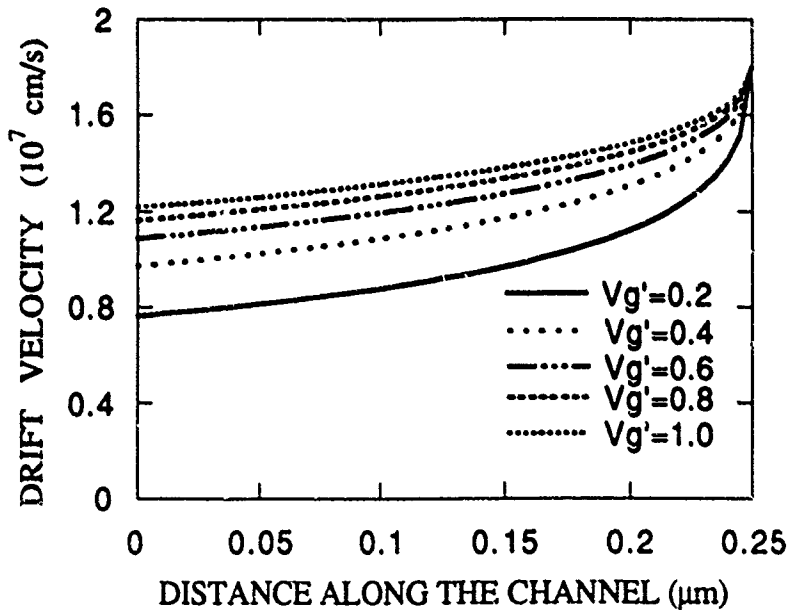


Figure 9. Velocity Distribution in $0.25\text{-}\mu\text{m}$ length channel of GaAs HEMT at room temperature.

It can easily be seen that the carriers are not travelling throughout the channel at the saturation velocity of 1.8×10^7 cm/s. The carrier velocity is lower on the source end. Only at the drain end, the carrier velocity is saturated. As channel becomes smaller, more electrons tend to travel near the saturation velocity.

Figure 7 indicates that the performance of the HEMT's at 77 K and 4.2 K will not be substantially different as saturation velocity is essentially the same at these temperature. This may be important information for cryoelectronics, as HEMT operating at 77 K may be much more economical than those operating at liquid helium temperature, but still without substantial loss about their performance.

6. CONCLUSION

An overview of the velocity-field profiles for materials of various dimensionalities is given. It is shown that under nondegenerate conditions, if a constant mean free path may be assumed, the drift velocity is limited by the appropriate thermal average of the magnitude of the velocity for the given dimensionality. The presence of an electric field tends to order the otherwise random electronic motion in its direction. For degenerate samples, the numerical calculations show that the saturation velocity tends to overshoot the thermal average of the magnitude of the velocity. This is due to the expansion of the Fermi sphere (or hemisphere in the strong electric field which has now to accommodate twice as many electrons than that in the zero electric field). But due to the experimental conditions present in the sample, the transfer to higher valleys is also possible. Unfortunately, very little is known about the transport parameters of the higher satellite valleys. Moreover, because of the ellipsoidal nature of the valley, the effective mass is a tensor. Anisotropies in this tensor can give anisotropies in the direction of current flow.

A few comments about the intrinsic transport which is directly related to the electron temperature can be made. The concept of hot electron temperature is extensively used in the literature to define electric-field-induced change in energy of the electron. As one can easily see this concept will be valid if the bands remain flat in the electric field. When electric field is applied and the current is flowing, the bands tilt in the

sample. Thus an electron after completing a mean free path will sink in the conduction band by an amount $e \ell_e$, and holes tend to float by an amount $e \ell_h$. This decreases the bandgap by an amount equal to $e (\ell_e + \ell_h)$. The decrease in bandgap enhances the number of electron hole pairs in strong electric field (carrier multiplication). If bandgap is assumed to be constant at zero field value, the carrier multiplication can be renormalized in terms of change in temperature, which is perhaps a better definition for an effective electron temperature as it involves both the conduction and the valence band. The results of this study will be reported in a separate communication.

When velocity-field profiles are considered in modelling FET's, it is found that the usual pinchoff effect at the onset of current saturation is absent. Actually, pinchoff phenomena appear when constant mobility, independent of an electric field, is used in modelling a transistor. When the velocity saturation effect, as present in the velocity-field profiles is used, the carrier density at the onset of saturation is found to be constant.¹² For obvious reasons, when the electric field is very high at the drain end, as is the case, the electrons do not follow the linear behavior in velocity-field relationship as predicted by Ohm's law. After the saturation point in I-V characteristics of the FET, carrier multiplication yields a large number of intrinsic carriers, which keep the channel open and current continues to flow. This explanation seems to be closer to the experimental observation than that the flow of carriers is through depletion layers as is modelled in the published literature. This carrier multiplication, perhaps, is also the source of noise which is normally present on the drain end.

These are some of the observations where velocity-field profiles may influence the modelling of modern nanostructure devices. We, therefore, hope that the results presented here will prove useful in understanding the world of future quantum device.

ACKNOWLEDGEMENTS

I would like to acknowledge the warm hospitality of Research Division of the Solid State Electronics Directorate of Wright Laboratory at the Wight-Patterson Air Force Base. Their cooperation made this stay highly productive. In particular, Gary McCoy, Ken Nakano, and Chern Huang were wonderful hosts for providing an environment conducive to

independent research. Chris Bozada is to be thanked for the valuable help he provided in setting up the Macintosh workstation without which this work would not have been possible. Many conversations with David Look have given me some directions for the future, for which I am grateful.

REFERENCES

1. V. K. Arora, Jpn. J. Appl. Phys. **24**, 537(1985); J. Appl. Phys. **54**, 824(1983).
2. K. Hirakawa and H. Sakaki, J. Appl. Phys. **63**, 803(1985).
3. W. T. Masselink, T. S. Henderson, J. Klem, W. F. Kopp, and H. Morkoç, IEEE Trans. Electron Dev. **ED-33**, 639(1986).
4. K. K. Thornber, J. Appl. Phys. **51**, 2127(1980).
5. W. Shockley, Bell Syst. Tech. J. **30**, 990(1951).
6. F. Capasso, T. P. Pearsall, and K. K. Thornber IEEE Electron Dev. Lett. **EDL-2**, 295(1981).
7. M. Dresden, Rev. Mod. Phys. **33**, 265(1961).
8. K. W. Böer, *Survey of Semiconductor Physics*, Van Nostrand Reinhold, New York, 1990, pp. 696-725.
9. S. Zukotynski and W. Howlett, Solid State Electron. **21**, 35(1978).
10. C. M. Wolfe, N. Holonyak, and G. Stillman, *Physical Properties of Semiconductors*, Prentice-Hall, Englewood Cliffs, N. J., 1989, pp. 112-118.
11. M. A. Green, J. Appl. Phys. **67**, 2944(1990).
12. D.L. Scharfetter and H. K. Gummel, IEEE Trans. Electron Dev. **ED-16**, 64(1982).
13. C. Jacoboni, C. Canali, G. Ottaviani, and A. A. Quaranta, Solid State Electron. **20**, 77(1977).
14. W. T. Masselink, N. Braslau, W. I. Wang, and S. I. Wright, Appl. Phys. Lett. **51**, 1533(1987).
15. J. A. Cooper and D. F. Nelson, J. Appl. Phys. **54**, 1445(1983).
16. A. A. Ketterson, W. T. Masselink, J. S. Gedymin, J. Klem, C.-K. Peng, W. F. Kopp, H. Morkoç, and K. R. Gleason, IEEE Trans Electron Dev. **ED-33**, 564(1980).
17. W. Fawcett, A. D. Boardman, and S. Swain, J. Phys. Chem. Solids **31**, 1963(1970).
18. C. Canali, C. Jacoboni, F. Nava, G. Ottaviani, and A. Alberigi Quaranta, Phys. Rev. B **12**, 2265(1975).
19. V. K. Arora and M. B. Das, Electron. Lett. **25**, 820(1989).
20. V. K. Arora and M. B. Das, Semicond. Sci. & Tech. **5** (1990).

SOL-GEL WAVEGUIDE LASER FABRICATION

Dr. Raymond Zanoni

Recently there has been growing interest in developing solid-state integrated optical lasers. At British Telecom a waveguide laser was formed by Nd ion implantation in YAG¹, at NTT a neodymium doped SiO₂ film was fabricated by CVD onto a silicon substrate², at Thomson-CSF in France a waveguide and amplifier were demonstrated in LiNbO₃³, and ion exchange waveguide lasers have been made in neodymium doped glasses⁴. The intent of this investigation is to study the feasibility of fabricating waveguide lasers using sol-gel materials. "Sol-gel" processing is a low-temperature route for making glasses. The ability to chemically modify or dope the sol-gel together with the capability of simplified processing by means of spin coating, spraying, or vapor depositing the sol-gels makes these materials ideal candidates for novel, low-cost integrated optical components in a variety of military and civilian applications.

Sol-gel processing of inorganic ceramic and glass materials began in the mid-1800's with studies of silica gels⁵. In 1940 Tanner and Lockhart first reported the development of SiO₂ films made by the sol-gel process⁶. Renewed interest in this technology has led to the development of new multifunctional materials over the past decade⁷. The sol-gel process has been used effectively to form glasses: SiO₂, TiO₂, SiO₂-TiO₂, indium tin oxide coatings, ZrO₂, Al₂O₃, etc.⁸ Both rare earth⁹ and dye doped sol-gel laser materials have been made¹⁰. To date, integrated optical amplifiers and lasers have not been made with sol-gel materials. The sol-gel process combined with optical waveguide technology promises to open up a wide range of novel integrated optical device applications.

If integrated optical components can be fabricated in sol-gels, then the next step will lead to the development of waveguide amplifiers and lasers. Below, several types of sol-gel waveguide lasers are illustrated: channel waveguide lasers, distributed feedback lasers, and a mode-locked laser using coupled cavities. Figure 1 illustrates typical channel waveguide lasers which can be

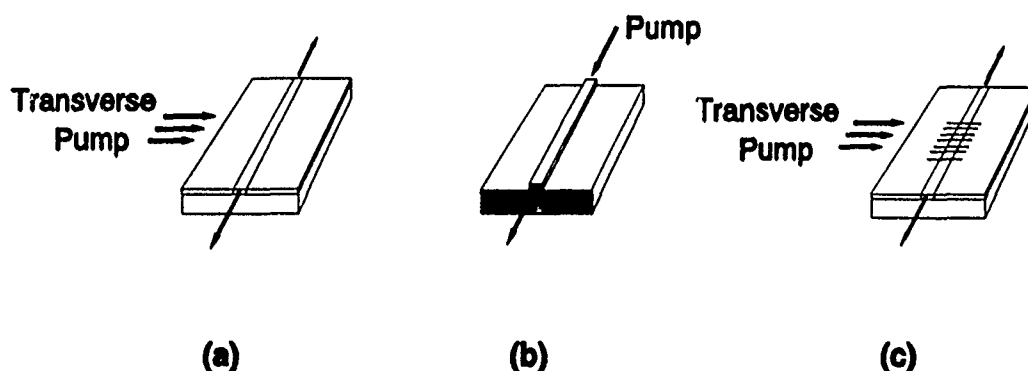


Figure 1. Channel waveguide lasers. A) Buried channel waveguide, B) Ridge waveguide, and C) Distributed Feedback laser.

either transversely or end-fire pumped by diode lasers. In Fig. 1a a channel waveguide is formed by doping a laser active material into a sol-gel film. The laser cavity is formed by coating dielectric mirrors onto the ends of the channel waveguide. The laser is pumped transversely by guiding light into the laser active region through the planar sol-gel film. Laser radiation is guided by total internal reflection within the optical channel. Proton exchanged Nd:MgO:LiNbO₃ waveguide lasers have produced up to 14 mW of CW optical power at 1085 nm¹¹. Fig 1b illustrates a ridge waveguide laser which can be made by reactive ion milling a laser active sol-gel film. The laser can be optically pumped by end-fire coupling light into the end of the channel waveguide. Laser light is outcoupled from the channel waveguide laser by a partially reflecting dielectric coating on the end-face of the channel. In Fig 1c a distributed feedback laser is illustrated where a periodic corrugation is etched into a sol-gel film to form a grating resonator for the waveguide laser. This eliminates the need for dielectric mirror coatings to make the resonator.

Distributed feedback resonators can operate at a single frequency by adjusting the pump power, therefore, these lasers are particularly useful for injection seeding high power lasers.

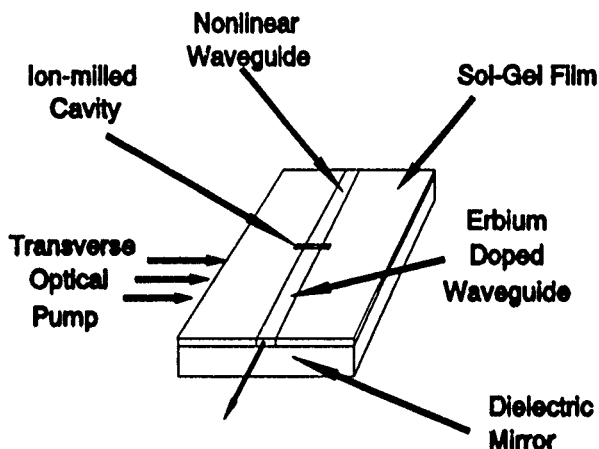


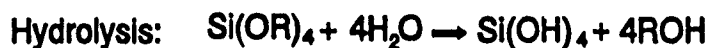
Figure 2. A coupled cavity laser is illustrated where the laser doped ridge waveguide is weakly coupled to a ridge waveguide which has been doped with a nonlinear optical material with a large nonlinear refractive index. This device can be expected to produce pulses widths of approx. .1 to 10 ps wide at repetition rates of approx. 30 GHz.

Figure 2 illustrates a coupled cavity laser which is expected to produce short, high repetition rate laser pulses. The coupled cavity laser works on the principle that short, high intensity pulses will have an intensity dependent phase shift in the nonlinear cavity formed from the nonlinear cavity. The nonlinear phase shift will in effect modulate the path length of the nonlinear cavity such that the laser cavity can be mode-locked. Only those pulses which circulate in phase with the laser cavity round trip time will add constructively to produce a mode-locked sequence of short pulses. Hence the name "additive pulse mode-locking". This type of laser was first developed by Mollenauer and Stolen¹² and further developed by Fujimoto and Haus¹³. With appropriate design it may be possible to construct devices which produce soliton pulses for dispersion free propagation on fiber optical communication systems. However the fundamental issue in applying this new technology depends upon the fabrication of low loss waveguides before sol-gels can be viewed as a serious alternative to existing waveguide material systems.

The objective of the summer research project at Wright Patterson has been to study the feasibility of fabricating channel waveguides in sol-gel materials for making optical amplifiers and lasers. Practical questions remain regarding the feasibility of processing these materials into low loss optical structures. This summer several types of sol-gel systems have been studied for possible use as thin film hosts for laser active species: ORMOSIL's, Titanium Butoxide/TMOS, and TMOS. The issues of importance in these studies were film shrinkage, ease of film fabrication, transparency and film quality. In this work it is shown that standard photolithographic methods can be used to make ridge channels in sol-gel films. With further work in reducing particulate contamination it should be feasible to make light guides with sol-gel films.

MATERIALS

The process for making silica glass is accomplished easily with the sol-gel processing method. For example, an alkoxide silicon precursor [tetraethylorthosilicate (TEOS) or tetramethylorthosilicate (TMOS)] can be used to form a colloidal suspension of silica by the addition of water through a hydrolysis and condensation reaction:¹⁴



With the addition of distilled water to the alkoxide precursor the mixture begins to hydrolyze and condense to form a silica gel. The SiO_2 formed by the hydrolysis and condensation reaction will remain in a clear colloidal suspension provided the pH of the solution is adjusted with hydrochloric acid. The solution forms an SiO_2 gel which is a porous three dimensional network. Upon aging and drying (or post baking) the pores can be eliminated leaving behind a dense glass (densification). Silicate glasses are not the only glasses which can be made by the sol-gel process.¹⁵ A variety of nonabsorbing metal oxide materials are listed in Table 1. For optical applications an admixture of TiO_2 and SiO_2 can yield films whose refractive index is continuously adjustable over the range of 1.45 to 2.3. Many of the starting compounds are readily available from chemical supply houses and the recipes for preparing the sol-gel materials have been published and are available in the chemical literature.

Oxide	Starting Compound	n	Absorbing Below (nm)
Al ₂ O ₃	Al(NO ₃) ₃ · 9H ₂ O	1.62	250
CeO ₂	Ce(NO ₃) ₃ · 6H ₂ O	2.11	400
HfO ₂	HfOCl ₂ · 8H ₂ O	2.04	220
In ₂ O ₃	In(NO ₃) ₃	1.95	420
Nd ₂ O ₃	Nd(NO ₃) ₃	(Inhom.)	
SiO ₂	Si(OR) ₄	1.455	205
SnO ₂	SnCl ₄	(Inhom.)	350
Ta ₂ O ₅	TaCl ₅	2.1	310
ThO ₂	ThCl ₄ , Th(NO ₃) ₄	1.93	220
TiO ₂	TiCl ₄ , Ti(OR) ₄	2.3	380
Y ₂ O ₃	Y(NO ₃) ₃	1.82	300
ZrO ₂	ZrOCl ₂	1.72	340

Table 1. Characteristics of organogenic metal oxide coatings from Schroeder.¹⁵

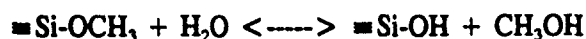
There are three types of sol-gel reactions which were used to investigate the feasibility of making channel waveguides. The first, mixture I, was the reaction outlined earlier for making SiO₂ from TMOS mixed with water. The second process, mixture II, involved making an organically modified silicate glass by copolymerizing TMOS with methyl methacrylate (this is called an ORMOSIL).¹⁶ The third process, mixture III, involved mixing TMOS with Titanium Butoxide to make a composite SiO₂/TiO₂ glass.¹⁷ The issues in preparing these materials during the summer were: a) shrinkage, b) ease of film fabrication c) transparency and d) thin film quality.

The preparation of mixture I followed the work by Yoldas and Schroeder.^{5,18} This mixture can be used to make thin films by dip coating, but the volume contracts by nearly a factor of 2 after densification. This is due to the replacement of the methyl groups in TMOS by oxygen when the SiO₂ network is formed. The shrinkage of the material during curing is a significant problem when making thin films on the order of 1 μm thick, thinner films can be made easily. Typically films thicker than approximately .5 μm form cracks. The cracking is due to the film shrinkage. The film thickness is difficult to control for films prepared by mixture I because the viscosity of

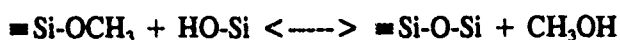
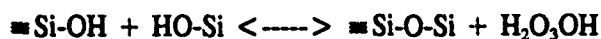
the solution changes on a time scale comparable to the preparation time. This makes spin coating films of a desired film thickness difficult to achieve without active monitoring of the spin dope viscosity. Work with this mixture was not continued, because of the difficulty in making crack free films and because the film thickness was difficult to control. In follow on research it is hoped that this simple mixture can be spray coated onto a hot substrate so that densification occurs during deposition in a clean environment without stressing the film.

The second mixture for making sol-gel films showed more promise in terms of minimal shrinkage.¹⁶ The recipe for making ORMOSIL sol-gel materials consists of a co-polymerization of TMOS, methyl methacrylate (MMA) and TMSPM [(3-trimethoxysilyl)propyl methacrylate]. This chemical process produces an SiO₂ network chemically bonded to PMMA through three chemical reactions (see Figure 3) which result in the ideal structure illustrated in Figure 4.

1. Hydrolysis - TMOS + TMSPM



2. Polycondensation - TMOS + TMSPM



3. Polymerization - MMA + TMSPM

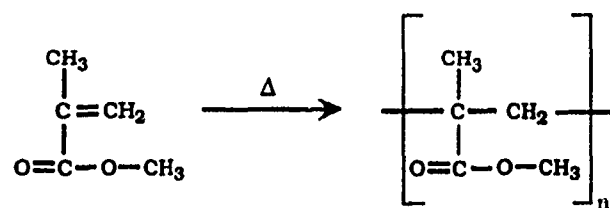


Figure 3. Chemical reactions for ORMOSIL.

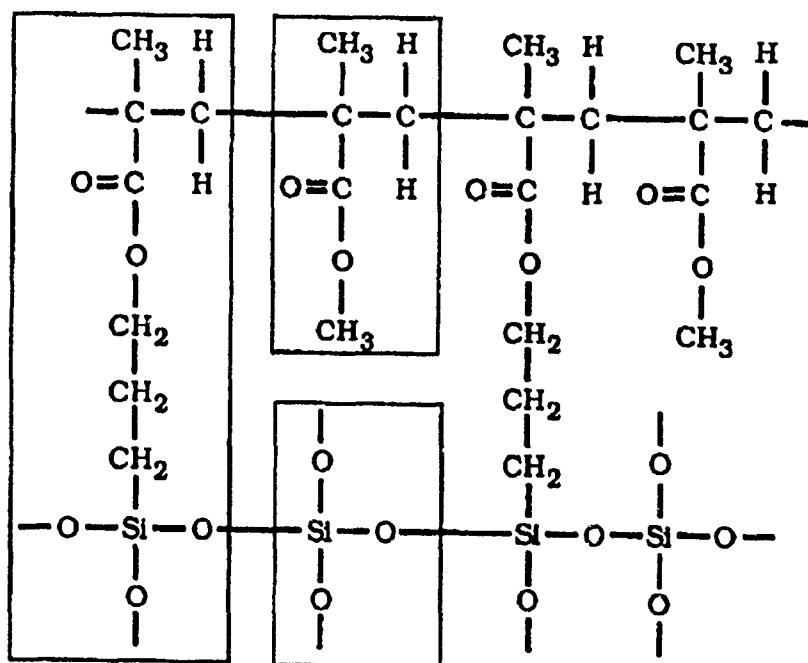


Figure 4. The ideal structure which is ultimately formed after the copolymerization.

Samples were prepared by reacting equal amounts of TMOS and TMSPM with 3.5 times as much 0.04 N HCL. After stirring the solution for 1/2 hour, MMA was added. A small quantity of benzoyl peroxide is added in order to initiate the polymerization reaction - the amount of benzoyl peroxide is inversely proportional to the molecular weight of the sol-gel. The solution is then heated to 70° C and held at that temperature for 1-4 hours. Films are prepared by spin coating a viscous solution onto a substrate. The films can be hardened by post baking.

In making these materials the solution becomes cloudy upon exposure to the atmosphere. This is due to the formation of large colloidal particles which scatter light. The problem can be resolved by coating the ORMOSIL in an inert atmosphere where the films can be dried before exposure to the atmosphere. The facilities for coating in an inert atmosphere were not available so this method of film fabrication was not pursued further. It is expected that the ORMOSIL will be investigated in future research because of the following advantages of the ORMOSIL materials:

- 1) Reduced shrinkage over conventional sol-gel materials
- 2) Low temperature processing temperature < 150° C
- 3) Low porosity
- 4) Transparency
- 5) Easily prepared into thin films

The third method (Titanium Butoxide/TMOS) was studied in order to make sol-gel films.¹⁷ The films were fabricated using an acid catalyzed solution of TMOS which was prepared by mixing water with TMOS in a mole ratio of 2:1 and mixed for 30 minutes. Titanium butoxide was reacted

with a complexing agent, 2,4 pentanedione in a molar ratio of 1:1 ($\text{SiO}_2\text{-TiO}_2$) and stirred for four days. This solution was diluted 1:1 by volume with distilled isopropanol prior to spinning.

The films were deposited onto single crystal silicon wafers 2" in diameter. The solutions were spin coated at 3000 RPM for 30 seconds. The coated substrate was then allowed to dry overnight in an oven at 60 degrees centigrade. Thickness measurements were made using a DekTak profilometer. Unlike films prepared from mixture I the complexing agent inhibits the densification of the film so that the spin coating process is easier to control. Thin film samples 1 μm thick were fabricated in this manner.

Ridges were reactively ion milled into the sol-gel film using standard photolithographic techniques. First, a sol-gel film was spin coated onto a silicon substrate, and then the film was heated to dry the film. The sol-gel film was overcoated with Shipley 1400-27 photoresist with a thickness of 1.5 μm and then the sample was exposed through a mask which had channel widths as small as 1 μm in width. The patterned photoresist was then developed to leave behind a photoresist mask which formed the mask for the reactive ion-milling process. The sample was reactively ion-milled and the remaining photoresist was washed off, leaving behind an array of sol-gel channels. Figure 5 illustrates the steps involved in making the ridge channels by reactive ion milling.

(A) CLEAN SUBSTRATE



(B) SPIN SOL-GEL



(C) SPIN PHOTORESIST



(D) PATTERN AND DEVELOP



(E) REACTIVE ION ETCH



(F) REMOVE PHOTORESIST



Figure 5. Photolithographic procedure for making a ridge channel in a sol-gel film.

Below is a photograph of a reactively ion-milled sol-gel film. These results show that it is feasible to reactively ion-mill the sol-gel films, however, there are problems with particulate contamination of the films. Future work will address the issue of filtering the sol-gel solutions carefully before spinning the films. This will reduce the particle contamination.

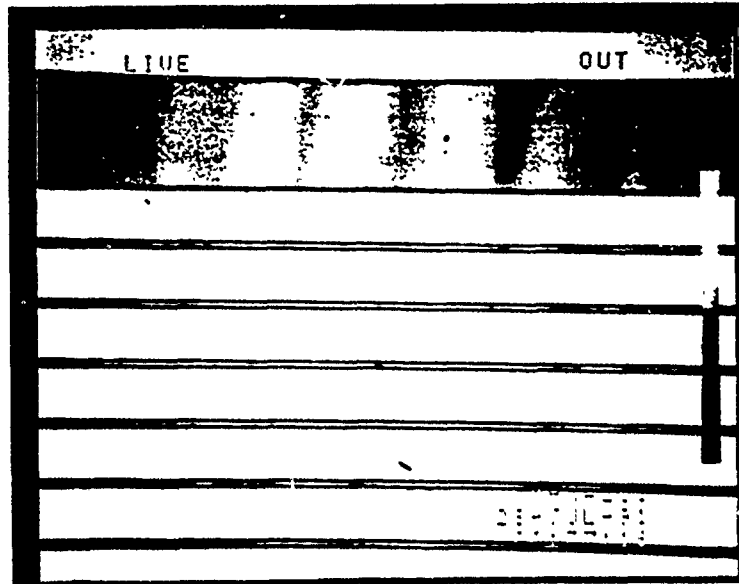


Figure 6. 5 μm wide ridges reactively ion etched in a sol-gel film approximately .18 μm thick.

CONCLUSIONS

Thin sol-gel films were made by spin coating a solution of Titanium Butoxide and TMOS onto silicon substrates. Ridge channels were reactively ion-etched into the sol-gel film by standard photolithographic methods. These channels were not adequate for waveguiding because the solutions were contaminated with particles. By properly filtering the sol-gel solutions it is believed that channels can be made with sufficient quality to guide light. If light guides can be made in the sol-gel films then it should be feasible to make laser amplifiers and oscillators by doping the sol-gel materials with either dyes or rare earth elements.

Acknowledgements. During this summer project Prof. Paras Prasad and Dr. Ryszard Burzynski from Laser Photonics Technology in Buffalo, NY. provided invaluable advice on material processing issues.

REFERENCES

1. Chandler P.J.; Field S.J.; Hanna D.C.; Shepard D.P.; Townsend P.D.; Tropper A.C.; Zhang L.; *Elect. Lett.* **25**, 1989, p 986.
2. Hibino Y.; Kitagawa T.; Simazu M.; Hanawa F.; and Sugita A.; "Neodymium-doped silica optical waveguide laser on silicon substrate," *IEEE Photonics Technol. Lett.* **1**, November 1989, p 349-50.
3. Lallier E., Pocholie J.P., Papuchon M., de Michell M., Li M.J., Ostrowsky D.B., Grezes-Besset C., and Pelletier E., "Nd:MgO:LiNbO₃ waveguide laser and amplifier," *IEEE/Lasers and Electro-Optics Society OSA, Integrated Photonics Research*, Vol. 5, TuJ6, March 1990.
4. Najafi S.I., Wang W., Currie J.F., Leonelli R., and Brebner J.L., *IEEE Photon. Tech. Lett.* **1**, 109 (1989); Mwarania E.K., Reekie L., Wang J., and Wilkinson J.S., "Low-threshold monomode ion-exchange waveguide lasers in neodymium-doped BK-7 glass," *Elect. Lett.* **26**, 16, August 1990 p 1317; Sanford N.A., Malone K.J., and Larson D.R., "Integrated-optic laser fabricated by field-assisted ion-exchange in neodymium-doped soda-lime-silicate glass," *Opt. Lett.*, **15**, NO. 7, April 1, 1990, p 366-368.
5. Ebelmen, M. *Ann. Chimie Phys.* **16**, (1846), p 129; Ebelmen, M. *C.R.Acad. Sci.* **25**, (1847), p 854; Graham, T.J. *Chem.Soc.* **17**, (1864), p 318.
6. H.A. Tanner and L.B. Lockhart, *J. Opt. Soc. Am.* **36**, p 701 (1946).
7. Hench L.L. and West J.K., "The Sol-Gel Process," *Chem. Rev.* **1990**, no. 90, p 33-72.
8. Schroeder, H; *Opt. Acta*, Vol. 9, 249 (1962); Mackenzie, J.D.; *J. Non-Cryst. Solids*, Vol. 41, 1 (1982); Mackenzie, J.D.; In *Ultrasonic Processing of Ceramics, Glasses and Composites*; Hench, L.L., Ulrich, D.R., Eds.; Wiley: New York, 1984; 15; Wenzel, J. In *Glass. Current Issues*; Wright, A.F.; Dupuy, A.F.; Eds.; Martinus Nijhoff: Dordrecht, Netherlands, 1985; p 224.
9. Berry, A.J.; King, T.A., "Characterization of doped sol-gel derived silica hosts for use in tunable glass lasers," *Journal of Physics. D, Applied Physics* **22**, October 14, 1989, p 1419-22.
10. Avmir, D.; Kaufman, V.R.; Reisfeld, R.; "Organic Fluorescent Dyes Trapped in Silica and Silica-Titania Thin Films by the Sol-Gel Method. Photophysical, Film and Cage Properties," *Journal of Non-Crystalline Solids* **74**, p. 395 (1985); Altshuler, G.B.; Bakhanov, V.A.; Dulneva, E.G.; Erofeev, A.V.; Mazurin, O.V.; Roskova, G.P.; and Tsekhomskaya; "Laser based on dye-activated silica gel," *Opt. Spectrosc.* **62**, 709 (1987); Knobbe E.T., Dunn B., Fuqua P.D., and Nishida F., "Laser Behavior and Photostability Characteristics of Organic Dye Doped Silicate Gel Materials", *Applied Optics* **29**, 2729 (1990); Knobbe E.T., Dunn B., Fuqua P.D., Nishida F., and Zink J.I., "Laser Behavior in Organic Dye Doped Sol-Gel Materials", Fourth International Conference on Ultrastructure Processing (John Wiley, New York, in press).

11. E.Lallier, J.P. Pocholle, M. Papuchon, M. de Micheli, M.J. Li, Q. He, D. B. Ostrowsky, C. Grezes-Beset, and E. Pelletier; "Efficient Nd:MgO:LiNbO₃ Waveguide Laser," *Electronics Letters* .
12. L.F. Mollenauer and R.H. Stolen, "The Soliton Laser," *Optics Letters* **9**, p 13, (1984).
13. Fujimoto J.G., "New technologies for ultrashort pulse generation in solid state lasers", *Opt. Phot. News* **2**, March 1991, 8-13.; Mark J.; Liu L.Y.; Hall K.L.; Haus H.A. and Ippen E.P., "Femtosecond pulse generations n laser with a nonlinear external resonator", *Opt. Lett.* **14**, 1989, 48.
14. Nogues J.R. and LaPaglia A.J., "Processing Properties and Applications of Sol-Gel Silica Optics," *SPIE Vol. 1168*, 1989 p 61-73.
15. H. Schroeder, "Oxide Layers Deposited from Organic Solutions," *Physics of Thin Films* (Edited by George Hass and Rudolf E. Thun), **5**, p 87, Academic Press, New York (1969).
16. Capozzi, C.A. and Pye, L.D.; "Preparation and Characterization of PMMA modified SiO₂ Host Material for Organic Dye Molecules," *SPIE 970*, "Properties and Characteristics of Optical Glass," p 135, (1988).
17. Weisenbach, L.; Davis, T.L.; Zelinski, B.J.J.; Roncone, R.L.; and Weller-Brophy, L.A.; "Processing of SiO₂-TiO₂ thin Film Waveguides," *Mat. Res. Soc. Symp. Proc.* **180**, 1990 Materials Research Society P. 377 (1990); Dale, G.W.; Fox, H.H.; Zelinski, B.J.J.; and Weller-Brophy, L.A.; "Sol-Gel Synthesis of Thin Films for use as Planar Waveguides," *Mat. Res. Soc. Symp. Proc.* **180**, 1990 Materials Research Society P. 371 (1990).
18. Yoldas, B.E. "Monolithic Glass Formation by Chemical Polymerization," *Journal of Materials Science*, **14**, p 1843-1849 (1979); Yoldas, B.E. "Deposition and Properties of Optical Oxide Coatings from Polymerized Solutions," *Applied Optics*, **21**, p 2960-2964 (1982).

**HYPERSONIC VEHICLE CONTROL STRATEGIES:
PRELIMINARY CONSIDERATIONS**

**Dr. Daniel J. Biezad
AFOSR 1991 Faculty Research Program**

**Mr. Phuong Vu
AFOSR 1991 Graduate Student Research Program**

**Aeronautical Engineering Department
Cal Poly State University
San Luis Obispo, CA 93407**

presented to

**Mr. Chuck Suchman
AFOSR Research Focal Point
WL/FIGC
WPAFB, Ohio 45433-6553**

" This document may contain information subject to the International Traffic in Arms Regulation (ITAR) or the Export Administration Regulation (EAR) of 1979, which may not be exported, released, or disclosed to foreign national inside or outside the United States without first obtaining an export license. A violation of the ITAR or EAR may be subject to a penalty of up to 10 years imprisonment or fine of not more than \$1,000,000 or both under 22 U.S.C. 2778 or Section 2410 of the Export Administration Act of 1979. Include this notice with any reproduced part of this document. "

ABSTRACT

Preliminary research in the area of hypersonic vehicle (HSV) control was accomplished to prepare for a proposal submission to AFOSR (including an extensive literature review). Linearized state-space models of a generic HSV configuration, obtained from Systems Technology Inc (STI), were catalogued and investigated using the controls analysis packages "CC Version 4" for IBM-compatibles and using MATLAB/SIMULAB for the MAC computer family. Tutorial and analysis "command files" were generated in "MACRO" form (CC-IBM) and in "M-FILES" (MATLAB-MAC).

The following research goals were established and investigated as time permitted:

- (1) Identify the governing key control issues in hypersonic "equilibrium" flight.
- (2) Investigate viable longitudinal loop closure control strategies (called "minimal SCAS" strategies by STI) for a succession of equilibrium points in the hypersonic envelope that define a particular mission phase.
- (3) Monitor and prevent excessive control deflection and deflection rates.
- (4) Apply new MIMO stability and robustness metrics which are applicable to the control strategies and present them in a form suitable for analysis.
- (5) Identify and apply handling qualities metrics which will provide insight into pilot-in-the-loop hypersonic flight, especially in the vital area of predicting flying qualities "cliffs".

the architecture, past experience and practice may be applied in a more conventional manner.¹⁰

There are a host of factors (called "governing properties" by STI) in hypersonic flight that may be considered key control issues.¹¹ Included among them is the precise longitudinal control required during rapid accelerations and decelerations when equilibrium conditions are difficult to identify. The first goal of proposed future research will be to investigate whether classical control strategies will result in architectures where gain scheduling is feasible.

For example, hypersonic climbout may include transition at Mach 3 to maximum dynamic pressure, then a Mach 6 climb at reduced dynamic pressure due to ramjet limits.¹² This may be loosely interpreted as flying through configurations P1BP, P2BP, P3BP, P4BP, P10BP, P4CP, P10CP, and P16CP of Reference 7 (See Appendix D). The control architectures to be developed will be tested on the above configurations for powered ascent, and those developed for descent will similarly be applied to successive points for unpowered descent. (If cooling totally dominates descent the flying qualities issues may be secondary to precise automatic control of flight path trajectory).

The second goal of proposed future research is to investigate the effects of control limiting and time delay on ascent and descent trajectories. This will be especially important for powered hypersonic flight where extreme sensitivities are anticipated between engine and airframe.¹³ The third goal will be to apply some of the new measures of MIMO stability to the above configurations.^{14,15} Finally, a pilot-in-the-loop analysis is proposed based on the Neal-Smith models as modified for super-augmented vehicles.¹⁶ One promising approach is the relationship between closed-loop extended bandwidth and pilot rating, which may be used to anticipate hypersonic flying qualities "cliffs" (Ref 16: pp 37).

This report reviews the HSV bare airframe dynamics for one generic, but not necessarily representative, HSV configuration. Two "minimal SCAS" strategies are then discussed for this configuration. Although the resulting architectures are multi-input, multi-output (MIMO), an attempt is made to close successive loops in a meaningful way so that insight that relates key variables is not lost. Classical analysis tools are used where appropriate, including "system

increases, resulting in a new increase in "equilibrium" acceleration (see also "centrifugal relief" comments in Ref 1: pp4).

HSV Longitudinal Modes. The HSV configurations of Appendix D are longitudinally unstable at high Mach numbers (above $M=6$) whether powered or unpowered. Longitudinal control power, as expected, is reduced with power on. Many configurations also show an increase in forward thrust as α is increased (positive X_α). A unique feature of the HSV, moreover, is the existence of altitude stability derivatives due to the density gradient.

The 5th order longitudinal modes (phugoid, short period, density) may be either over or under-damped. Coupling between the phugoid and density modes may occur at low dynamic pressure (Ref 1: pp28, Ref 17).

As an example of longitudinal dynamics, consider the HSV configuration P24CP for $M=20$ and $q_{bar}=2000$ psf, powered. The figures to follow were created with the STI_RPT CC macros. Figure 1a shows the instability in the longitudinal response due to elevator deflection ($-\delta e$). Note that the zeros of Figure 1b for pitch rate are not the same zeros as the pitch angle zeros as shown in Figure 2a. This is due to the inertial rotation of the vertical.¹⁸ The integral of pitch rate, q/s , thus does not equal the horizon reference angle, θ , even when there is no bank.

The system survey in Figure 1b illustrates the primary objective of pitch stabilization for highly augmented aircraft. A PI-compensator will be used to stabilize the $1/T_{sp2}$ mode and to replace the airframe $1/T_{\theta 2}$ zero with an effective zero of $1/T_q$ set by the designer. This will be discussed later in Section 3.1.

2.3 Lateral Modes. The HSV configurations of Appendix D are laterally "classical" in that they exhibit a roll mode, Dutch roll, and spiral. An excellent summary of configuration properties is found in Section III of Reference 1. Lateral modes were not investigated during this research period but may be included in the research proposal.

(PLOT GENERATED BY @STI_RPT2 MACRO)

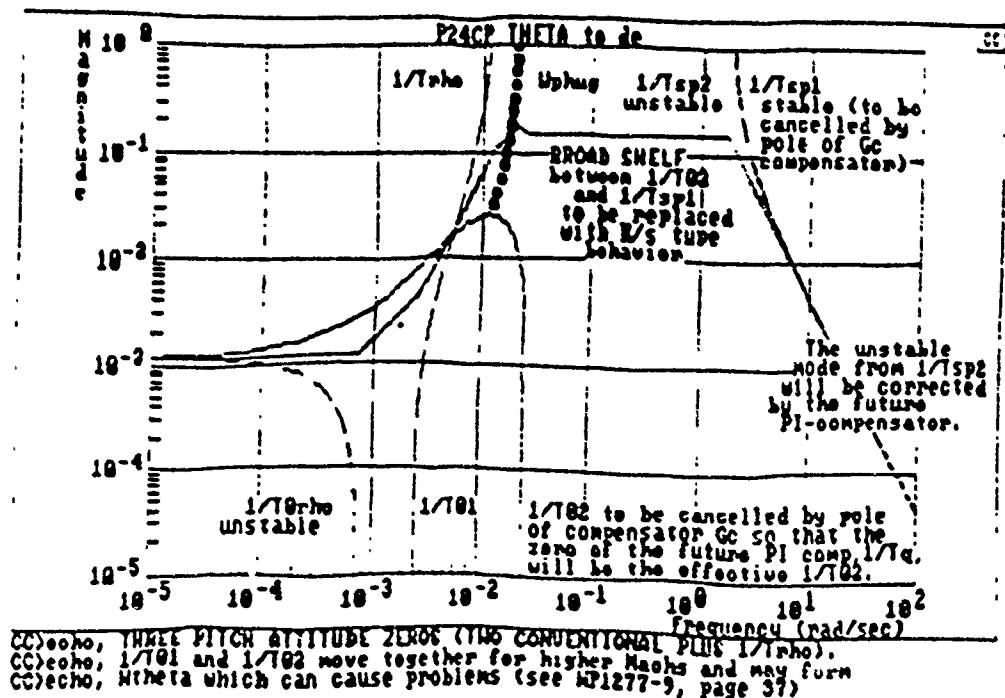
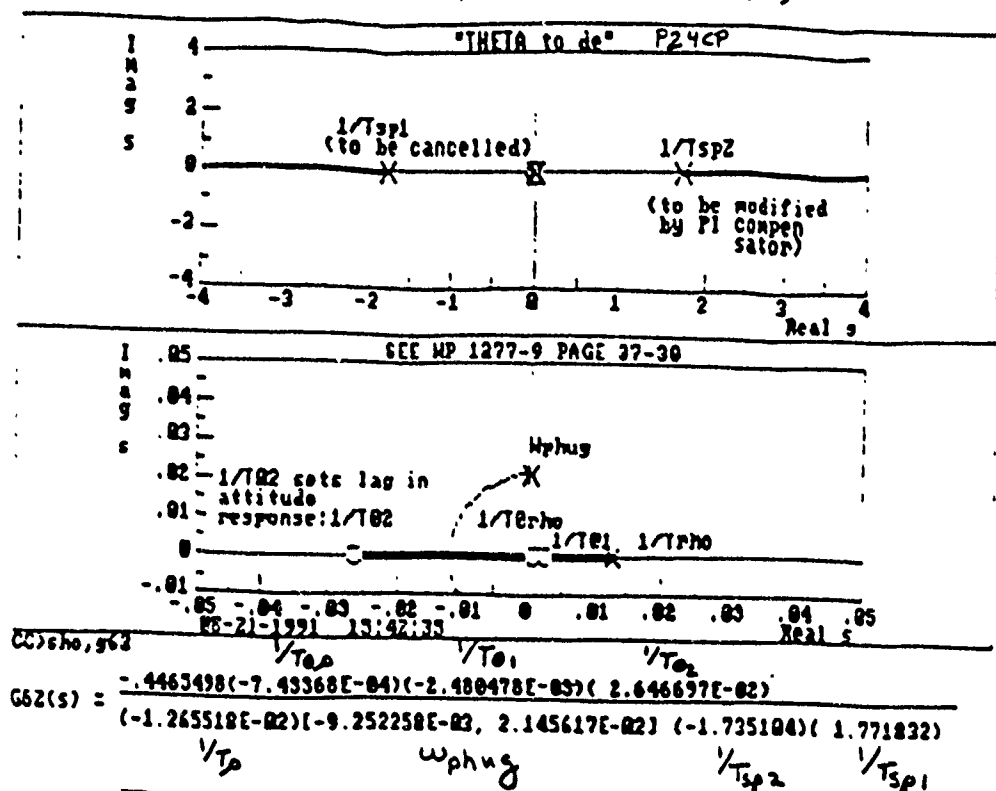


FIGURE 2. SYSTEM SURVEY OF MACH 20, $\bar{q}_0 = 2000$ psf POWERED HSV CONFIGURATION P24CP θ/δ_0 TRANSFER FUNCTION

3. MINIMAL "SCAS" STRATEGIES

Because of the sensitivity of thrust/airframe coupling to inlet flow (i.e. to α , β , and Mach), uncommanded fluctuations of angle of attack and sideslip should be minimized. The initial loop closures that effectively determine the aircraft as perceived by the pilot, or minimal "SCAS", thus should minimize the effect of inlet flow variations. Past experience has shown that for robustness the system should be simple in concept and implementation so that it is potentially more effective in handling the inevitable uncertainties of HSV design.^{19,20} Finally, the evaluation of minimal "SCAS" strategies should be tested using flying qualities metrics that are applicable to high order control systems and to systems where the stability derivatives are not known precisely (the Neal-Smith and the bandwidth criteria, for example, satisfy these requirements).

The two minimal "SCAS" strategies examined in this report are the rate command attitude hold (RCAH) and the angle of attack command and hold (AAH) systems. If normal HSV operation consists of additional loop closures as presented to the pilot (path tracking command, for example), the minimal SCAS should still provide adequate flying qualities in the event of automatic system failure or override by the pilot. Minimal SCAS analysis will include, therefore, the closure of a path tracking loop in proposed future research.

3.1 SUPER-AUGMENTATION IN PITCH.

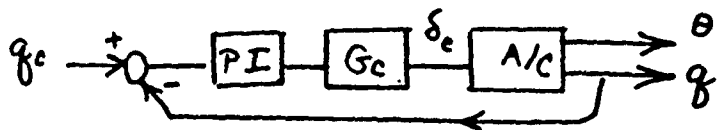
This augmentation scheme has been a prime topic of investigation by Systems Technology Inc (STI). The systems approach advocated by STI²¹ has matured and advanced to the point where task-tailored flight controls are feasible.^{22,23} The concept is currently being applied to selected HSV configurations of Appendix D (e.g. P24CP). The advantage of this approach over emerging multivariable control strategies^{26,27} lies in its simplicity, insight, and foundation based on past successes (Space shuttle, X-29).

The fundamental idea of superaugmented pitch control for an unstable airframe (i.e. one which has an unstable short period root ($j/T_{sp2} < 0$) is to replace the zero ($1/T_{\theta 2}$) controlling lag in the attitude response with a zero ($1/T_q$) of a PI-compensator (see Figure 3a). The goal is to change the broad, level "shelf" in the bode plot of q/q_c (known to cause flying qualities difficulties and illustrated in the SIGGY plot of Figure 2) with a frequency response having a more "flyable" K/s type of shape (as shown in the Bode plot of Figure 3).

The compensator G_c in Figure 3 helps to do this by cancelling the airframe $1/T_{\theta 2}$. It also cancels the airframe stable short period root $1/T_{sp1}$ so that the resulting root locus will have dominant second order roots (see the root locus in Figure 4) where dominant frequency and damping may now be chosen by setting K_q in the PI-compensator.

For HSV flight control this scheme is complicated by two difficulties. First, the lower frequency zeros of q/δ_e may be non minimum-phase (i.e. in the right half plane as in Figure 2). This will result in tracking performance as shown in Figure 4. This behavior is only safe if a pilot is continually attentive in the control loop. Other uncertainties in design, moreover, including the need for automatic control and the inherent lack of safety associated with unstable modes in flight, however slow they may be, justify the search for a stable minimal "SCAS".

The second difficulty is due to the rotation of the vertical, making the pitch reference θ different than the integral of pitch rate, q/s . Reasons for preferring θ to q/s are documented in Reference 25 (page 3). Figure 3b shows the change in the resulting transfer functions. Although the zeros of q/δ_e are no longer the zeros of θ/δ_e , standard superaugmentation approximations apply in the mid-frequency range (Ref 25: pp 3). The effect of non minimum phase zeros is now aggravated, but essentially of the same character as before in that they primarily affect long period instabilities. Appendix G discusses the rotation of the vertical and proposes some corrections to Reference 24 (STI Working paper-1277-8).



(a) $\theta = \delta/\lambda$

$$\underbrace{\frac{K_q (1/T_{\delta})}{1}}_{PI} \underbrace{\frac{K_c (1/T_{sp1})}{(1/T_{\theta 2})}}_{G_c} \underbrace{\frac{K_{\theta} (1/T_{\theta 1}) (1/T_{\theta}) (1/T_{\theta 2})}{(1/T_{\lambda}) (E_{ph}, w_{ph}) (1/T_{sp1}) (1/T_{sp2})}}_{G_{\delta}^{\theta} \text{ IF } \theta = \delta/\lambda} \underbrace{1}_{G_{\delta}^{\theta}}$$

(b) $\theta \neq \delta/\lambda$
ROTATION OF VERTICAL

$$\underbrace{\frac{K_{\delta_0} (E_{\delta_0}, w_{\delta_0}) (1/T_{\delta_1} \neq 1/T_{\theta 1}) (1/T_{\delta_2} \approx 1/T_{\theta 2})}{(1/T_{\lambda}) (E_{ph}, w_{ph}) (1/T_{sp1}) (1/T_{sp2})}}_{G_{\delta}^{\theta} \text{ IF } \theta \neq \delta/\lambda} \underbrace{\frac{N_{\delta_c}}{N_{\delta}}}_{G_{\delta}^{\theta}}$$

(c) P24CP

$$\underbrace{\frac{-9.95 (0.82)}{1}}_{PI} \underbrace{\frac{(1.77)}{(0.0249)}}_{G_c} \underbrace{\frac{-0.447 (-0.075, 0.09) (0.0117) (0.025)}{(-0.0127) (0.147) (-1.74) (1.77)}}_{\substack{A/C \\ \text{EXAMPLE}} G_{\delta}^{\theta}}$$

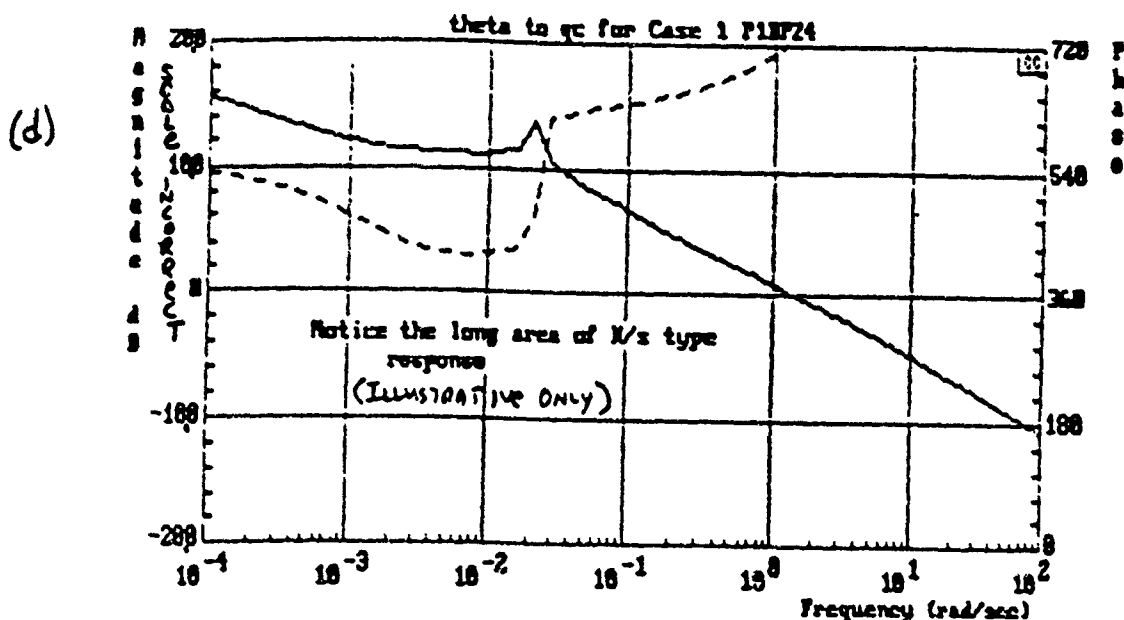
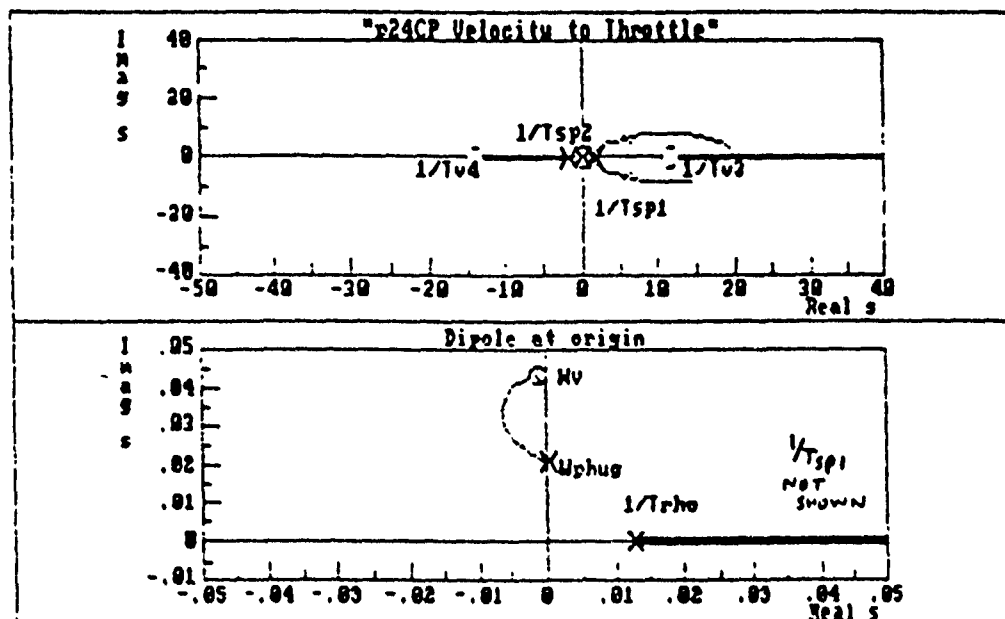
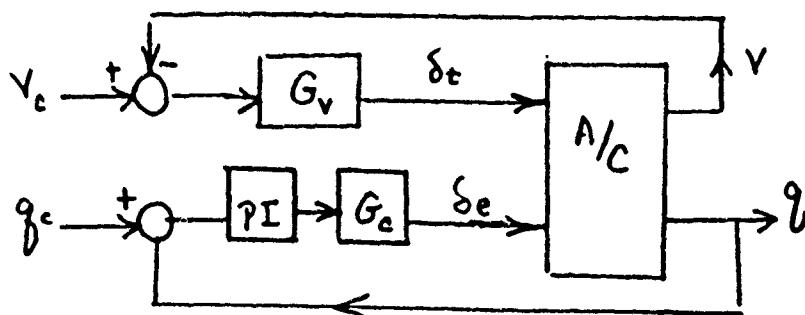


FIGURE 3. Pitch Supercorrection of an Unstable Aircraft (CC MACRO STIB)
 (a) WHEN Altitude Reference θ is δ/λ (NON-HYPersonic FLIGHT)
 (b) WHEN θ AND δ/λ DIFFER (ROTATION OF VERTICAL IN HYPERSONIC FLIGHT)
 (c) FOR HYPERSONIC CONFIGURATION P24CP
 (d) BODE Plot of COMPENSATED CONFIGURATION



$$G(s) = \frac{(-3.88)(-.0261)(-.0431)(-11.7)(14.2)}{(-.0127)(-.00925)(.0215)(-1.74)(1.77)} = \frac{\Delta V(\Delta)}{\delta_e(\Delta)}$$



$$G_v = K_v(1 + T_v s)$$

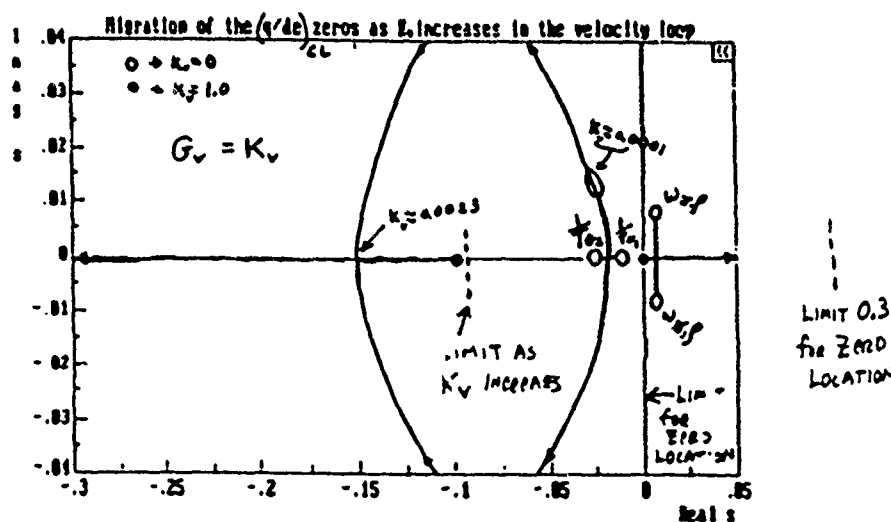


Figure 5. (a) Velocity to Throttle Root Locus Survey for Mach 2.0 P24CP
 (b) Multi-Loop Strategy with Velocity Loop Closed
 (c) Pitch Loop Zero Migration as K_v is Varied in Velocity Loop.

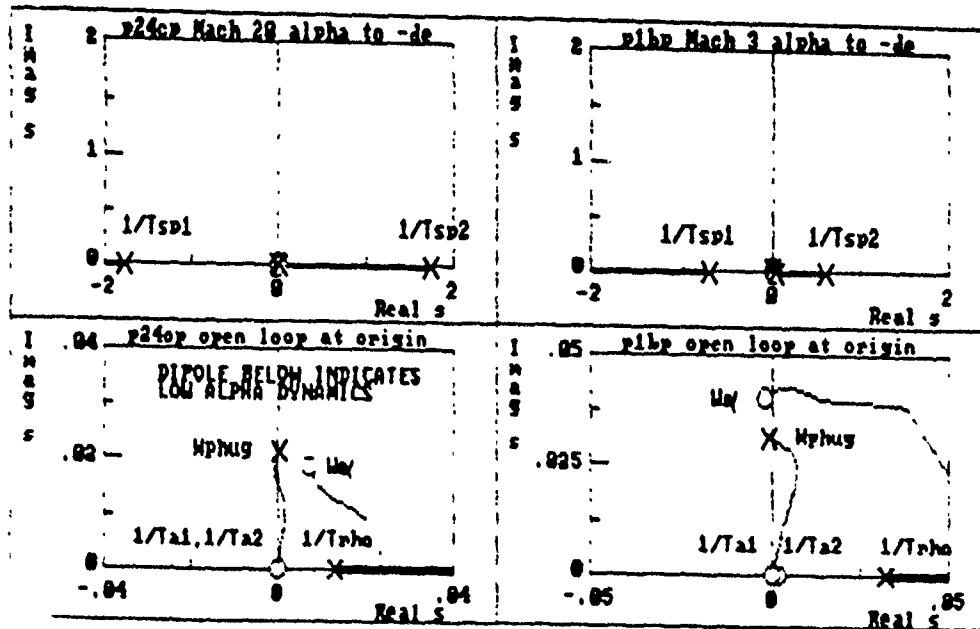
3.2 AUGMENTATION STRATEGIES USING ANGLE OF ATTACK

There are three reasons for considering angle of attack stabilization for hypersonic vehicles. The first is that alpha-stabilization presents a relatively conventional and stable vehicle to the pilot (Ref 10: pp 443-446). It further stabilizes the phugoid mode which, though usually unimportant in conventional aircraft, may be significant in HSV aircraft susceptible to phugoid coupling with the density mode (Ref 17). This stabilizing characteristic, however, is very similar to that provided by super-augmented pitch rate command and stabilization systems.

Since alpha-stabilization tends to maintain relative wind constant, fluctuations of HSV thrust should be minimized. Such fluctuations cause changing forces, moments, and possibly coupled airframe oscillations, all detrimental to controlled HSV flight. Moreover, it is possible that angle of attack must be precisely controlled due to envelope-limiting flight corridors. In this area alpha command and stabilization should control inlet flow conditions relative to the atmosphere better than a pitch rate command, attitude hold (RCAH) system. Moreover, there are rotation of the vertical effects causing horizon reference θ to be different than the integral of pitch rate, q/s , which a RCAH system must consider.

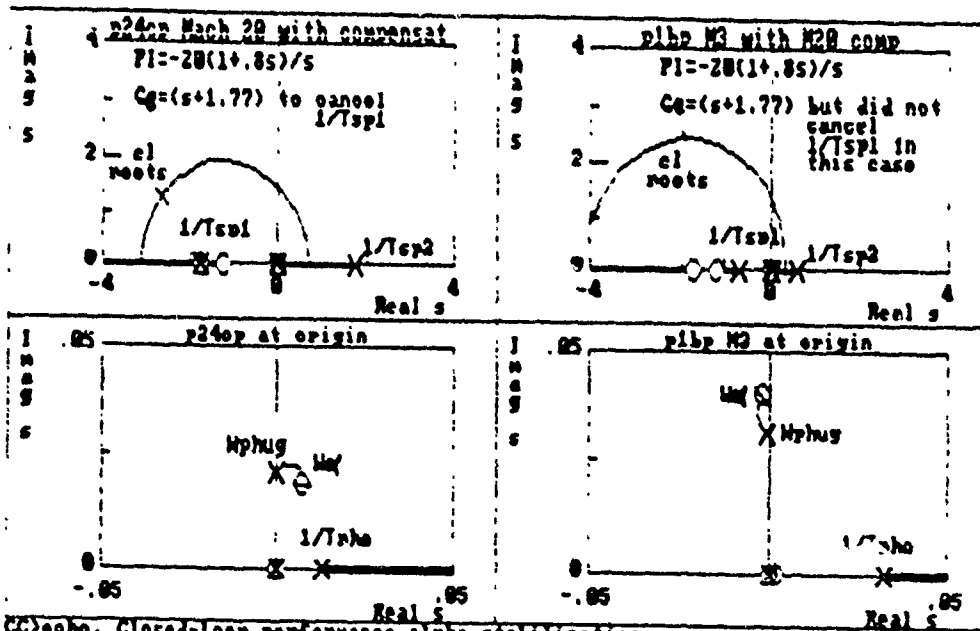
Alpha-stabilization will also reduce any roll-induced α to β coupling, critical for HSV flight to avoid beta-induced motions, heating, engine/airframe coupling, and adverse effects of engine unstart. A pitch rate command system may aggravate this type of sideslip coupling to angle of attack.

The downside of alpha-stabilization is the sensor suite required, which may be unavailable for practical HSV configurations, and the susceptibility of such systems to control limiting at high gain. The sensor difficulty may be alleviated by computing alpha and its derivative with a state observer or estimator. The pilot, who will probably not be flying relative to an actually observed horizon, would receive this information via an appropriate heads-up display (HUD). Command limiting may be required to avoid excessive external surface deflection rates.



$$G_{-de}^{\alpha} = \frac{.0027(0)(-8.1E-5)(-.347, .02)(52.3)}{(-.0127)(-.00925, .0215)(-1.74)(1.77)} \quad G_{-de}^{\alpha} = \frac{.00617(0)(-180E-5)(.059, .04)(352)}{(-.0374)(.021, .0314)(-.6)(.72)}$$

M20 M3



M20

M3

Figure 6. Angle of Attack Stabilization at Mach 20 and Mach 3
using the Mach 20 compensator
 $PI = -20(1+.8A)/A$ $G_c = (s+1.77)$

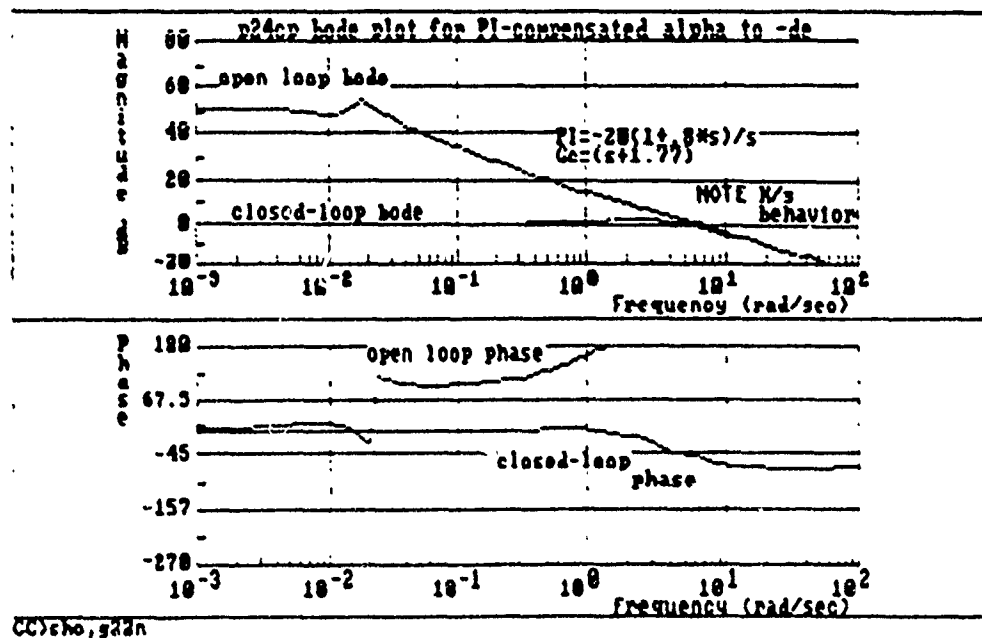


Figure 7. Open Loop Bode Plot for Mach 20 P24cp with Compensation in Alpha Forward Loop
 $PI = -20(1 + 0.8s)/s$
 $G_c = (s + 1.77)$

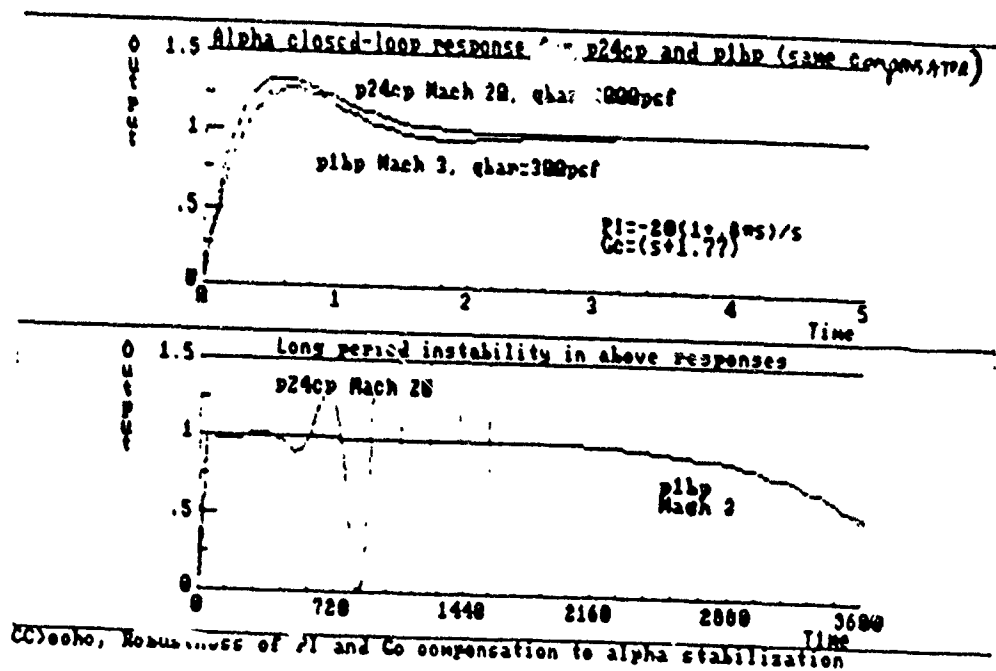


Figure 8. Closed-Loop Time Responses illustrating Short Term Robustness and Long Term Instability of Mach 20 and Mach 3 HSV Configurations using Mach 20 Compensator

4. SPECIAL CONSIDERATIONS

4.1 CONTROL LIMITING

Since an augmented, unstable aircraft tends to return to its unstable modal behavior whenever control limiting occurs (see Ref. 9), it is essential that any control strategy be tested by monitoring control deflection and rate as a function of open loop gain (i.e. system bandwidth). Rate limited actuators may be simulated by first order lags using transfer functions or as augmented state equations in state-space representation. Proposed research into this area will use both schemes. CC Macro @STI5 has been developed as a tool to investigate control limiting. CC Macro STI6 analyzes the resulting system made by @STI5.

4.2 TIME DELAY

The ill effects of time delay on flying qualities are well known. Although such "lumping" of time delay into one point of the control system is not rigorous, it does effectively convey the loss of performance and tendency towards instability. Proposed research will vary time delay between 0.0 and 0.2 seconds and investigate its effects on loop performance.

4.3. MULTI-LOOP SYSTEM STABILITY

Figures of merit for the stability of multi-variable flight control systems are not yet well established in industry. However, much theory has been developed in this area that is promising and which should be investigated. A distinction may be made between "nominal" and "robust" stability. Current flying qualities guidelines, as given in MIL-STD-1797, emphasize "equivalent" systems to determine nominal stability measures of damping and time constants. These systems may be poor indicators of stability²⁹ and be totally inappropriate when unstable modes are approximately cancelled by non minimum phase zeros.

Multi-loop stability margins and open-loop bandwidth are used to specify MIMO robust stability margins.^{14,15} It is not known how these new measures will be used to affect HSV design. These topics will be covered in proposed future research, and the control strategies

developed will be checked for both nominal and robust stability.using both independent and uniform measures.

4.4. FLIGHT PATH ANGLE RESPONSE

It is assumed that flight path control will be a dominant consideration in HSV flight. A path loop thus is anticipated to be closed around the minimal SCAS regardless of the type of control strategy chosen. The path bandwidth is an important determination of the type of tasks which may be safely accomplished.²² For HSV flight it will be important to know whether configurations are phase margin limited (typical) or gain margin limited (oscillation prone). Guidance for applying bandwidth criterion is explained in MIL-STD-1797 (see also page 31 of Reference 16). Bandwidth metrics will be proposed for future research.

4.5. PILOT-IN-THE-LOOP ANALYSIS

The revised boundaries of the Neal-Smith criterion (Ref 16: pp36) predict pilot-in-the-loop performance ratings given the aircraft and control system transfer functions. Unfortunately, these boundaries are not known for any task involving HSV flight. It is clear, however, that aircraft sensitivity to task demands or pilot technique is an important factor determining flying qualities "cliffs". This sensitivity may be approximated by plotting predicted pilot rating over a range of realistic task bandwidths (Ref 16: pp 37). Rapid deterioration in rating is indicative of excessive sensitivity and latent poor handling qualities. It is proposed that HSV sensitivity to task bandwidth be determined in future research.

5. CONCLUSIONS AND RECOMMENDATIONS

The major conclusions and recommendations of this report are listed below:

(1) The super-augmented minimal SCAS strategy is viable for controlling either pitch rate or angle of attack and presents a "flyable" aircraft to the pilot in the short term. It is recommended that these strategies be evaluated for multi-loop nominal and robust stability, control limiting, the inclusion of time delay, and pilot-in-the loop behavior.

(2) Angle of attack super-augmentation may be preferable to pitch rate control due to its direct control of inlet flow to minimize thrust/airframe coupling. It also reduces α to β coupling while rolling and the chance of unstart. It is recommended that the difficulties of implementing this scheme using achievable sensor dynamics and computation be investigated.

(3) The primary difference in the longitudinal modes between HSV dynamics and conventional unstable aircraft configurations lies in the low frequency instabilities caused by the height, density gradient, and phugoid coupling. The rotation of the vertical and centrifugal relief are very long period phenomena that should not affect control law operation in the short term. It is recommended, however, that the long period instabilities (non-minimum phase zeros) be eliminated by an appropriately compensated velocity loop.

(4) Controls analysis packages were found to be indispensable in working with the large number of HSV generic configurations. It is recommended that macros (and/or M-files) be developed to provide rapid review and access to design data and strategies.

REFERENCES

1. Myers, T.T., Klyde, D.H., Larson, Greg, "Hypersonic Open-Loop Vehicle Analysis," STI WP 1277-9, June 1991.
2. Drummond, A.M., "Performance and Stability of Hypervelocity Aircraft Flying on a Minor Circle," Progress in Aerospace Sciences, Chapter 3, pages 137-221, 1972. (see also AFFDL TR 65-218).
3. Etkin, B., "Longitudinal Dynamics of a Lifting Vehicle in a Circular Orbit," UTIA Rep. No. 65, AFOSR, TN 60-191, Feb. 1960.
4. Myers, Thomas T., "Low Frequency Longitudinal Dynamics and Control of Hypersonic Vehicles," STI WP 1277-10, June 1991.
5. Larson, G.L., Pierson, W.L., "Linear Equations of Motion for Hypersonic Flying Qualities," STI WP 1277-13 (Rockwell International), 12 May 1991.
6. Larson, G.L., Hunter, G., "Linear Models for Hypersonic Flying Qualities," STI WP 1277-14, 7 July 1990.
7. Klyde, David H., "Generic Hypersonic Vehicle State Space Models," STI WP 1277-6D, 16 April 1991.
8. Myers, T.T., McRuer, D.T., Johnston, D.E., "Flying Qualities and Control System Characteristics for Superaugmented Aircraft," TR 1202-1, STI, Contract NAS2-11388, Sept 84.
9. McRuer, D.T., Johnston, D.E., Myers, T.T., "A Perspective on Superaugmented Flight Control: Advantages and Problems," Journal of Guidance, Control, and Dynamics, Volume 9, Number 5, Sept-Oct 1986, pp 530-540.
10. McRuer, D., Ashkenas, I., Graham, D., Aircraft Dynamics and Automatic Control, Princeton University Press, 1973.
11. "Hypersonic Flying Qualities," STI & Rockwell Proposal 694, 16 June 1989.
12. Larson, G., and Ono, W., "Military Missions for Hypersonic Flying Qualities Research," NA 90-106, SNO 13, Rockwell Intl., P.O. Box 92098, L.A., CA 90009, May 1990.

13. McRuer, Duane T., Ashkenas, Irving L. and Johnston, Donald E., "Hypersonic Technology Planning, Flying Qualities and Control Issues/ Features for Hypersonic Vehicles," TR2361-1, May 1989.
14. Anderson, Mark R., Abbas, Emami-Naeini, and Vincent, James H., "Measures of Merit for Multivariable Flight Control," SCT Rep. 6664-500-1, Contract F33615-90-C-3611, Feb. 21, 1991.
15. Yeh, H., Ridgely, D. B., and Banda, S.S., "Non-conservative Evaluation of Uniform Stability Margins of Multivariable Feedback Systems." J.G.C., Vol. 8 #2, Mar.- Apr. '85, pp. 167-174.
16. Advisory Group for Aerospace Research and Development, NATO, "Handling Qualities of Unstable Highly Augmented Aircraft," AGARD Advisory Report No. 279, May 1991, 116 pages.
17. Klyde, D.H., Mitchell, D.G., "Causes of Phugoid and Density Mode Coupling for a Hypersonic Vehicle," STI WP 1277-5, 18 Dec 1990.
18. Myers, Thomas T., "The Effect of the Earth's Curvature on Hypersonic Aircraft Dynamics," STI WP 1277-4, June 1991.
19. Wendel, Thomas R., "Flight Control Synthesis to Meet Handling Qualities Specifications: An Evaluation of Nine Control Law Synthesis Techniques," Vol. I, McDonnell Aircraft Company, 20 March 1989 (Issued 17 July 1987).
20. Wendel, Thomas R. "Flight Control Synthesis to Meet Handling Qualities Specifications: An Evaluation of Nine Control Law Synthesis Techniques," Vol. II, McDonnell Aircraft Co, 5 June 1989.
21. McRuer, D. and Graham, D., "Eighty Years of Flight Control: Triumphs and Pitfalls of the Systems Approach," Journal of Guidance and Control, Vol. 4, No. 4., July-August 1981, pp 353.
22. Mitchell, David G., Aponso, Bimal L., and Duane T. McRuer, "Task-Tailored Flight Controls: Vol. 1 -- Ultra Precision Approach and Landing System, NASA CR 182066, November 1990.
23. Myers, Thomas T., Aponso, Bimal L., and Parseghian, Zareh, "Task-Tailored Flight Controls: Vol. II - Enhanced Fighter Maneuverability," NASA CR 182067, November 1990.
24. Myers, Thomas T., "SCAS Conceptual Design for the Hypersonic Flying Qualities Simulation," STI WP 1277-11, June 1991.

25. Klyde, David H., Myers, Thomas T., "Preliminary Superaugmented Pitch Loop Design for a Generic Hypersonic Vehicle," SCI WP 1277-8, April 1991.

26. Ridgely, D. Brett, and Banda, Siva S., "Introduction to Robust Multivariable Control," AFWAL-TR-85-3102, Feb. 1986.

27. Maciejowski, J.M., Multivariable Feedback Design, Addison-Wesley, 1989.

28. Thompson, Peter M., Program CC Version 4 Tutorial and User's Guide, STI, November, 1988.

29. Bacon, B.J., Schmidt, D.K., "Fundamental Approach to Equivalent System Analysis," AIAA Journal of Guidance, Control, and Dynamics, Vol. 11, No. 6, Nov.-Dec. 1988, pp. 527-534.

```

CC> ***** A. PROGRAM CC ENVIRONMENT *****
CC> *****
CC> A.1 ABBREVIATIONS.
CC>
CC>      UG      CC TUTORIAL AND USER'S GUIDE
CC>      V1      CC VOLUME 1
CC>      V2      CC VOLUME 2
CC>      ENV(f,m,d)  USER'S) ENVIRONMENT (3 DOS) SUBDIRECTORIES)
CC> *****

```

CC> A.2 ENVIRONMENT.

CC> A CC user's environment, ENV(f,m,d), consists of three DOS
 CC> subdirectories (f,m,d) that are user specified to organize work and to
 CC> avoid clutter. There may be separate environments for different tasks,
 CC> problems, or tutorials, and the environments may reside on the hard disc,
 CC> or on designated floppies. Each environment consists of a subdirectory
 CC> for CC files preceded with \$\$ in their title (CC automatically puts the
 CC> \$\$ prefix on these files); a subdirectory m for macros; and a
 CC> subdirectory d for "stored" and "recalled" data files in arbitrary (or
 CC> default) DOS directories. The environment ENV(f,m,d) is specified by
 CC> the user under OPTION 2 of the SETUP command (UG: pp 372).

CC> Three user environments are described here. ENV1 is the base user
 CC> environment for general use with macros that arrived with the CC
 CC> program (see UG: Appendix E). ENV2 is an environment set up within
 CC> a DOS directory called c:\cc\st1 to work on a particular problem which
 CC> has its own set of macros. (f,m,d) for ENV2 are thus all located within
 CC> c:\cc\st1. ENV3 is an environment set up for a floppy disk on a:
 CC> drive. Floppy drive environments are slow but useful for storage,
 CC> transport, and backup. The table below summarizes the environments:

ENV(f,m,d)	f	m	d
ENV1 (Tutorial Workspace)	c:\cc\files	c:\cc\macros	c:\cc\data
ENV2 (ST1 Workspace)	c:\cc\st1\files	c:\cc\st1\macros	c:\cc\st1\data
ENV3	a:\files	a:\macros	a:\data

echo, There are also macros that will automatically set ENV2, ENV3, and
echo, ENV3. They are called SETCC, SETST1, and SETA respectively. Before
echo, these macros are used the subdirectories f and m must exist as
echo, listed in the prior table.

echo,
echo, A.3 MANUALS.

echo,
echo, The CC manuals are very informative but in some areas lack a
echo, tutorial focus for the novice user. One way to get started is to
echo, read the following references:

echo,
echo, UG: pp 1-4,10,18,22,83-86,330 (Intro, Macros, ENV(f,m,d))
echo, V1: pp 108 (Structure, How to Quit)
echo, UG: Appendix D, E (Help, Command and Macro List)

echo,
echo, Then run the DJB tutorial macros in order (DJB1, DJB2, etc) and
echo, read the referenced material within the macros. Familiarity with
echo, and continued use of personal macros will increase user friendliness
echo, and satisfaction with this powerful program.

pause
echo,
echo, The following is a partial list of errors found in the manuals:

echo, V1: pp 117 use o/i for proper order
echo, V1: pp 163 G(N,3,1) should be G(N,3,0)
echo, V1: pp 164 10(s+5) should be 20(s+5)
echo, V1: pp 168 missing g3 in Mason Gain Rule TF

pause
echo,
echo, Finally, a word of caution. Many commands will not accept variables
echo, passed into an argument list through nested macros. Labelling of plots
echo, within a macro cannot be done if the plot (or root locus) is called as a
echo, result of an IF statement. TRIAL and ERROR are often required, so keep
echo, macros short and nest them when possible. This will aid in the
echo, inevitable troubleshooting.

echo,
echo, You are now ready to run the DJB# macros. The CC volumes should
echo, be nearby for reference. The list of files below came from the
echo, DJB_MACS file in ENV1:

echo,
echo, DJB1 MACROS and HELP
echo, DJB2 Passing parameters in MACROS
echo, DJB3 Introduction to Windows capability in CC
echo, DJB4 Bode Plots and REDO example
echo, DJB5 Data Files and Matrices, Part 1
echo, DJB6 Manipulation of Transfer Functions
echo, DJB7 Using a: drive hypersonic vehicle (HSV) files
echo, DJB8 Data Files and Matrices, Part 2
echo, DJB9 Introduction to the Equation Interpreter

echo,
echo, NOTE: This appendix was printed from the DJB macro.

B. Tutorial CC Macros

DJB USER ENVIRONMENT ENF(f,m,d)
DJB1 MACROS and HELP
DJB2 Passing Parameters in MACROS
DJB3 Intro to Windows
DJB4 Bode plots and REDO
DJB5 Data Files & Matrices, Part 1
DJB6 Manipulation of Transfer Functions
DJB7 Using a: drive HSV (hypersonic vehicle) files
DJB8 Data Files & Matrices, Part 2
DJB9 Intro to the Equation Interpreter
DJB_BODE Generic Aid for Bode Plots.
DJB_TIME Generic Aid for Time Plots.

C. Hypersonic Vehicle (HSV) Macros

STI0 TUTORIAL ON HSV QUADRUPLES AND TF MATRICES
STI1 Strip Chart of a quadruple with selected step input.
STI1F Strip Chart with N and alpha plots for long mode
STI1Y Strip Chart with Ny and beta plots for lateral mode
STI1_1 Long Strip Chart Simulation with "No Power" labels.
STI1_2 Long Strip Chart Simulation with "Power" labels.
STI1_3 Lateral Strip Chart Simulation with "Lateral" labels.
STI2 Extract TF from a TF MATRIX.
STI3 Sys Surv #1 given TF (Bode, Step response, Root loci)
STI3_1 Label Root Locus Plot with $\zeta=1,10,100$
STI4 Sys Surv #2 given TF (Bode, Root Locus, SIGGY)
STI5 SISO Plant G with Comp K, Fdbk F, Preflt P, & GAIN
STI5_1 Compute OUTF,YRC,YR,ERC,ER,URC,UR,BRC,BR for STI5 SISO
STI5_2 Header for STI5 SISO system and definitions
STI6 Closed Loop Survey of STI5 SISO system
STI6_1 Bode magnitudes for STI5 SISO closed-loop system
STI6_2 PHASE plots for STI5 SISO closed-loop system
STI6_3 Time plots for STI5 SISO closed-loop system
ST6_3A thru D Time plots for STI6 for .1 1 10 120 seconds
STI6_4 Root locus for STI5 SISO closed with GAIN
STI7 First half (root locus) of survey specialized for HSV configs.
STI7_1 Second half (siggy) of survey specialized for HSV configs.
STI7_2 Macro makes fixed time delays .025 to .3 sec for demo.
STI7_2A This makes a set of Fade transfer functions for STI7_2.
STI7_3 Root locus survey macro for TF with PADE and ACTUATOR delay.
STI7_4 Generic Bode Plot macro for use with STI7 macro family.
STI7_5 Generic Time Response macro for use with STI7 macro family.
STI8 Tutorial macro for STI working paper 1277-8 pitch design.
STI8_1 Continuation of STI8 for Case #4 of WP 1277-8 design.
STI8_2 Continuation of STI8 for Case #5 of WP 1277-8 design.
STI8_3 Continuation of STI8 for THETA vs q/s FEEDBACK (WP 1277-8).
DJB_BODE Generic macro aid for Bode plots.
DJB_BOD2 BODE OPEN & CLOSED for TF times GAIN (mag over phase: 2 win)
DJB_TIME Generic macro aid for Time plots.
STI_RPT1 Macro explains Figure 1 in AFOSR Final Report
STI_RPT2 Macro explains Figure 2 in AFOSR Final Report
DJB_SUR Survey of TF times GAIN (SIGGY,BODE,TIME responses)
DJB_SUR1 Survey of TF times GAIN (SIGGY over PHASE: 2 windows)
DJB_SUR2 Survey of TF times GAIN (SIGGY over R LOCUS: 3 windows)
DJB_SIG Generic SIGGY plot called by DJB_SUR macros

APPENDIX D. HSV Configurations

The 36 powered and unpowered generic HSV configurations are explained in this appendix as taken from References 1 and 7 (see also Refs 5, 6). The configurations are available in "quadruple" P format, which is a mapping in state-space given by

$$\begin{bmatrix} \dot{x} \\ \dot{y} \end{bmatrix} = \begin{bmatrix} A & B \\ C & D \end{bmatrix} \begin{bmatrix} x \\ u \end{bmatrix} = P \begin{bmatrix} x \\ u \end{bmatrix}$$

P \$\$plmn (Program CC quadruple file designation).

\$\$ Program CC designation of data element.

p Quadruple label.

l Number from 1 to 36 identifying Mach and qbar for configuration.

m Letter a for unpowered or b for powered (low Mach) or c (Mach>6).

n letter p (longitudinal mode) or y (lateral mode).

Example: \$\$p21ay is the quadruple file for Mach 12, qbar 700 psf,
unpowered, lateral mode.

Longitudinal State Vectors

$$x = [u \quad \alpha \quad q \quad \theta \quad h]^T \text{ (units feet, seconds, radians)}$$

$$u = [\delta_w \quad \delta_e \quad \delta_r \quad w_r]^T \text{ (units radians pounds, feet, seconds)}$$

$$y = [\alpha \quad \dot{\alpha} \quad q \quad N_{x(PCS)} \quad N_{x(CR)} \quad \theta \quad \dot{h} \quad u]^T \text{ (u for powered only cases)}$$

Lateral State Vectors

$$x = [\beta \quad p \quad r \quad \phi \quad \psi \quad y]^T \text{ (units feet, seconds, radians)}$$

$$u = [\delta_a \quad \delta_r \quad \delta_{\text{yaw}} \quad v_r]^T \text{ (units radians, pounds, feet, seconds)}$$

$$y = [\beta \quad \dot{\beta} \quad p \quad r \quad N_{y(PCS)} \quad N_{y(CR)} \quad \phi \quad \psi \quad \dot{y}]^T$$

Longitudinal configurations are located in the LONHSV directory and the lateral configurations are located in the LATHSV directory of the appropriately specified storage media (these directories are for government use only).

Example Flight Case Matrices

Longitudinal (Unpowered)

	Mach ->	3	6	10	12	15	20
qbar (psf)	300	1a	⁷ 7a	³ 10a	⁹ 11a	25a	31a
	500	2a	8a	14a	20a	26a	32a
	700	3a	9a	15a	21a	27a	33a
	1000	4a	10a	16a	22a	28a	34a
	1500	5a	11a	17a	23a	29a	35a
	2000	6a	12a	18a	24a	30a	36a

Longitudinal (Powered)

	Mach ->	3	6	10	12	15	20
qbar (psf)	300	1b	7b	1c	7c	13c	19c
	500	2b	8b	2c	8c	14c	20c
	700	3b	9b	3c	9c	15c	21c
	1000	4b	10b	4c	10c	16c	22c
	1500	5b	11b	5c	11c	17c	23c
	2000	6b	12b	6c	12c	18c	24c

TABLE 1a. UNPOWERED FLIGHT CONDITION MATRIX

Mach \bar{q} (psf)	3	6	10	12	15	20
300	-1.0 10.9	-1.0 12.2	-0.2 12.4	-1.0 10.9	-1.0 8.5	-0.2 5.0
500	-1.0 9.2	-1.0 11.5	-0.2 11.6	-1.0 10.5	-1.0 8.4	-0.2 5.9
700	-1.0 9.5	-1.0 12.0	-0.2 11.7	-1.0 10.9	-1.0 8.8	-0.2 7.5
1000	-1.0 11.5	-1.0 13.8	-0.2 12.5	-1.0 11.9	-1.0 10.0	-0.2 10.1
1500	-1.0 16.4	-1.0 17.6	-0.2 14.5	-1.0 14.5	-1.0 12.3	-0.2 14.4
2000	-1.0 21.9	-1.0 21.7	-0.2 17.1	-1.0 17.2	-1.0 15.2	-0.2 18.6

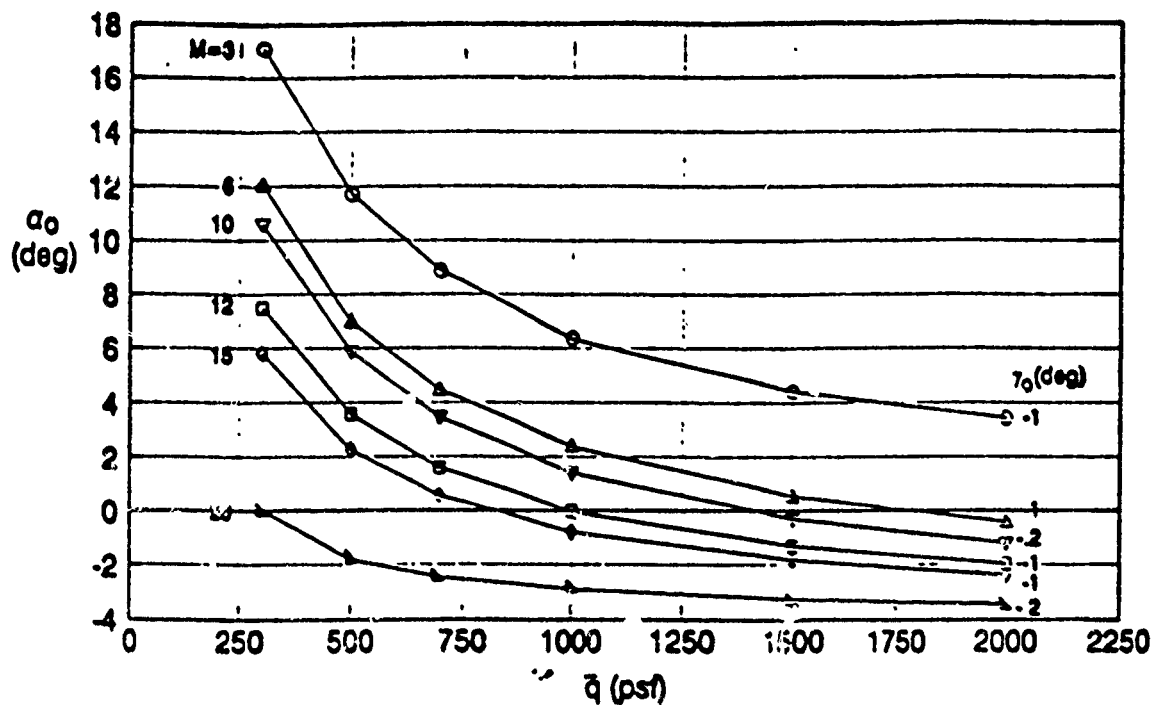
TABLE 1b. POWERED FLIGHT CONDITION MATRIX

Mach \bar{q} (psf)	3	6	10	12	15	20
300	3.8 7.9	0.42 0.31	0.47 6.9	0.47 6.0	0.18 4.4	0.14 8.2
500	3.8 3.3	0.42 5.0	0.47 1.9	0.47 1.7	0.18 1.3	0.14 8.5
700	3.8 0.14	0.42 8.5	0.47 1.8	0.47 1.2	0.18 0.83	0.14 9.1
1000	3.8 4.0	0.42 12.6	0.47 6.0	0.47 4.7	0.18 3.4	0.14 13.2
1500	3.8 7.9	0.42 18.0	0.47 11.3	0.47 9.1	0.18 7.0	0.14 19.0
2000	3.8 12.6	0.42 22.8	0.47 14.2	0.47 12.0	0.18 9.2	0.14 24.9

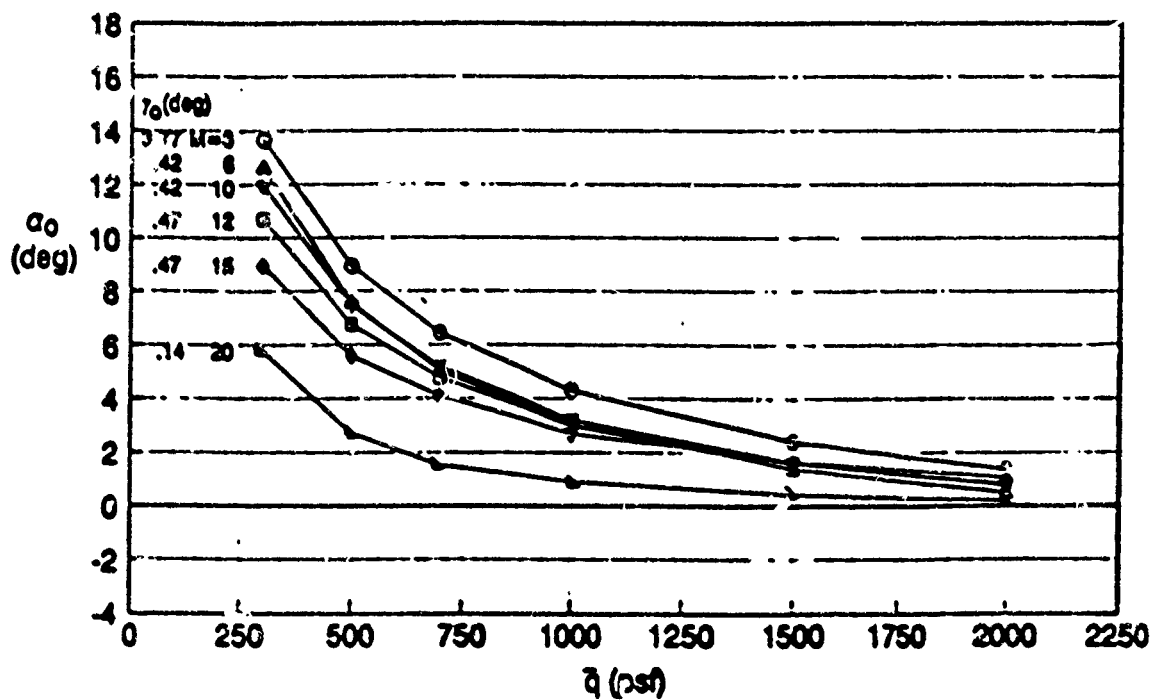
in each cell:

Top # - γ_0 (deg)

Bottom # - \dot{V}_T (ft/sec²)



a) Unpowered Cases



b) Powered Cases

Figure 3. Trim Angle of Attack and Flight Path Angle for the Flight conditions Investigated

Appendix E. M-file Environment (pages 32-34)

Appendix F. M-File Summary (pages 35-46)

Available on request (Macintosh MATLAB required)

A STUDY ON INTERFEROMETRIC TOMOGRAPHIC APPLICATION
OF
THE AERODYNAMIC EXPERIMENTAL FACILITIES AT WRIGHT LABORATORY

Soyoung S. Cha
Summer Research Faculty at Wright Laboratory
Department of Mechanical Engineering, University of Illinois at Chicago
P.O. Box 4348, Chicago, IL 60680

ABSTRACT

The Aeromechanics Division of the Flight Dynamics Directorate at Wright Laboratory conducts high-speed aerodynamic research in five in-house facilities. The experiments have depended heavily on classical surface-mounted probes. However, for investigation of modern aerodynamic problems and verification of computational codes, quantitative three-dimensional gross-field measurements are very desirable. Optical interferometric tomography can be very attractive in this aspect due to its noninvasiveness, instantaneous capture of a three-dimensional field, good measurement accuracy, and high spatial resolution. However, the practical application of the technique to existing facilities poses some challenges due to peculiar operating environments that produce ill-conditioned operational data. During a short period of his summer research program, the investigator carefully studied the existing facilities, quickly collected necessary information, and conducted evaluation. He then drew important results and corresponding conclusions in order to apply the interferometric tomographic technique to the aerodynamic research facilities.

1. Introduction

Interferometric tomography can be of great value, especially in high speed aerodynamic diagnostics, due to its noninvasiveness, instantaneous capture of a gross field, good measurement accuracy, and high spatial resolution. However, practical application of the technique to the existing wind tunnel facilities at the Wright Laboratory requires several problems to be thoroughly examined. During the short period of the summer research program, the investigator (Professor S. S. Cha) has carefully studied the operation conditions of the various facilities, quickly collected necessary information, and conducted fast hand-calculation. He then drew some important conclusions for implementing interferometric tomographic experiments with those existing facilities. The brief summary of his investigation procedures and results are summarized hereafter.

2. Facility Evaluation Scheme for Holographic Interferometric Tomography

Wind tunnel facilities are in general operated under harsh environments involving ambient and structural disturbances. These external noise sources, which are detrimental to interferometric experiments, cannot be completely eliminated without newly designing the system. When an acceptable external noise level is assumed, the most important factor for successful experiments is the facility capability to produce interferograms of a reasonable quality. Other elements of consideration, including simple facility modification for experiment accommodation and correction of refraction effects can be resolved without

difficulties.

2.1 Model Flows

The quality of interferograms to be produced depends on the flow fields to be measured. Real test fields can be very complex with much variation. Hence, we have chose only a few typical model fields for facility evaluation. The interferograms of other fields will more or less resemble these representative ones. Consequently, the interferometric behavior of the representative fields can provide valuable information on the facility capacity in producing quality interferograms. This approach is especially important for tomographic application where concerted planning and execution is very much required. When a drastically different flow field is tested, the procedures as outlined here can be followed for more accurate assessment: i.e., determination of test model sizes and facility operation conditions. In the model flow study, refraction effects are also evaluated to provide some guidelines in planning experiments.

The model flows, which are selected for facility evaluation and depicted in Figure 1, are: (1) two-dimensional external flow (2D-EF); (2) two-dimensional boundary layer flow (2D-BLF); (3) axisymmetric external flow (A-EF); (4) axisymmetric boundary layer flow (A-BLF). The axisymmetric models are sized such that the blockage is less than 15 percent of the test section area of the wind tunnel facility.

2.2 Facility Operation Conditions

Each facility operates with a relatively wide range of upstream flow conditions. In the evaluation calculation, the wide range of operation conditions was reflected except for subsonic and transonic

flows. For these flows, only a typical operation point was selected. Table 1 summarizes operation conditions employed for calculation of interferogram fringe number and refraction. It also shows the vibration severity of each facility.

2.3 Dimensions of Flow Models and Calculation Results

For the flow types depicted in Figure 1, and the operation conditions listed in Table 1, except the transonic/subsonic 2D-EF and A-EF, the flow fields and their corresponding interferograms can be determined, once the model parameters of θ , α , and W_f are provided as in Table 2. For those transonic/subsonic 2D-EF and A-EF models, their shapes need to be specified to determine the flow fields. Instead, the Mach number at a surface point where the fringe number was calculated was assumed to be 1.4 times greater than the free stream value as shown in Figure 1. With the additional information on W_f , D_g and D_∞ provided for these flows (see Table 2), the approximate fringe numbers and refraction effects could be estimated at the specified point.

L_f represents the distance where the flow field properties and interferometric data were calculated. It is equal to the model length for A-EF. It may be difficult to measure turbulent boundary layers. Consequently, L_f was chosen from L_{max} or the test section length for 2D-BLF and from the value corresponding to L_{max} or the model length for A-FLB, whichever is shorter.

For the given upstream flow conditions and model parameters as discussed thus far, the flow field properties, including δ , D_g and D_∞ at the distance L_f , were calculated and listed in Table 2. The number of interferometric fringes formed across the region indicated in Figure 1

were also calculated and summarized in Table 3. The number of fringes formed changes substantially when the operation conditions are varied as shown in Table 1. As indicated, the calculation was conducted at the location of L_1 if specified.

If the density gradient or the field size is large, refraction becomes prominent. The refraction effects can be computationally corrected after experiments or minimized by proper experiment arrangement. The significance of refraction effects is summarized in Table 4. The calculation was based on crude approximation: however, it can provide good guidelines. Refraction can also be significant at the expansion wave corner of 2D-EF. The distance d_e , where the interferogram can be influenced by refraction, is also tabulated in Table 4.

3. Conclusion and Summary

Based on the approximate calculation, the feasibility of producing appropriate interferograms was evaluated for individual flow models and facilities as summarized in Table 5. The evaluation criteria are as follows:

(1) The number of fringes should be sufficient enough above the acceptable external disturbance level to produce a good signal/noise ratio.

(2) The fringe spacing should be large enough for accurate detection of individual fringes.

The optimum number of fringes formed across a field, which satisfy the above criteria, may range from few to about 40. The quality of extracted interferometric data also depends on other factors including optical hardware and data reduction software. Hence, the evaluation

that is provided here cannot be ultimately conclusive. The structure as well as the floor vibration level, which was assessed during facility operation through physical touch, are also analyzed in the table.

By considering various facility characteristics and operating conditions, an attempt was made, as shown in Table 5, to rank the expected performances in interferometric application. For the individual facilities, the following specific comments can be made.

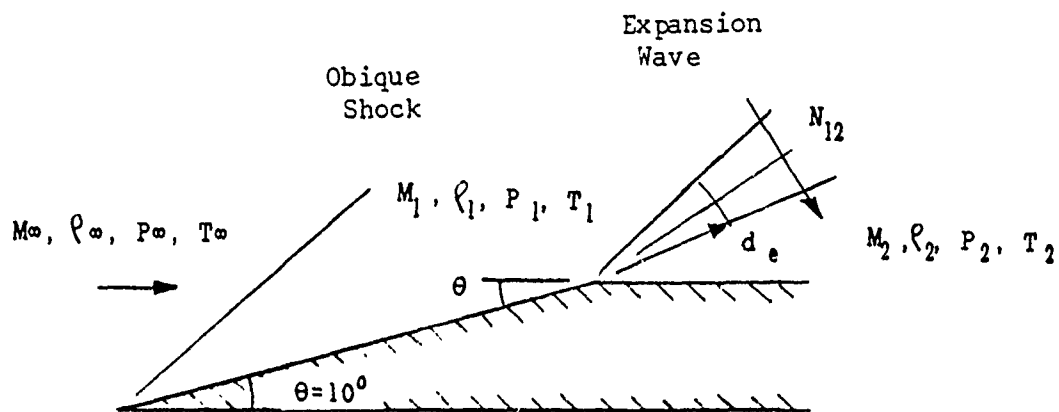
(1) M3: The current test-section windows, being a little small and off-centered, need to be redesigned for interferometric application. The solid ground floor is an advantage.

(2) M6: The facility allows a wide range of operation conditions and thus easy optimization of experiments. The large windows and vibration-less-sensitive ground floor are attractive for hologram recording. This may be the best candidate for interferometric application.

(3) HWT: This facility operates rather quietly, offsetting its drawback of being on the second floor. The calculation indicates that approximately one interferometric fringe can be formed for the two-dimensional flows. The multipath interferometric technique may enhance the signal to a sufficiently high level for this type of flows. It requires further investigation.

(4) SARL: The calculation demonstrates the feasibility of producing a reasonable number of fringes: however, severe vibration and less-rigid structure can limit the interferometric application without major modification of the structure and instrument support.

As indicated earlier, the current study adopted very simplifying approaches due to the time limitation and the complexity of problems. However, the discussions presented here should provide some valuable information for future experiment planning.



* M, ρ, P, T = Mach number, density, pressure, temperature

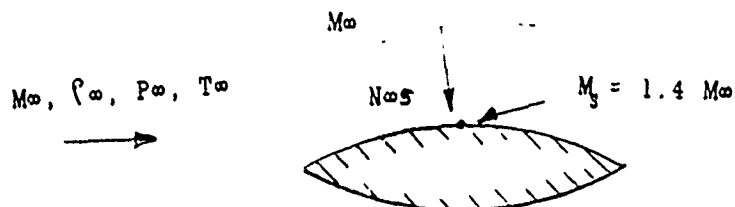
d_e = radius within which refraction becomes prominent at the expansion

θ = compression and expansion wave

N = number of fringes formed in an interferogram across the region indicated by subscripts

Subscripts $\infty, 1, 2$ = regions of the free stream, after the oblique shock, after the expansion wave

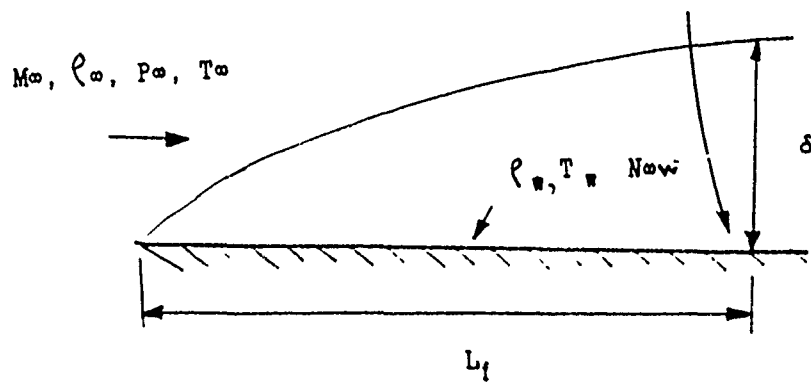
Supersonic Flow



*Subscript S = region just outside the boundary layer

Transonic or Subsonic Flow

(a) Two-dimensional external flow (2D-EF) model.

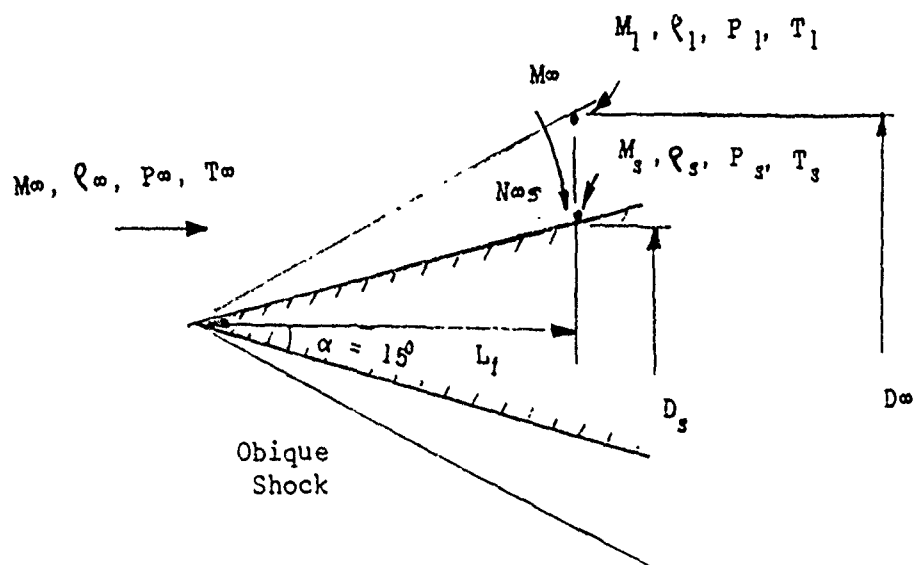


* L_f = length where the flow and fringe data are calculated

δ = boundary layer thickness

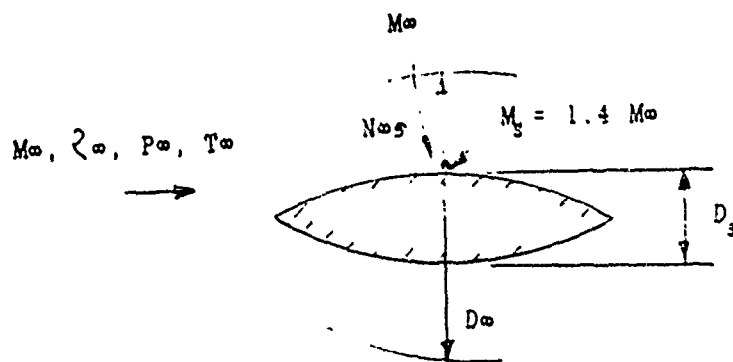
subscript w = wall

(b) Two-dimensional boundary-layer flow (2D-BLF) model.



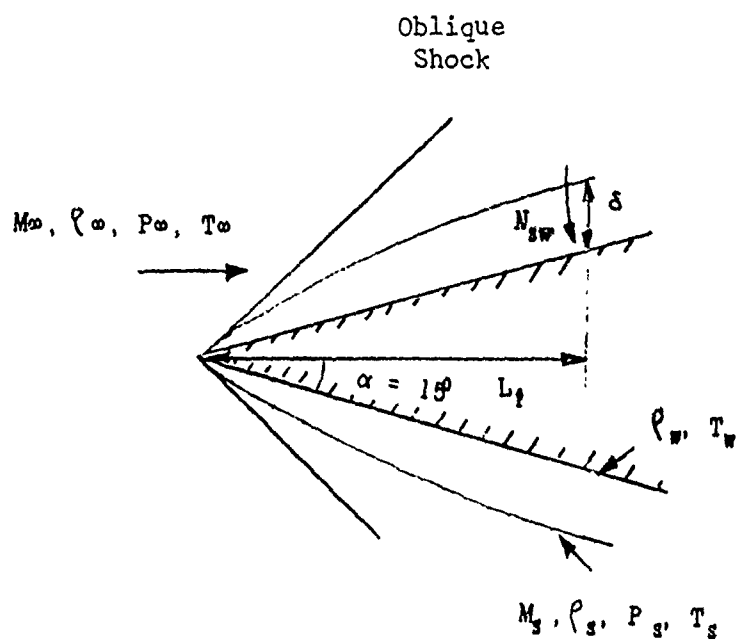
* D_∞, D_s = diameters of the free stream and model surface at L_1
 α = half cone angle

Supersonic Flow



Transonic or Subsonic Flow

(c) Axisymmetric external flow (A-EF) model.



(d) Axisymmetric boundary-layer flow (A-BLF) model.

Figure 1. Typical flow models selected for facility evaluation in interferometric measurements.

TABLE 1. Wind Tunnel Operation Conditions, Selected or Observed for Facility Evaluation in Interferometric Measurements

OPERATION CONDITION*	FACILITIES†				
	M3	M6	TGF		HWT
			Supersonic	Transonic	Subsonic
M _∞	3.0	6.0	3.0	0.85	0.85
Re/Ft	10 ⁷ ~10 ⁸	1.5X10 ⁶ ~3X10 ⁷	0.9x10 ⁵ ~3.67x10 ⁶	7.3x10 ⁶	2.0x10 ⁶
To (K)	477	1000		559	1800
Po (psia)	65~560	100~2100	0.69~27.8	25.7	7.64
Test Section (in)	8.2x8x23.2	12.4x28	24x24x30	18x15x30	24x24x30
	(H WxL)	(DxL)		(HxWxL)	
Facility Vibration**	I	I		H1	L
					(DxL)
					(HxWxL)
					VH1
					34-12
					530
					14.7
					120x84x180
					3.73x10 ⁵
					0.6x10 ⁶ ~1.0x10 ⁶
					12
					0.6

† : M3 = Mach 3 High Reynolds Number Facility
M6 = Mach 6 High Reynolds Number Facility
TGF = Trisonic Gasdynamic Facility
HWT = 20 Inch Hypersonic Wind Tunnel
SARL = Subsonic Aerodynamic Research Laboratory

*: M_∞ = Free Stream Mach Number, Re = Reynolds Number, To = Stagnation Temperature, Po = Stagnation Pressure,
H = Height, W = Width, L = Length, D = Diameter

**: VH1 = Very High, H1 = High, I = Intermediate, Lo = Low, Vlo = Very Low

TABLE 2. Dimensions of Flow Models from Which Fringe Numbers are calculated: See Table 1 and Figure 1.

FLOW MODELS*

FACILITIES

	M3	L16	TGF		HWT	SARL
			Supersonic	Transonic		
2D-EF: θ	10^0	10^0	---	---	10^0	---
W_f (m)	0.2	0.25	0.6	0.38	0.5	2.1
2D-BLF: W_f (m)	0.2	0.25	0.6	0.38	0.8	2.1
L_{max} (ft)	0.5-0.05	3.3-0.17	55-1.4	0.69	8.3-5	13.4
L_f (ft)	0.5-0.05	2.3-0.17	2.3-1.4	0.69	3.3	13.4
δ (mm)	5.8×10^{-1} - 5.8×10^{-2}	6.9 - 4.2×10^{-1}	12.8 - 1.6	0.48	3.2×10^{-2} - 2.5×10	9.2
A-EF: α	15^0	15^0	---	---	15^0	---
L_f (in)	6.5	7.0	18.6	---	14.4	---
D_g (in)	3.5	3.8	10.0	5.0	7.7	12.0
D_{∞} (in)	6.2	4.9	17.6	10.0	8.8	24.0
A-BLF:						
α	15^0	15^0	---	---	15^0	---
L_{max} (ft)	3.7×10^{-1} - 4.3×10^{-2}	2.5 - 1.2×10^{-2}	4.3×10^{-1}	---	3.1×10^{-2} - 1.9×10^{-2}	---
L_f (ft)	3.6×10^{-1} - 4.18×10^{-2}	5.8×10^{-1} - 1.2×10^{-2}	1.63 - 1.3	---	1.2	---
δ (mm)	2.2×10^{-1} - 2.5×10^{-2}	1.1 - 1.1×10^{-2}	4.7 - 0.61	---	2.5×10^{-1} - 1.9×10	---

* W_f = Depth of Field

L_{max} - Maximum Length to be a Laminar Boundary Layer

TABLE 3. Approximate Calculation of Number of Fringes at the Points Indicated in Figure 1 and Conditions Listed in Table 1 and 2, Respectively.

	FACILITIES						
	<u>M3</u>	<u>M6</u>	<u>TGF</u>		<u>HWT *</u>	<u>SARL</u>	
			<u>Supersonic</u>	<u>Transonic</u>	<u>Subsonic</u>		
2D-EF: N_{12} Nos	22-185	2.9-60	0.6-23	--- 51	--- 1.5-2.5	--- 111	
2D-BLF: N_{sw}	20-170	1.79-36	0.5-21	36	0.51-0.85	46	
A-EF: Nos	12-103	1.0-22	0.6-24	15	0.13-0.22	14	
A-BLF: N_{sw}	0.50-0.49	0.18-0.05	0.05-0.5	---	$0.88 \times 10^{-2} \sim 1.3 \times 10^{-2}$	---	34-14

*The inaccuracy of these approximate calculations may be very large for the HWT flows.

TABLE 4. Flow Models for Which Refraction Effects Needs to be Corrected in Interferometric Measurements: See Figure 1 and Table 1-2 for Approximate Calculation Conditions.

FLOW MODELS	FACILITIES					
	<u>M3</u>	<u>M6</u>	<u>TGF</u>		<u>HWT</u>	<u>SARL</u>
			<u>Supersonic</u>	<u>Transonic</u>	<u>Subsonic</u>	
2D-EF: de(mm)	15-49	6.9-32	4.3-27	---	---	7.3-9.4 ---
2D-BLF:	Yes	No-Yes	No-Yes	Yes	Yes	No Yes
A-EF:	No	No	No	No	No	No
A-BLF:	No	No	No	---	---	No ---

*: de = Distance from the corner within which refraction of the expansion wave needs to be considered (see Fig 1)
 Yes = Consideration required.
 No = Not required.

TABLE 4. Flow Models for Which Refraction Effects Needs to be Corrected in Interferometric Measurements: See Figure 1 and Table 1-2 for Approximate Calculation Conditions.

	FACILITIES					
	<u>M3</u>	<u>M6</u>	<u>TGF</u>		<u>HWT</u>	<u>SARL</u>
			<u>Supersonic</u>	<u>Transonic</u> <u>Subsonic</u>		
2D-Σ: de (mm)	15~40	6.9~32	4.3~27	--- ---	7.3~9.4	---
2D-BLF:	Yes	No~Yes	No~Yes	Yes Yes	No	Yes
A-EF:	No	No	No	No No	No	No
A-BLF:	No	No	No	--- ---	No	---

*: de = Distance from the corner within which refraction of the expansion wave needs to be considered (see Fig 1)
 Yes = Consideration required.
 No = Not required.

TABLE 5. Evaluation of the Facility Appropriateness for Interferometric Measurements Based on Feasibility of Proper Interferometric Data Acquisition: See Fig 1 and Tables 1-4.

FLOW MODELS

FACILITIES *

	<u>M3</u>	<u>M6</u>	<u>TGF</u>			<u>HWT</u>	<u>SARL</u>
			<u>Supersonic</u>	<u>Transonic</u>	<u>Subsonic</u>		
(1) Ability to produce appropriate interferograms under no external disturbances.							
2D-EF:	A~S	S~A	S~A	A	A	F**	A
2D-BLF:	S~N	S~A~S	N~A	S	A	F**	A
A-EF:	A~S	S~A	S~A	A	A	N	A
A-BLF:	N	N	N	---	---	N	---
(2) Vibration:	A	A	S	S	S	A	N
(3) Overall Ranking for Interferometric Tomography†	A	A	S	F	F	F	N

*: A = Application Recommended, S = Skeptical, F = Further Study Required, N= No Recommendation

**: For HWT, the Multipath Interferometric Technique is Suggested as a Trial to Increase Fringe Numbers and thus Measurability.

†: By no Means, Rigorous Ranking is Possible: However, this can Provide Some guidelines

(This Page Intentionally Left Blank)

**EVALUATION OF THE ANALYTICAL DESIGN PACKAGE (ADP)
FOR FRAMELESS TRANSPARENCY PROGRAM**

David M. Russell, Ph.D. Student
Joe Chow, Assistant Professor
Clarkson University, Potsdam, New York

Acknowledgment

We are very grateful to Group Leader Robert McCarty, Program Leader William Pinnel, and Aerospace Engineer Kevin Roach for their support and for providing us with a comfortable working atmosphere. In particular, we would like to thank Kevin for his help and guidance throughout this research period and efforts in communicating our findings to General Dynamics. The Flight Dynamics Laboratory and the Air Force Office of Scientific Research are also appreciated for the sponsorship of this research. Finally, we want to thank the people of the Aircrew Protection Branch, who have made this summer a rewarding and fun experience.

Abstract

The increasing demand for more efficient transparency design, low cost manufacturing, and longer service life has lead to the concept of frameless transparencies for high performance fighter and trainer type aircraft. The frameless transparency program investigates the use of a transparent panel which directly interfaces with the aircraft structure without using a frame. Computer programs, such as Patran, MAGNA, STAPAT, and C-Mold, have been used to create, assess and optimize traditional transparency designs. However, these stand alone programs can be difficult to run, as the user is expected to be quite proficient with all procedures for running these programs. To aid in the transparency design procedure, an Analytical Design Package, ADP, is being developed by General Dynamics (GD), which integrates these computer programs into one module. The main

objective of this project is to test and validate the ADP, and ensure that it is easier to use compared to using the stand alone analysis programs. This involves the evaluation of the ADP's user interface and translation programs. The procedures used in evaluating the ADP and the results of the evaluation are documented in this report.

1. Introduction

Presently the windows and canopies for high performance fighter and trainer type aircraft are made of transparency assemblies which, consist of transparent panels mounted in reinforcing metal frames. The frame serves as an interface between the transparent panel and the aircraft structure. The manufacture of these transparency assemblies involves heating previously extruded flat sheets and forcing them to conform to a mandrel, or tool, which has the desired contour. After going through the proper heating cycles, the desired shape is achieved and retained. The transparent panel is then edge trimmed and mounted in a frame. The presence of the frame reduces the structural integrity and dramatically increases the cost of manufacturing and maintenance. The manufacture and implementation of a frameless transparency program would result in projected savings of over \$600M for the F-16 fleet alone. But, the cost of molds for frameless transparencies requires that the designers fully investigate a design before a mold is made.

New injection molding processes have demonstrated potential for directly forming transparencies from plastic resins with attachment hardware directly integrated into a molded transparency [1]. These new processes form frameless transparencies by injecting molten resins into a high precision mold. This fabrication method allows for high precision thickness control, achieving superior optical quality in viewing areas, edge reinforcement, and accommodation of transparency to aircraft

interface. In order to develop and validate this process, a frameless transparency program has been initiated by the Aircrew Enclosures Group at Wright Laboratory (WL). An integral part of this project is the ADP, which was developed to aid in producing a frameless transparency design.

The ADP is a design tool which integrates the necessary analysis tools, used to iteratively converge on a transparency design. It is capable of producing a frameless transparency design with integrated aircraft interface, mold design, and molding process parameters. The four major areas of the transparency design process are unified by the ADP, these areas are; computer aided design (CAD), structural finite element analysis, aerodynamic heating and transient thermal analysis, and injection molding analysis. The programs used in these areas are, Patran, MAGNA (Materially and Geometrically Nonlinear Analysis), STAPAT (Specific Thermal Analyzer Program for Aircraft Transparencies), and C-Mold, respectively. The integration of the different analysis programs allows the user to converge on a design quickly, reducing the time and cost required to produce a frameless transparency design.

2. Research Objective

The objective of this research is to test and evaluate the ADP. This package, designed and written by General Dynamics (GD), integrates the analysis programs used by the Aircrew Enclosure Group at Wright Laboratory, (WL/FIVR). The analysis programs incorporated in the ADP have been validated by the original software developers and/or WL. Therefore, the emphasis of this project is to evaluate the ADP's user interface, translation programs, and the general overall operation of the package. The final goal of this project is to ensure that the ADP is user friendly, operates smoothly, and correctly shares data between the various analysis programs.

3. ADP Evaluation Procedure

The evaluation of the package was divided into three major phases;

1. Test the menu system and user interface,
2. Check the data translation programs, and
3. Run a transparency through a complete design cycle in the ADP.

The activities during each of these phases are described in the following subsections of this report. The ADP is still in the development stage and had to be assessed accordingly. This required an approach which evaluated and tested the high level functionality, (user interface), before the low level translating programs. The idea being that, it doesn't matter if the data can be translated between programs if the user can't run the programs. As errors were encountered, Software Incident Reports, SIRs, were created and passed on to GD, where the problems could be fixed.

The core program of the ADP is the Executive Control Processor (ECP) program. The ECP is the root menuing system which consolidates the four main computer programs, (Patran, MAGNA, STAPAT, and C-Mold), the file translators, and a materials database manager, (FTPMAT). The ECP organizes related options, according to these tasks, into a tree structure menu system, and, can be run using a textual or graphical mode. The graphical mode of operation was used exclusively through this evaluation procedure.

3.1 Testing the ADP's Menu System

The first goal in evaluating the ADP was to make sure that the menu system is easy to use, well organized, and self explanatory. Most of this evaluation was performed on ADP Version 1.1, (ADP V1.1), but continued through the later versions.

Evaluation of the ADP V1.1 began (1 July 91), by traversing all possible menu paths, without running any analysis. Any difficulties and errors encountered were documented. These errors were organized into a report which was sent on to GD (11 July 91). This report resulted in 48 SIRs, of which 13 still remain unresolved (Sept 91). As later versions of the ADP were delivered, all the SIRs which remained open were checked to see if they had been resolved. Due to the vast extent of problems with the ECP portion of the ADP, it was hard to proceed with evaluating the ADP further.

When ADP V1.2 was delivered (8 July 91), it was evaluated in a manner similar to ADP V1.1. This was done to see which problems had been resolved and locate any new errors. This evaluation resulted in the creation of 11 SIRs (17 July 91), of which 4 still remain unresolved (Sept 91). The delivery of ADP V1.2a (19 July 91), was a vast improvement over the previous versions and allowed for greater testing of the ADP's functionality, e.g. data translations.

3.2 Data Translation Verification

The main objective of this evaluation phase was to test the ADP's data translation programs. One of GD's major efforts, in the development of the ADP, is the development and/or modification of file translators between the various analysis programs. The ADP uses Patran for the and post processing of the analysis models. By running various analysis programs on sample models, created in Patran, one can find out whether or not the file translators between various analysis programs are operating correctly.

Two models were used for testing the ADP's ability to set up an analysis, run the analysis, and then review the results. One of the models used for testing at this level was a confirmation frameless transparency,

CFT. The other model was a much simpler model, DMR. This model was a crude estimation of the CFT. These models were used to test the various data translation tasks within the ADP because, the analysis would run quicker and the cause of any problems would be easier to locate. In order to test all of the translating programs, it was necessary to perform the analyses and subsequent post processing of the results. The validity of the results obtained was not as important as demonstrating that the ADP was able to process the data. The general procedure for running MAGNA, STAPAT (STAHET and TAP), and C-Mold programs inside the ADP is as follows;

- (1) On Iris workstation prepare the analysis model inside Patran.
- (2) Prepare input files for the appropriate analysis programs.
- (3) Run the analysis.
- (4) Convert the analysis results to a Patran format.
- (5) Review results inside Patran.

In the case of running MAGNA and STAPAT one had to also be concerned with the data transfer between the Iris Workstation and the Cray computer, where the MAGNA and STAPAT programs reside.

Evaluation of the ADP translation programs began with version 1.2, and continued with version 1.2a. The unresolved short comings of the ADP V1.1 made evaluation at this level difficult. Even with the problems that still existed in the ECP portion of the ADP, it became obvious that GD had put much of their effort into the data translation between the different analysis codes. After the arrival of ADP V1.2a only 12 new SIRs were written (16 Aug 91) of which only 3 remain unresolved (Sep 91).

The evaluation of the ADP up through version 1.2a resulted in a total of 71 SIRs (16 Aug 91). Of these SIRs, 20 still have to be resolved. Of these unresolved SIRs, 7 are considered to be serious. There has been much

improvement in the ADP and it is nearly useable at this point in the evaluation. Two areas of investigation remain. The first area that needs to be worked out is the use of a centralized materials database. This problem grew to be such a large problem, that it quickly became beyond the scope of this project. Another problem is the use of Patran Control Language, PCL, to aid in post-processing. Due to the extent of problems early in the evaluation of the ADP, and the late inclusion (Aug 91) of the PCL into the ADP, not enough effort could be devoted to testing the PCL.

During this phase of evaluating the ADP, a draft of the ADP Users Manual was proof read. Comments have been made on this working draft of the ADP User Manual, which was then sent to GD (Sept 91). This was done so that any confusion in using the ADP could be clarified and incorporated into the User's Guide. These suggestions and comments are to be incorporated into the next draft of the ADP User's Guide.

3.3 F-16 Trial Data Set

With delivery of ADP V1.2b (16 Aug 91), most of the pressing problems have been fixed and the ADP is 'usable'. At this time a full scale F-16 transparency model, which is significantly larger than the CFT models, was used to further evaluate the ADP. This geometry was run through one complete design iteration, using the ADP. It was shown that the temperature results from TAP and the pressure results from STAHET can be superimposed on the MAGNA model, and that the displacements and stresses due to the temperatures and pressures encountered during flight conditions can then be calculated. The F-16 trial data set, provided by GD, consists of two data files, a forebody geometry and a canopy geometry. These two files contain all the geometrical data required for generating the necessary meshes for a complete design cycle.

The design process began with creating the forebody mesh for STAHET and a canopy mesh suitable for TAP. STAHET and TAP were then run and the results viewed in Patran. (Figures depicting various results are at the end of this report.) Figure 1 shows the STAHET results in the area of the forebody where the canopy resides, and Figure 2 shows the TAP results at the end of a simple flight mission. (The left side of Figure 2 shows the canopy with the front portion cut away.) STAHET and TAP were run completely through the ADP, with relatively little difficulty. These results were then applied to a MAGNA mesh of the same canopy.

MAGNA requires a different mesh than TAP, so a new mesh had to be created. After creating a new mesh for MAGNA, simple boundary conditions were applied. The canopy centerline was restrained to model the symmetry and the edge was clamped. An appropriate loading condition was then imposed. (6 psi was applied to the interior surface, to simulate cabin pressure.) The STAHET pressures and the TAP temperatures were then applied to the model using the PCL programs STAHET_MAGNA and TAP_MAGNA, respectively. This is when the most trouble was encountered, during this level of evaluation of the ADP. Approximately 6 new serious SIRs were created as a result of these PCL programs. After quite a bit of side stepping and a few tricks, (to resolve problems with the PCL), the STAHET and TAP results were successfully applied to the MAGNA mesh. At this point static analysis of the MAGNA mesh was performed. Figure 3 shows the shaded contours of the deflections as a result of this static analysis.

With the static analysis performed, the next task was to perform a birdstrike analysis. (MAGNA has the capability of modeling the highly nonlinear effects of a bird striking a canopy at flight velocities.) Before performing this analysis, the proper time integration step size had to be determined. This was accomplished by running a frequency analysis in MAGNA. (The second mode shape from this frequency analysis is shown in

Figure 4.) With this frequency analysis performed, the proper step size can be determined and used for the birdstrike analysis. This analysis was then performed, and the results, (von Mises stresses on the front portion of the deformed model), at 0.001 seconds into the birdstrike are displayed in Figure 5. Other than the problems encountered in translating the TAP and STAHET results into the MAGNA mesh, the only major problem with running MAGNA within the ADP is the omission of the material properties from the MAGNA input deck. For this analysis, the material properties were input manually.

With the MAGNA analysis complete the only thing left to test was C-Mold. The testing of C-Mold was the easiest part of the ADP's evaluation. Other than creating the model in Patran, everything is done entirely within C-Mold, including material selection. C-Mold however, requires a completely different mesh made entirely of shell or plate elements. Evaluation of C-Mold during this phase was limited to the translation of the mesh, created in Patran, into C-Mold.

Testing the ADP during this phase of the evaluation resulted in the creation of 24 new SIRs (Sept 91). Of these SIRs, 5 are related to the PCL and 5 to the materials database. Of these 24 SIRs, 18 are considered to be serious.

4. Concluding Remarks:

The evaluation of the ADP's user interface, translating programs, and overall functionality has resulted in a total of 95 SIRs. Of these 95 SIRs, 44 remain to be resolved (Sept 91). 25 of these unresolved SIRs are considered to be serious. The materials database accounts for the largest part of these open SIRs, with 10 to be resolved, 6 of which are serious.

The PCL programs, e.g. STAHET_MAGNA and TAP_MAGNA, account for 7 more of the unresolved serious SIRs. The appendix of this report contains a summary/status document, which was created to aid in tracking the SIRs.

During the period of this evaluation (1 July through 6 Sept 91), the usability of the ADP has been greatly improved. The status of the ADP usability is summarized by the following statements;

1. The ECP is useable and nearly complete.
2. STAHET and TAP can be run with relatively little difficulty.
(Most of the problems should be easily fixed.)
3. Only minor problems exist in translating a Patran mesh into C-Mold. (C-Mold functionality within the ADP was not further tested.)
4. The PCL needs to be more completely tested. It is a source of many problems and confusion.
5. MAGNA can not be run using the ADP. The user must find ways to resolve the serious problems with the PCL and materials database.
6. The materials database manager FTPMAT is the greatest source of problems. (This area needs to be completely investigated in order to come up with an alternative solution.)
7. When the unresolved SIRs are fixed, development of the ADP should be virtually complete.

Compared to stand alone analysis programs, a fully operational ADP has the following advantages;

- 1) It is an integrated package, thus allowing the user to move from one analysis program to another easily.
- 2) The ADP is menu driven and most of the options are fairly self explanatory.
- 3) The procedure for running an analysis is significantly simplified. Most of the steps, which are normally done manually,

have been automatd by the ADP.

- 4) In general, the user needs to know less about the individual analysis programs, in order to run them.

Although currently there are many problems with the ADP it has shown a lot of potential for becoming an excellent design tool, capable of producing a frameless transparency design. Patran, MAGNA, STAHET and TAP, and C-Mold are successfully unified by the ADP. Integration of the different analysis programs allows the user to converge on a design quickly. And, a designer could be quickly and easily trained to use the ADP when the ADP becomes fully functional. The general feeling about the ADP is; When the remaining SIRs and the materials database problems are resolved, WL/FIVR will have a design tool which will greatly aid in the design process of a frameless transparency.

References:

1. Fuller, D. B., "Direct Forming Processes for Aircraft Transparencies", Loral Defense Systems-Arizona, Conference on Aerospace Transparency Materials and Enclosures Vol. 1, April 1989, pp 522-554, WRDC-TR-89-4044.

Appendix:

WL/FIVR SIR STATUS SUMMARY

Legend --- S# -- Suggested changes or non-critical errors.
C# -- Serious errors which must be corrected.
E# -- CRITICAL errors.
FIVR SIR# -- FIVR's SIR tracking number.
WL# -- GD's # for tracking WL originated SIRs.

S3 ---- Closed. WL1.1.27, WL1.1.29
S4 ---- Closed. WL1.1.3
S5 ---- Closed. WL1.1.5
S6 ---- Closed. WL1.1.10
S7 ---- Closed. WL1.1.29
S8 ---- Closed. WL1.1.32, WL1.1.39
S9 ---- Closed.
S11 ---- Closed.
S12 ---- Closed. WL1.1.41
S13 ---- Closed. WL1.1.44
S14 ---- Closed. WL1.1.45
S16 ---- Closed.
S17 ---- Closed. WL1.1.51
S18 ---- Closed. WL1.1.53
S19 ---- Closed. WL1.1.53
S20 ---- Closed. WL1.1.55
C1 ---- Closed. WL1.1.6, WL1.1.36
C2 ---- Closed. WL1.1.9, WL1.1.21, WL1.1.38
C3 ---- Closed. WL1.1.28
C4 ---- Closed. WL1.1.14
C5 ---- Closed. WL1.1.20
C6 ---- Closed. WL1.1.25
C7 ---- Closed.
C9 ---- Closed. WL1.1.33
E1 ---- Closed. WL1.1.66
E2 ---- Closed. WL1.1.67
E3 ---- Closed. WL1.1.26
E4 ---- Closed. WL1.1.68
E5 ---- Closed. WL1.1.29
E6 ---- Closed. WL1.1.30
E7 ---- Closed. WL1.1.34
E8 ---- Closed. WL1.1.37
E9 ---- Closed. WL1.1.42
E10 ---- Closed. FIVR SIR16, WL1.2.78
E11 ---- Closed. WL1.1.54

S1 ---- OPEN. Use of '...'.
FIVR SIR17, WL1.2.77, 1.1.1
S2 ---- OPEN. Use of '...'.
FIVR SIR17, WL1.2.77, WL1.1.2, WL1.1.4, WL1.1.11,
WL1.1.31, WL1.1.35, WL1.1.48

S10 ---- OPEN. A centralized default database is to be established.
FIVR SIR18, WL1.2.63
S15 ---- OPEN. FTPMAT Browse material, menu order.
WL1.1.46
S24 ---- OPEN. Each window should have its own title.
FIVR SIR15, WL1.2.80
S25 ---- OPEN. PATMAG should reference MAGNA variable names.
WL1.1.71
S26 ---- OPEN. Work directory name to be put on the second line of the
status/input box.

FIVR SIR4, WL1.2.84

S27 --- OPEN. NEXT and PREV window debate settled through the reorganization of PATSTAHET data input. Specifically submenus for Mission Data.

FIVR SIR10, WL1.1.8, WL1.1.17, WL1.1.43, WL1.2.79

C8 ---- OPEN. Cancel instability in FTPMAT.

WL1.1.40

C10 --- OPEN. Some kind of filter is needed. Even backspaces are treated as separate characters.

FIVR SIR19, WL1.1.12, WL1.1.22, WL1.2.76, WL1.2.99

C11 --- OPEN. FTPMAT filename defaults use #'s.

WL1.1.47

C12 --- OPEN. List of files is wrong.

FIVR SIR9, WL1.2.81

C13 --- OPEN. Cancel doesn't work. File 'c' is used, etc..

FIVR SIR8, WL1.2.82

----- New Errors V1.2 -----

E12 --- Closed. WL1.2.49

E13 --- Closed. FIVR SIR1, WL1.2.72

E14 --- Closed. FIVR SIR2, WL1.2.71

E15 --- Closed. FIVR SIR5, WL1.2.85

E16 --- Closed. FIVR SIR12, WL1.2.65

E17 --- Closed. FIVR SIR13, WL1.2.70

E18 --- Closed. FIVR SIR14, WL1.2.69

S21 --- OPEN. Input of time for mission, in PATTAP, it is unclear.

FIVR SIR6, WL1.2.66

S28 --- OPEN. PATCMOLD and PATCCOOL are the only two places the option of inputting the Neutral file name is not given.

FIVR SIR3, WL1.2.87

S29 --- OPEN. Make changing directories permanent.

FIVR SIR7, WL1.2.83

E19 --- OPEN. FTPMAT Memory Fault coredump.

FIVR SIR11, WL1.2.64

----- New Errors V1.2a -----

S22 --- Closed. FIVR SIR30, WL1.2.96

S23 --- Open/Closed. Source code. FIVR SIR22, WL1.2.62

E20 --- Closed. FIVR SIR21, WL1.2.88

E21 --- Closed. FIVR SIR26, WL1.2.93,

E22 --- Closed. FIVR SIR27, WL1.2.90, WL1.2.90

E23 --- Closed. FIVR SIR29, WL1.2.95

E24 --- Closed. FIVR SIR31, WL1.2.97

E25 --- Closed. FIVR SIR32, WL1.2.98

E26 --- Closed. FIVR SIR23

S30 --- OPEN. In PATTAP there is a message window that 'flys' by and can't be read. To be mentioned in the manual.

FIVR SIR24, WL1.2.91

S31 --- OPEN. Separate options for running just TAP or just STAHET are to be created.

FIVR SIR25, WL1.2.92

C14 --- OPEN. Monitoring jobs using user 'ADP'.

FIVR SIR20, WL1.2.75

----- New Errors V1.2b -----

S32 --- OPEN. File names used in side C-Mold to be mentioned in manual.
FIVR SIR35

S33 --- OPEN. Incorporate resolution of FIVR SIR38 in the manual.
FIVR SIR39

S34 --- OPEN. Improve FTPMAT data entry.
FIVR SIR40

S35 --- OPEN. Invalid TAPPAT error message.
FIVR SIR41

S36 --- OPEN. STAHET input deck title ends on second line.
FIVR SIR52

S37 --- OPEN. Wrong message after ending C-Mold.
FIVR SIR55

C15 --- OPEN. Parent window processes locked out.
FIVR SIR33

C16 --- OPEN. C-Mold file name inconsistency.
FIVR SIR34

C17 --- OPEN. STAHET_MAGNA needs to delete FIELD 1.
FIVR SIR44

C18 --- OPEN. Existence of FIELD 1 causes STAHET_MAGNA to bomb.
FIVR SIR46

C19 --- OPEN. STAHET_MAGNA applies pressures to nodes instead of faces.
FIVR SIR48

C20 --- OPEN. Extraneous data in PATSTAHET menus.
FIVR SIR53

C21 --- OPEN. ISMO not always 1.
FIVR SIR54

C22 --- OPEN. Invalid C-Mold option.
FIVR SIR56

E27 --- OPEN. STAHET control deck missing ALT. and MACH data.
FIVR SIR36

E28 --- OPEN. FTPMAT is extremely unstable.
FIVR SIR37

E29 --- OPEN. FTPMAT. The units conflict between analyses.
FIVR SIR38

E30 --- OPEN. TAPPAT unable to process nodal data.
FIVR SIR42

E31 --- OPEN. TAP_MAGNA only interpolate onto the "rim", and then is
unable to process the data.
FIVR SIR43

E32 --- OPEN. STAHET_MAGNA error mapping because of streamlines.
FIVR SIR45

E33 --- OPEN. STAHET_MAGNA doesn't work if other temps already exist.
FIVR SIR47

E34 --- OPEN. No material data is put into the MAGNA input deck.
FIVR SIR49

E35 --- OPEN. TAP RENUMBER renumbers elements wrong.
FIVR SIR50

E36 --- OPEN. NSL not put into STAHET input deck.
FIVR SIR51

Summary of OPEN/Closed SIRs.

	S#	C#	E#	Total
Open	13	6	1	20
Pre V1.2b Closed	18	8	25	51
Totals				
Grand	31	14	26	71
New Problems V1.2b	6	8	10	24
Total Open Problems	19	14	11	44
Total Closed Probs.	17	8	25	51
Grand Total	37	22	36	95

Figures:

Figure 1. STAHET temperature results of the forebody in the region of the canopy.

Figure 2. TAP temperature results of a canopy after a simple flight mission.

Figure 3. MAGNA static deflections due to applied STAHET pressures and TAP temperatures.

Figure 4. MAGNA frequency analysis results, the 2nd mode shape.

Figure 5. MAGNA birdstrike results. 0.001 seconds into the strike of a 4 pound bird at 500 knots.

A MASSIVELY PARALLEL ALGORITHM FOR LARGE-SCALE NONLINEAR COMPUTATION

S. K. Dey
Mathematics Department
Eastern Illinois University
Charleston IL 61920

Abstract

A perturbed functional iterative scheme (PFIS) discussed in [1] is now modified with massive parallel computation for large-scale nonlinear models. Several implicit finite difference models were successfully solved by this technique. However, the algorithm is yet to be tested on a massively parallel machine like a CM2 machine. The algorithm is fully vectorized and is called PVPFI (Parallel Vectorized Perturbed Functional Iteration). While solving implicit finite difference equations PVPFI eliminates inversions of block matrices for 2D models and block-of-block matrices for 3D models which are generally required for most implicit finite difference solvers. Furthermore, PVPFI minimizes linearization, reduces the number of arithmetic operations significantly and generates a high degree of accuracy. With appropriate number of parallel processors, the algorithm should converge quadratically.

1. The Basic Concept

Let us consider an equation

$$f(x) = 0$$

Let us represent this equation as $x = g(x)$.

Picard's iteration is

$$x_{k+1} = w_k + g(x_k), \quad k = 0, 1, 2, \dots$$

Let us introduce a perturbation parameter and write a new iterative scheme as

$$x_{k+1} = w_k + g(x_k)$$

Where w_k = the value of the perturbation parameter at the k th level of iteration.

Let us assume that this method converges after $k+1$ iterations. Then,

$$w_k + g(x_k) = g(w_k + z_k), \quad z_k = g(x_k).$$

Let us assume that w_k is small and terms of the order w_k^2 may be neglected. Then, expanding the right side by Taylor's series and neglecting terms of the order w_k^2 , we get

$$w_k + g_k = g(g_k) + w_k \cdot g'(g_k).$$

giving

$$w_k = \frac{g(g_k) - g_k}{1 - g'(g_k)}.$$

Thus the computational algorithm is : (at some kth iteration)

#1 With x_k known, compute $g_k = g(x_k)$

#2 compute $w_k = \frac{g(g_k) - g_k}{1 - g'(g_k)}.$

#3 compute $x_{k+1} = w_k + g_k.$

The method fails if $g'(g_k) = 1$. The method converges if at some k

$$w_k < \xi$$

Where ξ is positive and arbitrarily small.

This algorithm is a combination of Picard's method and Newton's method.

2. The Algorithm (PVPFI)

The same concept may now be extended to solve large-scale nonlinear models with massive parallel computations.

Let us consider a two-dimensional nonlinear finite difference model expressed as

$$F_{ij}(U) = 0 \tag{2.1}$$

$$i = 1, 2, \dots, I \quad ; \quad j = 1, 2, \dots, J$$

$$U = (U_1 \ U_2 \ \dots \ U_I)^T$$

$$U_i = (U_{i1} \ U_{i2} \ \dots \ U_{iJ})^T$$

Our objective is to solve (2.1) for U . The subscript i stands for the number of points along the x-axis and the subscript j stands for the number of points along the y-axis. Thus, in the computational field, there are I no. of points along the x-axis and j -no. of points along the y-axis.

Let us develop now a parallel vectorized perturbed functional iteration (PVPFI) to solve (2.1).

Let us express (2.1) as

$$U_{ij} = G_{ij}(U) \quad (2.2)$$

$$i = 1, 2, \dots, I ; \quad j = 1, 2, \dots, J$$

In terms of the elements of the block-vector U (2.2) may be expressed as:

$$U_i = G_i(U) \quad (2.3)$$

This notation signifies that for each $i = 1, 2, \dots, I$ we solve a unique nonlinear system for $j = 1, 2, \dots, J$. And this may be done in parallel. This means that if we have a machine with I no. of parallel processors, each processor will solve for U_i which is a vector with J number of components.

That means the i th processor will solve for $U_{i1}, U_{i2} \dots U_{iJ}$

($i = 1, 2, \dots, I$). We also note that U is a vector with a total number of components equal to (IJ) . Thus, each subsystem (2.3) is an underdetermined system.

Let us assume that at the k th iteration we know U^k (U^k = values of U at the k th iteration; here k is not an exponent).

Let $G_{ij}^k = G_{ij}(U^k)$.

Introducing perturbations, let us express an iterative scheme as:

$$U_{ij}^{k+1} = w_{ij}^k + G_{ij}^k \quad (2.4)$$

where w_i^k = the perturbation parameter to be computed.

Let $G^k = (G_1^k \ G_2^k \ \dots \ G_I^k)^T$

Let us assume that the method has converged after k iteration. Let U_i^* = the root.

$$\text{Then } U_i^k = U_i^{k+1} = G_i^k = U_i^* = G_i^*.$$

Then from (2.4)

$$W_{ij}^k + G_{ij}^k = G_{ij}(G_1^k, G_2^k, \dots, G_{i-1}^k; W_{i1}^k + G_{i1}^k, W_{i2}^k + G_{i2}^k, \dots, W_{iJ}^k + G_{iJ}^k; G_{i+1}^k, \dots, G_I^k) \quad (2.5)$$

Assuming that terms of the order W_{ij}^2 may be neglected and expanding the rightside of (2.5) by Taylor's theorem, we get

$$W_{ij}^k + G_{ij}^k = G_{ij}(G^k) + \sum_{m=1}^J W_{im}^k \frac{\partial G_{ij}(G^k)}{\partial U_{im}} \quad (2.6)$$

$$\text{where } G_{ij}(G^k) = G_{ij}(G_1^k, G_2^k, \dots, G_I^k)$$

From (2.6)

$$\begin{aligned} - W_{i1}^k \frac{\partial G_{ij}(G^k)}{\partial U_{i1}} - W_{i2}^k \frac{\partial G_{ij}(G^k)}{\partial U_{i2}} - \dots + (1 - \frac{\partial F_{ij}(G^k)}{\partial U_{ij}}) W_{ij}^k \\ - \dots - W_{iJ}^k \frac{\partial G_{ij}(G^k)}{\partial U_{iJ}} = G_{ij}(G^k) - G_{ij}^k \end{aligned}$$

This equation holds for $j = 1, 2, \dots, J$ for each i . (2.4)

Thus, we have a linear system given by

$$(I - A_i) W_i^k = G_i(G^k) - G_i^k \quad (2.5)$$

$$\text{Where } A_i = \begin{bmatrix} \frac{\partial G_{i1}(G^k)}{\partial U_{i1}} & \frac{\partial G_{i1}(G^k)}{\partial U_{i2}} & \dots & \frac{\partial G_{i1}(G^k)}{\partial U_{iJ}} \\ \frac{\partial G_{i2}(G^k)}{\partial U_{i1}} & \frac{\partial G_{i2}(G^k)}{\partial U_{i2}} & \dots & \frac{\partial G_{i2}(G^k)}{\partial U_{iJ}} \\ \vdots & \vdots & \ddots & \vdots \end{bmatrix}$$

$$\begin{array}{c}
 \vdots \\
 \left[\begin{array}{ccc}
 \frac{\partial G_{iJ}(G^k)}{\partial U_{i1}} & \frac{\partial G_{iJ}(G^k)}{\partial U_{i2}} & \dots \frac{\partial G_{iJ}(G^k)}{\partial U_{iJ}}
 \end{array} \right] \\
 i = 1, 2, \dots, I.
 \end{array}$$

Each A_i is a $J \times J$ Matrix.

Solving (2.5) we get

$$W_i^k = (I - A_i)^{-1} (G_i(G^k) - G_i^k). \quad (2.6)$$

Thus, if there are I number of processors, each processor will invert a $J \times J$ matrix and compute W_i^k .

Thus, the algorithm is:

Assuming that at some k th iteration U^k is known,

Step #1. Compute $G_i(G^k)$.

From the shared memory location, the (IJ) number of values of G^k will be used by each processor and then each i th processor will compute $G_i(G^k)$.

Then $B_i^k = G_i(G^k) - G_i^k$

will be computed for $i = 1, 2, \dots, I$.

Step #3 Then each i th processor will compute (in parallel)

$$W_i^k = (I - A_i)^{-1} B_i^k \quad (2.7a)$$

$$U_i^{k+1} = W_i^k + G_i^k \quad (2.7b)$$

$i = 1, 2, \dots, I$

Let us now take an example and illustrate the use of this algorithm.

An Illustration

$$\text{Solve } U_t + UU_x + UU_y = 0. \quad (2.8)$$

$$U(x, y, 0) = 1 + 0.5(x+y)$$

$$U(0, y, t) = \frac{1 + 0.5y}{1 + t}$$

$$U(x, 0, t) = \frac{1 + 0.5x}{1 + t}$$

$$\text{The analytical solution is } U = \frac{1 + 0.5(x+Y)}{1 + t}$$

In the conservative form, the equation is:

$$U_t + \frac{1}{2} (U^2)_x + \frac{1}{2} (U^2)_y = 0 \quad (2.9)$$

An implicit finite difference scheme with upwind differencing is:

$$\begin{aligned} U_{ij}^{n+1} = U_{ij}^n - \frac{\Delta t}{2\Delta x} \{ (U_{ij}^{n+1})^2 - (U_{i-1,j}^{n+1})^2 \} \\ - \frac{\Delta t}{2\Delta y} \{ (U_{ij}^{n+1})^2 - (U_{i,j-1}^{n+1})^2 \} \end{aligned} \quad (2.10)$$

Where U_{ij}^n = value of U at x_i , y_j , and t_n .

Let us denote $U_{ij}^n = U0_{ij}$ and $U_{ij}^{n+1} = U_{ij}$.

Then the difference equation is:

$$U_{ij} = G_{ij}(U) \quad (2.11)$$

$$\text{Where } G_{ij}(U) = U0_{ij} - a (U_{ij}^2 - U_{i-1,j}^2)$$

$$- b (U_{ij}^2 - U_{i,j-1}^2) \quad (2.12)$$

$$a = \Delta t / 2\Delta x, \quad b = \Delta t / 2\Delta y.$$

Now we have to set the matrix A_i .

$$A_i = \begin{bmatrix} \frac{\partial G_{i1}}{\partial U_{i1}} & \frac{\partial G_{i1}}{\partial U_{i2}} & \dots & \frac{\partial G_{i1}}{\partial U_{iJ}} \\ \vdots & \vdots & \ddots & \vdots \\ \frac{\partial G_{iJ}}{\partial U_{i1}} & \frac{\partial G_{iJ}}{\partial U_{i2}} & \dots & \frac{\partial G_{iJ}}{\partial U_{iJ}} \end{bmatrix} \quad (2.13)$$

each element is evaluated at G^k .

$$G_{i1} = U_{i1} - a (U_{i1}^2 - U_{i-1,1}^2) - b (U_{i1}^2 - U_{i0}^2)$$

$U_{i0} = a$ boundary element = constant.

$$\frac{\partial G_{i1}}{\partial U_{i1}} = -2(a+b) U_{i1}$$

All other elements of the 1st row are zeros.

$$\text{Now } G_{i2} = U_{i2} - a (U_{i2}^2 - U_{i-1,2}^2) - b (U_{i2}^2 - U_{i1}^2).$$

$$\frac{\partial G_{i2}}{\partial U_{i1}} = -2b U_{i1}, \quad \frac{\partial G_{i2}}{\partial U_{i2}} = -2(a+b) U_{i2}$$

All other elements in the row are zeros.

Finally,

$$G_{iJ} = U_{iJ} - a (U_{iJ}^2 - U_{i-1,J}^2) - b (U_{iJ}^2 - U_{iJ-1}^2)$$

$$\text{Here } \frac{\partial G_{iJ}}{\partial U_{iJ-1}} = -2b U_{iJ-1}, \quad \frac{\partial G_{iJ}}{\partial U_{iJ}} = -2(a+b) U_{iJ}.$$

All other elements in the Jth row are zeros.

Thus, A_i is a lower triangular matrix for each i .

Now the algorithm works as follows:

At a given time, step t_n we will solve for U_{ij} iteratively. Let us assume that at some k th iteration U_{ij}^k are all known.

Then

Step #1 For $i = 1, 2, \dots, I$
 For $j = 1, 2, \dots, J$

 Compute $G_{ij}(U^k)$ using (2.12).

 Call them G_{ij}^k . (These values are now known.)

Step #2 Use the values of G_{ij}^k from step #1 and

 For $i = 1, 2, \dots, I$
 For $j = 1, 2, \dots, J$

 Compute $G_{ij}(G^k)$ using

$$G_{ij}(G^k) = U_{ij} - a\{(G_{ij}^k)^2 - (G_{i-1,j}^k)^2\} \\ - b\{(G_{ij}^k)^2 - (G_{ij-1}^k)^2\}$$

$$\text{and} \quad B_{ij}^k = G_{ij}(G^k) - G_{ij}^k$$

Step #3 Now evaluate all the elements of the matrix A_i replacing U_{ij}^k by G_{ij}^k for all i and j .

Invert $(I - A_i)$ and compute $W_i^k = (I - A_i)^{-1} B_i^k$

Notice that the method is fully vectorized. Each processor collects data from a shared memory, and processes information completely independent of the information processed in parallel by other processors.

Finally,

Step #4 Compute $U_i^k = W_i^k + G_i^k$

(is computed by each i th processor $i = 1, 2, \dots, I$)

This algorithm is fully vectorized.

Convergence criterion is : for some k . if $\max_1 (|w_i^k|) < \epsilon$

ϵ = positive and arbitrarily small.

the method converges.

The model has been solved with the following inputs

$\Delta x = 0.02$, $\Delta y = 0.02$, $\Delta t = 0.0025$ (see Appendix)

3. Operation Counts and the Rate of Convergence

To solve $F_{ij}(U) = 0$ $i = 1, 2, \dots, I$ and $j = 1, 2, \dots, J$, we need to compute (IJ) number of unknowns. If we solve this nonlinear system by Newton's method, at each iteration, we need to invert a matrix $(IJ) \times (IJ)$. To invert such a matrix $I^3 J^3$ number of operations are required. For the present algorithm we need to invert I number of $J \times J$ matrices requiring $I(J^3)$ number of operations.

Let us assume that, at a given time, step

N_1 = no. of iterations for Newton's method to converge.

N_2 = no. of iterations for the present scheme to converge.

O_1 = total no. of operations for Newton's method.

O_2 = total no. of operations for the present scheme.

$$\text{Then, } O_1 = N_1 I^3 J^3$$

$$O_2 = N_2 I J^3$$

$$\text{Thus, } O_2 = \left(\frac{N_2}{N_1} \right) \cdot \frac{I}{I^2} \cdot O_1$$

Without using parallel computation, it has been found that $N_2 = N_1$.

However, even if we assume that $N_2 = 2N_1$,

$$O_2 = \frac{(2)}{I^2} O_1 \quad (3.1)$$

Thus, the present scheme uses much less operational counts than Newton's method.

Newton's method inverts the (IJ) x (IJ) matrix and generates a quadratic rate of convergence. The present scheme does not invert such a huge matrix and, as such, it does not have a quadratic rate of convergence.

Let us now discuss the rate of convergence quite thoroughly.

In order to do this, we need the following information:

Let us assume that $f(x, y)$ is sufficiently smooth. Let

$$\begin{aligned} f(x + h, y + k) &= f(x, y + k) + h \frac{\partial f(x, y+k)}{\partial x} + \frac{h^2}{2!} \frac{\partial^2 f(x, y+k)}{\partial x^2} + \dots \\ &= f(x, y) + k \frac{\partial f}{\partial y} + h \frac{\partial f}{\partial x} + hk \frac{\partial^2 f}{\partial x \partial y} \\ &\quad + \frac{h^2}{2!} \frac{\partial^2 f(x, y+k)}{\partial x^2} + \dots \end{aligned} \quad (3.2)$$

Let us consider two processors processing two equations in parallel.

$$U_1 = G_1(U_1, U_2) ; \quad U_2 = G_2(U_1, U_2) \quad (3.3)$$

Here,

$$w_1^k = \{ G_1(G^k) - G_1^k \} / \{ 1 - G_{1,1}(G^k) \} ; \quad G_1^k = G_1(U_1^k, U_2^k)$$

$$U_1^{k+1} = w_1^k + G_1(U_1^k, U_2^k) \quad G_{1,1} = \text{partial . derivative with respect to } U_1 .$$

similarly,

$$w_2^k = \{ G_2(G^k) - G_2^k \} / \{ 1 - G_{2,2}(G^k) \} ; \quad G_2^k = G_2(U_1^k, U_2^k)$$

$$U_2^{k+1} = w_2^k + G_2^k$$

Let U_1^* , U_2^* = the roots.

$$\text{Then, } U_1^* = G_1(U_1^*, U_2^*) = G_1(G_1^*, G_2^*) ; \quad G_1^* = G_1(U_1^*, U_2^*)$$

$$U_2^* = G_2(U_1^*, U_2^*) = G_2(G_1^*, G_2^*)$$

Now,

$$\begin{aligned} U_1^{k+1} - U_1^* &= w_1^k + G_1^k - G_1^* \\ &= \{G_1(G^k) - G_1^*\} / \{1 - G_{1,1}(G^k)\} + G_1^k - G_1^* \\ &= \{G_1(G^k) - G_1^* - (G_1^* - G_1^k)G_{1,1}(G^k)\} / \{1 - G_{1,1}(G^k)\} \end{aligned}$$

$$\text{Using (3.2) } (G_1^* = G_1^k + \delta_1^k, \quad G_2^* = G_2^k + \delta_2^k)$$

$$\begin{aligned} G_1^* &= G_1(G_1^*, G_2^*) = G_1(G_1^k + \delta_1^k, G_2^k + \delta_2^k) \\ &= G_1(G_1^k, G_2^k) + \delta_1^k \frac{\partial G_1(G^k)}{\partial U_1} + \delta_2^k \frac{\partial G_1(G^k)}{\partial U_2} \\ &\quad + \delta_1^k \delta_2^k \cdot \frac{\partial^2 G_1(G^k)}{\partial U_1 \partial U_2} + \frac{1}{2!} (\delta_1^k)^2 \frac{\partial^2 G_1(G^k)}{\partial U_1^2} + \dots \end{aligned}$$

Then,

$$U_1^* - U_1^{k+1} = \left\{ \frac{\partial G_1(G^k)}{\partial U_2} \left[1 - \frac{\partial G_1(G^k)}{\partial U_1} \right] \right\} \delta_2^k$$

$$+ \text{ terms of the order } (\delta_1^k)^2$$

$$(\text{Assume } \delta_2^k \sim \delta_1^k)$$

Similarly,

$$U_2^* - U_2^{k+1} = \left\{ \frac{\partial G_2(G^k)}{\partial U_1} / \left[1 - \frac{\partial G_2(G^k)}{\partial U_2} \right] \right\} \delta_1^k + \text{terms } O(\delta_2^k)^2.$$

Thus, if two processors are activated simultaneously, each processor will generate a quadratic rate of convergence for the individual iterate.

The same is true if both U_1 and U_2 are two vectors.

4. A Matrix Free Version of the Algorithm

Here to solve

$$U_{ij} = G_{ij}(U)$$

$$U = (U_1 \ U_2 \ \dots \ U_I)^T$$

$$U_i = (U_{i1} \ U_{i2} \ \dots \ U_{iJ})^T$$

We use the following steps:

For $i = 1, 2, \dots, I$; For $j = 1, 2, \dots, J$

$$\text{Step \#1} \quad \text{Compute } W_{ij}^k = \{ G_{ij}(G^k) - G_{ij}^k / [1 - \frac{\partial G_{ij}(G^k)}{\partial U_{ij}}] \} \quad (4.2)$$

$$\text{Step \#2} \quad \text{Compute } U_{ij}^k = W_{ij}^k + G_{ij}^k \quad (4.3)$$

If $F_{ij}(U) = U_{ij} - G_{ij}(U)$, then (4.2) and (4.3) are equivalent to

$$\text{Step \#1} \quad U_{ij}^{k+1/2} = G_{ij}(U^k)$$

$$\text{Step \#2} \quad U_{ij}^{k+1} = U_{ij}^{k+1/2} - \{ F_{ij}^{k+1}(U^{k+1/2}) / [\frac{\partial F_{ij}(U^{k+1/2})}{\partial U_{ij}}] \}$$

Thus, the present scheme is a combination of two methods which are both vectorized. If r_1 = rate of convergence of the first method and r_2 = rate

of convergence of the second method, the rate of convergence of the new scheme is $r_1 r_2$.

5. Discussion

The present scheme may be expressed as:

$$U_i^{k+1/2} = G_i(U^k)$$

$$U_i^{k+1} = U_i^{k+1/2} - F_2^l(U_i^{k+1/2})^{-1} F_i(U_i^{k+1/2})$$

$$i = 1, 2, \dots, I; \quad F_i(U) = U_i - G_i(U)$$

Both steps are fully vectorized, both steps may be implemented in parallel machines, and if the first step converges, the second step must converge (by the definition of $f_i(U)$).

The first step, as it is, has a slow rate of convergence. Thus, the second speeds up the rate of convergence of the first step.

The second step, by itself, requires an initial guess to be close to the root, and generally converges for monotone functions. These are eliminated by the first step.

Independent of the initial guess, it has been found, that the method converges [1]. However, it was for the non-parallel, non-vectorized version. In that version, convergence properties were established using D-mapping analysis. This is the first part of our project in the future.

We are primarily interested in computing time-accurate solutions of flow models.

6. Conclusion

A massively parallel vectorized perturbed functional iterative scheme has been presented here. Even without using parallel processors, the method seems to be effective for solving nonlinear PDE's. However, in the near future, we need to do the following:

1. A rigorous mathematical analysis of convergence; and computational study of many nonlinear PDE's.
2. Applications to Navier-Stokes' type equations.
3. Applicability (or implementation of the method) in a SIMD and/or MIMD type machine.
CM-2 type machine applicability

4. Acceleration of the rate of convergence.

I believe that parallel programming is very essential for all large-scale computations. It is the wave of the (near) future.

Bibliography

1. S. K. Dey, Numerical Solution of Nonlinear Implicit Finite Difference Equations of Flow Problems by Perturbed Functional Iterations. Computational Fluid Dynamics. (W. Kollman Edited), Hemisphere, New York, 1980.
2. S. K. Dey, Numerical Solution of Euler's Equation by Perturbed Functionals. Lect. Notes in Appd. Maths, Vol. 22, '85. Am.Math.Soc.
3. G. Fox, M. Johnson, et al, Solving Problems on Concurrent Processors, Vol. 1, Prentice Hall, 1988.

An Appendix

For the model equation (2.8), with $\Delta x = 0.2 = \Delta y$, $\Delta t = 0.0025$, at time = 1 sec, $EMAX = 2.2892 \times 10^{-3}$ (decreasing), where $EMAX = \max_{ij} (|u_{ij}^n - U_{ij}^n|)$

u_{ij} = the analytical solution

U_{ij} = The computed solution

No artificial viscosity was added. The code was written with Mr E. Josyula at the Computational Fluid Dynamics center of Wright-Patterson AFB.

In order to seek for global convergence, we first made an initial guess at a given time step twice the value of U at the previous-time step and then (12) times the values of U at the previous time step. This is done arbitrarily. Still, the algorithm brought U inside the domain of convergence and the method converged.

This phenomenon was expected. However, it must be studied mathematically in the near future.

FINAL REPORT

United States Air Force Office of Scientific Research

1991 Summer Research Program

Decentralized Control of Flexible Structures

with Uncertain Interconnections

George T. Flowers

Assistant Professor

Department of Mechanical Engineering

Auburn University, AL 36849-5341

August 23, 1991

DECENTRALIZED CONTROL OF FLEXIBLE STRUCTURES WITH UNCERTAIN INTERCONNECTIONS

**George T. Flowers
Assistant Professor
Department of Mechanical Engineering
Auburn University, AL 36849-5341**

Introduction

Typically, control strategies are developed assuming that the controller has access to all the states of the system (or at least their estimates). For many large scale systems, such a formulation is not practical. Adequate control may require too many states for it to be practical to deal with all simultaneously or the system may be geographically extended such that communication of states back to a central controller is prohibitively expensive and involves excessive time delays. The solution to this problem has been to develop decentralized control techniques that are based only upon local states which are convenient subsets of the total system states. This field has advanced rapidly in recent years. Such techniques have been shown to be effective for many large scale systems, including power distribution networks, telecommunication networks, and large, flexible structures.

There has been a great deal of recent interest in the decentralized control of flexible structures. For decentralized control design, a flexible structure can be modelled as a collection of flexible appendages attached to a flexible support structure. Knowledge of the components (support structure and appendages) is typically fairly complete and can usually be modelled quite adequately using linear mode shapes and frequencies. However, knowledge of the interconnection dynamics is typically not so complete. The interconnections may be nonlinear (a pinned interconnection with friction, for example) and a great deal of uncertainty may exist

with regard to adequate models (both with regard to functional form and parametric configuration). Therefore, it is natural to address the issue of decentralized control for a flexible structure in terms of substructures subjected to external disturbances due to uncertain interconnection forces.

The current work is concerned with studying techniques for vibration suppression and tracking of large flexible structures with uncertain interconnections using decentralized control techniques. This report serves to document the work that has been conducted by the author on this subject. It consists of three major parts. First, a discussion of background material and previous work in this area is presented. A control strategy that is currently being investigated by the author is discussed in the second section. The third section describes important areas for future work and goals that should be achieved if decentralized control strategies are to be successfully implemented for flexible structures with uncertain interconnections.

Previous Work

There are several ways of designing decentralized control systems for flexible structures with uncertain interconnections that have been discussed in the control system literature. The following will describe two of the most promising techniques – suboptimal fixed-gain methods and adaptive methods – and identify the advantages and disadvantages of each.

Suboptimal fixed-gain strategies

For a decentralized model consisting of substructures with the interconnection forces considered as disturbance inputs, it is natural to describe the system by considering the disturbance as a random excitation. A standard formulation in this regard is Linear Quadratic Gaussian (LQG) control techniques (Sandell, et al., 1978; Singh, 1981; Siljak, 1991). In order to implement this controller design procedure, the structure is first subdivided into N subsystems that can be described by the equations:

$$\dot{x}_i = A_i x_i + \sum_{j=1}^N A_j^C x_j + B_i u_i \quad (1)$$

Robust optimal controllers are designed for each subsystem using LQG techniques independently of the interconnections. That is, the controllers are designed for the subsystems described by the equations:

$$\dot{x}_i = A_i x_i + B_i u_i \quad (2)$$

with the cost functions:

$$J_i = \int_0^\infty (x_i^T R_{xx} x_i + u_i^T R_{uu} u_i + u_i^T R_{xu} x_i) dt \quad (3)$$

The decentralized control laws are linear functions only of the local states x_i :

$$u_i = k_i x_i \quad (4)$$

If the controllers are sufficiently robust, the responses of the connected system will be stable.

In order to motivate the discussion of decentralized control concepts, a simple model will be discussed and decentralized control system design procedures applied to it. The simple model is illustrated in Figure 1. It consists of four identical masses connected by springs of varying stiffnesses. This system will be decomposed into two substructures. The first substructure consists of M_1 , M_2 , and K_1 . The second substructure consists of M_3 , M_4 , and K_3 . The interconnection is K_2 .

Consider the following representation for a decentralized model:

$$\dot{\vec{x}}_i = (A_i^m) \vec{x}_i + \sum_{j=1}^n (A_j^I) \vec{x}_j$$

For the simplified model studied here, the system matrices are:

$$\begin{aligned}
\begin{pmatrix} \ddot{x}_1 \\ \ddot{x}_2 \\ \dot{x}_1 \\ \dot{x}_2 \end{pmatrix} &= \begin{pmatrix} 0 & 0 & -20 & 20 \\ 0 & 0 & 20 & -20 \\ 1 & 0 & 0 & 0 \\ 0 & 1 & 0 & 0 \end{pmatrix} \begin{pmatrix} \dot{x}_1 \\ \dot{x}_2 \\ x_1 \\ x_2 \end{pmatrix} \\
&+ K_2 \begin{pmatrix} 0 & 0 & 0 & 0 \\ 0 & 0 & 0 & -1 \\ 0 & 0 & 0 & 0 \\ 0 & 0 & 0 & 0 \end{pmatrix} \begin{pmatrix} \dot{x}_1 \\ \dot{x}_2 \\ x_1 \\ x_2 \end{pmatrix} \\
&+ K_2 \begin{pmatrix} 0 & 0 & 0 & 0 \\ 0 & 0 & 1 & 0 \\ 0 & 0 & 0 & 0 \\ 0 & 0 & 0 & 0 \end{pmatrix} \begin{pmatrix} \dot{x}_3 \\ \dot{x}_4 \\ x_3 \\ x_4 \end{pmatrix} \\
\begin{pmatrix} \ddot{x}_3 \\ \ddot{x}_4 \\ \dot{x}_3 \\ \dot{x}_4 \end{pmatrix} &= \begin{pmatrix} 0 & 0 & -1 & 1 \\ 0 & 0 & 1 & -1 \\ 1 & 0 & 0 & 0 \\ 0 & 1 & 0 & 0 \end{pmatrix} \begin{pmatrix} \dot{x}_3 \\ \dot{x}_4 \\ x_3 \\ x_4 \end{pmatrix} \\
&+ K_2 \begin{pmatrix} 0 & 0 & 0 & 0 \\ 0 & 0 & -1 & 0 \\ 0 & 0 & 0 & 0 \\ 0 & 0 & 0 & 0 \end{pmatrix} \begin{pmatrix} \dot{x}_3 \\ \dot{x}_4 \\ x_3 \\ x_4 \end{pmatrix} \\
&+ K_2 \begin{pmatrix} 0 & 0 & 0 & 0 \\ 0 & 0 & 0 & 1 \\ 0 & 0 & 0 & 0 \\ 0 & 0 & 0 & 0 \end{pmatrix} \begin{pmatrix} \dot{x}_1 \\ \dot{x}_2 \\ x_1 \\ x_2 \end{pmatrix}
\end{aligned}$$

Notice that the parameters were deliberately chosen so that the frequencies of each of the subsystems are distinctly separated.

Applying LQG techniques to the uncoupled subsystems ($K_2=0$) produces the following closed loop uncoupled systems:-

$$\begin{aligned}
\begin{pmatrix} \ddot{x}_1 \\ \ddot{x}_2 \\ \dot{x}_1 \\ \dot{x}_2 \end{pmatrix} &= \begin{pmatrix} -2.1 & -0.7 & -21.7 & 20.3 \\ 0 & 0 & 20 & -20 \\ 1 & 0 & 0 & 0 \\ 0 & 1 & 0 & 0 \end{pmatrix} \begin{pmatrix} \dot{x}_1 \\ \dot{x}_2 \\ x_1 \\ x_2 \end{pmatrix} \\
\begin{pmatrix} \ddot{x}_3 \\ \ddot{x}_4 \\ \dot{x}_3 \\ \dot{x}_4 \end{pmatrix} &= \begin{pmatrix} 0 & 0 & -1 & 1 \\ -1.1 & -2.1 & 1.3 & -2.7 \\ 1 & 0 & 0 & 0 \\ 0 & 1 & 0 & 0 \end{pmatrix} \begin{pmatrix} \dot{x}_3 \\ \dot{x}_4 \\ x_3 \\ x_4 \end{pmatrix}
\end{aligned}$$

The actuator locations are specified a priori as:

$$[B_1] = \begin{pmatrix} 1 & 0 \\ 0 & 0 \end{pmatrix} \quad [B_2] = \begin{pmatrix} 1 & 0 \\ 0 & 0 \end{pmatrix}$$

A root locus plot of the closed loop system for variations in the parameter K_2

is shown in Figure 2. Notice that two of the branches (those associated with the interconnection mode) become unstable for a suitably large value of K_2 . Thus, the closed loop system is unstable for sufficiently stiff interconnections.

If the actuator locations are changed slightly so that

$$[B_1] = \begin{pmatrix} 1 & 0 \\ 0 & 1 \end{pmatrix} \quad [B_2] = \begin{pmatrix} 1 & 0 \\ 0 & 0 \end{pmatrix}$$

the root locus plot shown in Figure 3 is produced. Notice that for this case the responses will not be unstable for any positive value of K_2 . Thus, a possible strategy for decentralized control is to concentrate on designs that are stable regardless of the interconnection strength.

For centralized control systems LQG techniques rely heavily on the use of the separation property, by which the state estimator is decoupled from the controller. As a result, the controller and estimator can be designed separately and combined to produce the required controller/estimator combination. With regard to decentralized control, such a strategy does not follow immediately without some qualification. The separation property holds only at the price of exchange of state estimates between the subsystems (Siljak, 1991). In general, this is an undesirable circumstance. One of the primary motivations for decentralized control is the distribution of the control effort among several local controllers that can act independently. If information exchange is required for a stable controller/estimator combination, then a break in the information exchange could result in unstable and catastrophic responses. As a result, it is probably a wise strategy to design the estimator and controller concurrently.

Advantages

1. Inherently robust controller designs have been demonstrated by Siljak (1991).
2. LQG techniques employ straightforward, well established design strategies which are available on many control system design software packages.

Disadvantages

1. In general, techniques do not exist for designing truly optimal controllers for decentralized systems. While the subsystem controller designs can be made optimal for the unconnected subsystems, the combined designs are not optimal due to interconnection effects. Thus, a principal objective of optimal control (i.e., optimizing control effort) will not be realized by this strategy. In fact, a truly optimal controller for a decentralized control system may be nonlinear (Wittenhausen, 1968).
2. LQG type controllers may not be stable for all interconnection strengths. That is, the controllers may not be adequately robust to account for interconnections of an arbitrary amplitude (as illustrated by the example system). Thus to insure stability, bounds for the interconnection strength are required.
3. Excessively high gains may be used in an effort to make the control system robust in the presence of interconnection dynamics. In part this is due to the inability of suboptimal techniques to take full advantage of the sometimes stabilizing effects of interconnections.

Adaptive Control Strategies

An area of current rapid development is the field of adaptive control theory. Researchers in the area of decentralized control have recently begun to investigate and apply adaptive techniques. Since such methods typically result in lower closed loop feedback gains, they appear to offer in many cases significantly improved noise rejection characteristics as compared to fixed-gain strategies. A number of investigators have made important contributions to this field. Among them are Hmamed and Radouane (1983), Ioannou and Kokotovic (1983), and Ioannou and Reed (1988). Much of this work has been directed toward using model reference adaptive controllers (MRAC) for the decentralized control of unknown subsystems as if they were disconnected from each other. Gavel and Siljak (1989) describe an adaptive method for designing a decentralized control system for a system with known sub-

systems that will be stable regardless of the magnitude of the interconnection forces. This technique consists of first developing controllers that stabilize the unconnected subsystems. This can be done using LQG techniques, pole placement, or any other convenient method. Then, adaptive controllers of the form

$$u_i^A = \Phi_i [K_i^A] \{x_i\} \quad (4)$$

where

$$\dot{\Phi}_i = -\{x_i\}^T [G_i] \{x_i\} \quad (5)$$

are applied to each of the subsystems of equation (1). G_i must be symmetric and positive definite. H_i is the symmetric, positive definite solution to the matrix Liapunov equations:

$$A_{m_i}^T H_i + H_i A_{m_i} = -G_i \quad (6)$$

Choose a symmetric, positive definite matrix R_i . The local adaptive feedback law is then:

$$u_i^A(t) = -\Phi_i(t) R_i^{-1} B_i^T H_i x_i \quad (7)$$

Siljak (1991) demonstrates this adaptive feedback scheme and shows that the resulting behavior is globally bounded.

This technique was applied to the simple four-mass example system. The following parameters were chosen for adaptive controller design.

$$[G_1] = \begin{pmatrix} 0 & 0 & 0 & 0 \\ 0 & 0 & 0 & 0 \\ 0 & 0 & 1 & 0 \\ 0 & 0 & 0 & 1 \end{pmatrix} \quad [G_2] = \begin{pmatrix} 0 & 0 & 0 & 0 \\ 0 & 0 & 0 & 0 \\ 0 & 0 & 1 & 0 \\ 0 & 0 & 0 & 1 \end{pmatrix}$$

and

$$[K_1^A] = \begin{pmatrix} 10 & -5 & 10 & -5 \\ 0 & 0 & 0 & 0 \end{pmatrix} \quad [K_2^A] = \begin{pmatrix} 0 & 0 & 0 & 0 \\ 10 & -5 & 10 & -5 \end{pmatrix}$$

The results were quite impressive. As can be seen from Figure 5, the system was stabilized very effectively by this technique.

The primary advantage of most adaptive decentralized control strategies lie in their inherent stability. A properly designed adaptive controller can be made to be stable for any value of interconnection coupling strength.

The primary disadvantage of decentralized adaptive strategies lie in the nature of most adaptive strategies to simply increase the gains of the system so as to insure stable responses of the closed loop system. In fact, the method of Gavel and Siljak (1989) is explicitly a high-gain adaptive scheme. Such an approach can result in saturation of the actuators and excessively high gains that magnify external noise effects. Note that from a physical perspective, an actuator has a limited range of force output. Outside of that range, saturation occurs. While the closed loop gains can often be made less than those for a sufficiently robust fixed-gain controller, they are often significantly higher than is required for adequate performance. Little effort is made to exploit the (sometimes) stabilizing effects of interconnection forces to reduce the magnitude of the adaptive control forces.

Advantages

1. Robust control strategies can be developed in the face of unknown interconnection forces.
2. The techniques of adaptive control can be applied to nonlinear models as well as nonlinear interconnections. Such techniques provide important advantages in particular for tracking problems that require a large amplitude motion.
3. Allows for the opportunity to take advantage of the stabilizing effects of interconnections (possibly through an adaptive gain strategy that transfers control

energy from overdamped states to underdamped states).

Disadvantages

1. Adaption schemes result in nonlinear, time-varying controllers that are often difficult to analyze. Multiple solutions, limit cycles, etc. are possible.
2. The resulting controllers are not optimal and may require excessive control effort.
3. State estimation is still necessary and the estimator/controller designs must still be performed concurrently for decentralized control with no information exchange.

Work to Date

A developmental study for a modified adaptive control strategy that allows for the use of interconnection forces to advantage is currently being conducted. The proposed idea for implementing such an algorithm is based upon adaptive schemes for modifying the control laws on-line. It is basically a model reference adaptive control (MRAC) strategy applied in the context of decentralized control. The conceptual design for this algorithm is as follows.

1. Select a design configuration for each subsystem, A_i^D .
2. Consider the actual dynamics of the i^{th} subsystem to be

$$\dot{x}_i = A_i x_i + b_i u_i + \delta_i(x) \quad (8)$$

where x represents all of the states of the structure and $\delta_i(x)$ is an uncertain, possibly nonlinear interconnection function. u_i is a linear function of the local subsystem states

$$u_i = K_i x_i \quad (9)$$

3. Using a finite number of measured signals, fit the following dynamical model to (8):

$$\dot{x}_i = \bar{A}_i x_i \quad (10)$$

4. Formulate an error function between the desired subsystem dynamics A_i^D and the estimated dynamics \bar{A}_i as:

$$E_i = \text{Norm}(A_i^D - \bar{A}_i) \quad (11)$$

5. Minimize this error function with respect to the elements of K_i subject to constraints on the maximum actuator forces.
6. Modify the controller force in accordance with the results of the previous step and return to step 3.

Note that the above algorithm implicitly accounts for the interconnection coupling effects in the approximate subsystem dynamics \bar{A}_i . The proposed strategy offers the distinct advantage of avoiding excessively high adaptive gains by explicitly modifying the control laws to account for any stabilizing effects that may result from interconnection effects. In addition, the adaptive methods of Gavel and Siljak explicitly require that the decoupled subsystems be stabilized so as to avoid instabilities if the interconnections deteriorate or fail completely. The proposed method does not impose this requirement since it automatically stabilizes to specified design values.

In order to motivate and illustrate the usage of the adaptive algorithm developed in this work, the decentralized control problem for several simplified flexible structural models will be examined and the implementation of control strategies for these structures discussed. The models are presented in Figures 1. and 2. The first model is a very simple spring-mass model. The second model is much more complex. It consists of a flexible truss acting as a support structure. Attached to this primary support by a pin connection is a boom truss. Provisions are made for an actuator to provide a control input to the structure from this location. An antenna is attached to the boom truss with a pin and similar arrangements are made for a control actuator at this location. This model serves as a "proof of concept" structure to demonstrate the effectiveness of the proposed adaptive control technique for large-scale structural systems.

Critical Issues and Areas for Further Research

The foregoing discussion has served to identify strengths and weaknesses for two control methods that provide great promise for the development of improved strategies for the decentralized control of flexible structures. Research efforts can contribute most directly to this area by addressing some of the weaknesses that have been previously discussed. In order to develop an improved controller design strategy, the natural next step is to attempt to combine optimal and adaptive control methods in a manner that will take maximum advantage of the strengths of each. The following suggestions for further research are studies related to such an effort and to associated issues that are of concern. The issues can be separated into four general categories:

1. Dynamical strategies

- a. **Investigation of techniques for using the stabilizing effects of interconnections to some advantage.** It has been noted by a number of authors that decentralized control techniques, in general, treat interconnection forces as undesirable destabilizing forces that require increased gains to overcome. In many cases, interconnection forces actually provide some stabilizing effects (at least for particular modes). Techniques need to be developed that exploit any stabilizing influence that interconnections may provide to avoid excessive demands on the actuator forces and to produce responses that are as close as possible to the desired behavior (in terms of response speed, frequencies, damping ratios, etc.). Such an approach could lead to significantly improved performance and life expectancy (less wear and tear) for the controlled structure.
- b. **Study of other possible time varying and nonlinear controller schemes and the dynamical implications of such control strategies.** The adaptive controller schemes that have been mentioned previously impose time varying and nonlinear effects on the controlled system. It is well known that nonlinear systems can behave in ways that are greatly different (in a qualitative

as well as quantitative manner) from linear systems. Limit cycles, multiple solutions, chaos, etc. may result from the presence of inappropriate nonlinearities. On the other hand, improvements in performance may result from the presence of appropriate nonlinearities (as demonstrated by the adaptive and cubic controllers). Assessments need to be made of the influence of nonlinear elements (absolute value, quadratic, or cubic control algorithms, for example) on global dynamical responses and stability. The associated implications for the performance of the controlled systems should be evaluated.

2. **Optimization strategies** – Development of optimal techniques for forming adaption matrices. The adaptive techniques for decentralized control systems that have been developed by Siljak and others place no optimality conditions on the adaption matrices (K_i^A and G_i). Their work is only concerned with establishing the conditions on these matrices for the stabilization of the connected system with local feedback. Clearly such strategies could lead to excessive controller forces unless some effort is made to select the respective matrices in an optimal manner. This issue should be addressed and appropriate techniques (ones that work) developed.
3. **State estimation and the separation property**. As was noted previously, the separation property holds for decentralized control strategies only under the condition that the state estimators for the decentralized subsystems exchange states with each other. It may be possible (since the interconnection forces are modelled as unknown disturbance forces in the adaptive scheme) to establish a separability condition without interchange of state estimates. Such a result could greatly simplify controller design and improve the independence of each controller.
4. **Additional issues**
 - a. **Investigation of fixed-gain design strategies that will be stable regardless of the strength of the interconnections.** As was noted previously, it is possible to design controllers for some systems that retain their sta-

bility characteristics regardless of the magnitudes of the interconnection forces. The implications of such a strategy should be evaluated for large scale flexible structures. If possible, appropriate design criteria should be established for implementing such an approach.

- b. **Investigate techniques for posing the optimization problem so as to account for information structure and communication costs.** As has been mentioned previously, truly optimal controllers have not been developed for decentralized systems. Some have suggested that this may be due, in part, to the ill-posing of the optimization problem with regard to the costs of a decentralized information structure and the costs associated with communication between the various subsystems. On the other hand, some have suggested that further research may show that truly optimal control for decentralized systems is an impossible task or is so extremely difficult that it is not worth the effort it entails. Successful resolution of optimization issues associated with this problem would be a significant contribution to the field of decentralized control theory. (This is a very complex issue.)

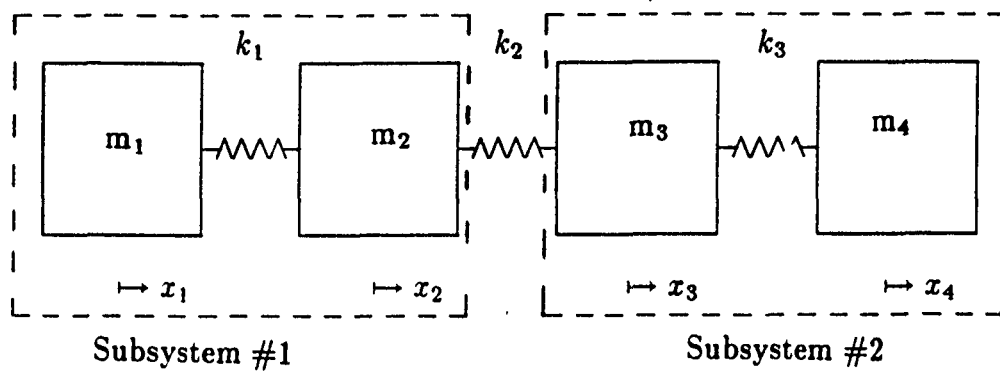


Figure 1.: Simple flexible structure model

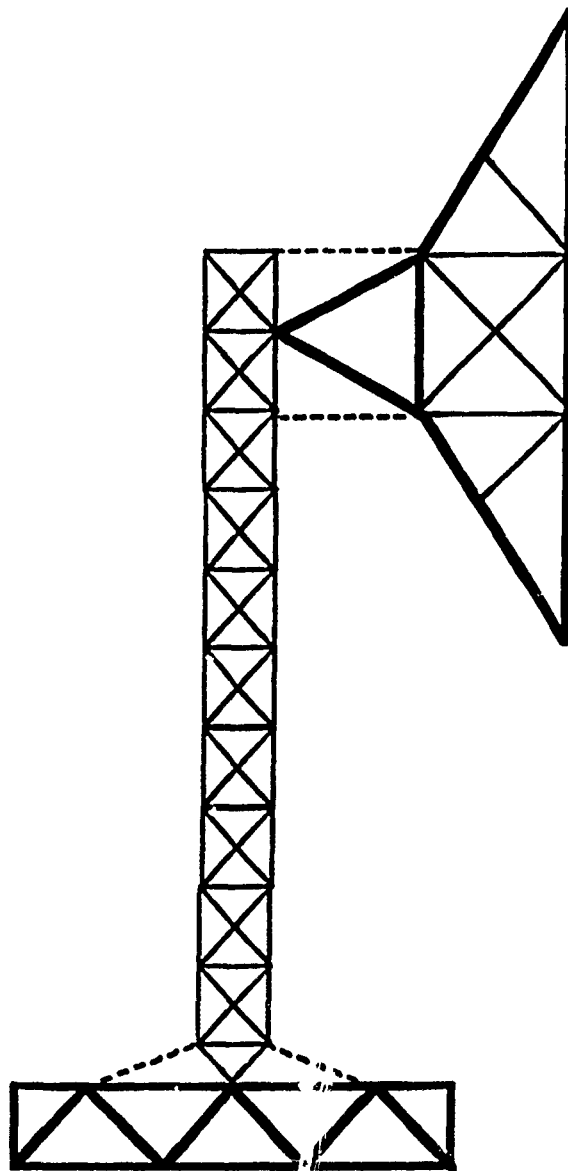


Figure 2: Multi-body truss model

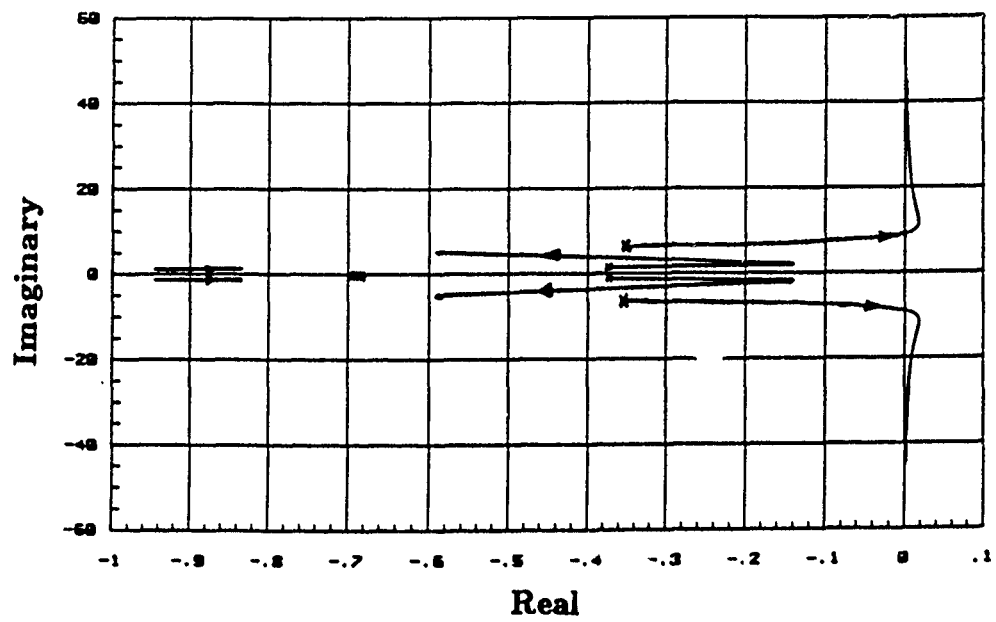


Figure 3.a: Root locus for simple system

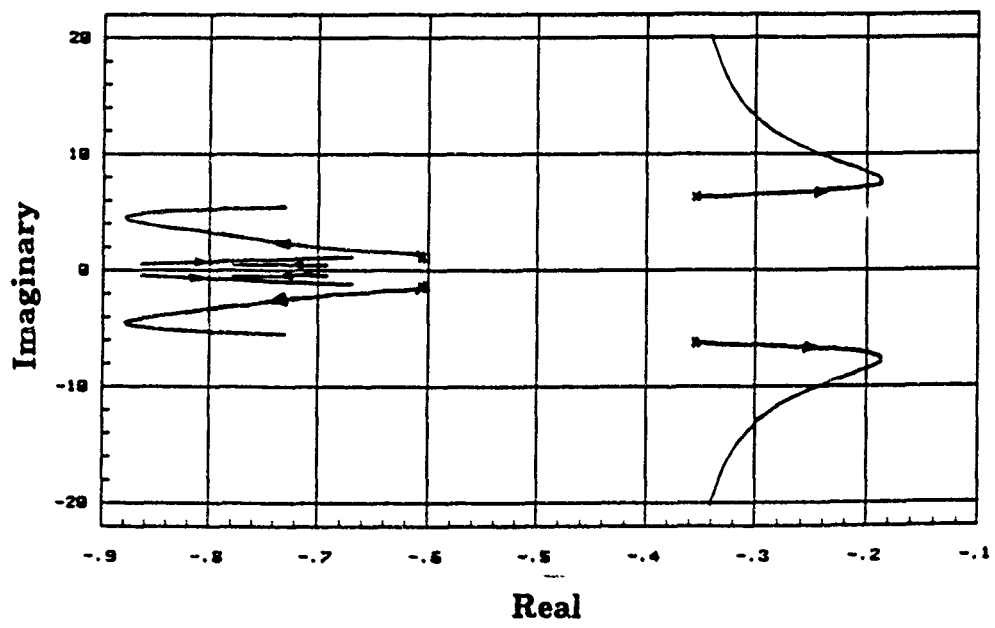


Figure 3.b: Root locus for simple system

Time History

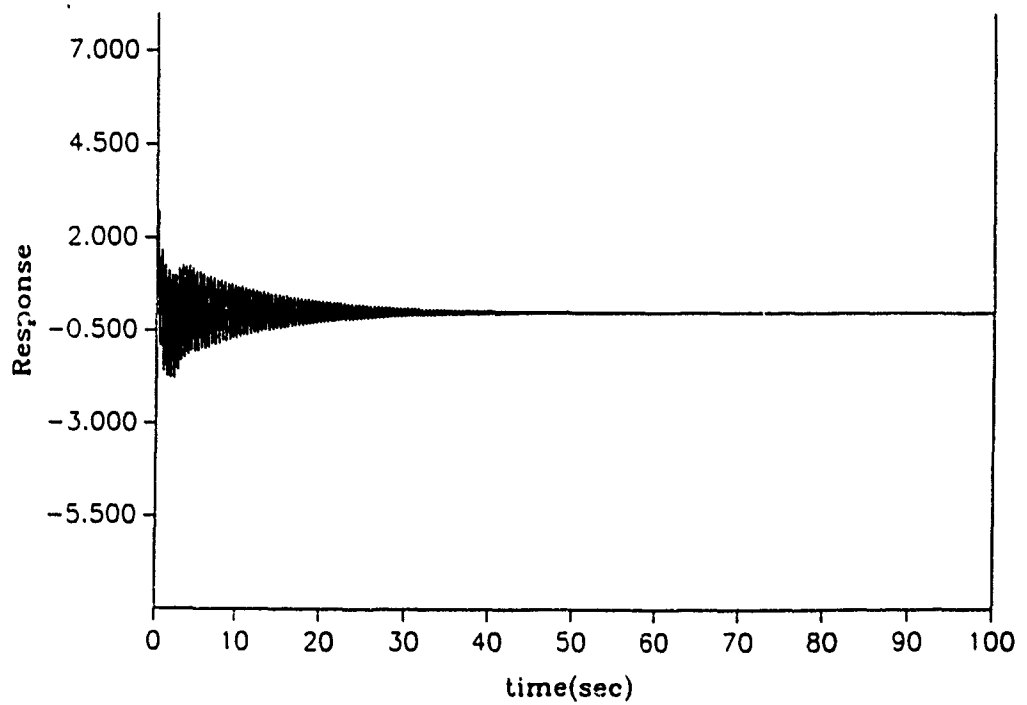


Figure 4: Time response with adaptive feedback gains

References

- Craig, J.J., *Adaptive Control of Mechanical Manipulators* Addison-Wesley Publishing Company, Reading, MA, 1988.
- Derecho, A.T., Freskakis, G.N., and Fintel M., *A Study of the Effects of the Frequency Characteristics of Ground Motion on Nonlinear Structural Response*, Proceedings of the International Symposium on Earthquake Structural Engineering, St. Louis, Missouri, USA, August 1976, pp. 21-36.
- Gavel, D.T., and Siljak, D.D., *Decentralized Adaptive Control: Structural Conditions for Stability*, IEEE Transactions on Automatic Control, Vol. 34, No. 4, April 1989, pp 413-426.
- Hmamed, A., and L. Radouane, *Decentralized Nonlinear adaptive feedback stabilization of Large-scale interconnected systems*, IEE Proceedings, Vol. 130-D, 1983 PP. 57-62.
- Ioannou, P.A., and P.V. Kokotović, Adaptive Systems with Reduced Models, Springer, New York, 1983.
- Ioannou, P.A., and P.V. Kokotović, *Robust Design of Adaptive Control*, IEEE Transactions on Automatic Control, Vol. AC-29, 1984, pp. 202-211.
- Ioannou, P.S., *Decentralized Adaptive Control of Interconnected Systems*, IEEE Transactions on Automatic Control, Vol. AC-31, No. 4, April, 1986, pp. 291-298.
- Ioannou, P.A., and J.S. Reed, *Discrete-time Decentralized Control*, Automatica, Vol. 24, 1988, pp. 419-421.
- Kailath, T. Linear Systems, Prentice-Hall, Inc., 1980.
- Lewis, F.L., Optimal Estimation, John Wiley and Sons, New York, 1986.
- Mao, Cheng-Jyl, and Lin, Wei-Song, *On-Line Decentralized Control of Interconnected Systems With Unmodelled Nonlinearity and Interaction*, Proceedings of the 1989 Automatic Controls Conference, Vol. 1, pp. 248-252.
- Rao, S.S., Pan, T.S., and Venkayya, V.B., *Modeling, control, and design of flexible structures: A survey*, Applied Mechanics Review, vol. 43, no. 5, part 1, may 1990, pp. 99-117.
- Sandell, N.R., Varaiya, P., Athans, and Safonov, M.G., *Survey of Decentralized Control Methods for Large Scale Systems*, IEEE Transactions of Automatical Control, Vol. AC-23, No. 2, April 1978, pp. 108-128.
- Siljak, D.D., *Parameter Space Methods for Robust Control Design: A Guided Tour*, IEEE Transactions on Automatic Control, Vol. 34, NO. 7, July 1988, pp. 674-688.
- Siljak, D.D., Decentralized Control of Complex Systems, Academic Press, Inc., 1991.
- Singh, M.D., Decentralised Control, North-Holland Publishing Company, Amsterdam, 1981.

Yang, C.Y., Random Vibration of Structures, John Wiley and Sons, New York, 1986.

Young, K.D., *A Distributed Finite Element Modeling and Control Approach for Large Flexible Structures*, AIAA Guidance, Navigation, and Control Conference, Minneapolis, MN, Aug. 1988, AIAA, pp. 253-263.

Witenhausen, H.S., *A Counter Example in Stochastic Optimal Control*, SIAM Journal of Control, No. 6, 1968, pp. 131-147.

**COMPUTATIONAL PREDICTION OF STATIC AND ROLLING RESPONSE OF AN
AIRCRAFT TIRE ON A RIGID SURFACE AS A PRELUDE TO WEAR STUDIES**

by

MANJRIKER GUNARATNE, P.E.

**Assistant Professor
Dept. of Civil Engineering and Mechanics
University of South Florida
Tampa, FL. 33615**

**formerly
Assistant Professor
Dept. of Civil Engineering
Tennessee State University
Nashville, TN. 37204**

**Submitted to
Landing Gear Systems Group
Wright-Patterson Air Force Base
Dayton, Ohio**

**and
Research and Development Laboratories
Culver City, California**

ACKNOWLEDGMENT

The author is indebted to Mr. John P. Medzorian, of the Landing Gear Systems Facility, Wright-Patterson Air Force Base for the invaluable advice with regard to WPAFB computational facilities and the collaboration in tire studies. The author also wishes to thank Mr. Paul Ulrich of the above institution for the inspiration and facilities provided during the research period. His thanks also extend to Dr. Arnold Mayer, Mr. Igors Skriblis and Mr. Adolf Harris for their cooperation at different stages of the summer faculty program. Finally, the AFOSR summer research faculty award sponsored by Research and Development Laboratories is gratefully acknowledged.

ABSTRACT

The 3-dimensional finite element program TIRE3D is used to predict the static and rolling response of a KC-135 aircraft tire on a rigid surface. The tire tread and the casing are modeled respectively by 20-node brick elements and 16-node layered shell elements. As for the constitutive relations, Mooney-Rivlin model was used for the tread material while orthotropic properties based on laminate theory were used for the cord-rubber casing.

It was found that the numerical results were in remarkable agreement with the static tire load test data. Although the program possesses the capability of incorporating visco-elastic rubber behavior, numerical stability under rolling was achieved only under elastic conditions. Further, a simple numerical procedure was developed to determine the slip velocities at nodal points on the rolling tire contact patch. Determination of slip velocities is certainly a useful stride in the analytical prediction of tire wear.

TABLE OF CONTENTS

	Page
ACKNOWLEDGMENT	i
ABSTRACT	i
LIST OF FIGURES	ii
CHAPTER 1. Introduction	1
CHAPTER 2. Program implementation	4
CHAPTER 3. Determination of slip velocities	14
CHAPTER 4. Conclusion	21
REFERENCES	22

LIST OF FIGURES

	Page
1.1 Finite element configuration of half cross-section	2
1.2 Finite element configuration in the hoop direction	3
2.1 Static load-deflection curve for isotropic elasticity	5
2.2 Static load-deflection curve for Mooney-Rivlin elasticity	6
2.3 Contact patch pressure contours (static, isotropic elasticity)	10
2.4 Contact patch pressure contours (static, Mooney-Rivlin elasticity)	10
2.5 Contact patch 3-D pressure distribution (static loading)	11
2.6 Fully loaded spinning tire (spinning velocity 10 rad./sec.)	12
2.7 Contact patch pressure contours for spinning tire	13
2.8 Contact patch finite element configuration for spinning tire	13
3.1 Displacements of a point on the contact patch	17
3.2 Contact patch finite element configuration for partly loaded rolling tire	17

CHAPTER 1

Introduction

Objective:

A new research program sponsored by the Flight Dynamic Directorate is underway to develop tires with substantially improved life. One major task of this program is to formulate an analytical-numerical model of the aircraft tire takeoff and landing process. A complete understanding of the aircraft tire behavior during the entire ground operation is essential to accomplish the above task. The different maneuvers associated with the ground motion are : spinup, roll, yawed/cambered roll, braked roll, and taxiing-cornering.

Most of these features can be computationally modeled by the TIRE3D finite element program by the Computational Mechanics Co. Inc. for the NASA Langley Research Center. The work presented here recounts the author's research efforts to use the above computer program to investigate the behavior of a KC-135 tire during ground operation, in a way that it could be utilized in the tire wear research program.

Finite element model

The tread region of the KC-135 tire is modeled by 20-node brick elements while 16-node layered shell elements are used to model the cord-rubber composite in the casing (TIRE3D manual, 1990). The finite element configuration in the radial (K), meridional (J), and the hoop (I) directions used in the present work is depicted by Figs. 1.1 and 1.2.

The general cord-rubber structure in the KC-135 tire is assumed to be a balanced symmetric one with a total of 14 plies each with a thickness (t) of 0.027" and a crown angle of 39° . It was realized from the laminate theory for cord-rubber plies that the constitutive matrix in the finite element formulation is unaltered by using a balanced symmetric ply arrangement of $\theta/-\theta/-\theta/\theta$ of 4 plies by increasing the ply thickness accordingly. Thus, a modified ply thickness of 0.0945" (i.e. $14 \times 0.027/4$) was used in the model. The theoretical formulation is straightforward and hence omitted for brevity.

Scope of report

The program results for various load cases and the constitutive relations used in the current study are discussed in Chapter 2. In Chapter 3, the methodology used for determining slip velocities is elaborated with a numerical example. The geometric and material data used as well as computed deflections and stresses of the KC-135 tire are shown respectively in the data file (APPENDIX I) and the output file (APPENDIX II) submitted directly to John P. Medzorian of FIVMA/WRDC at WPAFB.

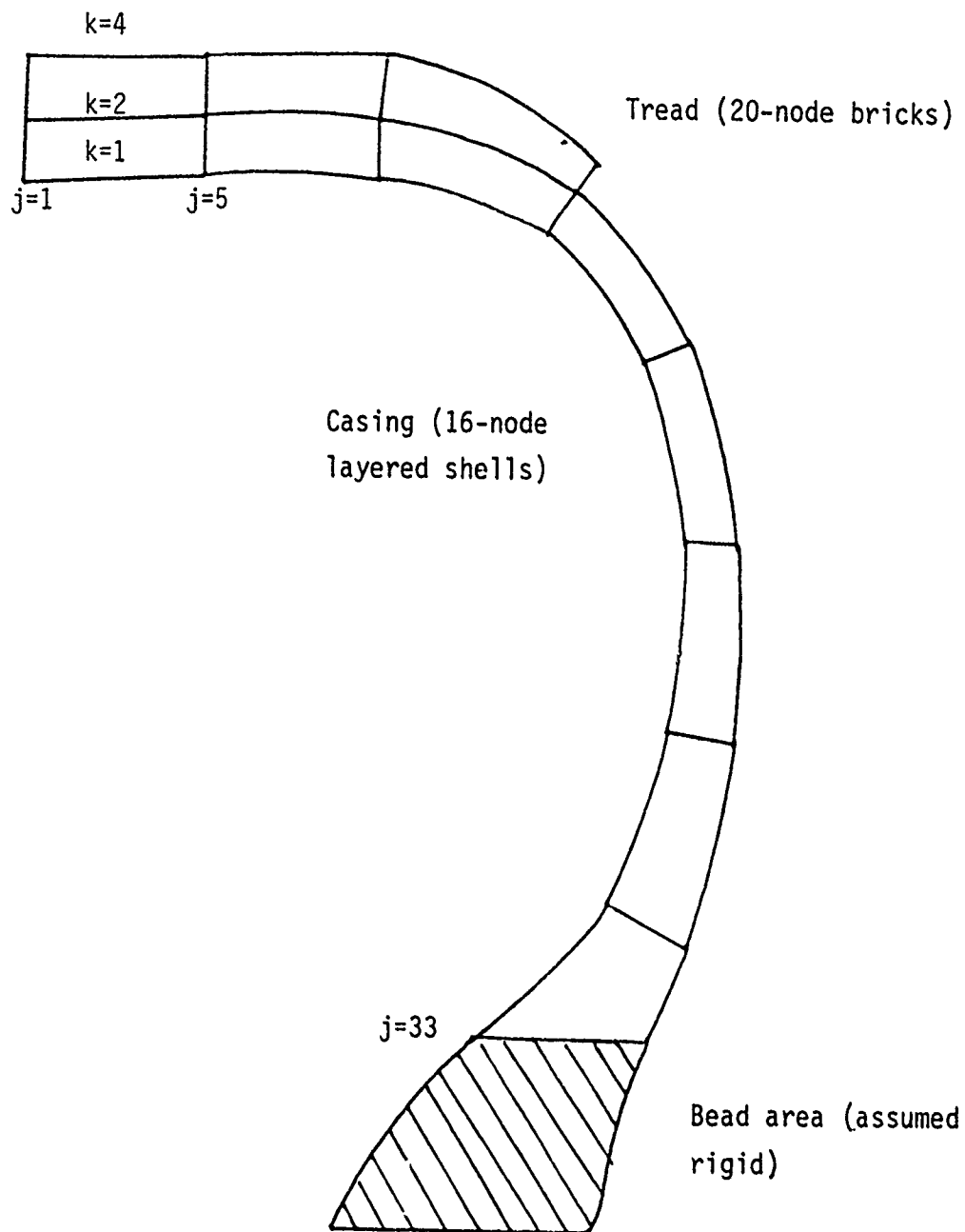


Fig. 1.1 Finite element configuration of half cross-section

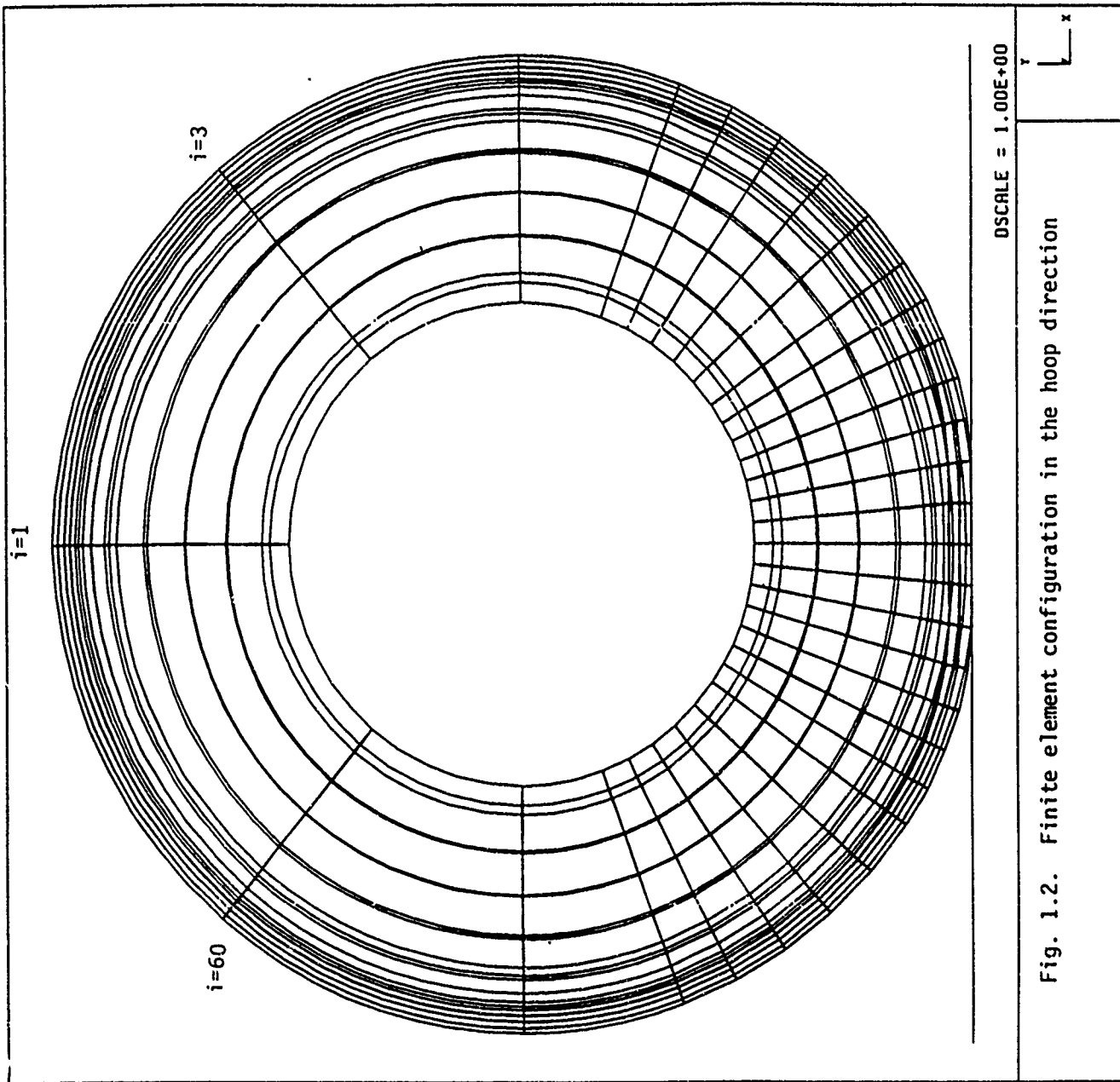


Fig. 1.2. Finite element configuration in the hoop direction

CHAPTER 2 .

Program Implementation

Application of inflation pressure and tire load

In order to evolve a stable solution, inflation pressurization (170 psi) was done in three steps (Appendix I). The rated KC-135 tire load is 39600 lbs. However, as seen from the input data (Appendix I), the load was also applied in many sufficiently small increments to ensure stability. The load deflection results for static loading were compared with experimental data. As seen in Figs. 2.1 and 2.2, remarkable agreement is obtained both for isotropic and Mooney-Rivlin elasticity.

Determination of tire deflection due to inflation pressure

TIRE3D program results do not provide the contact plane position after the inflation pressurization. Therefore, the author had to devise the following simple methodology to determine the above position and thus the tire deflection.

Inspection of the experimental load-deflection curves indicate linearity (proportionality) for small loads (< 2-3 kips for KC-135 tires). Thus, as seen in Table 1, two relatively small load increments (W_1 and W_2) were applied in the above range to estimate the contact plane positions (H_1 and H_2). Then, if the unknown contact plane position after the pressurization is H , the following proportionality relation can be used to find H :

$$\frac{W_1}{W_2} = \frac{H - H_1}{H - H_2}$$

Once H is known, the tire deflection for any other load W_3 can be determined as $H - H_3$.

As the applied load approached the rated load with increased deformations, convergence problems were experienced with isotropic elasticity. To circumvent this problem it was decided to use the Mooney-Rivlin elastic model especially suited for rubberlike material undergoing large deformations. Hence, the theoretical aspects of the above model are discussed in the ensuing section.

Mooney - Rivlin model

If the stretch ratio λ of an elastic substance in a given direction is defined as:

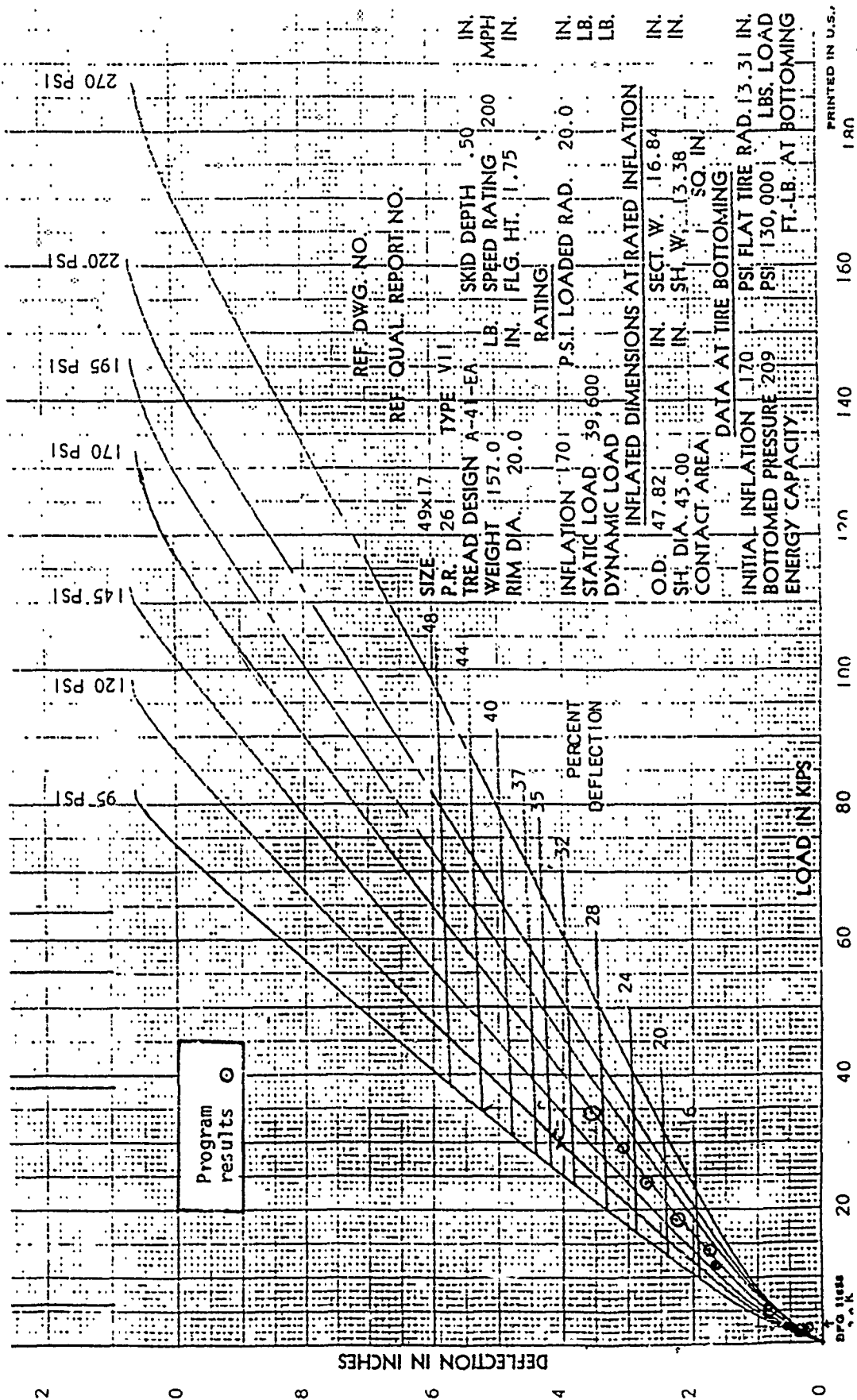


Fig. 2.1 Static load-deflection curve for isotropic elasticity

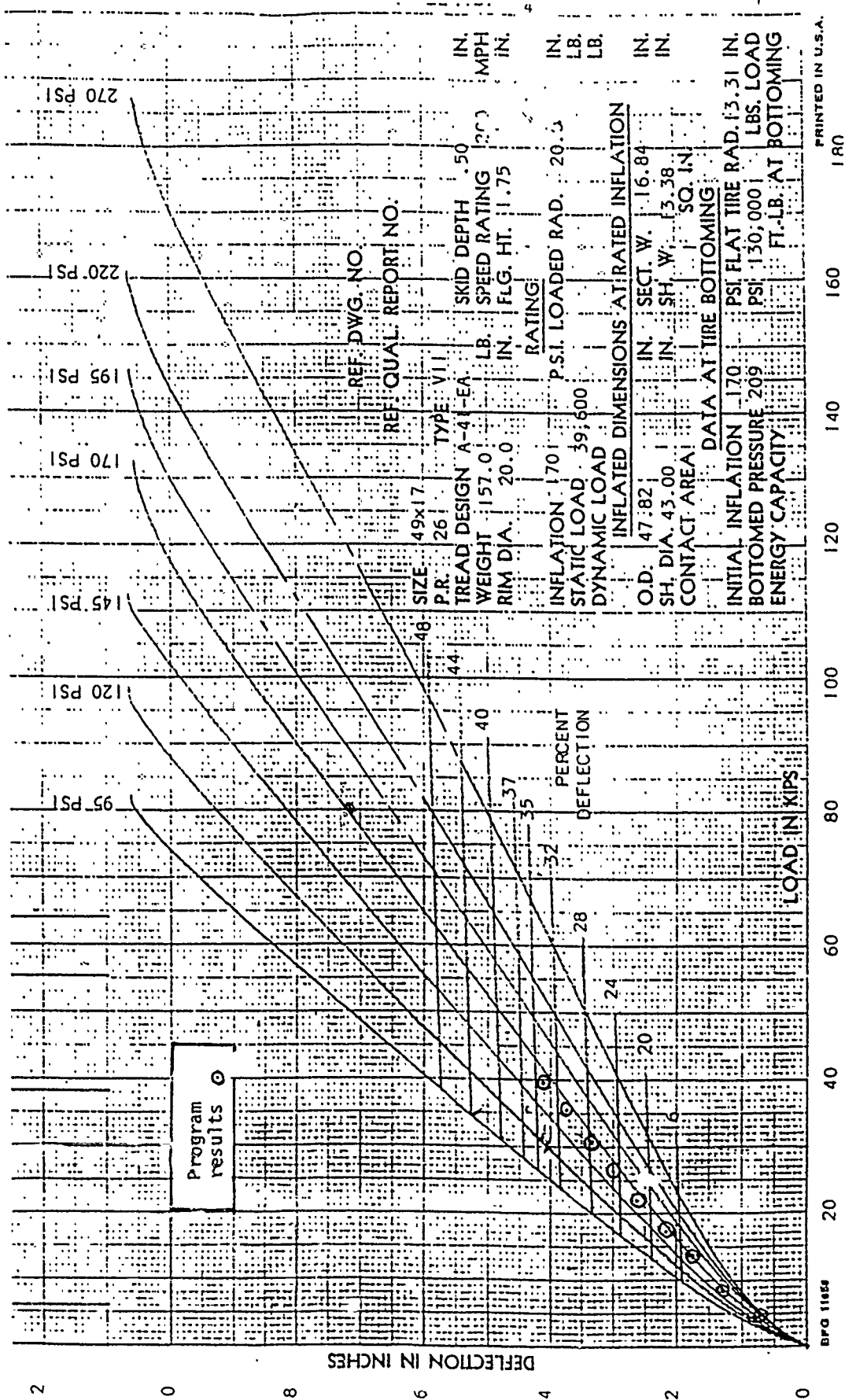


Fig. 2.2 Static load-deflection curve for Mooney-Rivlin elasticity

$$\lambda = \text{final length/initial length} \quad (2.1)$$

Mooney (1940) expressed the strain energy density of a material as:

$$W = C_1 (\lambda_1^2 + \lambda_2^2 + \lambda_3^2 - 3) + C_2 (1/\lambda_1^2 + 1/\lambda_2^2 + 1/\lambda_3^2 - 3) \quad (2.2)$$

where λ_i are the principal stretches and C_1 and C_2 are material constants.

Mooney (1940) also showed that C_1 and C_2 can be related to the shear modulus G and a "new large deformation elastic constant" H , as follows:

$$C_1 = (G + H)/4 \quad (2.3)$$

$$C_2 = (G - H)/4 \quad (2.4)$$

It follows from Eqns. (2.3) and (2.4) that,

$$G = 2 (C_1 + C_2) \quad (2.5)$$

for an incompressible elastic material undergoing large deformations. Also, since $\nu = 0.5$ for an incompressible material,

$$E = 3 G = 6 (C_1 + C_2) \quad (2.6)$$

Thus, W can now be expressed as:

$$W = G/4 \cdot \sum (\lambda_i - 1/\lambda_i)^2 + H/4 \cdot \sum (\lambda_i^2 - 1/\lambda_i^2) \quad (2.7)$$

Stress - strain energy relationship for uniaxial loading

The condition for incompressibility (no volume change) can be expressed as,

$$\lambda_1 \cdot \lambda_2 \cdot \lambda_3 = 1 \quad (2.8)$$

For a simple isometric stretch λ in the 1st principal direction, it follows from Eqn. (2.8) that,

$$\lambda_2 = \lambda_3 = 1/\lambda \quad (2.9)$$

The following strain-energy expression can be written by considering a unit cube of the material:

$$dW = \sigma \cdot \lambda_2 \cdot \lambda_3 (d\lambda)$$

Using Eqn. (2.9),

$$dW = \sigma \cdot 1/\lambda \cdot (d\lambda)$$

Therefore,

$$\sigma = \lambda \, dW/d\lambda \quad (2.10)$$

Experimental determination of C_1 and C_2

When the result in (2.9) is substituted in Eqn. (2.7), one gets

$$W = G/4 \cdot E(\lambda) + H/4 \cdot F(\lambda) \quad (2.11)$$

$$\text{where } E(\lambda) = 2(\lambda + 1/\lambda) + \lambda^2 + 1/\lambda^2 - 6 \quad (2.12)$$

$$\text{and } F(\lambda) = -2(\lambda + 1/\lambda) + \lambda^2 - 1/\lambda^2 \quad (2.13)$$

Since, from Eqn. (2.10)

$$\sigma = \lambda \, dW / d\lambda$$

$$\sigma = G/2 \cdot \lambda (\lambda + 1)(1 - 1/\lambda^3) + H/2 \cdot \lambda (\lambda - 1)(1 - 1/\lambda^3) \quad (2.14)$$

Finally, G and H can both be determined by fitting Eqn. (2.14), to an experimental σ Vs. λ curve.

Mooney (1940) defined the ratio H/G as

$$\alpha = H/G \quad (2.15)$$

and determined α to be 0.223 for Tread stock rubber.

Mooney - Rivlin constants used for KC-135 tire

In implementing the TIRE3D program, elastic moduli (E) values of 800 psi and 400 psi were assumed for tread and liner material respectively as well as a α value of 0.223.

Thus Eqns. (2.3) - (2.6) in conjunction with Eqn. (2.15) produces the following C_1 and C_2 values:

	C_1 (psi)	C_2 (psi)
Tread	82	51
Liner	41	26

Selection of the range of travel velocities

The problem of variation of slip conditions within the contact patch for different travel velocities has been addressed by Oden and Lin (1985). In their work, they defined the following two limits of travel velocity:

Upper limit = V_{0a} = Average contact particle velocity

Lower limit = V_{0r} = Rigid contact particle velocity

If the travel velocity $V_0 = V_{0a}$, the slips are minimal whereas if $V_0 = V_{0r}$, the full slip condition is obtained.

It is easily seen that

$$V_{0r} = \omega H \quad (2.16)$$

where H is the deflected vertical position of the foundation.

An approximate expression for V_{0a} can be found using the following logic:

The average velocity of the undeflected outer surface = ωR_o

Then, the imaginary flow rate through the undeflected area $= \omega R_o (R_o - R_i)$

Similarly, the imaginary flow rate through the deflected area $= V_{0a} (R_o - H)$

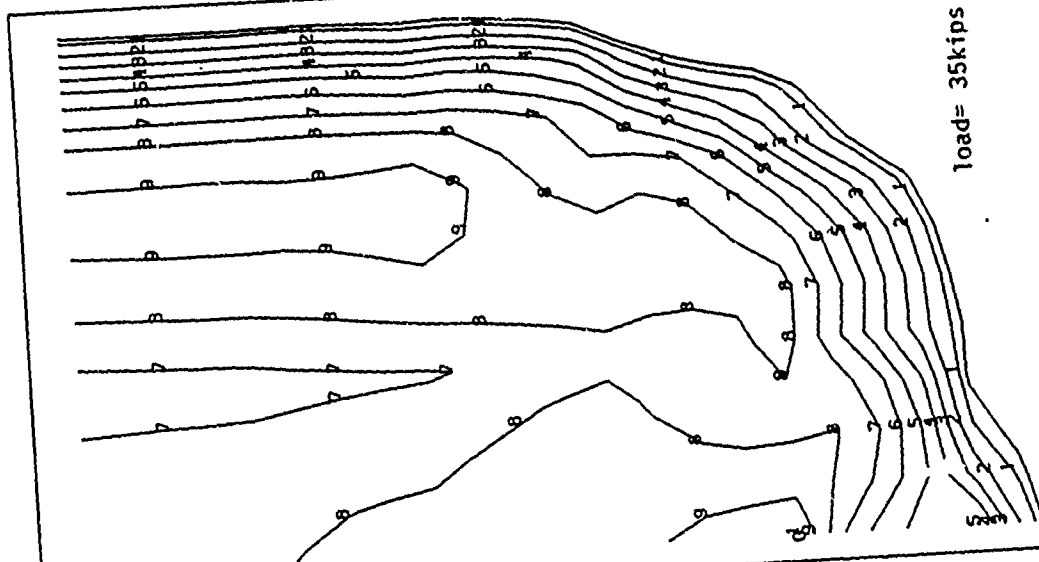
By equating the imaginary flow rates, one obtains

$$V_{0a} = \omega R_o (R_o - R_i) / (H - R_i) \quad (2.17)$$

Both the above limits of travel velocity are important in the analysis of slip velocities through the contact patch. However, due to time limitations only the effect of the lower limit of travel velocity was considered. Hence, the input data file contains a travel velocity obtained from Eqn. (2.16).

Program results

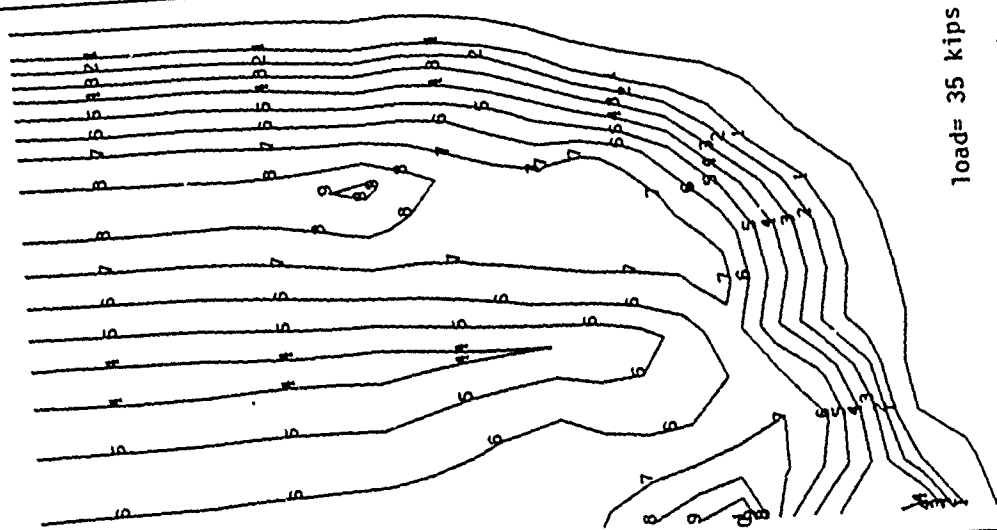
Some of the versatile post-processing provisions of TIRE3D for static loading/spinning are illustrated in Figs. 2.3 to 2.8. One straight rolling case was also run for a spinning velocity of 264.8 rad./s. and a corresponding travel velocity of 5280 in/s. (Eqn. 2.16). Due to time restrictions, this run had to be abandoned at a spinning and travel velocities of 75.4 rad/s. and 1508 in/s respectively. The contact patch corresponding to this run is shown in Fig. 3.2 which is used later for slip velocity calculations.



load= 35kips

PEZIZONE CONTACTS MAX(10)= 234.9 MIN(10)= 19.2 INTERVAL= 21.6

Fig. 2.3. Contact patch pressure contours (static, isotropic elasticity)



load= 35 kips

PEZIZONE CONTACTS MAX(10)= 235.6 MIN(10)= 35.7 INTERVAL= 25.3

Fig. 2.4 Contact patch pressure contours (static, Mooney-Rivlin elasticity)

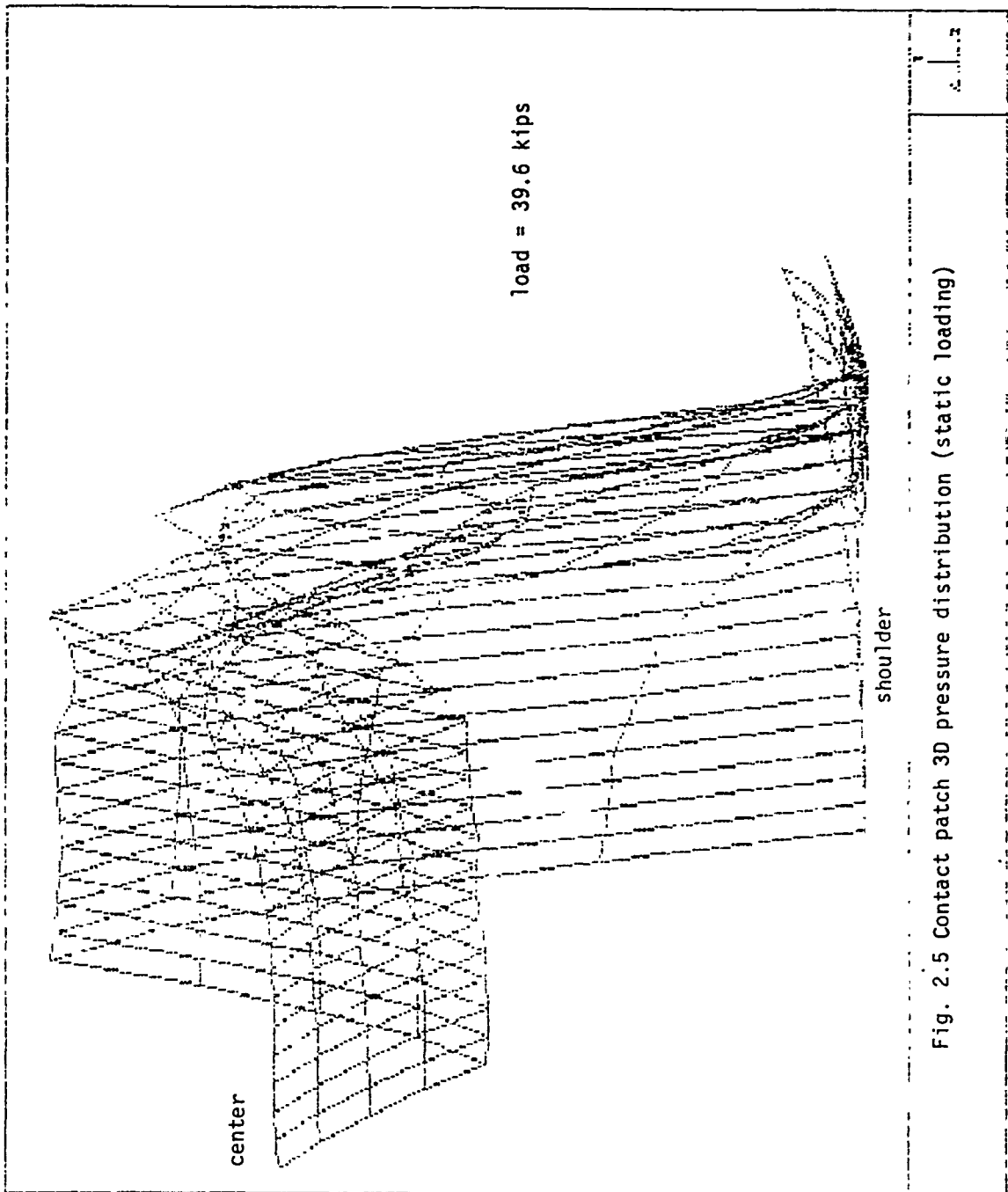
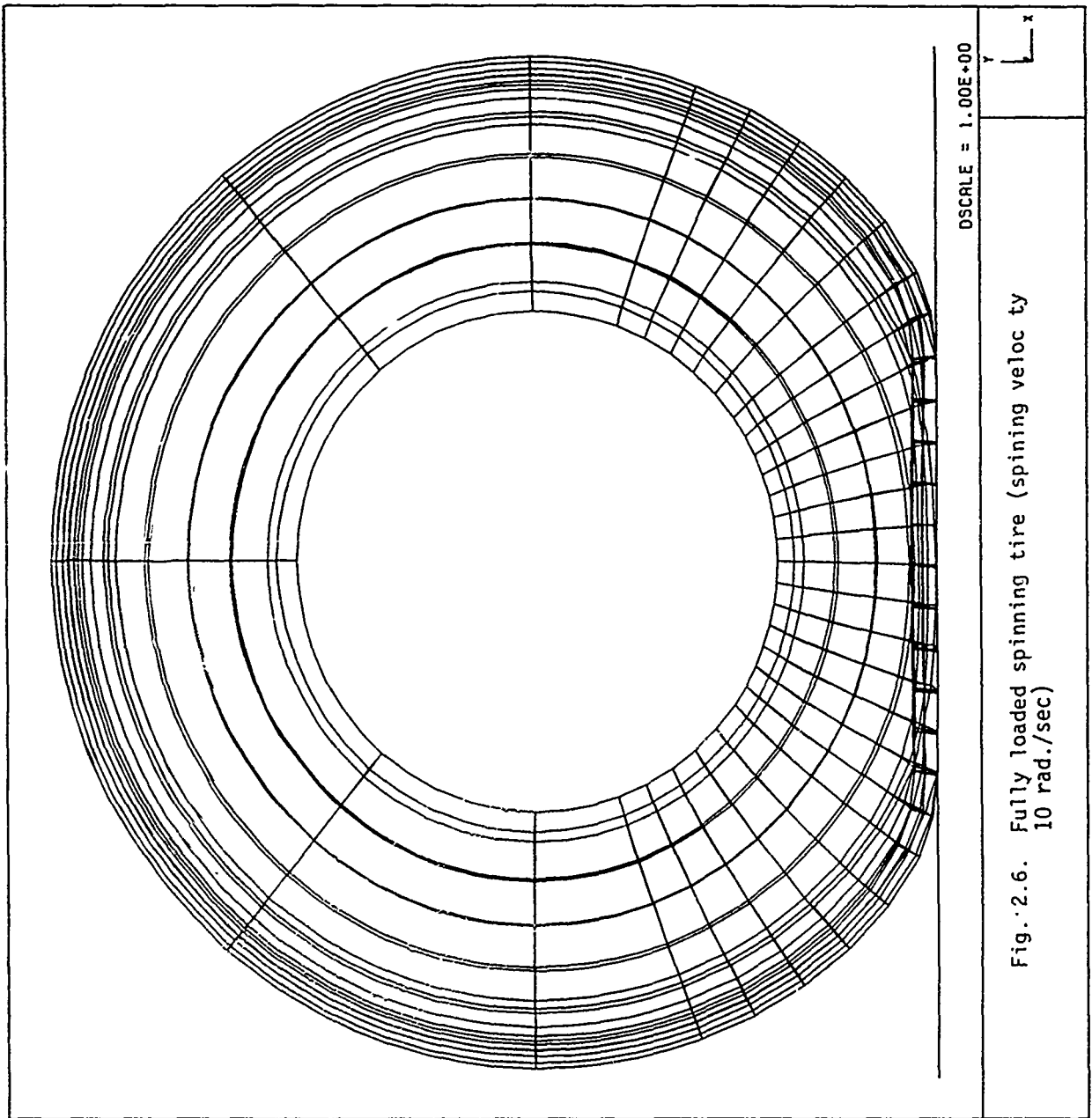
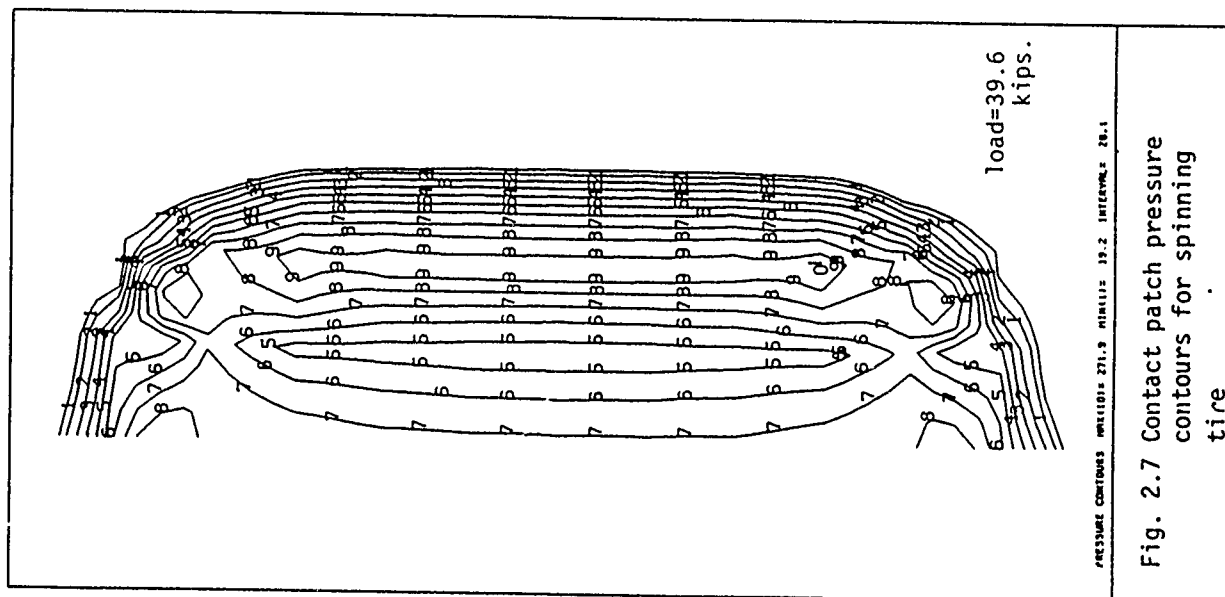
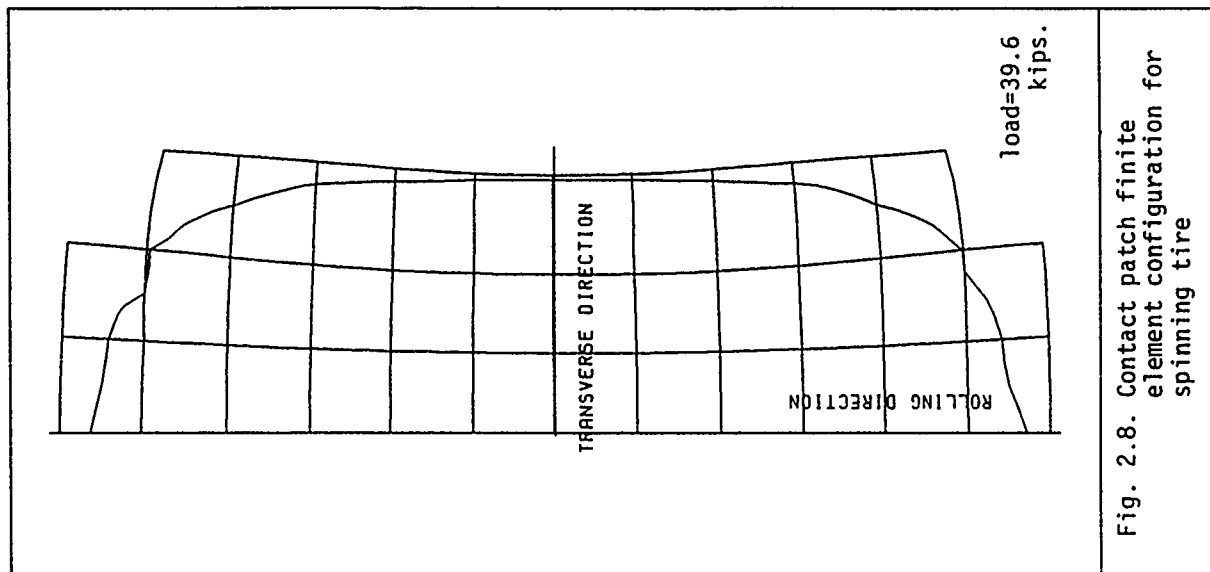


Fig. 2.5 Contact patch 3D pressure distribution (static loading)





CHAPTER 3

Determination of Slip Velocities

When a tire rolls on a foundation, the slip velocity w_t at a point on the contact patch (Γ) is defined as:

$$\bar{w}_t = \bar{V} - \bar{V}_0 \quad (3.1a)$$

where \bar{V} = absolute particle velocity of a point on Γ .
 \bar{V}_0 = foundation velocity

If the foundation does not move, then

$$\bar{w}_t = \bar{V} \quad (3.1b)$$

Particle Velocity in cartesian coordinates

The following formulation due to Faria et. al (1989) can be used to determine the absolute particle velocity \bar{V} on the contact patch. First, the motion of a particle must be separated into three components, which are 1) translational component equal to the tire center velocity (v_{o1}), 2) rigid body rotation about tire the center and 3) deformation due to the contact constraint.

If \bar{x} is the position vector of a particle X in the deformed tire, and if $\bar{y}(t)$ denotes the position vector of the point that would have been occupied by X had the tire been rigid, then

$$\bar{x} = \chi (\bar{y}(t))$$

where χ is an invertible map from the reference configuration to the deformed cylinder. \bar{x} is only an implicit function of time t due to the assumed steady state conditions. Then, the velocity field without the translational component is obtained as:

$$\begin{aligned} \bar{v} &= \dot{\bar{x}} \\ &= \partial \bar{x} / \partial \bar{y} \cdot \partial \bar{y} / \partial t \end{aligned}$$

In terms of the components, this can be rewritten as:

$$v_i = \partial x_i / \partial y_1 \cdot \partial y_1 / \partial t + \partial x_i / \partial y_2 \cdot \partial y_2 / \partial t + \partial x_i / \partial y_3 \cdot \partial y_3 / \partial t \quad (3.2)$$

Using the following notation for different maneuvers,

- ω = spinning angular velocity
- Ω = cornering angular velocity
- γ = camber
- α = slip angle

$$\partial y_1 / \partial t = \Omega y_3 \cos \gamma - (\omega + \Omega \sin \gamma) y_2 \quad (3.3a)$$

$$\partial y_2 / \partial t = (\omega + \Omega \sin \gamma) y_1 \quad (3.3b)$$

$$\partial y_3 / \partial t = -\Omega y_1 \cos \gamma \quad (3.3c)$$

Further, it is noted from the above discussion that u , the deformation of a particle is given by,

$$u = x - y \quad (3.4)$$

Thus,

$$\partial x_i / \partial y_i = \partial u_i / \partial y_i + 1 \quad (3.5)$$

$$\partial x_i / \partial y_j = \partial u_i / \partial y_j \quad (3.6)$$

where u_i are the cartesian components of u .

Substituting Eqns. (3.5) and (3.6) in Eqn. (3.2) results in:

$$V_1 = (\partial u_1 / \partial y_1 + 1) \cdot \partial y_1 / \partial t + \partial u_1 / \partial y_2 \cdot \partial y_2 / \partial t + \partial u_1 / \partial y_3 \cdot \partial y_3 / \partial t \quad (3.7a)$$

$$V_2 = \partial u_2 / \partial y_1 \cdot \partial y_1 / \partial t + (\partial u_2 / \partial y_2 + 1) \cdot \partial y_2 / \partial t + \partial u_2 / \partial y_3 \cdot \partial y_3 / \partial t \quad (3.7b)$$

$$V_3 = \partial u_3 / \partial y_1 \cdot \partial y_1 / \partial t + \partial u_3 / \partial y_2 \cdot \partial y_2 / \partial t + (\partial u_3 / \partial y_3 + 1) \cdot \partial y_3 / \partial t \quad (3.7c)$$

Then, by using expressions (3.5) and (3.6) in Eqns. (7), one obtains the most general expression for the particle velocity as:

$$V_1 = (\partial u_1 / \partial y_1 + 1) \cdot [\Omega y_3 \cos \gamma - (\omega + \Omega \sin \gamma) y_2] + \partial u_1 / \partial y_2 \cdot (\omega + \Omega \sin \gamma) y_1 - \partial u_1 / \partial y_3 \cdot \Omega y_1 \cos \gamma \quad (3.8a)$$

$$V_2 = \partial u_2 / \partial y_1 \cdot [\Omega y_3 \cos \gamma - (\omega + \Omega \sin \gamma) y_2] + (\partial u_2 / \partial y_2 + 1) \cdot (\omega + \Omega \sin \gamma) y_1 - \partial u_2 / \partial y_3 \cdot \Omega y_1 \cos \gamma \quad (3.8b)$$

$$V_3 = \partial u_3 / \partial y_1 \cdot [\Omega y_3 \cos \gamma - (\omega + \Omega \sin \gamma) y_2] + \partial u_3 / \partial y_2 \cdot (\omega + \Omega \sin \gamma) y_1 - (\partial u_3 / \partial y_3 + 1) \cdot \Omega y_1 \cos \gamma \quad (3.8c)$$

However, in the special case of a straight rolling tire, since

$$\begin{aligned} \Omega &= 0 \\ \gamma &= 0 \\ \alpha &= 0 \end{aligned}$$

the above expressions for velocity simplify to

$$V_1 = -(\partial u_1 / \partial y_1 + 1) \cdot \omega y_2 + \partial u_1 / \partial y_2 \cdot \omega y_1 \quad (3.9a)$$

$$V_2 = -\partial u_2 / \partial y_1 \cdot \omega y_2 + (\partial u_2 / \partial y_2 + 1) \cdot \omega y_1 \quad (3.9b)$$

$$V_3 = - \partial u_3 / \partial y_1 \cdot \omega y_2 + \partial u_3 / \partial y_2 \cdot \omega y_1 \quad (3.9c)$$

Finally, by incorporating the translational velocity (center velocity, v_{o1}), the absolute particle velocity is obtained as:

$$V_1 = -(\partial u_1 / \partial y_1 + 1) \cdot \omega y_2 + \partial u_1 / \partial y_2 \cdot \omega y_1 + v_{o1} \quad (3.10a)$$

$$V_2 = - \partial u_2 / \partial y_1 \cdot \omega y_2 + (\partial u_2 / \partial y_2 + 1) \cdot \omega y_1 \quad (3.10b)$$

$$V_3 = - \partial u_3 / \partial y_1 \cdot \omega y_2 + \partial u_3 / \partial y_2 \cdot \omega y_1 \quad (3.10c)$$

Contact patch particle velocity in cylindrical coordinates

A simpler formulation was done to obtain particle velocities on the contact patch by Tielking (1984). The corresponding expressions applicable only on the contact patch are as follows:

$$V_1 = -(\partial u_\theta / \partial \theta + R - u_r) \cdot \omega \cos \theta + (\partial u_r / \partial \theta + u_\theta) \cdot \omega \sin \theta + v_{o1} \quad (3.11a)$$

$$V_2 = 0 \quad (3.11b)$$

$$V_3 = - \partial u_z / \partial \theta \cdot \omega \quad (3.11c)$$

where

R = Length of the radius of contact patch point considered.

u_r , u_θ , and u_z are the cylindrical components of u in Eqn. (3.4).

Interpretation of particle velocities on the contact patch

According to Fig. 3.1, it is seen that

$$y_1 = R \sin \theta \quad (3.12a)$$

$$y_2 = -R \cos \theta \quad (3.12b)$$

$$u_1 = u_\theta \cos \theta - u_r \sin \theta \quad (3.13c)$$

$$u_2 = u_\theta \sin \theta + u_r \cos \theta \quad (3.13d)$$

It is known that

$$\partial u_1 / \partial \theta = \partial u_1 / \partial y_1 \cdot \partial y_1 / \partial \theta + \partial u_1 / \partial y_2 \cdot \partial y_2 / \partial \theta \quad (3.14)$$

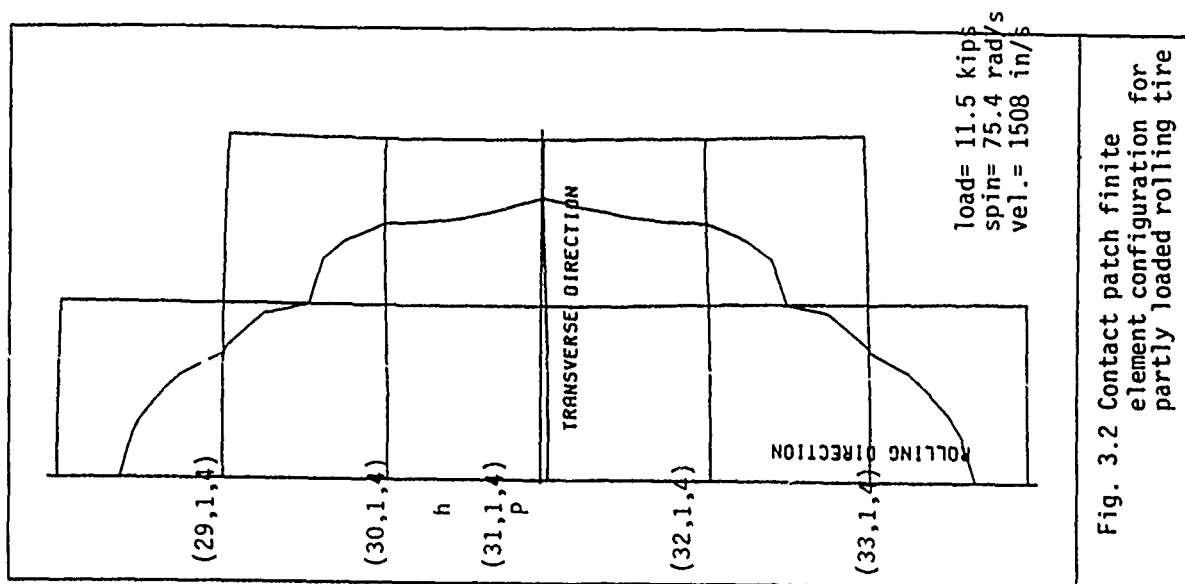


Fig. 3.2 Contact patch finite element configuration for partly loaded rolling tire

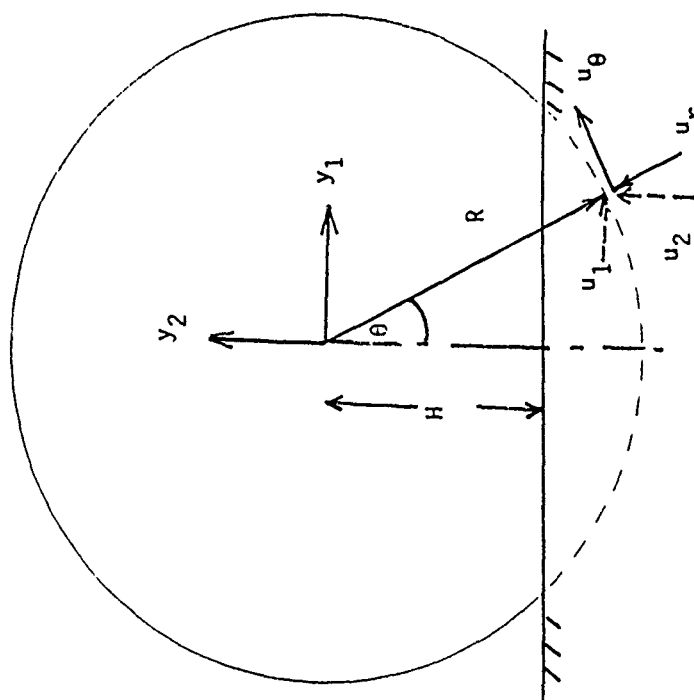


Fig. 3.1 Displacements of a point on the contact patch

Then, by differentiating Eqns. (3.12)

$$\begin{aligned}\partial u_1/\partial \theta &= \partial u_1/\partial y_1 \cdot R \cos \theta + \partial u_1/\partial y_2 \cdot R \sin \theta \\ &= -\partial u_1/\partial y_1 \cdot y_2 + \partial u_1/\partial y_2 \cdot y_1\end{aligned}\quad (3.15)$$

Further, by differentiating Eqn. (3.13a), one obtains

$$\partial u_1/\partial \theta = (\partial u_\theta/\partial \theta - u_r) \cos \theta - (\partial u_r/\partial \theta + u_\theta) \sin \theta \quad (3.16)$$

Hence, expressions (3.15) and (3.16) yield

$$-\partial u_1/\partial y_1 \cdot y_2 + \partial u_1/\partial y_2 \cdot y_1 = (\partial u_\theta/\partial \theta - u_r) \cos \theta - (\partial u_r/\partial \theta + u_\theta) \sin \theta$$

Finally, since $y_2 = -R \cos \theta$, it is seen that the expressions for V_1 (Eqns. 3.10a and 3.11a) produce similar results.

Furthermore, from Eqn. (3.15) it can be deduced that

$$\partial u_2/\partial \theta = -\partial u_2/\partial y_1 \cdot y_2 + \partial u_2/\partial y_2 \cdot y_1 \quad (3.17)$$

By recognizing that u_2 and u_3 are one and the same, it becomes clear that the expressions for V_3 (Eqns. 3.10c and 3.11c) are also the same.

It can also be deduced from Eqn. (3.15) that,

$$\partial u_2/\partial \theta = -\partial u_2/\partial y_1 \cdot y_2 + \partial u_2/\partial y_2 \cdot y_1 \quad (3.18)$$

Further, Fig. 3.1 depicts that any element on the contact patch must have a vertical displacement component (u_2) given by:

$$u_2 = R \cos \theta - H \quad (3.19)$$

Thus,

$$\partial u_2/\partial \theta = -R \sin \theta = -y_1 \quad (3.20)$$

Now, comparison of Eqns. (3.18) and (3.20) yields,

$$-\partial u_2/\partial y_1 \cdot y_2 + \partial u_2/\partial y_2 \cdot y_1 = -y_1$$

Hence, it follows that the expressions for V_2 (Eqns. 3.10b and 3.11b) give similar results as well.

Approximation of displacement gradients

It is necessary to determine the nodal displacement gradients to obtain nodal slip velocities from Eqns. (3.10) and

(3.1b). However, most finite element programs such as TIRE3D provide only the displacements at the element nodes. Hence, the author used the following numerical approximations to compute the nodal displacement gradients.

Determination of $\partial u_i / \partial y_1$

For the lagging area,

$$\partial u_i / \partial y_1(I) = [-3 u(I) + 4u(I+1) - u(I+2)]/2h \quad (3.21)$$

For the leading area,

$$\partial u_i / \partial y_1(I+2) = [u(I) - 4u(I+1) + 3 u(I+2)]/2h \quad (3.22)$$

For inner nodes,

$$\partial u_i / \partial y_1(I) = [u(I-2) - 4u(I-1) + 4u(I+1) - u(I+2)]/2h \quad (3.23)$$

where I is the loop direction coordinate used in the TIRE3D and h is the distance interval in the direction 1 (Fig. 3.1).

Determination of $\partial u_i / \partial y_2$

For the entire region,

$$\partial u_i / \partial y_2(K) = [-3 u(K) + 4u(K-2) - u(K-3)]/2k \quad (3.24)$$

where K is the radial direction coordinate used in the TIRE3D and k is the distance interval in the direction 2 (Fig. 3.1).

Estimation of slip velocities

In order to illustrate the application of Eqns. (3.10) and (3.1b), the slip velocity of the point P on the contact patch (Fig. 3.2), is predicted below.

Since P is at the centerline of a straight rolling tire, the slip velocity is in the rolling direction. Thus, only Eqn. (3.10a) is applicable in this case.

Estimation of $\partial u_i / \partial y_1$

In this case, Eqn. (3.23) is applied observing that P is an inner node with $I=31$ (Figs. 1.2 and 3.2). It must be remembered that TIRE3D produces cumulative displacements and hence, the displacements due to load deformation should be obtained by subtracting the inflation pressure displacements from the final displacements.

To illustrate this the author has provided the relevant final displacements in Table II.1 (Appendix II) and the relevant

inflation displacements in Table II.2 (Appendix II). As the deformation of a given point (ex. I=30, J=1 and K=4) the user should be utilize the difference between the displacements in the corresponding rows (ex: 30,1,4) in the above tables.

$$\text{Further, } h = H \tan \phi$$

where ϕ = angle interval in the hoop direction (= 5° in the contact patch region) and H (Fig. 3.1) is the contact plane vertical position (= 22.363 in. from the program output).

$$\begin{aligned} \text{Thus, } \partial u_1 / \partial y_1 &= [u(29,1,4) - 4u(30,1,4) + 4u(32,1,4) - u(33,1,4)] / 2h \\ &= -0.0324 \end{aligned}$$

Also, by recollecting that y_i are the undeformed coordinates of the tire, Fig. 3.1 shows that,

$$\begin{aligned} \text{and } y_2 &= -(H + u_2) = -23.343 \text{ in.} \\ y_1 &= -u_1 = 0.131 \text{ in.} \end{aligned}$$

Estimation of $\partial u_1 / \partial y_2$

In this case, Eqn. (3.24) can be applied using Tables II.1 and II.2 in the above described manner considering k as the tread thickness.

$$\text{Then, } k = 0.65 \text{ in.}$$

$$\begin{aligned} \text{Thus, } \partial u_1 / \partial y_2 &= [-3u(31,1,4) + 4u(31,1,2) - u(31,1,1)] / 2k \\ &= 0.08 \end{aligned}$$

$$\begin{aligned} \text{Since, } \omega &= 75.4 \text{ rad/s (for partly loaded tire)} \\ \text{and } v_{o1} &= 1508 \text{ in/s} \end{aligned}$$

Finally, the slip velocity (Eqns. 3.1b and 3.10a)

$$V_1 = 55.98 \text{ in/s.}$$

It is noted that the slip velocity at P is small when compared with the travel velocity of 1508 in/s.

The above procedure can be easily computerized and hence the TIRE3D program can be made to predict the slip velocities at every nodal point on the contact patch.

CHAPTER 4

Conclusion

The TIRE3D computer code was found to predict the actual static response of a tire remarkably well with both linear elastic and Mooney-Rivlin elastic constitutive models. Instabilities were however encountered for linear elasticity under large deformations. This condition was rectified by using the Mooney-Rivlin model.

Although the analytical results for rolling could not be checked with experimental values, the solutions obtained were stable and adjudged to be reasonable. The inability of the present version of TIRE3D to accomodate visco-elasticity is a drawback especially in analyzing high speed tire response such as that of HVVs tires. However, there is optimism that a near future version of TIRE3D will be devoid of these problems.

It is well established that tire wear is produced by tractions and strains set up by interfacial rubber-pavement slip. As illustrated in Chapter 3, the program results were successfully used to estimate slip velocities on the contact patch. The algorithm used to determine slip velocities is a numerical one and hence is approximate. Yet, it is advantageous in a programming perspective as its very numerical nature makes it compatible with the rest of the TIRE3D code!

Moreover, Appendix II (Tables II.3 and II.4) shows a sample output of TIRE3D where the shear stresses (tractions) on the contact patch are also predicted. Thus, this initial study has shed light into means of analyzing two vital factors leading to wear. Hence it certainly is a significant stride towards analytical prediction of tire wear.

Recommendations for extended research

Recent research (Veith, 1982) has shown that the maneuvers contributing most to tire wear are 1) braked rolling and 2) cornering. In the case of aircraft tires, spinup associated with landing could make a major contribution to wear as well. A review of literature (Gough, 1958, Veith, 1982) indicates the complexity involved in determining the tractions and strains generated during above maneuvers. The present work has demonstrated that the TIRE3D program is capable of revealing the traction and slip distributions during static loading and rolling. Therefore, a future study using TIRE3D to analyze the traction and slip distribution on the contact patch during braked rolling, cornering and spin-up will be invaluable to analytical tire wear studies.

The validity of a future tire wear model formulated based on TIRE3D can be ascertained only by checking the present results with experimental measurements whenever possible. This is especially needed for spinning and rolling conditions. Experimental

corroboration of contact patch vertical pressure distribution (Figs. 2.3 - 2.5 and 2.7) and strain distribution (Appendix I) are two such possibilities. The existing experimental evidence obtained from bias tire tests tend to support the pressure distributions shown in Figs. 2.3 - 2.5 and 2.7 where the pressure peaks are closer to the tire shoulder than to the center. The anticipated results from the collaborative experimental study between the Landing Gear Systems Group, Wright-Patterson AFB and the University of Michigan Transportation Research Center should yield adequate test results for this venture.

Another factor often assumed to be a simple constant in analytical models is the coefficient of friction representing the pavement roughness. The variation of frictional resistance due to environmental conditions such as moisture and the tire speed itself is generally overlooked for simplicity. Since the coefficient of friction used in TIRE3D to model the pavement roughness plays a vital role in traction and strain distribution on the contact patch, a profound investigation of the tire-pavement frictional characteristics will be immensely useful in obtaining more meaningful analytical results for wear.

REFERENCES

Computational mechanics Co., Inc., "Tire user's manual", Austin, Texas, 1990.

Faria, L.O., Bass, J.M., Oden, J.T., and Becker, E.B., "A three-dimensional rolling contact model for a reinforced rubber tire", Tire Science and Technology, Vol. 17, No. 3, July-Sep. 1989, pp. 217-233.

Gough, V.E., "Tire-to-ground contact stresses", Presentation to the Stress Analysisi Group Conference on Contact Stresses, London, May, 1958.

Mooney, M., "A theory of large deformations", Journal of Applied Physics, Vol. 11, Sept. 1940.

Oden, J.T., Lin, T.L., and Bass, J.M., "A finite element analysis of the general rolling contact problem for a viscoelastic rubber cylinder", Tire Science and Technology, Vol. 16, No. 1, Jan. - March 1988, pp. 18-43.

Tielking, J.T., "A finite element tire model", Tire Science and Technology, Vol. 11, Nos. 1-4, Jan. - Dec. 1984, pp. 50-63.

Veith, A.G., "The wear of pneumatic tires, a review", Department of Mechanical Engineering, University of Akron, August 1982.

1991 USAF SUMMER FACULTY RESEARCH PROGRAM/
GRADUATE STUDENT RESEARCH PROGRAM

Sponsored by the
AIR FORCE OFFICE OF SCIENTIFIC RESEARCH
Conducted by the
Research & Development Laboratories

FINAL REPORT

Depley of Laminated Panels with Perforation due to impact

Prepared by: John Lair and David Hui
Academic Rank: Graduate Student and Associate Professor
Department and Mechanical Engineering
University: University of New Orleans
Research Location: WRDC/FIVST
USAF Researcher: Greg Czarnecki
Date: September 29, 1991

Deply of Laminated Panels with Perforation due to Impact

by

John Lair and David Hui

ABSTRACT

Deply techniques were used in composite material laminated plates were used in low velocity impact of panels where there no perforation occurs. Some preliminary data were obtained by Foos (1989). Such deply technique by pyrolysis (heat it in an oven at approx 800 deg F for about 40 min and then separate the plies with a scalpel) has not been commonly applied on perforated plates. Such deply technique will give more accurate delaminated areas and hole sizes than C-Scan techniques. Further, matrix cracks were observed in deply laminates which cannot be observed by C-Scan. Six panels from previous composite panels perforated by spherical projectiles (Altamirano 1991) are used for deply and the separated plies are analyzed in an image processing machine. The delaminated areas are seen quite clearly since they were pre-soaked in gold chloride prior to heating in an oven.

1. INTRODUCTION

The purpose of the work is to determine whether more information can be obtained from deply techniques than from the traditional C-Scan photos. The panels were soaked in gold chloride liquid prior to heating in an oven so that it will leave a gold imprint on the plies which can be easily visualized. The size and shape of the delaminated area as a function of the plies were observed and measured using an image processing machine.

Figure 1a,b shows typical actual size photos of two adjacent plies from the 365 ft./sec. test taken from the

ACKNOWLEDGEMENTS

The authors would like to thank the guidance of Dr. Arnold Mayer and the assistance of Greg Czarnecki during the course of the research. The literature search on the subject of damage of composite panels due to projectile impact was performed at Wright Patterson Air Force Base library and the assistance of the library staff is gratefully acknowledged. The encouragements of James Hodges, Marty Lentz, Eric Fletcher and Pat Petit were appreciated.

Altamirano (1991) test program. The boundaries of the delamination zone were marked with white paint. Such painting was not necessary in the image processing machine since the gold imprints were clearly observable, they are shown only for xeroxing purposes. The matrix cracking can be seen in ply 14 of Fig. 1 and a often occurring "H" shaped deply area can be seen in ply 15. These two plies were adjacent to one another ply 14 being closer to the impact face. The side of the ply closest to the impact face is shown in both cases.

Figure 2a-2f shows graphs of the delamination areas and hole sizes. It can be seen that there exist drastic changes in delamination areas from one ply to the next ply. The hole sizes for relatively low impact velocities (365 ft/sec) would be smaller than that from higher velocities (879, 1013, 2777, 4476, 5817 ft/sec). On the other hand, the delamination areas would be larger for smaller velocities since one can expect that most of the damage would occur at velocities just above the V50.

Figure 3 shows a graph of the delamination volume and hole volume versus the energy absorption of the panels divided by the mass of the 1/2 inch diameter spherical steel projectile, using the deply technique. The energy absorption is defined as the difference between the initial and residual kinetic energies of the projectile. It can be seen that the delamination volume decreases for the first three lower velocities and then increases for the remaining three higher velocities. The hole volume tends to reach an asymptotic value for higher energy absorption. Figure 4 presents the same data taken from pixel count of C-Scan image.

Figure 5 shows a typical C-Scan photo of the entire laminated panel. The pixel count on C-Scan would enable one

to obtain the delamination volume and hole volumes. The delamination volumes measured from the C-Scan image were found to be larger than that obtained from deply technique. This is due to the fact that C-Scan can not detect delaminations which are smaller than those found near the surface. If a delamination overlays a undelaminated area, such undelaminated area is counted as delaminated area, thus overestimating the undelaminated area. On the other hand, the hole size was smaller on the C-Scan results than from the deply results. As these observations are based on the deply of only seven panels, they need to be substantiated by a enlargement of the test program.

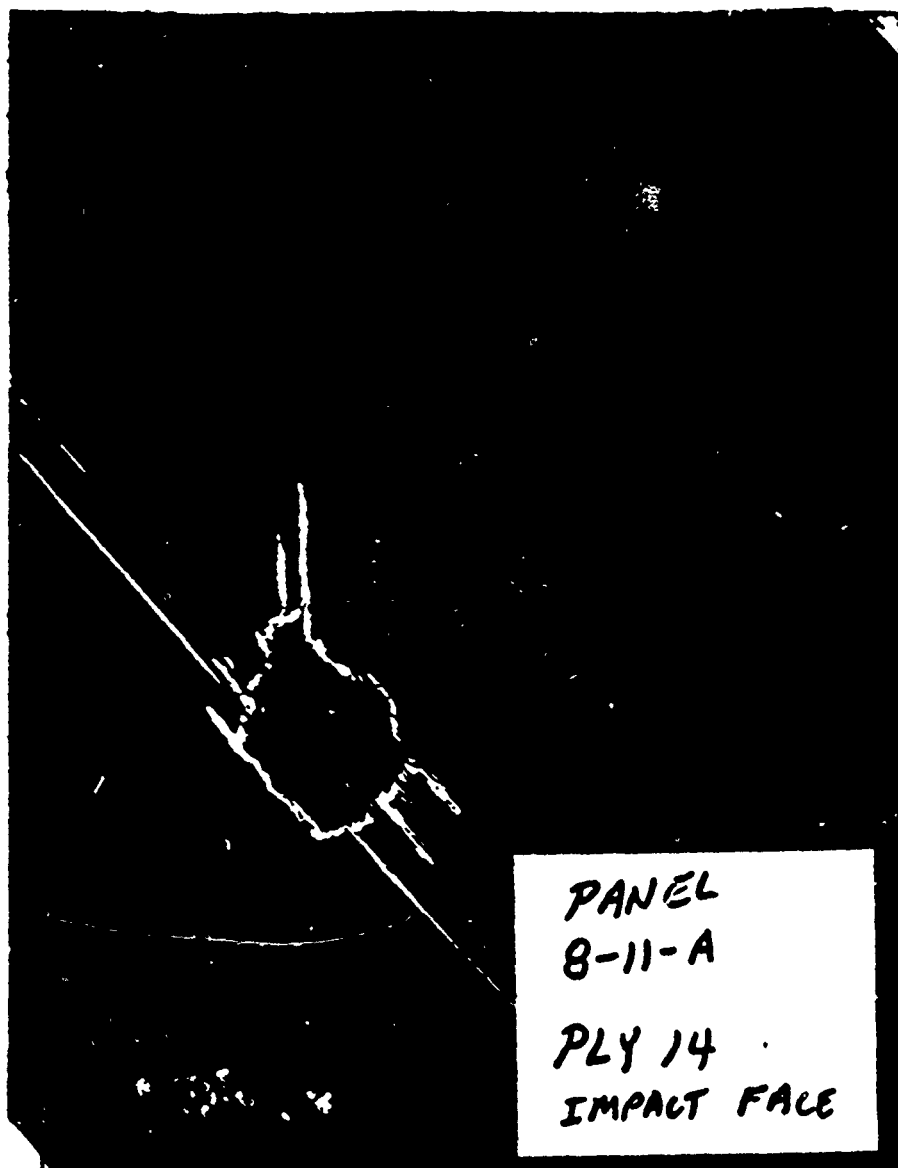
3. CONCLUSIONS

The deply technique was successfully employed to study the damage zone of laminated panels perforated by spherical indenter. Such deply technique was found to give valuable information on the size, shape and matrix cracks which could not be accurately observed by C-Scan photos.

REFERENCES

Altamirano, Magna, Experimental Investigation of High and Low Impact Energy Absorption of AS4/3502 Graphite/Epoxy Panels, M.S. Degree Thesis, University of New Orleans, New Orleans, LA, May 1991

Foos, Brian, Low Velocity Impact Damage Investigations of Composite Plates in a Drop Tower, M.S. Degree Thesis, The Ohio State University, Columbus, OH, March 1990

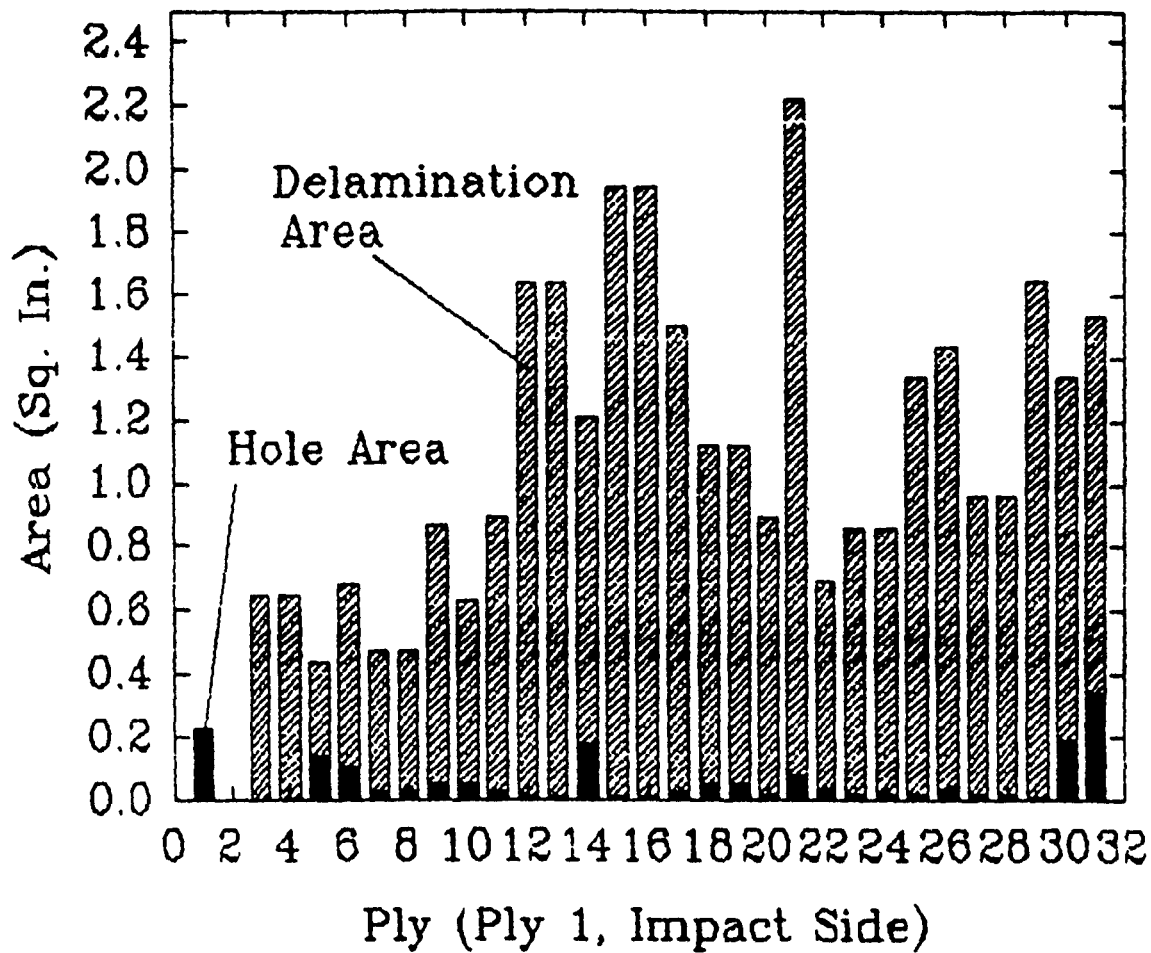


PANEL
8-11-A
PLY 14
IMPACT FACE

Figure 1a deplined lamina



Figure 1b deplied lamina



Damage at 365 ft./sec. impact velocity
From Deply technique

FIGURE 2a

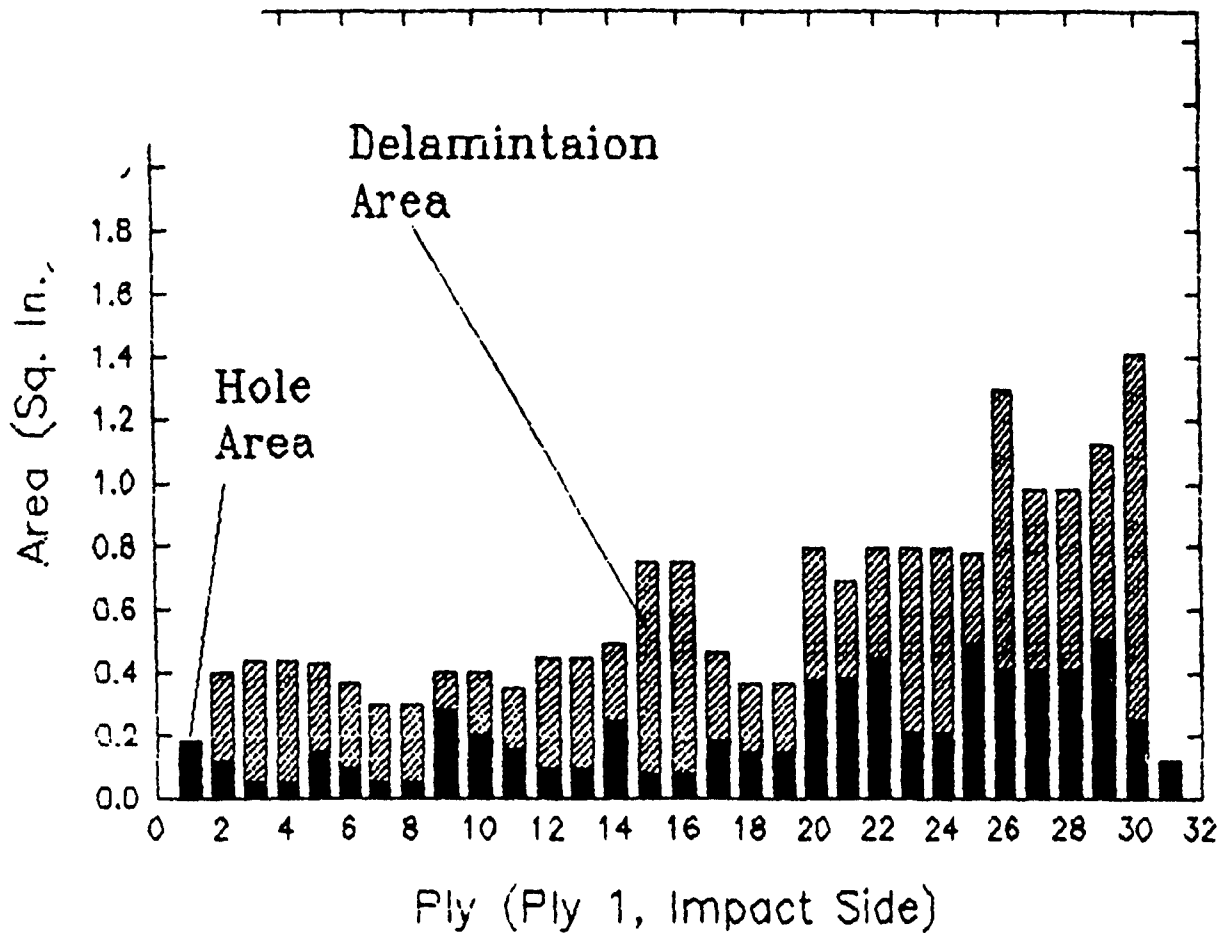


FIGURE 2b Damage at 879 Ft./Sec Impact Velocity.
From Depty Technique

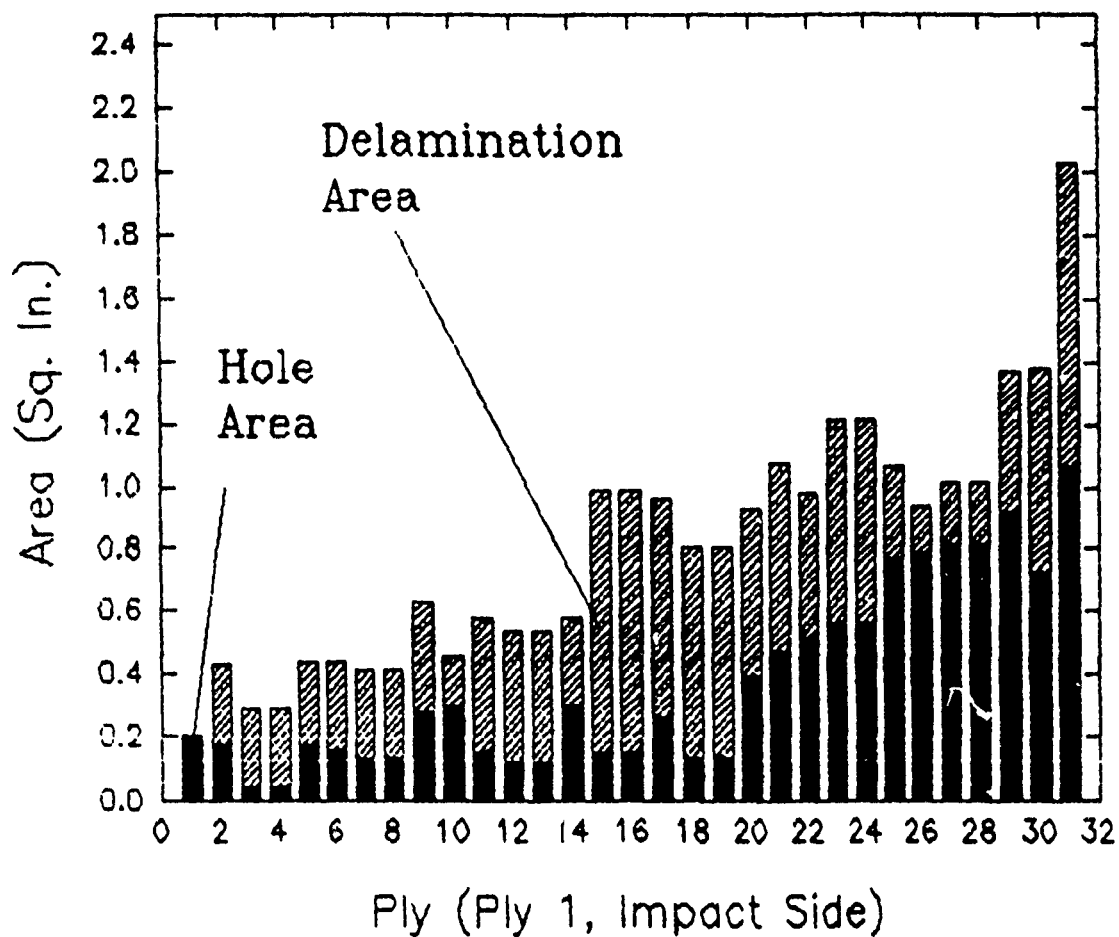


FIGURE 2c Damage at 1013 Ft./Sec. Impact Velocity
From Depty Technique

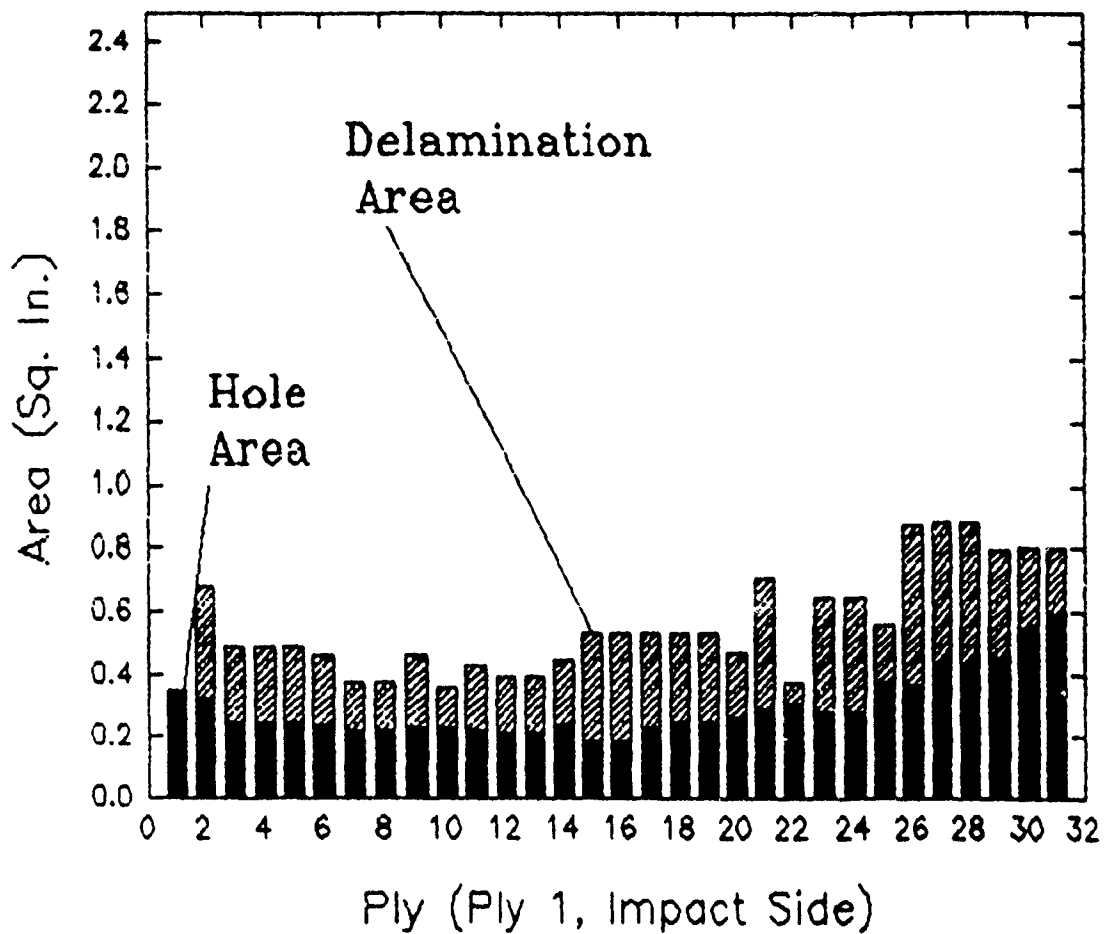


FIGURE 2d Damage at 2777 Ft./Sec. Impact Velocity
From Depy Technique

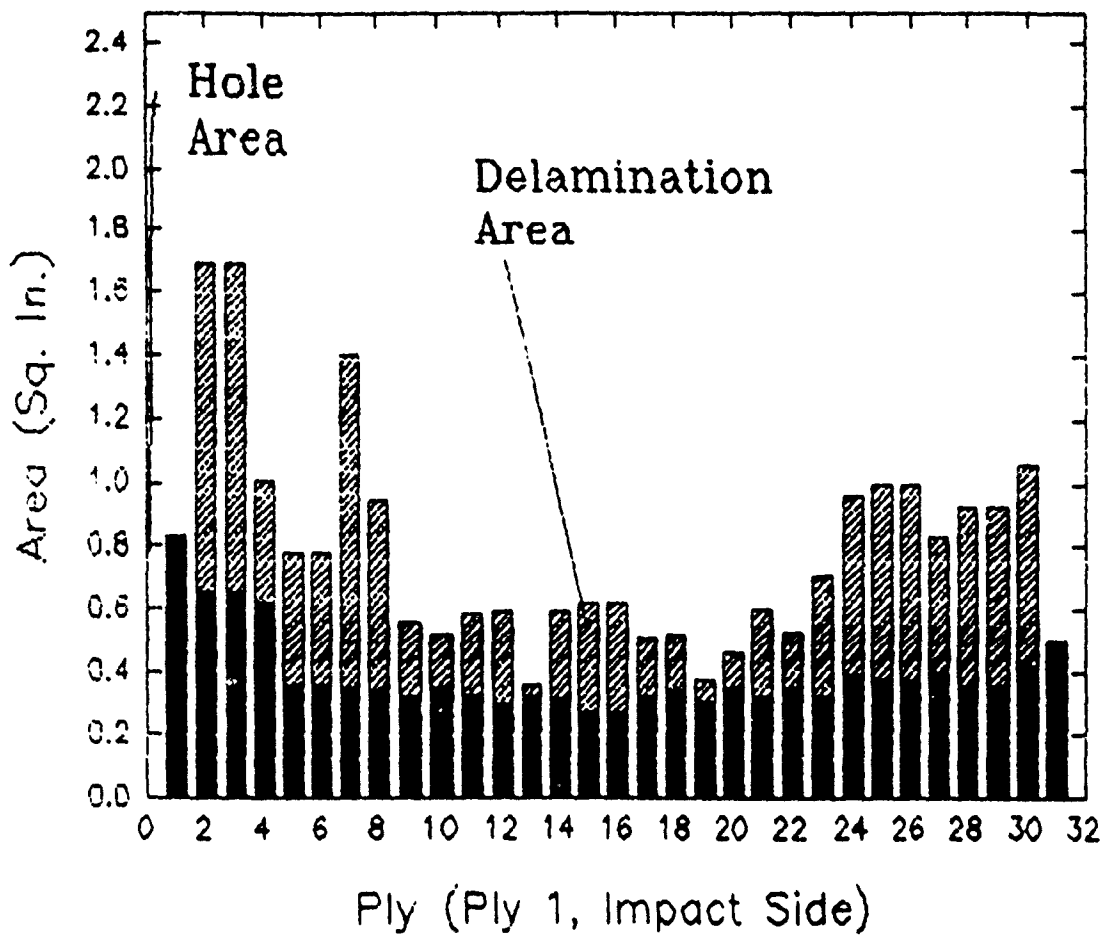


FIGURE 2e Damage at 4476 Ft./Sec. Impact Velocity
From Deply Technique

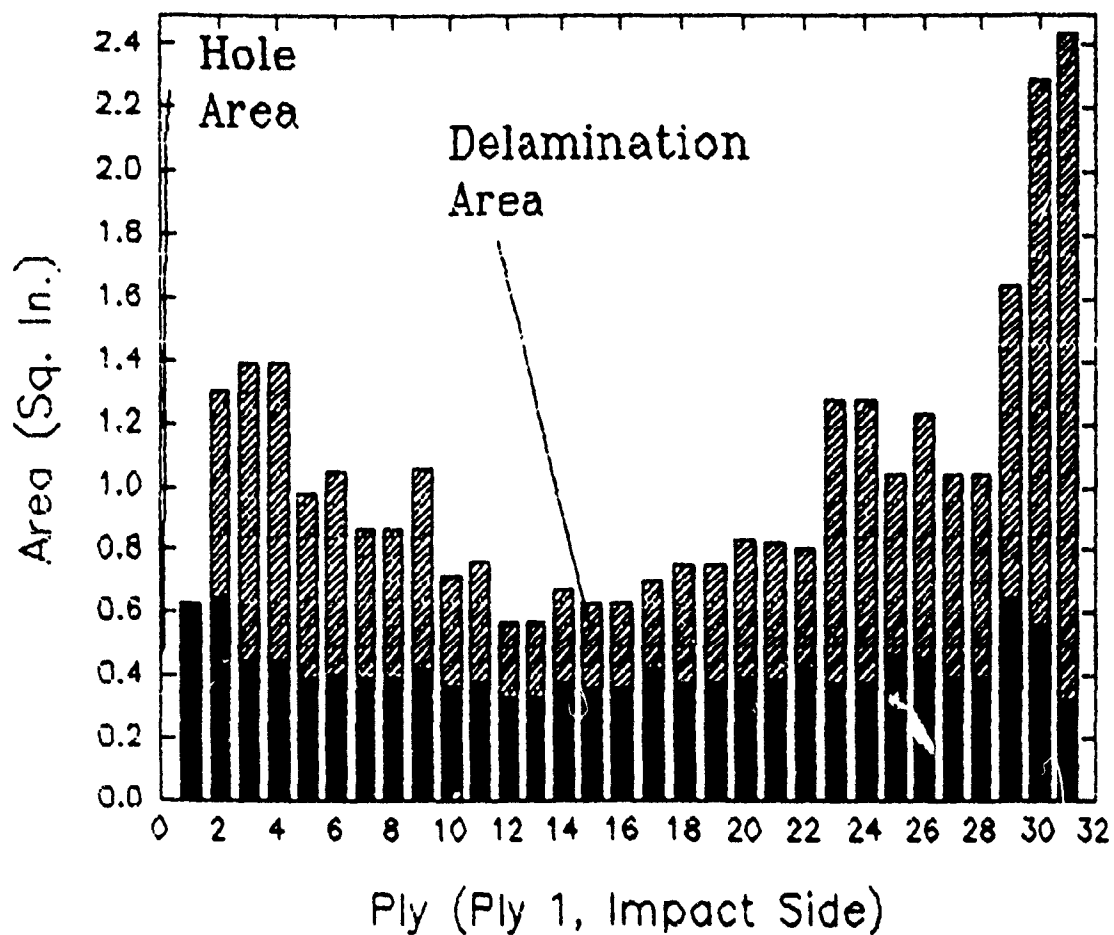


FIGURE 2f Damage at 5817 Ft./Sec. Impact Velocity
From Depty Technique

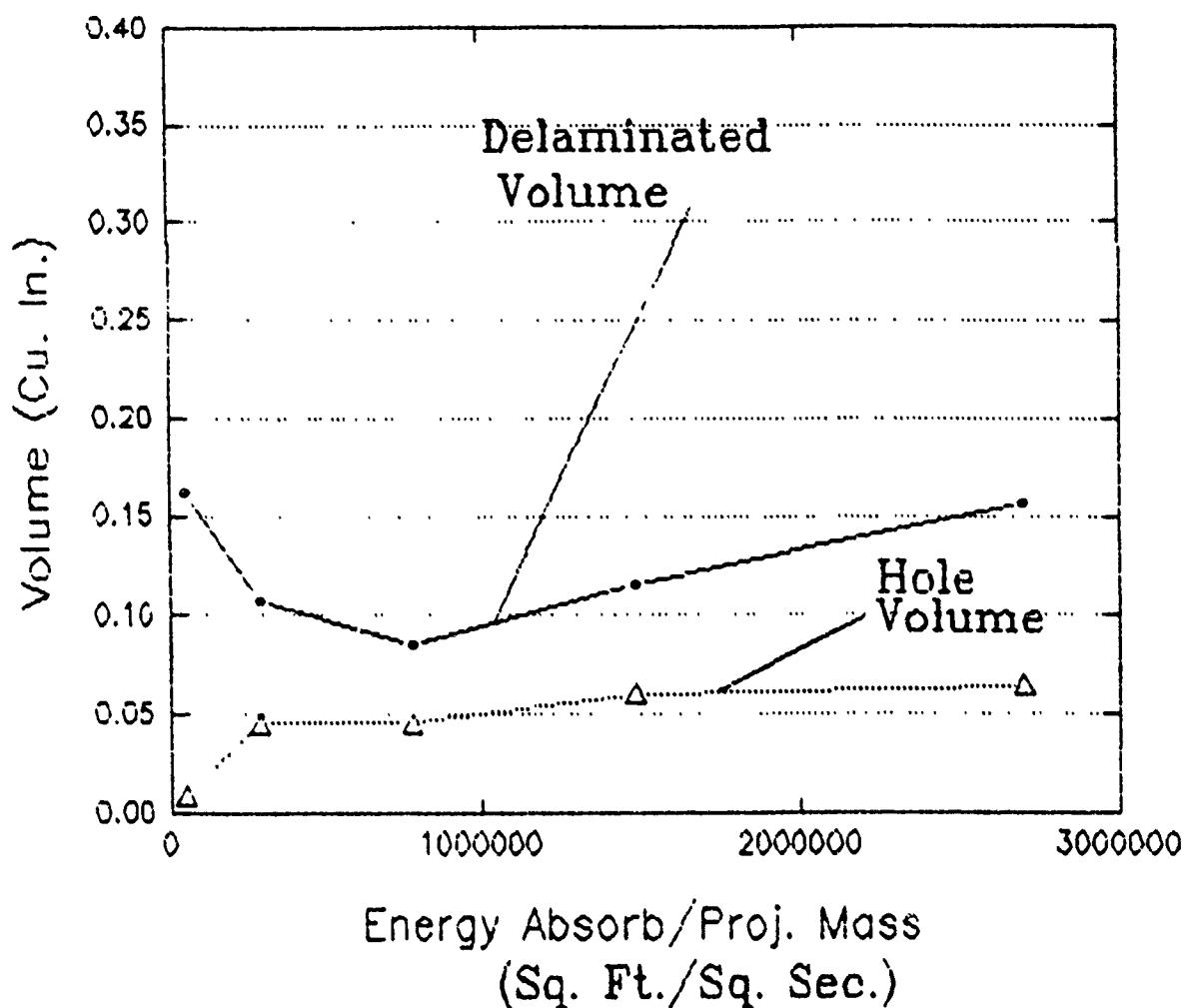


FIGURE 3 Projected Volume of Plug = 0.0314 Cu. In.

Damage Volume Vs Energy Absorbption
Using Deply Technique

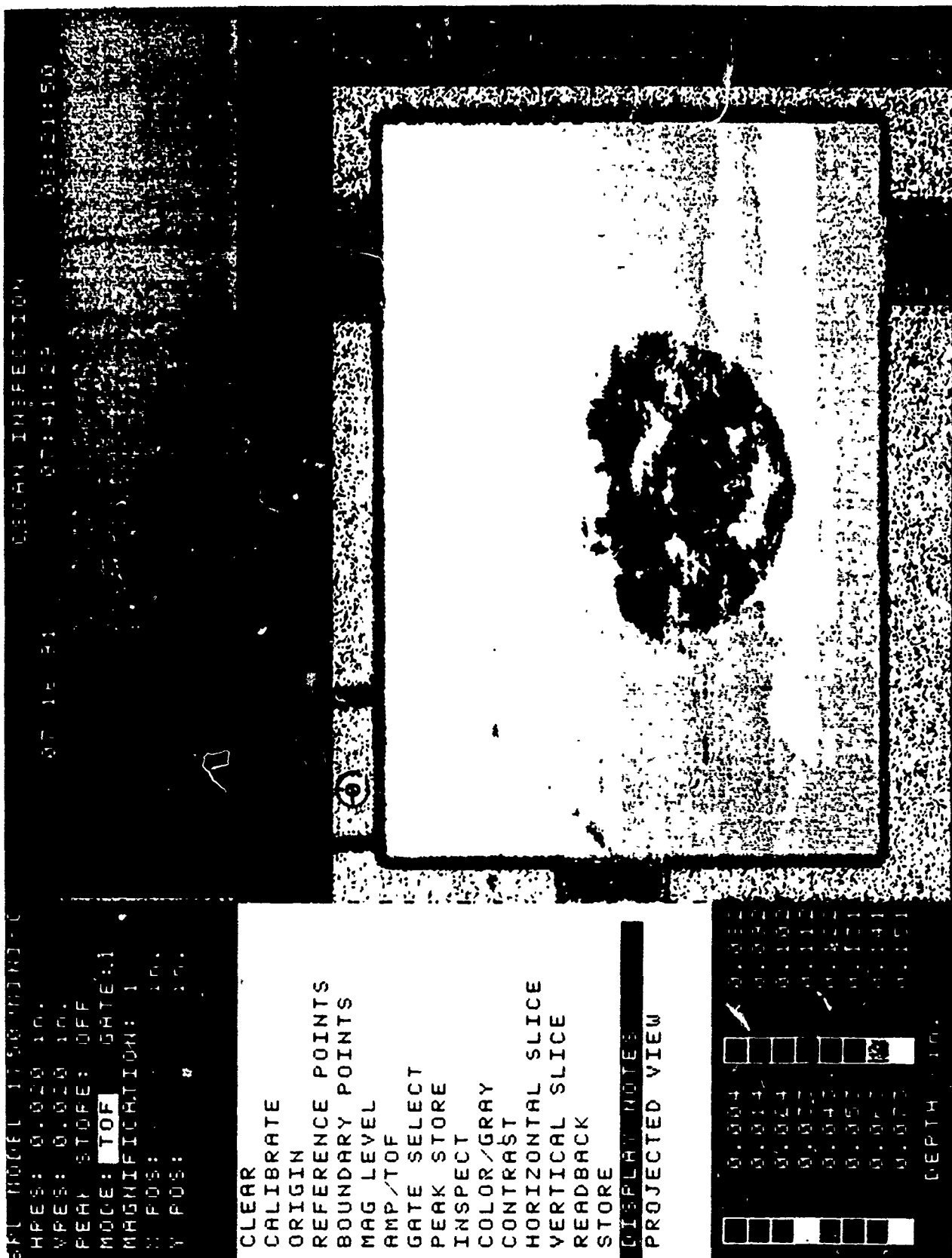


FIGURE 5 C-Scan image

1991 USAF-RDL SUMMER FACULTY RESEARCH PROGRAM

GRADUATE STUDENT RESEARCH PROGRAM

Sponsored by the

AIR FORCE OFFICE OF SCIENTIFIC RESEARCH

Conducted by the

The Research & Development Laboratories, Inc.

FINAL REPORT

Monitoring of Damage Accumulation for the Prediction of

Fatigue Lifetime of Cord-Rubber Composites

Prepared by:	Byung-Lip ("Les") Lee and Pat K. Hippo
Academic Rank:	Associate Professor and Graduate Student
Department and	Engineering Science and Mechanics
University:	Pennsylvania State University, Univ. Park, PA
Research Location:	Wright-Patterson Air Force Base Wright Research Laboratory Flight Dynamics Directorate Vehicle Subsystems Division Aircraft Launch and Recovery Branch
USAF Researcher:	John P. Medzorian
Date:	30 September, 1991
Contract No:	F49620-90-C-0076

Monitoring of Damage Accumulation for the Prediction of Fatigue Lifetime of Cord-Rubber Composites

by

Byung-Lip ("Les") Lee and Pat K. Hippo

ABSTRACT

The study examined the effect of a broad range of the combination between different loading parameters on the fatigue resistance of *model* cord-rubber composites. Among them, stress amplitude was found to play a dominant role in determining fatigue lifetime of composites with an exception of the case where minimum stress approaches zero. The observed higher rate of strength degradation of composites at the zero minimum stress may be attributed to the alteration of the failure mode. The process of damage accumulation of cord-rubber composites was accompanied by a continuous increase of cyclic strain (i.e. dynamic creep), temperature and acoustic emission (AE). The dynamic creep rate and the rate of temperature increase were inversely proportional to the fatigue life according to a power law. In contrast, the extent of dynamic creep at gross failure was found to be independent of stress amplitude. When the minimum cyclic stress was high enough, distinctly different rates of AE signal accumulation could be assigned to the debonding and delamination failure modes. The results demonstrated a great potential of the measurement of local strain change, heat generation and AE as a viable experimental technique for real-time monitoring of the damage accumulation process.

I. INTRODUCTION

Currently, the operational life of bias-ply aircraft tires used by the U.S. Air Force is certified by expensive dynamometer testing to specify the number of takeoff and landing cycles a tire may endure before replacement (1). An initiative is underway to realign this procedure where the emphasis is placed on more cost-effective laboratory prediction of tire durability supplemented with computer modeling capability. In this strategy, the initial goal is to define the fatigue fracture mechanisms of the tire carcass by identifying the parameters that control the process of damage accumulation for cord-rubber composite elements (2). Eventually, it is hoped a fatigue law can be formulated that will serve to predict the lifetime of the tire carcass on a reliable basis. These efforts could extend tire replacement intervals which ultimately would prove more cost-effective than existing criteria that now govern tire replacement.

The focus of this study addresses the above-stated goal of identifying the parameters which control the fatigue life of angle-ply tire carcass composites, with a special provision of establishing a viable experimental technique for real-time monitoring of damage accumulation process. Real-time monitoring of damage accumulation process in composite specimens is necessary for the fatigue fracture mechanism study. But, when established, it will also lay a technical basis for the future research activities of predicting the imminent failure of an actual tire carcass in the field. Past studies (2-7) showed that angle-ply cord-rubber composites exhibit unusually high level of interply shear strain under uniaxial tension. Above a critical value of interply shear strain, localized damage is induced in the form of *cord-matrix debonding*. Further increase of strain results in the initiation of *matrix cracking*. Under static loading, debonding and matrix cracking are widened and eventually developed into the *delamination* leading to the gross fracture of the composites.

The same sequence of failure modes was observed in cord-rubber composites under cyclic loading as long as minimum stress remains safely in the tensile regime (2). It was also observed that damage accumulation in the form of debonding and delamination is accompanied by a steady increase in temperature and local strain. The same study demonstrated that the above-described critical load for the onset of cord-matrix debonding constitutes a threshold level for semi-infinite fatigue life, i.e. *fatigue endurance limit*, of the composites. However, one complication to this generalized description of fatigue fracture mechanisms is the fact that the described sequence of failure modes is sometimes reversed when minimum cyclic stress is near zero. Our unpublished results indicated that the

delamination process appears to precede cord-matrix debonding in this situation. The clarification of this question requires a systematic study on the effects of minimum cyclic stress on the damage accumulation mode and fatigue life of tire carcass composites.

In this study, the damage accumulation process of cord-rubber composites was closely monitored under the different combinations of loading parameters such as stress amplitude and minimum stress. For real-time monitoring of damage accumulation, the acoustic emission (AE) analysis was utilized in addition to the measurement of changes in local strain and temperature. The damage accumulation under cyclic as well as static tensile loading is normally accompanied by AE events that are associated with the sudden release of energy (8). Based on this premise, appropriate monitoring of AE might lend insight into damage accumulation mechanisms which control the fatigue lifetime of the material. Numerous studies on other materials have shown that different failure modes generate distinctively different acoustic signatures (9-11). Therefore the use of AE analysis as a NDE tool for monitoring structural integrity could prove quite successful and valuable, particularly if the acoustic signature of the failure mode is known a priori.

Since the catastrophic failure of the tire carcass is often caused by delamination, there is great potential for the use of AE as a means of sensing imminent tire failures if the acoustic signature of the delamination mode is identified. However, surprisingly little work has been done with cord-rubber composites using AE analysis even though it is a technique that has been used for years with other structural materials such as metals and advanced fiber composites (9-11). AE is an elastic stress wave that travels through a material. As confirmed in other materials, its source is a sudden release of energy induced by plastic deformation or microcracking. AE technology (12) involves the detection and conversion of these mechanical stress waves into electrical voltage signals by piezoelectric transducers that are mounted on the specimen surface. Signal amplification and electronic processing of these transmitted waves then produce an acoustic signature.

Although described in a simplistic manner so far, AE does have some shortcomings that can limit its effectiveness. For example, external sources of noise may interfere with analysis. Often, a proper selection of the frequency monitoring range or threshold frequency settings on the AE instrument will minimize unwanted information, but they do not necessarily ensure their complete elimination. For instance, gripping noise from cyclic loading can not be fully removed. In other cases, its application to a particular structure may be inherently difficult. Monitoring of AE from an aircraft tire in service could pose

serious problems. These technology gaps that now exist would have to be overcome to establish AE analysis along with the measurement of material temperature or local strain as a real-time monitoring technique for damage accumulation.

II. OBJECTIVES OF THE RESEARCH EFFORT

The present investigation was undertaken in accordance with continuing efforts for the laboratory prediction of the durability of aircraft tire carcass. Two objectives were set forth. The first was to identify the loading parameters controlling fatigue lifetime of tire carcass composites, while the second was to establish the measurement of local strain change, heat generation and acoustic emission (AE) as a viable experimental technique for real-time monitoring of the damage accumulation process.

III. EXPERIMENTS

In consideration of its exploratory nature, a current phase of the study used *model* composites consisting of 2+2x0.25 steel wire cable reinforcement and a proprietary rubber compound matrix instead of the composites representing actual aircraft tire carcass. Composite laminate panels (8" long x 3" wide x 0.25" thick) were supplied by the Goodyear Tire & Rubber Company. To avoid tension-bending coupling, the laminates were constructed with a symmetric ply lay-up of +/- 23 deg cord angle. The end tabs were added to the specimens to prevent grip failures that could be experienced during mechanical testing. Coupon specimens of 0.75" width were machined from these panels and edge-polished on a grinding wheel. These angle-ply composite coupons were designed to maximize the interply shear strain which is a major contributing factor in composite failure (5-7).

To represent the circumferential tension of an aircraft tire in the footprint region, coupon specimens were subjected to both static and cyclic uniaxial tensile loading. For cyclic loading, various combinations of stress amplitude and minimum stress were implemented (Table 1) with a close monitoring of local strain, heat generation and AE. A cyclic frequency of 5 Hz was employed throughout the experiment. With regard to static loading, deflection rate was kept constant at 0.05 inch/min. In both static and cyclic testing, local axial and interply shear strain were estimated by measuring the displacement of line

markings drawn on the specimen edge (Figures 3 and 4 in *Ref. 2*). Temperature build-up as a function of fatigue lifetime was recorded with a thermocouple attached to the specimen surface. The location of the thermocouple was generally between the two AE transducers attached but on the opposing side of the specimen.

Finally the monitoring of AE was accomplished with Physical Acoustics Corporation LOCAN-AT instrumentation (*12*). Considering that the test results are highly dependent on wave signal processing techniques, a study was performed under static loading to assess the influence of the following three factors and their combinations on the AE behavior of cord-rubber composites: the type of piezoelectric *transducer* (Physical Acoustics R50, Dunegan D9230A, Dunegan N30W); a frequency range of bandpass filter for *preamplifier* (100-1200 KHz wide band and 400-600 KHz narrow band); a frequency range of bandpass filter for *amplifier* (100-300 KHz, 400-600 KHz, 100-1200 KHz). Since the frequency range of the bandpass filter for LOCAN-AT amplifier was found to play a secondary role, it was fixed at 400-600 KHz in the rest of the program. In the final test set-up for cyclic loading, one R50 transducer was connected to a wide bandpass preamplifier while the other R50 transducer was connected to a narrow bandpass preamplifier.

These two transducers were mounted to the specimen using masking tape and rubber bands. A small amount of vacuum grease was placed between the transducer and the specimen to ensure air gaps would not permit acoustic wave reflection interference. Both transducers occupied one side of the specimen and were spaced about 1.5" apart center to center. In general, AE monitoring for a given specimen was initiated immediately before start-up of the mechanical testing instrument so that all AE activities would be included for analysis. For signal data processing, the following settings were used for key variables:

Gain	20 db
Amplitude threshold	45 db
Peak definition time (PDT)	20 μ s
Acoustic event definition time (HDT)	150 μ s
Acoustic event lockout time (HLT)	300 μ s

IV. RESULTS AND DISCUSSION

As stated earlier, our current study plans to examine the effects of loading parameters on the fatigue resistance of tire carcass composites. Although allocated numbers of specimens were too few to form a sound statistical database (Table 1), the loading conditions employed in this screening study covered a broad range of the combination between stress amplitude, maximum stress, minimum stress, and the ratio of minimum-to-maximum stress (R-ratio). Among these loading parameters, stress amplitude was found to play a dominant role in determining the fatigue lifetime of cord-rubber composites (Figures 1 and 2). The curves of maximum cyclic stress vs the logarithm value of fatigue life generated at four different levels of minimum stress were dissimilar. However, when the values of stress amplitude instead of maximum stress were plotted against fatigue life, the S-N curves were shown to be similar with an exception of the case where the minimum stress approaches zero. This series of plots also illustrates that at a given stress amplitude, the effect of R-ratio on fatigue lifetime is negligible. Again, an exception is evident at zero minimum stress.

When the minimum cyclic stress is near zero, the S-N curve of cord-rubber composites exhibit a steeper slope with a shortened fatigue lifetime in the normal loading range (Figure 2). A steeper slope of the S-N curve at a given static (or single cycle) strength means a higher rate of strength degradation. The observed higher rate of strength degradation of composites at the zero minimum stress may be attributed to the alteration of failure modes as observed in the past. As long as the minimum stress is safely in the tensile regime, cord-rubber composites exhibit debonding of the cord from the surrounding rubber matrix prior to the development of delamination. However, when the minimum stress approaches zero, microbuckling of laminates may occur and, as a result, the delamination process could precede cord-matrix debonding. Several attempts were made to confirm the change of failure mode using visual means, but no concrete results were obtained so far.

In this study, the damage accumulation process of cord-rubber composites could be monitored under a broad range of the combination between stress amplitude and minimum stress. The process of damage accumulation was accompanied by a continuous increase of cyclic strain and temperature. As a universal trend, the increase of cyclic strain undergoes three stages (Figure 3). After an initial stepwise increase in strain, the strain increases at a progressively slower rate until reaching a constant rate at about 20% of the fatigue life. In the second region, the cyclic strain increases at a constant rate which will be referred as

dynamic creep rate hereafter. In this region which ranges from 20 to 80% of the fatigue life, the damage takes the form of cord-matrix debonding and matrix cracking with no delamination observed. Above 80% of the fatigue life, partial delamination appears at the specimen edge. In this final stage, the cyclic strain increases at a progressively higher rate eventually leading to a catastrophic failure by gross delamination. The increase of specimen temperature was found to follow a similar pattern, but a final spike of temperature was less pronounced than the final increase of cyclic strain.

One major finding was that the dynamic creep rate and the rate of temperature increase are a good indication of the fatigue lifetime for the composites. As shown in Figures 4 and 5, the logarithm value of the fatigue life is inversely proportional to the logarithm value of the dynamic creep rate or the rate of temperature increase according to a power law. Since the logarithm value of fatigue life is also inversely proportional to the stress amplitude, a power law relationship between the dynamic creep and the stored strain energy could be defined in our future work with more data available. It is interesting to note that the dependence of crack growth rate on the level of stored strain energy for rubbery materials follows a power law (4). The rate of temperature increase is expected to correlate with a part of strain energy dissipated during hysteresis. Aside from these questions on the roles in fracture mechanisms, the above results demonstrate the measurement of local strain change and heat generation as a viable experimental technique for real-time monitoring of the damage accumulation process.

Another important finding was that, in contrast to the case of dynamic creep rate, the extent of dynamic creep at gross failure which is defined as the increase of strain after initial stepwise imposition is roughly independent of stress amplitude (Table 1). All the specimens were found to fail when the maximum axial strain reaches approximately 30% above the level imposed by initial stepwise increase in strain (Figure 3). Although it may be premature to propose a formal criterion without additional data at different levels of frequency, the observation strongly suggests the existence of a critical level of dynamic creep for catastrophic failures of angle-ply cord-rubber composites and possibly for the tire carcass. A possible existence of a similar type of temperature threshold was assessed, but there seemed to be no correlation between the fatigue lifetime and the final temperature of the specimen just prior to catastrophic failure (Figure 6).

In addition to the measurement of changes in local strain and temperature, the study utilized AE analysis for real-time monitoring of damage accumulation in cord-rubber composites.

AE is compared to a damped sinusoid in signal processing and the following three parameters are used to characterize the intensity of the activities (12): the number of *AE events* (the number of stress wave generated), *AE counts* (the number of crossings of stress waves over a threshold value set to eliminate background noise), *AE energy* (the area under the stress waves). Under cyclic tension, AE occurs as soon as the loading starts (Figures 3 and 7). With progressive build-up of damage in composites, cumulative values of AE counts, events and energy generated were found to follow a pattern which is somewhat similar to that of dynamic creep (Figures 3, 8-10). However, this pattern was observed only when the minimum cyclic stress was high enough. The use of a lower minimum cyclic stress tended to generate an increasingly excessive amount of AE in early stage of deformation which is presumably caused by the friction of the specimens against the grips under hydraulically operated clamping pressure.

When the minimum cyclic stress was high enough, cumulative values of AE counts, events and energy for cord-rubber composites increase at a progressively slower rate eventually reaching a region with a constant rate of a very low value or a pseudo-asymptote (Figures 8-10). In this region, predominant modes of damage accumulation are still cord-matrix debonding and matrix cracking. Around 80% of the fatigue life, the cumulative values increase at a higher rate which is coincided with an appearance of partial delamination. Finally the cumulative values increase at an extremely high rate in catastrophic failure. Distinctly different rates of AE signal accumulation could be assigned to the debonding and delamination failure modes. For instance, the AE energy release rate, which is defined by normalizing the value of cumulative AE energy with the level of attendant increase of strain, was found to be approximately 100 and 5000 dB/inch deflection for debonding and delamination respectively (Figure 10, Table 2).

The values of AE energy release rate for delamination estimated under cyclic loading were independently verified by performing a separate experiment under static loading. Under static tension, cumulative values of AE counts, events and energy for cord-rubber composites follow a simpler pattern consisting of two different rates prior to gross failure (Figure 11). The accumulation of acoustic signals at a higher rate corresponded to the delamination failure while the accumulation of signals at a lower rate could be associated with the debonding process. The values of AE energy release rate measured under static loading were found to be in the same degree of order compared with the values obtained under cyclic loading (Table 2). The results on AE energy release rate discussed so far imply a great potential for AE monitoring as a means of sensing imminent gross failure of

tire carcass led by delamination based on its distinct acoustic signature. However, an extreme caution is urged in view of the excessive amount of background noise in the early stage of deformation when the level of minimum cyclic stress is lowered.

V. CONCLUDING REMARKS

With a special provision of establishing a viable experimental technique for real-time monitoring of damage accumulation process, this screening study examined the effect of a broad range of the combination between different loading parameters on the fatigue resistance of *model* cord-rubber composites. Among them, stress amplitude was found to play a dominant role in determining fatigue lifetime of composites. All the S-N (stress amplitude vs the number of cycles to failure) curves were found to be similar with an exception of the case where minimum stress approaches zero. When the minimum cyclic stress is near zero, the S-N curve of cord-rubber composites exhibits a steeper slope with shortened fatigue lifetime in the normal loading range. The observed higher rate of strength degradation of composites at the zero minimum stress may be attributed to the alteration of the failure mode.

The process of damage accumulation of cord-rubber composites was accompanied by a continuous increase of cyclic strain (i.e. dynamic creep) and temperature. In the region ranging from 20 to 80% of the fatigue life, the strain increases at a constant rate and the damage takes the form of cord-matrix debonding and matrix cracking. Above 80% of the fatigue life, partial delamination appears. In this final stage, the cyclic strain increases at a progressively higher rate eventually leading to catastrophic failure. The increase of specimen temperature follows a similar pattern. The dynamic creep rate and the rate of temperature increase were found to be inversely proportional to the fatigue life according to a power law. In contrast, the extent of dynamic creep at gross failure is roughly independent of stress amplitude. All the specimens were found to fail when the maximum axial strain grows by approximately 30% above the initially imposed one.

With a progressive build-up of damage in composites, cumulative values of AE counts, events and energy generated were found to follow a pattern which is similar to that of dynamic creep or temperature. However, the use of lower minimum cyclic stress tended to generate an increasingly excessive amount of AE in the early stage of deformation which is presumably caused by the friction of the specimens against the grips. When the minimum

cyclic stress was high enough, distinctly different rates of AE signal accumulation could be assigned to the debonding and delamination failure modes. The AE energy release rate was found to be approximately 100 and 5000 dB/inch deflection for debonding and delamination respectively. The values of AE energy release rate estimated under cyclic loading were independently verified by a separate experiment under static loading.

The results demonstrated the potential of the measurement of local strain change, heat generation and AE as a viable experimental technique for real-time monitoring of the damage accumulation process. AE monitoring seems to have a great potential as a means of sensing imminent gross failures of tire carcass led by delamination based on its distinct acoustic signature. However, an extreme caution is urged in view of excessive amount of background noise when the level of minimum cyclic stress is lowered.

VI. RECOMMENDATIONS

The following recommendations can be made for the future study on fatigue fracture mechanisms and monitoring of the damage accumulation process for cord-rubber composites:

- (1) Repeat the same type of fatigue fracture mechanism study in the case of nylon cord-reinforced composites which represent the actual aircraft tire carcass material with a systematic variation of *frequency*, *temperature* and the *ratio of minimum-to-maximum stress*. Perform a microscopic examination of damage accumulation modes and define the S-N curves for the onset of debonding and delamination as well as gross fracture.
- (2) Confirm the existence of a critical level of dynamic creep at a catastrophic failure for aircraft tire carcass composites. Check the degree of reversibility of local strain encountered during dynamic creep.
- (3) Assess the contribution of viscoelastic properties of constituent materials to the dynamic creep process of composites by performing static loading experiments at elevated temperatures. Determine how the process of damage accumulation interacts with material property changes.

- (4) Define the exact role of hysteretic heating in determining the fatigue lifetime of composites by performing *isothermal* cyclic testing. Cyclic testing in isothermal condition will resolve the issue of the possible interaction between hysteretic heating and the progressive increase of strain due to damage accumulation.
- (5) Assess the measurement of the AE response as a real-time monitoring technique for damage accumulation in the case of aircraft tire carcass composites. Examine the effects of amplitude threshold and check a possibility of selective monitoring of AE at the peak regions of sinusoidal loading curves (gating circuitry) to control background noise.
- (6) Assess the measurement of heat generation as a real-time monitoring technique for damage accumulation in the case of aircraft tire carcass composites. Measure the temperature response in the local regions of the composite specimen using needle type temperature sensors and thermography techniques.
- (7) Assess the failure modes of internally-pressurized composite tube under cyclic tension using a new specimen configuration with a predelaminated area.

Acknowledgements

We wish to thank the Air Force Systems Command and the Air Force Office of Scientific Research for sponsorship of this research. The Research and Laboratories, Inc. helped us in all administrative aspects of this program.

We sincerely appreciate continuing support and encouragement for this research work from Messrs. John P. Medzorian, Paul C. Ulrich and Aivars V. Petersons and Dr. Arnold H. Mayer at the Vehicle Subsystems Division of WL Flight Dynamics Directorate.

We are also very grateful to Dr. George P. Sendeckyj (WL Flight Dynamics Directorate, Structures Div.), Dr. Ran Y. Kim (Univ. of Dayton Research Inst.) and Dr. James M. Whitney (WL Materials Directorate, Non-Metallic Materials Div.) for their support of the research program. Mr. Harold Stalnaker (WL Flight Dynamics Directorate, Structures Div.) and Messrs. Ron Esterline and John Camping (Univ. of Dayton Research Inst.) played an essential role in this program by performing various mechanical testing.

Finally our sincere thanks should go to Drs. Alfredo G. Causa and Yao M. Huang (Goodyear Tire & Rubber Co.) for providing composite specimens.

References

- (1) S. N. Bcbo, "Fatigue Life of Aircraft Tires", *Tire Science and Technology*, Vol. 16, No. 4, p.208 (1988).
- (2) B. L. Lee, J. P. Medzorian, P. M. Fourspring, G. J. Migut, M. H. Champion, P. M. Wagner and P. C. Ulrich, "Study of Fracture Behavior of Cord-Rubber composites for Lab Prediction of Aircraft Tire Durability", *Soc. of Automotive Engineers Paper #901907*, Warrendale, PA (1990).
- (3) R. F. Breidenbach and G. J. Lake, "Mechanics of Fracture in Two-Ply Laminates", *Rubber Chemistry and Technology*, Vol. 52, p.96 (1979).
- (4) R. F. Breidenbach and G. J. Lake, "Application of Fracture Mechanics to Rubber Articles Including Tyres", *Philosophical Trans. Royal Soc. London*, Vol. A299, p.189 (1981).
- (5) J. D. Walter, "Cord-Reinforced Rubber" in Mechanics of Pneumatic Tires edited by S. K. Clark, U.S. Department of Transportation, Washington D.C. (1982)
- (6) J. L. Ford, H. P. Patel and J. L. Turner, "Interlaminar Shear Effects in Cord-Rubber Composites", *Fiber Science and Technology*, Vol. 17, p.255 (1982).
- (7) R. J. Cembrola and T. J. Dudek, "Cord/Rubber Material Properties", *Rubber Chemistry and Technology*, Vol. 58, p.830 (1985).
- (8) J. Lenain, "General Principles of Acoustic Emission", Dunegan-Endevco Technical Report DE 78-5 (1979).
- (9) A. Rotem, "Effect of Strain Rate on Acoustic Emission from Fibre Composites", *Composites*, Vol. 9, No. 1, p.33 (1978).
- (10) B. Harris, F. J. Guild and C. R. Brown, "Accumulation of Damage in GRP Laminate", *J. Physics D: Applied Physics*, Vol. 12, p.1385 (1979).
- (11) L. Carlsson and B. Norrbom, "Acoustic Emission from Graphite/Epoxy Composite Laminates with Special Reference to Delamination", *J. Materials Science*, Vol. 18, p.2503 (1983).
- (12) "8900 LOCAN-AT User's Manual", Physical Acoustics Corp (1988).

TABLE 1**Fatigue-Induced Changes in Strain and Temperature for Cord-Rubber Composites (5 Hz)**

Width	Load		Creep		Temp
	Max	Min	Total	Rate	Rate
inch	lbf	lbf	inch	inch/Kcycle	°F/sec
.719	800	0	.18	.51	.58
.721	800	0	.20	.36	.60
.712	800	100	.17	.27	-
.747	800	100	.17	.135	-
.775	800	200	.16	.03	.061
.727	800	200	.13	.023	.074
.702	800	400	.14	.0029	.00023
.737	800	400	.10	.0063	.000117
.733	750	250	.13	.0075	.0032
.794	750	250	.21	.0047	.00066
.743	710	390	.11	.0019	.000094
.740	710	390	.18	.0017	.000047
.714	700	0	.14	.12	.38
.733	700	0	.14	.18	.45
.733	700	100	.14	.078	.25
.727	700	100	-	-	.31
.738	700	200	.17	.021	.041
.742	700	200	.13	.020	.048
.746	600	0	.13	.080	.27
.732	600	0	.18	.156	.39
.711	600	100	.16	.031	.085
.727	600	100	.18	.039	.098
.722	600	200	.24	.0057	.0015
.741	600	200	.15	.0026	.00081
.729	500	0	.14	.016	.056
.723	500	0	.13	.025	.084
.710	500	100	.18	.0042	.0051
.770	500	100	.18	.0014	.0015
.730	400	0	.12	.0057	.032
.739	400	0	.09	.0025	.022

.15 Ave

TABLE 2

Acoustic Energy Release Rate for Delamination and Debonding
of Cord-Rubber Composites

Cyclic Loading (5 Hz)	Static Loading (.05 inch/min)	
Delamination	Delamination	Debonding
3500 (dB/inch deflection)	3400	80
4000	4850	80
6800	6800	120

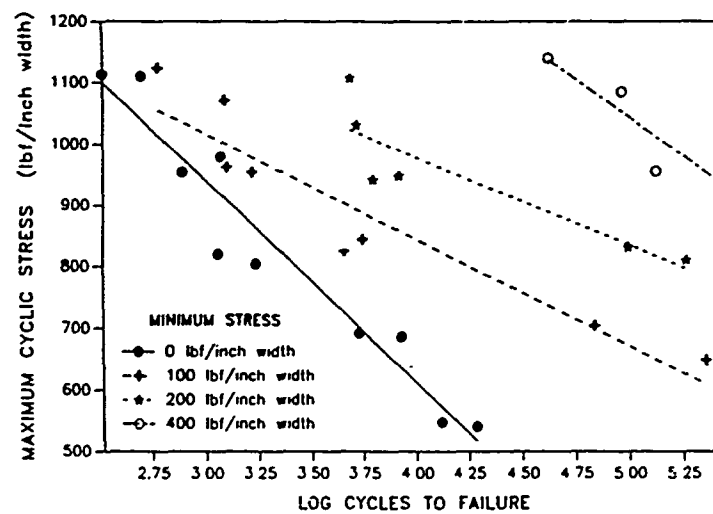


Figure 1

Maximum Cyclic Stress vs Fatigue Lifetime Curves for Cord-Rubber Composites

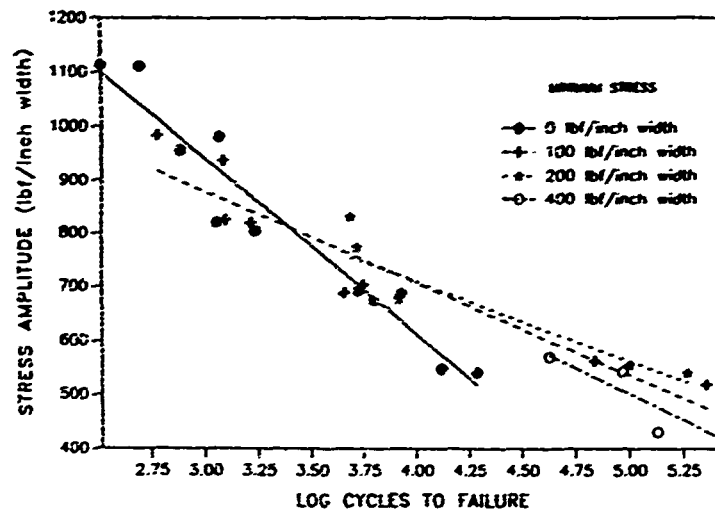


Figure 2

Stress Amplitude vs Fatigue Lifetime (S-N) Curves for Cord-Rubber Composites

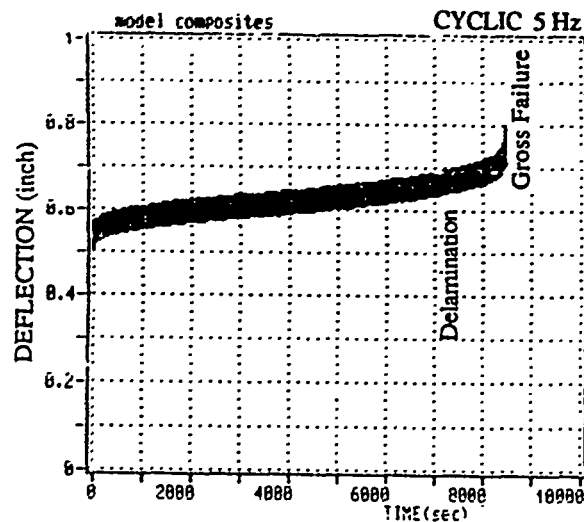


Figure 3

Increase of Strain under Cyclic Loading with Constant Stress Amplitude
(1140 lb/inch Maximum, 570 lb/inch Minimum, 5 Hz)

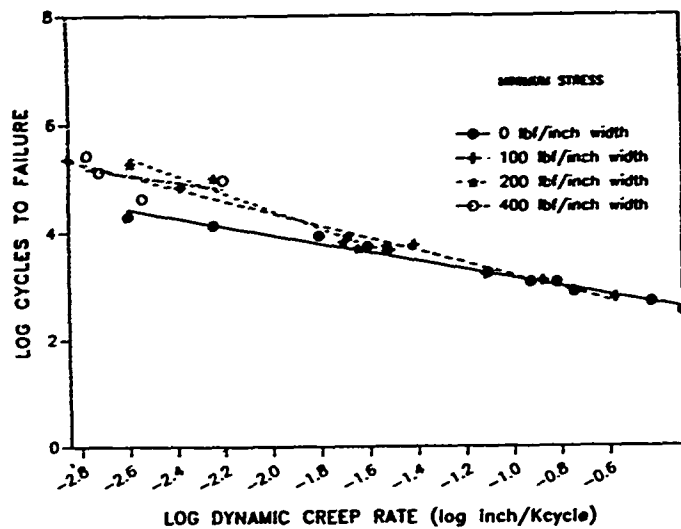


Figure 4

Fatigue Lifetime vs Dynamic Creep Rate

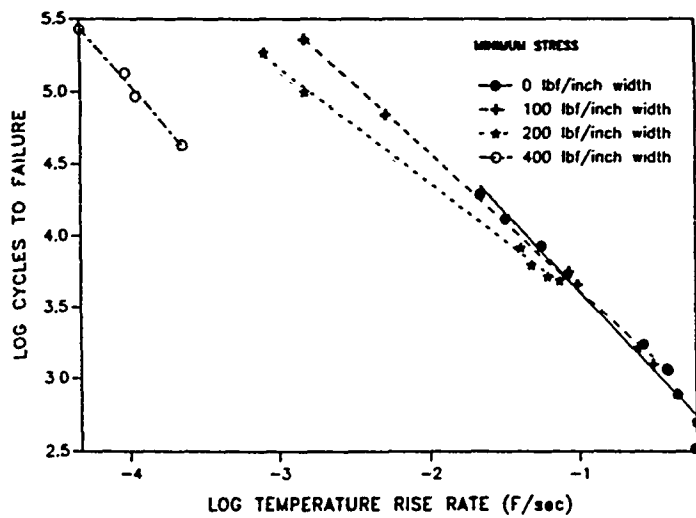


Figure 5

Fatigue Lifetime vs Specimen Temperature Rise Rate

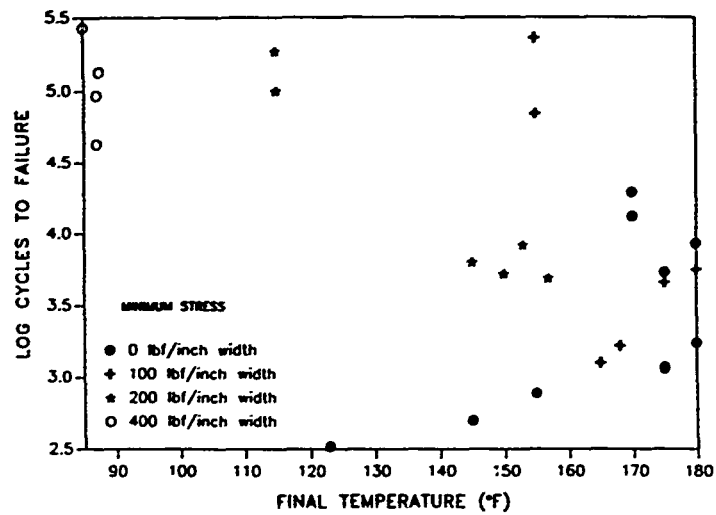


Figure 6

Fatigue Lifetime vs Final Specimen Temperature

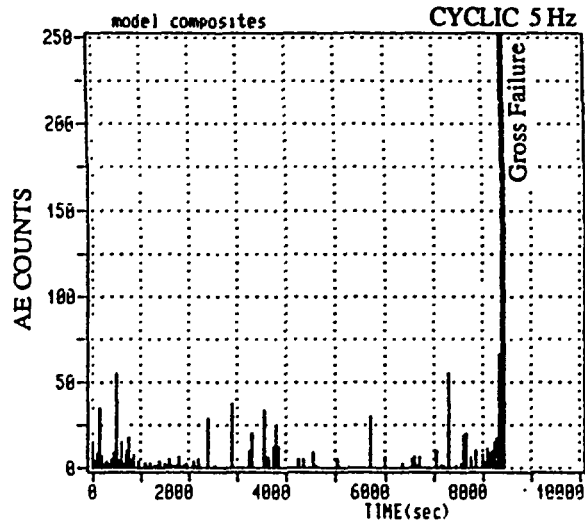


Figure 7

Acoustic Emission Count vs Time under Cyclic Loading
(1140 lb/inch Maximum, 570 lb/inch Minimum, 5 Hz)

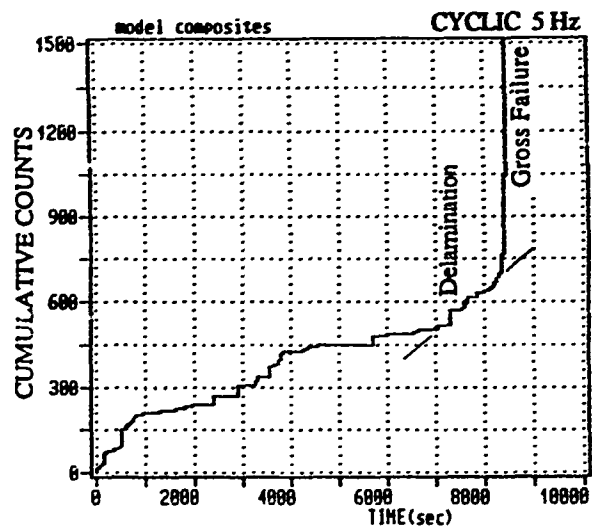


Figure 8

Cumulative Acoustic Emission Count vs Time under Cyclic Loading
(1140 lb/inch Maximum, 570 lb/inch Minimum, 5 Hz)

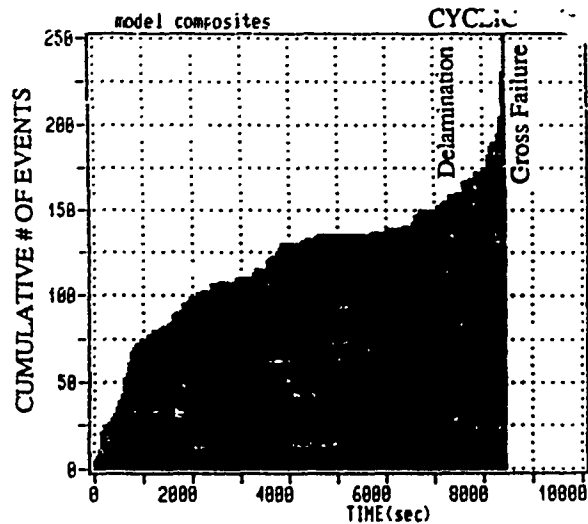


Figure 9

Cumulative Number of Acoustic Events vs Time under Cyclic Loading
(1140 lb/inch Maximum, 570 lb/inch Minimum, 5 Hz)

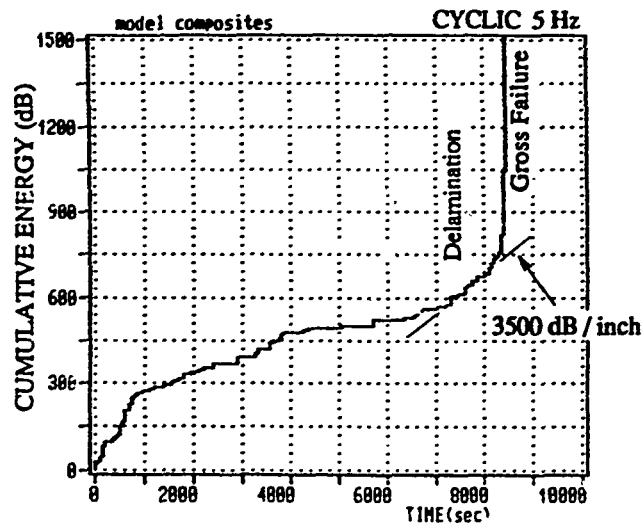


Figure 10

Cumulative Level of Acoustic Energy Released vs Time under Cyclic Loading
(1140 lb/inch Maximum, 570 lb/inch Minimum, 5 Hz)

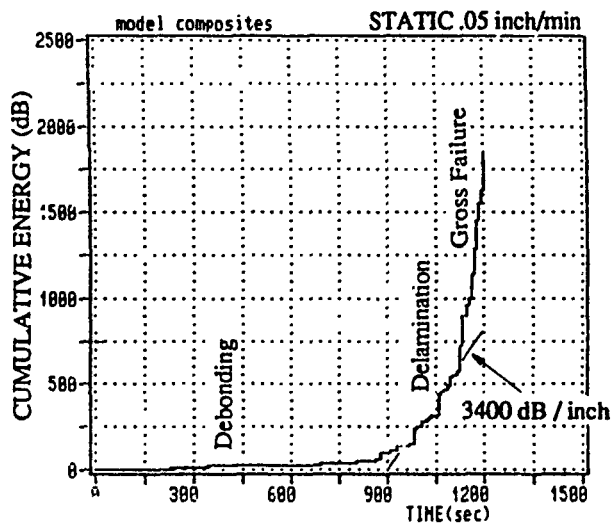


Figure 11

Cumulative Level of Acoustic Energy Released vs Time under Static Loading
(0.05 inch/min)

IN-FLIGHT STRUCTURAL COMBAT DAMAGE DETECTION AND EVALUATION FOR ENHANCED SURVIVABILITY OF MILITARY AIRCRAFT

Vernon C. Matzen
Associate Professor of Civil Engineering

ABSTRACT

A procedure is proposed for detecting - in flight - combat damage of military aircraft. This could be accomplished by using measured excitation and response data in a mathematical modelling technique known as system identification. An evaluation of the resulting damage information, using computational fluid dynamics algorithms and finite element models, would provide information on the relationship between the structural integrity of the aircraft and restricted flight variables such as speed and acceleration. This information, provided to the pilot in an obvious but unobtrusive manner, would make it more likely that the aircraft would be able to return to base, and do so without sustaining additional damage from normal maneuvers. Besides allowing for safer flight following damage, this information, if transmitted ahead, would allow repair crews to assemble the appropriate resources so that repairs could be made in the shortest possible time. To develop these ideas, a series of tests is conducted on a plate model having the configuration of an F-16 wing. Finally, a long-term project is proposed in which damage detection, evaluation, and pilot displays are developed to the point where they are implemented in a prototype model.

I. INTRODUCTION

When a military aircraft suffers ballistic damage, there are several possible outcomes. In the worst case, the aircraft might be lost with no opportunity for the pilot to eject. At the other end of the spectrum, the damage may be so light that the pilot can continue the mission with no degradation of the planes capability. It is the set of outcomes in between these two extremes that motivates the research described in this report. One possible scenario is this: An aircraft is hit but is able to maintain control and power. On the way back to the base, however, a hard turn subjects a damaged structural component

(such as a wing) to a load that it cannot withstand, and the aircraft (and perhaps the pilot) is lost. Had the pilot known the severity of the damage and the revised limits within which the damaged aircraft must be operated, there would be less likelihood of loss. As the cost of new military aircraft continues to increase, the importance of saving even a single aircraft becomes obvious.

Damage to any one of the many critical systems on military aircraft may be fatal. The ability to monitor the "health" of many of these systems is well developed; but for others, it is less well developed. In particular, the technology to detect structural damage rapidly and then immediately evaluate the consequences does not yet exist. The individual components of this technology do exist, however, in various stages of development.

Nondestructive testing techniques for structural damage detection can be classified broadly into local methods such as ultrasonic scanning and acoustic emissions, and global methods such as vibration testing. Global methods seem more attractive for this work because they can more easily accommodate remote testing and they provide information about large sections of the structure. The instrumentation needed for global vibration tests must be small enough to fit unobtrusively inside a structural component and, at the same time, be robust enough to withstand the rigors of normal flight as well as ballistic impact and explosion. Instrumentation such as embedded fibers and piezoelectric skins may in the future provide alternatives to the more commonly used accelerometers and strain gages. Data acquisition and signal processing hardware must also be compact and rugged. Advances are being made in all of these areas so that instrumentation availability should, in the near future, no longer be limiting factors.

Experimental modal analysis, a commonly used global method, can be used to obtain frequencies and mode shapes of a test structure; and these can in turn be used to update a finite element model of the structure. Alternatively, other techniques can be used to determine elements of the mass and stiffness matrices directly. In either case, changes in mathematical model parameters from an original, baseline, configuration to a model of the damaged aircraft can be used to infer both the location and the magnitude of damage. The usefulness of these techniques has been demonstrated using simple laboratory structures.

Assuming that identification software and instrumentation are sufficiently well developed so that tests can be conducted in flight, and the parameters obtained, the question remains: What do the parameters mean and how are they to be used? There are two ways to answer these questions. One is to perform a large number of either laboratory or numerical experiments, in each of which known damage exists. Parameters from these experiments, say in terms of frequencies and mode shapes, could be cataloged. Later,

when frequencies might be obtained from a damaged aircraft, this catalog could be consulted to determine the location and extent of damage. The other way to use parameters from a damaged aircraft is to update a mathematical model of the aircraft to reflect the damage. The advantage of using this updated model approach is that the resulting model could then be used to predict the structural response of the aircraft to various possible loading patterns.

The loading on aircraft structures comes from lift and drag forces, as well as the dynamic behavior of the aircraft itself. The ability to model the response of an aircraft to aerodynamic effects such as lift and drag using computational fluid dynamics (CFD) algorithms has been demonstrated for aircraft of moderate complexity. The usual way the problem is solved is to specify the speed, acceleration, elevation, and other aerodynamic quantities and then solve the aeroelastic equations to obtain the forces acting on the structure. Knowing these forces, the stresses in the structure can be computed using a finite element model (FEM). What we would like to be able to do is solve the problem

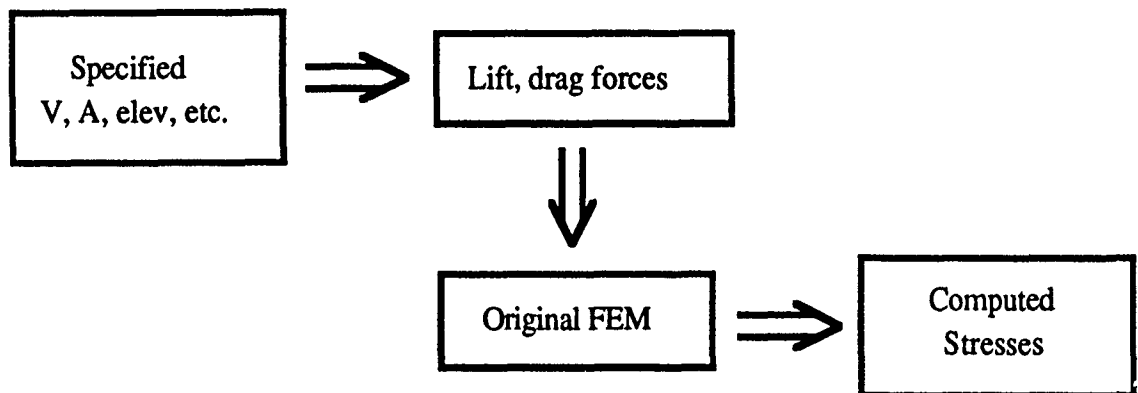


Figure 1. Standard Analysis Sequence

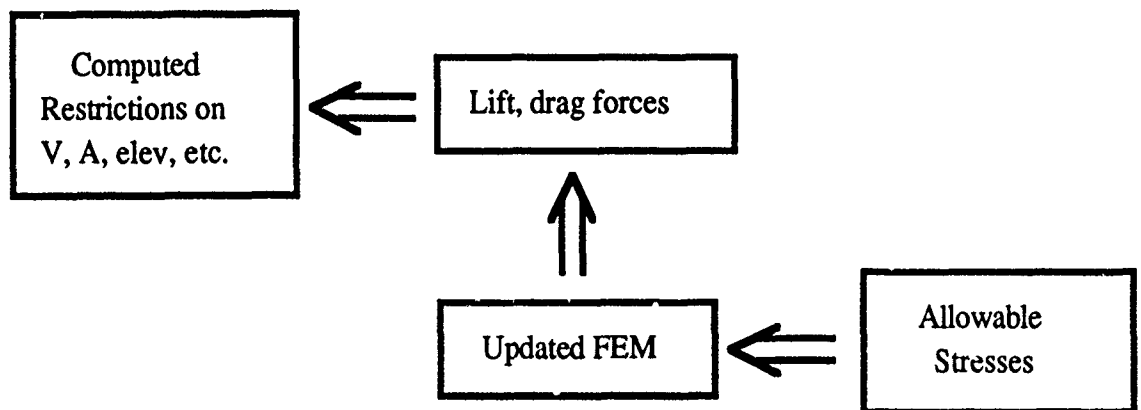


Figure 2. Inverse Analysis Sequence

backwards. In this inverse problem, we would specify the maximum allowable stresses the structure can withstand, and then, using the FEM of the damaged aircraft, solve for the corresponding lift and drag forces. The forces, in turn, would allow us to compute restrictions on the plan's maximum safe speed, acceleration, elevation, and so on. These two types of analyses - standard and inverse - are illustrated in Figures. 1 and 2.

The computational requirements for multiple solutions of the mathematical model described above are immense. It is not only the size of the models that will create difficulties, but also the speed with which they must be solved. As in other fields, however, rapid strides are being made in computing technology.

Advances in mathematical modelling, instrumentation, and computer technology make it possible to think about attempting to solve the in-flight damage detection and evaluation problem. The work performed at Wright Laboratories (WL) over the summer of 1991 included a background study of related research as well as a preliminary plan for a program encompassing the various aspects of the damage detection and evaluation research and development effort.

Section two of this report contains the results of my work over the summer which consisted of two parts. The first was a series of interviews with engineers at WL to find out about existing research which relates to structural damage detection. The second part was the continued development of my own damage detection algorithms. The third section of the report contains a description of a test program developed over the summer for conducting vibration tests on an F-16 plate model. In the fourth section of this report, an interdisciplinary program is proposed for creating a working prototype damage detection system for military aircraft including detection, evaluation, assessment of possible flight scenarios, determination of revised aircraft limitations, and pilot displays. The summary and conclusions are given in the fifth section. Section six contains the list of references.

II. RESULTS OF SUMMER INTERVIEWS AND ALGORITHM DEVELOPMENT

In the Flight Dynamics Directorate at WL, research related to the damage detection and evaluation problem has been performed in several branches. The following list was compiled this past summer from interviews I conducted with various engineers:

Wright Laboratories, Vehicle Subsystems Division, Survivability Enhancement Branch, Technology Group, Aircraft Battle Damage and Repair (ABDR)¹

Engineers from this group interview pilots and flight crews of planes that have sustained ballistic damage in combat. When possible, they also survey the damaged planes and talk to the ABDR mechanics and engineers.

Wright Laboratories, Survivability and Vulnerability Information Analysis Center (SURVIAC)

SURVIAC analyzes and classifies the effects of combat damage according to both the system (e.g. electrical, hydraulic, power, structural) and the primary cause of damage (e.g. fire, explosion, loss of pressure). Data are collected and statistics compiled on a wide array of military aircraft. A preliminary investigation of classified and unclassified information indicated that, whereas structural damage was not a large contributor to lost aircraft statistics, it was certainly not insignificant.

Wright Laboratories, Vehicle Subsystems Division, Survivability Enhancement Branch, Joint Live Fire Program (JLF)²

The JLF program, under the auspices of the Office of the Secretary of Defense, coordinates the testing of complete weapon systems or subsystems using controlled live ballistic fire. One JLF test was particularly pertinent to this study. It was a test of multiple shots on an F-16 wing, with the wing being repaired following each shot³. As part of this test, the Vibration Group from the Structures Division performed several modal tests on the wing for frequencies and mode shapes, both before and after ballistic damage and repair⁴. In addition, a finite element model was created to simulate the original, damaged, and then repaired wing for each shot⁵.

Wright Laboratories, Structures Division, Structural Dynamics Branch, Vibration Group⁶

This group is involved in the development of modal testing and modal identification techniques. They have built and will test a plate structure in support of this damage detection work. The test is described below.

Wright Laboratories, Structures Division, Structural Dynamics Branch, Instrumentation and Acquisition Group⁷

This group uses noncontact methods of vibration monitoring such as video holography for vibration monitoring. These methods are very attractive because they do not interfere with the structure and they have the potential of being used remotely. This equipment will be used in the testing described above.

Wright Laboratories, Structures Division, Analysis and Optimization Branch⁸.

ASTROS is a general purpose, large-scale computer code for optimization. The engineers in this group are seeking strategies for adapting the code so that it can be used for system identification. They have developed a prototype code called FRAMETUNE to demonstrate their ideas. So far, it has been used successfully in two tests: identification of flexibilities of the AMRAAM missile pylon connectors and of stiffnesses associated with a coplanar frame tested at the Air Force Academy. They are now modifying this code to identify different types of damping.

Wright Laboratories, Structures Division, Analysis and Optimization Branch, Aeroelasticity Group⁹.

Modern fighter aircraft utilize a large number of external weapon configurations, some of which can be flutter critical. Ejection of a given missile or bomb can instantly result in a dynamically unstable configuration. Adaptive control methods offer a direct approach which identifies the onset of unstable wing oscillations, and commands an appropriate control surface action to suppress flutter. Such an adaptive control approach has been demonstrated on computer models as well as in wind tunnel tests.¹⁰

Wright Laboratories, Flight Control Division, Flight Control Advanced Development Programs (ADP) Branch¹¹

Over the past ten years, this branch has been actively involved in the Self Repairing Flight Control System Program¹². The objective of this work was to reconfigure flight controls in such a way that the effects of control system failure, aircraft battle damage, and damage resulting from mid-air collision could be mitigated. In this procedure, the damage would be measured and then the control system commands would be immediately redistributed in such a way that normal maneuvering capability would be restored. "Damage detection" in this context is not have quite the same meaning as the term used elsewhere in this report. They do not locate or quantify damage directly, but rather, obtain "equivalent" damage.

The distinction is that they are concerned primarily with flight control and stability, whereas we are concerned primarily with structural integrity. The ADP Branch has used computer simulation and some flight testing to demonstrate the potential of their procedure. The following damage scenarios are examples of the ones they addressed:

1. Fuselage Damage: A NASTRAN finite element model was used to simulate damage to four separate sections of the fuselage of an F-15. Reductions of 25%, 50%, and 75% in both the mass and stiffness of the fuselage were considered. The effect of this damage was to change the fuselage bending frequencies to such an extent that they would lie outside the range of the Flight Control System data acquisition filters. A closed-loop instability would then cause the aircraft to experience an annoying and possibly dangerous high frequency vibration called "buzz". The solution was to sense the frequency of this unwanted structural mode and adjust the filter to eliminate it from the Flight Control System.
2. Partial Wing Loss: A NASTRAN finite element model was again used to model the damage, this time wing cutoffs of 25%, 35%, and 50%. A CFD program was used to determine the aeroelastic forces on the remaining structure. The solution to this wing-loss problem was to reconfigure the remaining control surfaces so that the aircraft would fly as if it were unimpaired.
3. Wing Hole Damage: Smooth holes from twenty to sixty inches in diameter, located in two different wing locations, were modeled using NASTRAN. Computer analysis showed that flutter would not be a problem; that the wing stresses near the holes would not be excessive; but that the effectiveness of the aileron would be decreased.
4. Jagged Edge Wing Damage: Both a jagged hole and a jagged partial wing loss were considered in this part of the study. The effect of the jaggedness is to cause turbulence and to increase the drag forces. In this analysis, using a finite element model, the partial wing loss created no difficulties while the jagged hole did create wing instability at a speed below the flutter speed.

NASA Johnson Space Flight Center.¹³

Modal analysis is being used as a diagnostic tool for on-ground health monitoring of the Space Shuttle. The procedure was extensively tested using an intentionally damaged Cessna aircraft. Changes in natural frequencies from baseline values are used to detect damage. The Modal Assurance Criterion for the new mode shapes is then used to locate

areas of the structure associated with the changed frequencies. In this way, a knowledgeable person can track down a failed part.

North Carolina State University, Civil Engineering Department.

Over the past fifteen years at NCSU, my students and I have developed several computer codes for the identification of structural parameters. In the most recent version, excitation and response data from a structure can be used to determine directly the elements of mass, damping, and stiffness matrices which make up the mathematical model of the structure. In the summer of 1990, as a participant in this Air Force Office of Scientific Research (AFOSR) program with the same group at WL, a graduate student and I demonstrated the usefulness of this technique for identifying damage in a cantilever beam.¹⁴ This year, besides conducting the interviews at WL, I continued to use my system identification program to investigate various aspects of damage detection. In addition, three graduate students who remained at NCSU in Raleigh worked on related topics. The following list gives a brief summary of these efforts:

1. The specific identification problem I considered at WL this summer was the possibility of using data from a reduced set of sensors to identify selected elements of the mass or stiffness matrices. This is a critical question in the identification process since it will never be possible to place sensors at every degree of freedom needed to define the structure. The structure I considered was a cantilever beam with support provided by a vertical and rotational spring at one end. The mathematical model, shown in Figure 3, contains four Bernoulli-Euler beam elements with consistent mass matrices.

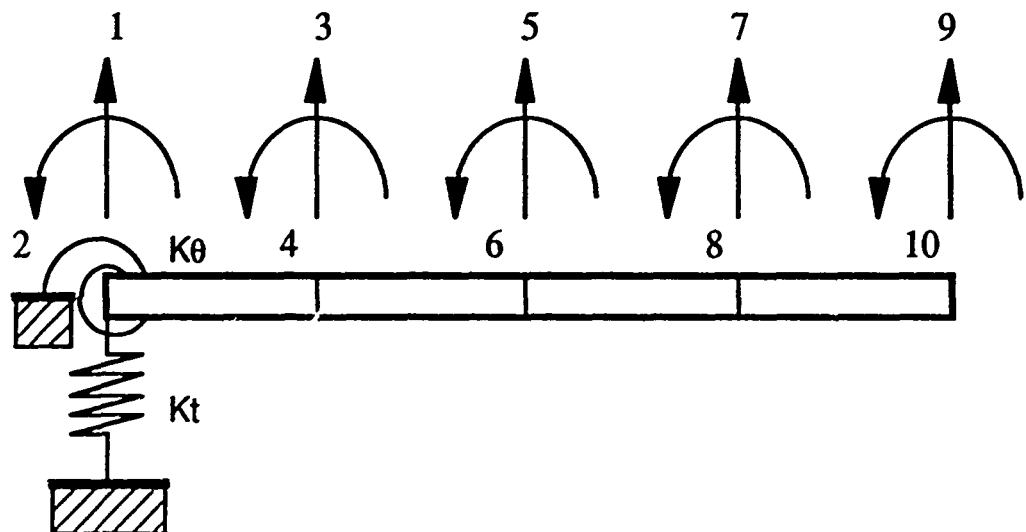


Figure 3. Four-Element, Spring-Supported Cantilever Beam

I simulated test data by assigning specific values to all of the physical parameters and then integrating the equations of motion. The excitation was from a pull-back-and-quick-release at the free end of the cantilever. For the identification program, initial values of the support stiffnesses were selected to be plus or minus ten percent of the original, assigned values. Results from the simulated tests are shown in Table 1.

Sensor Location (DOF)	No. of Function Evaluations	No. of Directions	Run Time (min)
1-10	65	9	18.85
1,3,5,7,9	56	8	16.00
3,7,9	31	7	9.47
9	26	6	7.95

Table 1. Identification Results From the Cantilever Beam Test

In each case, the program converged to the correct (assigned) spring stiffnesses. The fewer the number of sensors used, however, the quicker the convergence. I am not sure why this happened. One would think that the use of more data should lead to improved results and more rapid convergence. In a more realistic test, that is when the data are noisy and the model is imperfect, more sensors may in fact lead to superior results.

2. One of the shortcomings of the identification program used in the above study is that it solves the coupled equations of motion using a direct integration technique. While allowing the use of nonproportional damping matrices, the solution method does have difficulties associated with stability and numerical damping, especially at the very beginning of the response. A graduate student in Raleigh¹⁵ worked over the summer to incorporate a mode superposition solution procedure to replace direct integration, both for the solution of the mathematical model and for the sensitivity coefficients. With this solution technique, the parameters to be identified will still contain the elements of the mass and stiffness matrices, but damping will now be in terms of damping ratios.

3. Instead of using individual elements of the structure's mass and stiffness matrices as parameters, there could be a single parameter associated with each member's stiffness or mass matrix. This would be equivalent to using the modulus

of elasticity and mass density of each member as the parameters. This choice places additional constraints on the form of the model (it would no longer be possible to identify damage at an intermediate location in a single member¹⁶), but it greatly reduces the number of parameters to identify. Another graduate student¹⁷ worked on this approach over the summer. Using simulated data, he demonstrated that the method works quite well. More recently he had been using advanced computing techniques such as vectorized code on a supercomputer.

4. The most common approach to identification uses modal quantities as the parameters. Experimental modal analysis is a mature field and parameters such as frequency, damping ratio, and modal mass can be obtained quite routinely. The difficulty in using this approach for damage detection lies in relating a subset of the modal parameters to physical parameters. A third student in Raleigh¹⁸ is investigating various modal analysis approaches to damage detection.

III. F-16 PLATE MODEL TEST

Based on the work Harwood and I did last year, as well as my work this past summer, it seemed appropriate to begin a test sequence on a plate model. An unsymmetrical configuration was chosen so that problems associated with symmetric modes would be avoided. Because of the interest the ABDR group had in the F-16 wing, we decided to this shape for the plate model. The Vibration Group was looking for a benchmark structure, and they decided to select this F-16 plate model. The plate is shown in Figure 4. It will be tested by the Vibration Group first in its original, undamaged configuration, and then with damage of various magnitudes and locations. Details of the testing program are given below:

Instrumentation: Both contact and noncontact types will be used. Approximately thirty 2gm accelerometers will be attached to the plate. Video holography will also be used, both alone and in conjunction with the accelerometers. These tests should tell us whether or not mass loading by the accelerometers is significant. Accelerometer data will be gathered and stored using a ZONIC A/D system.

Loading: Both pull-back-and-quick-release tests and harmonic excitation will be used.

Support: The plate will be tested in a cantilevered configuration with the the plate in the vertical plane, and the axis of the wing extending horizontally away from the support. The

plate will be attached to a specially designed fixture which, in turn, will be attached to a six-inch thick steel base plate rigidly fixed to the floor.

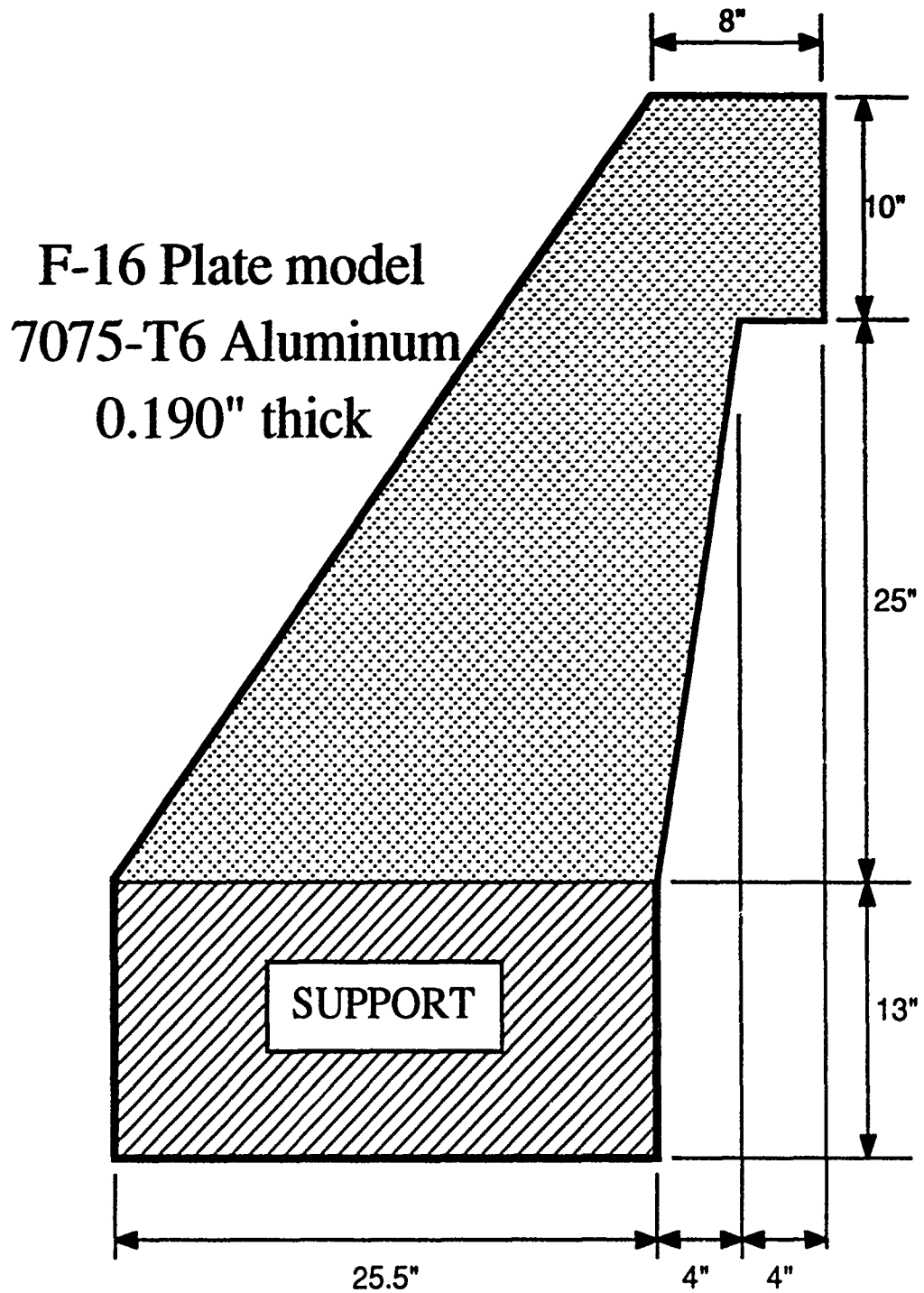


Figure 4. F-16 Plate Model

Schedule: The first test on the undamaged plate should be run during the fall of 1991, with data being made available by the end of the year. Tests on damaged plates will be conducted after the first sets of data are analyzed.

Identification: The two groups at WL interested in system identification, the Vibrations Group and the Analysis and Optimization Branch, will be using modal analysis techniques, while my students and I at NCSU will be using both modal and physical parameter methods. The reason for using more than one method of identification is that there is not yet a consensus on what the best approach to damage detection is. We will continue to consider all reasonable alternatives until an obvious choice becomes apparent.

IV. PROPOSED PROGRAM TO DETECT AND EVALUATE STRUCTURAL COMBAT DAMAGE

There are three major aspects to the development of this system. The first is the ability to detect combat damage in a timely manner. The second aspect is to evaluate the results. There are two subparts to this second aspect. The first subpart is to use this information to predict the plane's ability to perform various aspects of its mission. The second subpart is to determine the additional constraints that must be placed on the plane's speed and maneuverability to prevent further damage. Because this evaluation phase would detect the seriousness of the various ballistic hits, the information should be provided to ABDR personnel so that they could make the needed repairs more efficiently. The third aspect of the proposed program is to present this information to the pilot in a form that can be easily and quickly understood. The three aspects will be discussed separately.

1. **Damage Detection:** Recent journal articles on damage detection have been based on a variety of mathematical modelling schemes. Applications have included cantilever beams, symmetrical plates, and trusses^{19,20}. The use of wing-like structures, like the one described in section III, is the next major extension of this work. Future test structures might be box beams, tapered box beams, isolated wings, and then wings attached to a fuselage. The direction of damage detection software development will be towards quick, robust algorithms which require the minimum amount of instrumentation.

2. **Damage Evaluation:** After both the magnitude and location of the damage have been identified, the structural effects of the damage must be determined. This

is not a simple matter. As described earlier, the lift and drag forces on the aircraft are functions of the current speed as well as the several kinematic functions and their derivatives. If the control surfaces are reconfigured, then all of these variables and hence the loading on the aircraft will change. It is possible that, from a structural integrity point of view, this reconfiguration may exacerbate the damage and result in a more restricted flight condition than is necessary. Ideally, then, the reconfiguration would be based not only on stability and control considerations, but also on structural strength.

To determine the lift and drag forces on aircraft surfaces, it is necessary to use an analytical techniques such as CFD. A finite element program like NASTRAN can then be used to determine the corresponding structural response. These analyses will be based on a given set of flight variables. If the structural response exceeds safe limits, then the flight variables must be restricted. This inverse problem will in all likelihood require an iterative solution. At the present time, even one CFD analysis is very time consuming. Solutions to this problem, however, can be envisioned. Computers will become faster and algorithms more efficient. Entirely new approaches to finding the effects of aerodynamic and aeroelastic forces on a structure may be found.

3. **Pilot Display:** Following the determination of the revised limits on the aircraft's maneuverability and speed, this information needs to be given to the pilot in an unobtrusive but obvious form. It may be advisable to relate this information to ground personnel. Aircraft battle damage and repair personnel would benefit in that resources needed for repair or replacement could be on hand when the aircraft returns.

V. SUMMARY AND CONCLUSIONS

Through a series of interviews and study of existing work this summer at WL, it became apparent that it would be beneficial for pilots to have a near real time "health-monitoring" system for the plane's structural integrity. Such a system would indicate to the pilot any restrictions on the plane's capability that may have been caused by combat damage (other causes could be considered also). It was also apparent from these interviews that the technology to begin the development of such a system exists. Various groups at WL have been working, for over ten years in some cases, on different aspects of the

detection/evaluation problem. However, additional work could be done to integrate the areas of experimental mathematical modelling, aircraft controls, and battle damage repair.

In a series of numerical experiments on cantilever beams conducted this summer, we demonstrated that, at least in this one case, it was not necessary to have sensors at every DOF when using time-domain, physical-parameter system identification. This is a fortunate result since it will never be possible to place instrumentation at every DOF.

As part of the development of damage detection algorithms, an F-16 plate model was constructed and will be tested in both undamaged and damaged configurations. Researchers at both WL and NCSU will use the test data in their damage detection algorithms.

Finally, an outline was developed for a long range project to extend the research needed to develop a damage detection and evaluation procedure. The benefits of such a procedure, once implemented, would be fewer aircraft losses to combat damage and more rapid repair on damaged planes by ABDR crews.

VI. LIST OF REFERENCES

¹Contact: Mike Waddell

²Contact: Ralph Lauzze, Jr

³Ritter, Stephen Bruce 1Lt (1987). "Battle Damage Repairs Applied to Ballistically Damaged F-16 Wings," 61 JTCG/ME-9-13 and JLF-TR-87-5, pp. 100.

⁴Pacia, Arnel and Banaszak, David (1989). "Joint Live Fire F-16 Wing Modal Tests," AFWAL-TM-88-167-FIBG, 20 April 1989, 85 pp.

⁵Negaard, Gordon R., (1988). "Finite Element Analysis of F-16 Ballistic Tests," AFWAL-TR-88-3041.

⁶Contacts: Doug Henderson, Eob Gordon, and Joe Hollkamp

⁷Contact: Gene Maddux

⁸Contact: Major Mark Ewing

⁹Contact: Terry Harris

¹⁰Larimore, W.E. and Mehra, R.K. (1984). "Technical Assessment of Adaptive Flutter Suppression Research," Final Report AFWAL-TR-84-3052, (Scientific Systems, Inc, Cambridge, MA 02140) 80 pp.

¹¹Contact: Phil Chandler and Bob Yeager

¹²Hoy, Stephen and Havern, William (1991). "Volume II: Fuselage and Wing Damage Analysis and Development of Control Reconfiguration Concepts," DRAFT-Final Report AFWAL

¹³Contact: George Studor, USAF Reserves, Summer duty performed at WRDC.

¹⁴Matzen, V. C., and Harwood, C. E. (1990). "Ballistic Damage of Aircraft Structures: Detection of Damage Using Vibration Analysis." Final Report, AFFDL F49620-88-C-0053, Air Force Flight Dynamics Laboratory, Wright-Patterson Air Force Base, OH.

¹⁵Alok Jha, MS candidate.

¹⁶Harwood, Craig, "Global Nondestructive Damage Evaluation in a Cantilever Beam using Dynamic Response Data and System Identification." MS thesis, NCSU, see p. 52

¹⁷Hung-Shi, PhD student

¹⁸Shunyi Chen, PhD student.

¹⁹Hajela, P. and Soeiro, F.J.(1989). "Structural Damage Assessment as an Identification Problem," Recent Advances in Multidisciplinary Analysis and Optimization, Langley Research Center, pp. 1507-1520.

²⁰Hanagud, S., Meyyappa, M., and Craig, J.I. (1987). "Identification of Structural Damage Systems," Recent Trends in Aeroelasticity, Structures and Structural Dynamics, Florida Presses.

A REPORT ON ROBUST CONTROL DESIGN FOR STRUCTURED UNCERTAINTIES

Dr. Jenny L. Rawson

Abstract: A method is presented for the construction of design equations for low-order controllers to stabilize and provide disturbance rejection for uncertain plants. The multi-goal robust stability and performance problem is broken down into subproblems, each with a simple design goal. Design Riccati inequalities are easily written for each of the subproblems, then the various terms are collected from each to form design equations for the multi-goal problem. This method is based on theorems fundamental to μ -synthesis so that the results can be used to start the D-K iteration process in μ -synthesis.

Acknowledgements

I wish to thank the Air Force Systems Command and the Air Force Office of Scientific Research for sponsorship of this research. Thanks are due also to Research and Development Laboratories for help and guidance in all of the administrative aspects of this program.

John Bowlus and the people of the Control Analysis Group made this a most enjoyable and productive research period. Many members of the group went out of their way to help me. Capt. Andrew Sparks, as my Effort Focal Point, facilitated my work at the lab and spent much time answering questions. Dr. Siva Banda assisted with technical advice and took care of administrative details. Special thanks are due to Dr. Hsi-Han Yeh for providing an exciting research topic and spending many hours in discussion with me.

I. Introduction

The objective of this report is to present a method for the construction of design equations for low-order observers to stabilize and provide disturbance attenuation for uncertain plants. A single Riccati equation and a Riccati inequality result from the construction.

Other methods exist for the solution of this problem, but they have been mainly restricted to the full-order observer case. They also differ in other ways from this work as discussed in the following. Previously, Petersen [1], developed a method for the design of observers for stabilization with respect to additive perturbations of the state, input and output matrices of the plant. This requires the solution of two Riccati equations and the testing of a Riccati inequality. Disturbance rejection is not specifically mentioned. However, it is in the methods of Yeh, Banda, Bartlett and Heise [2], Veillette, Medanic and Perkins [3], and Jabbari and Schmitendorf [4]. The first models the real parameter uncertainties as additive disturbances to the nominal plant. Bernstein and Haddad's H_2/H_∞ controller [5] is then used to minimize an entropy (an upper bound of a linear quadratic cost) in addition to providing disturbance rejection and robust stability. An independent Riccati equation and a pair of coupled Riccati equations must be solved. Although the solution of the coupled equations is not difficult, the process is numerically intensive. The second also models the real parameter uncertainties as additive disturbances to the nominal plant, but uses the H_∞ controller from the paper by Doyle, Glover, Khargonekar and Francis [6]. A series of algebraic manipulations and a revision of a theorem by Willems [7] are used to obtain the conditions

under which the uncertain system is stable and the H_∞ disturbance rejection constraint is satisfied. The method by Jabbari et al. [4] for H_∞ design with plant uncertainty is a two-step process based on the fact that an observer degrades the performance of a state feedback system. The first step is to obtain state feedback gains to meet the disturbance rejection requirements despite perturbations in the plant state matrix. Then in the second step, an observer is designed, with an additional Riccati equation and a matrix inequality, for a specified increase in the H_∞ norm bound and decrease in the stability margin from those of state feedback system.

The main difference between this work and the above references is in the machinery for formulating the Riccati equalities or inequalities from design objectives. The basis for this is a set of three theorems by Doyle [8] in μ -analysis. The first theorem states that disturbance rejection can be measured by the H_∞ norm, the second gives the structured singular value (μ) as a non-conservative measure of robust stability of uncertain systems, and the third states that a constraint on μ is a necessary and sufficient condition for an uncertain system to be robustly stable and to remain in its H_∞ norm bound for disturbance rejection. These theorems form a powerful engine for generating design equations for multiple robustness and performance objectives in a simple and direct manner. A Riccati inequality can be written for the closed-loop system for each individual design goal, such as disturbance rejection or stabilization with respect to perturbations in a special parameter, using the first two of the above-mentioned theorems of Doyle. Then, with the aid of an extension of Willems' work [7] by Veillette et

al. [3], the third theorem enables the terms of the various inequalities to be collected to form one overall Riccati inequality, just as in a collection of terms to form the smallest common denominator, or in the collection of implicants in a logical equation. In this manner, a complex, multi-goal robust stability and performance problem breaks down into simple subproblems, each having only a simple design goal for which design equations are easy to write. The design equations of the multi-goal problem can then be constructed from the design equations of the subproblems. It is worth noting that, unlike other methods that deal with real structured uncertainty and robust performance, this method is not restricted to a specific observer. In this paper, the design equations are derived for Luenberger observers, although any other observer could have been used. It is shown that a single Riccati equation and a Riccati inequality result from this derivation. In addition, the Luenberger observer also requires a Sylvester equation to be satisfied.

It should also be noted that although Doyle's theorems point to the constraint of μ , this paper formulates the design equations to constrain the H_∞ norm only. Therefore, the real parameter uncertainties are treated as if they were complex parameter uncertainties, and full advantage is not taken of the uncertainty structure. A certain amount of conservatism is thus introduced. This fact was only recently pointed out by Khargonekar, Petersen and Zhou [9]. However, the formulations given in this paper can also be used as the first step of D-K iteration in μ -synthesis [8]. If μ -synthesis is carried out, the final result will be non-conservative. This is left for future research.

II. Problem Discussion

This section includes all of the background material needed to understand and solve the problem of low-order observer design for robust stabilization and performance. The first subsection below contains the basic theorems that are used to derive the main result in this report. The second is devoted to a description of the plant and observer to which the main result is applied later in Section III.

1. Mathematical Background

This subsection covers the mathematical for the derivation of the design Riccati equations for the observer. In the main result of this report, uncertainty is treated as complex and the knowledge of the structure of the uncertainty is not used to full advantage. However, the development here will be usable in the future to minimize the conservatism by employing μ -synthesis.

Consider the block diagram of Figure 1. The transfer functions G_{11} through G_{22} include plant and compensator dynamics along with any weighting functions needed for performance specifications. All uncertainty is placed in the feedback block Δ .

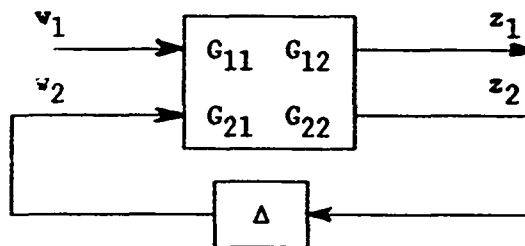


Figure 1. Perturbed System

The following three theorems from Doyle [8], form the basis for the method of derivation of design equations. The first theorem is a definition of the H_∞ norm of a transfer function in terms of the L_2 norms of the input and output signals.

Theorem A: Let $\Delta = 0$. Then, for any w_1 such that $\|w_1\|_2 < 1$, $\|z_1\|_2 < 1$ iff $\|G_{11}\|_\infty \leq 1$. ■

The next theorem concerns the robust stability of the system for nonzero Δ . Structured singular value (μ) is used to take advantage of the structure in the uncertainty. This is defined as follows. Let

$$\underline{\Delta} = \{\Delta = \text{diag}(\delta_1, \delta_2, \dots, \delta_m, \Delta_1, \Delta_2, \dots, \Delta_\ell) \mid \delta_i \in \mathbb{R}, \Delta_j \in \mathbb{C}^{k_j \times k_j}\}. \quad (2.2)$$

If there exists a $\Delta \in \underline{\Delta}$ such that $\det(I - H\Delta) = 0$, the structured singular value $\mu(H)$ of a transfer function H is:

$$1/\mu(H) = \min_{\Delta \in \underline{\Delta}} \{\sigma(\Delta) \mid \det(I - H\Delta) = 0\}. \quad (2.3)$$

Otherwise, $\mu(H) = 0$. With μ defined, the second theorem can be stated.

Theorem B: Let $\underline{B\Delta} = \{\Delta \in \underline{\Delta} \mid \sigma(\Delta) < 1\}$. The system of Figure 1 is stable for all $\Delta \in \underline{B\Delta}$ iff $\|G_{22}\|_\mu \leq 1$. ■

The third theorem gives conditions for stabilization and disturbance rejection by systems subject to structured perturbations. To include the extra requirement, a fictitious perturbation block $\Delta_{\ell+1}$ between z_1 and w_1 is appended to the system as in Figure 2. Define:

$$G = \begin{bmatrix} G_{11} & G_{12} \\ G_{21} & G_{22} \end{bmatrix} \quad (2.1)$$

Also define another function of H :

$$\|H\|_\mu = \sup_{\omega} \mu[H(j\omega)] \quad (2.2)$$

An important property of $\|H\|_\mu$ is that while it is not a norm, it is overbounded by the H_∞ norm. That is, $\|H\|_\mu \leq \|H\|_\infty$. This is used later in the development of design equations.

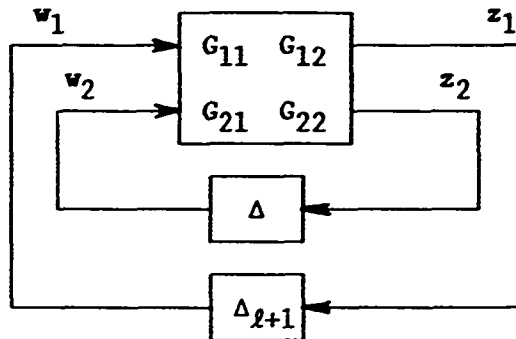


Figure 2. Perturbed System with Fictitious Uncertainty

Theorem C: The system is stable and $\|F_L(G, \Delta)\|_\infty < 1$ for all $\Delta \in \underline{\Delta}$ iff G is stable and $\|G\|_\mu \leq 1$ where μ is taken with respect to the augmented set $\tilde{\Delta} = \{\Delta - \text{diag}(\Delta_{l+1}, \Delta) \mid \Delta \in \underline{\Delta}\}$. ■

In Section III, the above three theorems are applied in a direct method to obtain Riccati design equations. In this report μ is dropped in favor of the H_∞ norm; there are well known methods for design with respect to this norm. In future work, μ will be used in order to include the structure of the uncertainty.

A theorem due to Veillette, et al. [3] is needed to obtain the desired Riccati inequalities.

Theorem D: Let (A_{c1}, C_{c1}) be a detectable pair. Then, A_{c1} is stable and $\|C_{c1}(sI - A_{c1})^{-1}B_{c1}\|_\infty \leq 1$ if there exists $P \geq 0$ such that

$$PA_{c1} + A_{c1}^T P + PB_{c1}B_{c1}^T P + C_{c1}^T C_{c1} \leq 0. \quad (2.3)$$

Veillette et al. also use the fact that if

$$PA_{c1} + A_{c1}^T P + PB_{c1}B_{c1}^T P + C_{c1}^T C_{c1} + Q \leq 0 \quad (2.4)$$

for some $Q \geq 0$, then

$$PA_{c1} + A_{c1}^T P + PB_{c1}B_{c1}^T P + C_{c1}^T C_{c1} \leq -Q \leq 0. \quad (2.5)$$

This theorem and fact are combined with Theorems A, B and C to obtain a method for deriving design equalities and inequalities.

2. Low-Order Observers

This subsection is concerned with the low-order observer to be used for stabilization and disturbance rejection in an uncertain plant. First, the plant is presented, along with any assumptions that are needed. Then, the same is done for the observer.

The plant has the state-space description:

$$\begin{aligned} \dot{x}(t) &= (A + \Delta A)x(t) + (B + \Delta B)u(t) + G_1 w_1(t) \\ y(t) &= Cx(t) \\ z_1(t) &= H_1 x(t) \\ z_2(t) &= H_2 u(t) \end{aligned} \quad (2.6)$$

where, $x \in R^n$ is the plant state vector, $u \in R^p$ the control input, $w_1 \in R^{p1}$ a disturbance input, $y \in R^m$ the measured output, and $z_1 \in R^{q1}$, $z_2 \in R^{q2}$ are controlled outputs. In order to be sure of attaining closed-loop stability, a few assumptions on the plant must be made:

- A1. (A, B) is stabilizable.
- A2. (A, C) is detectable.
- A3. $\text{Rank}(B) = p \leq n$.
- A4. $\text{Rank}(H_2) = q_2 \geq p$.

These assumptions are used in the design phase.

Now, suppose that state feedback design has been performed to obtain a set of gains K_c such that if the states were available, the control law would be $u = -K_c x$. However, if the states are not available, an observer must be used. A minimal-order observer can be described by the following equations:

$$\begin{aligned}\dot{x}_0(t) &= Fx_0(t) + Gu(t) + K_f y(t) \\ u(t) &= -Nx_0(t) - My(t)\end{aligned}\tag{2.7}$$

where, $x_0 \in R_{n-m}$. The observer states are an estimate of a linear combination of the plant states Tx , where T is chosen so that $[T^T C^T]^T$ is nonsingular. An error signal is defined as $e = Tx - x_0$. The error e is asymptotically stable if the following Luenberger constraint equations are satisfied [10]:

$$TA - FT = K_f C \tag{2.8}$$

$$G = TB \tag{2.9}$$

$$NT + MC = K_c \tag{2.10}$$

These equations are assumed to hold throughout this report.

III. Results

The main result of this report is in Theorem I below. With it, a Riccati inequality can be written for each individual design goal for a closed-loop system. Then these inequalities can be combined in a straight forward manner into a single inequality. If this inequality has a positive semi-definite solution, and a detectability condition is met, then all of the design goals are met *simultaneously*.

Some new definitions need to be made before the theorem is stated. Referring to Figure 3, let the transfer function L_{ij} from w_i

to $z_i, w_i, z_i \in R^{k_j}$ $i = 1, \dots, \ell$, have the state-space description:

$$\begin{aligned}\dot{\mathbf{x}}(t) &= \mathbf{A}_{cl}\mathbf{x}(t) + \mathbf{B}_i\mathbf{w}_i(t) \\ \mathbf{z}_i(t) &= \mathbf{C}_i\mathbf{x}(t)\end{aligned}\quad (3.1)$$

Block Δ_i represents either uncertainty in L_{ii} or a disturbance rejection criterion. It is assumed for now that $\sigma(\Delta_i) \leq 1$. Each subsystem has corresponding Riccati inequality:

$$\mathbf{R}_i(\mathbf{P}) = \mathbf{P}\mathbf{A}_{cl} + \mathbf{A}_{cl}^T\mathbf{P} + d_i\mathbf{P}\mathbf{B}_i\mathbf{B}_i^T\mathbf{P} + d_i^{-1}\mathbf{C}_i^T\mathbf{C}_i \leq 0. \quad (3.2)$$

Each inequality can be used to design compensation to meet the i^{th} design goal. That is, by Theorem D, if $(\mathbf{A}_{cl}, \mathbf{C}_i)$ is detectable and there exists a $\mathbf{P} \geq 0$ that satisfies (3.2), then \mathbf{A}_{cl} is stable and $\|\mathbf{L}_{ii}\|_\infty \leq 1$. If Δ_i represents uncertainty in the system, then by Theorem B, the uncertain system is stable for all Δ_i with $\sigma(\Delta_i) \leq 1$.

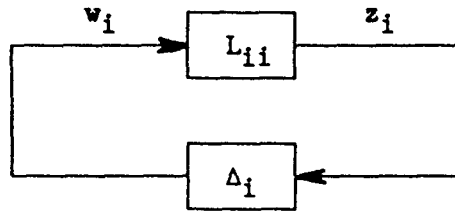


Figure 3. Subsystem for i^{th} Design Goal

For the combination of all ℓ design goals, let:

$$\mathbf{L} = \begin{bmatrix} L_{11} & L_{12} & \dots & L_{1\ell} \\ L_{21} & L_{22} & \dots & L_{2\ell} \\ \vdots & \vdots & \ddots & \vdots \\ L_{\ell 1} & L_{\ell 2} & \dots & L_{\ell \ell} \end{bmatrix} \quad (3.3)$$

as in Figure 4. Define a corresponding Riccati inequality

$$\mathbf{P}\mathbf{A}_{cl} + \mathbf{A}_{cl}^T\mathbf{P} + \sum_{i=1}^{\ell} d_i\mathbf{P}\mathbf{B}_i\mathbf{B}_i^T\mathbf{P} + \sum_{i=1}^{\ell} d_i^{-1}\mathbf{C}_i^T\mathbf{C}_i \leq 0 \quad (3.4)$$

formed by combining terms from the inequalities (3.2). Without loss of generality, w_1 is the disturbance input, z_1 controlled output, and all of the remaining w_i and z_i are associated with system parameter uncertainty. The uncertainties Δ_i , $i = 2, 3, \dots, \ell$ are combined in the set $\underline{B\Delta}'$ which is defined by:

$$\underline{\Delta}' = \{\Delta = \text{diag}(\Delta_2, \Delta_3, \dots, \Delta_\ell) \mid \Delta_i \in \mathbb{C}^{k_i \times k_i}\} \quad (3.5)$$

$$\underline{B\Delta}' = \{\Delta \in \underline{\Delta}' \mid \sigma(\Delta) < 1\} \quad (3.6)$$

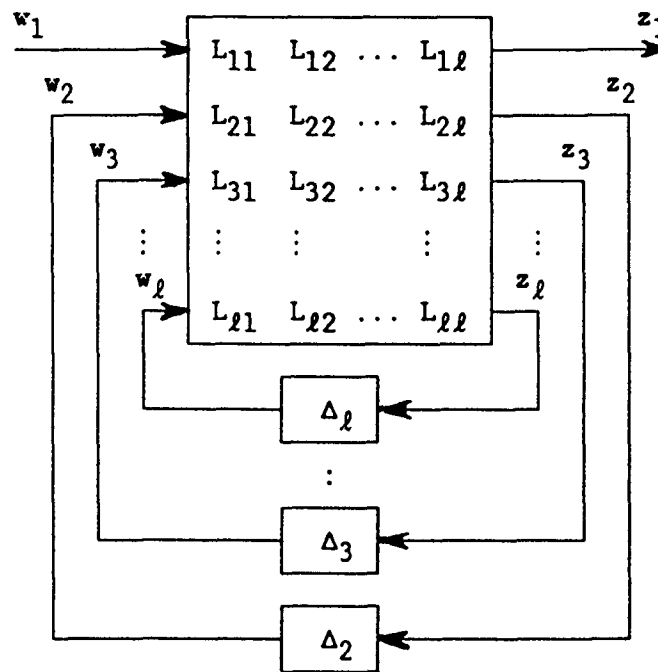


Figure 4. Perturbed System for Theorem I

Now it is possible to state the theorem.

Theorem I. If (A_{c1}, C_1) is detectable for one of the C_i and there exists a solution $P \geq 0$ to (3.4) for some $d_i > 0$, $i = 1, \dots, \ell$, then the system is stable and $\|F_1(L, \Delta)\|_\infty < 1$ for all $\Delta \in \underline{B\Delta}'$.

Proof: This can be performed in 4 steps.

1. Each inequality (3.2) has a solution $P \geq 0$. For any i , (3.4) can be reduced to (3.2) by moving the extraneous terms to the right-hand side of the inequality. Since these terms are positive semi-definite, the solution P of (3.4) will also solve (3.2).

2. A_{c1} is stable. Suppose that $\{A_{c1}, C_j\}$ is the detectable pair. Then by step 1 and Theorem D, A_{c1} is stable.

3. $\|L\|_\mu \leq 1$. The state-space description of L is $\{A_{c1}, [B_1 \ B_2 \ \dots \ B_\ell], [C_1^T \ C_2^T \ \dots \ C_\ell^T]^T\}$. Stability of A_{c1} trivially ensures the detectability of $\{A_{c1}, [C_1^T \ C_2^T \ \dots \ C_\ell^T]^T\}$, so that by Theorem D, a positive semi-definite solution to (3.4) implies that $\|DLD^{-1}\|_\infty \leq 1$. The rest follows since $\|L\|_\mu \leq \|DLD^{-1}\|_\infty$ for any $D = \text{diag}(d_1 I_{k1}, d_2 I_{k2}, \dots, d_\ell I_{k\ell})$ [8].

4. The remainder of the proof follows from Theorem C by letting

$$G_{11} = L_{11}; \quad G_{12} = [L_{12} \ L_{13} \ \dots \ L_{1\ell}]; \quad G_{21}^T = [L_{21}^T \ L_{31}^T \ \dots \ L_{\ell 1}^T]^T; \\ G_{22} = \begin{bmatrix} L_{22} & L_{23} & \dots & L_{2\ell} \\ L_{32} & L_{33} & \dots & L_{3\ell} \\ \vdots & \vdots & & \vdots \\ L_{\ell 2} & L_{\ell 3} & \dots & L_{\ell\ell} \end{bmatrix}; \quad \underline{A} = \underline{A}'; \quad \underline{B}\underline{A} = \underline{B}\underline{A}'.$$

Note that $\|L_{ii}\|_\infty \leq 1$, $i = 1, \dots, \ell$. ■

The next step is to apply this theorem to the task of obtaining Riccati inequalities for low-order observer design. Before this can be done, the plant uncertainties have to be described in terms that fit the above formulation. The uncertainties are decomposed as:

$$\Delta A = \sum_{j=1}^r D_j \Delta_j E_j; \quad \Delta B = \sum_{j=1}^r D_j \Delta_j F_j \quad (3.7)$$

with $\Delta_j \in R^{k_j \times k_j}$. The matrices D_j , E_j and F_j are fixed, with all of the

parameter variation appearing in the Δ_j . Furthermore, the uncertainty is bounded as

$$\sigma(\Delta_j) \leq \rho, \quad (3.8)$$

where D_j , E_j or F_j can be scaled so that for each j the perturbation of maximum norm achieves ρ . It is convenient to stack these matrices as:

$$\begin{aligned} \tilde{D} &= [D_1 \ D_2 \ \dots \ D_r]; \ \Delta = \text{diag}(\Delta_1 \ \Delta_2 \ \dots \ \Delta_r); \\ \tilde{E} &= [E_1^T \ E_2^T \ \dots \ E_r^T]^T; \ \tilde{F} = [F_1^T \ F_2^T \ \dots \ F_r^T]^T. \end{aligned} \quad (3.9)$$

With the uncertainties defined as above, the system can be represented as in Figure 5. Additional signals w_2 , w_3 , z_3 and z_4 are defined, and some scaling is introduced to make the system compatible with Theorem I. Requiring the norm of the transfer function from w_1 to $[z_1^T \ z_2^T]^T$ to be bounded by δ is the same as requiring the norm of the transfer function from w_1' to $[z_1^T \ z_2^T]^T$ to be bounded by 1.

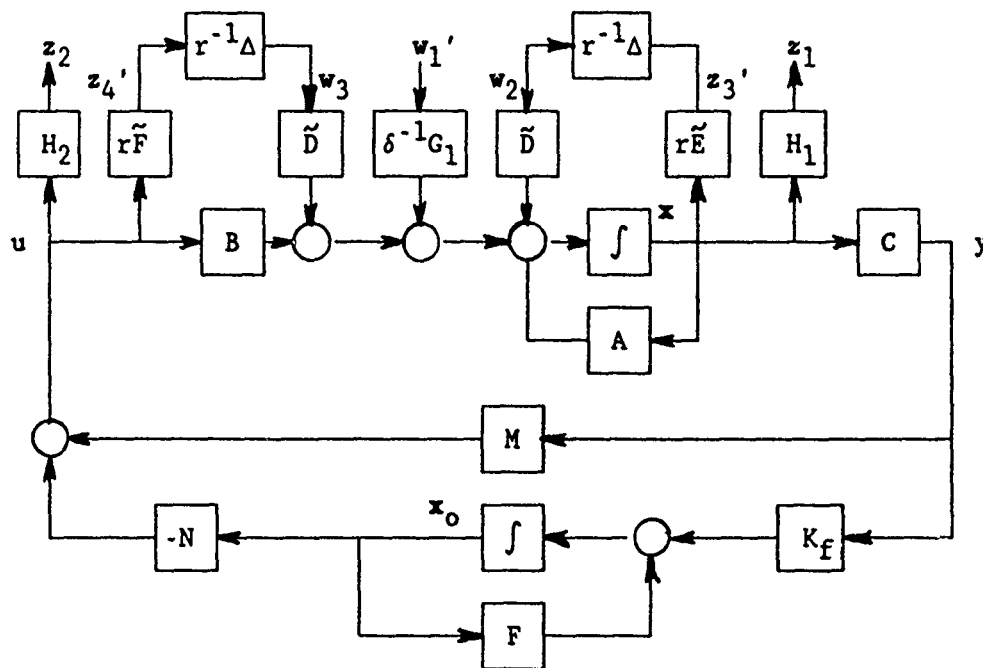


Figure 5. Perturbed System with Observer

Now a set of state equations can be obtained for each of the design goals individually: minimization of the effect of w_1 on $[z_1^T z_2^T]^T$, stabilization with respect to ΔA , and stabilization with respect to ΔB . It is possible to use $[x^T x_0^T]^T$ as the complete state of the closed-loop system, but the process is simplified by using $[x^T e^T]^T$, where $e = Tx - x_0$. This is done in each of the following subsections.

1. Disturbance Rejection

In this case, a Riccati equation is obtained for the nominal system. The norm of the transfer function L_{11} between w_1' and $[z_1^T z_2^T]^T$ is to be bound. Some simple manipulations and application of the Luenberger observer equations (2.8) through (2.10) yield:

$$A_{c1} = \begin{bmatrix} A - BK_C & BN \\ 0 & F \end{bmatrix}; B_1 = \begin{bmatrix} \delta G_1 \\ \delta TG_1 \end{bmatrix}; C_1 = \begin{bmatrix} H_1 & 0 \\ -H_2 K_C & H_2 N \end{bmatrix} \quad (3.10)$$

Detectability of (A_{c1}, C_1) follows from the detectability of (A, H_1) , the stability of F and the rank conditions on B and H_2 . This can be shown by recalling that a pair (A, C) is detectable iff for any $v \neq 0$, $v^T[A' - \lambda I \ C'] \neq 0$ for λ any scalar in the closed right-half complex plane. Veilleux, et al. use a similar procedure whenever they apply Theorem D [3]. If the disturbance rejection is the only concern, then, by Theorem D, $\|L_{11}\|_\infty \leq 1$ if there exists a $P \geq 0$ such that:

$$R_1(P) = PA_{c1} + A_{c1}^T P + PB_1 B_1^T P + C_1^T C_1 \leq 0, \quad (3.11)$$

Inequality (3.11) is used in subsection 4 where Theorem I is applied. However, if disturbance rejection alone is the concern, then a design equation and an inequality can be formed from (3.11). This is beyond the scope of this report; details may be found in [11].

2. Stabilization with Respect to ΔA .

Now the concern is with stabilization of the system when there is uncertainty in the A matrix. The disturbance rejection goal is dropped and ΔB set to zero. If the Δ_j are bounded as in (3.8), then, by Theorem A, the closed loop system is stable if the norm of the transfer function between w_2 and z_3 is bounded by ρ . This is the same as bounding the norm of the transfer function between w_2 and z_3' by 1. The state matrices for this case are:

$$A_{c1} = \begin{bmatrix} A - BK_C & BN \\ 0 & F \end{bmatrix}; B_2 = \begin{bmatrix} \tilde{D} \\ T\tilde{D} \end{bmatrix}; C_2 = [\rho\tilde{E} \quad 0] \quad (3.12)$$

Note that A_{c1} is the same as for the disturbance rejection case. If (A, \tilde{E}) is detectable and F is stable, then (A_{c1}, C_2) is detectable. By Theorem D, $\|L_{22}\|_\infty \leq 1$, and, hence, the system is stable for all $\Delta_2 = \Delta$, bounded as in (3.8), if there exists a $P \geq 0$ such that:

$$R_2(P) = PA_{c1} + A_{c1}^T P + PB_2 B_2^T P + C_2^T C_2 \leq 0, \quad (3.13)$$

3. Stabilization with Respect to ΔB .

The last goal to consider individually is stabilization with respect to ΔB . It is desired to bound the norm of the transfer function between w_3 and z_4' . For this, the state matrices are:

$$A_{c1} = \begin{bmatrix} A - BK_C & BN \\ 0 & F \end{bmatrix}; B_3 = \begin{bmatrix} \tilde{D} \\ T\tilde{D} \end{bmatrix}; C_3 = [\rho^{-1}\tilde{F}K_C \quad \rho^{-1}\tilde{F}N] \quad (3.14)$$

The Riccati inequality corresponding to this transfer function is:

$$R_3(P) = PA_{c1} + A_{c1}^T P + PB_3 B_3^T P + C_3^T C_3 \leq 0, \quad (3.15)$$

4. Disturbance Rejection and Stabilization with ΔA and ΔB .

This subsection addresses the design of an observer so that the closed-loop system is stable and the transfer function between w_1 and

$[z_1^T \ z_2^T]^T$ is bounded by δ for all allowable perturbations of the plant state matrix A and input matrix B . Theorem I is applied to the Riccati inequalities set up in subsections 1, 2 and 3. Combining (3.11), (3.13) and (3.15) gives:

$$R(P) = PA_{c1} + A_{c1}^T P + P(d_1 B_1 B_1^T + d_2 B_2 B_2^T + d_3 B_3 B_3^T)P + d_1^{-1} C_1^T C_1 + d_2^{-1} C_2^T C_2 + d_3^{-1} C_3^T C_3 \leq 0, \quad (3.16)$$

It is known already that (A_{c1}, C_1) is a detectable pair, so that if there exists a $P \geq 0$ and a set of observer and state feedback gains which satisfy (3.16), then the above goals are attained simultaneously. A design equation and an inequality to be tested can be derived from (3.16) by first assuming that $P = \text{diag}(P_1, P_2)$ as before and making use of a matrix inequality from [4] three times. Setting

$$K_c = [d_1^{-1} H_2^T H_2 + (d_3 \rho^2)^{-1} \tilde{F}^T \tilde{F}]^{-1} B^T P_1 \quad (3.17)$$

yields:

$$R(P) \leq \begin{bmatrix} U_{11} & U_{12} \\ U_{21} & U_{22} \end{bmatrix} \quad (3.18)$$

where,

$$U_{11} = P_1 A + A^T P_1 + d_1^{-1} H_1^T H_1 + d_2^{-1} \rho^2 \tilde{E}^T \tilde{E} + P_1 (d_1 (1 + \alpha) \delta^{-2} G_1 G_1^T + d_2 (1 + \beta) \tilde{D} \tilde{D}^T + d_3 (1 + \gamma) \tilde{D} \tilde{D}^T - B [d_1^{-1} H_2^T H_2 + (d_3 \rho^2)^{-1} \tilde{F}^T \tilde{F}]^{-1} B^T) P_1 \quad (3.19)$$

$$U_{22} = P_2 F + F^T P_2 + d_1^{-1} N^T H_2^T H_2 N + (d_3 \rho^2)^{-1} N^T \tilde{F}^T \tilde{F} N + P_2 T [d_1 (1 + \alpha^{-1}) \delta^{-2} G_1 G_1^T + d_2 (1 + \beta^{-1}) \tilde{D} \tilde{D}^T + d_3 (1 + \gamma^{-1}) \tilde{D} \tilde{D}^T] T^T P_2 \quad (3.20)$$

for any $\alpha, \beta, \gamma > 0$. Also, $U_{12} = U_{21}^T = 0$.

The goal is to find $P_1, P_2 \geq 0$ such that $U_{11}, U_{22} \leq 0$. A design equation can be obtained from (3.19) since the 0 matrix is negative semi-definite. So $\alpha, \beta, \gamma, d_1, d_2, d_3 > 0$ are adjusted until there is a $P_1 \geq 0$ which solves:

$$\begin{aligned} P_1 A + A^T P_1 + d_1^{-1} H_1^T H_1 + d_2^{-1} \rho^2 \tilde{E}^T \tilde{E} \\ + P_1 (d_1 (1 + \alpha) \delta^{-2} G_1 G_1^T + d_2 (1 + \beta) \tilde{D} \tilde{D}^T + d_3 (1 + \gamma) \tilde{D} \tilde{D}^T \\ - B [d_1^{-1} H_2^T H_2 + (d_3 \rho^2)^{-1} \tilde{F}^T \tilde{F}]^{-1} B^T) P_1 = 0 \end{aligned} \quad (3.21)$$

Then, K_c is determined by (3.17). The remaining observer gains are not obtained via a Riccati equation, but are a product of some other design method. Whatever method is used, the gains must be such that with the same $\alpha, \beta, c, d_1, d_2$, and d_3 as in (3.21) there is a $P_2 \geq 0$ which gives $U_{22} \leq 0$. These scalar parameters may have to be adjusted and (3.21) re-solved for a new P_1 if at first there are no practicable observer gains which result in a $P_2 \geq 0$. Methods for systematically doing this, as well as methods for observer design, are the subject of future work.

IV. Conclusions

This paper has demonstrated how to quickly derive Riccati design equations for problems with multiple design goals. The process involves writing a simple Riccati inequality for each of the subgoals, then combining the terms from each into an inequality incorporating all of the goals. The existence of a solution to this more complex inequality guarantees that all of the multiple design goals can be met at the same time. This method is based on theorems which are fundamental to μ -synthesis, so the results can be used to start the D-K iteration process in μ -synthesis. Lastly, unlike other methods that deal with real

structured uncertainty and robust performance, this method is not restricted to a specific observer. Any observer could have been used.

V. Bibliography

- [1] I. R. Petersen, "A Riccati equation approach to the design of stabilizing controllers and observers for a class of uncertain linear systems," *IEEE Transactions on Automatic Control*, vol. AC-30, no. 9, pp. 904-907, Sept. 1985.
- [2] H.-H. Yeh, S. S. Banda, A. C. Bartlett and S. A. Heise, "Robust design of multivariable feedback systems with real parameter uncertainty and unmodelled dynamics," *1989 American Control Conference*, Pittsburgh, PA, pp. 662-670, June 1989.
- [3] R. J. Veillette, J. V. Medanic and W. R. Perkins, "Robust stabilization and disturbance rejection for systems with structured uncertainty," *Proceedings of the 28th Conference on Decision and Control*, Tampa, FL, pp. 936-941, Dec. 1989.
- [4] F. Jabbari and W. E. Schmitendorf, "Effects of using observers on stabilization of uncertain systems," *1991 American Control Conference*, Boston, MA, pp. 3131-3136, June 1991.
- [5] D. S. Bernstein and W. M. Haddad, "LQG control with an H_∞ performance bound: a Riccati equation approach," *IEEE Transactions on Automatic Control*, vol. AC-34, no. 3, pp. 293-305, Mar. 1989.
- [6] J. C. Doyle, K. Glover, P. P. Khargonekar and B. A. Francis, "State-space solutions to standard H_2 and H_∞ Control Problems," *IEEE Transactions on Automatic Control*, vol. AC-34, no. 8, pp. 831-847, Aug. 1989.

- [7] J. C. Willems, "Least squares stationary optimal control and the algebraic Riccati equation," *IEEE Transactions on Automatic Control*, vol. AC-16, no. 6, pp. 621-634, Dec. 1971.
- [8] J. C. Doyle, "Structured uncertainty in control system design," *Proceedings of the 24th Conference on Decision and Control*, Ft. Lauderdale, FL, pp. 260-265, Dec. 1985.
- [9] P. P. Khargonekar, I. R. Petersen and K. Zhou, "Robust stabilization of uncertain linear systems: quadratic stabilizability and H_∞ control theory," *IEEE Transactions on Automatic Control*, vol. AC-35, no. 5, pp. 356-361, Mar. 1990.
- [10] J. O'Reilly, *Observers for Linear Systems*. London: Academic Press, 1983.
- [11] H. H. Yeh, J. L. Rawson and S. S. Banda, "Robust Control of Uncertain Systems," submitted for possible publication in *1991 American Control Conference*, Chicago, IL, June 1992.

EXPERIMENTAL INVESTIGATION OF THE INFLUENCE OF CONSTRAINED-LAYER DAMPING TREATMENT ON PARAMETRIC AND AUTOPARAMETRIC RESONANCES IN NONLINEAR STRUCTURAL SYSTEMS

Lawrence D. Zavodney
Assistant Professor

Joseph A. Schudt
Graduate Research Assistant

Department of Engineering Mechanics
The Ohio State University
209 Boyd Laboratory
155 West Woodruff Ave
Columbus, Ohio 43210

1 2 ABSTRACT

The influence of viscoelastic constrained-layer damping treatment on parametric resonances of single-degree-of-freedom (SDOF) systems and autoparametric resonances of multiple-degree-of-freedom (MDOF) nonlinear systems possessing internal resonance was investigated. The results show that commercially available aluminium-backed treatment is effective in suppressing parametric resonances of a particular mode; it essentially adds linear viscous damping to the system and moves the regions of parametric resonance away from the frequency axis. In the MDOF systems the damping affects the nonlinear coupling between modes and can suppress the modulation between modes. In general, its effect is to reduce the regions of nonlinear modal interaction and, in some cases, actually suppress it entirely with a sufficient amount of damping treatment. Experimental results include slow swept-sine excitations at constant amplitude and slow swept-amplitude excitations at constant frequency. Particular attention was paid to the nonlinear resonances and the modal interaction regions bounded by the Hopf bifurcation.

2.0 INTRODUCTION

Parametric resonances are not uncommon in structural vibrations. Zavodney¹ and Zavodney, et al²⁻⁴ have provided a summary of parametric resonance in SDOF nonlinear structural systems. Damping is a common method of controlling or reducing vibration for externally excited resonances. However, damping plays quite a different role in parametrically excited systems. When systems exhibit nonlinear behavior, the analysis is more complicated; the nonlinearity affects the system response along with the damping, so it is not always obvious what part the damping plays in the response. Zavodney and Shihada⁵ investigated the influence of the linear viscous damping coefficient on the fundamental and principal parametric resonances of SDOF systems possessing quadratic and cubic nonlinearities. The results showed that linear viscous damping plays a significantly different role; if reduction in amplitude at resonance is the objective, then in some cases certain critical levels of damping must be exceeded--otherwise one can increase the damping coefficient by an order of magnitude but realize less than 5% reduction in the response amplitude.

When the structure possesses more than one mode, as is usually the case, there is the possibility of nonlinear modal coupling. When modes are coupled, it is possible to exchange energy from a directly excited mode to another mode. The end result is that more than one mode is participating in the response and, hence, the structure is vibrating at other frequencies in addition to the frequency of the excited mode--which is not always the same as the excitation frequency. As a result the analysis becomes even more complicated. Attempting to find appropriate mathematical models for these behaviors is extremely difficult. One particular mathematical model may describe one type of behavior, but when the excitation frequency is changed by only 0.1 Hz, the behavior is something else--qualitatively and quantitatively--i.e., a bifurcation has occurred. The

nonlinear coupling responsible for this behavior is further enhanced if the structure possesses an internal resonance; an internal resonance occurs whenever any natural frequencies are commensurate (i.e., in a 2:1, 3:1, 3:2, etc. ratio). When a structure simultaneously possesses an internal resonance and appropriate nonlinear coupling terms, it is possible for one mode to parametrically excite another mode; this phenomenon is called an autoparametric resonance. When this happens, the nonlinear effects are greatly intensified and completely dominate the response. Nayfeh and Zavodney⁶ and Balachandran and Nayfeh⁷ provided a theoretical model and experimental results showing that such behavior can lead to long-time responses that are not steady-state; mathematically a Hopf bifurcation has occurred.

The objective of this project was to conduct experiments on nonlinear SDOF and MDOF flexible structures using the experimental facilities at Wright Laboratory to study the effects of damping on parametric and autoparametric resonance. The experiments were performed on structures fabricated from uniform prismatic beams and lumped masses. These types of structures were easy to prepare and tune--i.e., by adjusting the position of the masses the resonant frequencies could be changed. This was essential for the MDOF structure when an internal resonance was desired.

3.0 SINGLE-DEGREE-OF-FREEDOM STRUCTURE

Experiments were performed on a flexible beam carrying a lumped mass; this structure is shown in Figure 1. The excitation was a base displacement (along the axis in the vertical direction) at a frequency twice that of the first flexural mode of the cantilever beam. The resonant response that ensues is called a principal parametric resonance. The experiments consisted of frequency sweeps at constant-amplitude acceleration and amplitude sweeps at constant frequency. The amplitude was held constant by a computer-controlled feedback loop; as the

frequency was changed, the corresponding excitation amplitude required adjustment to keep the acceleration level constant. The excitation level was chosen as large as possible without causing excessive amplitudes of displacement; it turned out that a level of 0.350 g's was selected. The response was measured by strain gages mounted at the base of the lower beam.

The frequency response of the structure before application of the damping treatment for two levels of excitation is shown in Figure 2. It shows that the system is softening because it bends to the left. Zavodney¹ and Zavodney and Nayfeh⁸ performed experiments on similar structures and found responses that exhibited hardening behavior. It turns out that the relative length (i.e., flexibility) of the beam determines, in part, whether the system is hardening or softening. These experiments were conducted by increasing the frequency of excitation very slowly while simultaneously keeping the table acceleration constant. The arrows indicate jumps; for example, when the excitation level is 0.350 g's (denoted by the circles), the response jumps up to the large amplitude and then slowly decreases as the frequency is increased. When the frequency is decreased, the response follows the same curve but extends it somewhat. The response eventually jumps down to the trivial response. The response for the 0.250-g excitation level is qualitatively the same but at a lower amplitude. Additional experiments were performed with one strip and two strips of viscoelastic damping treatment as shown in Figures 3 and 4, respectively. For the lower excitation level, the parametric resonance was completely suppressed using only two strips of damping treatment. Two 0.10-inch strips of damping treatment cover only 5% of the surface area of the beam between the support and the lumped mass. In summary, increased application of the damping treatment reduces the amplitude of the resonant response, and reduces the region of parametric instability.

The regions of parametric resonance in the excitation-amplitude versus the excitation-frequency plane were also determined. These experiments were

performed by repeating the frequency response experiments for different levels of excitation and plotting only the bifurcation points where either the trivial response becomes unstable (during both a sweep up and a sweep down) or a nontrivial response jumps to the trivial response. An example is shown in Figure 5. This figure shows three boundaries; the inner-most region (bounded by the two curves on the right) represents the loss of trivial stability for the linear system; the additional curve on the far left represents the extension of the instability region caused by the overhang due to the softening nonlinearity in the system. Because nontrivial responses exist at excitation frequencies below those predicted by linear theory, the system is said to possess a subcritical instability. This overhang is reduced for increased damping levels as shown in Figures 6 and 7.

A summary of the bifurcation boundaries showing only the region where nontrivial responses exist is shown in Figure 8. As the equivalent linear viscous damping coefficient increases, the instability regions move away from the frequency axis. From this figure one can see that the only way to completely suppress a parametric resonance is to shift the instability region far enough away from the axis so that it is completely removed from the area of interest.

4.0 MULTIPLE-DEGREE-OF-FREEDOM STRUCTURE

Experiments were performed on a multiple-degree-of-freedom (MDOF) structure. The objective was to study the effect of viscoelastic damping treatment on the autoparametric resonance (modal interaction) caused by the simultaneous occurrence of appropriate nonlinear coupling terms with an internal resonance. The structure used for these experiments is shown in Figure 9; it has been studied by several researchers^{7,9,10}. It was chosen because it was easy to fabricate and could be easily tuned (to create an internal resonance) by adjusting the lengths of the beams and position of m_2 . The procedure for applying damping treatment to the SDOF structure was used for the MDOF structure: thin strips of 0.10-inch

width damping treatment were applied in increasing numbers to each beam, effectively increasing the damping of the structure.

The responses of this structure--both to impulse and harmonic excitation--are very complicated. The primary source of the quadratic modal-coupling nonlinearity in this structure is the asymmetrical geometry. When an internal resonance exists, this nonlinear coupling is significantly intensified and can dominate the response; when this happens the response amplitudes can be three or four times larger than the linear response. This happens whenever one mode is (directly or parametrically) excited; the response initially consists of the excited mode--which is the linear response. Because of the internal resonance (in this case it appears as a 2:1 frequency ratio between the first and second mode), whenever the second mode is excited, it acts as a parametric excitation to the first mode. As a result, when appropriate conditions exist, the first mode will also be excited. Because it is a parametric excitation, the response requires many cycles to achieve a steady state.

The purpose of applying the damping treatment was to eliminate (or at least attenuate) the large amplitude responses that are caused by nonlinear modal coupling (e.g., saturation and modulation). Hence, to ascertain these effects, both frequency sweeps at constant amplitude and amplitude sweeps at constant frequency were performed for three levels of damping treatment. The labels correspond to the following amounts of damping treatment: the unmarked (or back plane) for none, "I" for two strips on each beam (17% of the surface area), "II" for six strips on each beam (50%), and "III" for 100% coverage.

The experiments were performed at very high levels of excitation. Previous studies^{6,7,9,10} have shown that under some conditions, nonlinear responses can be achieved with very small levels of excitation (on the order of 20 mili-g's). In the experiments performed here, the excitation levels were on the order of 100 mili-g's--five times that required to solicit a nonlinear response consisting of coupled

modes. This large excitation level was used to extend the range for which damping treatment could be applied; in other words, more damping treatment could be applied before the nonlinear motion was expected to be suppressed.

The structure shown in Figure 9 was tuned such that the first resonance occurred at 4.012 Hz and the second resonance occurred at 8.040 Hz; this corresponds to an internal resonance detuning of +0.016 Hz, or +0.20% (of the second resonant frequency). This was as close as feasibly possible to perfect tuning on a real structure; a tuning closer to 0% could be accomplished at the expense of more painstaking effort (i.e., moving the lower beam into the clamped support in 0.001-inch increments and repeating the experiments until the desired detuning is achieved). After each application of damping treatment, the model was retuned to get as close as possible to 0.0%. Experiments for a slightly detuned structure were also performed; the detuning was accomplished by increasing the mass of m_2 (by adding a small screw). In this case, the resonances occurred at 3.750 Hz and 7.750 Hz, which corresponds to a detuning of +0.25 Hz, or +3.2%. The results of these experiments are qualitatively the same, but the increased internal-resonance detuning causes skewing of the frequency-response curves and increases the region where modulated responses occur. Due to the length restrictions of this report, these results are not discussed here.

The undamped structure had the largest response levels. The frequency responses for the structure without and with three amounts of damping treatment are presented in one figure; this 3-D perspective viewing aids in seeing the qualitative and quantitative changes caused by the increased damping. When the first mode is directly excited with a high-level excitation, the response is nonlinear, as shown in Figure 10. Figure 10(a) shows the first mode response and Figure 10(b) shows the second mode response. The frequency axis is shown normalized with respect to the excitation frequency (because the addition of the

damping treatment caused the frequencies to shift slightly) and the response amplitude (displacement of m_1) is represented in units corresponding to the ratio of the lower mass displacement amplitude to the length of the lower beam. This scaling provides a convenient comparison of the results of all of the experiments. For example, the peak amplitude of the response of the first mode is approximately 8% of the length of the lower beam.

The response of the untreated structure shows the most interesting behavior. As the frequency of excitation is increased from 0.90, the amplitude initially grows until the second mode is excited; this happens at a frequency near 0.98. As the frequency is increased further, the amplitude of the first mode decreases dramatically--almost four times! When a Hopf bifurcation occurs near a frequency of 1.0 no steady-state responses are possible. This region is denoted by dots which represents an "average" amplitude. Actual variations are shown later in the amplitude response curves shown in Figure 12. As the frequency is further increased, the amplitude of response increases until it jumps down (at the first mode frequency of 1.072) to the linear response; the linear response consists only of the directly excited mode--no other modes are present. If the frequency is decreased from above, the jump up occurs at a lower frequency (i.e., 1.044) than did the jump down during a sweep up. This indicates an overhang or double-valued steady-state response. Theory shows that these two solution branches are connected by an unstable solution branch; this is shown by the dashed line on the response (note--there are no data points for this dashed line because they cannot be realized in the laboratory). Further decreases in the excitation frequency cause the response to follow the same path as that followed during the sweep up. The frequency response shown in this curve is almost symmetrical; because it is slightly skewed to the right, it indicates slight positive detuning of the internal resonance.

In summary, the frequency response curve shows four distinct types of motions that are possible when the excitation frequency is near the first mode: (1) the linear solution where only the directly excited mode participates in the response, (2) a region where nonlinear coupling is present and causes two steady-state solutions to exist--the linear one and a nonlinear one, (3) a nonlinear response where the modes achieve steady-state amplitudes, and (4) a region where no steady-state solutions exist.

As damping treatment is applied to the structure, response amplitudes are attenuated. However, certain trends can be observed in Figure 10. The first application of damping treatment consisted of two strips on each beam (17%). Both response peaks are broadened (indicating increased damping); the peak at the lower frequency is almost eliminated while the response peak at the upper frequency is reduced in amplitude sufficiently to eliminate the hysteresis. The second application of damping treatment (six strips, 50%) causes further peak smoothing. The third application (100%) almost completely eliminates the modal coupling. In summary, the damping treatment can attenuate the modal responses, and it appears that a sufficient quantity could eliminate the nonlinear coupling altogether.

A direct excitation to the second mode is shown in Figure 11. Similar observations can be made from these curves shown in a 3-D perspective plot. The three curves correspond to the same amounts of damping treatment used for the direct excitation to the first mode shown in Figure 10. In Figure 11 the frequency axes correspond to a nondimensionalization with respect to the excitation frequency; hence the second mode has a resonance at 1.0 and the first mode, representing a frequency of one-half that of the excitation, has a resonance at 2.0. The indirectly excited mode (i.e., the first mode) remains trivial until it is strongly (and nonlinearly) coupled to the second mode; when it is, the amplitude of the second mode is drastically attenuated. Furthermore, during a sweep down,

there is no jump up in the second mode response--only a jump down--because the lower branch merges with the upper branch; it is not a turning point bifurcation as was the case for a direct excitation to the first mode as seen in Figure 10. The first mode demonstrates both a jump up and a jump down during a frequency sweep. For the third application of damping treatment, the nonlinear coupling between the modes is completely suppressed.

Experiments were also conducted to measure the amplitude response at selected frequencies of excitation; these curves are cuts across a particular frequency response curve shown in Figure 10. For the case of no damping treatment, a cut at a frequency of 1.004 passes through the modulation region. The amplitude response at this frequency is shown in Figure 12. As the amplitude of excitation is increased, the system experiences a Hopf bifurcation and begins to modulate; i.e., energy begins to flow back and forth between the two modes. As the amplitude of excitation is increased, the mean tends to increase and the maximum excursions increase.

At a frequency of 1.067 the frequency response curve (for no damping treatment) in Figure 10(a) shows a double value. An amplitude sweep through this region, as shown in Figure 13, reveals a jump phenomenon. When starting on the lower branch, increasing the amplitude of excitation causes a jump up to the upper branch; decreasing the amplitude of excitation causes a jump down at a lower value of the amplitude of excitation.

When the maximum damping treatment was applied, there was essentially one qualitative response; Figure 14 shows an amplitude sweep through the resonance at a frequency of 0.979. Although the curves are quite tame, they show nonlinear coupling because the second mode is excited. Even though the excitation is driving the first mode, some of the energy is channeled into the second mode.

Amplitude excitation experiments were also performed for a direct excitation to the second mode. Figure 15 shows a cut across the 0.998 frequency line (the 1.999 frequency line for the first mode) in Figure 11(b) for the structure with no damping treatment applied. Although the second mode is directly excited, its response is attenuated; instead the energy goes into the first mode which responds like a parametrically excited SDOF system. An amplitude sweep at the 1.057 frequency line (2.119 for the first mode) in the region of the overhang is shown in Figure 16. During the experiment, the amplitude of the excitation was increased slowly. At 0.32 g's rms, the linear solution becomes unstable. However, the divergence is so slow that it is possible to stay on the unstable solution long enough to locate the equilibrium points. These are shown in the figure as circles without a solid line connecting them. However, by waiting long enough, the response goes to the steady-state nonlinear solution which is shown with the solid line. During a sweep down, the response follows the upper curve rather than the lower curve. At an excitation level of 0.075 g's rms, the response jumps down to the linear response on the lower branch and remains there. Note that the overhang region in Figure 11 is qualitatively different than the overhang region in Figure 10; hence, it is not surprising to see a qualitative difference in the double solution region of Figures 13 and 16.

When damping treatment was applied to the structure, the regions of multiple solutions contracted and eventually disappeared. For small levels of excitation the linear solution appears, as shown in Figure 17. At this frequency of excitation (0.992 for the first mode, 1.991 for the second mode), when the excitation level exceeds 0.09 g's, the second mode saturates. The energy that is put into the system at the second-mode natural frequency is passed into the first mode; essentially the second mode is parametrically exciting the first mode. Hence, the first mode response appears to have a parametric type response.

5.0 SUMMARY

A series of experiments were performed to study the effect of commercially available viscoelastic damping treatment on parametric and autoparametric resonances in nonlinear systems. Both SDOF and MDOF structures were used; they consisted of flexible beams and masses. For the SDOF structure, experiments were conducted at several levels of excitation and it was found that the damping treatment was particularly effective in reducing and even suppressing the resonance entirely. For the 2DOF system, the particular case of an internally resonant structure was considered. The qualitative and quantitative effects of the damping treatment were determined for very large excitation levels; it was observed that the damping treatment first reduces the nonlinear modal coupling and modulation regions and then reduces the amplitude of response. For the case of direct excitation to the second mode, damping treatment was capable of eliminating the nonlinear coupling, even when the internal resonance detuning was on the order of 0.20%.

6.0 REFERENCES

1. Zavodney, L.D., "A Theoretical and Experimental Investigation of Parametrically Excited Nonlinear Mechanical Systems," Ph.D. Dissertation, Virginia Polytechnic Institute and State University, 1987.
2. Zavodney, L.D. and Nayfeh, A.H. "The Response of a Single-Degree-of-Freedom System with Quadratic and Cubic Nonlinearities to a Fundamental Parametric Resonance," *Journal of Sound and Vibration*, 1988, Vol 120, 63-93.
3. Zavodney, L.D., Nayfeh, A.H. and Sanchez, N.E., "The Response of a Single-Degree-of-Freedom System with Quadratic and Cubic Nonlinearities to a Principal Parametric Resonance," *Journal of Sound and Vibration*, 1989, Vol 129, 417-442.
4. Zavodney, L.D., Nayfeh, A.H. and Sanchez, N.E., "Bifurcations and Chaos in Parametrically Excited Single-Degree-of-Freedom Systems," *Nonlinear Dynamics*, 1990, Vol 1, 1-21.
5. Zavodney, L.D. and Shihada, S.M., "The Role of Damping in the Suppression of Parametric Resonances in Nonlinear Systems," *Proceedings of Damping '89*, West Palm Beach, Florida, February 8-10, 1989, FBD-1 - FBD-22.
6. Nayfeh, A.H. and Zavodney, L.D., "Experimental Observation of Amplitude- and Phase-Modulated Responses of Two Internally Coupled Oscillators to a Harmonic Excitation," *Journal of Applied Mechanics*, 1988, Vol 110, 706-710.
7. Balachandran, B. and Nayfeh, A.H., "Nonlinear Motions of Beam-Mass Structure," *Nonlinear Dynamics*, 1990, Vol 1, 39-62.
8. Zavodney, L.D. and Nayfeh, A.H., "The Non-Linear Response of a Slender Beam Carrying a Lumped Mass to a Principal Parametric Excitation: Theory and Experiment," *International Journal of Nonlinear Mechanics*, 1989, Vol 24, 105-125.
9. Zavodney, L.D. and Hollkamp, J.J., "Experimental Identification of Internally Resonant Nonlinear Structures Possessing Quadratic Nonlinearity," *Proceedings of the 32nd Structures, Structural Dynamics and Materials Conference*, Baltimore, Maryland, 8-10 April, 1991, 2755-2765.
10. Haddow, A.G., Barr, A.D.S., and Mook, D.T., "Theoretical and Experimental Study of Modal Interaction in a Two-Degree-of-Freedom Structure," *Journal of Sound and Vibration*, 1984, Vol 97, 451-473.

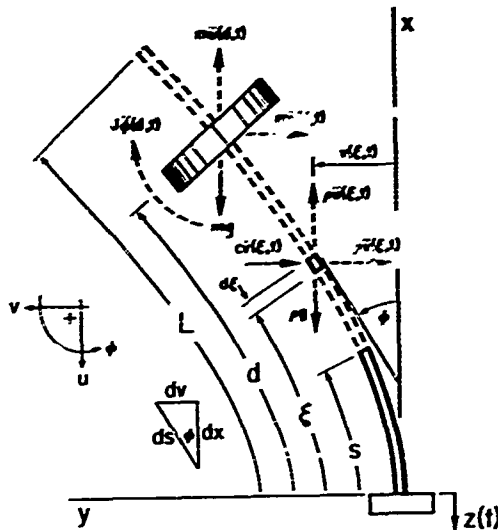


Figure 1. Structure consisting of a flexible beam carrying a lumped mass used for the SDOF experiments. Constrained-layer damping treatment was applied in thin 0.10-inch strips on both sides to incrementally increase the level of damping in the structure. The model was attached to a shaker head that was oscillating in the vertical direction.

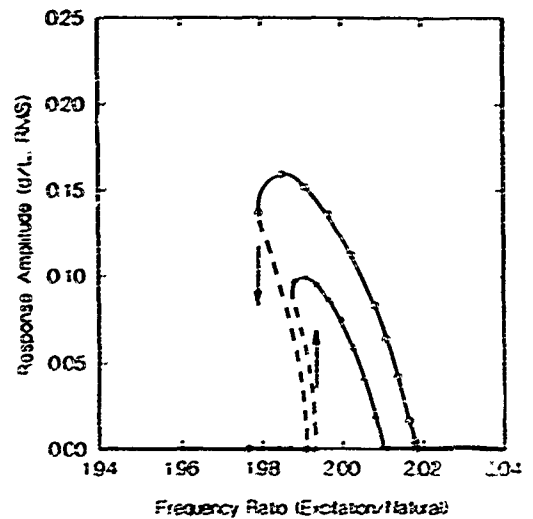


Figure 3. Frequency-Response at two levels of excitation for the SDOF structure with one strip of damping treatment applied.

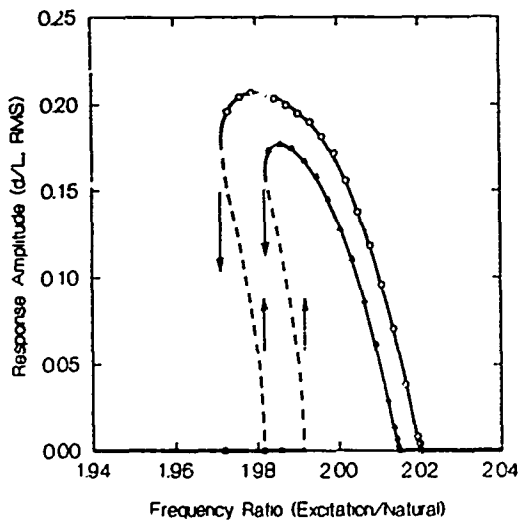


Figure 2. Frequency-Response for the SDOF structure before damping treatment was applied for two levels of excitation (0.25 and 0.35 g's rms). The bending of the curves to the left indicates that the system is softening. These curves were obtained by sweeping the frequency up and down through the region of principal parametric resonance at a rate slow enough such that a steady-state amplitude was maintained.

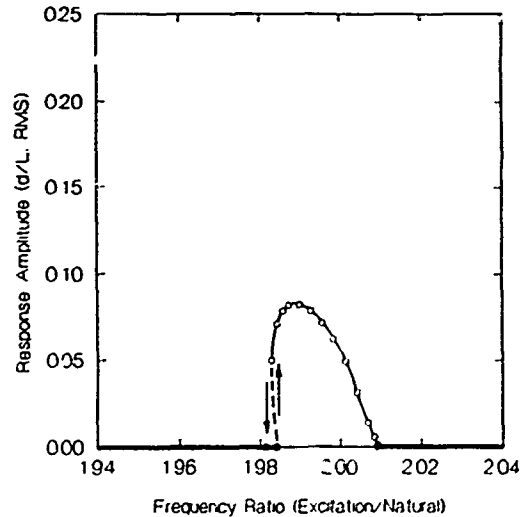


Figure 4. Frequency-Response at two levels of excitation for the SDOF structure with two strips of damping treatment applied. Note that the resonance for the smaller excitation level is completely suppressed.

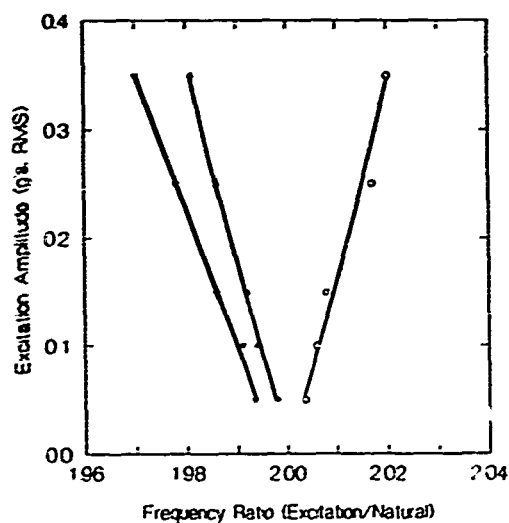


Figure 5. Bifurcation diagram showing the instability regions of the principal parametric resonance for the beam before the damping treatment was applied. The curve on the far left represents the bifurcation boundary caused by the overhang observed in Figure 2 which is caused by the softening behavior. It represents a subcritical instability.

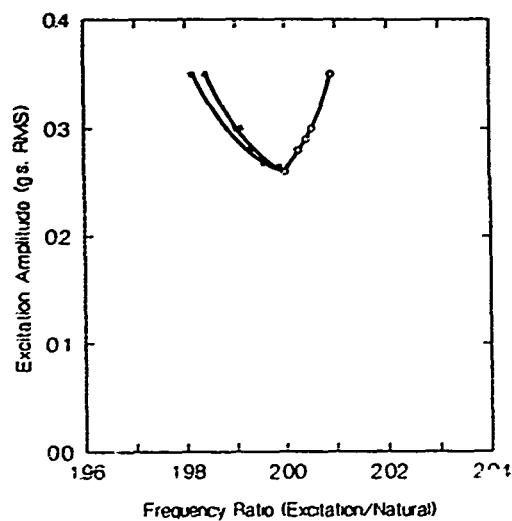


Figure 7. Bifurcation diagram showing the instability regions of the principal parametric resonance for the beam with two strips of damping treatment.

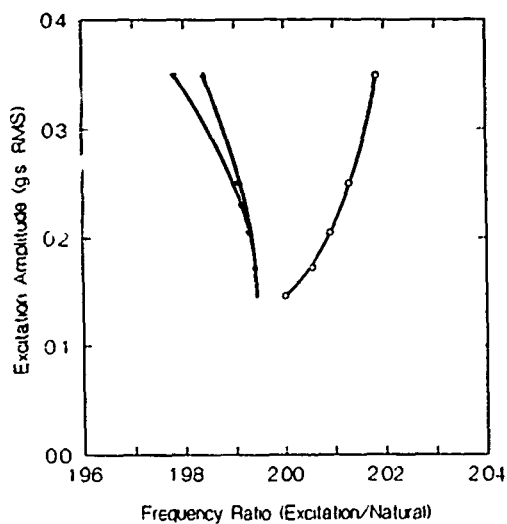


Figure 6. Bifurcation diagram showing the instability regions of the principal parametric resonance for the beam with one strip of damping treatment.

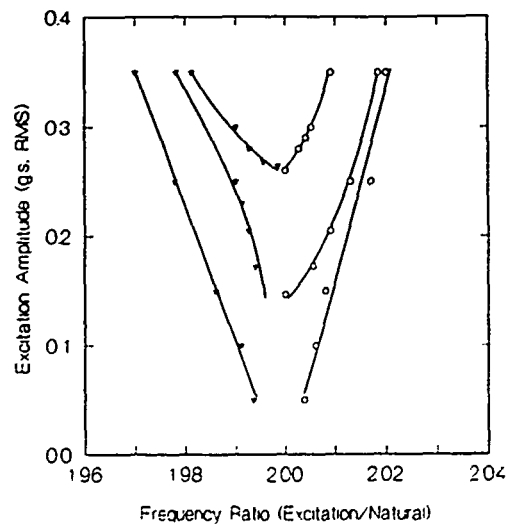


Figure 8. Bifurcation diagram summarizing the region where nontrivial responses exist for three levels of damping. Increased damping treatment causes the instability region to migrate away from the frequency axis and contract.

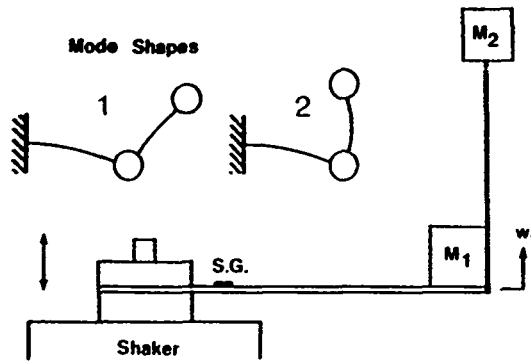


Figure 9. Structure used for the MDOF experiments. By adjusting the length of the lower beam and the position of the second mass, the first and second resonant frequencies could be adjusted. The higher modes and out-of-plane modes were not excited during the experiments; hence a 2DOF model can be used to adequately describe the observed behavior.

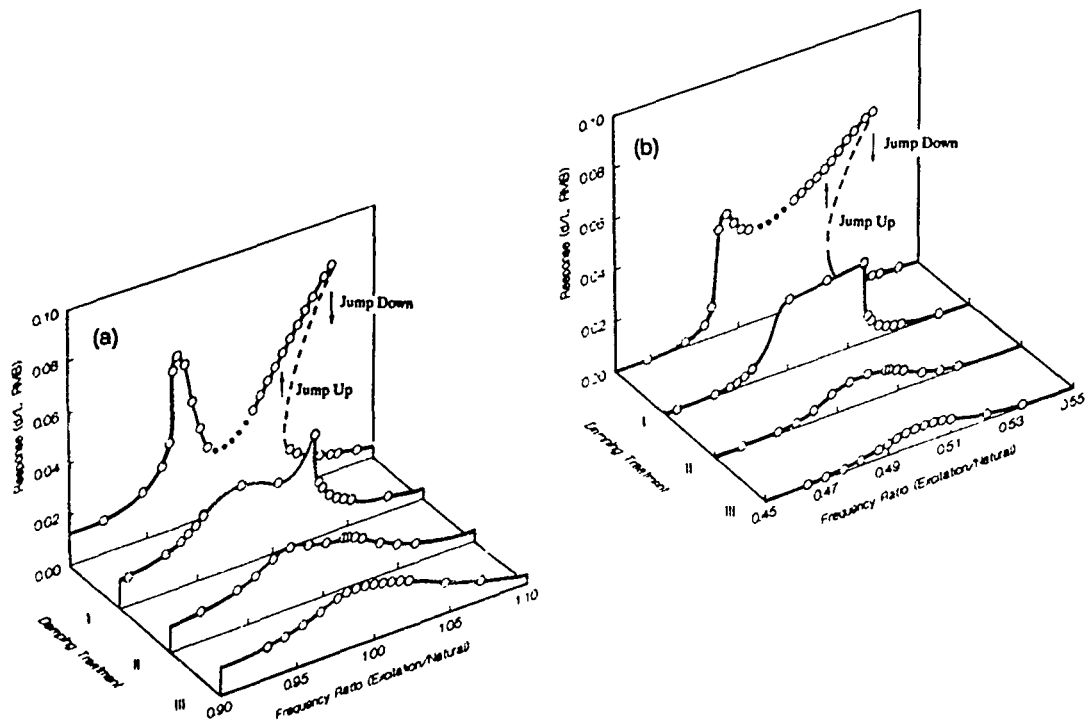


Figure 10. Frequency response of the 2DOF structure with +0.20% detuning (for no damping treatment) for a direct excitation to the first mode: (a) shows the first mode response and (b) shows the second mode response. Although attempts were made to have a perfect internal resonance, there is some small amount of detuning as evidenced from the unsymmetrical nature of the response curves.

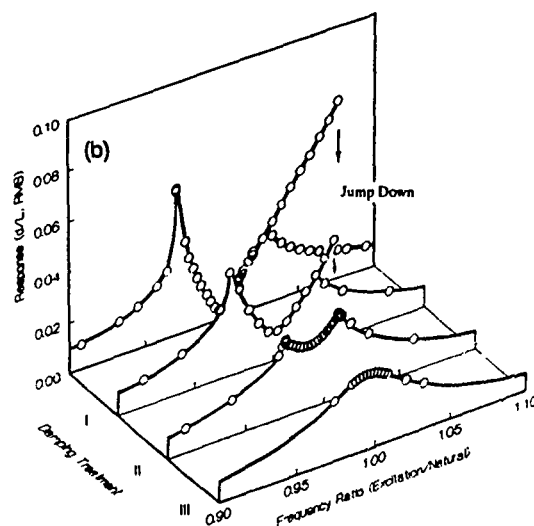
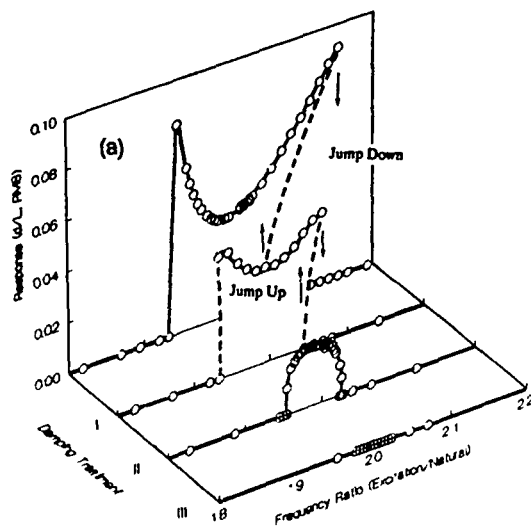


Figure 11. Frequency response of the 2DOF structure with +0.20% detuning (for no damping treatment) for a direct excitation to the second mode: (a) shows the first mode response and (b) shows the second mode response.

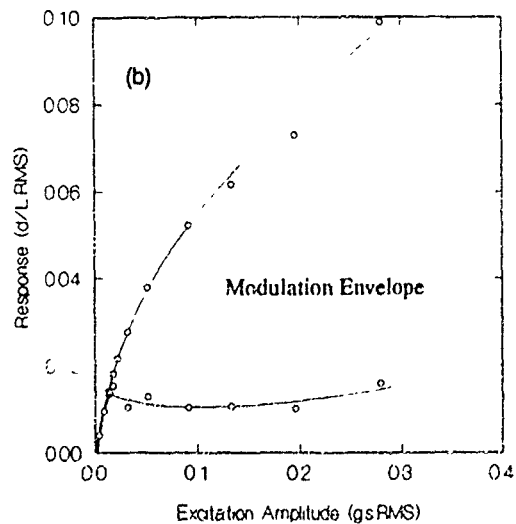
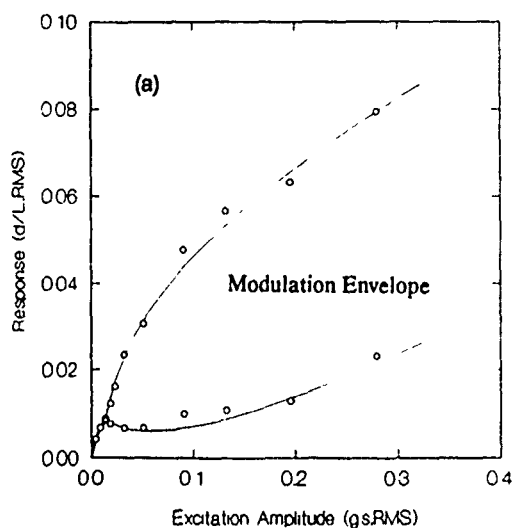


Figure 12. Amplitude response of the 2DOF structure with +0.20% detuning and no damping treatment for a direct excitation to the first mode at a frequency of 1.004. This frequency corresponds to the modulation region in Figure 10. The curves approximate the bounds on the modulation: (a) first mode amplitude, (b) second mode amplitude.

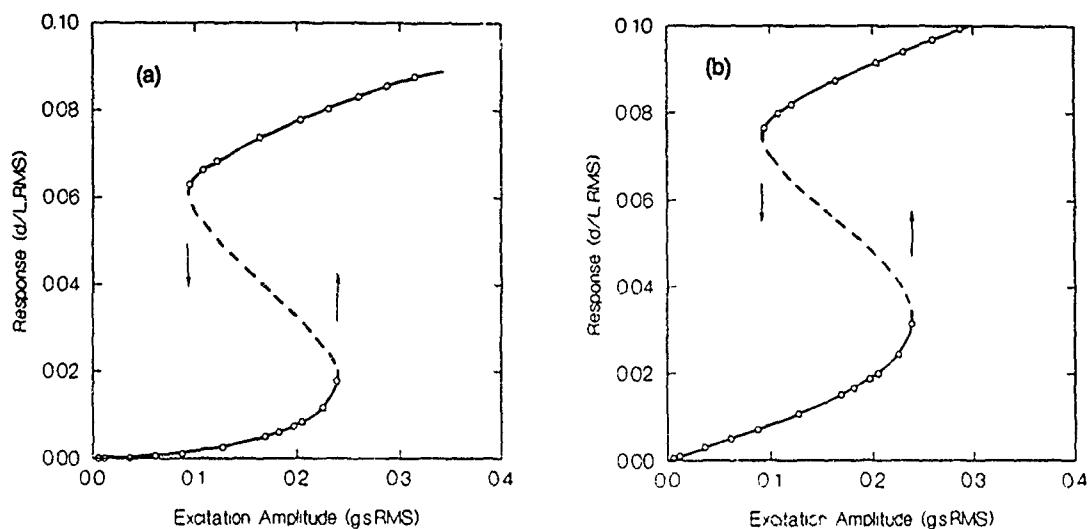


Figure 13. Amplitude response of the 2DOF structure with +0.20% detuning and no damping treatment for a direct excitation to the first mode at a frequency of 1.067. This frequency corresponds to the overhang region in Figure 10. The curves approximate the bounds on the modulation: (a) first mode, (b) second mode.

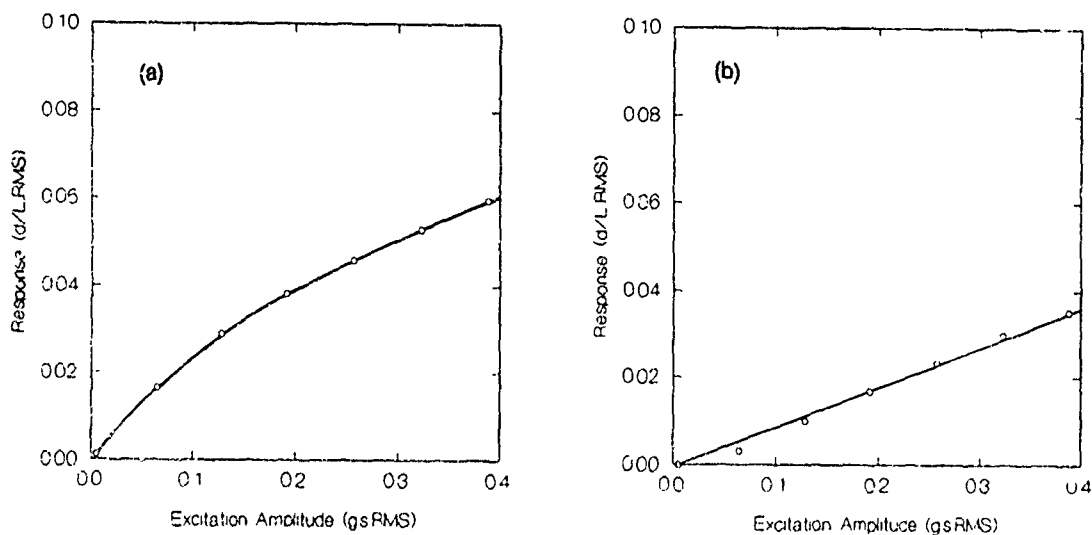


Figure 14. Amplitude response of the 2DOF structure with +0.29% detuning for the highly damped case for a direct excitation to the first mode at a frequency of 0.979. This frequency corresponds to the resonance region in Figure 10. The curves approximate the bounds on the modulation: (a) first mode, (b) second mode. These curves should be compared to Figure 12 to see the effect of the damping treatment--it completely suppresses the modulation and attenuates the amplitude of the response.

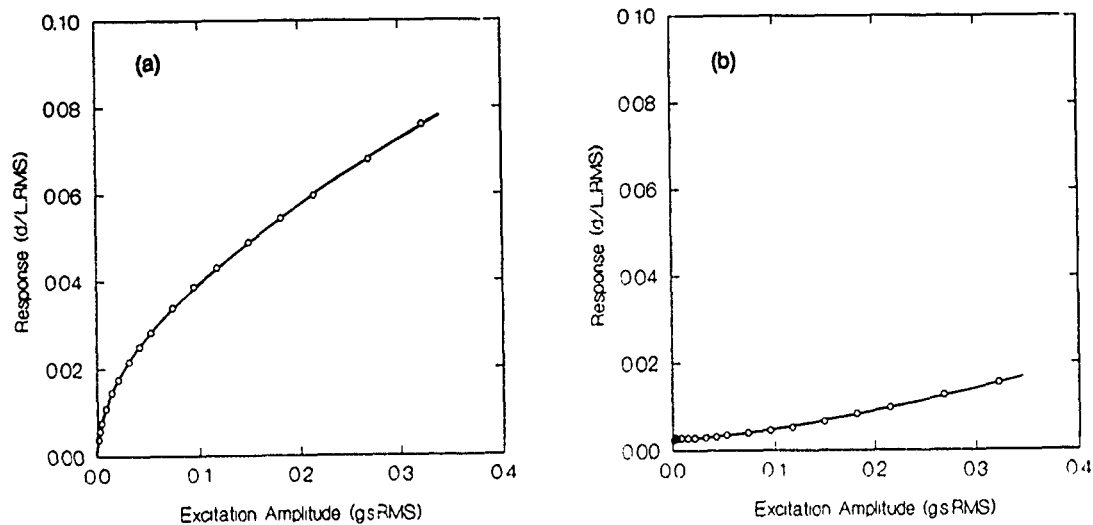


Figure 15. Amplitude response of the 2DOF structure with +0.20% internal resonance detuning for the case with no damping treatment for a direct excitation to the second mode at a frequency of 0.998. This frequency corresponds to the resonance region in Figure 11(b): (a) first mode, (b) second mode.

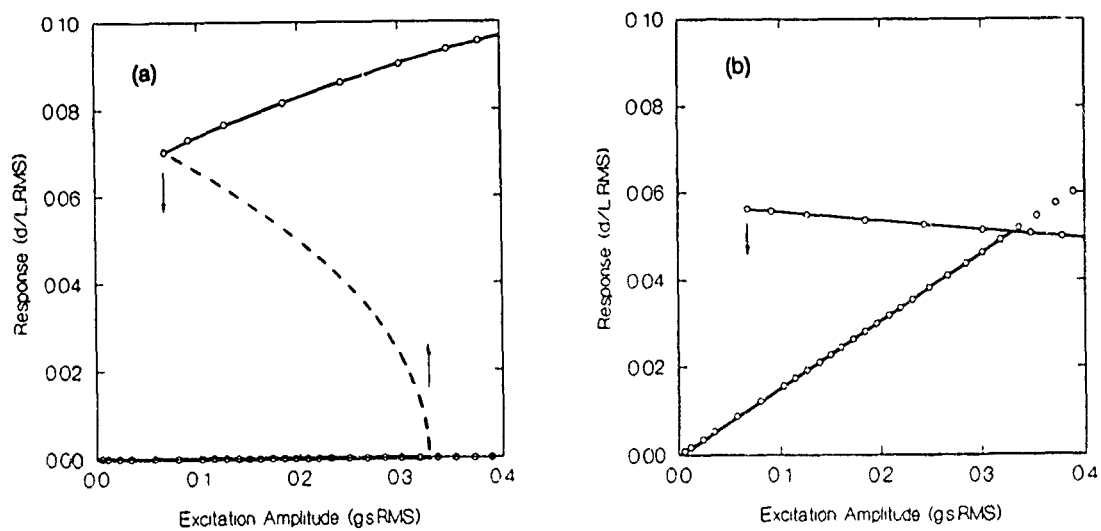


Figure 16. Amplitude response of the 2DOF structure with +0.20% internal resonance detuning for the case with no damping treatment for a direct excitation to the second mode at a frequency of 1.057. This frequency corresponds to the overhang region in Figure 11(b): (a) first mode, (b) second mode.

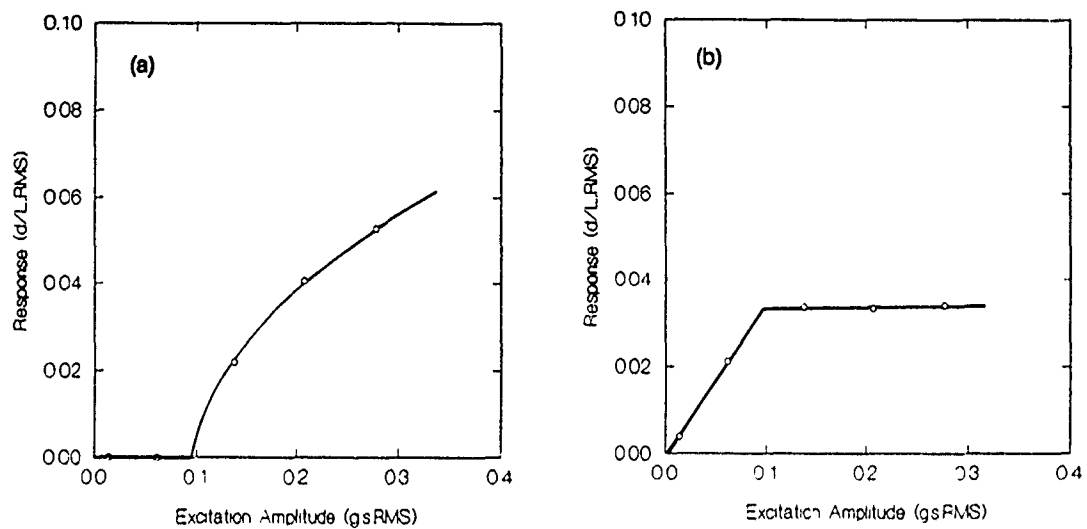


Figure 17. Amplitude response of the 2DOF structure with +0.29% internal resonance detuning for the highly damped case for a direct excitation to the second mode at a frequency of 0.992. This corresponds to the peak response in Figure 11: (a) first mode, (b) second mode.

SEMI-EMPIRICAL SELF-CONSISTENT CALCULATIONS OF GAAS SURFACE RESTRUCTURING

by
Dr. Shashikala Toke Das
Physics Department,
Kent State University, Trumbull campus, Warren, OH 44483
RDL Summer Faculty Research Program
ID#32, for Dr. Donald L. Dorsey
at WL/MLPO, Wright-Patterson AFB, OH 45433-6533
Summer 1991

ABSTRACT

A semi-empirical molecular orbital program (MOPAC) was used for determining the position and binding energy of arsenic atoms adsorbed on a gallium arsenide substrate. Total energy calculations are performed for different cluster sizes to determine the difference between the binding energies of an arsenic atom adsorbed on the $(\overline{111})$ surface of GaAs at the hexagonal-closed-pack (T4) and zincblende sites. It was found that the surface layer termination and the size of the cluster were very important in determining the binding energy accurately. The binding energies of As atoms at both sites were found to be of the same order of magnitude, supporting the recently proposed model for the $(\sqrt{19} \times \sqrt{19})$ reconstruction of the surface, which was based on scanning tunneling microscopy observations [1]. The present work also establishes that semi-empirical approaches of the kind adopted here are appropriate for such surface studies from consideration of both speed and accuracy.

I INTRODUCTION

For the past several years the surface structures of binary polar semiconductors such as GaAs have been of great interest due to the important role they play in the epitaxy of thin film heterostructure materials and devices. Because GaAs is a direct gap semiconductor and the mobility of the electrons is greater in GaAs than in Silicon, there is a prospect for much faster optoelectronic devices based on GaAs, provided that appropriate interfaces can be devised. Typically these structures are grown by molecular-beam epitaxy (MBE), metalorganic chemical vapor deposition (MOCVD) or some variant of these techniques. The resulting surfaces are studied by scanning tunneling microscopy (STM), low-energy electron diffraction (LEED), reflective high energy electron diffraction (RHEED) and X-ray diffraction. The Ga terminated (111) surface and As terminated ($\overline{1}\overline{1}\overline{1}$) surface have been previously studied by these techniques [1,2]. Depending on the growth conditions a rich variety of patterns, such as (2X2), (3X3) and ($\sqrt{19} \times \sqrt{19}$) surface reconstructions have been observed. Several models have been proposed based on ab initio theoretical calculations [3,4] to understand these patterns. On the ($\overline{1}\overline{1}\overline{1}$) surface, the As-rich (2x2) surface can be described by an arsenic trimer model. The surface composition of GaAs for this reconstruction allows for all As dangling bonds to be filled and all Ga dangling bonds to be empty. Energy is thus minimized and the surface is semiconducting [1]. The ($\sqrt{19} \times \sqrt{19}$) reconstruction, however, has an odd number of atoms per unit cell, and therefore cannot be fully compensated in this manner. The driving mechanism for formation of the ($\sqrt{19} \times \sqrt{19}$) reconstruction is still not fully understood.

Two groups have reported theoretical attempts to explain surface restructuring by total energy minimization calculations. The ab initio calculations of Kaxiras et al. [3,4] determine the total energy based on the pseudo-potential approximation coupled with the density functional theory. The (2X2) surface reconstruction observed under Ga-rich conditions on the (111) surface of GaAs has been successfully explained by this approach [3]. However, the models proposed for the (2x2) and ($\sqrt{19} \times \sqrt{19}$) reconstruction based on their calculations for the ($\overline{1}\overline{1}\overline{1}$) surface are not in agreement with the recent STM measurements of Biegelsen et al.[1]. These workers, using a similar calculation technique, found that an As-trimer model,

consistent with the STM results, had the lowest energy of all possible structure for the GaAs $(\bar{1}\bar{1}\bar{1})$ (2×2) reconstruction. The unit cell structure proposed for the $(\sqrt{19} \times \sqrt{19})$ reconstruction, however, was too large a system to be verified by their total energy minimization calculation.

The present work is aimed at understanding the $(\bar{1}\bar{1}\bar{1})$ surface restructuring from the variational approach (as opposed to the density functional approach) using a semi-empirical technique. We want, in particular, to find the difference in the binding energies between the two inequivalent positions of As atoms adsorbed on the $(\bar{1}\bar{1}\bar{1})$ surface in the $(\sqrt{19} \times \sqrt{19})$ reconstruction model proposed by Biegelsen et al.[1]. The arrangement of the atoms in the vicinity of an As atom in the T4 site [1] is shown in Fig.1. We refer to the other As atom position as a zincblende site, as it corresponds to the "correct" position relative to the bulk crystal structure. The primary difference between the two sites is the presence of a bulk Ga atom directly beneath the adsorbed arsenic atom, at a distance of three atomic layers for the T4 site and five atomic layers for the zincblende site. This is shown in Fig. 2. The large unit cell proposed for the $(\sqrt{19} \times \sqrt{19})$ surface reconstruction contains a hexagonal ring formed by six As atoms with three in the T4 site and three in the zincblende site as shown in Fig.3. Thus calculations of the relative binding energies of As atom at these positions is helpful in understanding the formation of the $(\sqrt{19} \times \sqrt{19})$ unit cell. The top view of the largest cluster of atoms considered here in these positions is shown in Fig. 4. The position of the adsorbed As atom is indicated as T4 and Z at the HCP (T4) site and the zincblende site, respectively.

The quantum mechanical nature of the many body problem makes it infeasible to handle a large cluster of atoms by ab initio methods due to computer memory and CPU time limitations. Semi-empirical methods, on the other hand, do not claim the theoretical completeness or validity of ab initio methods but are distinguished by adequate speed and versatility such that one can perform meaningful calculations on large clusters at a reasonable cost. We have used here the semi-empirical, self-consistent molecular orbital package MOPAC [5] for calculating the total energies with geometry optimization for GaAs clusters of different sizes to estimate the binding energy of the As atoms. The package has been successfully used in the past for various molecular and polymer calculations. To the best of my knowledge, the present work is the first time this method has been used for semiconductor studies. This

package is essentially a version of the MNDO/3 semi-empirical scheme of Dewar et al [6,7]. This scheme, essentially, solves the self-consistent field (SCF) equations appropriate for a given system where the one and two electron integral parameters for the valence atomic orbitals are determined from prototype systems on the basis of various experimentally measured properties such as ionization potential, electron affinity, heat of formation and dipole moments [8]. It is generally recognized that, in an indirect way, the semi-empirical methods such as MNDO/3 include a great deal of correlation which is absent in strictly ab initio SCF methods. For the problem at hand, which involves Ga and As atoms, the correlation plays a very important role. We therefore believe that the above semi-empirical approach is ideally suited for the present investigation.

We will first briefly discuss the method and then present the results of our calculations.

II METHODOLOGY

The main assumptions in the MNDO semi-empirical models are:

- (1) Only the valence electrons of atoms determine the electronic properties of materials. The core electrons are basically frozen around the atomic nucleus and follow it faithfully to new positions. The valence electrons on the other hand redistribute themselves to minimize their energy depending on the surrounding environment.
- (2) Only the s and p electrons of each atom of the cluster are considered. The d and f electrons are considered to be localized around the nucleus of the atom and are regarded as core.
- (3) The atomic orbitals used to construct the molecular orbitals are assumed to have zero differential overlap between different centers.

Based on the above assumptions, the SCF Molecular Orbital problem is solved as follows:

The molecular orbitals are expanded as a linear combination of atomic orbitals (LCAO).

$$\Psi_{\lambda}(r) = \sum_i C_{\lambda i} \phi_i(r),$$

where the atomic orbitals $\phi_i(r)$ are chosen to be of the Slater type (STO), centered on all the atoms of the molecule. The expansion

coefficients (C's) are obtained by solving the Roothan Hartree-Fock equations self-consistently[5].

$$|F - \epsilon_{\lambda} S|C_{\lambda} = 0,$$

where S is the overlap matrix (having non-zero off diagonal elements only on the same atoms) and F is the Fock matrix, given by:

$$F_{ij} = h_{ij} + \sum_k l(\langle ij|kl \rangle - 1/2 \langle killj \rangle) P_{kl},$$

h_{ij} is the one electron Hamiltonian matrix, P_{kl} is given by

$$P_{kl} = \sum_{\lambda} C_{\lambda k} C_{\lambda l}$$

and $\langle ij|kl \rangle$ are the two electron repulsive integrals.

The heat of formation of a cluster of atoms is defined to be the total energy required to form the cluster starting from the individual atoms and is given by

$$\Delta H_F = E_{\text{elect}} + E_{\text{nucl}} + \sum_A E_{\text{el}}(A) + \sum_A \Delta H_f(A)$$

Here the total electronic energy of the system is calculated from

$$E_{\text{elect}} = 1/2 \sum_{ij} P_{ij} (h_{ij} + F_{ij})$$

The repulsion energy of the ionic cores, E_{nucl} , is given by

$$E_{\text{nucl}} = \sum_{AB} E_n(A, B) = \sum_{AB} Z_A Z_B \langle AA|BB \rangle,$$

where Z_A and Z_B are the charges on the cores of atoms A and B and $\langle AA|BB \rangle$ is the repulsion integral approximated in terms of the internuclear separation and other adjustable parameters, $E_{\text{el}}(A)$ is the energy required to ionize the valence electrons of atom A, and the $\Delta H_f(A)$ is the heat of atomization for atom A.

The heat of formation is calculated self-consistently with the externally specified precision for a given geometry of atoms. The geometry optimization procedure is then used to find the positions of

atoms in the cluster and the energy of formation of the cluster. The binding energy of an atom is calculated by taking the difference between the heats of formation of the cluster of atoms including the atom at the optimized geometry and the reference energy, which is the heat of formation of the cluster of atoms without the atom. The atomic clusters used for the calculations are chosen to satisfy the crystal symmetry and the cluster size is increased to include the first, second and then the third nearest neighbors to see their effects on the binding energy of the As atom. The crystalline environment for small clusters of atoms is simulated by tying off the dangling bonds by "pseudo"- As or "pseudo"- Ga capped bonds in the lowest layer atoms. The semi-empirical parameters for the "pseudo"- As atoms are basically the hydrogen atom parameters, adjusted to exhibit the electronegativity of an As atom.

III RESULTS

The accuracy of the semi-empirical parametrization of the Hamiltonian matrix is tested by calculating the dipole moment of the GaAs molecule. For an interatomic distance of 2.82645 Å the dipole moment calculated by our method of 5.66 Debye compares very well with the value of 5.78 Debye obtained by Gayen et al. who used a strictly ab initio method [9]. The charge on the Ga atom in the diatomic GaAs molecule calculated by our method (-0.44e) is also of correct sign and magnitude (0.50e) when compared with their results showing the approximately correct electronegativity of the As atom by reproducing for the GaH molecule the same dipole moment as found for GaAs at its equilibrium separation.

Using MOSOL [10], the solid state version of MOPAC, we optimized the distance between gallium and arsenic atoms in a three-dimensional GaAs crystal containing 80 atoms and found that the optimized value of the GaAs bond length is 2.5009 Å. This differs by only 2.1% from the experimentally reported value of 2.4479 Å. The dissociation energy of GaAs as determined by Miller et al [11] for the (111) surface of GaAs and hence its bond strength is 112 Kcal/mol. We calculated the bond strength of GaAs by adding the heat of formation of the GaAs molecule (-27.4 Kcal) at 2.4469 Å to the heat of formation of the As atom (72.3 Kcal) and the Ga atom (65.4 Kcal). The value obtained was 110.3 Kcal/mol which is in excellent agreement with the reported value. The charge on each Ga atom is found to be negative. Thus we see the covalent bonding in solid GaAs in accordance with that obtained by X-ray studies of

Attard et al. [12] and by the nonlocal pseudopotential model band calculations of Chelikovsky and Cohen [13]. The vibrational frequencies calculated, however, are in poor agreement with the experimental values.

We next attempted to reproduce the ab initio cluster calculations on Selenium adsorbed on the 100 surface of GaAs reported by Gayen et al.[14,9]. We found the stable position of an adsorbed Se atom on the Ga^6As^4 cluster to be at 1.517 Å from the gallium plane which is in good agreement with their calculated value of 1.587 Å. The total energy calculations of the $\text{Ga}^6\text{As}^4\text{Se}^{2-}$ cluster shows the stable position of the two Se atoms to be at 2.683 Å from the Ga plane. This differs slightly from the value obtained by Gayen et al [14] and can be accounted for by the flatness of the energy curve as a function of Se atom position. The calculated binding energy of the Se atom of 2.34 eV is also of the same order as that obtained by them [9]. The charges on the Ga and As atoms in the Ga^6As^4 cluster, however, differ with the values reported by them. The energies of excited virtual states were also not in agreement with their results. We conclude that although the semi-empirical code MOPAC gives reliable results for the total energy and the geometry optimization, the excited energy levels are probably not reliably calculated. The calculated charge distribution on the atoms is also different when we compare them with the ab initio results for large clusters. These differences may be partly attributed to the built-in correlation in our parameters as mentioned before and to the neglect of the configuration interactions. The point deserves future investigations.

The results of the binding energy calculations for As atom adsorbed on the $(\bar{1}\bar{1}\bar{1})$ surface at the two sites are summarized in Tables I and II. It can be inferred from these results that (1) The accurate value of the binding energy of an As atom at the surface of GaAs can be obtained only if one includes four to six surface layers and second nearest neighbors on the surface. (2) The proper bulk termination of the cluster is important for getting the binding energy of surface-adsorbed atoms accurately with a smaller number of layers. (3) The difference in the binding energy of the As atom at the two sites is very small (~0.4 eV).

In summary we can say that these calculations support the model proposed by Biegelsen et al [2] for the $(\sqrt{19} \times \sqrt{19})$ surface reconstruction. Before one can conclusively validate this model for

the surface restructuring, however, one has to do the challenging task of total energy calculations for the proposed large unit cell. The formation of equilateral triangle-shaped islands observed by them must also be explained.

The total energy calculation for the largest cluster considered in these calculations took about ten hours of CPU time on a micro-VAX machine. Thus it will be feasible to do calculations on larger atomic clusters.

IV CONCLUSION

In conclusion we have shown that the semi-empirical code MOPAC is reliable for determining the total energy of III-V semiconductors. This code has the force algorithm already built into it such that it is possible to carry out dynamical simulations using this code. Activation energies for surface diffusion by atomic hopping may thus be calculated. The exploration of these applications is under consideration.

This work was performed at the Electronic and Optical Materials Branch of Wright Laboratory (WL/MLPO), Wright-Patterson Air Force Base, under the summer faculty program sponsored by AFSOR. Dr. G. Medrano of the Polymer Branch of Wright Laboratory (WL/MLBF) is gratefully acknowledged for making available the MOPAC & MOSOL code and many helpful discussions.

REFERENCES

- (1) D. K. Biegelsen, R. D. Bringans, J. E. Northrup and I. E. Swartz, Phys. Rev. Letters **65**,452, 1990
- (2) K.W. Haberern and M. D. Pashley, Physical Review B, **41**,3226, 1990
- (3) E.Kaxiras, Y. Bar-yam, J. D. Joannopoulos & K. C. Pandey, Physical Review B, **35**,9625,1987
- (4) E.Kaxiras, Y. Bar-yam, J. D. Joannopoulos & K. C. Pandey, Physical Review B, **35**,9636,1987
- (5) James J. P. Stewart J. Computer Aided Molecular Design, **4**,1,1990,

James J. P. Stewart, Quantum Chemistry Program Exchange, QCPE
no.455

(6) M.J.S. Dewar, D. H. Lo and C. A. Ramsden, J. Am. Chem. Soc.
97,1311,(1975)

(7) R.C.. Bingham, M.J.S. Dewar, D. H. Lo, J. Am. Chem. Soc. 97,
1285,1294,1302,1307 (1975)

(8) James J. P. Stewart, Journal of computational chemistry,
10,221,1989

(9) private communication, from Gayen et al.

(10) James J. P. Stewart, Quantum Chemistry program exchange,
QCPE program no. 495

(11) Donald P. Miller, James G. Harper, and Thomas R. Perry, J.
Electrochem. Soc. 108, 1123(1961)

(12) A.E. Attard, F.A. Mifsud, A.K. Sant, and J.A. Sultana, J. Phys. C
2,816 (1969)

(13) J.R. Chelikowsky and M.L. Cohen, Phy. Rev.B 24,2081 (1981)

(14) Sanjukta Gayen, Walter C. Ermler, Claude J. Sandroff, J. Chem.
Phys., 94, 729, 1991

FIGURE CAPTIONS

(1) The positions of atoms around the As atom adsorbed on GaAs
($\overline{111}$) surface at Hexagonal closed packed (T4) position

(2) The positions of atoms around the As atom adsorbed on GaAs
($\overline{111}$) surface at the zincblende site.

(3) The proposed model of the ($\sqrt{19} \times \sqrt{19}$) surface unit cell on the
GaAs ($\overline{111}$) surface.

(4) Top view of largest cluster of atoms used for finding the binding
energy of As atom adsorbed at T4 and zincblende sites (indicated by
T4 and ZB)

TABLE I

Binding energy of As atom at a height Z above the top Ga layer on the (111) surface at the T4 site

Cluster size	No. of layers	Heat of form. (KCAL)	Z (Å)	Reference. energy (KCAL)	Binding energy (KCAL)
Ga⁴As³	3	150.0	0.91	162.5	12.5
^cGa⁴As³	3	149.3	0.96	163.7	14.4
*Ga¹⁶As⁸	4	203.8	0.51	237.4	33.6
^aGa¹⁶As⁸	3	243.0	1.26	278.3	35.3
^aGa¹⁹As¹⁶	5	159.8	0.71	197.3	37.5

*** The Cluster is terminated by a pseudo As atom**

^a Bulk surface simulation is not done.

^c The GaAs bond length for this calculations was taken as 2.4479Å, while the rest of the calculations were based on a bond length of 2.4495Å

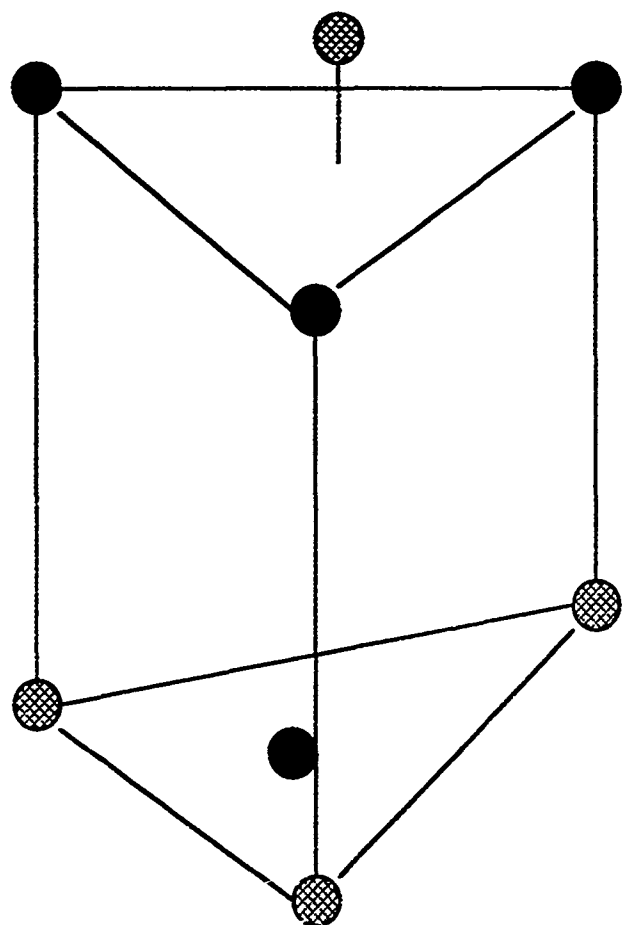
TABLE II

Binding energy of As atom at a height Z above the top Ga layer on the (111) surface at the zincblende site.

Cluster size	No. of layers	Heat of form. (KCAL)	Z (Å)	Reference. energy (KCAL)	Binding energy (KCAL)
^a Ga ³ As ³	3	154.0	0.79	170.0	15.9
*Ga ¹⁶ As ⁸	4	214.0	0.68	237.4	23.4
^a Ga ¹⁹ As ¹⁶	5	168.9	0.70	197.3	28.4

* The Cluster is terminated by a pseudo As atom

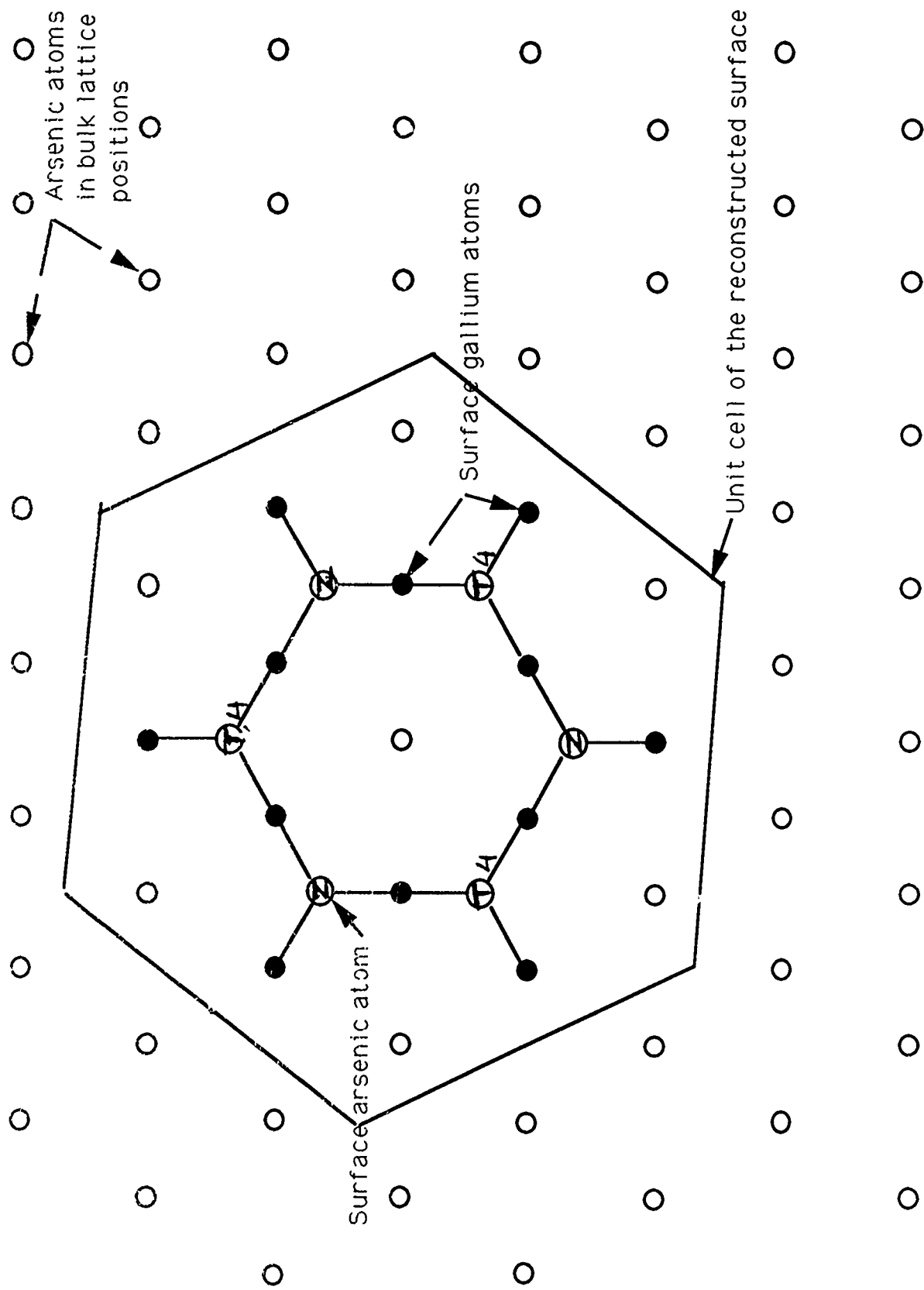
^a Bulk surface simulation is not done.




● Ga


⊗ As


Gallium Arsenide $[111]B \sqrt{19} \times \sqrt{19} R23.4^\circ$ Surface Reconstruction

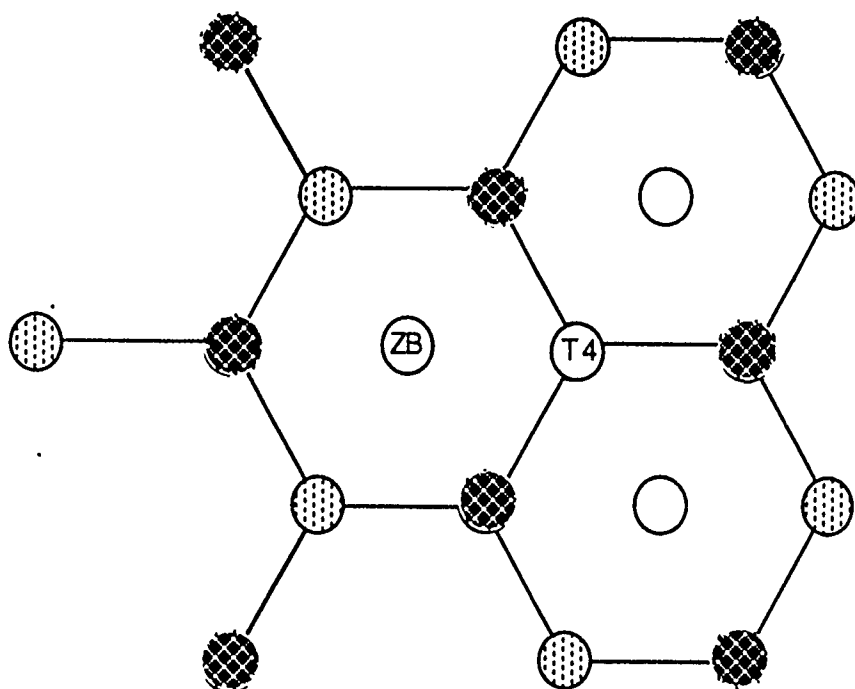


Ga₈As₈Ga₈As₈ CLUSTER

Ga III & As IV layer 

Ga V layer 

Ga I & As II layer 



1991 AFOSR SUMMER FACULTY RESEARCH PROGRAM

Conducted by

Research & Development Laboratories

5800 Uplander Way

Culver City, CA 90230-6608

FINAL REPORT

**X-RAY CRYSTALLOGRAPHIC STUDIES OF MODEL SYSTEMS
FOR RIGID ROD POLYMERS AND OF MOLECULES WITH POTENTIAL
NONLINEAR OPTICAL PROPERTIES**

Submitted by: Albert V. Fratini, Ph.D.

Title: Professor

**Department and
University: Department of Chemistry
University of Dayton
Dayton, Ohio 45469-2357**

**Research Location: WL/MLBP
Wright-Patterson AFB, Ohio 45433**

Date: September 1991

INTRODUCTION

The Polymer Branch of the Materials Directorate at Wright Laboratory, Wright-Patterson Air Force Base is engaged in a materials development program aimed at generating organic polymeric materials having structural and nonlinear optical (NLO) applications. The research program is a multi-faceted one, incorporating the areas of synthesis, processing, characterization, structure-property correlation, and the design and predictive features of computational chemistry methods. Organic materials are considered to be structurally diverse and multifunctional, and as a result, are expected to exhibit more long-term promise than inorganic materials.

The morphological characterization of polymers frequently involves the use of x-ray scattering techniques. The determination of ordered polymer structure generally involves first studying the structure of the various polymer repeat units by single crystal x-ray diffraction methods, followed then by a detailed packing analysis of polymer chains. Knowledge of polymer structure can lead to meaningful structure-property correlations.

The crystal structures of several model systems were determined during my ten-week experience this summer. Three of the compounds function as model structures for methyl-pendant polybenzobisthiazole polymers (PBZT). The substitution of alkyl groups on the polymer backbone is known to affect the solubility characteristics of these polymers. This is similar to the improved solubility observed when methyl groups are substituted on the backbone of polythiophene and polyphenylene.

The two substituted thiophene compounds have potential NLO applications. All kinds of materials are potential candidates to express third-order susceptibility. Eventually, practical considerations such as ease of fabrication become more important than the magnitude of the nonlinearity. Polythiophene, polyaniline and polypyrrole have been well-studied as electroactive materials.

EXPERIMENTAL

9-(2-Thienyl) anthracene, $C_{18}H_{12}S$ (X9106RT)

The compound, $C_{18}H_{12}S$, an anthracene derivative containing a thiophene ring (See Fig. 1), was examined using an optical microscope in order to find a data collection crystal with good size and external appearance. The crystal was mounted on a glass fiber attached to a goniometer and then placed on an Enraf Nonius CAD4 x-ray diffractometer. The crystal was centered optically and a polaroid rotation photograph revealed that the crystal diffracted at high angle. Data collection was initiated once the preliminary work was completed.

9,10-(di-2-Thienyl) anthracene, $C_{22}H_{14}S_2$ (X9108RT)

Yellow cubical crystals of this second anthracene derivative (See Fig. 1) were recrystallized from ethanol. They were examined under an optical microscope and a crystal was selected for data collection on the basis of its size and extinction characteristics. As before, the crystal was mounted on a glass fiber attached to a goniometer and aligned optically on the diffractometer. The structure analysis showed this first crystal to be disordered.

A second crystal was chosen from a batch of crystals recrystallized from isopropanol to see if the disorder problems were solvent dependent. A polaroid photograph of the crystal showed that the crystal did not diffract x-rays adequately, and the crystal was discarded. Another crystal from the isopropanol batch was mounted in a similar manner. It was also not fit for data collection. Work on this structure determination was stopped until better crystal can be grown. Preliminary work has shown that more ordered crystals can be grown from the melt phase.

9-(2-Nitrovinyl) anthracene, $C_{16}H_{11}NO_2$ (X9005RT)

Crystals of this anthracene derivative, $C_{16}H_{11}NO_2$, (X9005RT) were rather small, but a number were chosen as candidates for data collection. A total of four crystals were mounted and polaroid photographs were taken of them. The photographs did not show intense or high angle reflections. Work on this compound was halted because of the lack of good crystals for data collection. Work is continuing to try to grow larger crystals.

2-(2-Vinylethynylbenzene)anthracene, C₂₄H₁₆ (X9006RT)

Crystals of C₂₄H₁₆ (X9006RT) (See Fig. 1) were fine, yellow needles. One was chosen for its size and apparent good optical quality and mounted as described previously. A polaroid rotation photograph showed weak reflections at low angles and little or no diffraction spots at high angles. Another crystal was mounted with similar results. Further work on this structure was halted until larger crystals could be obtained.

Dimethyl PBT (X9101RT) and meta-monomethyl PBT (X9103RT) model compounds

Diffraction quality crystals were obtained from Dr. Fred Arnold and Mr. Tom Vance. They were mounted and aligned as described previously.

Ortho-monomethyl PBT model compound, C₂₂H₁₆S₂N₂ (X9102RT)

Crystals of the o-monomethyl PBT model compound, C₂₂H₁₆S₂N₂ (X9102RT), were small, colorless and needle-shaped (See Fig. 1). An x-ray rotation photograph showed only weak, low angle reflections. Another crystal was mounted and it showed a few high angle reflections, but rather weak in intensity. A preliminary search for x-ray reflections did not reveal meaningful data for this crystal. Another crystal was mounted that was larger than the earlier crystals. The polaroid showed more reflections, but after a preliminary search this crystal also proved to be inferior for data collection purposes.

Still an additional crystal was mounted. It showed high angle reflections on the polaroid photograph and looked somewhat promising after a automated search on the diffractometer. The fifth crystal that was mounted proved to be suitable for data collection.

RESULTS

9-(2-Thienyl) anthracene, C₁₈H₁₂S (X9106RT)

The reflection intensities were analyzed using the SDP system of crystallographic software. Crystal data and calculated results are presented in Tables 1 - 8. PLUTO drawings of the structure, including single molecule and packing diagrams, are displayed in Fig. 2. The structure was refined to a R value of 0.057. A disorder in the thiophene ring caused a problem in the refinement of the structure. The H atom attached to the C atom opposite the S atom would be pulled in towards the C atom during refinement. A literature search showed that crystals of other compounds containing thiophene rings were also disordered. The refinement was temporarily halted until a suitable method could be found to handle the disordered structure.

9,10-(di-2-Thienyl) anthracene, C₂₂H₁₄S₂ (X9108RT)

The data were analyzed with the SDP package. Pluto drawings of the structure are presented in Fig. 3. Crystal data and the results of the analysis are shown in Tables 1 and 9 - 13. The refinement was halted at an R value of 0.181. The thiophene rings again were disordered, the disorder revealing itself at an earlier stage in the refinement process. Further analysis of the structure was discontinued until a method could be found to treat the disorder.

Methylated PBT model compounds

Data collection parameters were changed in some cases in the attempt to obtain better data sets. Two sets of equivalent reflection data were collected for X9102RT. All structures were solved using the program SHELX and the SDP system. The refinement of the methyl PBT compounds is still in progress and the final calculated parameters will be published at a later date. Single molecule PLUTO drawings are shown in Fig. 4.

DISCUSSION

9-(2-Thienyl) anthracene, $C_{18}H_{12}S$ (X9106RT)

The two ring segments are planar (See Table 8). The dihedral angle between the thiophene and anthracene moieties is 72° . The thiophene is disordered as evidenced by peaks in the difference map corresponding to two different ring orientations.

9,10-(di-2-Thienyl) anthracene, $C_{22}H_{14}S_2$ (X9108RT)

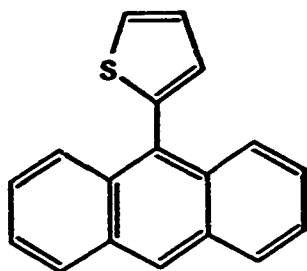
The refinement could not be completed since the thiophene rings were disordered. The molecule is located on a center of symmetry and the dihedral angle between the thiophene and anthracene rings is 83° .

Table 14 shows a comparison of the thiophene molecular parameters for a series of six substituted thiophene compounds. (Literature values are unpublished and supplied by Dr. S. Simonsen of the University of Texas). The slightly shortened S-C bond and the longer C2-C3 distance in 6 reflect a disordered ring. The 1.337 Å value for C1-C2 is consistent with conjugation of the ring with the olefinic bond of the side chain.

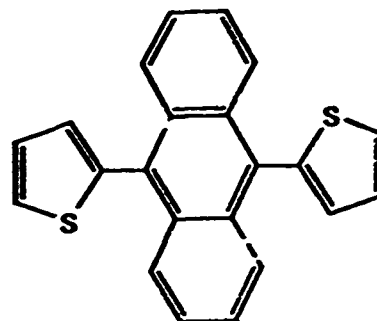
Methylated PBT model compounds

A comparison of the inter-ring torsion angles for the methylated PBT model compounds is shown in Fig. 7. AM1 calculations show that the minimum energy conformation corresponds to a rotation angle of 30° for an orthomethyl substitution when benzene is attached to benzothiazole (Connolly and Dudis, to be published in *Macromolecules*). For the case of dimethyl substitution, the minimum energy corresponds to an angle of rotation of 90° . A detailed analysis of the cell packing is in progress.

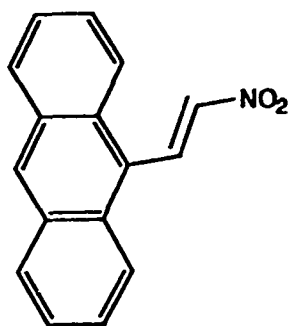
Fig. 1 Compounds



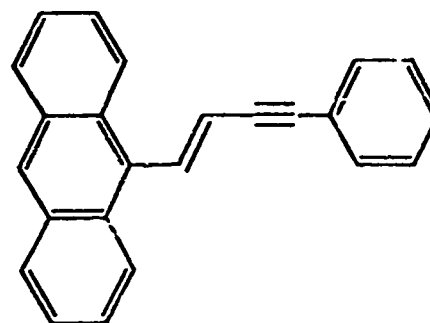
**9-(2-thienyl) anthracene
X9106RT**



**9,10-(di-2-thienyl)anthracene
X9108RT**

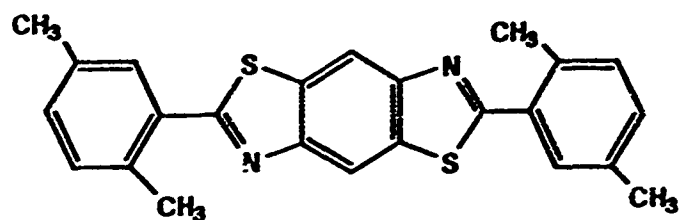


**9-(nitrovinyl) anthracene
X9005RT**

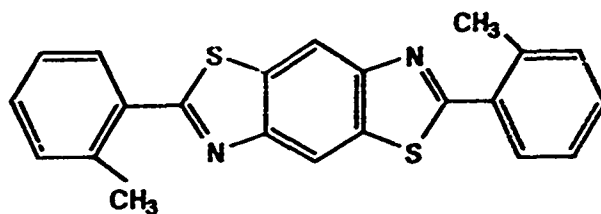


**9-(2-vinyl ethynyl benzene) anthracene
X9006RT**

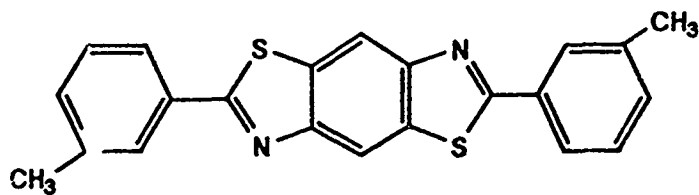
Fig. 1 Compounds Continued



**dimethyl PBT model compound
X9101RT**



**ortho-mono methyl PBT model compound
X9102RT**



**meta-mono methyl PBT model compound
X9103RT**

Fig. 2 PLUTO Drawing and Packing Diagram of X9106RT

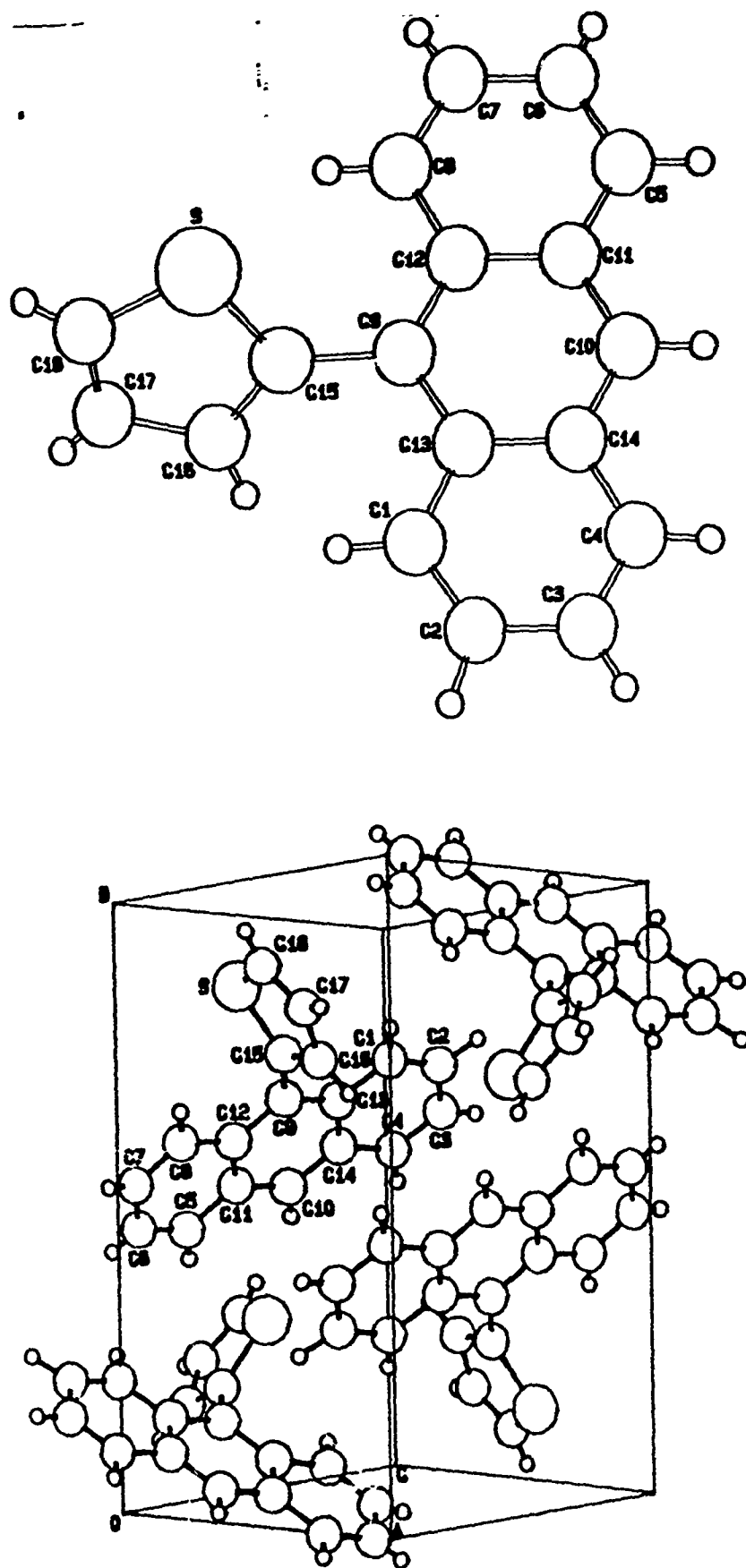


Fig. 3 PLUTO Drawing and Packing Diagram of X9108RT

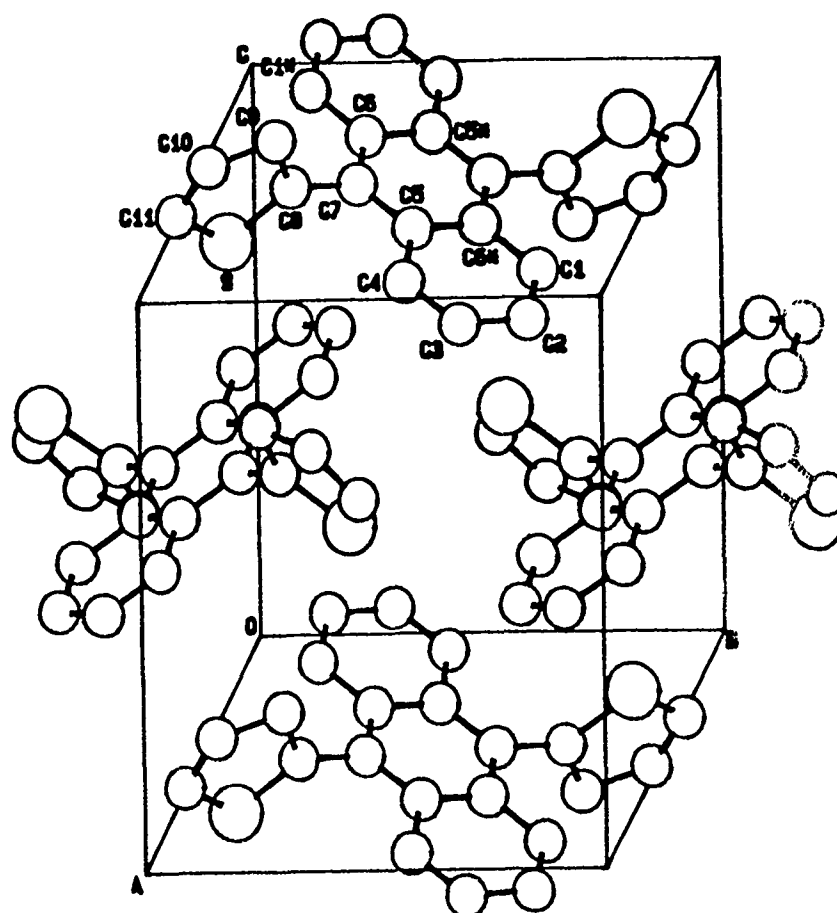
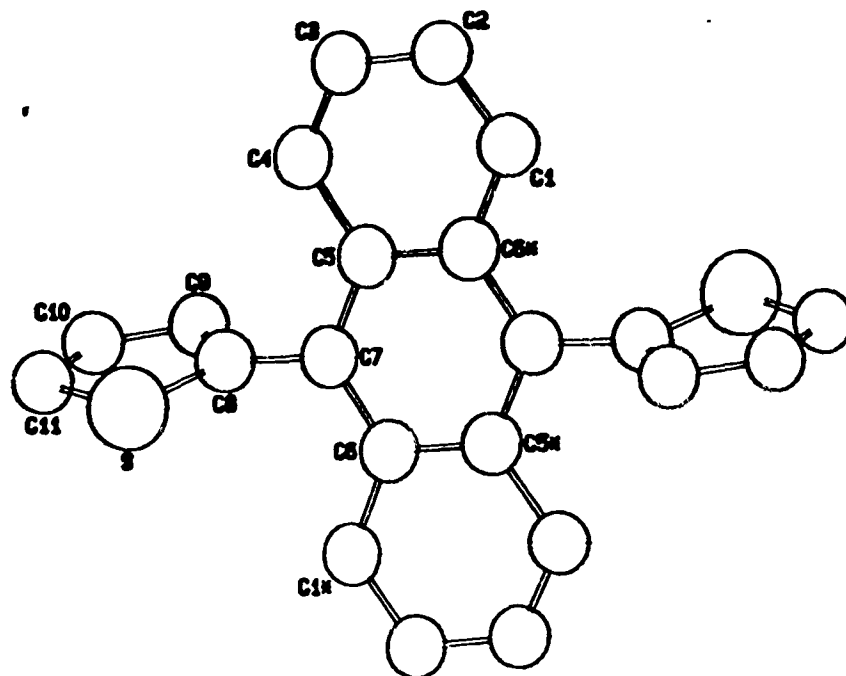


Fig. 4 PLUTO Drawings of Methylated PBT Model Compounds

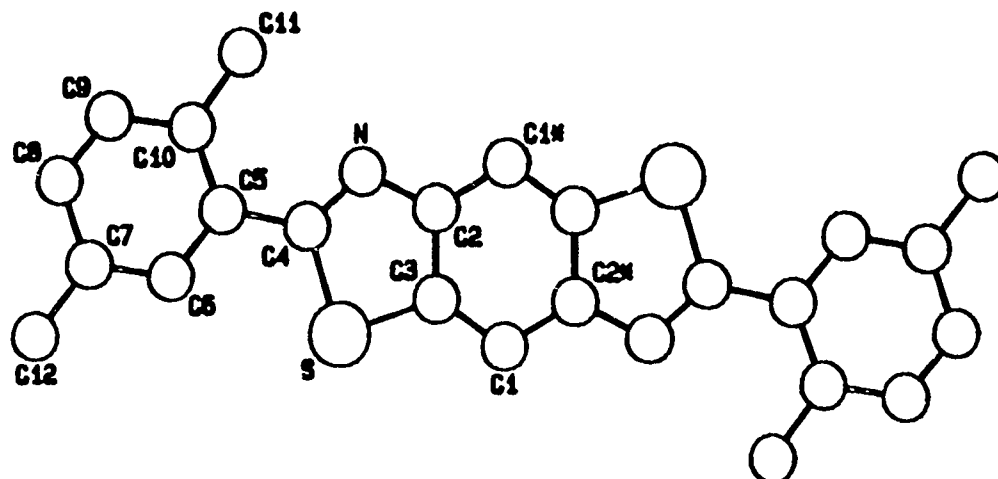
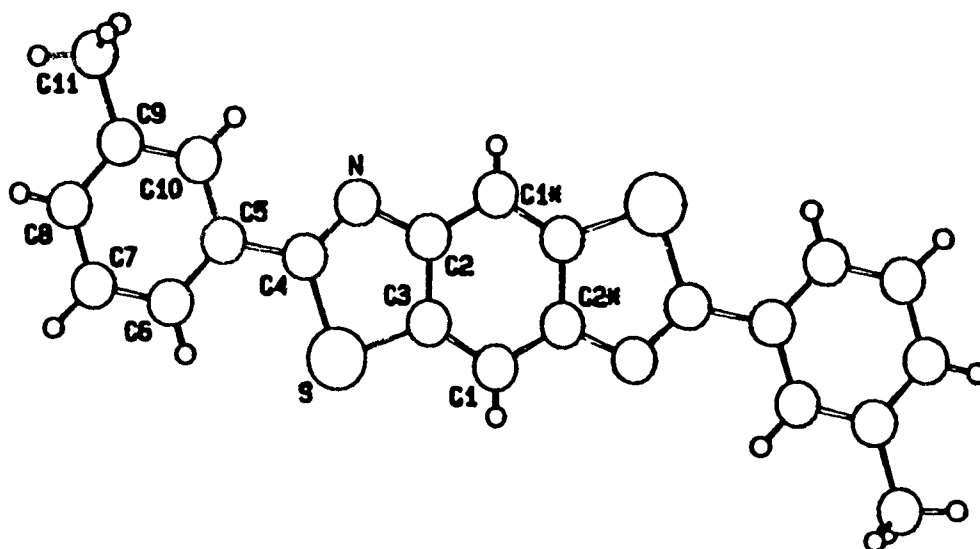
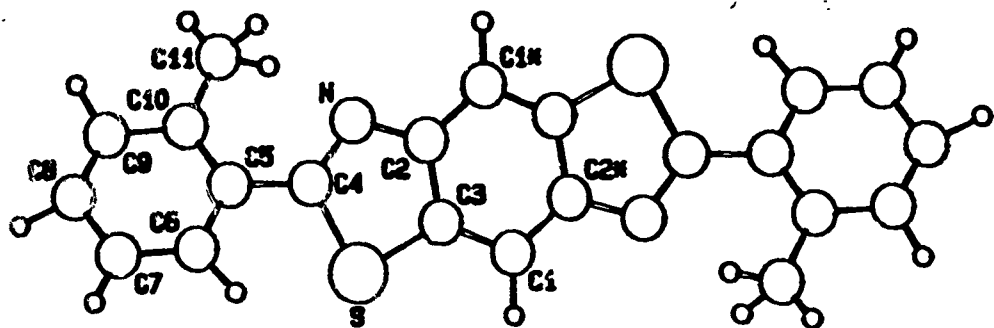


Fig. 5 Unit Cell Packing Diagram of X9102RT

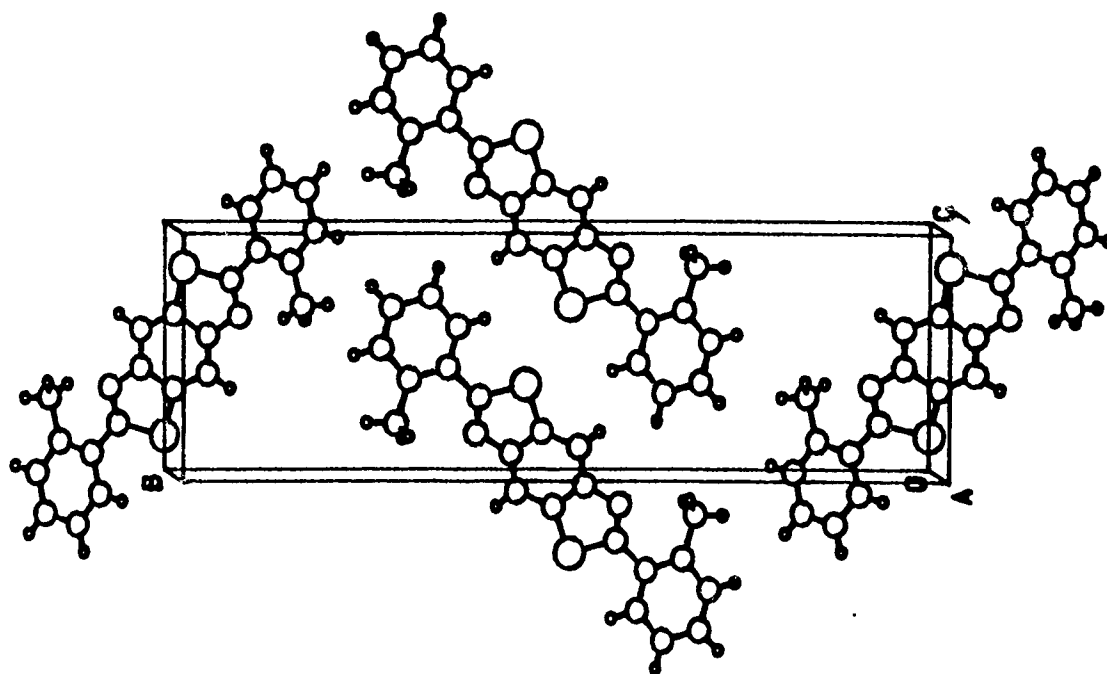


Fig. 6 Unit Cell Packing Diagram of X9103RT

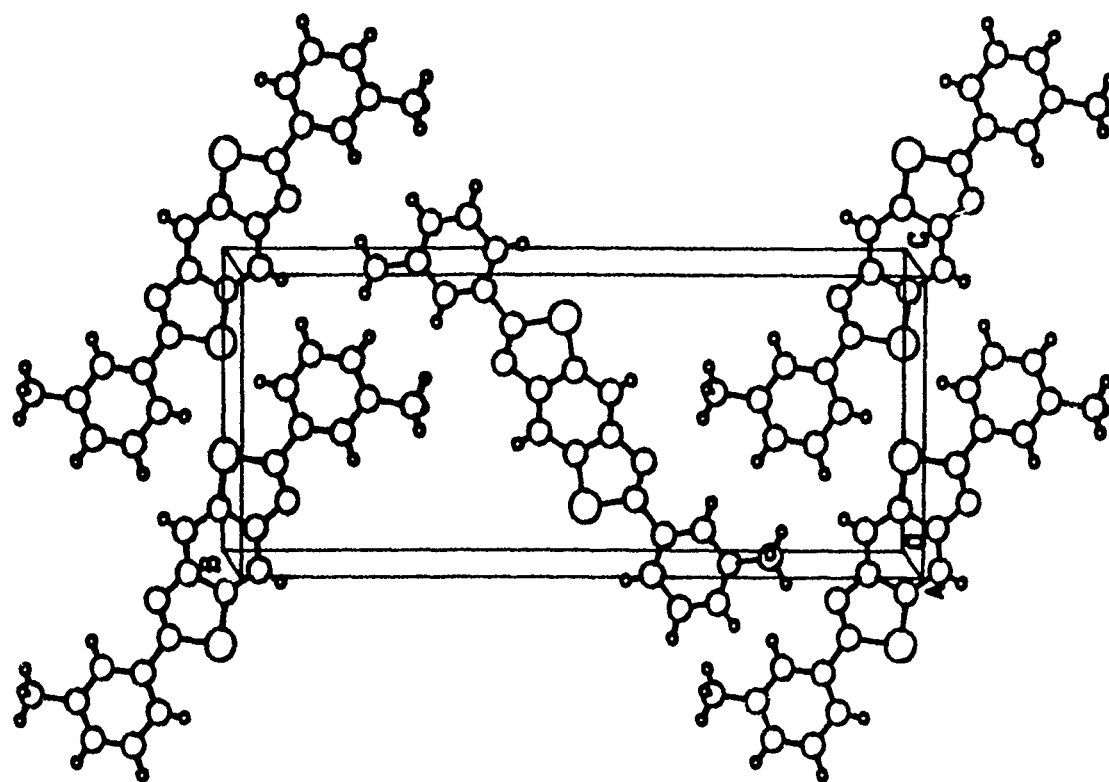


Fig. 7 Summary of Torsion Angles for PBT Model Compounds

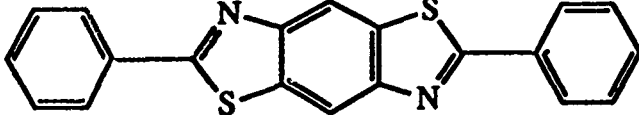
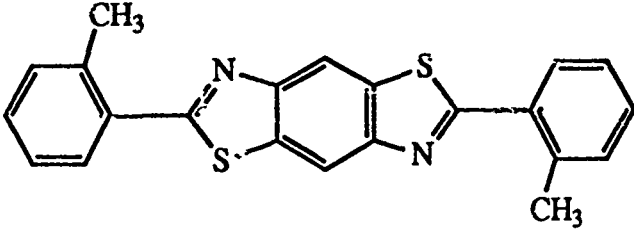
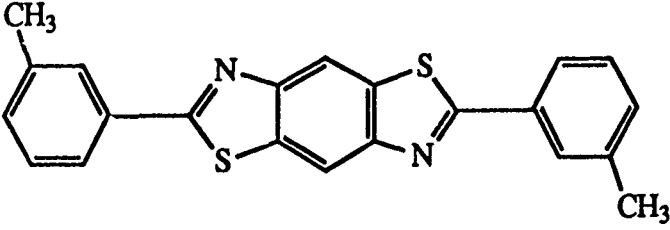
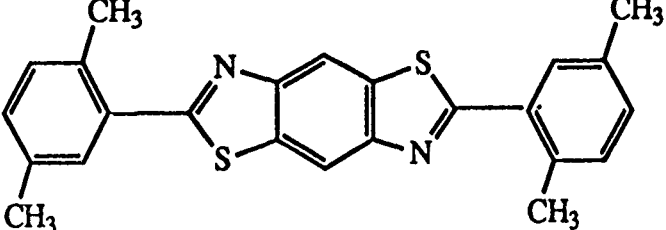
Compound	Torsion Angle
	23°
	30°
	2°
	17°

Table 1 Crystal Data

Crystal Code	X9106RT	X9108RT
Formula	$C_{18}H_{12}S$	$C_{22}H_{14}S_2$
Formula Weight	260.367	342.485
F(000)	548	356
Crystal Dimensions	0.4 x 0.5 x 0.6	0.3 x 0.2 x 0.4
Radiation	MoK α	MoK α
Wavelength	0.71073	0.71073
Temperature	23° C	23° C
Crystal Form	monoclinic	monoclinic
Space Group	P2 ₁ /n	P2 ₁ /c
Cell Constants	a= 9.270	a=9.820
	b= 12.573	b=9.212
	c= 11.952	c=10.153
	α = 90.0	α =90.00
	β = 110.73	β =115.40
	γ = 90.0	γ =90.00
Volume	1302.8	829.7
Z	4	2
Density	1.33 g/cm ³	1.37 g/cm ³
Absorption Coefficient	2.2 cm ⁻¹	
Scan Type	ω :2 θ	ω :2 θ
Scan Width	0.8+0.34 tan θ	0.8+0.34 tan θ
No. Unique reflections	3783	2404
No. I > 3 sigma(I)	2622	1161
R	0.057	0.181
Weighted R	0.093	0.175

Table 1 Crystal Data Continued

Code #	X9101RT	X9102RT	X9103RT
Formula	$C_{22}H_{20}S_2N_2$	$C_{22}H_{16}S_2N_2$	$C_{22}H_{16}S_2N_2$
Formula Weight	400.57	372.514	372.514
F(000)	840	388	388
Crystal Dimensions	1.1 x 0.34 x 0.91	0.2 x 0.1 x 0.5	0.1 x 0.2 x 0.4
Radiation	MoK α	MoK α	MoK α
Wavelength	0.71073	0.71073	0.71073
Temperature	23° C	23° C	23° C
Crystal Form	orthorhombic	monoclinic	monoclinic
Space Group	Pbca	P2 ₁ /n	P2 ₁ /n
Cell Constants a	7.7347(6)	4.0196(3)	4.0277(1)
b	14.5177(3)	27.0608(6)	23.1076(9)
c	17.6825(9)	8.1091(2)	9.4213(3)
α	90.00	90.00	90.00
β	90.00	95.8869	102.1447
γ	90.00	90.00	90.00
Volume (Å ³)	1985.6	877.4063	857.2234
Z	4	2	2
Density (g/cm ³)	2.68	1.410	1.443
Absorption Coefficient (cm ⁻¹)	2.68	3.0	3.0
Scan Type	$\omega:2\theta$	$\omega:2\theta$	$\omega:2\theta$
Scan Width	1.1+0.34 tan θ	0.8+0.34 tan θ	0.9+0.34 tan θ
Unique Reflections Measured	2816	2560	2498
Reflections I > 2 σ (I)	1655	1056	1098
R	0.098	0.065	0.049
Weighted R	0.122	0.076	0.055

Table 2. Bond Distances in Angstroms for X9106RT

<u>Atom 1</u>	<u>Atom 2</u>	<u>Distance</u>
S	C15	1.715(2)
C5	C11	1.423(3)
C10	C14	1.389(2)
S	C18	1.685(3)
C6	C7	1.405(4)
C11	C12	1.430(4)
C1	C2	1.368(4)
C7	C8	1.362(4)
C13	C14	1.432(3)
C1	C13	1.427(3)
C8	C12	1.428(3)
C15	C16	1.434(3)
C2	C3	1.426(4)
C9	C12	1.418(2)
C16	C17	1.457(3)
C3	C4	1.344(3)
C9	C13	1.411(3)
C17	C18	1.332(3)
C4	C14	1.438(3)
C9	C15	1.483(3)
C5	C6	1.347(4)
C10	C11	1.396(3)

Numbers in parentheses are estimated standard deviations in the least significant digits.

Table 3. Bond Angles in Degrees for X9106RT

Atom 1	Atom 2	Atom 3	Angle
C15	S	C18	93.1(1)
C13	C9	C15	119.7(2)
C4	C14	C10	121.2(2)
C2	C1	C13	121.3(2)
C11	C10	C14	121.6(3)
C4	C14	C13	119.0(2)
C1	C2	C3	120.5(2)
C5	C11	C10	121.4(3)
C10	C14	C13	119.8(2)
C2	C3	C4	120.1(2)
C5	C11	C12	119.0(2)
S	C15	C9	122.6(1)
C3	C4	C14	121.4(2)
C10	C11	C12	119.6(2)
S	C15	C16	111.5(2)
C6	C5	C11	121.1(2)
C8	C12	C9	122.8(2)
C9	C15	C16	125.9(2)
C5	C6	C7	120.4(2)
C8	C12	C11	118.1(2)
C15	C16	C17	107.9(2)
C6	C7	C8	121.1(2)
C9	C12	C11	119.1(2)
C16	C17	C18	115.0(2)
C7	C8	C12	120.5(2)
C1	C13	C9	123.0(2)
S	C18	C17	112.6(2)
C12	C9	C13	120.6(2)
C1	C13	C14	117.7(2)
C12	C9	C15	119.6(2)
C9	C13	C14	119.2(2)

Numbers in parentheses are estimated standard deviations in the least significant digits.

Table 4. Positional Parameters and Their Estimated Standard Deviations for X91G6RT

Atom	x	y	z	B(A ²)
S	0.02537(8)	0.83135(5)	0.42660(6)	5.04(1)
C1	0.4683(2)	0.7215(2)	0.5391(2)	3.58(4)
C2	0.6249(3)	0.7177(2)	0.5693(2)	4.20(5)
C3	0.6928(2)	0.6497(2)	0.5064(2)	4.15(5)
C4	0.6029(2)	0.5894(2)	0.4156(2)	3.76(4)
C5	0.0915(3)	0.4561(2)	0.1649(2)	4.34(5)
C6	-0.0624(3)	0.4523(2)	0.1373(2)	4.93(6)
C7	-0.1339(3)	0.5165(2)	0.1987(2)	4.38(5)
C8	-0.0500(2)	0.5834(2)	0.2876(2)	3.58(4)
C9	0.2068(2)	0.6565(1)	0.4134(2)	2.90(3)
C10	0.3452(2)	0.5275(2)	0.2877(2)	3.56(4)
C11	0.1851(2)	0.5252(2)	0.2562(2)	3.32(4)
C12	0.1134(2)	0.5903(2)	0.3198(2)	3.05(3)
C13	0.3685(2)	0.6577(1)	0.4446(2)	3.00(3)
C14	0.4377(2)	0.5912(2)	0.3802(2)	3.13(3)
C15	0.1346(2)	0.7206(2)	0.4835(2)	3.06(3)
C16	0.1447(2)	0.6998(2)	0.6041(2)	3.37(4)
C17	0.0543(3)	0.7805(2)	0.6373(2)	4.66(5)
C18	-0.0111(3)	0.8529(2)	0.5532(3)	4.98(5)
H1	0.569(3)	0.235(2)	0.415(2)	2.3(5)*
H2	0.293(2)	0.242(2)	0.362(2)	1.6(5)*
H3	0.696(3)	0.147(2)	0.972(2)	3.1(6)*
H4	0.648(3)	0.537(2)	0.380(2)	2.2(5)*
H5	0.642(2)	0.083(2)	0.622(2)	2.0(5)*
H6	0.372(3)	0.083(2)	0.582(3)	4.4(7)*
H7	0.767(3)	0.511(3)	0.189(2)	3.7(6)*
H8	0.596(3)	0.130(2)	0.167(2)	2.1(5)*
H10	0.612(2)	0.513(2)	0.754(2)	1.6(4)*
H16	0.201	0.644	0.654	3.7(7)*
H17	0.458(4)	0.268(3)	0.785(3)	5.2(8)*
H18	0.575(3)	0.415(2)	0.951(2)	3*

Starred atoms were refined isotropically. Anisotropically refined atoms are given in the form of the isotropic equivalent displacement parameter defined as:

$$(4/3) * [a^2*B(1,1) + b^2*B(2,2) + c^2*B(3,3) + ab(\cos \gamma)*B(1,2) + ac(\cos \beta)*B(1,3) + bc(\cos \alpha)*B(2,3)]$$

Table 5. Root-Mean-Square Amplitudes of Thermal Vibration in Angstroms for X9106RT

Atom	Min.	Int'med.	Max.
S	0.202	0.254	0.294
C10	0.174	0.206	0.250
C1	0.196	0.213	0.229
C11	0.182	0.200	0.231
C2	0.208	0.233	0.249
C12	0.176	0.191	0.220
C3	0.194	0.216	0.271
C13	0.172	0.191	0.219
C4	0.179	0.203	0.264
C14	0.168	0.190	0.234
C5	0.192	0.243	0.263
C15	0.181	0.194	0.214
C6	0.201	0.259	0.282
C16	0.158	0.214	0.239
C7	0.213	0.240	0.252
C17	0.182	0.228	0.303
C8	0.202	0.213	0.223
C18	0.189	0.217	0.326
C9	0.175	0.181	0.217

Table 6. Torsional Angles in Degrees for X9106RT

Atom 1	Atom 2	Atom 3	Atom 4	Angle
C18	S	C15	C9	179.23 (0.18)
C15	C9	C13	C1	-2.41 (0.28)
C18	S	C15	C16	-0.50 (0.17)
C15	C9	C13	C14	176.79 (0.17)
C15	S	C18	C17	-0.28 (0.22)
C12	C9	C15	S	-73.12 (0.22)
C13	C1	C2	C3	0.27 (0.33)
C12	C9	C15	C16	106.58 (0.23)
C2	C1	C13	C9	177.67 (0.20)
C13	C9	C15	S	110.16 (0.19)
C2	C1	C13	C14	-1.53 (0.30)
C13	C9	C15	C16	-70.14 (0.26)
C1	C2	C3	C4	0.73 (0.35)
C14	C10	C11	C5	-177.10 (0.19)
C2	C3	C4	C14	-0.40 (0.33)
C14	C10	C11	C12	0.46 (0.29)
C11	C10	C14	C4	177.09 (0.19)
C3	C4	C14	C10	-178.92 (0.21)
C11	C10	C14	C13	-0.92 (0.29)
C3	C4	C14	C13	-0.89 (0.30)
C5	C11	C12	C8	-0.50 (0.28)
C5	C11	C12	C9	177.90 (0.18)
C10	C11	C12	C8	-178.12 (0.18)
C11	C5	C6	C7	-0.18 (0.37)
C10	C11	C12	C9	0.28 (0.27)
C6	C5	C11	C10	178.20 (0.22)
C1	C13	C14	C4	1.82 (0.27)
C6	C5	C11	C12	0.63 (0.32)
C1	C13	C14	C10	179.87 (0.18)
C5	C6	C7	C8	-0.40 (0.38)
C9	C13	C14	C4	-177.42 (0.17)
C6	C7	C8	C12	0.52 (0.35)
C9	C13	C14	C10	0.63 (0.27)
C7	C8	C12	C9	-178.40 (0.20)
C7	C15	C16	C17	1.07 (0.22)
C7	C8	C12	C11	-0.07 (0.30)
C13	C9	C12	C8	177.76 (0.18)
C9	C15	C16	C17	-178.66 (0.19)
C13	C9	C12	C11	-0.56 (0.26)
C15	C9	C12	C8	1.08 (0.27)
C15	C16	C17	C18	-1.32 (0.29)
C15	C9	C12	C11	-177.25 (0.17)
C12	C9	C13	C1	-179.09 (0.18)
C16	C17	C18	S	0.99 (0.29)
C12	C9	C13	C14	0.11 (0.27)

Table 7. General Displacement Parameter Expressions - U's for X9106RT

Name	U(1,1)	U(2,2)	U(3,3)	U(1,2)	U(1,3)	U(2,3)
S	0.0730(3)	0.0506(3)	0.0752(3)	0.0167(2)	0.0352(2)	0.0058(3)
C1	0.0478(8)	0.0387(9)	0.0514(9)	-0.0003(8)	0.0200(6)	-0.0019(8)
C2	0.050(1)	0.049(1)	0.062(1)	-0.0050(9)	0.0201(8)	0.001(1)
C3	0.0422(8)	0.052(1)	0.067(1)	0.0007(9)	0.0233(7)	0.012(1)
C4	0.0479(8)	0.047(1)	0.0587(9)	0.0066(8)	0.0317(6)	0.0112(8)
C5	0.067(1)	0.055(1)	0.0429(9)	0.002(1)	0.0198(8)	-0.0089(9)
C6	0.063(1)	0.064(1)	0.052(1)	-0.004(1)	0.009(1)	-0.014(1)
C7	0.0483(9)	0.057(1)	0.056(1)	-0.002(1)	0.0117(8)	-0.002(1)
C8	0.0454(8)	0.0433(9)	0.0484(9)	0.0033(8)	0.0179(6)	0.0018(8)
C9	0.0430(7)	0.0335(8)	0.0377(7)	0.0053(7)	0.0189(5)	0.0043(6)
C10	0.0566(8)	0.0425(9)	0.0454(8)	0.0071(8)	0.0296(6)	0.0009(7)
C11	0.0526(8)	0.0404(9)	0.0367(7)	0.0024(8)	0.0200(6)	0.0015(7)
C12	0.0462(8)	0.0351(8)	0.0370(7)	0.0049(7)	0.0178(6)	0.0051(7)
C13	0.0437(8)	0.0330(8)	0.0409(7)	0.0032(7)	0.0196(5)	0.0058(6)
C14	0.0450(7)	0.0387(8)	0.0422(7)	0.0052(7)	0.0241(5)	0.0088(7)
C15	0.0412(7)	0.0350(8)	0.0435(8)	0.0017(7)	0.0194(5)	-0.0009(7)
C16	0.0459(8)	0.049(1)	0.0405(7)	-0.0011(7)	0.0241(5)	-0.0109(7)
C17	0.061(1)	0.068(1)	0.0592(9)	-0.012(1)	0.0352(7)	-0.0236(9)
C18	0.0502(9)	0.051(1)	0.097(1)	-0.0036(9)	0.0368(8)	-0.023(1)

The form of the anisotropic displacement parameter is:

$\exp[-2\pi i\{h^2a^2U(1,1) + k^2b^2U(2,2) + l^2c^2U(3,3) + 2hkabU(1,2) + 2hlacU(1,3) + 2klbcU(2,3)\}]$ where a,b, and c are reciprocal lattice constants.

Table 8. Least-Squares Planes for X9106RT

The equation of the plane is of the form: $A \cdot x + B \cdot y + C \cdot z - D = 0$
 where A,B,C & D are constants and x,y & z are orthogonalized coordinates.

Plane	A	B	C	D	Atom	x	y	z	Distance	Esd
1	0.1619	0.7349	-0.6585	3.0222	-----Atoms in Plane-----					
					C1	2.0606	9.0710	6.0259	0.010	0.002
					C2	3.3823	9.0257	6.3609	-0.030	0.003
					C3	4.2815	8.1696	5.6614	-0.053	0.003
					C4	3.8320	7.4115	4.6443	-0.013	0.002
					C5	0.1475	5.7357	1.8453	0.002	0.003
					C6	-1.1573	5.6878	1.5384	-0.043	0.003
					C7	-2.0798	6.4972	2.2200	-0.046	0.003
					C8	-1.6788	7.3340	3.2133	-0.020	0.002
					C9	0.1692	8.2550	4.6200	0.029	0.002
					C10	1.9821	6.6331	3.2154	0.056	0.002
					C11	0.6321	6.6027	2.8640	0.047	0.002
					C12	-0.3017	7.4219	3.5731	0.030	0.002
					C13	1.5352	8.2701	4.9686	0.032	0.002
Chi Squared = 3104.										
2	-0.7405	-0.5742	-0.3491	-6.5034	-----Atoms in Plane-----					
					S	-1.5697	10.4527	4.7687	-0.001	0.001
					C15	-0.7982	9.0596	5.4072	0.004	0.002
					C16	-1.2142	8.7984	6.7494	-0.006	0.002
					C17	-2.1916	9.8160	7.1162	0.005	0.003
					C18	-2.4449	10.7210	6.1868	-0.002	0.003
Chi Squared = 19.										
3	0.1604	0.7357	-0.6580	3.0314	-----Atoms in Plane-----					
					C1	2.0606	9.0710	6.0259	0.008	0.002
					C2	3.3823	9.0257	6.3609	-0.034	0.003
					C3	4.2815	8.1696	5.6614	-0.059	0.003
					C4	3.8320	7.4115	4.6443	-0.020	0.002
					C5	0.1475	5.7357	1.8453	-0.002	0.003
					C6	-1.1573	5.6878	1.5384	-0.045	0.003
					C7	-2.0798	6.4972	2.2200	-0.046	0.003
					C8	-1.6788	7.3340	3.2133	-0.019	0.002
					C9	0.1692	8.2550	4.6200	0.029	0.002
					C10	1.9821	6.6331	3.2154	0.051	0.002
					C11	0.6321	6.6027	2.8640	0.043	0.002
					C12	-0.3017	7.4219	3.5731	0.030	0.002
					C13	1.5352	8.2701	4.9686	0.030	0.002
					C14	2.4479	7.4324	4.2477	0.034	0.002

Chi Squared = 3346.

Dihedral Angles Between Planes:

Plane No.	Plane No.	Dihedral Angle
1	2	108.18 +- 0.06
1	3	0.10 +- 2.64
2	3	108.15 +- 0.06

Table 9 Bond Distances in Angstroms for X9108RT

<u>Atom 1</u>	<u>Atom 2</u>	<u>Distance</u>
S	C8	1.67(1)
C3	C4	1.35(3)
C7	C8	1.51(2)
S	C11	1.70(1)
C4	C5	1.47(2)
C8	C9	1.56(2)
C1	C2	1.41(3)
C5	C7	1.42(2)
C9	C10	1.40(2)
C1	C6	1.44(2)
C6	C7	1.40(2)
C10	C11	1.33(2)

Numbers in parentheses are estimated standard deviations in the least significant digits.

Table 10 Bond Angles in Degrees for X9108RT

<u>Atom 1</u>	<u>Atom 2</u>	<u>Atom 3</u>	<u>Angle</u>
C8	S	C11	89.8(7)
C5	C7	C6	120(2)
C7	C8	C9	123.2(9)
C2	C1	C6	119(2)
C5	C7	C8	119(1)
C8	C9	C10	98.1(8)
C3	C4	C5	119(1)
C6	C7	C8	121(2)
C9	C10	C11	123(1)
C4	C5	C7	121(2)
S	C8	C7	119.8(7)
S	C11	C10	112(1)
C1	C6	C7	122(2)
S	C8	C9	117.0(8)

Numbers in parentheses are estimated standard deviations in the least significant digits.

Table 11 Positional Parameters and Their Estimated Standard Deviations for X9108RT

<u>Atom</u>	<u>x</u>	<u>y</u>	<u>z</u>	<u>B(A2)</u>
S	0.6937(7)	0.1194(7)	0.9782(7)	9.8(2)
C1	0.460(1)	0.246(1)	1.143(1)	3.8(3)
C2	0.335(1)	0.240(1)	1.177(1)	4.4(3)
C3	0.764(1)	0.642(2)	0.857(1)	4.6(3)
C4	0.752(1)	0.522(2)	0.928(1)	4.1(3)
C5	0.625(1)	0.510(1)	0.968(1)	3.4(2)
C6	0.481(1)	0.373(1)	1.071(1)	3.1(2)
C7	0.605(1)	0.385(1)	1.038(1)	3.2(2)
C8	0.722(1)	0.267(1)	1.083(1)	3.7(3)
C9	0.8712(7)	0.2728(8)	1.2260(9)	1.6(2)
C10	0.934(1)	0.143(2)	1.209(2)	10.1(4)
C11	0.866(1)	0.054(2)	1.095(2)	7.8(4)
H1	0.529	0.168	1.167	4.9*
H2	0.349	0.258	1.274	5.7*
H3	0.238	0.217	1.103	5.7*
H4	0.828	0.719	0.910	5.9*
H5	0.709	0.649	0.754	5.9*
H6	0.824	0.445	0.951	5.3*
H7	0.908	0.343	1.302	2.1*
H8	1.030	0.116	1.282	13.2*
H9	0.896	-0.044	1.101	10.2*
H10	0.786	0.090	1.008	10.2*

Starred atoms were refined isotropically. Anisotropically refined atoms are given in the form of the isotropic equivalent displacement parameter defined as:

$$(4/3) * [a^2*B(1,1) + b^2*B(2,2) + c^2*B(3,3) + ab(\cos \gamma)*B(1,2) + ac(\cos \beta)*B(1,3) + bc(\cos \alpha)*B(2,3)]$$

Table 12 Root-Mean-Square Amplitudes of Thermal Vibration in Angstroms for X9108RT

<u>Atom</u>	<u>Min.</u>	<u>Int'med.</u>	<u>Max.</u>
S	0.261	0.353	0.422
C6	0.167	0.201	0.220
C1	0.188	0.224	0.239
C7	0.180	0.198	0.223
C2	0.208	0.225	0.270
C8	0.190	0.201	0.256
C3	0.183	0.251	0.276
C9	0.061	0.118	0.206
C4	0.181	0.245	0.250
C10	0.118	0.232	0.563
C5	0.198	0.209	0.216
C11	0.127	0.242	0.471

Table 13 Least-Squares Planes for X9108RT

The equation of the plane is of the form: $A \cdot x + B \cdot y + C \cdot z - D = 0$
 where A,B,C & D are constants and x,y & z are orthogonalized coordinates.

Plane	A	B	C	D	Atom	x	y	z	Distance	Esd
1	-0.1731	-0.4318	-0.8852	-10.1904	-----Atoms in Plane-----					
					C1	-0.4544	2.2868	10.4773	0.007	0.013
					C2	-1.8416	2.2065	10.7920	0.003	0.014
					C3	3.7685	5.9270	7.8666	0.015	0.014
					C4	3.3452	4.8104	8.5063	0.004	0.013
					C5	1.9164	4.6943	8.8755	-0.025	0.012
					C6	0.0722	3.4406	9.8119	0.007	0.011
					C7	1.4200	3.5541	9.5134	-0.011	0.011

Chi Squared = 7.

2	0.7204	0.4719	-0.5083	-2.1932	-----Atoms in Plane-----					
					S	2.5488	1.1011	8.9724	-0.012	0.007
					C8	2.3770	2.4665	9.9360	0.019	0.014
					C9	3.2276	2.5024	11.2474	-0.018	0.009
					C10	3.9725	1.1756	11.0141	0.011	0.016
					C11	3.7129	0.4226	9.9677	0.001	0.018

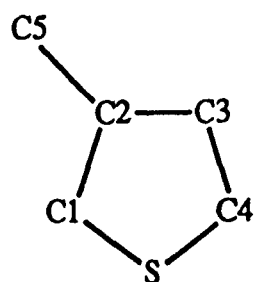
Chi Squared = 9.

Dihedral Angles Between Planes:

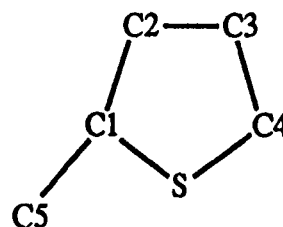
Plane No. Plane No. Dihedral Angle

1 2 83.02 +- 0.54

Table 14 Summary of Bond Distances and Bond Angles for PBT Model Compounds



- (1) N-3-thienylphthalimide
 (2) 3-phenoxyethylthiophene
 (3) 3-p-nitro-3-phenoxyethylthiophene



- (4) 9-(2-thienyl) anthracene
 (5) 2-(2-benzthiazolyl)-1-(2-thienyl) ethene
 (6) 2-(2-nitroethyl)thiophene

Table . Bond Distances of Thiophene compounds

Bond	(1)	(2)	(3)	(4)	(5)	(6)
S-C1	1.728(3)	1.710(1)	1.708(2)	1.715(2)	1.721(3)	1.691
S-C4	1.700(4)	1.711(1)	1.709(2)	1.685(3)	1.687(4)	1.675
C1-C2	1.416(5)	1.365(2)	1.394(3)	1.434(3)	1.389(4)	1.337
C2-C3	1.416(5)	1.428(2)	1.415(3)	1.457(3)	1.446(4)	1.493
C3-C4	1.370(4)	1.366(2)	1.372(3)	1.332(3)	1.357(6)	1.316
C2-C5	1.508(5)	1.496(2)	1.490(3)			
C1-C5				1.483(3)	1.450(4)	1.451

Table . Bond Angles of Thiophene compounds

Bond	(1)	(2)	(3)	(4)	(5)	(6)
S-C1-C2	108.1(2)	111.6(1)	109.7(1)	111.5(2)	112.0(2)	113.4(4)
C1-C2-C3	114.3(3)	112.5(1)	113.8(2)	107.9(2)	109.4(3)	109.1(4)
C2-C3-C4	111.3(3)	112.2(1)	111.6(2)	115.0(2)	114.2(3)	112.1(5)
C3-C4-S	112.6(3)	111.6(1)	109.7(1)	112.6(2)	111.6(3)	113.1(5)
C1-S-C4	93.6(2)	92.2(1)	93.2(1)	93.1(1)	92.7(2)	92.3(3)

COMPUTER-AIDED PROCESS PLANNING FOR GRINDING OPERATIONS

**Rakesh Govind
Professor
University of Cincinnati
Mail Location 171
Cincinnati, Ohio 45221**

ABSTRACT

Research was conducted on the development of a systematic approach for computer-aided process planning as applied to grinding operations. A decision making module using fuzzy sets was developed for grinding wheel selection. The module was tested on several industrial problems, with good success. A quantitative description of the grinding process was developed and a computer program for grinding cycle design was developed. Two cases have been presented here to demonstrate the results from the grinding cycle module.

Future work will involve the integration of the decision module and the grinding cycle design program with a process planning system, such as METCAPP.

INTRODUCTION

This final report discusses the grinding process planning problem starting with the part requirements and ending with the rough and finish feedrates, dressing parameters and cycle time to achieve the desired part quality. The important grinding process variables and their relationships are presented. These variables and equations

are used to calculate the rough feedrates consistent with the desired surface finish, the wheelwear corresponding to the desired stock removal and grinding time required.

The process planning problem starts with the part drawing or database describing the part dimensions, the tolerances, concentricity requirements, roundness, cylindricity or flatness, squareness, surface finish, surface integrity, cycle time and production requirements. This initial data must be processed to determine the appropriate machine tool(s), grinding cycle parameters, and inspection equipment to produce "finished parts" satisfying all specifications.

In planning grinding operations, it is necessary to define the various inputs and outputs, and to develop relationships between them. In the case of a typical grinding process, the relationships between the Machine Characteristics, the Grinding-Process Characteristics, and the Machine Input Variables is shown in Figure 1. Accordingly, the specific task for this project was to generate the proper feeds and speeds for the grinding-machine controller.

In planning grinding operations, it is important to distinguish between the Grinding Machine and the Grinding Process. Typical inputs to the Grinding Machine are:

feedrate or down feed, wheel and work speed, depth of dress, and sparkout time, as shown in Figure 2. The input to the Grinding Process is the normal force developed at the wheelwork interface, and the Wheel Sharpness. The tangential force, power, stock-removal rate, wheelwear rate, and surface finish are the output variables of the grinding process.

Grinding Machines can be classified according to the type of surface they produce. This includes Cylindrical (external and internal), surface, creep feed, tool grinders, and others. Figure 3 is a generalized representation of all grinding systems. The wheel and workpiece are connected to the machine slide and bed by system springs. The infeed rate is the input to the grinding system and the normal force F_n is the input to the grinding process.

GRINDING OPERATIONS

Each individual workpiece may require a number of surfaces to be ground, and if several of these surfaces can be created in one operation, high production efficiency would be achieved. High production efficiency can also be achieved if multiple operations can be performed for one staging of the workpiece thereby reducing the number of additional setups, part handling, and insuring squareness and concentricity.

Multiple grinding operations can be performed simultaneously by using a CNC grinder with two wheelheads mounted on the same cross-slide, or by using "compound wheels", where several cutting surfaces, or wheels, are provided on the same wheel-head.

For this report, the study was confined to single grinding operations. Later, as the module is developed further, the possibility of multiple grinding operations can be considered.

RESULTS

Selection of the Grinding Wheel:

Grinding wheel selection was achieved by developing a query-based decision making module using the Frill Logic Support System (Baldwin, 1989). The main element in grinding wheel selection is to select the type of bond, which is either based on the criteria of resiliency and form stability requirements, or the criteria of material removal characteristic. The approach used here was either a Dempster design or an overall consensus approach between the two different criteria's of resiliency/ form stability and material removal characteristics.

Fuzzy sets were specified in the beginning of the information base. A description of fuzzy set "high res" (for high resiliency) is as follows: On a resiliency scale (empirically derived) of 1 to 60, high resiliency can be defined as starting from 24 (with a zero % high resiliency value) to 60 (with 100% high resiliency value).

Using the fuzzy reasoning and Dempster design approach for bond selection numerous industrial problems were tried with very good results. An example problem with the result obtained is given below.

Example: The problem involves the bond selection for the grinding wheel which gives high form, low resiliency and precise geometry.

Using the Dempster design approach, "Rubber" as a bond material was found to be the most favorable, with 94% confidence. Using the overall consensus approach, the same material (Rubber) was found to be the most favorable with 72% confidence.

Quantitative description of the Grinding Process:

Grinding cycle analysis is required for every grinding operation. It involves analysis of the grinding parameters with regards to the grinding machine stiffness and power,

and grinding wheel specifications. In general, the grinding cycle analysis can be subdivided into two parts: (1) general analysis (common to all types of grinding); and (2) specific analysis, depending on the type of grinding operation, such as internal, surface, centerless, and center-type.

Table 1 details the quantitative equations used to describe the grinding operation and arrive at a grinding cycle design. Plots A through H have been attached in Appendix I. A computer program was developed to implement the equations (Table 1) and hence automate the task of grinding cycle design.

Table 2 gives a typical user consultation example of grinding cycle design using the quantitative equations.

Computer-Aided Process Planning for Grinding:

Based on the equations developed in the previous section, the grinding performance of various configurations can be analyzed using the computer programs developed in this project study. Grinding cycle parameters can be generated in terms of geometrical input data.

Two case studies have been presented here to demonstrate the results that have been obtained for computer-aided process planning for grinding operations.

Case 1: Grind a 24 mm hole in AISI52100 and M50 steel. The grinding wheel selection module had recommended two wheels, namely 22.22 mm and 17.78 mm diameter. This data was then entered into the grinding cycle analysis module, as summarized in Table 3.

The grinding cycle analysis results are given in Table 4. Note that the threshold force intensity for the new large wheel grinding AISI52100 is four times as large as that for the "used" wheel because of the larger diameter. This causes the "new" wheel to cut less freely and thus a 70% reduction in feedrate or force from the breakdown value of the new wheel.

For the M50 material, there is a great difference in active cycle time for the "new" and "used" wheels. This is again caused by the much larger threshold force intensity.

Case 2: Grind a 75 mm hole, 125 mm long with a 0.3 mm radial stock using a 64 mm diameter "new" wheel and a 50 mm diameter "used" wheel. Table 5 gives the input data.

Table 6 gives the grinding parameters and output performance for both reciprocate roughing and multiplunge roughing. The program gives the amount of wheelwear expected, the finish feedrate to achieve the desired

surface finish, and the active grind time for reciprocate roughing (feedrate grinding) and for multiplunge roughing (force adaptive) methods.

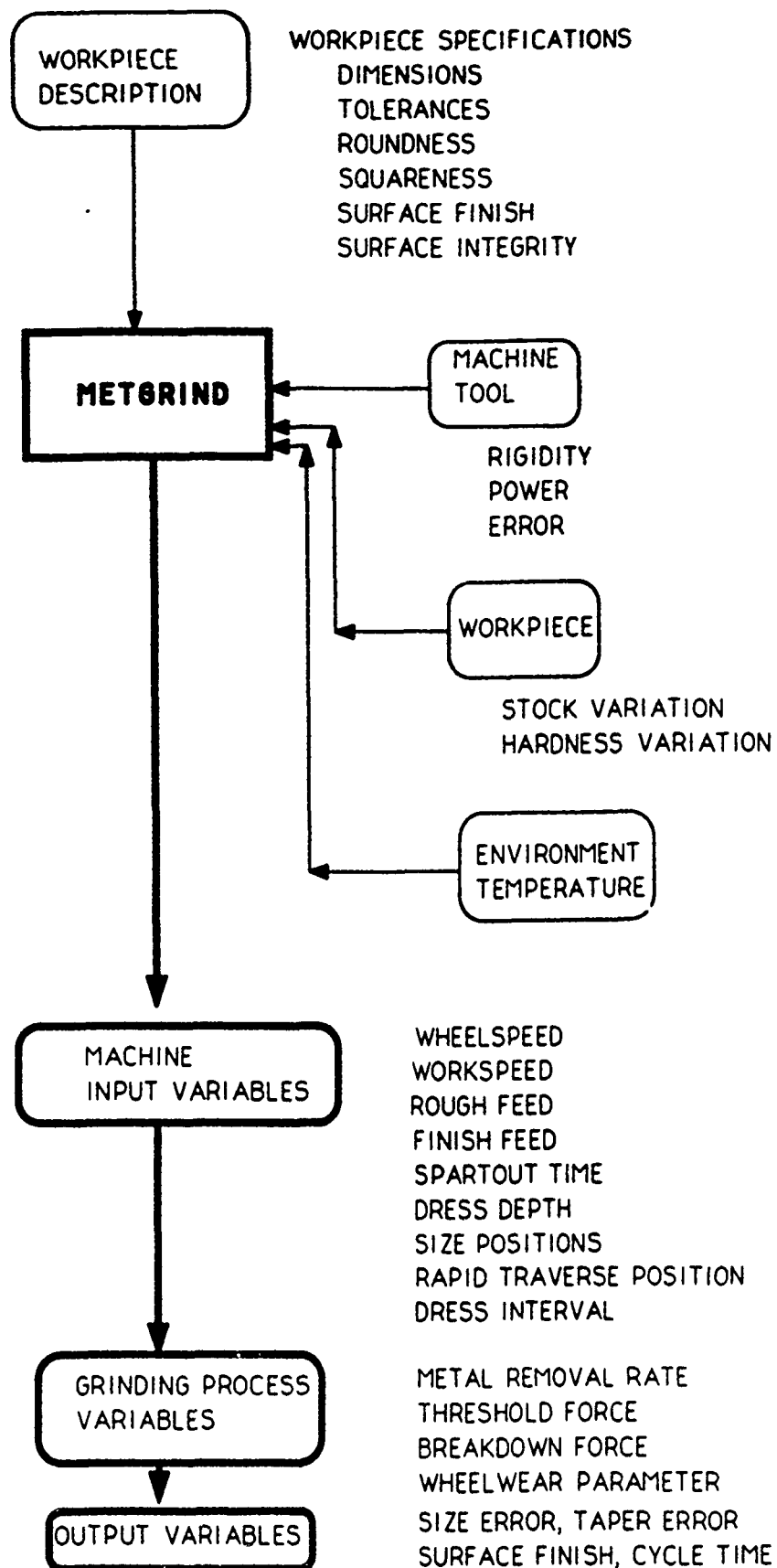
CONCLUSIONS

A decision making module for grinding wheel selection was developed using the Frill Logic Support System. The system was tested on several industrial problems with good success. The grinding wheel selection was then used in the grinding cycle analysis module for calculating the grinding cycle operating parameters. This module was a FORTRAN program that used quantitative equations to calculate the desired parameters.

Two case studies have been presented to demonstrate the computer-aided process planning approach for grinding operations.

Further development efforts will focus in integrating the grinding wheel selection and grinding cycle analysis module with the process planning system METCAPP. This will enable the METCAPP system to provide detailed information on all grinding operations as required by the process plan. It is expected that this system integration will be achieved as a continuation of this project, through the Research Initiation Program.

FIGURE 1: FLOWCHART FOR GRINDING PROCESS PLANNING

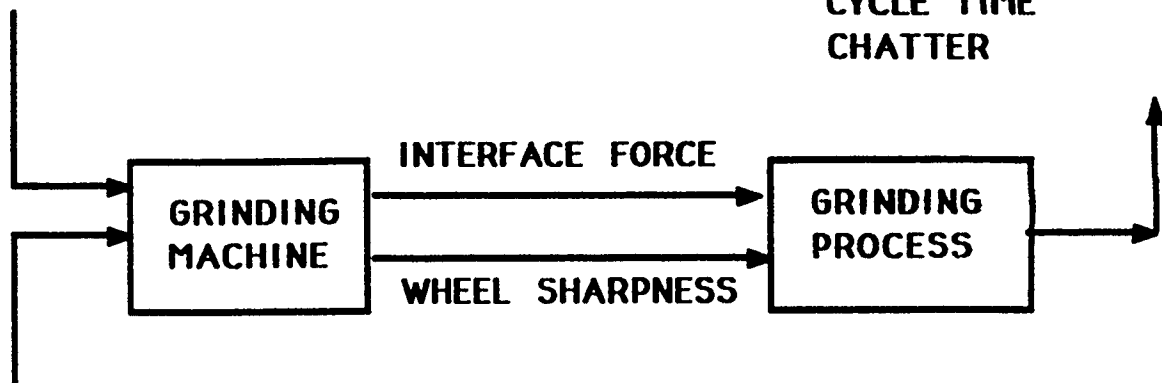


INPUTS

**FEEDRATE
WHEELSPEED
WORKSPEED
DRESS DEPTH
DRESS LEAD
SPARKOUT TIME**

OUTPUTS

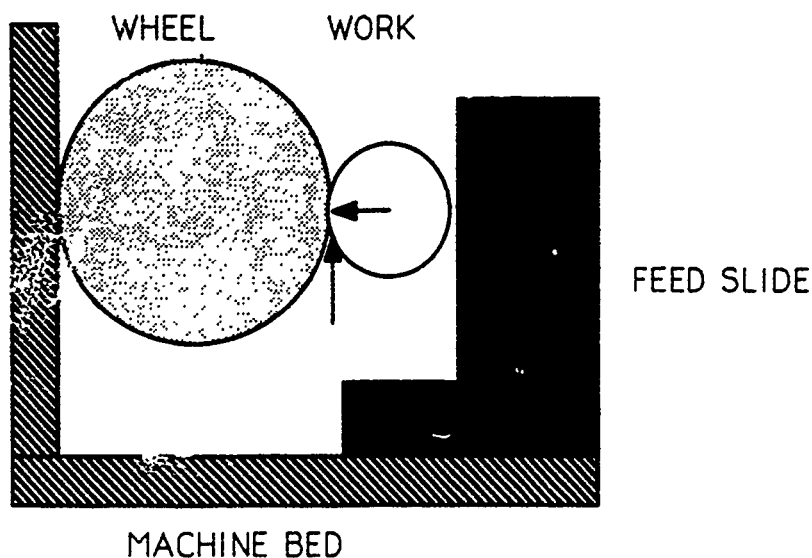
**CONCENTRICITY
ROUNDNESS
TAPER
SIZE TOLERANCE
SURFACE FINISH
SURFACE INTEGRITY
CYCLE TIME
CHATTER**



**STOCK VARIATIONS
HARDNESS VARIATIONS
SYSTEM RIGIDITY
STOCK RUNOUT**

FIGURE 2. INPUT/OUTPUT VARIABLES FOR GRINDING MACHINE AND GRINDING PROCESS

FIGURE 3: GENERALIZED REPRESENTATION OF ALL GRINDING SYSTEMS



- F_n FORCE NORMAL TO CONTACT SURFACES PER INCH OF WHEEL WIDTH
- F_t FORCE TANGENT TO CONTACT SURFACES PER INCH OF WHEEL WIDTH
- f_t WORKPIECE INFED RATE
- F_{bd} THRESHOLD FORCE INTENSITY, WHEEL
- F_{th} THRESHOLD FORCE INTENSITY, WORKPIECE
- V_f FEEDRATE OF CROSS SLIDE
- V_s SURFACE SPEED OF GRINDING WHEEL
- v_w RATE OF RADIAL WORKPIECE REMOVAL
- V_w SURFACE SPEED OF WORKPIECE
- v_s RATE OF RADIAL WHEEL WEAR
- Z_s VOLUMETRIC RATE OF WHEEL WEAR
- Z_w VOLUMETRIC RATE OF STOCK REMOVAL OR MATERIAL REMOVAL RATE
- Y WHEEL-WEAR REMOVAL PARAMETER
- Y_w METAL REMOVAL PARAMETER
- a DEPTH OF GRIND PER PASS
- b WIDTH OF GRIND
- bc CROSS FEED RATE (SURFACE GRINDING)
- D_s DIAMETER OF WHEEL
- D_w DIAMETER OF WORKPIECE

TABLE 1: EQUATIONS USED TO DESCRIBE THE GRINDING OPERATION

Knowledge Base	Database	Algorithm	Remarks
1 Find $(Q' \times U)$ available 2 Select Q' value 3 Find U using Plot A 4 Check $(Q' \times U)_{act} \leq (Q' \times U)_{ava}$ 5 Find $(R)_{act}$ from Plot B 6 Check $(R)_{act} < (R)_{des}$ If condition 6 not met Then Lower Q' and Repeat Steps	Plot A: $(Q' \text{ Vs } U)$ Plot B: $(Q' \text{ Vs } R)$	$N = Q' \times W \times U$	Constraint #1: Power based on Wheel Width Constraint #2: Surface Finish desired
7 Find $FN1$ 8 Find $(FN1/SS)$ 9 Check $\therefore (FN1/SS) \leq \text{Size Tol}$ If condition 9 not met Then Lower Q' and Repeat Steps	Table A: MU based on Workpiece Hardness and Material	$FN1 = (33000 \times Q' \times W \times U) / (MU \times V_s)$	Constraint #3: Static Stiffness check
10 Find S_f and S_r 11 Find (L/T) rate			Constraint #4: Minimum Set-Up Cost

TABLE 1 (Continued): EQUATIONS USED TO DESCRIBE THE GRINDING OPERATION

Knowledge Base	Database	Algorithm	Remark
1. Select grain type using Plot C	Plot C: Grain type - ((Mat., Mat. Hard))	N.A	<u>Grain type selection</u>
2. Select grit type using Plot D	Plot D: Grit type - ((DE-I.D/O.D))	$DE = \frac{Dw \times Ds}{Dw + Ds}$	<u>Grit type selection</u>
3. Select bond type using Plot E	Plot E: Bond type - ((F.S., R))	N.A	<u>Bond selection</u> F.S: Form stability R: Resiliency
4. Select structure using Plot F 5. Adjust structure based on actual RPM	Plot F: Structure - ((DE, d, RPM)) RPM : 6500 or 8000	N.A	<u>Structure selection</u>

N.A : Not Applicable

TABLE 1 (Continued): EQUATIONS USED TO DESCRIBE THE GRINDING OPERATION

Knowledge Base	Database	Algorithm	Remark
1. Select coolant using Plot G	Plot G: Coolant type - $f(Q)$, Cleanliness	N.A	Coolant type selection
2. Select specific flow rate using Plot H	Plot H: Sp. Flow rate VC - $f(d)$	N.A	Flow rate selection
3. Calculate the fluid pressure (VC)	N.A	$VC' = VC + W$	N.A

N.A: Not Applicable

TABLE 1 (Continued): EQUATIONS USED TO DESCRIBE THE GRINDING OPERATION

Knowledge Base		Database	Algorithm	Remark
1 Find DE_{new}	$DE_{worn} \times 1.5$	Decrease of DE by a factor of 1.5 causes wheel to act one grade softer	N.A	Wheel soft acting Increase wheel hardness by the ratio amount
2 Find - Total grinding cycle time (min)		N.A	$T_m = T_f$ $T = \frac{3.14 D \times S}{Q'}$	Cutting time cal. $T_c = T_r + T_m + T_f + 0.1$

N.A : Not Applicable

Remark: The remaining steps are identical to the steps involved for centerless grinding.

NOMENCLATURE FOR TABLE 1

Q'	: Specific material removal rate in in ³ /min/in
U	: Specific energy in hp/in ³ /min
W	: Wheel width in inches
Ra	: Surface finish in micro-inches
FN1	: Normal force in lbs
SS	: Static stiffness in lbs/inch
MU	: Coefficient of friction
Vs	: Grinding wheel speed in ft/min
S	: Total stock in inches
Sf	: Finish stock in inches
Sr	: Rough stock in inches
L/T	: Through feed rate in in/min
DE	: Equivalent diameter in inches
Ds	: Diameter of grinding wheel in inches
Dw	: Diameter of workpiece in inches
I.D	: Inner diameter in inches
O.D	: Outer diameter in inches
F.S	: Form stability
R	: Resiliency
VC'	: Specific flow rate in gal/min/inch
VC	: Fluid pressure in gal/min
Tc	: Cutting or cycle time in mins
Tr	: Rough machining time in mins
Tm	: Medium machining time in mins

NOMENCLATURE FOR TABLE 1 (continued)

Tf : Finish machining time in mins

TABLE 2: TYPICAL USER CONSULTATION FOR A GRINDING CYCLE DESIGN

Types of grinding areas:

1. Centerless Grinding
2. Center type Grinding
3. Internal Grinding
4. Micro-centric Grinding
5. Cam Grinding

Select your grinding application area : [3]

Please ANSWER the following queries..

Enter the workpiece material code

1. Cast iron/steel
2. Tool steel
3. Super alloys

: [2]

Hardness (HRC) : [62]

Stock (inches) : [0.012]

Surface finish (micro inches) : [16]

Tolerance (inches) : [0.0005]

Grinding wheel speed (ft/min) : [12000]

Grinding wheel diameter (inches) : [1.5]

TABLE 2: TYPICAL USER CONSULTATION FOR A GRINDING CYCLE DESIGN
(Continued)

WELCOME
TO
INTERNAL GRINDING MODULE

Please ANSWER the following queries:

Bore size (inches) : [1.85]

Bore length (inches) : [0.75]

Enter the following:

Finish stock (inches) : [0.001]

Medium stock (inches) : [0.002]

The following is the output from the program

Equivalent diameter (D_e) = 7.9286 inches

The ideal wheel speed (V_s) = 9000 ft/min

Total grinding time (t_g) = 0.166 min.

Rough Grinding Calculations:

Specific energy (U) = 15.427 hp/in³/min.

Horse power (HP) = 4.936 hp

Coefficient of friction (μ) = 0.246

Normal force (F_{N1}) = 55.18 lbs/inch

TABLE 2: TYPICAL USER CONSULTATION FOR A GRINDING CYCLE DESIGN
(Continued)

Wheel hardness and structure selection : K10

Enter the available HP = [6]

HP requirement O.K

Finish Grinding Calculations:

Specific energy (U) = 19.9 hp/in³/min

Horse power (HP) = 1.59 hp

Normal force (FN1) = 17.8 lbs/inch

Wheel hardness and structure selection : F14

The available static stiffness should be greater
than 110369.65 lbs/inch.

$Q' = 0.11 \text{ in}^3/\text{min}/\text{in}$

J O B C O M P L E T E D

Table 3: Input data for Case 1 example

New Wheel diameter	22.22 mm
Used Wheel diameter	17.78 mm
Grit size	80
Wheel Hardness	K
Wheel Structure	6
Bore diameter	24.13 mm
Length of Bore	25.4 mm
Rockwell hardness	63 C
Desired Surface Finish	0.375 um
Max. Stock	0.813 mm
Min. Stock	0.711 mm
Rough Stock Runout	0.254 mm
Final Runout	5.0 um

Table 4: Grinding Cycle analysis results for case 1 example

	Materials			
	AISI52100		M50	
	Used Wheel	New Wheel	Used Wheel	New Wheel
Stock required for roundup	0.439 mm	0.421 mm	0.456 mm	0.254 mm
Roundup time	3.06 sec	3.12 sec	5.82 sec	19.56 sec
Rough Grind time	3.36 sec	3.54 sec	6.24 sec	28.62 sec
Dress Time	0.67 sec	0.67 sec	0.67 sec	0.67 sec
Sparkout time	2.00 sec	0.80 sec	2.10 sec	2.10 sec
Active cycle time	6.03 sec	5.01 sec	9.01 sec	29.40 sec
Rough Grind Feedrate (mm/sec)	0.13	0.123	0.0711	0.0137
Wheelspeed	30,000	30,000	30,000	30,000

Table 5: Input data for Case 2 example

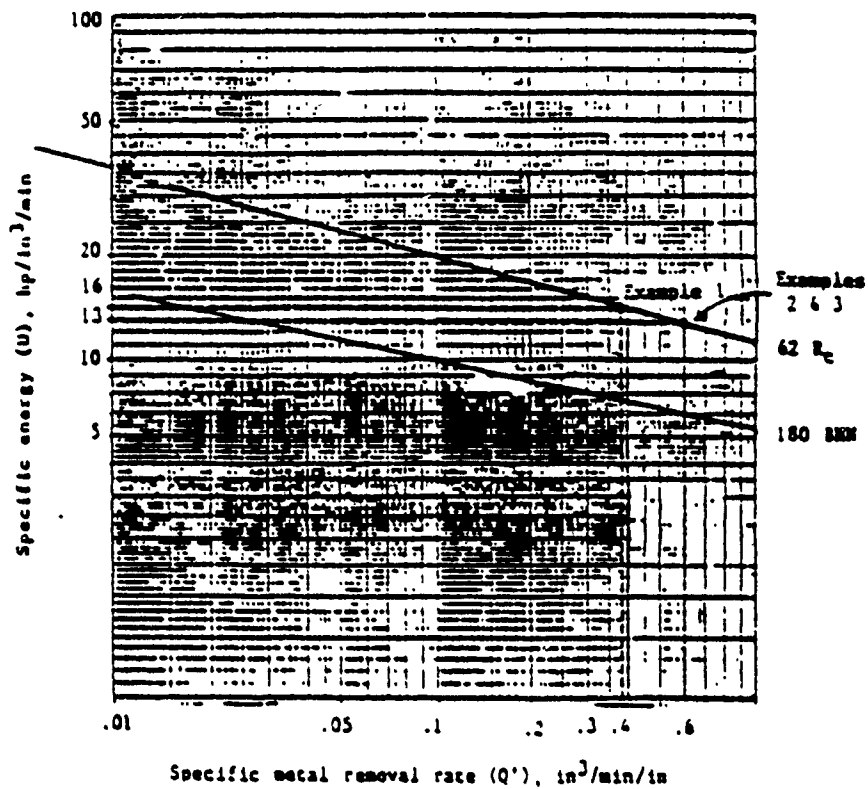
New Wheel diameter	64 mm
Old Wheel diameter	50 mm
Grit Size	80
Surface Finish	80 um
Length of Bore	125 mm

Table 6: Output of Grinding Cycle Analysis for Case 2 example

	New Wheel	Used Wheel
Grinding Force (n)	427.8	427.8
Rough Feedrate (um/sec)	49.7	90.2
Finish Feedrate	28.8	47.6
Sparkout time (sec)	2.4	2.5
Active Grind time (sec) (feedrate)	45.6	35.5
Active Grind Time (sec) (force adaptive)	22.8	17.6

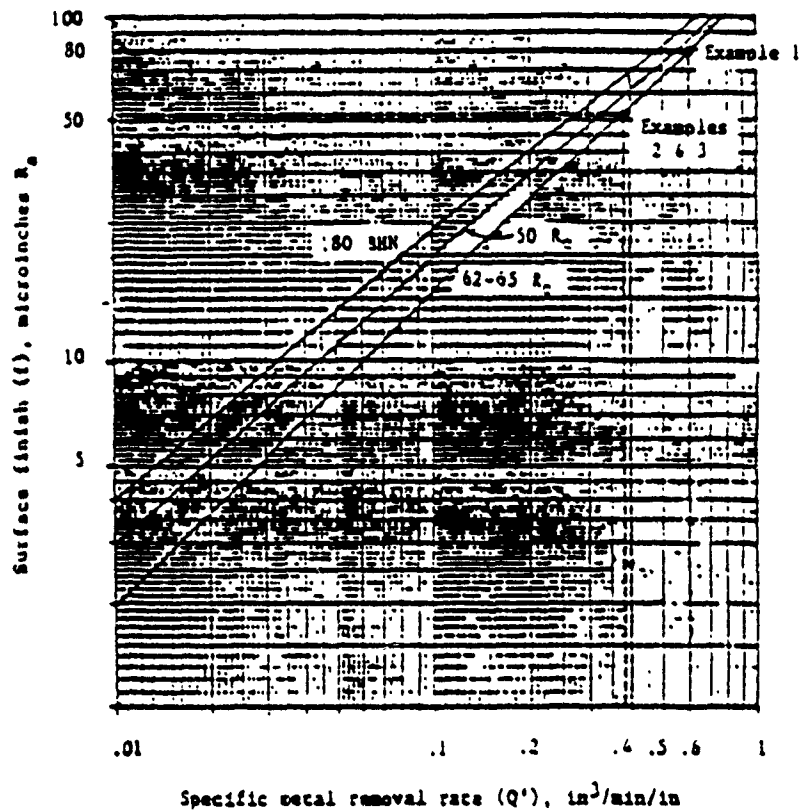
APPENDIX I: PLOTS A THROUGH H AS REFERRED TO IN TABLE 1

OD and ID Grinding with Conventional Abrasives
Carbon Steel and Ball Bearing Steel (9000 sfm)

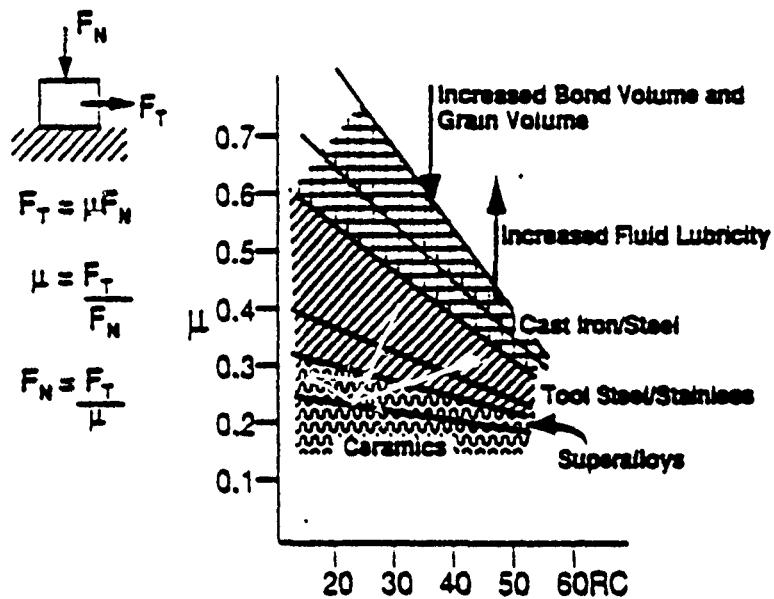


Plot A: Machine Power Limitation Diagram (Q' Vs. U)

OD and ID Grinding with Conventional Abrasives
Carbon Steel and Ball Bearing Steel (9000 s/m)

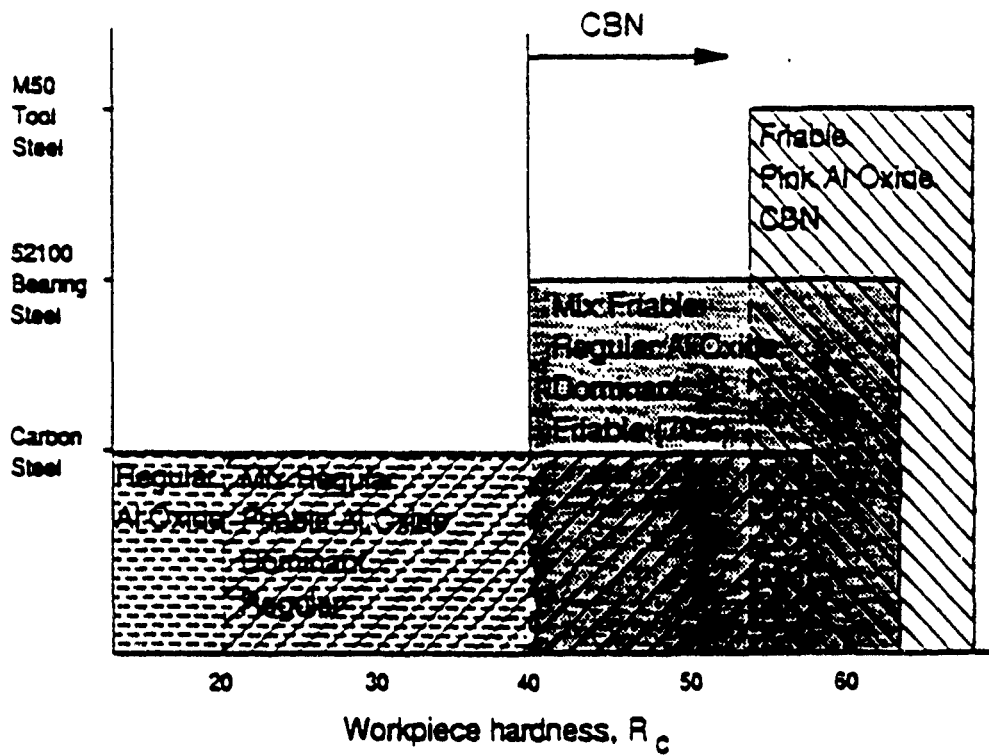


Plot B: Surface Finish Relationship to Specific Metal Removal Rate (Q' Vs. R_a)

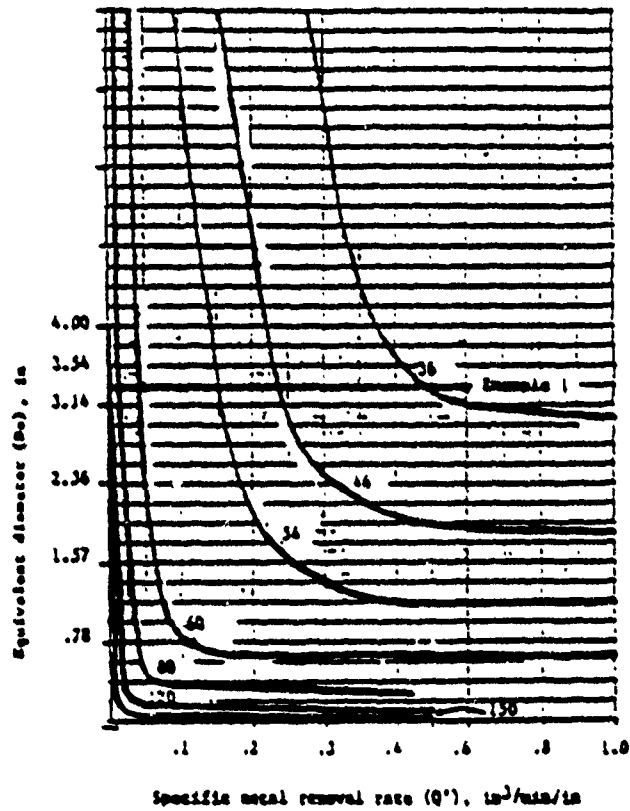


- 1 Determine F_T from Power Measurement
- 2 Estimate μ from Chart
- 3 Calculate F_N

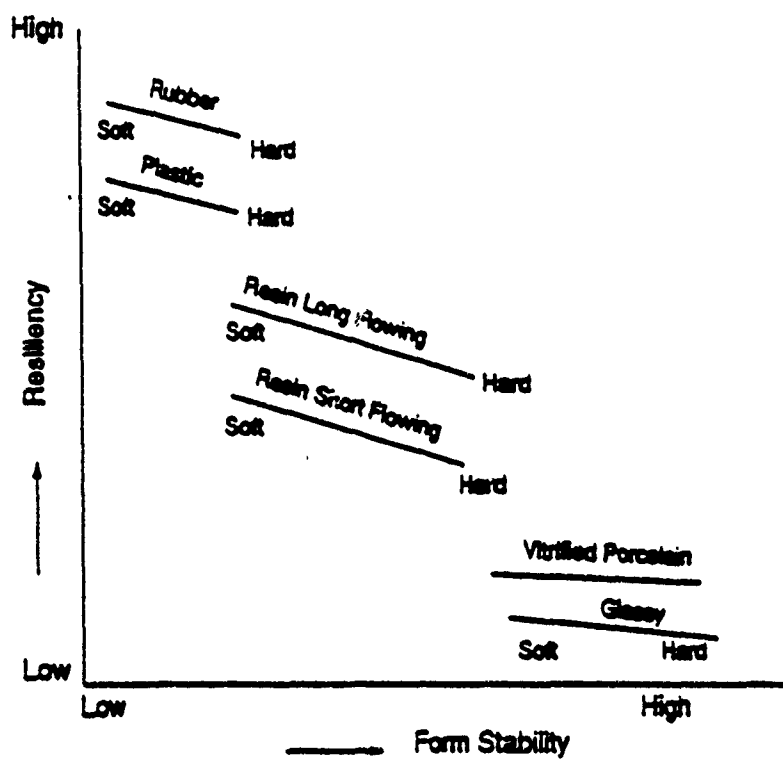
Table A: MU (Coefficient of Friction) based on Workpiece Material Hardness and Material



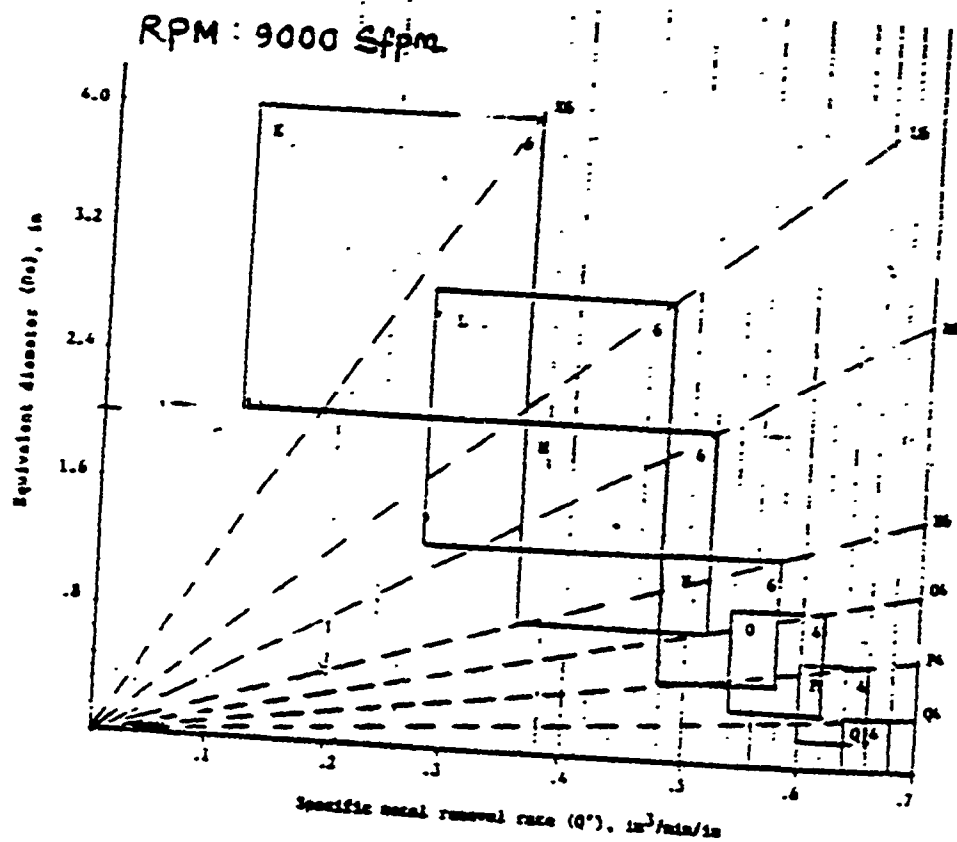
Plot C: Grain Type Selection Based on Material and Material Hardness



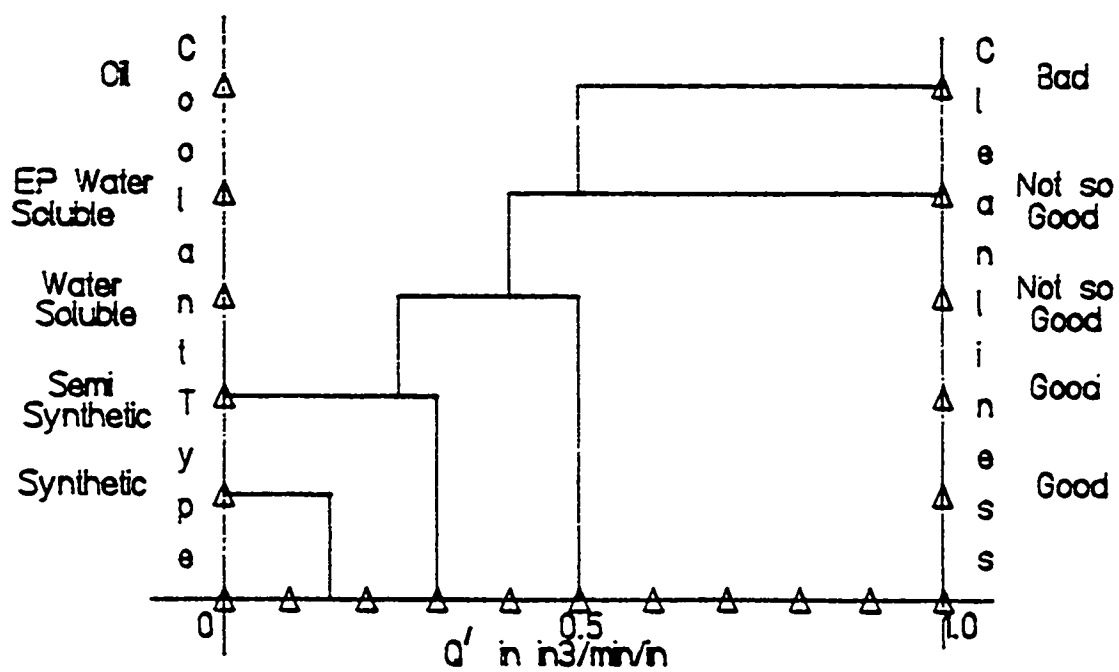
Plot D: Grit Type Selection Based on Material and Material Hardness



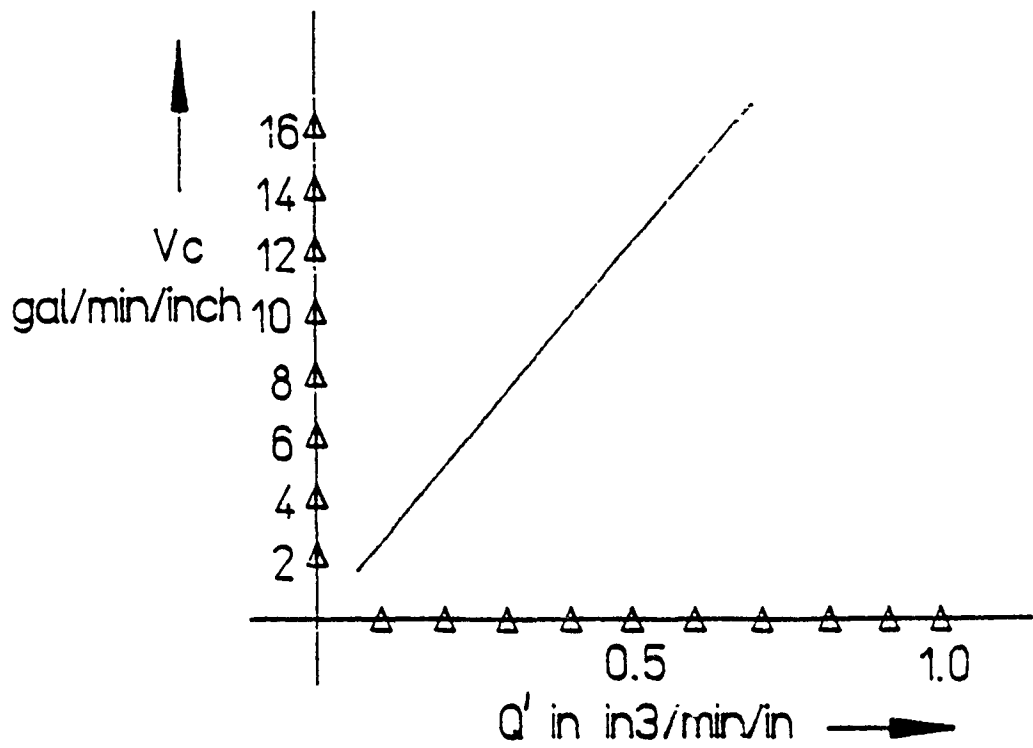
Plot E: Bond Type Selection Based on Resiliency and Form Stability Desired



Plot F: Structure Selection Based on D_e , Q' , and RPM



Plot G: Coolant Type Selection Based on Q' , and Cleanliness



Plot H: Specific Flow Rate Selection Based on Q'

TRANSMISSION ELECTRON MICROSCOPY of DEFORMATION at the INTERFACE of Ti-6-4 // SCS6 SiC FIBER COMPOSITES

WARREN J. MOBERLY
Assistant Professor at Stevens Institute of Technology

Abstract

Numerous FEM calculations have predicted plastic deformation to first occur at the interfaces of Ti-alloy-matrix // SiC-fiber composites, both as a result of thermal processing and/or as a result of applied external stress. This research utilizes TEM to experimentally observe the early stages of deformation at the interface region of a Ti-6Al-4V // SCS6 SiC composite containing three parallel, continuous fibers. The as-processed composite, which displayed a less extensive chemical reaction at the interface as compared to that typically reported, exhibited dislocations in the α -Ti grains near the interface only in regions between closely spaced fibers. In some grains these dislocations appeared in "rows" parallel to, and displace ~ 0.5 microns from, the interface. After being pulled in tension to $\sim 1/2\%$ plastic strain, significant dislocation multiplication had occurred throughout all of the matrix. A slightly higher dislocation density was observed in the α grains of the matrix region between fibers. Grains contiguous to the interface exhibited dislocations in both "rows" parallel to and perpendicular to the matrix / fiber interface. However, only the dislocations in rows perpendicular to the interface exhibit pile-ups at grain boundaries. In addition, significant planar slip (often associated with oxygen impurities in Ti alloys) was observed in the matrix grains in close proximity to the interface, especially between fibers.

Introduction

The purpose of this summer research was to use transmission electron microscopy (TEM) to observe deformation at the interface of Ti-6 wt.% Al-4 wt.% V // SCS6 (SiC) fiber composites. A primary concern of this study was to determine the influence of "constrained"¹ deformation occurring at and/or near fiber/matrix interfaces. This constrained deformation is addressed in light of thermal stresses arising due to coefficient of thermal expansion (CTE) mismatch between matrix and fiber², localized deformation during processing, intermetallic phases forming at the interface due to chemical reaction between fiber and matrix^{3 4 5 6 7 8 9}, geometrical spacing of fibers, localized deformation due to fiber fragmentation, and of course difference in strength of fiber and matrix.

The broad scope of this problem must consider many aspects of deformation: from that occurring during thermal processing and/or as a result of reactions occurring due to interface instability, to deformation and interface breakdown occurring during thermal cycling which will be incurred during use as a structural component of aircraft, to deformation occurring due to the load bearing aspects of structural components, and finally to failure modes that may be incurred. Typically breakdown of the composite structure, both physically and chemically, occurs at its weakest juncture: the interface. Either of the basic components of the composite, the matrix and the fiber, is alone easily studied, modelled and characterized for its properties. However, the interfaces tend to control the properties when these two components are in composite form. Thus this study uses microscopy to focus on the interfacial region and establish the role the interface plays during the onset of plastic deformation.

An extensive part of this summer research was promoted as a learning experience, with regards to the defined problem, the material system in general, and the development of new techniques in TEM analysis, (both for experimental acquisition and for computer modeling). Although most researchers of composites consider constrained deformation at interfaces in composites as a given, little microstructural analysis has been conducted to experimentally elaborate on the deformation at the interface. The present material system, Ti-6-4 // SCS6, is considered because of both the relative ease of producing these composites and the extensive knowledge available on each of the constituents. The chemical stability of this interface has also been characterized by many researchers. In addition, understanding this material system is seen as a prelude to studying and understanding deformation at the interfaces of intermetallic-matrix composites (for example, with Ti-11 wt.% Al-14 wt.% Nb and other titanium aluminides combined with various fibers). Much of the development of TEM analysis of the interfaces of composites shall be discussed in this report. Due to the advent of computers, TEM analysis becomes an interactive process between the operation of the TEM and computer analysis. Computer image simulation has become a necessary component of the analysis of high resolution imaging¹⁰. Likewise, traditional analytical microscopy can take advantage of simulation of electron diffraction¹¹ aspects (selected area diffraction patterns, convergent beam electron diffraction patterns, Kikuchi maps, etc.) to help interpret TEM results and even predefine the TEM experiment.

A major component of any TEM analysis is the preparation of TEM specimens. This is especially true when particular microscopic regions of material are desired to be analyzed. Without successful thinning of material to where it is electron transparent (generally a difficult, time-consuming, and learning process), the actual TEM analysis

becomes impossible. Another major consideration of the TEM specimen preparation is the possible alteration of the material area of interest during the specimen preparation. Such specimen preparation artifacts, whether altering the chemistry, crystal structure, and/or the physical microstructure, must be determined and accounted for, if they are not entirely prevented. Thus a major portion of this research involved establishing methodologies for preparing different TEM samples to secure analytical results of different aspects of the composites. A more detail description of the TEM sample preparation procedures is provided in Appendix I.

One aspect of this research considered both possible artifacts associated with TEM sample preparation in conjunction with ease of producing an abundance of material of interest which is electron transparent. Some samples were observed using the High Voltage Electron Microscope, operated at 1500 keV, at the National Center for Electron Microscopy, Lawrence Berkeley Laboratories, Berkeley CA. Such a high voltage TEM, as compared to traditional microscopes that operate at 100 to 200 keV, affords the opportunity of more "electron transparency" (i.e. thicker regions of material can be penetrated by the 1500 keV electrons.) One consideration is the trade-off between the ease of preparing a thicker sample (and/or the availability of more region of material that is electron transparent) which can be analyzed by HVEM versus the lesser availability of HVEM scopes. In addition, the possible additional artifacts of radiation damage caused to the samples by the higher energy electrons must be addressed. However, the more motivating factor for utilizing the HVEM in this research was to address reports in the literature¹² which claim the need for performing HVEM in order to obtain correct results on the extent of deformation and dislocation densities in composites. (It has been well established that, given a driving force, a dislocation will try to climb to a surface, annihilate itself, and thereby lower the strain energy of the system. It has been long feared that a TEM sample, with the top and bottom surface being so close, will lose many of its dislocations to the surfaces, hence causing TEM analyses to always underestimate the actual dislocation density of a material.)

Literature Review

This research historically derives its basis from research by Ashby, *et. al.*¹³ which considered ductile wires in a brittle matrix. In that study cracks were induced into the matrix surrounding the wire. When pulled in tension, the wires were constrained so that necking was hindered. Thus the Von Mises stress was lowered, and a higher applied stress was required in order to cause plastic flow in the metal wires. In addition, Finite

Element Modelling (FEM) has shown that the highest stress is actually displaced radially away from the interface¹⁴.

The material system in the present research has a ductile (and weaker) matrix with brittle high strength fibers. When FEM is used to model the stresses surrounding the SiC fibers in a Ti matrix¹⁵, the effective residual stress due to coefficient of thermal expansion (CTE) mismatch is calculated as decaying away from the interface. In such composites, where the constrained deformation analysis of Ashby is not considered, it is expected that when a tensile stress is applied the first deformation occurs at the interface.

The concepts of constrained deformation play a role in two aspects of this material system. When two fibers are closely spaced, there arises a region of ductile material mostly surrounded by brittle material. In these matrix regions between fibers, the geometrical configuration approaches that of Ashby research, and constrained deformation may be expected (i.e. plastic deformation may be expected to occur first at a spacing away from the interface). The second source of constrained deformation occurs after pulling the tensile sample past the fracture strain of the fibers. As each fiber fragmentation event occurs, the load that was carried by the fiber must be transferred to the surrounding matrix. (The local stress is actually highest in these regions, as the fiber no longer supports a load across the fracture.) Thus the matrix region in the vicinity of a fiber fracture exhibits a constrained stress state. When these two aspects are combined, one considers the stress on a thin section of matrix material which is sandwiched between two fractured fibers. When stressed in tension, this thin region of matrix wishes to neck; however, the constraining fibers attached to the matrix above and below the location of the fracture constrain the matrix material and lower the effective stress. Thus the matrix can support a higher than expected load after fiber fragmentation has occurred.

Other composites comprising a ductile matrix have been studied with TEM to observe the occurrence of deformation (i.e. dislocation motion) in the region closest to the fiber (or strengthening particle). Certain researchers¹⁶ claim that high voltage electron microscopy in thick regions of TEM samples must be conducted in order to obtain proper results of dislocation densities that correlate with the mechanical test data. The dislocations close to the composite interface, after being thinned to form the TEM sample, are believed subject to annihilation with a free surface (and/or the interface). Such may be the case for composites where the strengthening phase is smaller than the grain size of the matrix phase, and typically embedded in the matrix. *In situ* HVEM heating experiments on thicker regions of Al / SiC composites have even shown the emission of dislocations from the particle (or fiber) interface as the residual thermal stresses build rise above the yield stress of the Al upon cooling^{17 18}.

For the present composite system, the grain size is two orders of magnitude smaller than the fiber diameter. Thus the emission of dislocations from the interface of the fiber may not be expected in all grains, especially as many α grains are not contiguous with the fiber interface. However, the presence of different intermetallic phases at the interface warrant the use of HVEM to establish whether or not dislocations annihilate themselves with free surfaces and interfaces in thin TEM samples. In addition, the large size of the fiber, relative to the α grain size, will result in a similar microscopic stress state at the interface in many neighboring grains. Thus the relative orientation of each grain will dictate the nature of dislocation pile-ups within each grain.

Experimental Procedure

For this study composites were processed with three parallel fibers in a metal matrix, which were subsequently pulled in tension. The fibers used for this experiment were Silicon Carbide (SCS6) fibers manufactured by Textron Specialty Materials¹⁹. [These fibers are processed with successive Chemical Vapor Deposited coatings, with the outermost coating being enriched in carbon. The purpose of these outer, amorphous coatings is to prevent the formation of detrimental notches while handling fibers, which in turn would result in premature fracture of the fibers.] The fibers were laid in a row between two rolled metal foils of Ti-6Al-4V alloy, vacuum hot pressed and then hot-isostatic pressed (HIP) at $\sim 1200^\circ\text{C}$ for two hours. Finally, tensile specimens were spark cut with a gauge section that is 3 mm by 2 mm by 2 inches long. Considering the entire cross section of the tensile bar, the fibers made up only 0.8% of the volume fraction of the gauge section. Since the fibers were placed with only a small separation between them, the "localized" volume fraction of fibers (i.e. based on the separation between fibers) was as high as 47%. As has been reported in previous research²⁰, the temperature of processing results in a chemical reaction between the SCS6 fibers and the Ti (plus Al and V) alloy. Some contradicting reports²¹ have been published with regards to the crystallography and sequence of layers of the various phases that form at the interface. In addition, the extent of formation of phases such as titanium silicide (Ti_5Si_3) and titanium carbide is dependent on the extent of thermal processing. As shall be discussed in more detail, the thermal history experienced while processing these composites appears to limit the extent of formation of these interface phases as compared to microstructures typically described in reported literature.

The mechanical testing was performed in conjunction with a study on fiber fragmentation. [The principal investigators of the fiber fragmentation studies at Wright Patterson are S. Krishnamurthy and I. Roman.] In this study, fiber fragmentation is

monitored during tensile testing by using acoustic emission techniques. The primary purpose of this research is to establish which acoustic emission signals correspond to individual fiber fragmentation events. Correlating acoustic signals with secondary fragmentations and other deformation modes (such as the onset of slip deformation in the matrix and possible slippage at the fiber/matrix interface) in composites is also of interest²². In order to correlate the acoustic emission research and this TEM study of deformation at the fiber/matrix interface, the tensile tests were all performed while being monitored for acoustic emission.

Due to the difficulty and time consumed to process material, and the limited time allotted for this summer research program, only two successful tensile tests were performed of the composites containing three fibers. One sample was pulled in an increasing load tensile test until failure occurred at a total elongation of 19%. Numerous fiber fractures occurred in this sample; however, load transfer to the Ti-6-4 matrix prevented overall rupture of the tensile bar until significant necking had occurred. The second tensile specimen was pulled in tension past yielding of the matrix and stopped just after three acoustic signals were observed. A metallographic analysis, with repeated tests, is now being conducted to establish if the three acoustic signals correspond exactly with three fiber fragmentation events, if the fragmentation events occurred in each of the three fibers, and if the three fractures occurred in the same local region. The total plastic strain obtained in the second tensile specimen was 0.5% to 0.6%.

Experimental Results & Discussion

Mechanical Test Results

Room temperature tensile tests were conducted while being monitored for acoustic emission. (These mechanical tests are part of an ongoing project of S. Krishnamurthy and I. Roman at Wright Patterson AFB.) The stress / strain curve acquired for the 1/2% deformed sample is presented in Figure 1a. The dashed straight line indicates the 0.2% offset yield strength to be ~950 MPa. The onset of yielding occurs with limited strain hardening. The stress / strain curve acquired for the 19% deformation sample, not presented, exhibited minor strain hardening prior to necking. (It is noted that the presence of only three fibers in this metal matrix composite results in a stress / strain behavior nearly identical to the matrix alloy.) The associated acoustic emission spectrum, Figure 1b, exhibits little activity until ~1.2% strain (of which >0.7% is calculated to be elastic strain), when a strong signal is observed. It is noted that this acoustic signal occurs after the 0.2% offset yield strain on the corresponding stress / strain curve. A horizontal expansion of this

spectrum (Figure 1c) indicates that actually three signals are detected at nearly the same strain. These strong acoustic signals are presumed to be the result of fiber fragmentation events. (Further studies are being conducted to see if the three fragmentation events are in neighboring regions of the three individual fibers, in neighboring regions of a single fiber, or randomly located throughout the fibers. Figure 2 is a zerox copy of an optical micrograph of a single fiber composite sample deformed to final tensile fracture, where the fiber has undergone numerous fragmentation events. Since many of the fragmentation events do not represent "clean breaks" of the fiber, as would occur in a free-standing fiber, it is probable that fragmentation events, and associated acoustic emission signals, occur in a collective fashion, possibly as a result of shock waves vibrating back and forth. The importance of observing the first fiber fragmentation events, and of ideally performing a TEM analysis in the matrix regions near these first fiber fragmentation events, is readily apparent.)

Transmission Electron Microscopy Results

Over ten different TEM samples, prepared from the as-processed, ~1/2% plastic deformation, and ~19% deformed composites, were extensively analyzed during this initial research period. The 19% deformation sample exhibited high dislocation densities, such that observing individual dislocations, or even rows of dislocations was essentially impossible. The deformation was so extensive everywhere that it was difficult to determine if any variations in the dislocation density existed in local regions, for example at the fiber / matrix interface. Thus the majority of the TEM analysis centered on the as-processed composite without any tensile deformation and the tensile sample which had been pulled to 1/2% deformation. In the following TEM data, the presented results concentrate on one TEM sample from each condition, with those results being basically representative of all samples analyzed. (Often in TEM analyses, a greater disparity of results is acquired in a single sample than on average exists between samples.) The TEM results are presented with regards to the different geometrical regions of the composites, the different extents of deformation, and the different incident voltages of the electron beam in the TEMs used for analysis. This last factor of electron voltage is often correlated with the thickness of the area of analysis.

The cross-sectioned TEM sample of the as-processed composite, after preparation, is exhibited in Micrograph 1a. This image was acquired with an optical microscope using transmitted illumination, with white regions representing where holes were perforated in the TEM sample by ion milling. The thin circular sections are the region of the interface which milled most slowly, i.e. the compound phases that formed at the interface during

thermal processing. In addition, part of the matrix grains adjoining the interface phases remains after ion milling. [This sample was actually observed numerous times in the TEMs between intermittent ion milling, with all TEM observations occurring prior to the optical microscopy. Thus microstructural information was obtained from regions in the matrix that are not directly adjoining the interface, but are represented by hole in Micrograph 1a.] Micrograph 1b is a schematic of Micrograph 1a indicating different areas of TEM analysis that are presented in later micrographs.

Micrograph 2 is an optical image of the representative TEM sample made from the 1/2% deformed tensile bar. Again in this case it is evident that the SiC fibers are essentially ion milled away, although less thin interface region exists as compared to Micrograph 1. Again this sample was analyzed with TEM at various stages of the ion milling process. In the configuration as imaged in Micrograph 2a, the primary thin area exists in the matrix regions between where fibers existed. Micrograph 2b is a schematic which indicates the location from whence subsequently presented TEM micrographs have been acquired.

TEM Results on Extent of Interface Reactions

Although thermodynamic stability of the interface was not a primary focus of this research, a microstructural study of deformation at an interface must address the microstructure that does exist at the interface, and especially any unexpected differences in microstructure that may exist. As a point of fact, the Ti alloy - silicon carbide interface is not thermodynamically stable; and in light of the required thermal treatments to process these composites, chemical reactions to form new interface phases are considered the rule and not just a theoretical concern. Unlike computer modeling, where the thin region of "interface material" may be incorporated as part of either the matrix or the fiber²³, these interface phases may play an important role in a TEM investigation of deformation at the interface.

Two practically simple aspects are the effect of these interface phases on TEM sample preparation and the recognition/identification of these interface phases so that possible deformation in these phases is not erroneously studied as deformation in the matrix. The first is addressed in Appendix I on TEM sample preparation. The resistance to ion milling of the compound phases that form at the interface hinders the thinning of the interface region of the matrix. However, this same resistance to thinning results (in ideal cases such as exhibited in Micrograph 1) in thin area in much of the interface all at the same juncture. This section considers the TEM results of interface phases observed in this study and compares those results to observations made by other researchers. Judgement on the significance of differences in these composites, as compared to composites of the same

materials studied by others, is not treated as a major purpose of this initial research and is limited to a minor discussion in the following paragraphs.

Interface phases were observed to have formed as a result of reaction between the Ti alloy and the SiC fiber. Similar to results published by other researchers²⁴, discrete titanium carbide and titanium silicide layers were observed, with the titanium carbide layer being closest to the fiber. The TiC grains are smaller than 0.1 microns, and the TiC layer is more than a few grains wide, with a typical thickness of < 0.5 microns. This layer is consistently observed as a continuous layer. (However, a TEM analysis is limited to only local areas thinned by the sample preparation.) Micrographs 3 and 4, which are bright field (BF) electron micrographs, indicate the presence of the layer of fine TiC grains at the interface. This TiC layer often exhibits roughness in the radial direction of the fiber which can be up to five times the thickness of the TiC layer. In addition, TEM observations show this same level of roughness to be present at the interface between the two outer, amorphous coatings of the SiC fiber. In light of reported observations that the fractured interface in alpha Ti (6 wt.% Al - 4 wt.% V) / SiC composites is rougher than the interface in beta Ti (11 wt.% Al - 14 wt.% Nb) / SiC composites²⁵, the roughness of the TiC layer seems to be related to a roughness in the amorphous carbon coatings. SEM observations reported in the literature²⁶ imply the roughness at interfaces in Ti-6-4 / SCS6 SiC composites is due to preferential reaction of the β phase of the matrix during thermal processing. Since the Ti-11-14 / SiC composites, which consist primarily of the β phase, exhibit less roughness at the interface, and the interface roughness observed in this TEM analysis appears associated with the TiC layer, the amorphous carbon coating(s) are a more probable source of the roughness than preferential chemical reaction with the β phase.

The next layer observed at the interface encompassed a titanium silicide phase. A careful, in-depth analysis of this layer was not performed, yet all observed diffraction patterns were consistent with this phase having a hexagonal structure. [It is noted that apparently careful Convergent Beam Electron Diffraction (CBED) in a previous study²⁷ indicates the hexagonal symmetry does not exist.] Although basic electron diffraction can be somewhat lacking in a structural analysis, any observed diffraction patterns can easily be classified as being either consistent or inconsistent with a particular lattice. The possible crystal structures, that could exist and that are consistent with various diffraction patterns acquired from different titanium silicide grains, are presented in Appendix II. (It is noted that more than one titanium silicide phase, each with a different crystal structure, is considered a possibility.)

Although an exact analysis of the crystal structure of this titanium silicide layer has not been conducted, observations of the grain size and layer thickness are noted. The

titanium silicide grains are on the order of 0.5 microns in diameter, and consistently nearly an order of magnitude larger than the neighboring TiC grains. Likewise the up-to-two micron thickness of the titanium silicide layer is typically an order of magnitude greater than the thickness of the TiC layer. As mentioned previously, the extent of interface reaction that occurred during the thermal processing of these composites is substantially less than that reported in other composites similarly processed (although possibly with more severe thermal treatments). The discrepancies in the results of sizes of interface phases and relative layer thicknesses, as compared to published results, are being noted in a short article²⁸. In that note the implications of the kinetics of this interface reaction are addressed in light of the situation where no titanium silicide layer is forming.

TEM Results on Deformation in As-Processed Composite

The typical microstructure of the Ti-6-4 matrix far ($>100\text{ }\mu\text{m}$) from the interface of the composite has α (HCP) grains which are mostly free of dislocations after HIP processing. Although Micrograph 5 (a BF image) exhibits subgrains on the order of $1\text{ }\mu\text{m}$ in width, a more typical α grain is free of any substructure. [The black and white fringe contrast represents thickness fringes due to the wedge-shape nature of TEM metal foils. In addition, the cusps at the edge of the hole are a typical ion milling artifact.] In regions of α phase which are sandwiched between β (BCC) phase, however, dislocations are often present. Such a network of dislocations, which are visible in the $<1\text{ }\mu\text{m}$ wide α region in the center of Micrograph 6 (a BF image), are expected in two phase microstructures due to mismatch between lattices and differences in thermal expansion coefficients of the two phases. Since such regions of α phase make up a small volume fraction of the matrix, they are not considered of primary interest in this initial study. Also the regions of β phase, almost always present at triple points and often existing as fine lamellae alternating with α phase, do not comprise a major volume fraction. Thus the influence of the β phase on deformation is not considered in this study. [Actually the influence of β on deformation may be of critical importance because of its principal location at grain boundaries and triple points.] On the other hand, the β phase is reported to preferentially react with the SiC, thereby depleting the matrix of β near the interface.²⁹ Later micrographs of the interface will exhibit the lack of β at the interface.

The microstructures presented in Micrographs 3 and 4 are considered typical of interface regions that are not geometrically situated between fibers. (See schematic in Micrograph 1b for location of each TEM image.) In such typical cases no dislocations are observed in the β grain nearest to the interface, independent of whether or not the TiSi layer is present. [The "interface" is defined in this study as being between the α grains of the

matrix and whatever phases exist after processing.] As shall be discussed, however, α grains situated between fibers typically do have a few dislocations present. A select few grains which are not situated between fibers also exhibit dislocations. As most notably evidenced in Micrograph 7, however, dislocations are sometimes observed in the 2nd α grain away from the interface, with no dislocations observed in the α grain nearest the interface (even though this nearest grain is in a thicker region of the TEM sample).

The high voltage electron micrographs, Micrographs 8a through d, also exhibit many dislocations in the sole remaining location where the interface crescent of material is bridged to the matrix of the TEM sample. A large number of dislocations, compared to other grains of the as-processed composite, are present in each of the subgrains, which are imaged in Micrographs 8b through 8d after sequential small tilts in the microscope. Such a region, although thick enough to prevent electron penetration with the 2000FX (200 keV) TEM, might be expected to be highly stressed due to the final thinning of sample preparation. The penetrating power of the 1.5 million eV electrons enables imaging through these thick grains to establish that most of the dislocations in Micrograph 8 are in the second grain away from the interface phases. These particular dislocations are believed due to a sample preparation artifact. Likewise the dislocations imaged in Micrograph 7 are in a region of material which was also a "supporting bridge" at an earlier step in the ion milling process. The higher local stresses in these thin supporting bridges, which would arise during sample handling such as being dropped, is feared to have been sufficient to cause deformation. [It is remarkable that this sample in the thinned condition imaged in Micrograph 1 survived more than two round trips across country.]

Of most interest in the as-processed composite are the matrix α grains which are situated between the fibers. The α grains nearest the interface in this region consistently exhibit dislocations (see Micrographs 10, 11, and 12). Micrograph 9 is a low magnification ($\sim 2300\times$) image depicting how thin regions of α grains at the interface between the fibers remain after ion milling. Micrograph 10 is an enlarged magnification BF image exhibiting α grains with rows of dislocations, where the rows are perpendicular to the interface. The resistance of interface phases to ion milling results in the TiSi region and parts of α grains abutting the TiSi layer, being too thick for penetration by 200 keV electrons. Micrographs 11a and 11b are lower and higher magnification BF images, respectively, ($g = [10\bar{1}1]$) where the interface phases have been completely milled away to reveal a thinner section of an α grain neighboring the interface. Again rows of dislocation run almost perpendicular to the interface. Dislocation pile-up in the rows perpendicular to the interface occasionally appear to be present, but a more thorough analysis needs to be acquired.

Not all dislocations in α grains between fibers are present in rows that run perpendicular to the interface. Micrographs 12a and 12b exhibit two α grains, of four sequential interface α grains, which have a row of dislocations that is parallel to and displaced by ~ 0.5 microns from the interface. Consistent with observations of the 1/2% deformed sample that shall be discussed, no significant "pile-up" of dislocations at grain boundaries occurs for the rows (of dislocations) that are parallel to the interface.

TEM Results after 1/2% Plastic Deformation

Although 1/2% plastic deformation was deemed a small amount of strain prior to actual mechanical testing, the dislocation densities observed by TEM after 1/2% strain were sufficient as to eliminate possible information about early stages of deformation. [Future mechanical tests will be terminated at lower strains in order to provide a cleaner microstructure for dislocation analysis.] Most grains exhibited two or more active slip systems, with random dislocations often being typical in the matrix α grains far from (greater than one fiber radius) the fiber/matrix interface. Micrograph 13 is a bright field image acquired with a 2-beam condition of $g = [011]$. Some α grains of matrix far from the interface are judiciously sectioned such that longer, parallel dislocation loops are observed, as evidenced in the BF image ($g = [2110]$) of Micrograph 14. This preliminary study was not sufficient to establish whether any differences in dislocations densities and/or morphologies, as a function of geometrical location and/or crystallographic orientation of the α grain, existed in the matrix far from the interface.

Whereas the as processed composites ion milled such that matrix grains situated between two fibers ion milled through prior to the TiC and Ti_xSi_y at the interface, the matrix grains between fibers in the 1/2% deformed sample remained after the interface phases had been ion milled through. (This disparity, as evidenced in Micrographs 1 and 2, may have been influenced by the "work-hardened" metal grains being more resistant to ion milling.) Intermittent TEM observations and ion milling resulted in the situation observed in Micrograph 15, where the interface phases have just finished ion milling through, less than one α grain at each interface has been removed, and the matrix grains midway between the fibers are still present. (Whereas the original spacing between these two fibers was slightly less than 20 microns, now the remaining matrix region is ~ 12 to 14 microns wide.) This remaining matrix region exhibits a wide range of thickness, where the excessively long exposure time of Micrograph 15 results in the overexposure of any detail in some grains and yet no penetration of 200 keV electrons in the black regions. Extinction thickness fringes of a CBED analysis of a region similar to that of the area of Micrograph 16 (noted as being totally overexposed in Micrograph 15) determine this "thinner" area to

be between 0.2 and 0.4 microns thick. Such analyses of thickness fringes become somewhat questionable once thicknesses are close to or greater than one micron, as is the case for the black areas of Micrograph 15.

Micrographs 16a through 16e depict a series of bright field TEM images acquired of the same α grain at the different 2-beam conditions of $g = [10\bar{1}1]$, $g = [1010]$, $g = [01\bar{1}1]$, $g = [1\bar{1}01]$ and $g = [0002]$, respectively. These images primarily depict the region of an α grain that is the second grain away from the interface and displaced ~ 3 to 5 microns from the interface. Also exhibited is the grain boundary between the first and second grain, of which the projected intersection with the thin foil is nearly parallel to the fiber/matrix interface. Two different sets of dislocations, present as "rows" of dislocations, are imaged in Micrographs 16a and 16b, of which one set has the rows roughly perpendicular to the interface and the other set has rows nearly parallel to both the interface and the grain boundary. Micrographs 16c and 16e are acquired with imaging conditions ($g \cdot b = 0$) such that the dislocations in rows perpendicular to the interface have disappeared, thus establishing these dislocations to have a Burgers' vector of $b = [2110]$. Micrographs 16d and 16e are acquired with corresponding imaging conditions such that the dislocations in rows parallel to the interface have essentially disappeared, thereby determining these dislocations to have a Burgers' vector of $b = [11\bar{2}0]$. In addition, as the TEM sample is tilted to have the $[0002]$ zone axis parallel to the electron beam, the images of the dislocations lie parallel to each other and "flat" in the plane of the image. This implies that the $\langle 2110 \rangle$ type dislocations have slipped in the basal plane, (0002), rather than in a prismatic plane.

Although not as easily evidenced in this case as in Micrograph 17, the dislocations in rows perpendicular to the interface exhibit "pile-ups" of dislocations at the grain boundary (see Micrograph 16a). It is noted that dislocations appear which are not only "piled-up" at grain boundaries towards the interface, but also at grain boundaries facing away from the interface. On the other hand, lower magnification imaging, not included, indicates the dislocations in rows parallel to the interface do not exhibit pile-ups near where these rows intersect grain boundaries, (i.e. grain boundaries outside the field of view of Micrograph 16, which are essentially perpendicular to the fiber/matrix interface). Micrographs 16b and c exhibit parallel dislocations which are fairly evenly spaced.

Since this traditional $g \cdot b$ analysis of dislocations was enhanced through the use of a computer, a description of the analytical procedure is provided. With the grain of interest randomly oriented in the electron microscope, the sample is tilted (along both x and y axes) to pass through many 2-beam conditions, some of which appear to make the dislocations disappear. In a fairly straightforward manner, the 2-beam images of Micrographs 16a

through e , and corresponding diffraction patterns, may be obtained. If the microscope is well calibrated and is kept properly aligned during the tilting experiment, the type of 2-beam condition can be established through a simple measurement of the reciprocal lattice vector between diffraction reflections. However, a proper analysis of what the particular 2-beam conditions are requires measuring the various angles of tilt between each acquired image. Often "slop" in the tilting mechanism of the TEM holder, as well as possible bending in the TEM thin foil, lead to errors in measuring the angles of tilt, which in turn make difficult the determination of specific 2-beam conditions.

In the case of analysis of the 2-beam conditions of images of Micrographs 16a through 16e, a Kikuchi map of the α -Ti (HCP) structure was calculated with the Diffract Program³⁰ on the Macintosh II Computer. This Kikuchi map was rotated until a select stereographic triangle was obtained and enlarged, as viewed in Figure 3. This program not only produces the Kikuchi map but also allows for measuring angles between specific zone axes and specific 2-beam conditions. By comparing these calculations to the rough measurement of angles between different 2-beam conditions made while tilting in the microscope, the particular 2-beam conditions can be established on the Kikuchi map, as labelled in Figure 3.

A second method of analysis of 2-beam conditions actually integrates the computer calculations with the TEM tilting experiments while they are being performed. In this case a particular grain, as randomly oriented in the TEM foil, is tilted to obtain a zone axis diffraction pattern. After analysis of the diffraction pattern (using the Diffract program), the TEM sample is tilted, while measuring the angle(s) of tilt, until a second zone axis pattern is obtained. This zone axis pattern is also analyzed using Diffract, as are subsequent zone axis patterns which may be obtained. Using the known zone axis patterns and the angle (and direction) of tilt between zone axes, a Kikuchi map is generated and rotated to correspond to the crystallographic orientation of the grain. Figure 4 is such a Kikuchi map calculated for the grain of Micrograph 17, where the location of the $[1\bar{2}10]$ and $[01\bar{1}1]$ zone axis patterns acquired of the grain in Micrograph 17 are circled. (It is noted that the angle between these zone axes as calculated by the Diffract Program was 50.4° , and the roughly measured angle of tilt in the microscope was 50° . Quite often, electron microscopes are not so well aligned.) Now particular 2-beam conditions can be located on the Kikuchi map and used as a guide to determine what tilting angles should be used to acquire the 2-beam images of Micrographs 17a through 17d. In this case the dislocations were presumed to be of the $\langle 11\bar{2}0 \rangle$ type. Thus the sample was tilted to obtain the various 2-beam imaging conditions in Micrographs 17a through 17d of $g = [1011]$, $g = [10\bar{1}1]$, $g = [1\bar{1}01]$ and $g = [0002]$, respectively.

The grain imaged in Micrographs 17a through 17d is determined to be closer (2 - 3 microns) to the interface than the grain of Micrograph 16. Again two sets of dislocations are observed (see Micrograph 17a), with one set being roughly perpendicular to the interface and the second set being nearly parallel to the interface. The dislocation density imaged in this grain appears to be less than that observed in the grain of Micrograph 16; however, this disparity is actually related to the grain of Micrograph 17 being thinner (less than 200 nm). (The dislocation density disparity will be discussed in more detail in light of HVEM results.) The $\mathbf{g} \cdot \mathbf{b} = 0$ condition of Micrograph 17b results in the dislocations in rows that are perpendicular to the interface being almost invisible. Similarly, the $\mathbf{g} \cdot \mathbf{b} = 0$ condition of Micrograph 17c results in the dislocations in rows that are parallel to the interface being essentially invisible. Finally, the $\mathbf{g} \cdot \mathbf{b} = 0$ condition of Micrograph 17d results in both sets of dislocations being invisible. An analysis of these 2-beam conditions leads to a determination of the Burgers' vector of the perpendicular dislocations to be $\mathbf{b} = [1\bar{2}10]$ and the Burgers' vector of parallel dislocations to be $\mathbf{b} = [11\bar{2}0]$. Micrographs 17a and 17c depict the perpendicular dislocations as piling-up at the grain boundary. In this case the grain boundary imaged is actually "away from" the matrix / fiber interface. (Since the interface has actually been ion milled away, it is difficult to ascertain whether the grain boundary which was closest to the interface had dislocations "piling-up" at it or "emitting" from it. In addition, it is not known whether this grain was the first or second grain away from the interface.) The dislocations which occur in rows parallel to the interface (Micrograph 17b) do not appear to exhibit piling-up at the grain boundaries at either end of this grain.

Although not all dislocations in various grains near the interface can be classified as either perfectly parallel to or perpendicular to the interface, when such classifications are made, the results are consistent: Dislocations in rows that are parallel to the matrix / fiber interface do not exhibit significant pile-up at grain boundaries. On the other hand, dislocations in rows that are perpendicular to the interface do exhibit pile-up at grain boundaries, either grain boundaries facing the interface and/or those that face away from the interface.

Although the region of matrix material remaining between fibers is quite thick, a long exposure image, acquired with the 200 keV electron microscope, provides some microstructural information. In the low magnification BF image of Micrograph 18a, the thin areas at the edges of the hole are actually "washed out" due to the overexposure of the electron beam. This "bridge" of matrix material exhibits a minimum width of ~35 microns, as compared to the original ~40 microns of matrix that was present between fibers. (The BCC β phase exists as the dark phase present at triple points and along grain boundaries

between HCP α grains.) Since only 2-3 microns of matrix material has been completely removed at each interface, the grains at the edge of the holes are considered to have been within one to two grains of the interface. The higher magnification image of Micrograph 18b depicts a grain near the edge of the interface which ranges from a thickness of less than 100 nm to greater than 500 nm. Nevertheless, extending over the entire >5 micron width of this grain are regularly-spaced planar dislocations. Allowing for the fact that many dislocations may run out of the surfaces near the thinner edge, the dislocation density appears comparable in both the thick and thin region of the grain. The elongated loop nature of the dislocations becomes apparent in the thicker region of the grain, where the end of the loops are often contained within the thickness of the TEM sample. Such elongated dislocations are indicative of planar slip which is often observed in Ti alloys, especially when oxygen impurity atoms are present. (More detail of the significance of these planar dislocations is presented in the HVEM section.) In addition, the thickest region of this grain exemplifies one difficulty in trying to establish dislocation densities in the thick matrix material between fibers by using conventional lower voltage (200 keV) microscopy.

Results Comparing HVEM and Traditional TEM

Micrograph 19 depicts a BF image of a grain neighboring that of Micrograph 18b, acquired with a 2-beam condition $g = [10\bar{1}1]$. Again dislocations are observed in rows, of which those rows perpendicular to the fiber / matrix interface exhibit pile-up of dislocations at grain boundaries. This grain is the second grain away from the interface. In addition, the grain of interest goes from being fairly thin (and transparent to 200 keV electrons) near the interface to too thick for 200 keV electrons to penetrate in the region of the grain away from the interface. This same grain was observed using the High Voltage Electron Microscope (1.5 MeV) at the NCEM, LBL, Berkeley, CA. Micrographs 20a through 20b are BF images acquired with $g = [10\bar{1}0]$, $g = [11\bar{2}2]$, $g = [01\bar{1}2]$, respectively. The disappearance condition existing in Micrograph 20c is consistent with the Burgers' vector being of the type $\mathbf{b} = \langle 2110 \rangle$.

Comparing the TEM images acquired with the 200 keV microscope and the HVEM readily provides a difference in the sharpness of the images of dislocations. The nature of the electron beam interaction to provide diffraction contrast is such that better contrast imaging is provided with a lower acceleration voltage. Secondly, much of the grain which is viewed in the HVEM images is significantly thicker than the area of analysis in Micrograph 19. Absorption effects in these thicker regions also helps contribute to the more diffuse images in Micrographs 20a, 20b, and 20c. Although the aesthetics may not be as desirable in the HVEM images, the higher voltage electrons allow for greater

penetration and help establish that the dislocations in thicker regions substantiate observations made in thinner regions. Again dislocations in rows which are perpendicular to the interface appear as significantly more piled-up at grain boundaries. In addition, the number of dislocations per area does not increase as the grain becomes thicker, but rather the lengths of the individual dislocations are longer.

The power of the HVEM becomes more evident when images are acquired of the matrix α grains midway between fibers. These grains are approximately two times as thick as the thicker regions of the grain imaged in Micrograph 20. Micrograph 21a is a lower magnification BF image of the same region as Micrograph 18a, except acquired with the HVEM in a much shorter time of exposure. Higher magnification BF images, Micrographs 21b and 21c, are acquired with 2-beam conditions of $g = [01\bar{1}]$ and $g = [1\bar{1}0]$, respectively. Long straight dislocations extending entirely across the grain are indicative of planar slip. Many researchers, most notably J. Williams³¹ and G. Welsch³², have observed a correlation between the extent of planar slip and oxygen (or possibly carbon) contamination in titanium alloys. In this present study, the most significant planar slip is observed in α grains near to the fiber interfaces. This may indicate that carbon and/or oxygen diffuse out of the fiber and into the titanium matrix during thermal processing of the composite. The source of carbon is quite apparent, as the SCS6 fibers have enriched carbon coatings. Although no apparent source of oxygen contamination should be present in this system, Auger Electron Spectroscopy performed by other researchers has indicated that the SCS6 fibers are contaminated with significant oxygen on the surface prior to incorporation of these fibers into the composite. During thermal processing the chemical reaction between the titanium matrix and the SiC fiber may encourage the oxygen to diffuse into the surrounding α grains of Ti.

TEM analysis of grains significantly thicker than the grain in Micrograph 21 (greater than 1 micron in thickness) can be considered by utilizing HVEM. Micrographs 22a through 22d are acquired of the titanium matrix >30 microns from the fibers' interfaces. Micrograph 22a is a low magnification image which does not depict any grains with noticeable planar slip. Higher magnification BF images, Micrographs 22b, 22c, and 22d, were acquired with 2-beam conditions of $g = [11\bar{2}]$, $g = [10\bar{1}]$ and $g = [1\bar{1}0]$, respectively. As a result of this grain being thicker, these dislocations appear longer than the dislocations observed in Micrograph 21. However, the actual number of dislocations does not appear noticeably different, implying a similar dislocation density exists. (There exists the possibility that more dislocations were originally present in thinner regions near the interface, but during TEM sample preparation these thinned regions were susceptible to losing dislocations. This seems unlikely because long dislocations lying in the plane of the

TEM film should be more susceptible to the relaxation of stresses by dislocations leaving the thin film. Yet long planar dislocations are often present in the thin regions near the interface.) Probably the most apparent difference associated with the dislocations in Micrograph 22, as compared to the dislocations in grains closer to the interface (Micrograph 21), is that the dislocations in grains away from the interface do not exhibit planar slip. This implies that whatever contamination may exist, it does not exist far (>30 microns) from the interface. Thus the SCS6 fibers appear to be the source of impurity atoms which alter the nature of dislocations near the interface.

When thick regions of the matrix, more than one fiber radius from the interface, are analyzed, a somewhat lower dislocation density is observed. The low magnification image of Micrograph 23a depicts a region far from the interface, which also exhibits no planar slip. The BF images of Micrograph 23b, and 23c were acquired with 2-beam conditions of $g = [01\bar{1}1]$ and $g = [10\bar{1}0]$, respectively. Each bright field image exhibits a different set of dislocations as being visible. The difficulty in determining dislocation density, without first determining the exact TEM sample thickness, becomes evident when one compares the images of Micrographs 22c and 22d and Micrographs 23b and 23c. At first glance the grain far from the interface in Micrograph 23b may appear to have a greater dislocation density than the grain in Micrograph 22c. However, after considering that the grain in Micrograph 23b is substantially thicker and then recognizing that most of the dislocations in Micrograph 23b go across the grain and then loop back, it becomes apparent that the actual number of dislocations in Micrograph 23b is actually only $\sim 1/2$ the number counted in Micrograph 22c or 22d. (It is also important to tilt to different 2-beam conditions in order to account for all the dislocations.)

Many α grains in the matrix far from the interface of the 1/2% deformed sample exhibit few dislocations in very thin regions of the TEM samples. Micrograph 24a is a low magnification image depicting many grains with relatively low dislocation densities. Higher magnification BF images in Micrographs 24b and 24c, acquired at 2-beam conditions of $g = [01\bar{1}1]$ and $g = [2\bar{1}10]$, respectively, depict a fine dislocation network. This dislocation array, in light of the relatively clean microstructure in the surrounding grain, may be a residual subgrain boundary from the thermal processing of the composite.

The HVEM results provide a better statistical analysis of the dislocation densities in various regions. Although little difference is observed between the α grains at the interface and those α grains ~ 30 microns from the interface, a decrease in the dislocation density far (> one fiber radius) from the interface is observed. Since many of the analyses of "near-interface" grains were of α grains that are almost sandwiched between fibers, these grains may have been experiencing higher stresses due to overlapping stress fields from each

fiber, which in turn gave rise to dislocation densities as high as the dislocation densities of α grains immediately adjacent the fiber interface.

Summary

The primary purpose of this research is to determine if greater deformation occurs in matrix grains which are close to the interface of the fibers. Such preferred deformation is established by the presence of dislocations in α grains at the interfaces between fibers of the as-processed composite. Also a higher dislocation density exists between fibers, as compared to far from the interface, in the 1/2% deformed sample. In light of these results, it appears that the thermal stress arising due to CTE mismatch is sufficient to cause dislocation motion in α grains at only the interfaces which are between closely spaced fibers. In addition, the dislocations observed after only thermal processing are often displaced from the fiber interface by ~ 0.5 microns, possibly as a result of constrained deformation. However, the deformation is too extensive in both the 19% deformed and even the 1/2% deformed tensile specimens to ascertain whether constrained deformation results in dislocation motion in α grains right at the interface or away from the interface. (A continuation of this TEM research involves analysis of the earlier stages of deformation.)

Many of the dislocations observed near the interfaces, in both the as-processed and 1/2% deformed sample, were present as rows of dislocations. Those rows of dislocations which are perpendicular to the interface exhibit pile-ups at grain boundaries, whereas the rows of dislocations that are parallel to the interface are regularly spaced, with no pile-ups at grain boundaries. Since many of these dislocation pile-ups are observed in α grains which are not contiguous with the interface, these pile-ups are not considered a result of dislocation emission from the fiber interface. (Finite Element Models of the stress state near the interface indicate a preferred driving force for dislocation motion at 45° to the tensile axis and the radial direction. In cross sectioned TEM samples observed in this study, such dislocation motion results in the pile-ups perpendicular to the interface.)

This study utilized both a traditional (200 keV) voltage TEM and a high voltage (1500 keV) electron microscope. Comparing the results from these two microscopes provides information pertinent to the utilization of microscopy for materials analysis. Similar dislocation densities were observed in thin and thicker regions using these two microscopes. Dislocations in thicker regions were considerably longer, often looping back upon themselves all within the thickness of the TEM thin film. (In some of the thinnest regions of TEM samples, fewer dislocations were observed, probably as a consequence of the free surfaces being a sink for dislocation annihilation.) The HVEM enabled the

observation of dislocation pile-ups in thick regions of the matrix grains adjoining the interface. In addition, HVEM determined that planar slip had occurred (presumably as a consequence of oxygen contamination) in the α grains in thick regions between fibers.

Future Work

The as-processed composite exhibits a difference in dislocation density near the interface as compared to the bulk of the matrix, far from the interface. However after 1/2% deformation, enough dislocations are present everywhere such that it is difficult to unambiguously say that a higher dislocation density is present right at the interface boundary itself. Thus it is important to observe dislocation morphologies after less than 1/2% plastic deformation. Whereas the 1/2% deformation tensile test was stopped after three fiber fragmentation events, as measured by acoustic emission, it is believed earlier information in the acoustic emission signals may help determine the onset of plastic deformation (i.e. the earliest dislocation motion). These acoustic emission spectra may be used as a benchmark which determine when the tensile test should be truncated so as to provide appropriate TEM samples. These less-deformed samples should provide more evidence of enhanced deformation occurring at (or slightly displaced from) the interface.

The observance of dislocation pile-ups only perpendicular to the interface could also be studied in these less-deformed conditions. This initial analysis could not establish a preference of dislocation pile-ups away from or towards the interface. These pile-ups were observed in both the α grains contiguous to the interface, as well as the α grains second nearest to the interface. The less-deformed samples may distinguish whether pile-ups away from or towards the interface are preferred. Also, the presence of dislocation pile-ups in grains between fibers but further from the interface may be addressed, whether they are more or less prominent.

It is also important to observe composite samples having undergone greater than 1/2% plastic strain. A successful means of preparing TEM cross section samples, which may contain a fiber fragmentation event, has been developed. It would be useful to statistically analyze the dislocation densities in the region of fiber fragmentations in order to better understand the constrained deformation that occurs in such regions of the matrix.

The observance of planar slip primarily in α Ti grains near the interface, appears to be the result of oxygen (or carbon) impurities that have diffused into the matrix from the fiber during thermal processing. Since any future research is attempting to address differences in deformation near the interface, such a study must account for the role of this localized planar slip near the interface. Such a localization of a particular slip morphology,

as a result of composition variations, may have more influence than any load transfer effects due to the high strength and low ductility of the fibers.

It is also desirable to extend these TEM analyses of deformation at the interface to other composite systems. Initially comparisons of single fiber and multiple fiber composites, with different geometrical layout of the fibers, can be addressed. The present analysis indicated that fibers in close proximity result in deformation in the matrix region between fibers in the as-processed condition. How close fibers must be, before such deformation occurs, can be both theoretically modelled and observed experimentally with TEM. Additionally, different matrix materials such as titanium aluminide intermetallics should be processed, tested and characterized by TEM. These intermetallic-matrix composites (IMC) are important for their higher temperature applications. Two aspects of these IMCs will lead to differences in results as compared to the Ti-6-4 // SCS6 composites. First, these titanium aluminides have a greater CTE mismatch and have been modelled to undergo significant plastic deformation as a result of thermal processing. Secondly, these intermetallic phases are substantially more brittle than Ti matrix composites. Once a fiber fragmentation event occurs, these composites will be subject to crack propagation from the fractured fiber into the matrix. Thus the constrained deformation will be more complex to evaluate, but will also play a more important role.

REFERENCES

1. Ashby, M. F., F. J. Blunt & M. Bannister, *Acta Metall.*, V37, p.1847-1857, (1989).
2. Daehn, G. S. & G. Gonzalez-Doncel, *Metall. Trans.*, V20A, p.2355 (1989).
3. Rhodes, C.G. & R.S. Spurling, in *Recent Advances in Composites in the United States and Japan*, J. R. Wilson & M. Taya, eds., ASTM, Philadelphia, p.585-599 (1985).
4. Jones, C., C. J. Kiely & S. S. Wang, *J. Mater. Res.*, V4, p.327-335 (1989).
5. Hall, E. L., A. M. Ritter & N. Lewis, *General Electric Technical Report* #90CRD173, (1990).
6. Das, G., *Met. Trans.*, V21A, p.1571-1578 (1990).
7. Krishnamurthy, S., in *Titanium Aluminide Composites: Wright Laboratory Report* #WL-TR-91-4020, p.135-148 (1991).
8. Smith, P. R., C. G. Rhodes & W. C. Revelos, in *Titanium Aluminide Composites: Wright Laboratory Report* #WL-TR-91-4020, p.178-201 (1991).
9. Dudek, H. J., R. Leucht, R. Borath & G. Ziegler, *Mikrochim. Acta [Wien]*, II, p.137-148, (1990).
10. Mills, M. J., *Proceedings of the XIIth International Congress for Electron Microscopy*, Seattle p.448-449 (1990).
11. Stanley, J. & H. L. Fraser, *Diffract Program*, microdev Software, Hillsboro, OR, (1989).
12. Vogelsang, M., R. J. Arsenault & R. M. Fisher, *Metall. Trans.*, V17A, p.379-389 (1986).
13. *ibid.* ref. 1.
14. Evans, A. G. & R. M. McMeeking, *Acta Met.*, V34, p.2435 (1986).
15. Nimmer, R. P., R. J. Bankert, E. S. Russell & C. A. Smith, *Proceedings ASM Materials Conference*, Indianapolis, (1989).
16. *ibid.* ref. 12.
17. *ibid.* ref. 12.
18. Cottu, J-P & J-J Couderc, *J. Matls. Sci.*, V26, p.2985-2990, (1991).
19. Schoenberg, T., in *Titanium Aluminide Composites: Wright Laboratory Report* #WL-TR-91-4020, p.7-16 (1991).
20. *ibid.* refs. 3 through 9.
21. *ibid.* refs 3 and 4.
22. Roman, I. & S. Krishnamurthy, in preparation.
23. *ibid.* ref. 15.
24. *ibid.* refs. 3 through 9.
25. Krishnamurthy, S. to be published.
26. Bowden, D.M., *et. al.*, in *Titanium Aluminide Composites: Wright Laboratory Report* #WL-TR-91-4020, p.149-164 (1991).
27. *ibid.* ref. 4.
28. Moberly, W. J., D. B. Miracle & S. Krishnamurthy, to be published.
29. *ibid.* ref. 26.
30. *ibid.* ref. 11.
31. Williams, J.C. & G. Luetjering, *Proceedings of the 4th International Conference on Titanium*, Kyoto, Japan, p. 671, (1980).
32. Welsch, G., G. Luetjering, K. Gazioglu, & W. Bunk, *Met. Trans.*, V18A, p.169-176, (1977).
33. Commonwealth Scientific Corp. Bulletin # 137-89.

Appendix I: TEM Sample Preparation

As with most TEM investigations, one must establish a sample preparation methodology which not only provides an adequate analysis of the material problem, but also does not introduce artifacts. (I.e. the miniscule thin area of material being analyzed must be representative of the "bulk" material of interest.) Often the creation of a thin foil may result in a change in the local microstructure. As an example, the two-dimensional nature may allow for the alleviation of internal strain via the interaction of dislocations and the free surfaces. Measuring the dislocation density of very thin foils may result in values that are significantly less than actually existed in the "bulk" condition. Many methods for creating a thin foil involve possible heating of the sample. If such heating is excessive, diffusion and/or thermodynamic reactions may occur. In addition, the exposure of the thin foil to the environment may result in reactions (typically oxidation) that are not typical inside "bulk" materials. In light of all these possible artifacts, the following procedures for preparing TEM samples of these composites were considered quite successful by providing thin area in the interface regions of interest, and by limiting possible alterations of the microstructure due to the sample preparation.

TEM samples were prepared from sections of the center of the gauge section of the 19% strained and the 1/2% strained tensile specimens. Since these same specimens were to be also metallographically observed in a longitudinal cross section, a limited amount of material was available for TEM analysis. A diamond wafering saw was used to slice one ~0.5 mm thick section from the center of the 19% tensile specimen, and to slice four sections (each ~0.5 mm thick) from the 1/2% specimen. [The total removal of material from the 1/2% specimen, including that lost to cutting debris, was ~4 mm. This may have resulted in the actual region of fiber fragmentation having been lost.] In addition, TEM samples were obtained by sectioning the end tabs of the tensile specimens. Since the gripping pressure was ~ 25 MPa, well below the yield strength of the Ti matrix (>600 MPa at room temperature) and below the residual stresses arising from CTE mismatch during processing, the sections from these end tabs are taken as the undeformed (0% strain) condition. As the end tabs are much larger than the gauge section, both regions of the matrix alone as well as with fibers were available for analysis.

All TEM specimens were prepared by initially slicing a section ~ 0.5 mm thick with a low-speed diamond saw, using oil as a lubricant. The next step involved grinding specimens to a thickness of 0.15 to 0.2 mm thickness, using 600 grit SiC grinding papers for a final finish. It is noted that the SiC fibers are much more resistant to grinding than the Ti alloy matrix, resulting in the TEM sample being up to 0.1 mm greater in thickness in the region of the fiber as compared to the metal matrix far from the fiber. At this point, the

specimens from the tensile gauge section had x and y dimensions sufficiently small enough for the TEM. However, the specimens being prepared from the end tabs were punched to form 3 mm diameter samples. As indicated by the characterization of samples prepared from the Ti matrix in the end tabs, the various specimen preparation steps so far described do not result in deformation artifacts.

From this juncture, two separate preparation methods were attempted: electrochemical jet polishing and grinding / dimpling followed by ion milling. The first method was determined most appropriate for the samples of matrix metal alone because of its relative ease. However, the second method resulted in the best preparation of TEM samples of the composite interface. [A further study is being conducted which involves dimpling followed by electropolishing to produce TEM samples with extended electron transparent region at the fiber / matrix interface.] The electropolishing of the metal foils followed traditional methods of using an electrolyte that is cooled to $\sim -30^{\circ}\text{C}$. The electrolyte utilized was a mixture of three parts methanol and one part nitric acid. The dimpling and ion milling procedure of sample preparation of TEM cross sections of the composite interfaces was conducted in a variety of manners. Although each involves a combination of parts of different, well-established TEM cross section techniques, the variation in the combinations, and corresponding successes, warrant the following documentation. In all cases it is preferable to have final TEM samples which are 0.15 to 0.2 mm thick at the edges, for structural support, and yet have electron transparent material in the regions of the interfaces.

Since the grinding with SiC paper lead to fibers protruding from the sample, the first dimpling step actually used a 3 mm wide dimpling wheel. This wheel was used to polish flat both sides of the TEM samples to a finish of 1-3 micron diamond finish. Such a polishing step greatly reduces the extent of fiber protrusion, while not reducing the overall thickness of TEM samples to less than 0.1 mm. The next dimpling step uses a 1 mm wide dimpling wheel for creating a local dimple in the TEM sample. Three different methods of dimpling were utilized. One involved gluing the TEM sample to a 3 mm slotted Cu grid prior to dimpling which is centered on the fibers. (The Cu grid provides more support for handling the sample at later stages, so that fibers do not fracture and "fall out".) A second involved no Cu grid and dimpling centered on the fibers. (This method, although providing inconsistently prepared samples, was the quickest and occasionally provided the best results; i.e. the most thin area in the interface regions.) The third involved no Cu grid and having the dimple centered to one side of the fibers. (This method provided a means by which selective sections of the interface region were analyzed.) Initial dimpling was conducted with 6 micron diamond paste until the thickness in the center of the dimple

was less than 0.05 mm. Dimpling is subsequently conducted with 1 micron diamond until the thickness in the center of the dimple is < 20 microns.

For many of the TEM samples the translucent nature of the SiC fibers was used to an advantage, as well as utilizing a dimpling stage which has a transparent region below the TEM sample. Thus once the fibers were of a thickness < 30 microns, some light would be transmitted through the fibers using a transmitted light microscope. Micrograph 25 is an optical image acquired with transmitted illumination of a TEM cross-section sample after dimpling, but prior to ion milling. Not only does light penetrate through parts of the SCS6 fiber, but cracks in the fibers may be observed. (In this case the sample had been dimpled too thin, and the cracks were incurred while removing the sample from the dimpling table. However, careful sample preparation can prevent inducing any cracks, such that this means of imaging may be a means to determine if the TEM section is obtained from near a fiber fragmentation event.) In addition, as the dimpled region became thinner with subsequent dimpling, the color of the transmitted light would change from dark red to light yellow. Dimpling thinner than a thickness corresponding to bright orange or dark yellow (corresponding to $< 10 - 15$ microns) would result in the fibers becoming susceptible to fracturing and "falling out" of the TEM samples. Another use of observing the TEM samples with transmitted light is to observe if/when a fiber fragmentation event had occurred in the cross section region of that particular TEM sample. [It is hoped that this technique will provide for future research a means by which deformation in the matrix is related to fiber fragmentation events.]

After mechanically thinning by the final dimpling stage, the samples were thinned by physical ion beam milling (although a further study is being undertaken to use electropolishing after dimpling). The different materials comprising the composite ion mill at various rates³³, although exact etch rates are not well established. The Ti alloy etches slightly faster than crystalline SiC, whereas the titanium carbide and titanium silicide phases ion etch at a slower rate than the matrix or fiber. In many of the samples the region of the fiber is thinner and therefore will etch through first. The crystalline SiC coating of the fiber ion beam etches at a faster rate than the amorphous core and the amorphous, C-enriched, outer coatings. As a consequence a hole is typically formed in the crystalline part of the middle SiC fiber, followed by small holes in the Ti matrix, followed by the amorphous core of the SiC fiber, followed by the outer amorphous coatings of the fiber. It is noted that the titanium silicide interface layer, which formed during thermal processing of the composite, is the component of the composite which is most resistant to ion etching. Fortunately, this results in the last material remaining after ion etching to be the interface phases and grains of matrix material that are attached to the interface. An ideal TEM sample

will have a gradual wedge shape from the edge of the hole to the thicker regions of the sample, thereby providing "thin area" over a larger spatial area. However, these cross-section samples have a sharp wedge shape, being quite thick where the titanium silicide remains and thinned down to the hole over a region < 5 microns wide of matrix material.

Appendix II: Electron Diffraction Results on Titanium Silicide at Interface

The different diffraction patterns which were acquired from various separate titanium silicide grains at the interface of the as-processed composite are consistent with the following possible crystal lattices:

- a) Cubic $a_0 = 0.826 \text{ nm}$ (and probably a BCC-based superlattice, because {111} reflections are absent in a [112] pattern)
- b) Hexagonal $a_0 = 0.675 \text{ nm}$ $c_0 = 0.237 \text{ nm}$
- c) Hexagonal $a_0 = 0.675 \text{ nm}$ $c_0 = 0.474 \text{ nm}$ (HCP, as {0001} reflections are absent.)
- d) Hexagonal $a_0 = 0.675 \text{ nm}$ $c_0 = 0.333 \text{ nm}$

The Ti_5Si_3 phase is reported in literature as having a hexagonal structure with:

$$a_0 = 0.7429 \text{ nm} \quad c_0 = 0.5139 \text{ nm}$$

The ratio of a_0/c_0 is 1.446. This is essentially identical to the ratio of a_0/c_0 for the hexagonal lattice (c) above. This may imply a superlattice phase exists which has its lattice parameters slightly modified by additional elements, other than Ti and Si, that are incorporated in this phase.

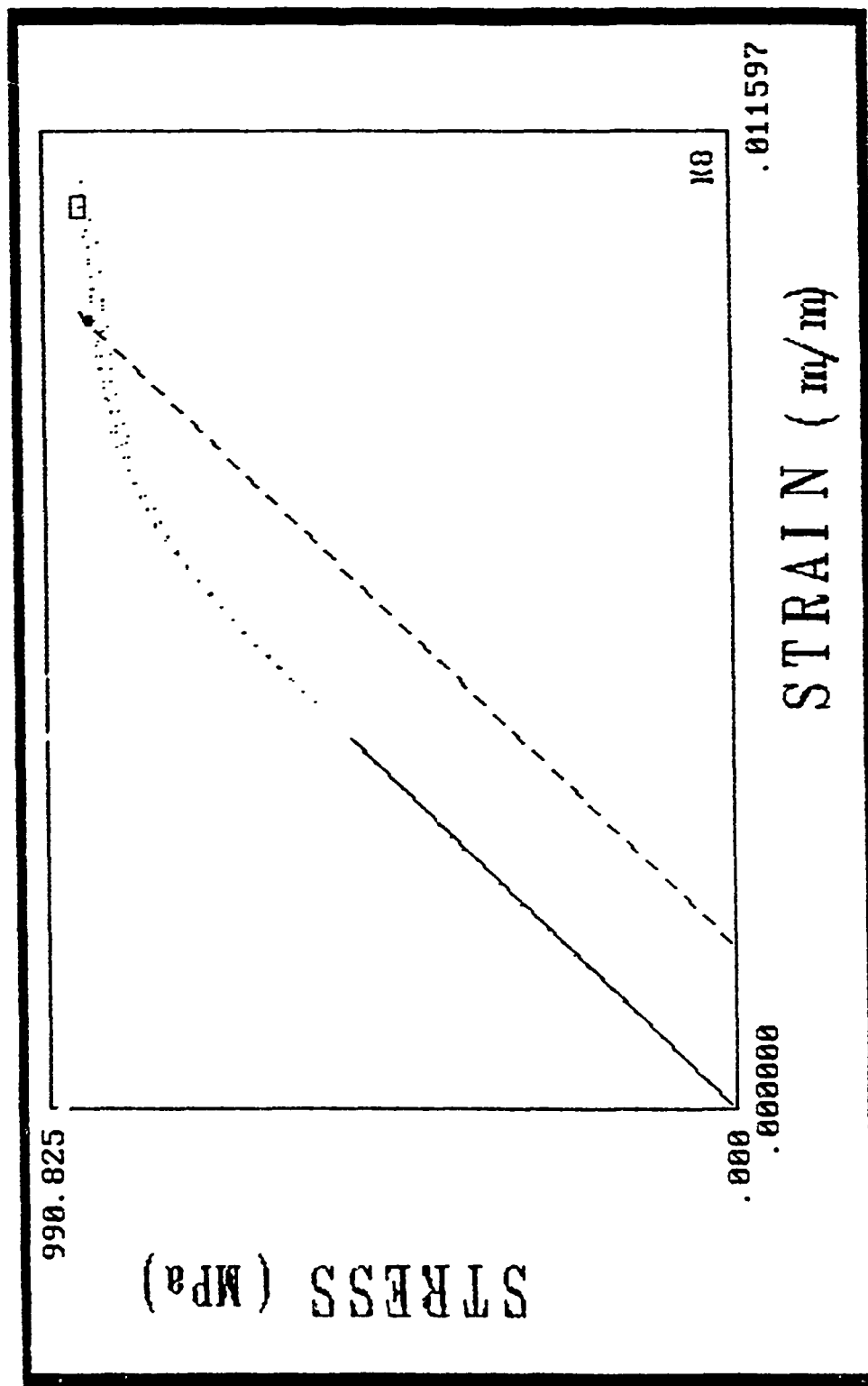


Figure 1a: Stress / strain curve for 1/2% deformed composite.

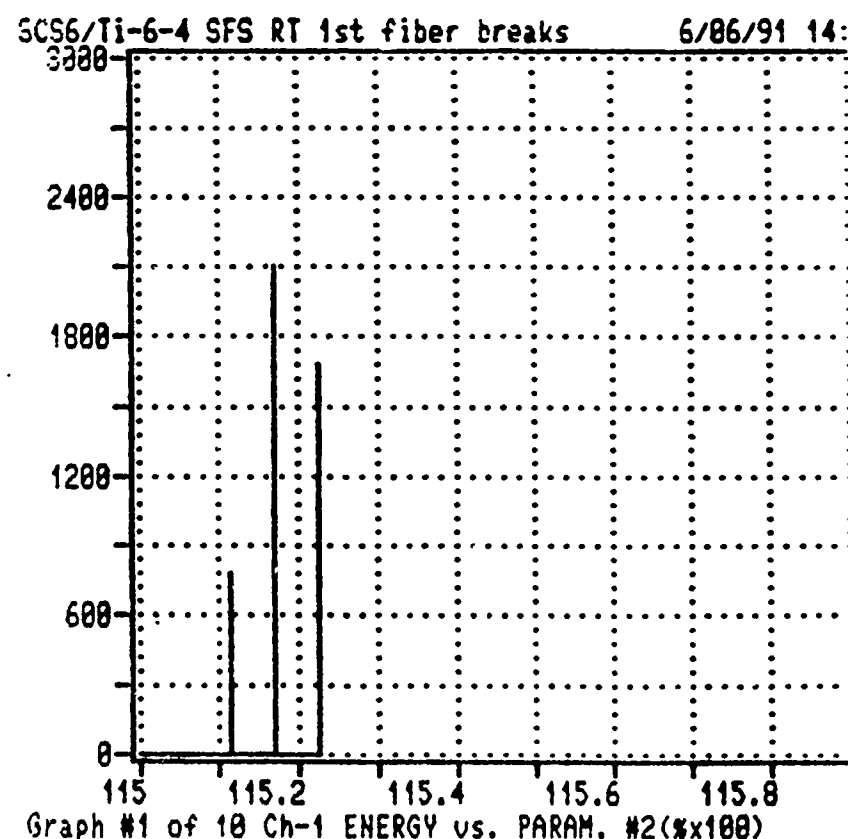
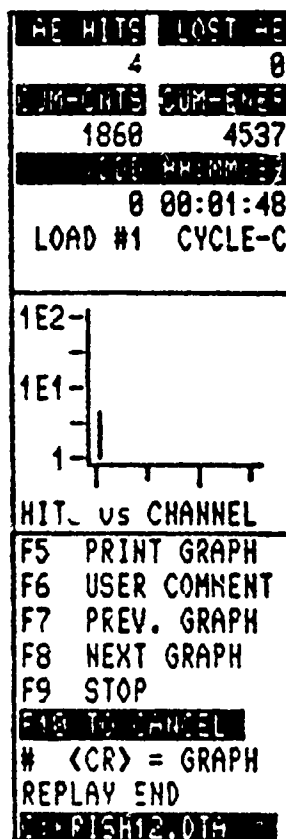
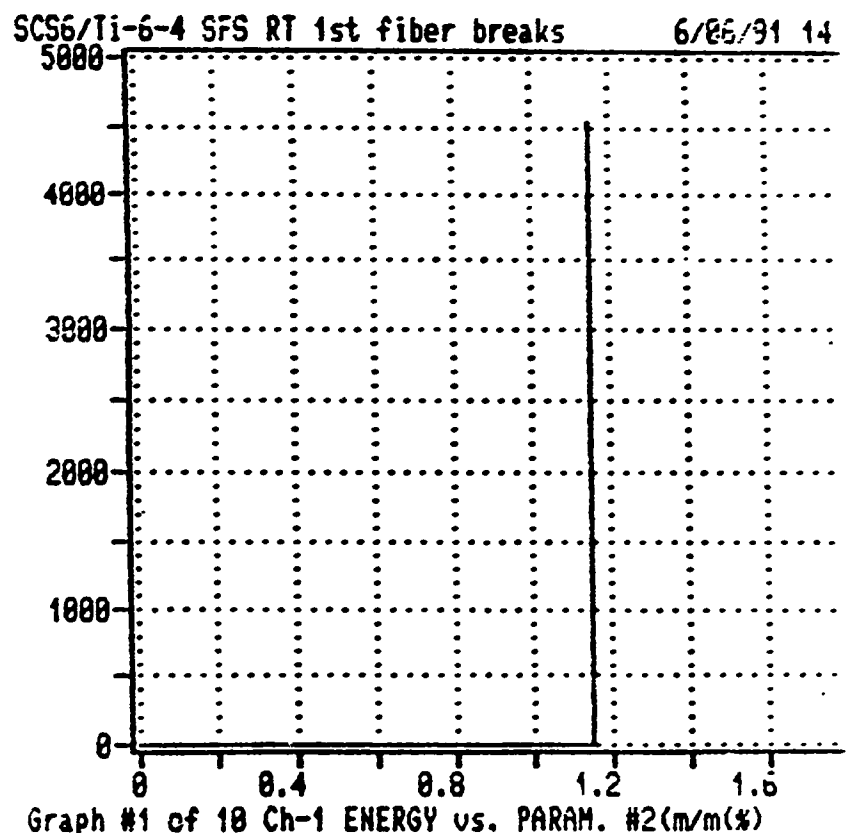
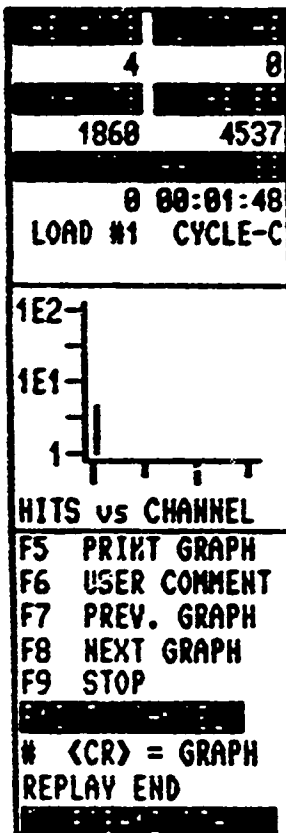


Figure 1b and 1c: Acoustic emission spectra acquired of the 1/2% deformed composite.

Ti-6 Al-4V / SCS-6
SINGLE FIBER COMPOSITE
TENSILE TEST (RT)

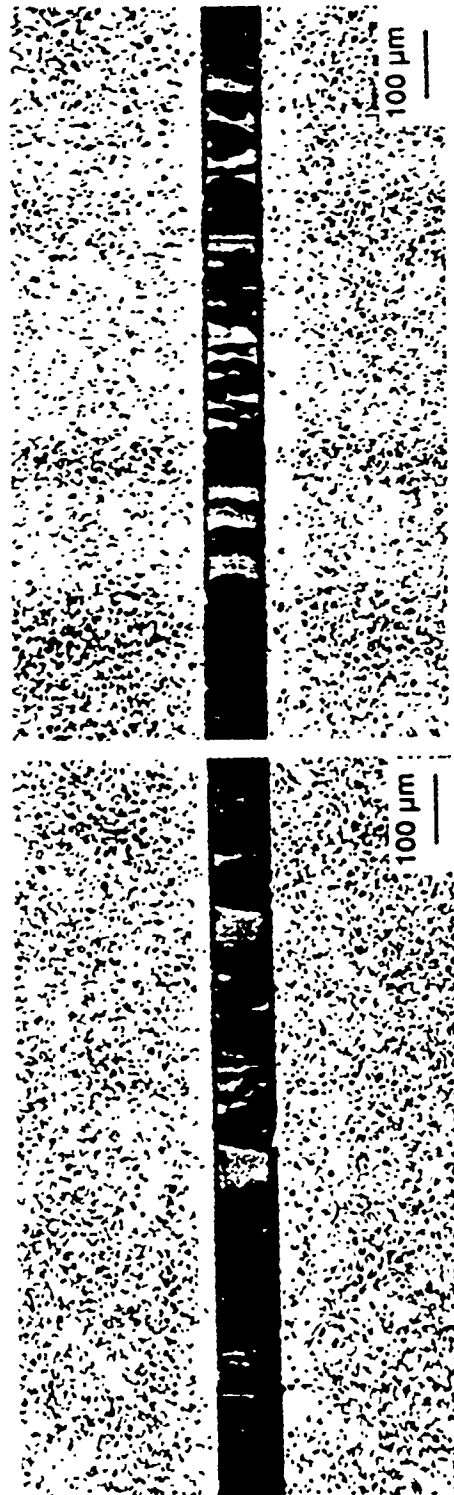


Figure 2: Optical micrograph of sectioned composite after tensile test to failure.

alpha Ti from TEM 6/25/91..figs 1730-1745

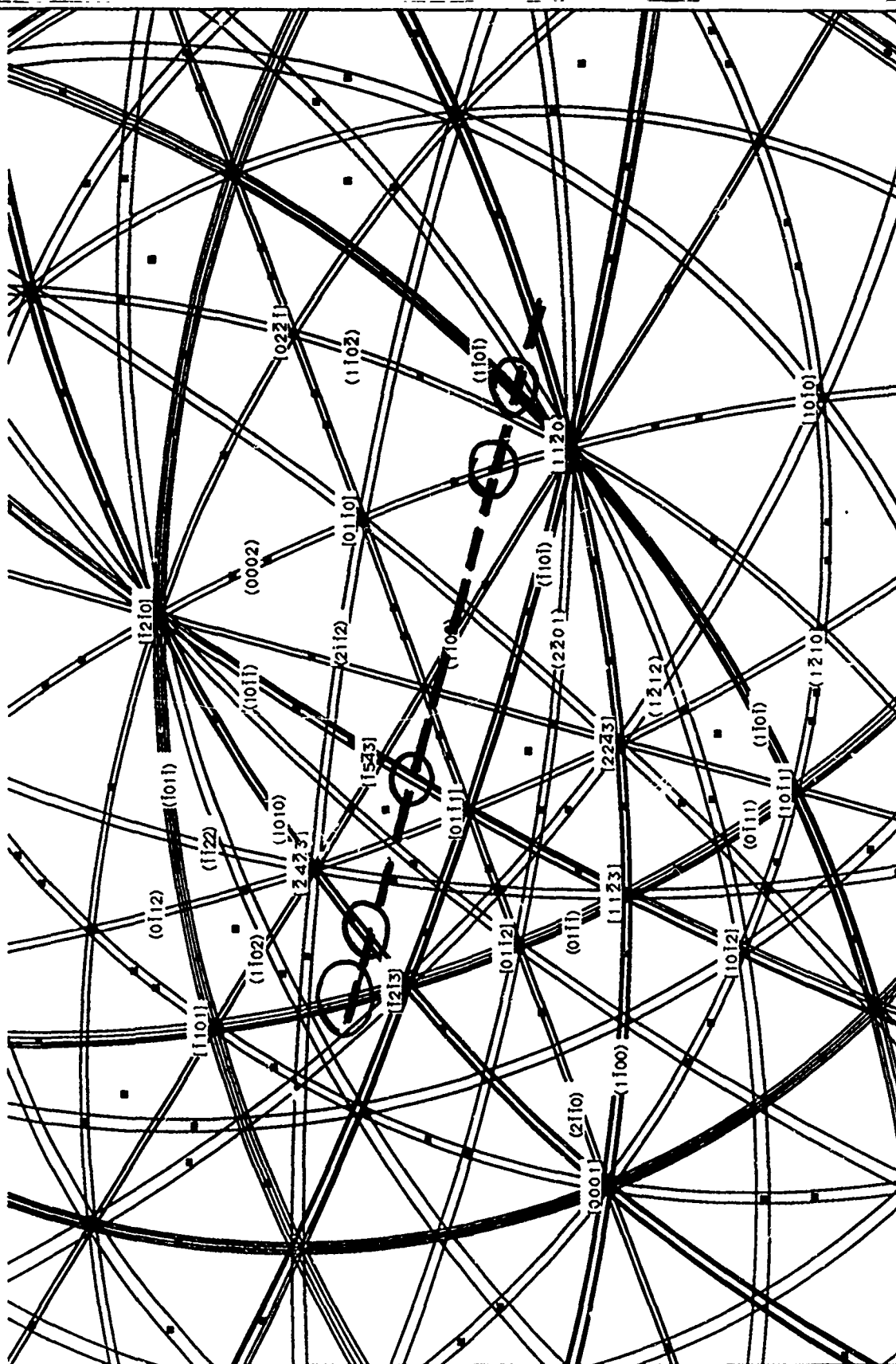


Figure 3: Kikuchi Map with 2-beam conditions of Micrographs 16a through 16e circled.

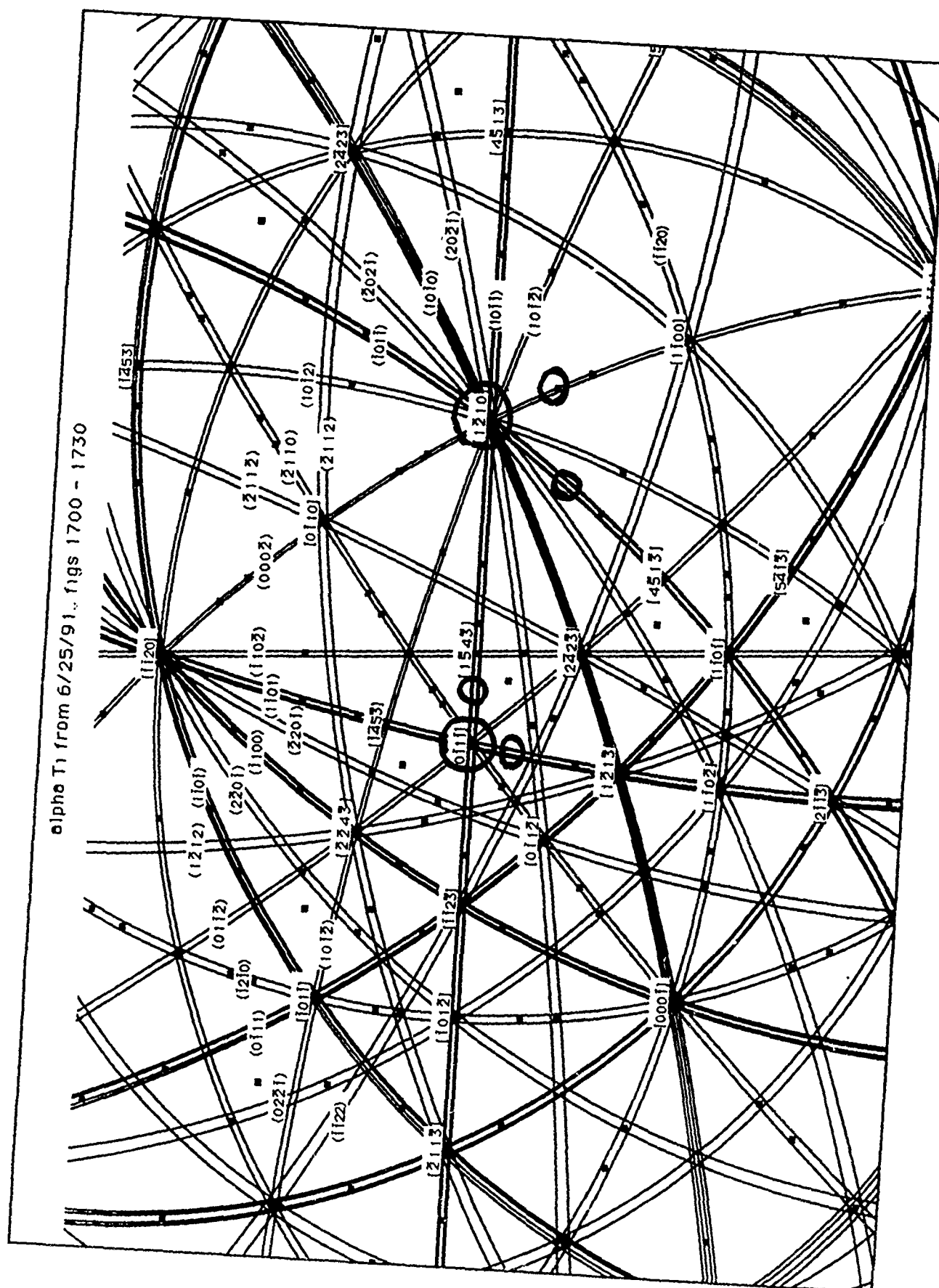
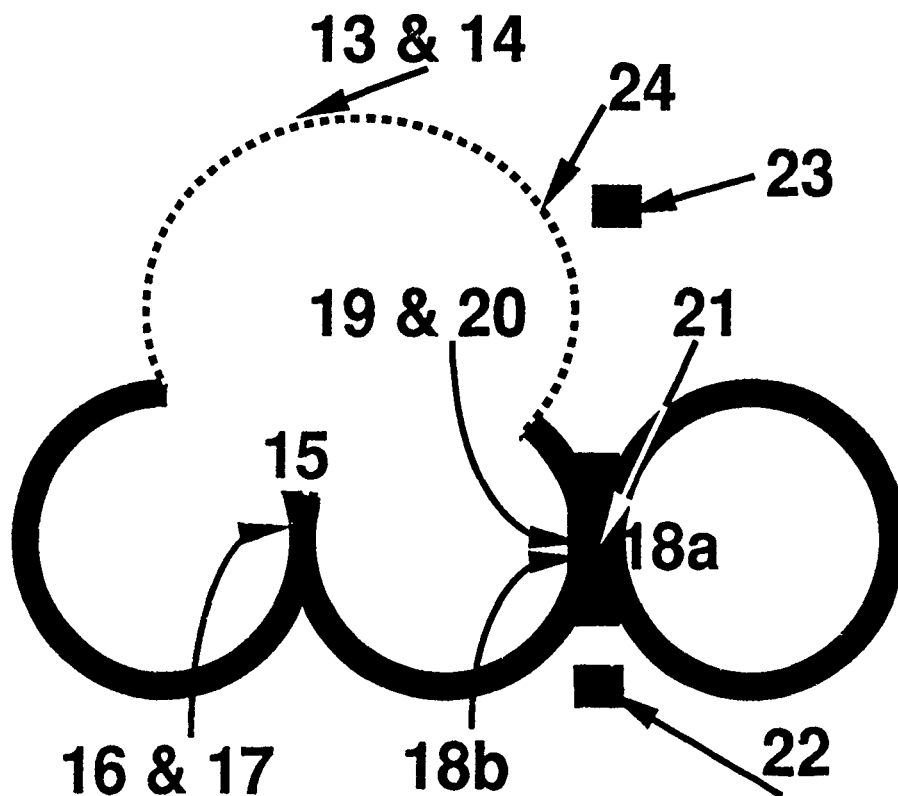
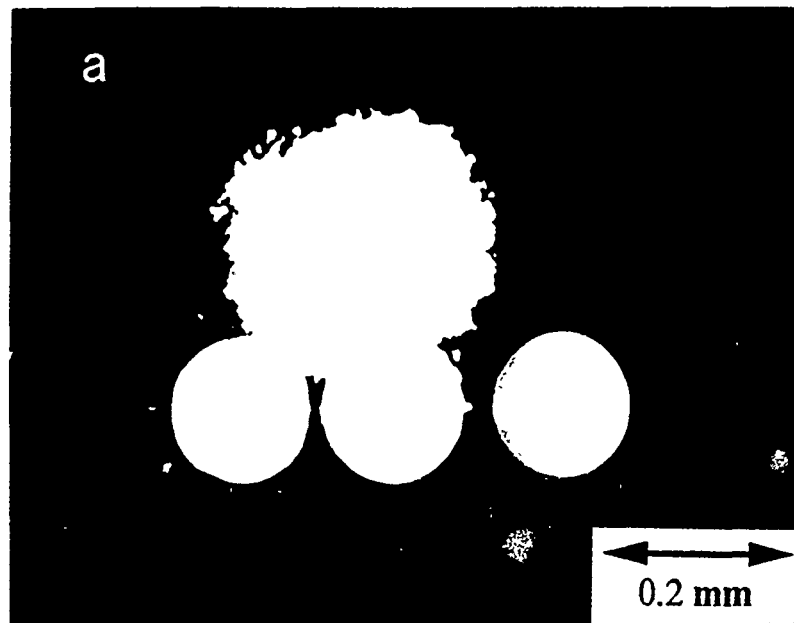
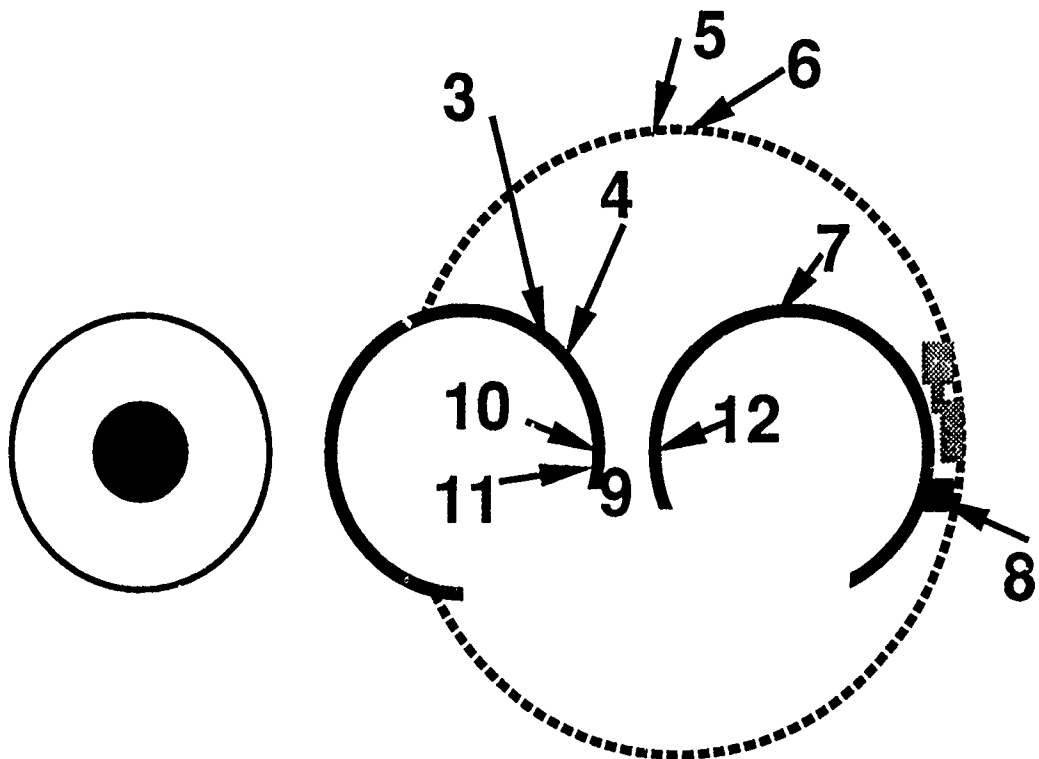
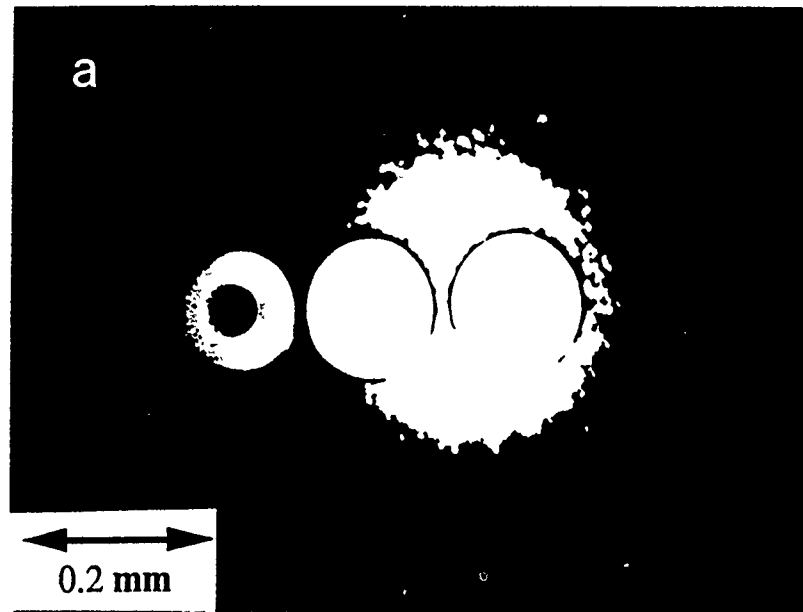


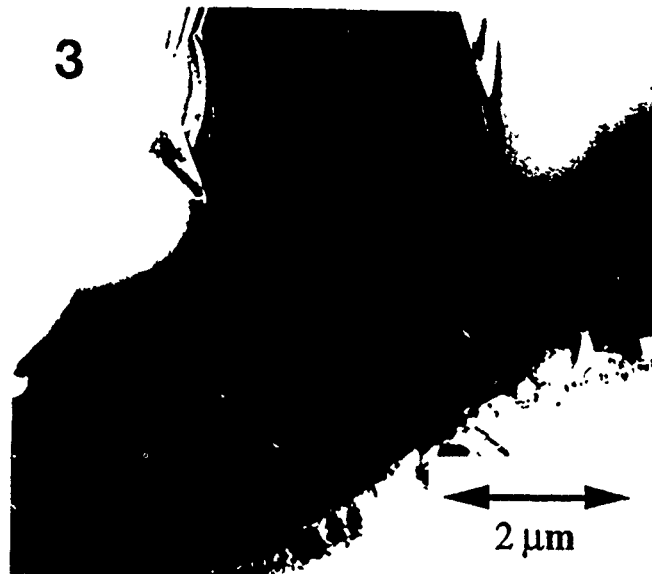
Figure 4: Kikuchi Map with locating zone axes and 2-beam conditions of Micrographs 17a through 17d circled.



Micrograph 2: (a) Optical image acquired with transmitted illumination of TEM sample prepared from the 1/2% deformed composite. The "bridges" are matrix Ti alloy between fibers remaining after ion milling. (b) A schematic of Micrograph 2a which indicates the specific locations from which the noted TEM images are acquired.

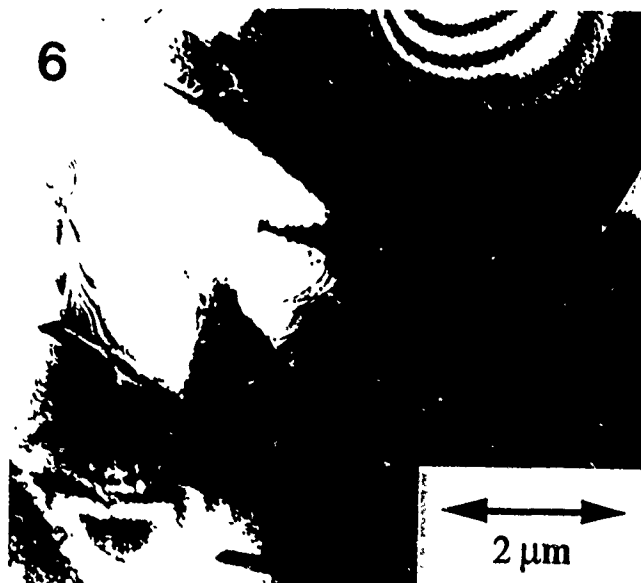


Micrograph 1: (a) Optical image acquired with transmitted illumination of TEM sample of as-processed composite. The thin crescents of material remaining after ion milling represent the interface between the fiber and the matrix. (b) A schematic of Micrograph 1a which indicates the specific locations from which the noted TEM images are acquired.



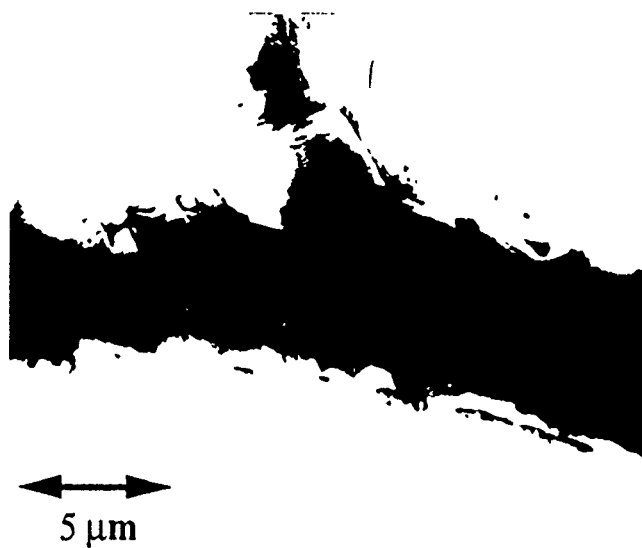
Micrograph 3: Bright Field (BF) TEM image acquired of the interface region of the as-processed composite. A layer, typically $<0.5 \mu\text{m}$ thick, of fine ($< 100 \text{ nm}$) TiC grains is present closest to where the outer coatings of the SiC fiber used to exist. The next layer, $\sim 1\text{-}2 \mu\text{m}$ thick, is comprised of titanium silicide grains ($\sim 0.5 \mu\text{m}$ diameter). Larger α grains ($\sim 5 \mu\text{m}$ diameter) of Ti are also depicted.

Micrograph 4: BF image of an interface region similar to that of Micrograph 3, except that no titanium silicide layer is observed. Such a "missing" layer is often observed.



Micrograph 5: BF TEM image acquired of a matrix α (HCP) Ti grain of the as-processed composite. The grains far from the interface are typically free of any dislocations, but occasionally contain subgrains ($\sim 1 \mu\text{m}$ diameter).

Micrograph 6: BF image depicting an α region sandwiched between β regions in the matrix of the Ti alloy. In such constrained, smaller regions of α phase, dislocations are often observed in the as-processed composite.

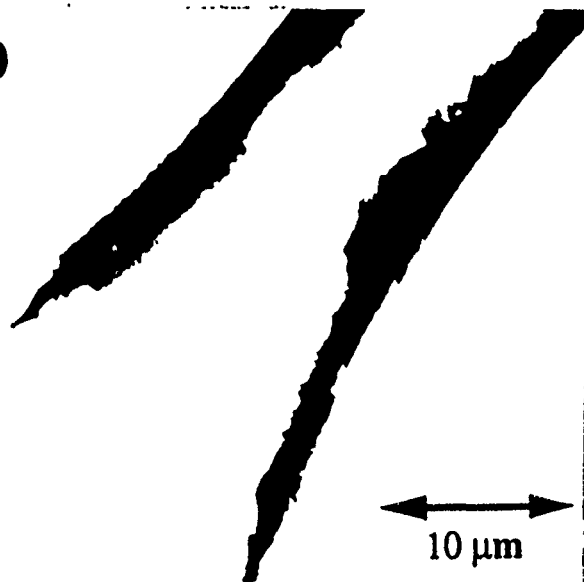


Micrograph 7: BF TEM image acquired of matrix α grains near the interface of the as-processed composite. Most grains exhibit no dislocations; however, an occasional second grain from the interface, as depicted here, does exhibit dislocations. In this case the dislocations are believed an artifact of sample preparation (see text).

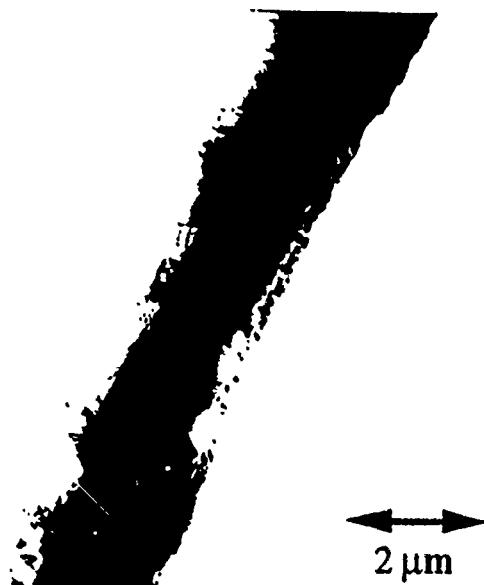


Micrograph 8: (a) BF low magnification TEM image acquired with the HVEM operating at an acceleration voltage of 1.5 MeV. These matrix α grains are the only grains which bridge the crescent interface region to the bulk of the matrix after sample preparation (see Micrograph 1b), and thus are expected to have been stressed. Higher magnification BF images (b), (c), and (d) are acquired after sequential small tilts to provide diffracting conditions that determine the presence of subgrains as well as dislocations within the subgrains. These dislocations are believed to be an artifact of sample preparation which has left this thin bridge of material experiencing high stresses whenever the crescent interface region is jostled.

9

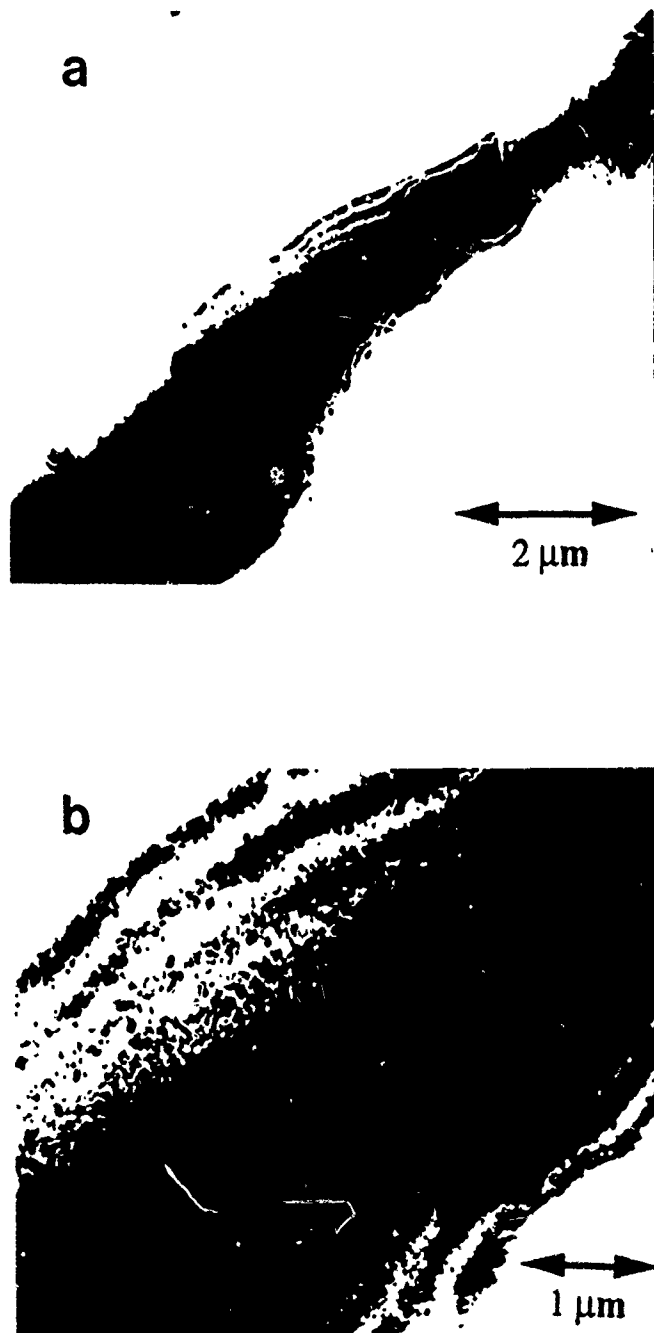


10

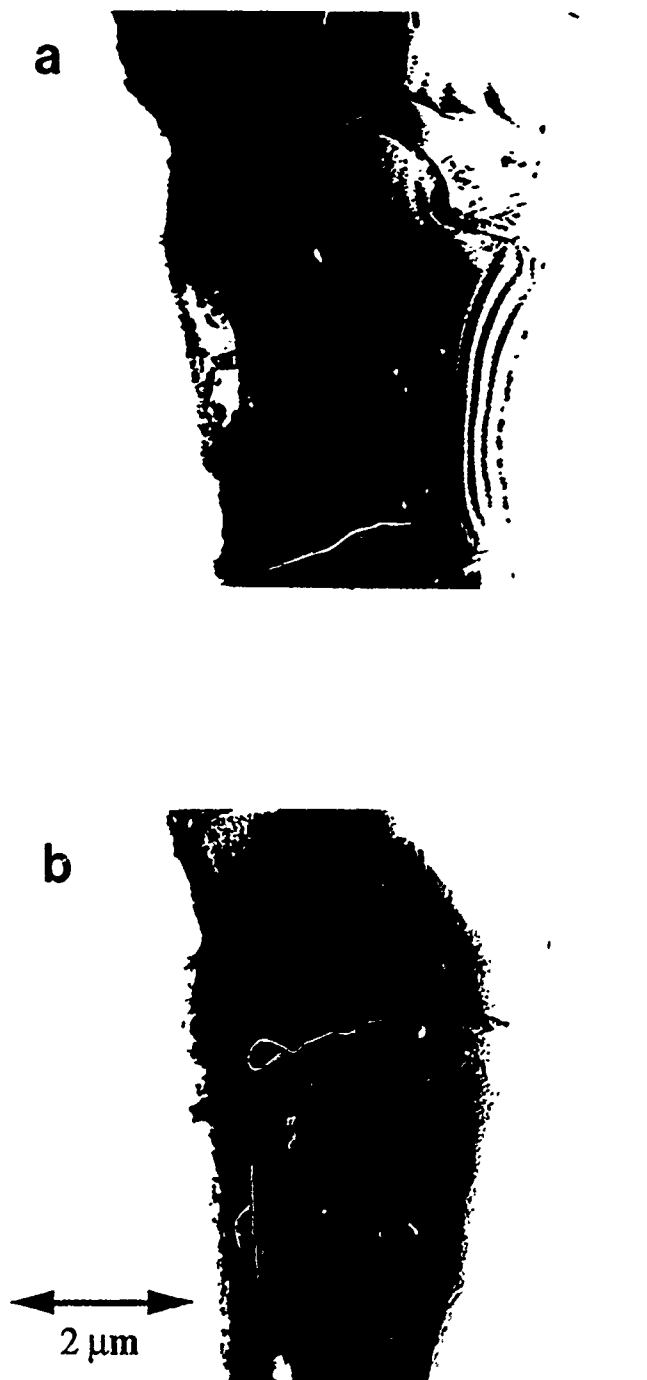


Micrograph 9: BF low magnification TEM image depicting thin regions of α grains at the interface of the fibers after ion milling the as-processed composite. Although these bridges of material are narrow, they are quite thick and not easily transparent to 200 keV electrons.

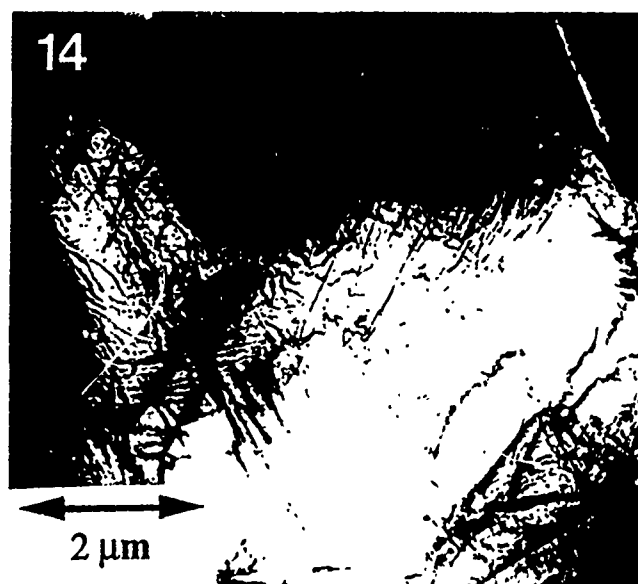
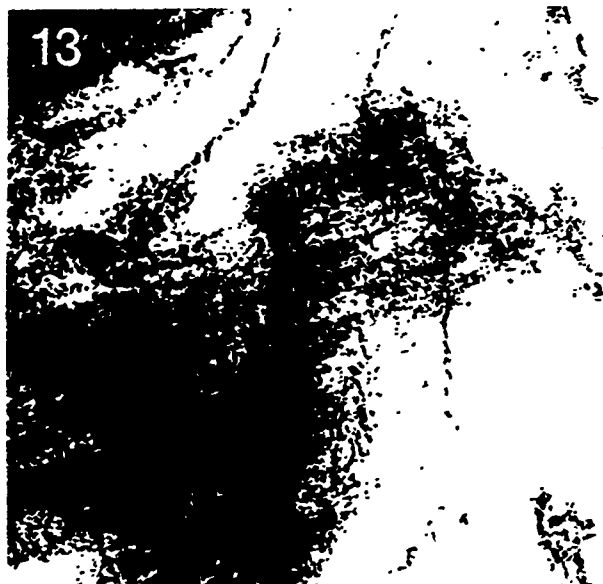
Micrograph 10: BF higher magnification TEM image depicting thin regions of α grains, at the interface of the as-processed composite, containing rows of dislocations. In this case the rows are perpendicular to the fiber / matrix interface.



Micrograph 11: (a) BF low magnification TEM image, acquired with a 2-beam condition of $g = [10\bar{1}1]$, of α grains at the interface of the fibers in the as-processed composite. (b) BF higher magnification image depicting rows of dislocations. Dislocation pile-up perpendicular to the fiber / matrix interface appears to have occurred, but more a definitive analysis is required.



Micrograph 12: (a) and (b) BF TEM images of two α grains, out of four sequential α grains at the interface of the as-processed composite, which exhibit a row of dislocations that is parallel to and displaced by ~ 0.5 microns from the interface.

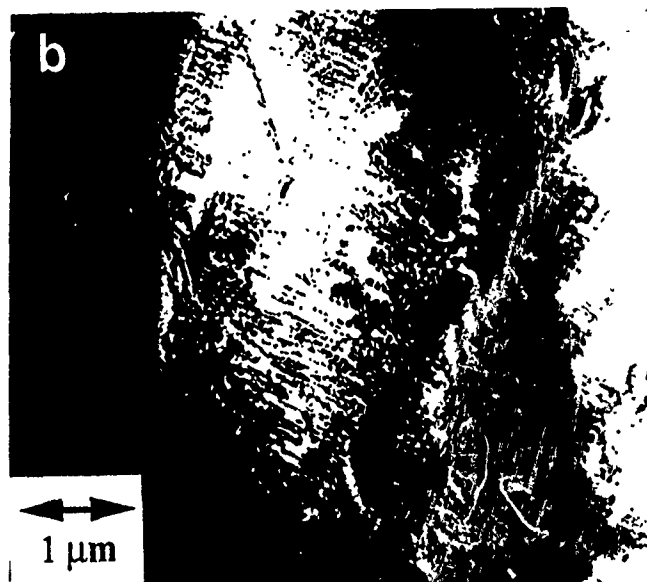


Micrograph 13: BF TEM image, acquired with a 2-beam condition of $g = [0111]$, of a typical α grain far from the interface in the 1/2% deformed composite sample.

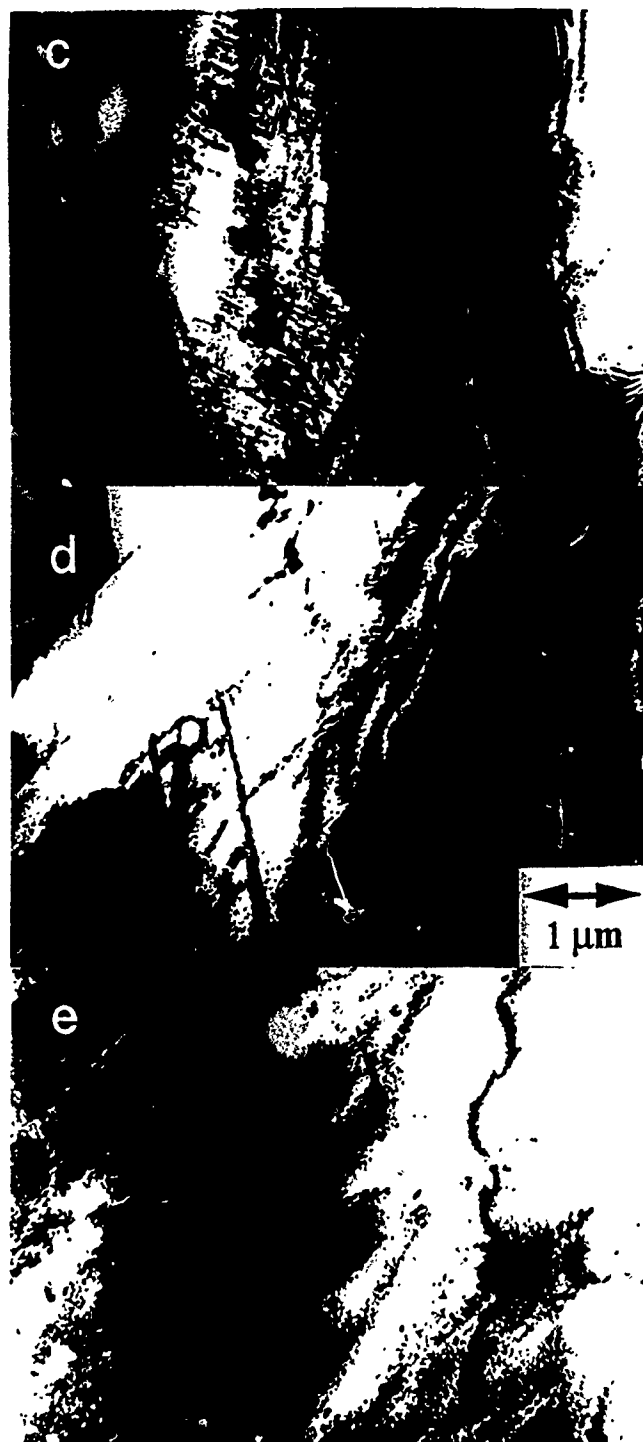
Micrograph 14: BF TEM image, acquired with a 2-beam condition of $g = [2\bar{1}10]$, of an α grain in the matrix far from the interface, which has been judiciously sectioned such that longer, parallel dislocation loops are observed.



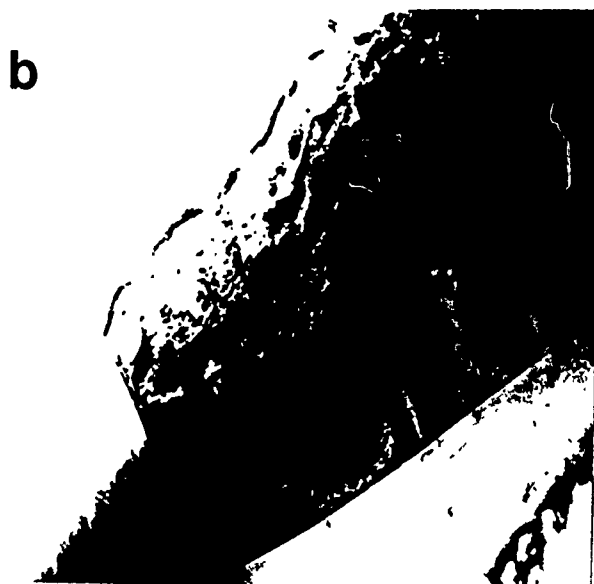
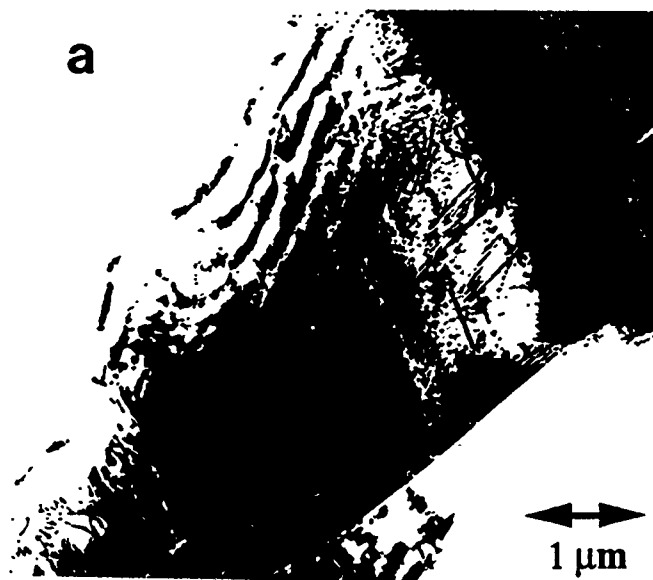
Micrograph 15: BF low magnification TEM image depicting the "bridge" of matrix α grains remaining from between two fibers after ion milling the 1/2% deformed composite sample. This bridge is quite thick; thus in order to obtain some electron transmission with 200 keV electrons, this image was acquired by overexposing the film. Thus the thin areas, from which the TEM analysis in Micrographs 16 and 17 are acquired, appear white in this image (see areas marked by "X").



Micrograph 16: (a) BF TEM image, acquired with a 2-beam condition of $g = [10\bar{1}1]$ of an α grain displaced 3 to 5 μm from the interface of the 1/2% deformed composite sample. This grain is the second grain from the interface. Two sets of rows of dislocations are present, with the more numerous sets that are visible being in rows that are approximately parallel to the interface and the second set having rows that are nearly perpendicular to the interface. (Lower magnification imaging, not included, indicate the dislocations in rows perpendicular to the interface exhibit pile ups at the grain boundary, whereas no significant pile ups are observed for the dislocations in rows parallel to the interface.) (b) BF image, acquired with a 2-beam condition of $g = [\bar{1}010]$, of the same α grain.



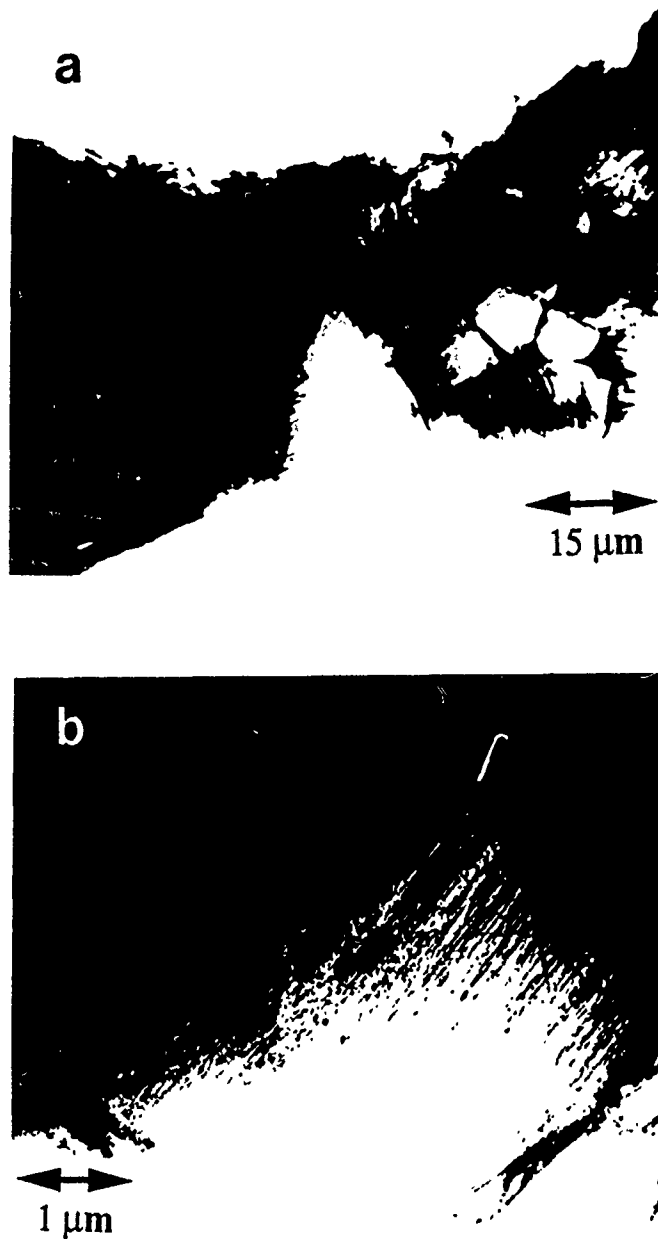
Micrograph 16: (c) BF TEM image, acquired with a 2-beam condition of $g = [01\bar{1}1]$ of the same α grain in the 1/2% deformed composite sample. Only the set of dislocations in the parallel rows are visible, with $g \cdot b = 0$ making invisible the second set of dislocations in rows that are perpendicular to the interface. (d) BF image, acquired with a 2-beam condition of $g = [1\bar{1}0\bar{1}]$, such that $g \cdot b = 0$ for the invisible dislocations in rows parallel to the interface. (e) BF image, acquired with a 2-beam condition of $g = [0002]$, such that $g \cdot b = 0$ for both sets of (invisible) dislocations. These imaging conditions establish the Burgers' vector of dislocations in rows parallel to the interface to be $b = [11\bar{2}0]$ and of the dislocations in rows perpendicular to the interface to be $b = [2110]$.



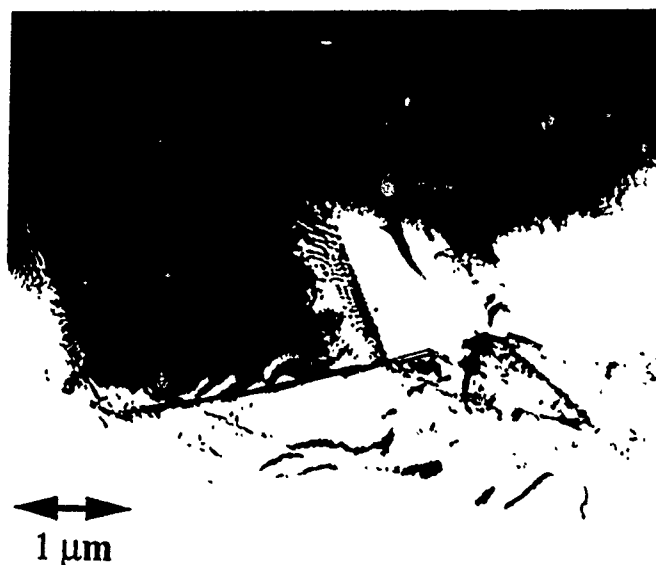
Micrograph 17: (a) BF TEM image, acquired with a 2-beam condition of $g = [\bar{1}011]$ of an α grain displaced 2 to 3 μm from the interface of the 1/2% deformed composite sample. Two sets of rows of dislocations are present, one set being in rows that are approximately parallel to the interface and the second set having rows that are nearly perpendicular to the interface. The dislocations in rows perpendicular to the interface exhibit pile ups at the grain boundary, whereas no significant pile ups are observed for the dislocations in rows parallel to the interface. (b) BF image, acquired with a 2-beam condition of $g = [10\bar{1}1]$, of the same α grain, such that $g \cdot b = 0$ for the almost invisible dislocations in rows perpendicular to the interface.

c**d**

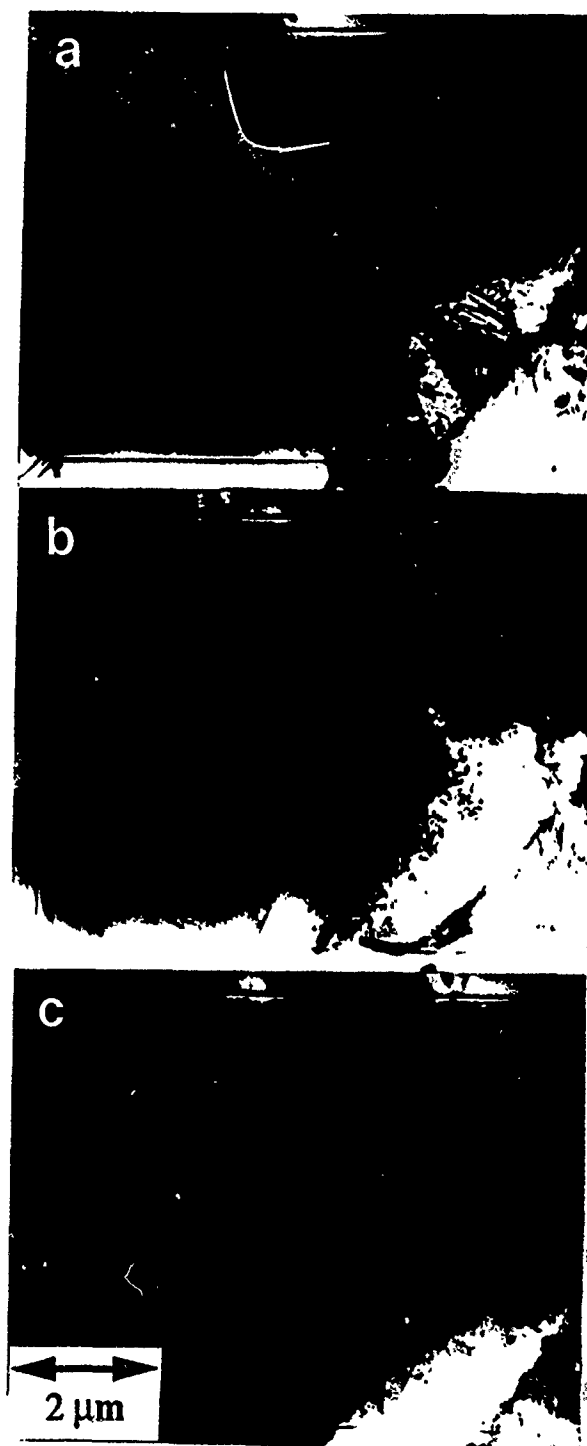
Micrograph 17: (c) BF TEM image, acquired with a 2-beam condition of $g = [1\bar{1}01]$ of the same α grain in the 1/2% deformed composite sample. Only the set of dislocations in the perpendicular rows are visible, with $g \cdot b = 0$ making invisible the second set of dislocations in rows that are parallel to the interface. (d) BF image, acquired with a 2-beam condition of $g = [0002]$, such that $g \cdot b = 0$ for both sets of (invisible) dislocations. These imaging conditions establish the Burgers' vector of dislocations in rows parallel to the interface to be $b = [11\bar{2}0]$ and of the dislocations in rows perpendicular to the interface to be $b = [1210]$.



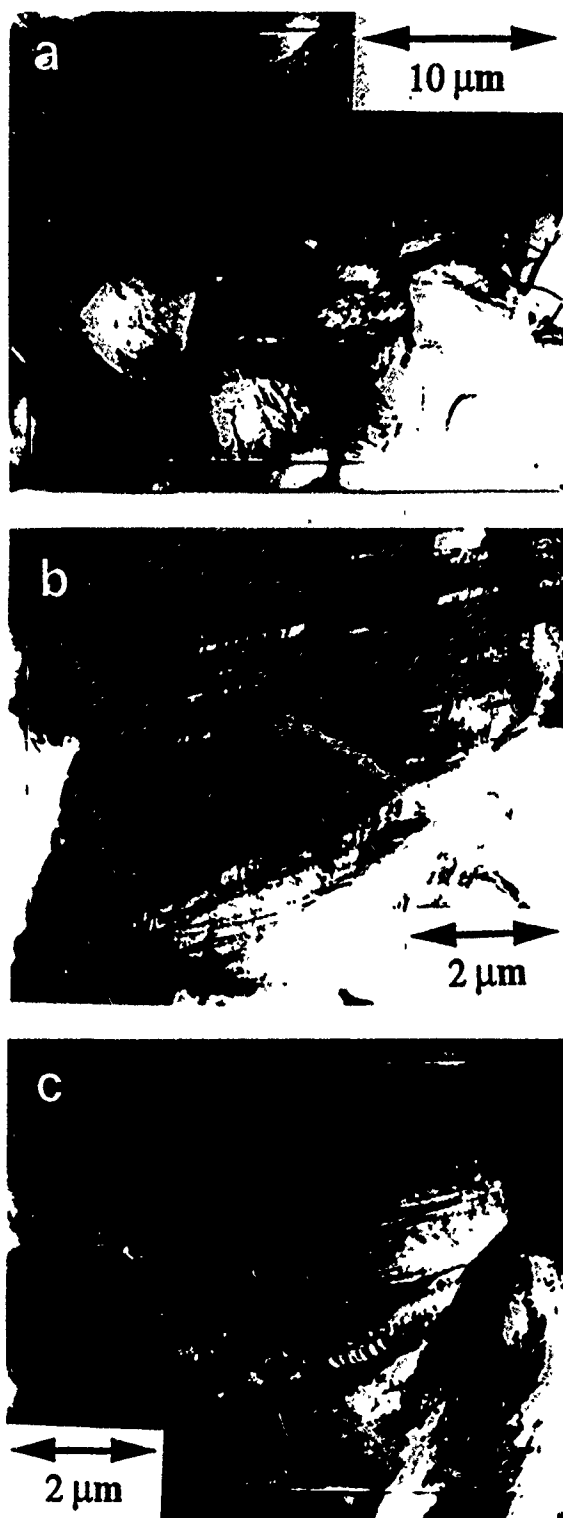
Micrograph 18: (a) BF low magnification TEM image acquired of a second bridge (~40 microns wide) of matrix between fibers in the 1/2% deformed composite sample. As with Micrograph 15, the edges of the hole (the interface regions) are not visible in this image due to the overexposure necessary to allow 200 keV electrons to penetrate the middle of the bridge. Much of the contrast in this image is due to the presence of β phase along grain boundaries and at triple points. Additional diffraction contrast within α grains is due to straight parallel dislocations extending across entire grains. This dislocation morphology is indicative of planar slip, which in turn is prominent in Ti alloys that contain impurities such as oxygen interstitials. (b) BF higher magnification image depicting a grain near the interface, which ranges in thickness from <100 nm to >500 nm. Elongated dislocation loops are readily apparent in thicker regions.



Micrograph 19: BF TEM image, acquired with a 2-beam condition of $g = [10\bar{1}1]$ of an α grain near the interface between fibers in the 1/2% deformed composite sample. Dislocations in rows which are perpendicular to the interface exhibit pile ups at the grain boundary closest to the interface. The grain becomes too thick to image with 200 keV electrons in regions away from the hole.



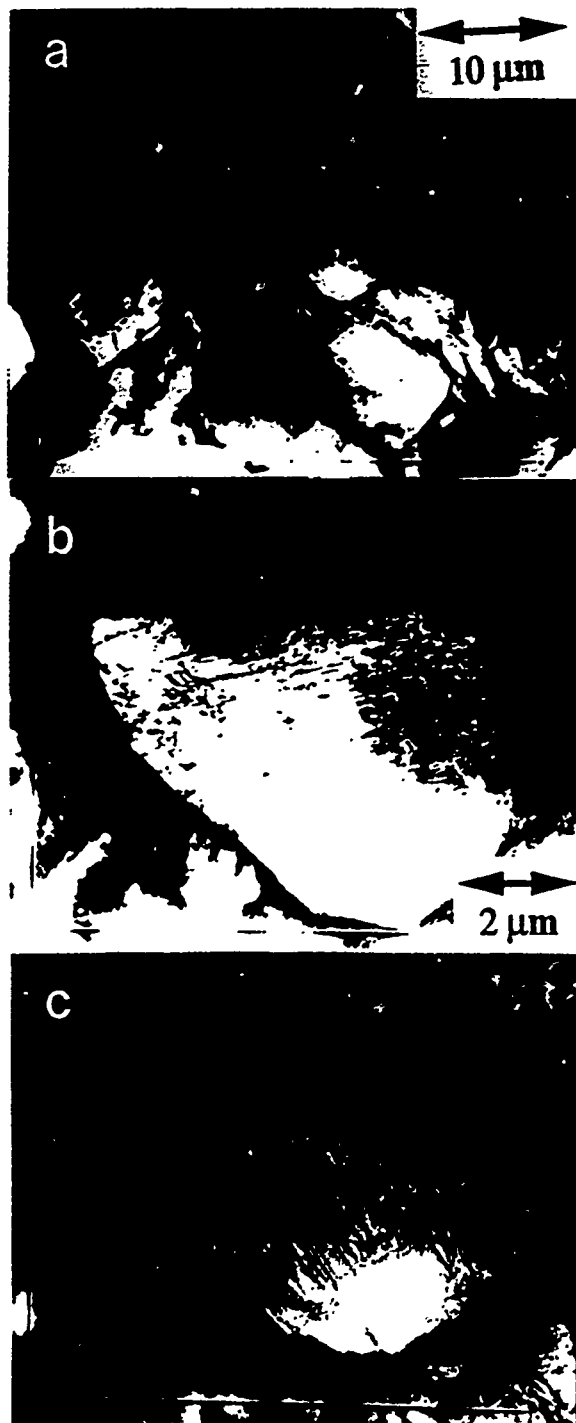
Micrograph 20: (a) BF TEM image, acquired of the same α grain and with the same 2-beam condition as in Micrograph 19, except this is an HVEM image acquired with 1.5 MeV electrons. The rows of dislocations which extend into much thicker regions of the grain are now observable, making it possible to see that these same rows of dislocations are not piled up at the opposite grain boundary. (b) BF HVEM image, acquired with a 2-beam condition of $g = [11\bar{2}2]$, of the same α grain near the interface in the 1/2% deformed composite sample. (c) BF HVEM image, acquired of the same α grain with a 2-beam condition of $g = [01\bar{1}2]$. The disappearance condition of $g \cdot b = 0$ is consistent with these dislocations having a Burgers' vector of the type $b = \langle 2110 \rangle$.



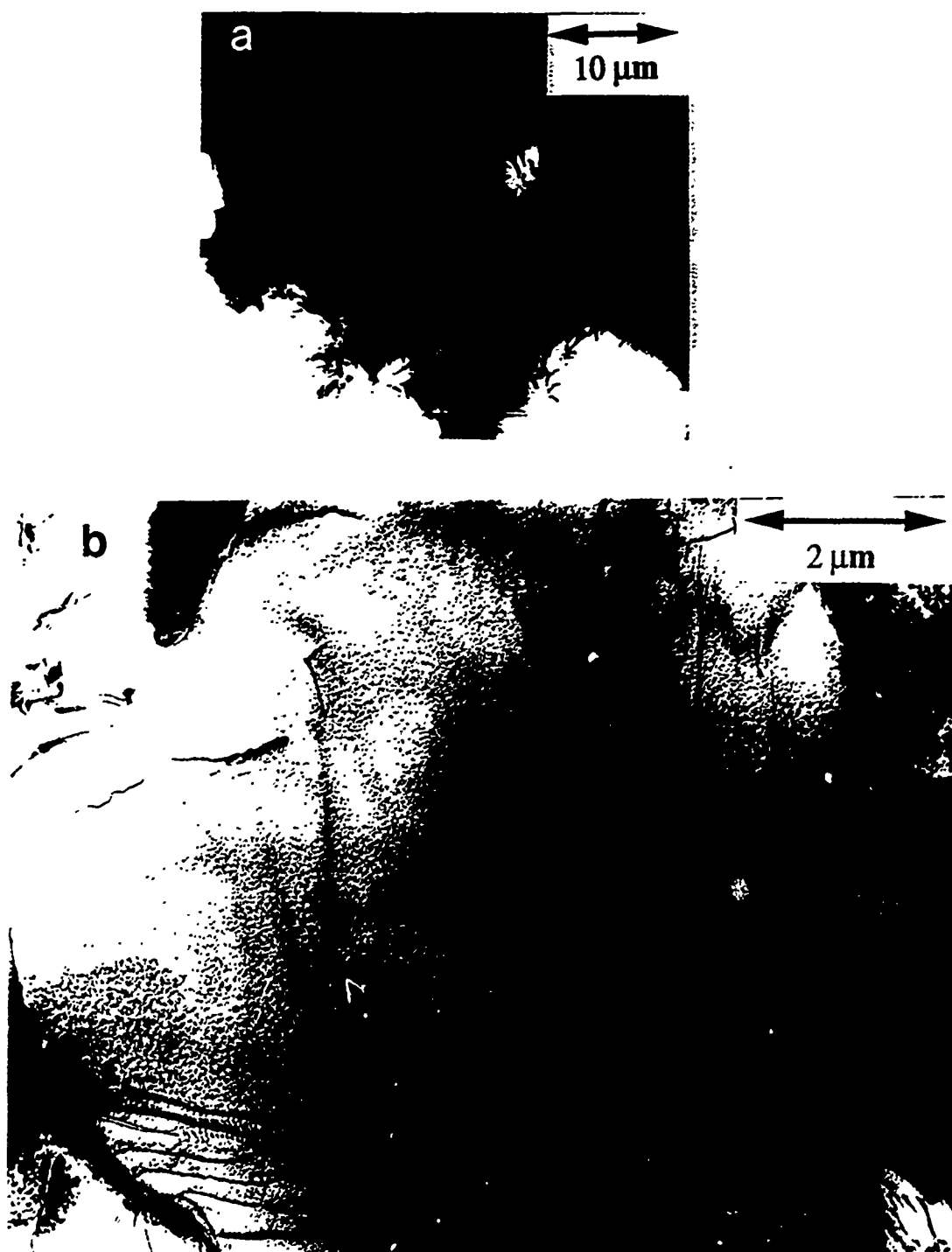
Micrograph 21: (a) BF low magnification image, acquired with the HVEM, of matrix grains directly between fibers and ~20 microns from each of the fiber interfaces in the 1/2% deformed composite sample. (See Micrograph 2b for location of area of analysis.) (b) BF HVEM image, acquired with a 2-beam condition of $g = [011]$, of an α grain with long straight dislocations indicative of planar slip (and presumably of oxygen diffusion from the SCS 6 fibers into the Ti matrix during thermal processing). (c) BF HVEM image, acquired with a 2-beam condition of $g = [110]$, of the same α grain.



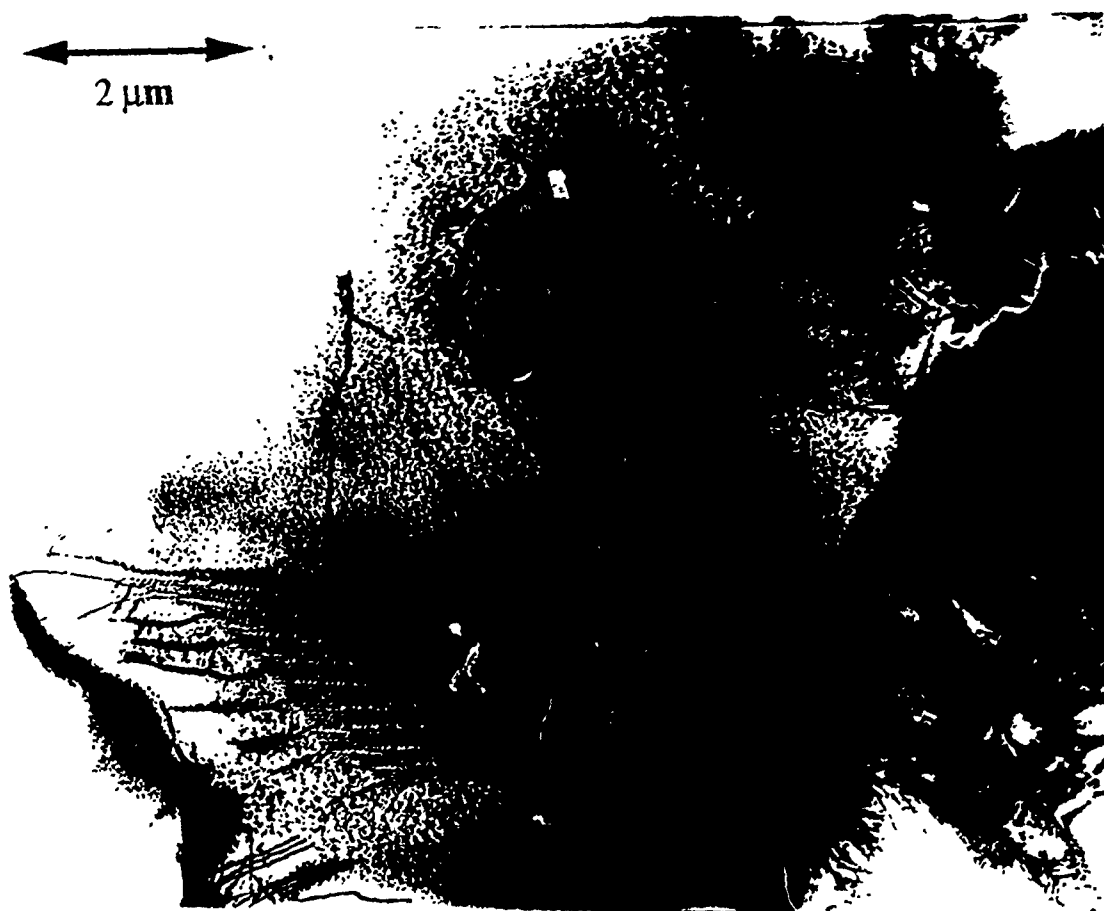
Micrograph 22: (a) BF low magnification image, acquired with the HVEM, of matrix grains not directly between fibers but <50 microns from each of the fiber interfaces in the 1/2% deformed composite sample. (See Micrograph 2b for location of area of analysis.) This region of the matrix was much too thick to be imaged with only 200 keV electrons. None of the grains imaged exhibit planar slip. (b) BF HVEM image, acquired with a 2-beam condition of $g = [11\bar{2}2]$. Two sets of dislocations are visible, but neither are they straight nor do they exist in parallel rows. (c) BF ($g = [10\bar{1}2]$) HVEM image with one set of dislocations invisible. (d) BF ($g = [1\bar{1}01]$) HVEM image. Although these dislocations have a different morphology as compared to dislocations closer to the interface, the dislocation density (based on the number of dislocations) is nearly the same.



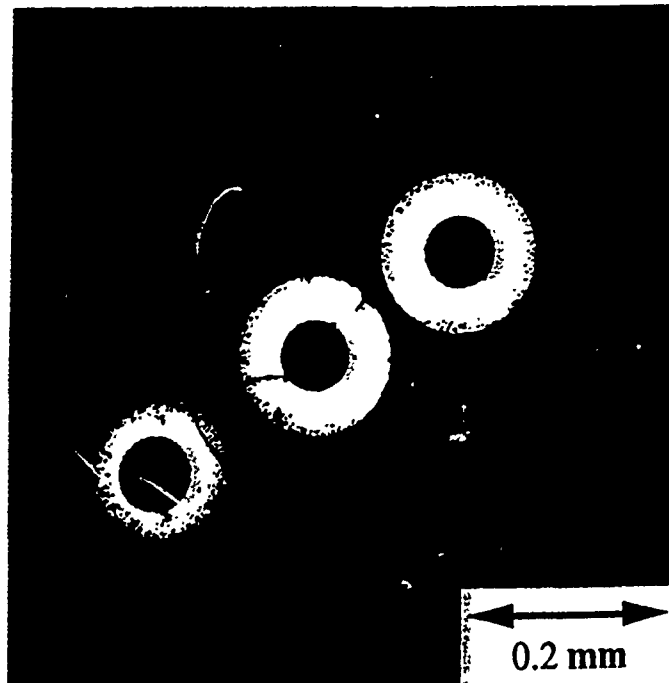
Micrograph 23: (a) BF low magnification image, acquired with the HVEM, of matrix grains far (greater than one fiber radius) from the fiber interface in the 1/2% deformed composite sample. None of the grains imaged exhibit planar slip. (b) BF HVEM image, acquired with a 2-beam condition of $g = [0\bar{1}11]$, exhibiting one set of dislocations as visible. (c) BF ($g = [10\bar{1}0]$) HVEM image with a second set of dislocations visible. After accounting for this grain being thicker than the grain in Micrograph 22, and recognizing that these dislocations loop back upon themselves, enables an analysis of the dislocation density far from the interface being less than the dislocation density between fibers (and near the interface).



Micrograph 24: (a) BF low magnification image, acquired with the HVEM, of matrix grains far (greater than one fiber radius) from the fiber interface in the 1/2% deformed composite sample. The grains in this thinner region exhibit a much lower dislocation density than grains near the interface of fibers. (b) BF HVEM image, acquired with 2-beam a condition of $g = [0111]$, which causes the disappearance of some dislocations and certain segments of the dislocation network.



Micrograph 24c: BF HVEM image, acquired with a 2-beam condition of $g = [2110]$. Compared to Micrograph 24b, different segments of the dislocation network are invisible. The fine network of dislocations present in this grain probably did not form as a result of deformation alone, but rather may be a result of the thermal processing. After accounting for these few dislocations, the dislocation density in this grain is quite low.



Micrograph 25: Optical micrograph, acquired with transmitted illumination, of a cross sectioned TEM sample after dimpling, but before ion milling. The SCS 6 fibers have been thinned sufficiently so as to allow much light to pass through. Cracks present in the fibers are made visible in this manner. (In this case, the cracks were caused by dimpling the sample too thin; however, careful sample preparation can prevent the formation of any new cracks. This would make possible determining the presence of fiber fragmentation events that reside within a TEM cross section sample.

ULTRASONIC BEAM PROPAGATION: DIFFRACTIONLESS BEAMS AND
BEAMS IN ANISOTROPIC MEDIA

Byron Newberry, Assistant Professor
Mark Preischel, Graduate Student
University of Cincinnati

ABSTRACT

Two problems were addressed during the summer research activity, both dealing with the propagation of ultrasonic beams as used in the nondestructive evaluation of materials. First, the possibility of making a transducer which produces an ultrasonic beam that does not diffract, or spread, as it propagates was explored. As a result of the work, such a beam was produced and a proposal for the construction of a practical device was developed. The second topic concerned the modeling of ultrasonic transducer beam propagation through anisotropic materials, such as fiber reinforced composites. As a result, simple formulas which predict the on-axis field profiles of beams in such materials were derived and validated through comparison with more complex models.

This report is broken into two sections describing each of these topics in detail.

I. PRODUCTION OF A DIFFRACTIONLESS ULTRASONIC BEAM

INTRODUCTION

The propagation of ultrasonic beams is a phenomenon of widespread interest to a variety of technologies including sonar, medical ultrasound, and nondestructive evaluation. One goal in most applications is the production of a narrow, highly collimated beam of sound. Rigid piston radiators have often been employed and have been thoroughly analyzed. This type of source has the generally undesirable attributes of a complicated near field interference structure as well as far field side lobes. Sources which produce a Gaussian amplitude distribution have been studied since, for this case, the previous disadvantages are eliminated. Unfortunately, Gaussian radiators are more difficult to manufacture [1,2]. Various types of focusing probes have also been analyzed for concentrating the sound in a narrow band over a short depth of field. Conically focussed, or axicon, probes have been examined for the purpose of extending the focal region for resolution over a greater depth of field.

One disadvantage common to all of the above sources, and indeed to any physically realizable source, is the phenomenon of beam spread due to diffraction.

Recently, in the optics literature, Durnin [3,4] has pointed out the existence of an axially symmetric harmonic solution to the scalar wave equation in the form of a transverse Bessel function modulated by an axially varying phase, $\phi(r,z) = J_0(\alpha r) \exp(j\beta z)$, where $k^2 = \alpha^2 + \beta^2$, and k is the wave number. When $\alpha=0$, this is just a plane wave solution. However, for $0 < \alpha < k$, we have a forward propagating field which has a beam-like transverse profile that does not vary with axial position, and is therefore diffractionless. The beam energy is not localized, however, but is instead infinite due to J_0 not being square integrable. Durnin analyzed a J_0 aperture approximation to a J_0 beam for the optical case and has shown both analytically and experimentally that a beam may be produced which can have a small spot size while retaining a significant depth of field over which the transverse profile is approximately constant. Initial attempts to produce a diffractionless acoustic beam have been reported by other investigators [5-7]. These have employed transducer arrays or transducer disks with radially varying poling or excitation. In this paper, we discuss an approach for the acoustic case analogous to the

method of Durnin and report the experimental generation of a nondiffracting J_0 Bessel beam. We also will discuss the potential for constructing a practical transducer via this approach.

EXPERIMENT

If the Bessel function solution is decomposed into an angular spectrum of plane waves, we find that the only wave vectors which contribute lie on the surface of a cone centered about the z axis and making an angle $\theta = \arcsin(\alpha/k)$ with it. Durnin showed, for the optical case, that this plane wave spectrum can be generated by a construction similar to that shown in Fig. 1, which is for the current acoustical case. A circular PZT piston transducer of radius a is used as the source. The center of the transducer disk is blocked by a circular disk of radius $b < a$ made of a highly attenuative material (in this case, polystyrene). The resulting effective source is a thin annulus.

An acoustically convergent lens of focal length F and diameter $2R$ is placed a distance F in front of the transducer. Each point on the ring radiates a spherical wave which the lens transforms into a plane wave traveling at angle $\theta = \arctan(a/F)$ relative to the z axis. Summing contributions from each point on the ring yields the

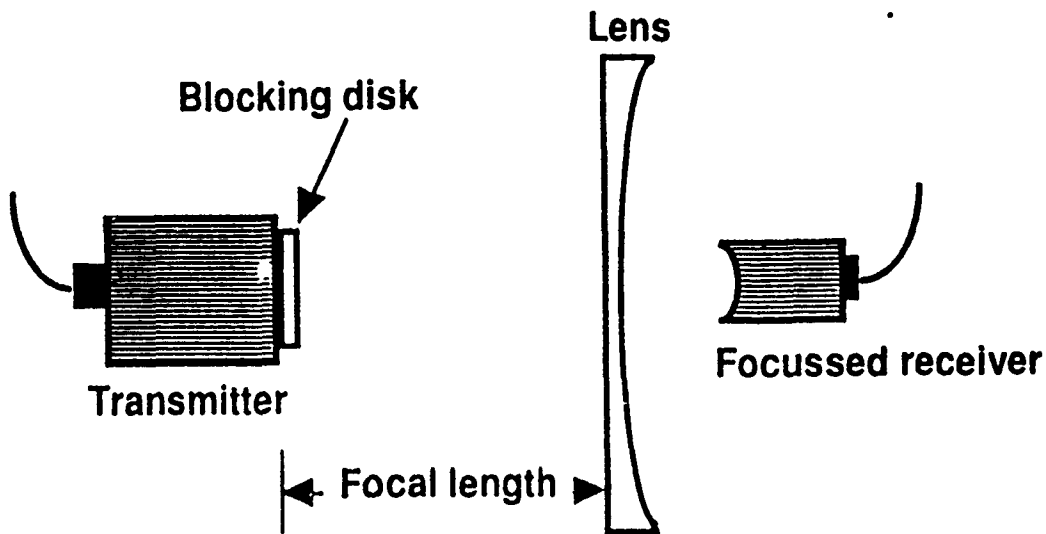


Figure 1. Experimental setup for producing diffractionless ultrasonic beam.

conical set of wave vectors necessary for a Bessel beam with width parameter $\alpha = (ka/F)(1+a^2/F^2)^{-1/2}$. If $a \ll F$, then $\alpha = ka/F$. The maximum possible depth of field is $z_{\max} = R/\tan\theta = RF/a$. Past this point, a shadow zone is produced due to the finite lens aperture.

A 0.25 inch radius, broadband transducer was used as the source. The blocking disk had a 0.22 inch radius. The lens was a 1.0 inch radius, fused quartz plano-concave which has an acoustical focal length of 6.85 inch in

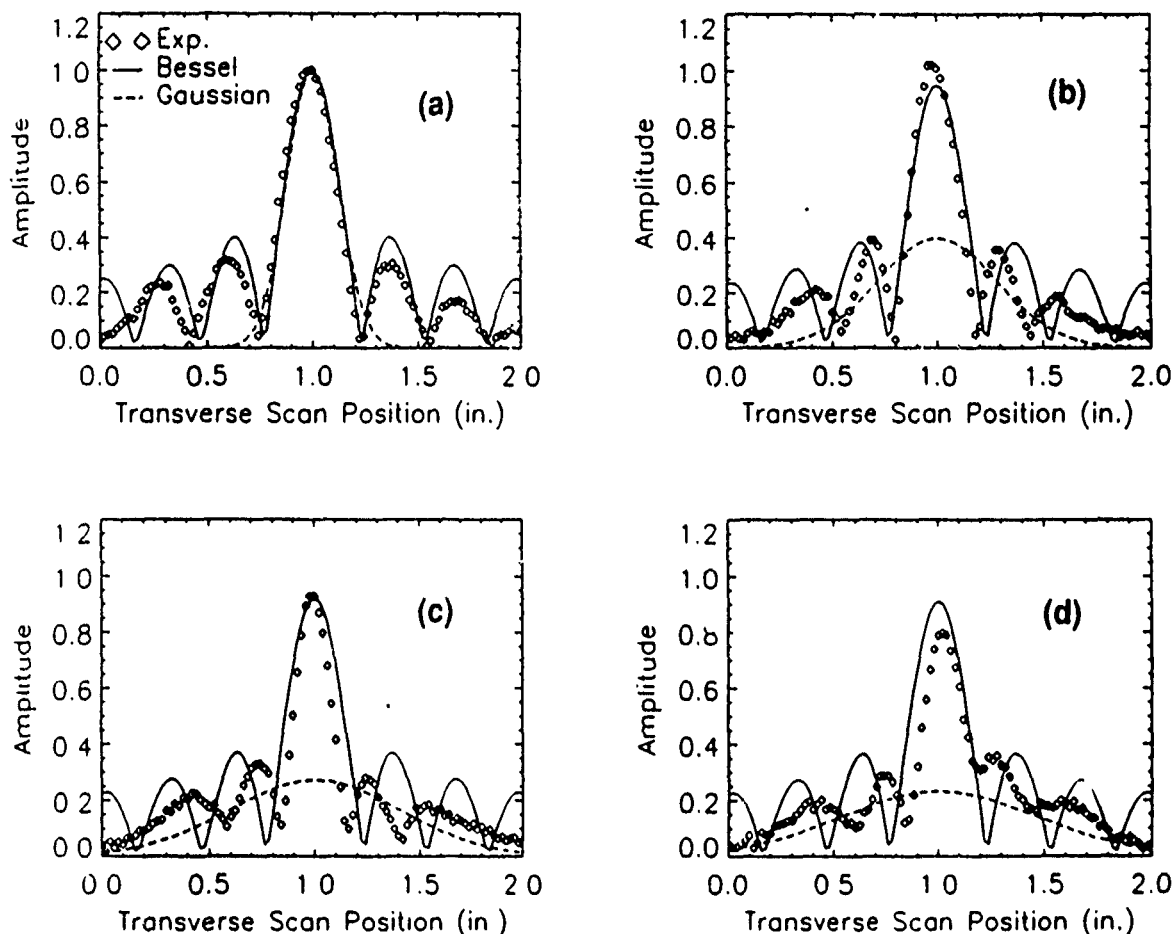
water. For measurement of the generated sound field, a 0.75 inch focal length, 0.25 inch radius transducer was scanned in a 2-D grid perpendicular to the beam axis. The focal spot of the receiver was much smaller than the Bessel beam width so that the measured amplitude profile should closely represent the actual Bessel beam profile at the axial distance corresponding to the focal point of the receiver.

The received rf waveform at each point in the scan grid was recorded and Fourier transformed to obtain the frequency spectrum. The amplitudes at particular frequency values were extracted for each point and plotted versus position in the scan grid, resulting in images of the transverse beam profiles at different frequencies and axial positions.

Figure 2a shows the data along a slice through the peak of the sound field transverse to the beam axis at 3 MHz, at an axial distance of $z=0.5$ inch past the lens. Also plotted is a J_0 function with $\alpha=10.4/\text{inch}$. This value of α , which gives a best fit to the data, corresponds to a ring radius of 0.224 inch, approximately the inner radius of the annulus. For comparison, a Gaussian beam with the same $1/e$ width as the main lobe of the Bessel function is also plotted ($w=0.17$ inch).

Figures 2b-d show the beam profile at distances of $z=10, 15,$ and 17.5 inches past the lens. The theoretical Bessel function has been scaled down at each axial distance to account for sound attenuation in water. It is apparent that the Bessel beam retains its initial width and amplitude to about 17.5 inches, although the side lobe structure has decayed. At 20 inches, which is not shown, the main lobe has broken down. The ideal z_{\max} for this case is 27.4 inches. At 17.5 inches, the Gaussian beam has decreased by approximately 80% from its initial amplitude. The Rayleigh range for the Gaussian is $z_r = \pi w^2 / \lambda = 4.6$ inch. The Bessel beam has propagated more than 3 times this distance without significant diffraction loss.

Because the source is a finite width annulus rather than an infinitesimal ring, a range of source radii contribute to the beam field, each producing a slightly different beam width parameter α . Since the phase parameter β varies with α , the wave becomes dispersive when the source has a finite width. This contributes to the breakdown of the Bessel profile before the ideal z_{\max} is reached.



2. Transverse profiles of Bessel beam at 3 MHz at axial distances of (a) 0.5 in., (b) 10 in., (c) 15 in., (d) 17.5 in.

The above results are quite exciting, although one disadvantage of the Bessel beam for the monochromatic case is the large magnitude of the side lobes. The beam is found to also be nondiffracting for the pulsed case. Figures 3a-d show the 2-D transverse profile scans of the peak-to-peak voltage of the rf waveform at various

distances from the lens. The pulsed beam is actually somewhat narrower than the 3 MHz case due to the contribution of higher frequencies. Also, the pulsed beam displays no sidelobes due to incoherent addition of the sidelobes at the different frequencies. Since ultrasonic scanning is often done in the pulsed mode, this shows promise for having a narrow, sharply peaked interrogating beam with a large depth of field.

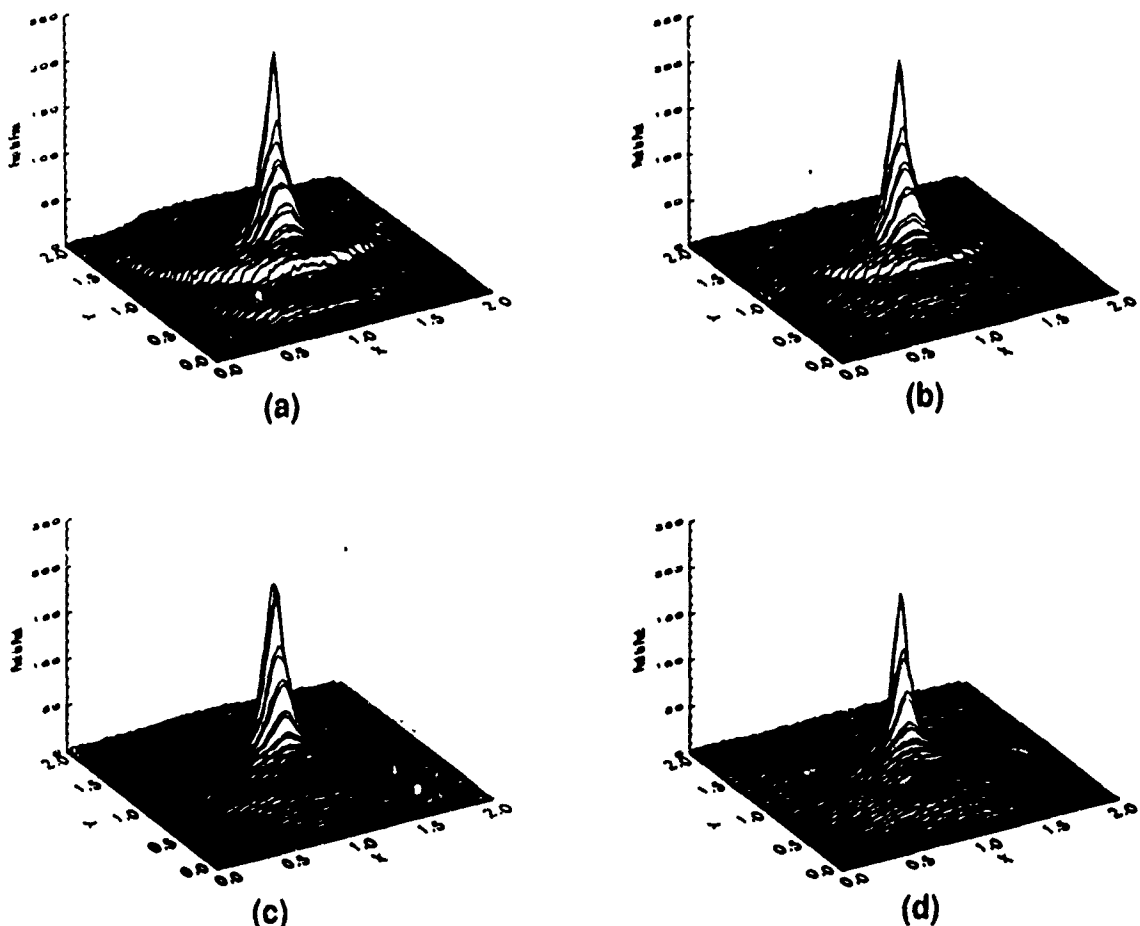


Figure 3. Transverse profiles of pulsed peak-to-peak voltage
(a) 0.5 in., (b) 5 in., (c) 10 in., (d) 15 in.

DISCUSSION

These results suggest that current ultrasonic transducer beam types can be greatly improved upon by the implementation of the diffractionless Bessel beam idea. The apparatus illustrated in Fig. 1, however, was contrived for the purpose of demonstrating the concept and is clearly not a practical one for ultrasonic inspection. However, it may be possible to construct a Bessel beam transducer by appropriately constructing a transducer element and lens combination. The manufacture should not be very different from that of a conventional focussed probe.

A proposed configuration is shown in Fig. 4. In this case, an annular transducer element is mounted on the planar surface of a thick plano-concave lens. The parameters such as annular radius and width, lens thickness, lens diameter, and lens radius of curvature must be chosen using thick lens theory to ensure that the annulus rests at the focal depth of the lens and that the desired characteristics of the beam are achieved. Further work on this subject will include the construction and testing of this transducer configuration.

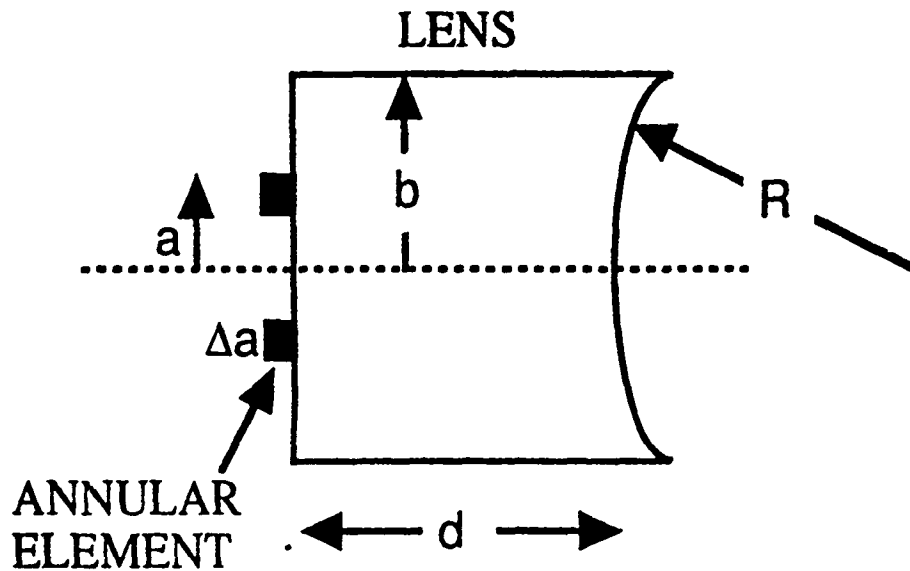


Figure 4. Proposed configuration for Bessel beam transducer.

REFERENCES

1. G. Du and M. A. Breazeale, J. Acoust. Soc. Am. 78, 2083-2086 (1985).
2. D. K. Hsu et al., IEEE Trans. Ultrason. Ferroelec. Freq. Contr. 37, 404-410 (1990).
3. J. Durnin, J.J. Miceli, and J.H. Eberly, Phys. Rev. Lett. 58, 1499-1501 (1987).
4. J. Durnin, J. Opt. Soc. Am. 4, 651-654 (1987).
5. R.W. Ziolkowski, D.K. Lewis, and B.D. Cook, Phys Rev. Lett. 62, 147-150 (1989).
6. D.K. Hsu, F.J. Margetan, and D.O. Thompson, Appl. Phys. Lett. 55, 2066-2068 (1989).
7. J.Y. Lu and J.F. Greenleaf, IEEE Trans. Ultrason. Ferroelec. Freq. Contr. 37, 438-447 (1990).

II. On-Axis Formulas for Ultrasonic Transducer Beams in Anisotropic Media

INTRODUCTION

The requirements of nondestructively inspecting cast steels, weldments, composites, and other inherently anisotropic materials have necessitated research aimed at better understanding ultrasonic wave propagation in these materials. Theoretical modeling can play an important role in the study of the unique effects, such as beam skew and excess beam divergence, which anisotropic materials have on ultrasonic transducer beams. The predictions of valid models can be used to help interpret nondestructive measurements and to help guide the choice of nondestructive inspection procedures by identifying configurations with the most promise of success. Much recent work has been devoted to this subject (for example Refs. [1-5]).

The purpose of the present work is to develop simple approximate formulas to predict the on-axis beam profile for ultrasonic transducers inspecting anisotropic materials. Many wave scattering theories assume plane wave incidence. These formulas can then be used, for example, to determine an incident wave amplitude for use with the scattering theories for predicting flaw response.

This approach has been used successfully in isotropic materials [6].

MODEL

The model configuration is shown in Fig. 1. A circular transducer of radius "a" and possibly focussed with focal length F is assumed to be insonifying a planar surface of an anisotropic solid from a water bath with an incident angle θ_i and standoff distance "d". The refracted phase velocity, V_p , is in the z-direction and has angle θ_r . The energy velocity, V_g , may have a skew angle ψ due to the anisotropy. Since the center of the beam energy will travel in the V_g direction, this will be defined as the beam axis, or z_{skew} . The only restriction will be that the plane of Fig. 1 must be a material symmetry plane.

The propagation of a time harmonic ultrasonic beam can be expressed in the form of an angular spectrum of plane waves, ASPW; i.e., a superposition of plane waves traveling in all directions, each with a particular amplitude

$$u(x,y,z) = e^{j\omega t} \frac{1}{(2\pi)^2} \int_{-\infty}^{\infty} \int_{-\infty}^{\infty} \phi(k_x, k_y) e^{-j(k_x x + k_y y + k_z z)} dk_x dk_y \quad (1)$$

where ϕ is the 2-D spatial Fourier transform of the sound generating source; in this case, a planar or focussed piston. A detailed discussion of the ASPW formulation for anisotropic materials is found in Ref. [4]. The key to this formulation is k_z , the component of the wave vector in the z -direction (the direction of phase propagation). Given k_x and k_y as the integration variables, k_z is found via the slowness surface of the material, which is derived from the elastic constants.

The ASPW formulation lends itself well to treating transmission of the beam through a plane interface since refraction of plane waves at a plane interface is well understood. Each plane wave in the superposition is analyzed as it passes through the interface and the resulting spectrum of refracted waves is recombined to yield the field in the solid. Roberts has done this rigorously with a numerical integration of the resulting integrals for the case of a transversely isotropic solid [3].

The objective at present is to make some key approximations which will allow a more nearly closed form solution for the axial component of the transmitted beam. This follows the approach previously used for the isotropic case [7]. The fundamental approximation is the

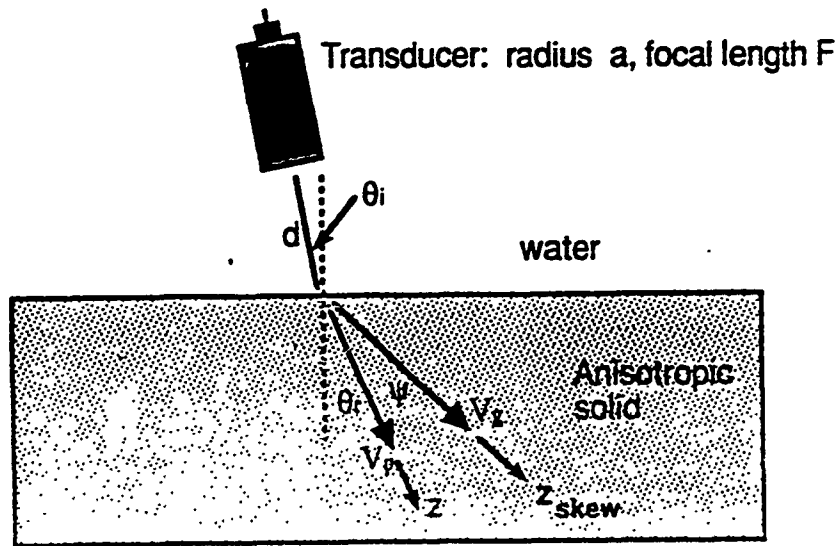


Figure 1. Mel configuration.

paraxial assumption; i.e., the beam is assumed to be well collimated, with most of the energy in the angular spectrum concentrated in plane waves travelling in the vicinity of the axial direction. Several consequences follow. Provided that the inspection configuration is well away from any critical angles, the transmission coefficient will vary slowly over the small angular spectrum and can be assumed a constant.

More significantly, the value of k_z is, for an anisotropic material, generally not available in closed form. However, the paraxial approximation allows a local approximation to the slowness as a second order (parabolic) surface. the parameters obtained from this

parabolic fit are the phase velocity in the axial direction V_p , the skew angle ψ , and the curvatures Δ_x and Δ_y of the slowness surface in the x - z and y - z planes (plane of Fig. 1 and the plane orthogonal to V_p). This parabolic approximation is detailed in Refs. [4,8,9]. The curvature terms control the rate of divergence (diffraction spread) of the beam.

After the procedure outlined above has been carried out and the approximations employed, then the majority of the resulting integrals may be evaluated exactly for the axial case and the amplitude of the displacement field along the z_{skew} -axis can be written as

$$u = e^{j\omega t} e^{-j(k_0 d + k_1 z)} C_s(S, \Delta S) \quad (2)$$

where k_0 is the wave number in the water, k_1 is the wave number associated with the V_p direction in the solid and $C_s(S, \Delta S)$ is given by the integral

$$C_s(S, \Delta S) = \frac{\sqrt{S^2 - \Delta S^2}}{2\pi} \int_0^{2\pi} \left\{ \frac{1 - e^{-j\pi(S - R + \Delta S \cos 2\theta)/(S^2 - \Delta S^2)}}{S - R + \Delta S \cos 2\theta} \right\} d\theta \quad (3)$$

where

$$R = (S^2 - \Delta S^2)a^2 / \lambda_0 F \quad (4)$$

$$S = \frac{z_{\text{skew}} \lambda_1 \cos \psi}{2a^2} [\Delta_y + \gamma^2 \Delta_x] + \frac{d\lambda_0}{a^2} \quad (5)$$

$$\Delta S = \frac{z_{\text{skew}} \lambda_1 \cos \psi}{2a^2} [\Delta_y - \gamma^2 \Delta_x] \quad (6)$$

$$\gamma = \frac{\cos \psi \cos \theta_i}{\cos(\theta_r - \psi)} \quad (7)$$

The parameters S and ΔS can be thought of as generalizations of the familiar nondimensional quantity used in transducer theory to define the nearfield length: $S = z\lambda/a^2$. The parameter γ is a "refraction parameter" related to the change in beam width due to refraction at the interface.

The integral in equation (3) is well behaved and can be easily evaluated with a call to a computer math library integration routine. This integral may also be evaluated exactly by expanding the denominator of the integrand in a Fourier series and integrating term by term to yield a series representation of the solution

$$C_a(S, \Delta S) = \frac{\sqrt{S^2 - \Delta S^2}}{\sqrt{(S-R)^2 - \Delta S^2}} \left\{ 1 - e^{-j\pi(S-R)/(S^2 - \Delta S^2)} \sum_{n=0}^{\infty} b_n J_n \left(\frac{\pi \Delta S}{S^2 - \Delta S^2} \right) \right\} \quad (8)$$

where

$$b_0 = 1, \quad b_n = 2(-j)^n \left\{ \frac{\sqrt{(S-R)^2 - \Delta S^2} - S + R}{\Delta S} \right\}^n, \quad n = 1, 2, \dots \quad (9)$$

The solution may be computed from equation (8).

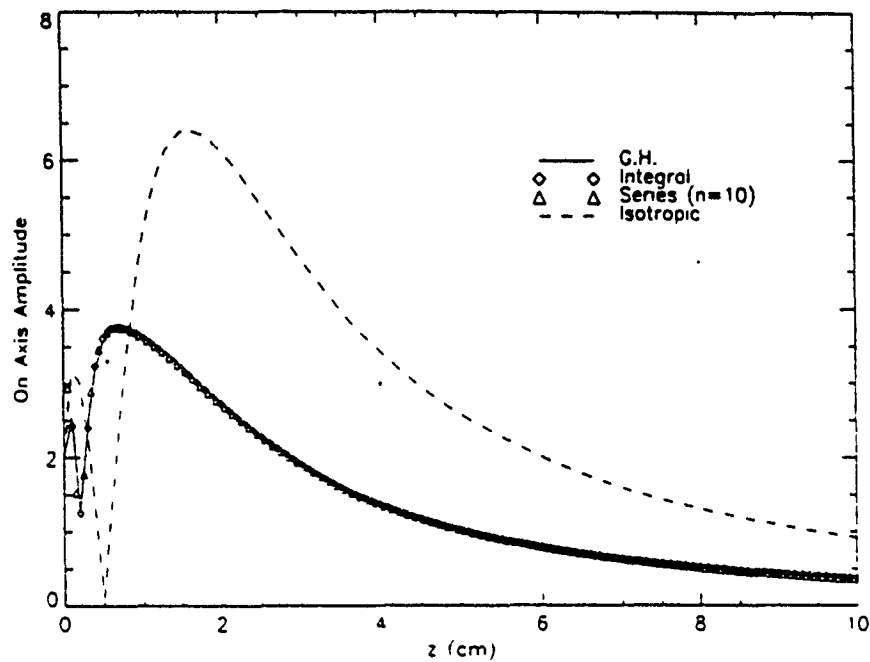
Convergence is generally achieved with less than 10 terms and more often less than 5 terms.

EXAMPLE CALCULATIONS

The on-axis formulas, both in integral form and series form, have been used to predict the axial profiles for ultrasonic inspection of a unidirectional graphite epoxy laminate. These predictions are compared with the predictions of the Gauss-Hermite beam model. The Gauss-Hermite beam model is a model which predicts the full-field within the paraxial approximation and which has undergone extensive experimental validation for cases including the one used here [4,8,9]. In order to illustrate the effects of the anisotropy, the axial profile which would be obtained in an isotropic material with the same nominal wavespeed are also shown on the figure.

Figure 2 shows the axial profile for a normal incidence inspection of a unidirectional composite using a focussed probe. The series and integ ~~al~~ computations are virtually identical with each other and with the Gauss-Hermite solution. One significant result is the reduction of the peak amplitude of the beam at the focal point as

compared to the isotropic material. This is due to the fact that the anisotropy causes the focussing parallel and perpendicular to the fibers to occur at different depths, thus spreading out the focal region.



- Normal incidence to unidirectional graphite-epoxy panel
- Focussed probe, $a=.635$ cm, $F=7.62$ cm, $d=2.54$ cm, frequency=5 MHz
- Wavespeed in solid = $.313$ cm/ μ s, $\Delta x=3.56$, $\Delta y=0$, $\gamma=0$

Figure 2. Axial profile in unidirectional composite.

CONCLUSIONS

A simple formalism, easy to numerically implement, has been derived for the prediction of the on-axis beam profile of an ultrasonic transducer inspecting an anisotropic material. The results of this beam model agree with those of the more general Gauss-Hermite beam model. These results can be used to better understand the effects that anisotropy has on ultrasonic inspections and to help interpret measurement data from anisotropic materials.

REFERENCES

1. J.A. Ogilvy, *Ultrasonics* 24, 337-347 (1986).
2. A.N. Norris, *Wave Motion* 9, 1-24 (1987).
3. R.A. Roberts, *Ultrasonics* 26, 139-147 (1988).
4. B.P. Newberry and R.B. Thompson, *J. Acoust. Soc. Am.* 85, 2290-2298 (1989).
5. J.L. Rose, K. Balasubramaniam, A. Tverdokhlebov, *JNDE* 8, 165-179 (1989).
6. R.B. Thompson and T.A. Gray, *J. Acoust. Soc. Am.* 74, 1279-1290 (1983).
7. R.B. Thompson and T.A. Gray, in Review of Progress in Quantitative NDE, edited by D.O. Thompson and D.E. Chimenti (Plenum Press, New York, 1983) Vol. 2A, p. 567.
8. E.P. Papadakis, F. Margetan, and B.P. Newberry, in Review of Progress in Quantitative NDE, edited by D.O. Thompson and D.E. Chimenti (Plenum Press, New York, 1990) Vol. 9A, p. 235.
9. F.J. Margetan, R.B. Thompson, and T.A. Gray, in Review of Progress in Quantitative NDE, edited by D.O. Thompson and D.E. Chimenti (Plenum Press, New York, 1991) Vol. 10A, p. 1539.

GEOMETRIC REASONING FOR PROCESS PLANNING

Dr. Joseph H. Nurre

Abstract

Geometric tolerance and dimensioning information is of primary importance in the design and manufacturing process. The current tolerance standard is intended to ensure the functionality of a part. This shifts more of the burden of understanding how to manufacture the geometry, to the process planner. In this report, the issues surrounding manufacturing to achieve a specified geometric tolerance is presented. Of particular interest in this report will be the topic of tolerance interaction among multiple features. A technique known as tolerance charting is presented as one method of handling geometric feature tolerance interaction. Tolerance charting is a highly structured technique which would lend itself to integration into an intelligent Computer Integrated Manufacturing system.

I. Introduction

The role of computers in design and manufacturing is expanding rapidly and has achieved widespread acceptance in industry.¹ Computer Aided Design (CAD) and Computer Aided Manufacturing (CAM), originally developed separately, have been brought together under the single umbrella of Computer Integrated Manufacturing (CIM). Current CAD systems, however, are little more than computerized drafting tables. They require the designer to construct physical features based on fundamental geometric primitives. The situation for CAM systems is similarly underdeveloped. CAM currently consists of a disperse collection of software packages, developed to address specific problems in manufacturing. An important goal when summing these two imperfect

systems together, is to achieve a CIM system which is greater than the sum of its parts. The Rapid Design System² is such a CIM system.

The Rapid Design System (RDS) is a fully integrated design and manufacturing software product which uses knowledge-based programming paradigms. The designer interfaces with the computer using a library of standard design features that help maintain the intent of the design, as well as, free the user from tedious drafting chores. The RDS can derive from the user's design appropriate manufacturing and inspection processes. This is done using a generative process planner. Furthermore, the RDS has an episodal associative memory to accumulate expertise on the design and how it relates to the manufacturing process. The generated process plan, and the changes subsequently made to that plan by the user, are remembered by the RDS. As the memory becomes populated, the RDS will assist the designer in satisfying manufacturing needs while designing the part.

Among the many pressing concerns to be addressed by the RDS development group is the handling of tolerancing information in the user's design. A major drawback of all current computer graphics systems is their reliance on nominal values to represent geometric features.³ The object oriented philosophy of the RDS will allow for a logical attachment of tolerances to the geometry.⁴ With the information properly attached to the model, the manufacturing process planner must assure a suitably manufactured part.

Research in the area of automated process planners is usually separated into generative process planners and group technology process planners.⁵ Group Technology process planners handle geometric tolerances by grouping them into similar classes.⁶ The manufacturing intelligence for handling process tolerance is provided by the programmer. This approach is not appropriate for the RDS which uses a generative process planner. It is interesting to note though that the episodal memory of the RDS will provide its own grouping of process technology. In the area of generative process planners a large body of research exists on the use of expert systems.⁷ The handling of manufacturing tolerances would be imbedded in the rules of the

knowledge-base. Expert systems tend to be brittle, however, requiring constant updating. In keeping with the concept of the RDS, tolerance reasoning for manufacturing would be more desirable.

There are four primary concerns in regards to tolerancing from the perspective of the process planner. These are: syntax, interpretation, consistency and process tolerance. Syntax refers to the standard in which the tolerance will be represented by the system. Interpretation requires an understanding of the tolerance standard, and its relationship to the manufacturing environment. Because more than one tolerance may be associated with any given feature, consistency must be assured among the different tolerances. Finally, to achieve design tolerance, the proper tools, machines and fixtures, with the appropriate accuracies, must be used to manufacture the part.

The four issues raised in the preceding paragraph will be addressed in the remainder of this report. Sections II through V will discuss syntax, interpretation, consistency and process tolerance respectively. In each section, the problem will be more clearly defined, and the likely approach for a solution will be discussed. The final section of this report will then summarize these issues.

II. Syntax


The syntax to be used by the RDS is the ANSI Y14.5M-1982 standard.⁸ This standard was created to ensure that dimensional and tolerance requirements, as related to actual feature design functions, are specifically stated and thus carried out.⁹ Furthermore, the ANSI Standard is intended to ensure the interchangeability of mating parts at assembly. The ANSI standard accepts tolerance information on individual features using the Feature Control Frame. A complete list of the geometric tolerances which can be used by the Feature Control Frame can be found in Reference 8.

Geometric tolerances can be classified into one of two categories. The first category is intrinsic tolerances which relate the shape of a

feature to an ideal geometry. For example, the roundness of a hole is determined by bounding the inner and outer diameters of that hole with ideal circles. The second category of tolerance information describes the relationship between two or more features. One example of this would be a positional tolerance. Positional tolerances specify a circular zone in which the center of the feature may fall.

In regards to the manufacturing process planner, tolerance of an intrinsic geometric form is a function of machine operation, tooling and sequencing. For instance, the roundness of a hole is controlled by the drill bit, and the speed and feed of the machine. To achieve a tighter roundness on a hole, one may need to follow the drilling operation with a boring operation. On the other hand, geometric tolerances, which describe the relationships among features, require a more sophisticated analysis. This arises from the fact that the machining datum may differ from the design datum due to fixturing or convenience. Furthermore, stack up error may result from multiple cuts on a single machine.

III. Interpretation

The ANSI standard is primarily a designer's standard. One of its primary purposes is to aid the analysis of interchangeability. In the example shown in Figure 1, the positional call out, , states that the center of the hole may fall anywhere within the shaded circular tolerance zone. A circular tolerance zone is appropriate for the designer concerned with mating parts. A drilled hole after all is completely symmetrical and interference is equally troublesome in any direction.

In regards to manufacturing, however, the machine used to create that hole, will be positioned along orthogonal linear axes. The geometric tolerance call out should be translated into a linear axis tolerance condition. As shown in Figure 1, the accuracy of the machine to be used is determined by a square tolerance zone which is enclosed by

the circular tolerance defined by the designer. Linear axes tolerances are more meaningful to the machinist with respect to the positioning functions of his machine.

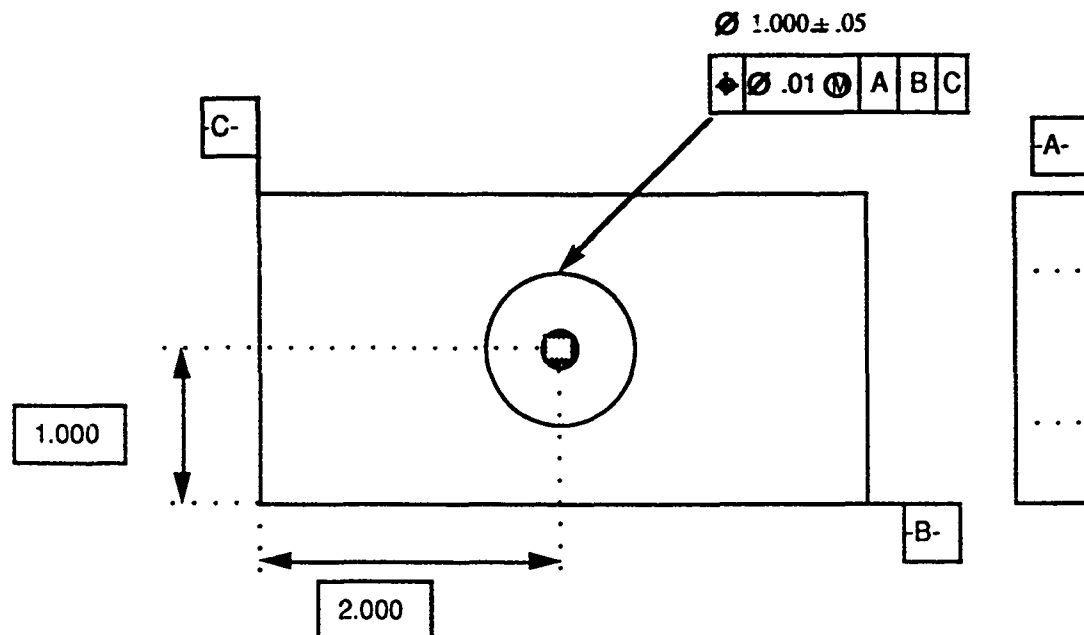


Figure 1. The Feature Control Frame shown in the upper right hand corner indicates a circular tolerance zone is being specified by the designer. The process engineer, however, will manufacture the part on a machine whose positional accuracies are specified along orthogonal axes. The square within the circular tolerance zone will determine the choice of machines.

Interpretation of the ANSI standard into a linear axis tolerance is not always as simple as fitting a box to a circle. In the example shown in Figure 2, the two holes have been toleranced with respect to each other as well as with respect to datum A. To interpret these ANSI positional tolerances into appropriate linear tolerances, one must first determine which of the control frames is more restrictive. This will obviously govern the values of a linear tolerance. Furthermore, the

machinist's choice of where he will zero his machine will also be important. This issue will be discussed in Section V. In conclusion, interpreting the ANSI Y14.5M standard requires translating positional tolerancing information into orthogonal axes tolerances.

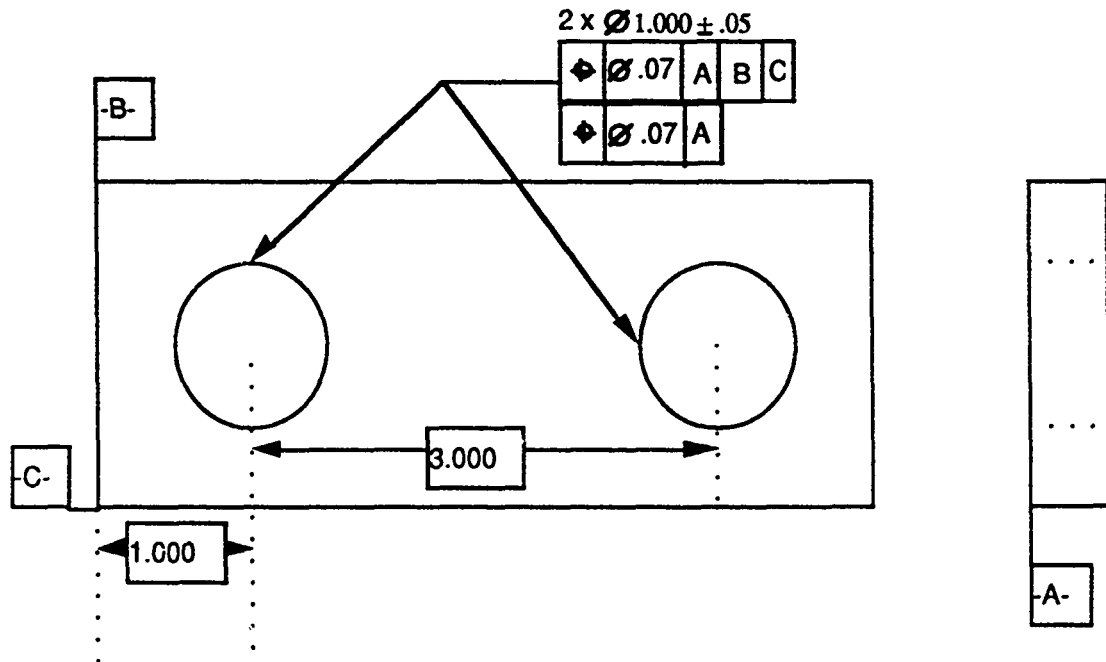


Figure 2. The possibility of multiple Feature Control Frames can make interpretation into linear axis tolerances difficult.

IV. Consistency

For tolerancing information to be inconsistent, a feature must have at least two tolerance call outs which are not equal along a linear axis. Many of the tolerance inconsistencies will be pointed out to the designer by the Feature Based Design Environment (FBDE) software in the RDS. In order not to be too restrictive, however, some potentially inconsistent call outs may be flagged by the FBDE with a warning, but allowed to pass to the process planner. Furthermore, because of the

need to interpret the Feature Control Frames into linear axes tolerances, the potential does exist for consistent ANSI Y14.5M designs to become inconsistent. Checking for consistency is simply a matter of checking for equivalence and, therefore, can be easily implemented with the interpreter.

V. Process Tolerance

A designer chooses a part's tolerance to make a design operational. His choice of datums and stack up are dependent on the functionality and interchangeability of the part. The process engineer chooses datums based on the ease of fixturing and the need to zero the machine. It is the job of the process engineer, therefore, to assure that tolerances chosen in the manufacturing process, meet or exceed the designer's specifications.

As stated in Section II, geometric tolerances can be divided into two categories: intrinsic to geometric form and relational to other features. Tolerances of geometric form are controlled by tooling and a machine's operational parameters. Tolerance of relative position are determined by machining accuracy and stack up due to multiple operations. Currently, the software package MetCAPP¹⁰ determines the tool selection, and the machine's speed and feed, which will result in a geometric form within design tolerance. A method known as tolerance charting is proposed to track stack up tolerances due to multiple operations.

The techniques of tolerance charting were first gathered into a single text by Oliver R. Wade¹¹ in 1967. Since that time, the method has been updated to reflect the current ANSI standards.¹² The underlying principles of the tolerance charts are very simple. Their primary importance to the process engineer is to help him keep his work organized. Using the charts is a very mechanical operation and lends itself easily to computer automation. General Motors, in fact, has developed proprietary software to perform this task.¹³

Tolerance charts can be used to achieve two different objectives. The first objective is to check the manufacturing processes for tolerance stack up and compare it with the designer's tolerance values. The second goal is to determine mean stock removal for different cutting operations and ensure it is appropriate to the operation.

In Figure 3, geometric tolerancing and dimensioning information is shown for a center slot, machined from a block of material. This figure will demonstrate the use of tolerance charting to verify design tolerances against the accuracies of the manufacturing process. In this case, the manufacturing process has been simplified for the sake of the example.

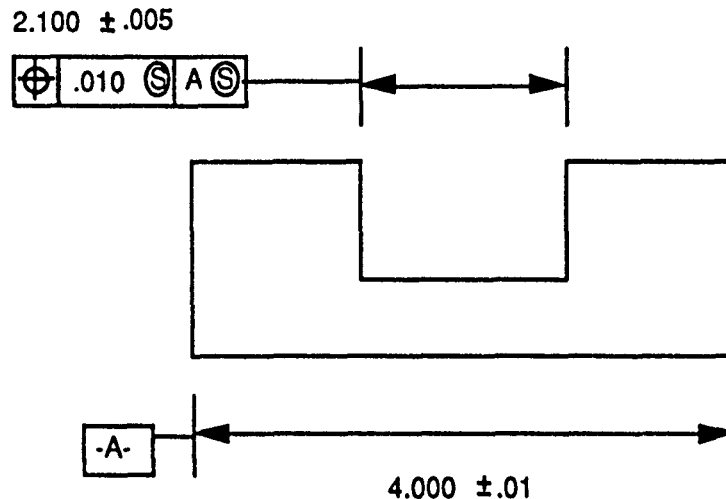


Figure 3. Tolerance specifications for a block with a slot. The slot's center is to be within .01 of an inch of the center of the block.

Let us assume that the part will be manufactured in four cuts. First, the width of the overall block will be established by a vertical mill. Next, a horizontal mill will be used to rough in the slot. Finally, the vertical mill will be used again, to cut the slot to its proper dimensions. The four cuts are represented on a tolerance chart

by lines with a single arrow as shown in Figure 4. The point of the arrow indicates the cutting plane, while the end of the arrow indicates the datum reference used by the machinist. Referring to LINE 6 of the chart, the vertical mill was zeroed at the left edge of the slot before cutting to the right edge. Lines on the chart with no arrows (ie. LINE 7) are called balance dimensions and are used to determine the resultant tolerances of multiple cuts.

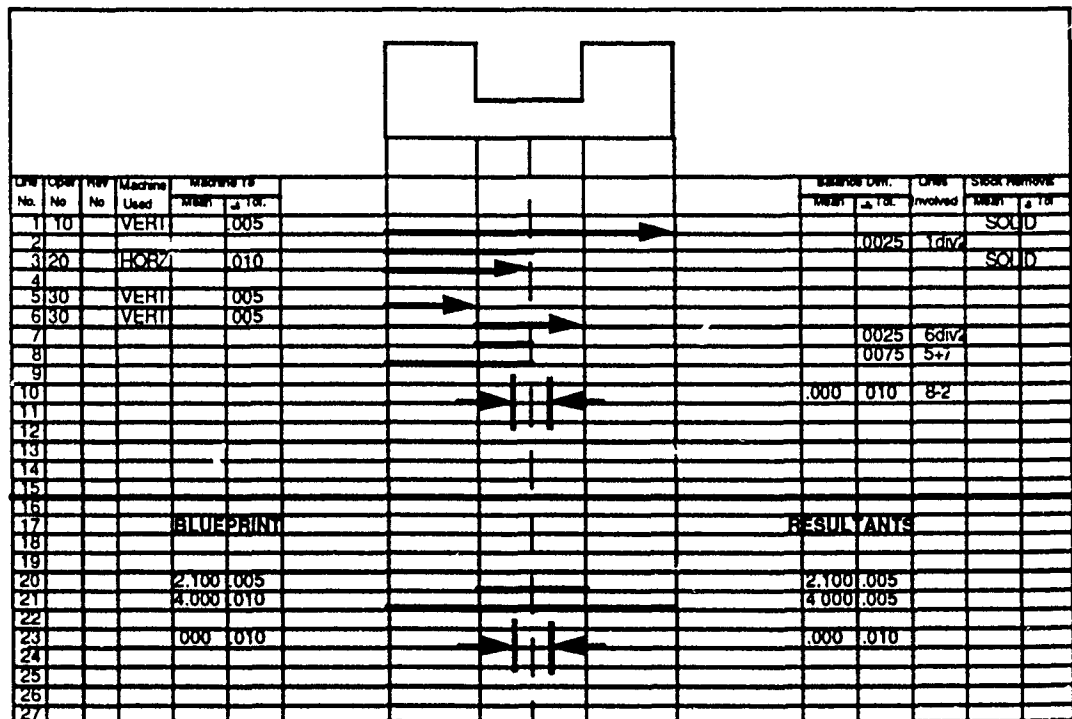


Figure 4. This tolerance chart is used to guarantee that the process plan (as described in the text) will satisfy the design requirements specified by the drawing in Figure 3.

Essentially, the operation of the tolerance chart is to generate the balance dimension lines which are equivalent to the blueprint dimension lines given at the bottom of the chart. For the chart shown in Figure 4, the tolerance of the block's width is completely determined

by the first cut. At the bottom of the chart, under the heading of "Blueprint" is the tolerance called for by the design. The tolerance established by the vertical mill is listed under the heading of "Resultants". A chart column titled "LINES INVOLVED", references LINE 1 as the cut that established that tolerance. Verifying that the slot is properly centered is done in LINE 10. The resultant tolerance is obtained by adding the tolerances of LINES 2 and 8, which are once again specified in the "LINES INVOLVED" column.

In this example all designer specifications are met by the manufacturing process. This can be seen by comparing the "Blueprint" column with the "Resultants" column. Can the manufacturing process be modified to bring the part out of spec without changing machine accuracies? Yes, from a tolerance chart, it can be determined that if the machinist chooses to use the left edge of the block as the datum for all the cuts, the slot size will be out of tolerance, although, it will still be properly centered.

In the example shown above, a single slot was cut from a block of material. Tolerance charting can actually handle more complicated situations, such as angular cuts and fillets. Furthermore, the tolerance chart can be used to assure that an appropriate amount of stock is removed by the cutting operation performed. This requires filling in the remaining columns of the chart. Examples of this procedure can be found in references 11 and 12.

The use of the tolerance chart helps the process engineer organize a procedural operation. In implementing the tolerance charts in the RDS, the underlying rules and procedures governing the chart will put in an algorithmic form. The output passed to the machinist need not be the tolerance chart in its current form. Only a process plan with datum references and fixturing is really necessary.

VI. Discussion

There is a need to intelligently handle tolerance call outs in the RDS for the generative process planner. The techniques of tolerance charting are well established and are a prime candidate for computer coding. The chart itself, need not be implemented, only its underlying principles. In order to proceed, however, first a linear axes tolerance interpreter with consistence checking will need to be written. After this step, it is recommended that the tolerance chart be installed into the RDS in two stages. The first stage will implement the tolerance checking process presented in the example of Section V. Tolerance checking for angular cuts and radii break out could be added as the FBDE of the RDS obtains those functionalities. The second stage of implementation would add the ability to check machining cuts for appropriate stock removal.

Experience with the tolerance chart is expected to further define what it means to have inconsistent tolerances with respect to a geometric feature. Additionally, some positional Feature Control Frame symbols, such as perpendicularity, which are not currently handled by tolerance charting, may also be better understood and implemented at a later date. The tolerance chart also has applications to assembly research. Implementing the tolerance chart as recommended above will not only add to the RDS but it will also increase the knowledge of the development team in areas of future research.

References

1. G. Halevi, *The Role of Computers in Manufacturing Processes*, John Wiley & Sons, Inc., New York, New York, 1980.
2. S.R. LeClair, "The Rapid Design System: Memory-Driven Feature-Based Design", *Proc. IEEE International Conf. on Systems Engineering*, Dayton, Ohio, August, 1991.

3. A.A.G. Requicha, "Representation of Geometric Features, Tolerances, and Attributes in Solid Modelers Based on Constructive Geometry", *IEEE Journal Robotics & Automation*, Vol. 2, No. 3, p. 156, 1986.
4. G.M. Radack, J.F. Jacobsohn, and F.L. Merat, "Positioning Features within the Rapid Design System", *Proc. IEEE International Conf. on Systems Engineering*, Dayton, Ohio, August, 1991.
5. G. Boothroyd and W.A. Knight, *Fundamentals of Machining and Machine Tools*, 2nd Edition, Marcel Dekker, Inc., New York, New York, 1989.
6. A. Kusiak, *Intelligent Manufacturing Systems*, Prentice Hall, Englewood Cliffs, New Jersey, 1990.
7. T-C Chang, *Expert Process Planning for Manufacturing*, Addison-Wesley Publishing Co., Inc., Reading, Massachusetts, 1990.
8. *Dimensioning and Tolerancing*, American National Standard Y14.5M-1982, American Society of Mechanical Engineers, New York, New York, 1983.
9. L.W. Foster, *Geo-metrics II*, Revised 1986 Edition, Addison-Wesley Publishing Co., Inc., Reading, Massachusetts, 1986.
10. *MetCAPP*, Institute of Advanced Manufacturing Sciences, Inc., Cincinnati, Ohio, 1990.
11. O.R. Wade, *Tolerance Control in Design and Manufacturing*, Industrial Press, Inc., New York, New York, 1967.
12. *Tool and Manufacturing Engineers Handbook, Volume 1: Machining*, Fourth Edition, Eds. T.J Drozda and C. Wick, Society of Manufacturing Engineers, Dearborn, Michigan, 1983.
13. J.E. Nicks, *BASIC Programming Solutions for Manufacturing*, Society of Manufacturing Engineers, Dearborn, Michigan 1982.

SYNTHESIS AND CHARACTERIZATION OF CHIRAL MESOGENS FOR USE IN CYCLIC SILOXANE LIQUID CRYSTALLINE MATERIALS

Steven K. Pollack

Assistant Professor of Materials Engineering

Dept. of Materials Science & Engineering

University of Cincinnati

498 Rhodes Hall, ML 12

Cincinnati, OH 45221-0012

ABSTRACT

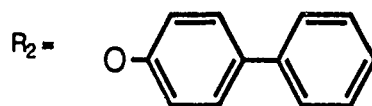
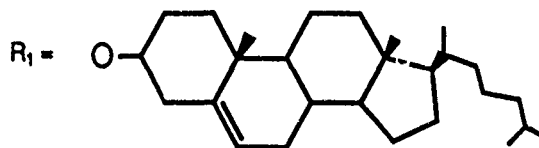
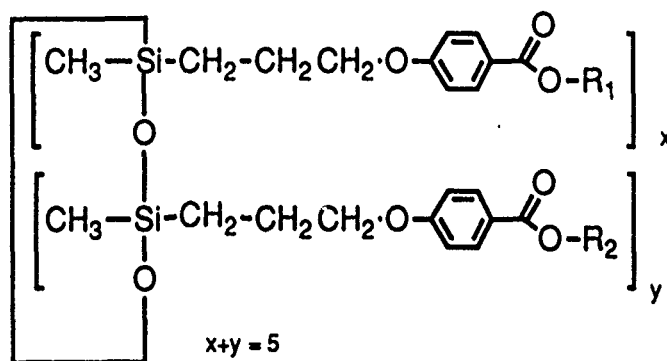
Chiral mesogens based on 1,3 dioxanes were synthesized in order to compare the physical properties and molecular packing of cyclic siloxane liquid crystals (CLC's) based on these new mesogens with those previously studied based on cholesterol as the cholesterogenic group. Molecular modelling was utilized to predict the relative compatibility of the 1,3-dioxane based mesogens and cholesterol with hydroxy biphenyl based mesogens. In an additional study, an efficient synthetic scheme was developed for the esterification of 1-(4-nitrophenyl)-propanol (NPP) using phase transfer catalyst conditions.

SECTION I

Synthesis of Chiral 1,3 Dioxane Based Mesogens

INTRODUCTION

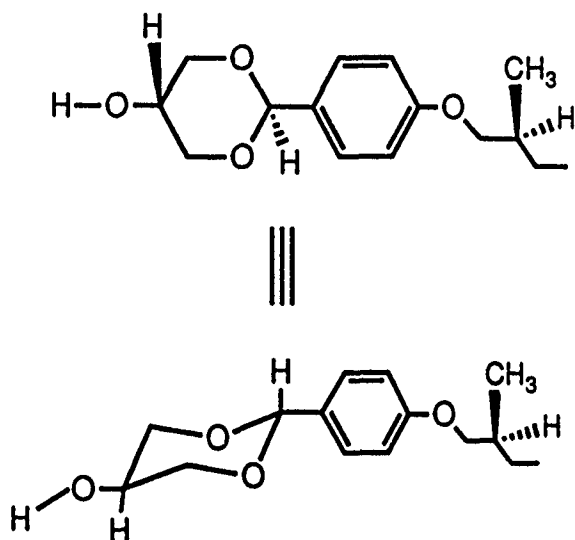
Research within the Materials Directorate the Laser Hardened Materials Branch has recently demonstrated that low molar mass cyclic siloxane side chain liquid crystals (CLC's) exhibit unique molecular superstructures in the solid state which may enhance their utility as matrices for nonlinear optical (NLO) applications¹⁻⁴. The materials previously described^{1,2,4} are based pentamethylcyclopentasiloxane rings with pendent mesogenic groups as shown below.



From the drawings it is readily noted that the two mesogens are of different length, the cholesterol being somewhat longer. It has been observed that at higher cholesterol concentrations, there is an apparent microphase separation and changes in the X-ray scattering patterns due, in principle, to the inability of the biphenyl and cholesterol mesogens to pack effectively inducing the production of cholesterol-rich lamella¹... This microphase separation is also evidenced in a reduced ability of form transparent films and continuous fibers at these higher cholesterol concentrations. Additionally the unsaturation in the cholesterol ring systems renders it somewhat susceptible to oxidation which may lead to loss of optical clarity during thermal processing, from photodegradation or through environmental effects.

It was felt by previous workers that the presence of the cholesterol groups was necessary to produce the fiber and film drawing properties of these materials as well as the introduction of a helical superstructure responsible for the materials ability to selectively reflect circularly polarized light at specific wavelengths. A number of other side-chain liquid crystalline polymers have been developed which incorporate other chiral mesogens as a means of obtaining cholesteric or chiral smectic liquid crystal phases⁵. The possibility existed that the use of these groups to replace cholesterol in the cyclic side-chain liquid crystal siloxanes might serve to both enhance the chemical stability of these materials as well as allow for the probing of the effects of changes in the chemical structure on the macroscopic properties of these materials.

To this end the synthesis of chiral mesogens of similar molecular dimensions to the biphenyl were undertaken. Following the work of Legrand⁶ and of Percec⁵, we synthesized the heterocyclic optically active alcohol.



trans-5-hydroxy-2-[4-(2-(-)(S)-methyl-butoxy)phenyl]-1,3-dioxane (HMBPD).

Legrand and his co-workers⁶ have demonstrated that acrylate polymers derived from trans-2-(4-cyanophenyl)-5-hydroxy-1,3-dioxane

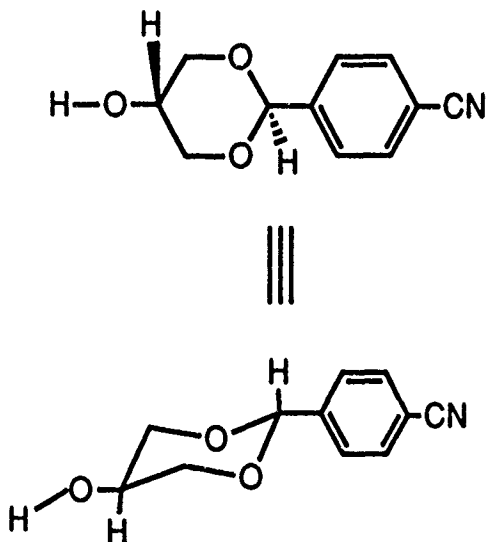


exhibit nematic liquid crystalline phases rather than the smectic phases typically seen in cyanobiphenyl containing side-chain liquid crystalline polymers.

Percec⁵ has shown that mesogens of the form

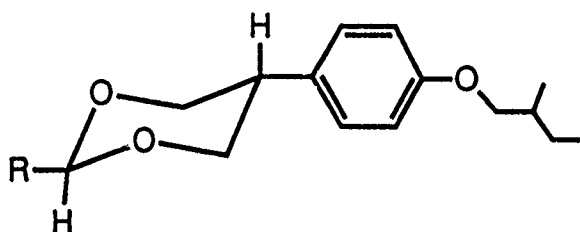
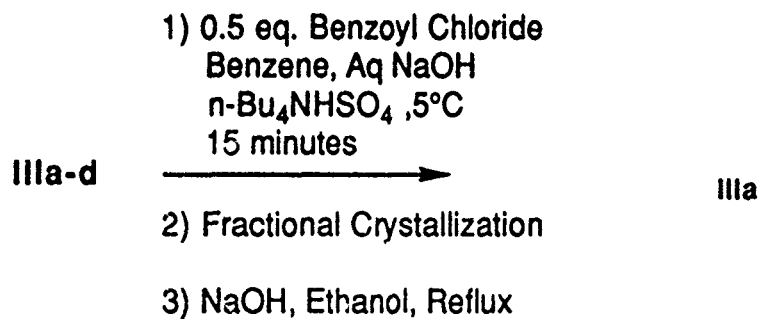
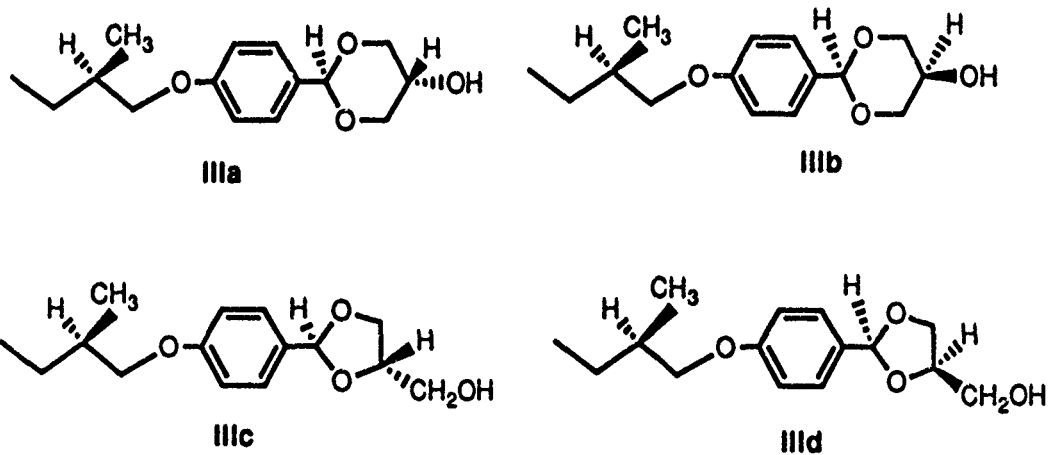
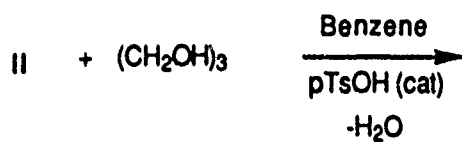
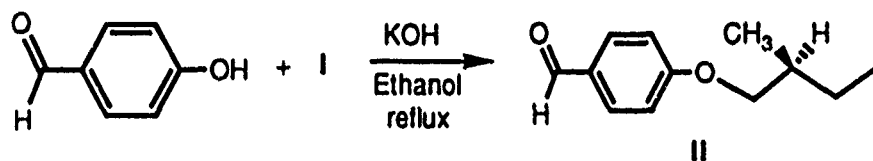
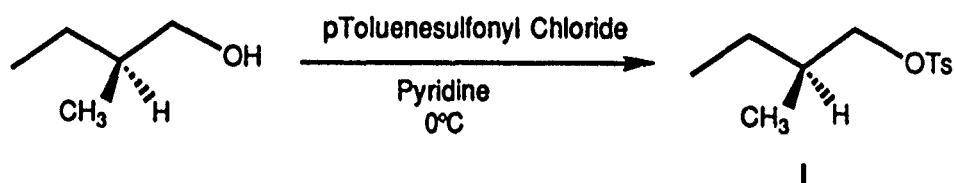


exhibit chiral smectic mesophases. We felt that the HMPBD system should provide either chiral smectic mesophases or cholesteric phases. Additionally, the absence of unsaturation in the dioxane ring should show enhanced thermal and photochemical stability.

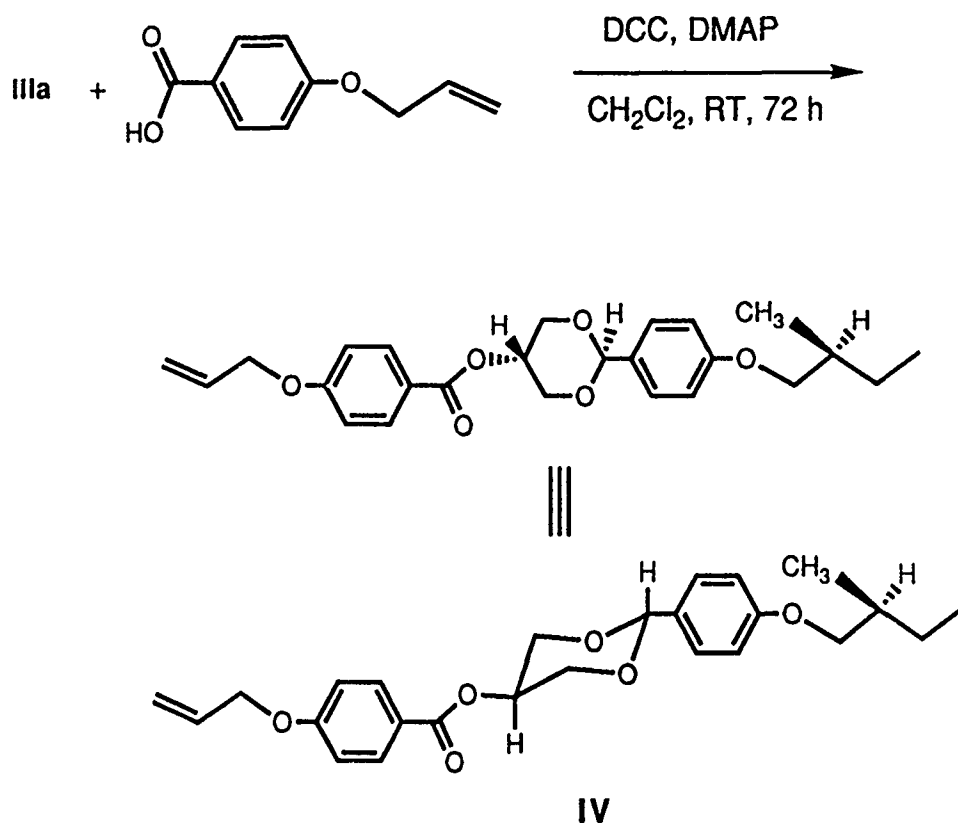
Once synthesized, the HMBPD was incorporated into a "leader group" for subsequent attachment to the precursor pentamethycyclopentasiloxane. . Cyclic siloxanes were then synthesized with various stoichiometries of HMBPD and hydroxybiphenol based mesogens and the physical and chemical behavior of these cyclic siloxane liquid crystals examined and compared with the equivalent cholesterol containing analogs.

The following reaction scheme was used to synthesize HMBPD

Reaction Scheme I



The acetalation reaction gave relatively low yields of the trans isomer, even after equilibration of the reaction mixture. The desired trans isomer of isomer of HBMPD (**IIIa**), isolated from the reaction mixture by selective benzoylation, fractional re-crystallization and saponification⁷ (total isolated yield 250 mg) was then reacted with 4-allyloxybenzoic acid in the presence of dicyclohexylcarbodiimide (DCC) and a catalytic amount of dimethylamino pyridine (DMAP)³ to form the reactive triad mesoçen **IV**.



Again, this reaction gave no better than a 50% overall providing 110 mg of the final olefin product. Finally **IV** and the 4-allyloxy benzoate of 4-phenylphenol (10% molar excess) were reacted with pentamethylcyclopentasiloxane in methylene chloride in the presence dicyclopentadienyl platinum(II) chloride as

a hydrosilation catalyst to form the LC cyclic siloxanes. This reaction was followed via observing the disappearance of the Si-H stretching vibration at 2140 cm^{-1} in the infrared. The product was purified by repeated precipitation from methylene chloride with methanol. The yield was quantitative based on pentamethylcyclopentasiloxane.

CHARACTERIZATION

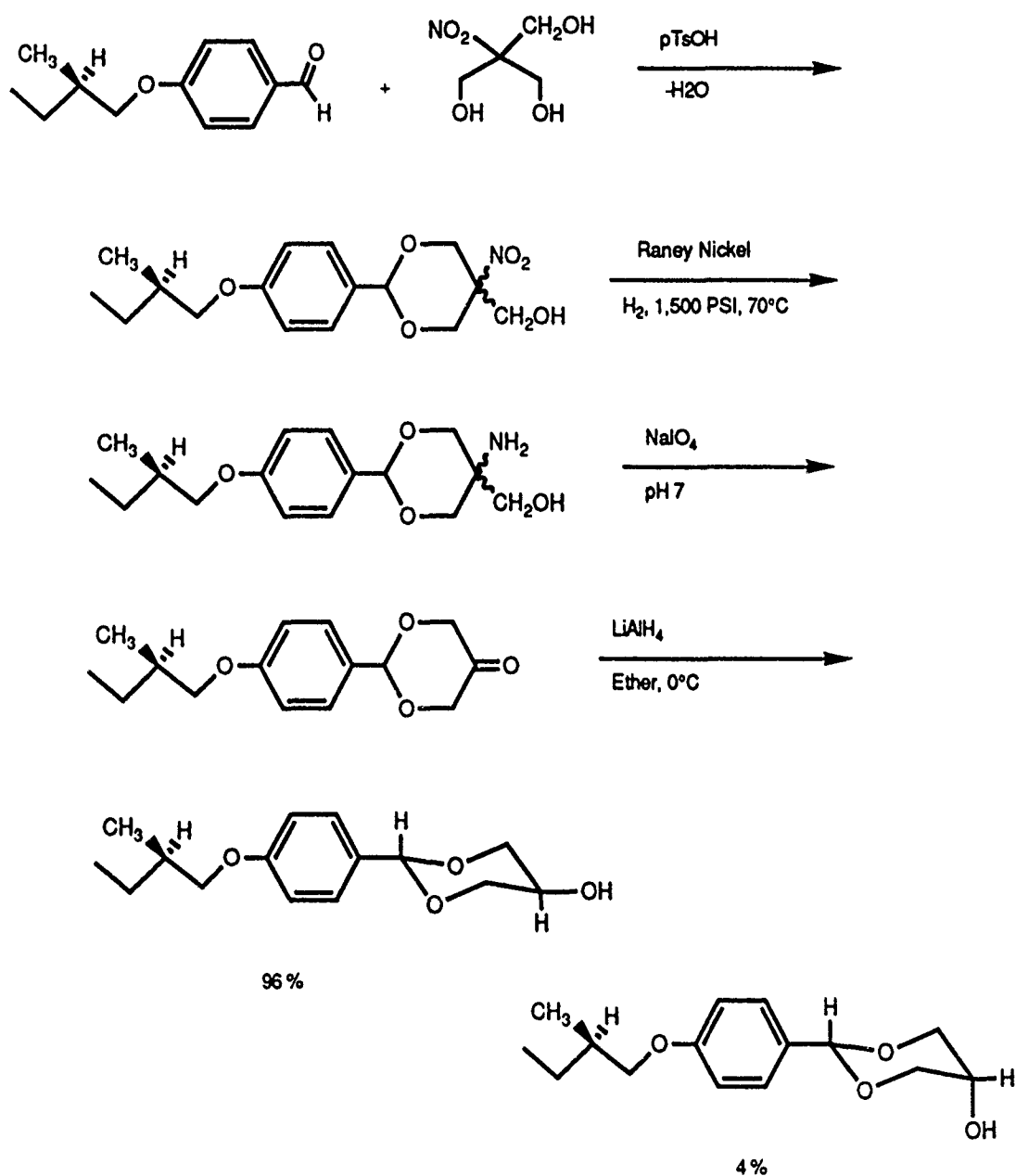
The olefin **IV** is a non-mesogenic compound exhibiting a melting point of 100°C . NMR and IR are consistent with its structure and will be reported elsewhere. The NMR of the compounds used in the initial hydrosilation study show traces of allyloxybenzoic acid as a contaminant.

The cyclic siloxane exhibited a glass transition at $\sim 75^{\circ}\text{C}$ and a clearing transition at $\sim 150^{\circ}\text{C}$. An additional transition was observed which disappeared upon multiple heatings. Optical microscopy exhibited cholesteric textures which were unaffected by multiple temperature cycles.

Fibers could be drawn from the material in the molten state. Wide angle X-ray diffraction of these fibers exhibited multiple orders along the meridian, consistent with the patterns observed for the cholesterol containing CLC's. The d-spacing of these reflection was determined to be 20.5 \AA , consistent with a rule of mixtures size of the the two constituent mesogens. One difference between the HMBPD based CLC and the cholesterol based CLC was that fin the former materials there was observed in addition to the meridional reflections, a "cybotactic" pattern, indicating some specialized packing due to this mesogen.

DISCUSSION

A major problem in this study was the low yield of the final chiral mesogen. This was due to two causes: 1) the non-specificity of the acetalation reaction and 2) the low yields of the esterification. We have since devised a synthetic scheme⁸⁻¹⁰ which alleviates these two problems is detailed below



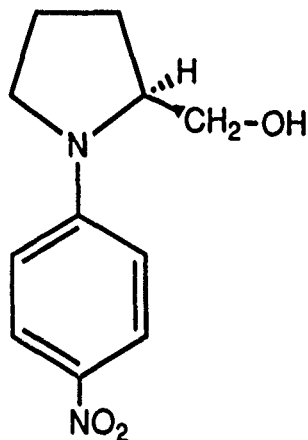
As shown the final reaction produced almost pure trans HMBPD (IIIa) in only a few steps. There is no formation of the dioxolane products (IIIc,d) at all. The other low yield step is the esterification via DCC/DMAP coupling. As we will discuss in Section 2, the use of phase transfer catalyst conditions⁷ in conjunction with the acid chloride of the 4-allyloxybenzoic acid¹¹ should give nearly quantitative yields. These reaction are currently being pursued. An additional benefit is that one is now in a position to economically modify the substitution of the phenyl ring in the dioxane mesogen. This is also under study. .

Until a complete range of compositions can be synthesized, we can say little about the nature of the mesophase of HMBPD based CLCs relative to the cholesterol based materials. Initial results indicate a similar ability to form glassy fibers with similar molecular packing arrangements. This work is in progress

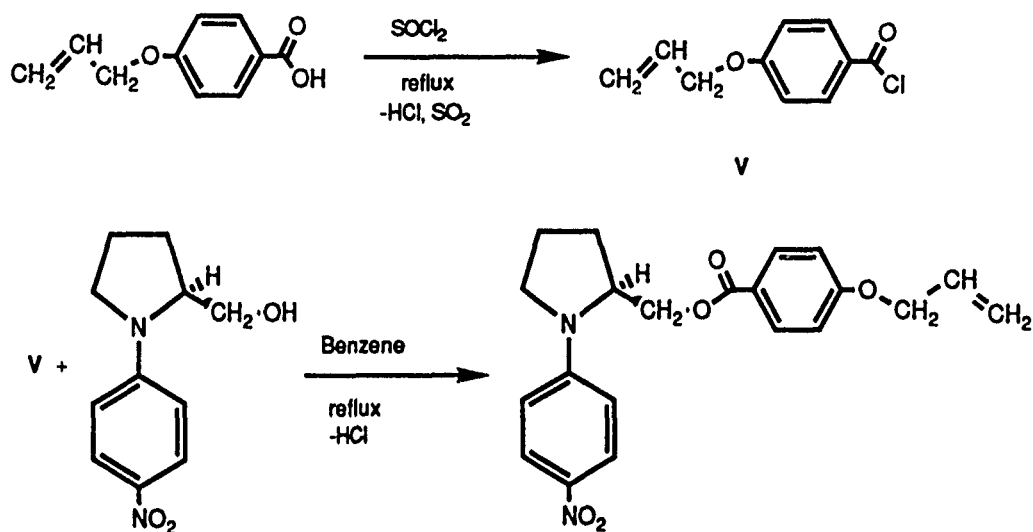
SECTION 2

Synthesis of Functionalized NLO Dyes

The compound 1-(4-nitrophenyl)-prolinol (NPP)



has been shown to have very high values of $\chi(2)$ in its crystalline form¹². This is due to the non-centrosymmetric nature of the crystalline state. NPP is optically active and has the potential to serve both as a non-linear optical chromophore as well as a cholesterogenic moiety. As such attempts were made to functionalize NPP for attachment to siloxane backbones. Attempts to form the 4-allyloxybenzoate derivative of NPP using the DCC/DMAP (see above) route proved unsuccessful. This may be due to the steric hindrance of the alcohol group on the NPP as well as its internal hydrogen bonding deactivating it. To circumvent the latter, we attempted to form the ester via Schotten-Bauman conditions using the acid chloride of 4-allyloxybenzoic acid (V), synthesized via the following reactions



The acid chloride preparation has been reported in the literature¹¹. After 24 hours, little ester had formed under these conditions. The reaction was re-attempted adding powdered K_2CO_3 as a scavenger for the HCl produced in the esterification. Again, the reaction gave little product. The reaction was attempted a third time using phase transfer catalysis (PTC) conditions⁷. Specifically, NPP and the acid chloride **V** were dissolved in 100 mL of benzene and 20 mL of a 50% (w/v) NaOH solution was added. Tetrabutyl ammonium bisulfite (TEBAH) (0.1 g) was added and the reaction mixture was vigorously stirred. TLC and IR showed rapid quantitative reaction to form the ester. However, if the mixture was then refluxed, a saponification reaction occurred rapidly, yielding the starting NPP and the sodium salt of 4-allyloxybenzoic acid. Thus the ideal reaction conditions are room temperature PTC conditions. Work on the attachment of the 4-allyloxy benzoate of NPP is currently in progress and the characterization of these compounds will be reported at a later date.

REFERENCES

1. Bunning, T.J.; Klei, Herbert E.; Samulski, E.T.; Adams, W.W.; Crane, R.J.
Air Force Technical Report WL-TR-91-4012.
2. Pachter, R.; Bunning, T.J.; Adams, W.W. accepted for publication.
3. Natarajan, L.V.; Bunning, T.J.; Klei, H.E.; Crane, R.J.; Adams, W.W.,
accepted for publication.
4. Kruezer, F.-H.; Andrejewski, D.; Haas, W.; Häberle, N.; Riepl, G.; Spes, P.
Mol. Cryst. Liq. Cryst. **199**, 1991, 345.
5. Hahn, B.; Percec, V. *Mol. Cryst. Liq. Cryst.* **157**, 1988, 125.
6. Legrand, C.; LeBorgne, A; Bunel, C.; Lacoudre, N.; Le Barny, P.;
Spassky, N.; Vairon, J.-P. *Makromol. Chem.* **191**, 1990, 2979.
7. Szeja, W. *Polish. J. Chem.* **57**, 1983, 609.
8. Marei, A.A.; Raphael, R.A. *J. Chem. Soc.* **1960**, 886.
9. Vorbrüggen, H. *Acta Chem. Scand.* **B36**, 1982, 420.
10. Jochims, J.C.; Kobayashi, Y.; Skrzalewski, E. *Tet. Lett.* **7**, 1974, 571.
11. Finkelmann, H.; Rehage, G. *Makromol Chem. Rapid. Commun.* **1**, 1980,
31.
12. Zyss, J.; Nicoud, J.F.; Coquillay, M. *J. Chem. Phys.* **81**, 1984, 4160.

1991 USAF-RDL SUMMER FACULTY RESEARCH PROGRAM

Sponsored by the
AIR FORCE OFFICE OF SCIENTIFIC RESEARCH

Conducted by the
Research & Development Laboratories

FINAL REPORT

Ab Initio Computational and NMR Relaxation Time
Investigations of Rotational Barriers and
Chain Dynamics in Perfluoropolyalkylethers

Prepared by:	Martin Schwartz
Academic Rank:	Professor
Department and	Chemistry Department
University:	University of North Texas
Research Location:	Materials Directorate WL/MLBT Wright-Patterson AFB Ohio 45433-6533
USAF Researcher:	Dr. Kent J. Eisentraut (Technical Focal Point) and Dr. Harvey L. Paige
Date:	September 12, 1991
Contract No:	F49620-90-C-0076

ABSTRACT

Like the perfluoropolyalkylethers, the barrier to internal rotation about the C-C bond in 1,1,2-trichloro-1,2,2-trifluoroethane [TCTFE] is affected by both steric and electronic substituent interactions. In order to establish a methodology for quantum mechanical investigations of PFPAE model compounds, the geometries, energies and vibrational frequencies of TCTFE were studied by *ab initio* calculations using basis sets ranging from 3-21G through 6-311G(2df). Bond lengths and angles calculated with the 6-31G(d) and 6-311G(d) bases were in close agreement with each other and with experimental results. Comparable energies of the equilibrium conformers and torsional barriers were obtained by MP2 calculations using the 6-31G(d), 6-311G(d) and 6-311G(2df) bases. The calculated equilibrium energy difference is in qualitative agreement with experimental results. It was concluded that results using the 6-31G(d) basis set provide satisfactory structural parameters and conformational energies, comparable to those obtained using larger polarized bases.

Fluorine-19 NMR spin-lattice (T_1) relaxation times were measured as a function of temperature and frequency for several PFPAE's. Derived correlation times and activation energies revealed that there exists a substantially greater barrier to rotation about C-C than C-O bonds in these systems. There is a significant variation in values of E_a obtained at two experimental frequencies (84.7 and 282.2 MHz), indicating that overall and internal polymer chain rotation affect the two measurements differently. Further analysis is in progress in order to separate the two reorientation mechanisms and to obtain a semi-quantitative experimental estimate of the barrier to internal rotation.

ACKNOWLEDGMENTS

I would like to thank the Air Force Systems Command and the Air Force Office of Scientific Research for sponsorship of this research and Research & Development Laboratories for the able administration of the Summer Faculty Research Program.

I am most indebted to Dr. Harvey L. Paige with whom I worked throughout the summer and look forward to our continued research together. His guidance and collaborative work on our projects made the summer far more productive and enjoyable than it could have been otherwise. I wish to thank Dr. Jim Liang, who is collaborating with Dr. Paige and myself on an ongoing research project.

I am most grateful to Dr. Kent J. Eisentraut, my Technical Focal Point, who furnished me with excellent summer facilities and was happy to help with any request I had.

Finally, I would like to thank all of the members of MLBT, whose friendship and camaraderie made my stay at the Materials Directorate a very enjoyable and rewarding experience.

1. INTRODUCTION

Perfluoropolyalkylether (PFPAE) fluids possess the viscoelastic, thermal and lubricity properties necessary to serve as effective, stable liquid phase lubricants.^{1,2} No currently available commercial PFPAE lubricants, however, are capable of operation at the temperature extremes and oxidative conditions required for lubrication of high performance gas turbine engines.

The viscoelastic properties of polymer fluids such as the PFPAE's are, of course, intimately connected to the chain flexibility in these systems which is, in turn, dependent upon the potential energy barriers to internal rotation about single bonds in the polymer. This summer, I have been engaged in two research projects designed to obtain a better understanding of chain mobility in PFPAE's. (1) In collaboration with Dr. Harvey L. Paige at the Materials Directorate, Wright Laboratory, Wright-Patterson AFB, I have begun *ab initio* and semi-empirical quantum mechanical modelling studies of rotational barriers in molecules related to perfluoroethers; (2) The students in my research group at the University of North Texas have been obtaining data on the frequency and temperature dependence of fluorine-19 NMR spin-lattice relaxation times (T_1) in model PFPAE compounds. This latter technique affords a direct measurement of the flexibility at various points along the polymer chain.

In the future, Dr. Paige and I plan to use the results of the quantum mechanical modelling studies in molecular dynamics simulations of the internal rotation in PFPAE chains. The results of these simulations will be compared to the experimental NMR measurements, which will provide an assessment of the accuracy of the calculations.

Ultimately, we expect to be able to use molecular modelling to predict the viscoelastic and conformational properties of these fluids, thus aiding in the molecular design of new PFPAE lubricants.

II. AB INITIO MOLECULAR ORBITAL STUDIES OF ROTATIONAL BARRIERS

Introduction The barriers to internal rotation about the C-O and C-C bonds and, hence, chain flexibility in PFPAE's depend upon both the electronic and steric properties of groups attached to the bonded atoms. Prior to beginning our investigations of the perfluoroethers, Dr. Paige and I decided to establish the methodology *via* studies of two halofluoroethanes, 1,1,2-trichloro-1,2,2-trifluoroethane ($\text{CCl}_2\text{F}-\text{CClF}_2$) [TCTFE] and 1,2-dichloro-1,1,2-trifluoro-2-iodoethane ($\text{CClF}_2-\text{CClFI}$) [DCTFIE]. The chlorine and iodine atoms in these molecules possess very different steric and electronic properties and provide us with the opportunity to assess the accuracy of the calculational procedures without the added complication of multiple internal rotations. The work on TCTFE has been completed and a paper has been prepared for publication.³ The computations have been completed on DCTFIE and the analysis will be completed this fall. In addition, Dr. James Liang of the Materials Directorate is obtaining experimental IR frequency and intensity data on the vibrations in DCTFIE, which will be compared with theoretical predictions. Results on the latter molecule will be presented in an article to be written at a later date.

Calculations *Ab initio* molecular orbital calculations were performed using the Gaussian-90⁴ program on a Cray X-MP/216 computer. In TCTFE, the two equilibrium geometries, C_1 and C_s , are termed gauche (G) and trans (T), respectively, to denote the relative positions of the lone fluorine (F_1) on the first carbon atom and the single chlorine

(Cl₁) on the second carbon; the transition state structures are called GT and GG'. The equilibrium and saddle point geometries were optimized with the following basis sets: 3-21G,⁵ 6-31G,⁶ D95,⁷ 6-31G(d)^{6,8} and 6-311G(d).^{8,9} Calculations on the four conformers were also performed with the 6-311G(2df)^{8,9} basis set using the 6-311G(d) geometries. Single point second order Møller-Plesset¹⁰ correlation energy calculations were performed with several of the largest basis sets.

For comparison with the *ab initio* results, MNDO,¹¹ AM1¹² and PM3¹³ semi-empirical energy calculations were performed with the program MOPAC.¹⁴ As above, all structural parameters were optimized for both equilibrium and transition state conformations.

Results and Discussion

Geometries Tabulated in columns 3-7 of Table 1 are the structural parameters for the trans conformer calculated with the various basis sets used in this study. The results from the D95 (double-zeta) basis set are not included since, not surprisingly, they are quite similar to those obtained with the 6-31G (doubly-split valence) basis.

One observes that structural parameters determined with the two polarized basis sets, 6-31G(d) and 6-311G(d) are generally quite close; calculated bond lengths are the same to within 0.002-0.006 Å and bond angles differ by an average of <0.4°. It is seen further from the table that $R(\text{CF}_2), R(\text{CF}_3) < R(\text{CF}_1)$, in agreement with the experimental observation¹⁵ that C-F bond lengths shorten with increasing fluorine substitution on a carbon.

Iwasaki¹⁶ has determined the structure of TCTFE by electron diffraction,¹⁷ and his results are given in the second column of Table 1. One finds that C-C and C-Cl bond lengths obtained with the

6-31G(d) and 6-311G(d) basis sets are in close coincidence to his values, whereas calculated C-F bond lengths are significantly shorter than experiment; the latter inequality is common to all large basis set SCF calculations on fluorocarbons.¹⁸ Considering the approximations employed in the experimental structure determination, the bond angles, too, are in quite satisfactory agreement with measured values.

Shown in the last four columns of the table are the structures of both equilibrium and saddle point configurations, determined with the 6-311G(d) basis set. As found in earlier *ab initio* studies of substituted ethanes,^{7,7} all bond lengths with the exception of C-C remain approximately constant, whereas the latter increases by 0.045-0.050 Å in the saddle point structures. One observes, also, that apparently equivalent angles appear to vary within a given conformation and between conformers. These variations can, in all cases, be explained by steric interactions. For instance, the observation that $\angle CCF_2 > \angle CCF_3$ in the G rotamer is due to the fact that fluorine F₂ has two gauche interactions with chlorine atoms compared to only one for F₃. Similarly, $\angle CCF_1$ and $\angle CCF_2$ are greatest in the GG' transition state, which is the only conformation in which they eclipse chlorine atoms.

Energies Displayed in Table 2 are the energies and energy differences (relative to the T conformer) calculated at the SCF and MP2 levels using the various basis sets. One finds that all *ab initio* calculations yield negative values for the energy difference, $\Delta E(G-T)$, which, at the SCF level, ranges from -0.7 to -0.8 kcal/mol for the two largest basis sets. The correlation energy correction is small, lowering ΔE by 0.0 to 0.2 kcal/mol. There is no further correction to the equilibrium energy difference arising from zero point vibrational

energy (ZPVE) and thermal contributions to the enthalpy (discussed in ref. 3). Thus the final calculated range is $\Delta E(G-T) = -0.6$ to -0.7 kcal/mol, which is in qualitative agreement with experimental estimates; $\Delta H(\text{exp}) \approx \Delta E(\text{exp}) = -0.25^{19}$ to -0.35^{20} kcal/mol.

One sees also from the table that both transition state energies, $\Delta E(GT-T)$ and $\Delta E(GG'-T)$, generally increase with size of the basis set. The correlation energy correction to $\Delta E(GT-T)$ is -0.0 to -0.3 kcal/mol. Together with a -0.4 kcal/mol correction from $\Delta[\text{ZPVE}]$ and $\Delta[H(T)-H(O)]$ (Ref. 3), one obtains a net energy barrier, $\Delta E(GT-T) = 8.7 - 9.1$ kcal/mol (with the three largest basis sets). This value lies within the range determined from ultrasonic relaxation measurements,²¹ $\Delta E(GT-T) = 5.0 - 10.0$ kcal/mol. It is somewhat higher than the estimate from the infrared torsional frequency;²¹ however, this latter measurement was subject to potentially large errors.

It is found that the second transition state, GG' , has a significantly lower energy than GT . With the correlation energy, $\Delta[\text{ZPVE}]$ and $\Delta[H(T)-H(O)]$ corrections, $\Delta E(GG'-T) = 6.8 - 7.2$ kcal/mol. The higher energy of the GT saddle point seems quite reasonable since there is a repulsive interaction between two eclipsed chlorine atoms which is not present in the GG' conformation.

Finally, we note that all three semi-empirical methods¹¹⁻¹³ predict that $\Delta E(G-T) > 0$, which disagrees with both experimental and *ab initio* results. Too, they predict that $\Delta(GT-T) < \Delta(GG'-T)$, in contrast to the *ab initio* calculations and to chemical intuition.

Vibrations Although not shown (see Ref. 3), vibrational frequencies were calculated for the G and T conformers using the 6-31G(d) basis set, and were multiplied by the standard scale factor, 0.90, to account for

corrections due to vibrational anharmonicity and electron correlation. The scaled frequencies were in quite satisfactory agreement with experimental data on the two rotamers, with errors of 1.2-1.8% for modes below 1000 cm^{-1} ; the error was somewhat greater (3.5%-4.2%) for the C-F stretching vibrations (above 1000 cm^{-1})

Conclusions The agreement between theoretical and experimental geometries, energies and vibrational frequencies were quite satisfactory when using the 6-31G(d) basis set, which provides evidence that this basis should provide an adequate characterization of the structures and energies in our planned computational investigations of model compounds for the perfluoropolyalkylethers.

Planned Investigations Dr. Paige and I have just begun a comparative *ab initio* study of perfluorobutane [$\text{CF}_3\text{CF}_2\text{CF}_2\text{CF}_3$] and perfluoroethylmethyl ether [$\text{CF}_3\text{CF}_2\text{OCF}_3$] in order to determine the effect replacement of CF_2 groups by oxygen atoms on the conformational energies and rotational barriers. We plan also to investigate whether the 3-21G(d) basis set yields satisfactory geometric structural parameters. If this proves true, it will permit us to perform more computationally efficient calculations on larger PFPAE model compounds. We also plan to initiate an investigation on the torsional potential energy surface in perfluorodimethoxymethane [$\text{CF}_3\text{OCF}_2\text{OCF}_3$] either later this fall or next spring. This molecule is of interest since one expects the torsional barriers to rotation about the the two $\text{CF}_2\text{-O}$ bonds to be mutually dependent upon both dihedral angles.

III. NMR RELAXATION TIME STUDIES OF PFPAE CHAIN FLEXIBILITY

Introduction The measurement of NMR Spin-Lattice (T_1) relaxation times is a well established technique to probe both the rates and

mechanisms of molecular reorientation in liquids and solution.²² The method has also been used quite profitably to characterize the conformational mobility of flexible chain polymers.^{23,24} To date, however, NMR relaxation has not yet been applied to study the polymer chain dynamics in perfluoropolyalkylethers.

As applied to the PFPAE's, the fluorine-19 relaxation time $[T_1(^{19}\text{F})]$ is a function of the rotational correlation time (τ_c) of the vector connecting the two fluorine atoms in a CF_2 group; i.e. $T_1^{-1} \propto \tau_c/R^6$, where R is the distance between the two fluorine nuclei. Qualitatively, τ_c is the time it takes for the ^{19}F - ^{19}F vector to rotate by one radian ($\approx 60^\circ$). The value of the correlation time, then, provides a direct measure of the polymer's flexibility in the region immediately surrounding a given perfluoromethylene group. For polymeric species such as the PFPAE's, τ_c may be a function of the frequency of the NMR experiment. The acquisition of data at two or more frequencies permits a determination of the mechanism of the internal rotation dynamics in the polymer chain.

During this summer, we have extended investigations begun during the past year to study the temperature and frequency dependence of NMR relaxation in a number of perfluoropolyalkylethers. The data acquisition is still in progress; below, we describe the preliminary results obtained to date.

Experimental Fluorine-19 NMR measurements were performed by students in my research group at the University of North Texas on (a) a JEOL FX90Q FT-NMR Spectrometer operating at $B_0=21.1$ kG [$\nu_0(^{19}\text{F})=84.7$ MHz], and (b) a Varian VXR-300 FT-NMR operating at $B_0=70.5$ kG [$\nu_0(^{19}\text{F})=282.2$ MHz]. Spin-lattice relaxation times were determined with the standard

Inversion Recovery Fourier Transform (IRFT) pulse sequence,²⁵ (180° - τ - 90° -Acq.), with 10-12 τ values plus $\tau \rightarrow \infty$. T_1 was calculated from the peak intensities by a non-linear fit to the three parameter magnetization equation.²⁶

The following experiments were performed this summer: (a) Temperature dependence of relaxation times in perfluoropoly(tetraethylene glycol), $R_fO[(CF_2CF_2O)_4CF_2O]_nCF_3$, $R_f=CF_3$, CF_3CF_2 (ML088-131) [Table 3];²⁷ (b) Temperature dependence of $T_1(^{19}F)$ in Fomblin-Z, $R_fO[CF_2O]_m[C_2F_4O]_n[C_3F_6O]_q$, $R_f=CF_3$, C_2F_5 (ML078-80) [Table 4]; (c) Temperature and frequency dependence of relaxation times in perfluoropoly(ethylene oxide), $CF_3O[CF_2CF_2O]_nCF_3$ (ML088-50) [Table 5]. Correlation times reported in Tables 3-5 were calculated using standard formulae.²⁸

Results and Discussion The temperature dependent rotational correlation times of perfluoropoly(tetraethylene glycol) are displayed in Table 3. One notes first that τ_c 's of the perfluoromethyl (CF_3) end groups [peaks 4 and 5] are lower than rotational times of perfluoromethylene (CF_2) groups in the middle of the polymer chain. This is to be expected since the internal rotation of the latter groups require cooperative reorientation about several adjacent bonds. One sees, however that the two CF_3 groups are not equivalent; the activation energy for rotation in the CF_3CF_2O - unit [peak 4] is substantially higher than in the CF_3O - group [peak 5] (4.5 versus 2.5 kcal/mol), which provides evidence that, as is intuitively reasonable, the barrier to rotation about a CF_3 - CF_2 bond is substantially greater than for a CF_3 -O bond. Further evidence for a lower barrier to rotation about C-O bonds is provided by a comparison of peaks 2, 3 and 6. The first two

resonances result from ^{19}F nuclei in CF_2 groups with one C-C and one C-O bond, whereas the third peak represents a group with two C-O bonds. The activation energy for rotation of the latter CF_2 unit is substantially lower (2.9 kcal/mol) than found in the two former peaks (3.8 and 4.1 kcal/mol) which, again, provides evidence for a markedly lower barrier to rotation about the C-O bonds in perfluoropolyalkylethers.

Table 4 contains correlation times obtained for the various resonances of Fomblin-Z as a function of temperature in the neat fluid. One observes the same trend found above in the simpler perfluoroether. Specifically, the activation energies for rotation of CF_2 groups containing both a C-C and C-O bond [peaks 1-4] are uniformly greater than those for perfluoromethylene units bonded to two oxygens [bands 7-9], which likely results from the higher barrier to internal rotation about the former bonds. Due to its greater molecular weight, with consequently greater correlation times, Fomblin-Z is almost assuredly not in the motional narrowing limit. Hence, a complete analysis of the reorientation in this molecule will require measurements of the frequency dependence of its relaxation times, which are currently in progress.

Displayed in Table 5 are the reorientational correlation times of perfluoropoly(ethylene oxide) as a function of temperature at two different fluorine-19 resonance frequencies (84.7 and 282.2 MHz). One observes that, as in perfluoropoly(tetraethylene glycol) and Fomblin-Z, both the values of τ_c and E_a for reorientation of the CF_3O - end group are lower than for other groups in the middle of the polymer chain. Most significantly, the activation energies of all resonances are markedly less in the high frequency (282.2 MHz) experiments. If all

motions in the polymer were at a frequency greater than ~300 MHz, one would expect results of the two experiments to be identical. Hence, it is clear that the low frequency measurements reflect two separate reorientational mechanisms, overall rotation superposed on the slower internal rotations about C-C and C-O bonds in the chain. In the coming month, we plan to fit the data with several theoretical models of chain reorientation,^{29,30} which will permit us to obtain a quantitative separation of the internal and overall polymer dynamics.

Future Studies Work is currently underway to determine the relaxation and correlation times of Fomblin-Z at a second ¹⁹F resonance frequency and to study relaxation in two other Fomblins of differing average molecular weights. As for perfluoropoly(ethylene oxide), the data will be fit to models which will permit separation of the rates and mechanisms of internal and overall molecular rotation and will, hopefully, provide semi-quantitative estimates of the barriers to internal rotation; these results will be correlated with the experimental viscosity indices. It is expected that, eventually, these experiments will yield an indication of the effects of structure (e.g. number of CF₂, C₂F₄, C₃F₆ units and their arrangement) on the viscosity-temperature characteristics of perfluoroethers and aid in the design of new PFPAE lubricants.

REFERENCES

1. Snyder, C. E., Jr.; Dolle, R. E., Jr. *ASLE Trans.* 1975, 19, 171.
2. Snyder, C. E., Jr.; Gschwender, L. J.; Tamborski, C. *Lubr. Eng.* 1981, 37, 344.
3. "Ab Initio Study of Conformational Energies and Rotational Barriers in a Chlorofluoroethane," H. L. Paige and M. Schwartz, *J. Phys. Chem.* (to be submitted).
4. Gaussian 90, Revision F; Frisch, M. J.; Head-Gordon, M.; Trucks, G. W.; Foresman, J. B.; Schlegel, H. B.; Raghavachari, K.; Robb, M.; Binkley, J. S.; Gonzalez, C.; Defrees, D. J.; Fox, D. J.; Whiteside, R. A.; Seeger, R.; Melius, C. F.; Baker, J.; Martin, R. L.; Kahn, L. R.; Stewart, J. J. P.; Topiol, S.; Pople, J. A.; Gaussian, Inc.: Pittsburgh, PA, 1990.
5. Pietro, W. J.; Francl, M. M.; Hehre, W. J.; Defrees, D. J.; Pople, J. A.; Binkley, J. S. *J. Am. Chem. Soc.* 1982, 104, 5039, and references contained therein.
6. (a) Hehre, W. J.; Ditchfield, R.; Pople, J. A. *J. Chem. Phys.* 1982, 56, 2257; (b) Hariharan, P. C.; Pople, J. A. *Theor. Chim. Acta* 1973, 28, 213.
7. Dunning, T. H., Jr.; Hay, P. J. In *Methods of Electronic Structure Theory*; Schaefer, H. F., III, Ed.; Plenum Press: New York, 1977; p 1.
8. Frisch, M. J.; Pople, J. A.; Binkley, J. S. *J. Chem. Phys.* 1984, 80, 3265.
9. (a) Krishnan, R.; Binkley, J. S.; Seeger, R.; Pople, J. A. *J. Chem. Phys.* 1980, 72, 650; (b) McLean, A. D.; Chandler, G. S. *ibid.* 1980, 72, 5639.
10. Møller, C.; Plesset, M. S. *Phys. Rev.* 1934, 46, 618.
11. Dewar, M. J. S.; Thiel, W. J. *Am. Chem. Soc.* 1977, 99, 4899.
12. Dewar, M. J. S.; Zebisch, E. J.; Healy, E. F.; Stewart, J. J. P. *J. Am. Chem. Soc.* 1985, 107, 3902.
13. Stewart, J. J. P. *J. Comput. Chem.* 1989, 10, 209, 221.
14. Stewart, J. J. P. *MOPAC: Version 5.0*; Frank J. Seiler Research Laboratory, U. S. Air Force Academy, Colorado Springs, Colorado, 80840.

15. (a) Harmony, M. D.; Laurie, V. W.; Kuczkowski, R. L.; Schwendeman, R. H.; Ramsey, D. A.; Lovas, F. J.; Lafferty, W. J.; Maki, A. G. *J. Phys. Chem. Ref. Data* 1979, 8, 619; (b) Hirota, E.; Tanaka, T.; Sakakibara, A.; Ohashi, Y.; Morino, Y. *J. Mol. Spectrosc.* 1970, 34, 222; (c) Typke, V.; Dakkouri, M.; Oberhammer, H. *J. Mol. Struct.* 1978, 44, 85.
16. Iwasaki, M. *Bull. Chem. Soc. Jpn.* 1959, 91, (a) 194; (b) 207.
17. In the structure determination of $\text{CCl}_2\text{F}-\text{CClF}_2$, the C-C bond length and the C-C-F and C-C-Cl bond angles were transferred directly from earlier investigations of $\text{CClF}_2-\text{CClF}_2$ and $\text{CCl}_2\text{F}-\text{CCl}_2\text{F}$. (Iwasaki, M. *Bull. Chem. Soc. Jpn.* 1958, 31, 1071).
18. (a) Dixon, D. A.; Fukunaga, T.; Smart, B. E. *J. Am. Chem. Soc.* 1986, 108, 1585, 4027; (b) Dixon, D. A. *J. Phys. Chem.* 1986, 90, 2038. (c) Dixon, D. A.; Arduengo, III, A. J. *ibid.* 1987, 91, 3195; (d) Dixon, D. A. *ibid.* 1988, 92, 86.
19. Braathen, G. O.; Gatial, A.; Klæboe, P.; *J. Mol. Struct.* 1987, 157, 73.
20. Klæboe, P.; Nielsen, J. R. *J. Mol. Spectrosc.* 1961, 6, 379.
21. Pethrick, R. A.; Wyn-Jones, E. *J. Chem. Soc. (A)* 1971, 54.
22. Boéré, R. T.; Kidd, R. G. *Ann. Rep. NMR Spectrosc.* 1982, 13, 319.
23. Heatley, F. *Ann. Rep. NMR Spectrosc.* 1986, 17, 189.
24. Hermann, G.; Weill, G. *Macromolecules* 1975, 8, 171.
25. Martin, M. L.; Martin, G. J.; Delpuech, J.-J. *Practical NMR Spectroscopy*; Heyden; London, 1980, Chap. 6.
26. Rodriguez, A. A.; Chen, S. J. H.; Schwartz, M. J. *Magn. Reson.* 1987, 74, 114.
27. In addition to the data in Table 3, measurement of the relaxation times in perfluoropoly(tetraethylene glycol) at several lower temperatures are currently in progress.
28. Ref. 25; Chap. 4.
29. Hall, C. K.; Helfand, E. *J. Chem. Phys.* 1982, 77, 3275.
30. Viovy, J. L.; Monnerie, L.; Brochon, J. C. *Macromolecules* 1983, 16, 1845.

Table 1. Calculated Structural Parameters^a

Parameter	Experiment ^b	T [3-21G]	T [6-31G]	T [6-31G(d)]	T [6-311G(d)]	G [6-311G(d)]	GT [6-311G(d)]	GG' [6-311G(d)]
R(CC)	1.54 (0.05)	1.523	1.529	1.549	1.552	1.550	1.599	1.595
R(CF ₁)	1.38 (0.02 ₁)	1.363	1.373	1.330	1.324	1.320	1.321	1.319
R(CF ₂)	1.33 (0.01 ₄)	1.345	1.360	1.318	1.313	1.311	1.311	1.311
R(CF ₃)	1.33 (0.01 ₄)	1.345	1.360	1.318	1.313	1.313	1.311	1.311
R(CCl ₁)	1.75 (0.02 ₇)	1.829	1.801	1.749	1.751	1.756	1.756	1.756
R(CCl ₂)	1.76 (0.02)	1.821	1.808	1.754	1.756	1.761	1.759	1.761
R(CCl ₃)	1.76 (0.02)	1.821	1.808	1.754	1.756	1.756	1.762	1.761
∠CCF ₁	107.1	106.1	105.5	104.9	105.6	107.6	106.6	109.4
∠CCF ₂	108 (1.5)	108.7	108.3	107.6	108.0	109.7	107.2	110.3
∠CCF ₃	108 (1.5)	108.7	108.3	107.6	108.0	108.3	110.0	110.3
∠CCCl ₁	112 (1.5)	112.6	114.6	114.5	114.0	112.1	115.9	112.1
∠CCCl ₂	112 (2.0)	111.3	112.0	111.6	111.3	109.5	114.6	111.2
∠CCCl ₃	112 (2.0)	111.3	111.9	111.6	111.3	111.4	111.0	111.2
∠F ₂ CF ₃	108.7	109.2	107.7	107.9	107.8	108.4	107.5	107.0
∠Cl ₂ CCl ₃	110.5 (1)	111.6	111.6	111.6	111.4	110.5	109.4	110.0
φ(F ₁ CCCl ₁)	59.5 (1.5)	180.0	180.0	180.0 ₆	180.0	58.0	120.4	0.0

a) Bond lengths in Angstroms and angles in degrees.

b) Reference 16.

Table 2. Calculated Conformational Energies

Basis set	T	G	GT	GG'
A. Total Energies (Hartrees)				
HF/3-21G	-1743.842 44	-1743.848 03	-1743.831 07	-1743.839 02
HF/6-31G	-1752.247 87	-1752.250 68	-1752.234 13	-1752.238 64
HF/D95	-1752.310 81	-1752.312 21	-1752.296 76	-1752.300 86
HF/6-31G(d)	-1752.458 57	-1752.460 12	-1752.443 56	-1752.447 07
HF/6-311G(d)	-1752.630 64	-1752.631 75	-1752.615 42	-1752.618 83
HF/6-311G(2df) //6-311G(d)	-1752.673 92	-1752.675 17	-1752.658 76	-1752.661 81
MP2/6-31G(d)	-1753.624 56	-1753.626 06	-1753.610 05	-1753.613 10
MP2/6-311G(d)	-1753.933 15	-1753.934 24	-1753.917 97	-1753.921 11
MP2/6-311G(2df) //6-311G(d)	-1754.277 79	-1754.278 75	-1754.263 01	-1754.265 66
B. Relative Energies (kcal/mol)				
HF/3-21G	0.00	-3.50	+7.14	+2.15
HF/6-31G	0.00	-1.76	+8.62	+5.79
HF/D95	0.00	-0.88	+8.82	+6.25
HF/6-31G(d)	0.00	-0.97	+9.42	+7.22
HF/6-311G(d)	0.00	-0.69	+9.55	+7.41
HF/6-311G(2df) //6-311G(d)	0.00	-0.79	+9.51	+7.60
MP2/6-31G(d)	0.00	-0.94	+9.11	+7.19
MP2/6-311G(d)	0.00	-0.68	+9.52	+7.55
MP2/6-311G(2df) //6-311G(d)	0.00	-0.61	+9.27	+7.61
MNDO	0.00	+0.82	+5.17	+7.23
AM1	0.00	+1.13	+5.15	+9.21
PM3	0.00	+0.81	+2.86	+3.44
Experiment	0.00	-0.25 ^a -0.35 ^d	+5.9 ^b +5-10 ^c	

a) Reference 19.

b) Reference 21. From torsional frequency (IR).

c) Reference 21. From ultrasonic relaxation.

d) Reference 20.

Table 3. NMR Correlation Times in Perfluoropoly(tetraethylene glycol),
 $R_fO[(CF_2CF_2O)_4CF_2O]_nCF_3$, $R_f=CF_3$, CF_3CF_2 (ML088-131)
 Bulk Fluid. $B_0 = 21.1$ kG [$\nu_0(^{19}F) = 84.7$ MHz]

Peak	Delta ^a	Assignment	23°C	49°C	73°C	-E _a
1	73.6 ppm	CF ₃ OCF ₂ CF ₂ O-	72 ps	41 ps	32 ps	3.3 kcal/mol
2	74.0	-OCF ₂ CF ₂ OCF ₂ O-	115	63	46	3.8
3	75.7	-OCF ₂ CF ₂ OCF ₂ CF ₂ O-	125	68	46	4.1
4	76.8	CF ₃ CF ₂ O-	31	20	10	4.5
5	108.2	CF ₃ OCF ₂ CF ₂ O-	35	23	19	2.5
6	112.6	-OC ₂ F ₄ OCF ₂ OC ₂ F ₄ O-	92	67	45	2.9

a) Chemical shifts are measured in ppm downfield from hexafluorobenzene

Table 4. NMR Correlation Times in Fomblin-Z,
 $R_f[CF_2O]_n[C_2F_4O]_q[C_3F_6O]_r$, $R_f=CF_3$, C_2F_5 (ML078-80)
 Bulk Fluid. $B_0 = 21.1$ kG [$\nu_0(^{19}F) = 84.7$ MHz]

Peak	Delta ^a	Assignment	-30°C	-3°C	23°C	50°C	76°C	-E _a ^b
1	74.2	OCF ₂ CF ₂ OCF ₂ O	337	180	101	60	42	3.4
2	75.9	OCF ₂ CF ₂ OC ₂ F ₄ O	419	247	139	79	56	3.3
3	79.5	OCF ₂ CF ₂ CF ₂ OCF ₂ O	420	171	85	59	35	3.9
4	81.1	OCF ₂ CF ₂ CF ₂ OC ₂ F ₄ O	371	139	67	52	16	4.6
5	106.9	CF ₃ OCF ₂ O	32	22	18	17	16	1.1
6	108.6	CF ₃ OC ₂ F ₄ O	72	42	21	9	7	3.9
7	109.5	OCF ₂ OCF ₂ OCF ₂ O	197	115	67	45	36	2.8
8	111.3	OCF ₂ OCF ₂ OC ₂ F ₄ O	284	162	97	60	45	3.0
9	112.9	OC ₂ F ₄ OCF ₂ OC ₂ F ₄ O	370	215	132	76	60	3.0

a) Chemical shifts are measured in ppm downfield from hexafluorobenzene

Table 5. NMR Correlation Times in Perfluoropoly(ethylene oxide), $\text{CF}_3\text{O}[\text{CF}_2\text{CF}_2\text{O}]_n\text{CF}_3$ (ML088-50)

5.A Bulk Fluid. $B_0 = 21.1 \text{ kG}$ [$\nu_0(^{19}\text{F}) = 84.7 \text{ MHz}$]

Peak	Delta ^a	Assignment	10°C	23°C	40°C	55°C	70°C	-E _a
1	73.6 ppm	$\text{CF}_3\text{OCF}_2\text{CF}_2\text{O}-$	115 ps	79 ps	51 ps	45 ps	30 ps	4.1 kcal/mol
2	75.7	$\text{CF}_3\text{CF}_2\text{OCF}_2\text{CF}_2\text{O}-$	218	163	111	87	58	4.1
3	75.8	$-\text{OCF}_2\text{CF}_2\text{O}-$	277	214	137	103	72	4.3
4	76.9	$\text{CF}_3\text{CF}_2\text{OCF}_2\text{CF}_2\text{O}-$	100	72	48	34	25	4.5
5	108.1	$\text{CF}_3\text{OCF}_2\text{CF}_2\text{O}-$	48	42	29	26	22	2.6

5.B Bulk Fluid. $B_0 = 70.5 \text{ kG}$ [$\nu_0(^{19}\text{F}) = 282.2 \text{ MHz}$]

Peak	Delta ^a	Assignment	10°C	23°C	40°C	55°C	70°C	-E _a
1	73.6 ppm	$\text{CF}_3\text{OCF}_2\text{CF}_2\text{O}-$	127 ps	86 ps	71 ps	55 ps	43 ps	3.3 kcal/mol
2	75.7	$\text{CF}_3\text{CF}_2\text{OCF}_2\text{CF}_2\text{O}-$	184	134	115	90	67	3.1
3	75.8	$-\text{OCF}_2\text{CF}_2\text{O}-$	225	196	167	134	106	2.4
4	76.9	$\text{CF}_3\text{CF}_2\text{OCF}_2\text{CF}_2\text{O}-$	92	62	48	35	29	3.7
5	108.1	$\text{CF}_3\text{OCF}_2\text{CF}_2\text{O}-$	41	34	28	24	21	2.1

a) Chemical shifts are measured in ppm downfield from hexafluorobenzene

b) Activation energies are given in kcal/mol

On Photoreflectance Spectra from Two Dimensional Electron Gas in GaAs/AlGaAs Heterojunctions

by
Michael Sydor
Physics Dept.
University of Minnesota, Duluth
RDL Summer Faculty Research Program
ID#140, for Dr. William Mitchel
at MLPO/WPAFB
Summer 1991

ABSTRACT: We use differential Photoreflectance and indirectly modulated photoreflectance to examine the signature from high mobility Two-dimensional electron gas in GaAs/AlGaAs heterojunctions. The samples with the highest electron mobility show an additional photoreflectance signal at ~ 1.45 eV. The signal can be attributed to the optical transitions from the valence band to the second conduction subband (E_1). Indirect Photoreflectance obtained by modulating the sample slightly off the probe illumination, accentuates the 1.45 eV signal. The amplitude and time dependence of the indirectly modulated Photoreflectance appears to depend on sample quality and may thus be useful in optical assessment of electronic materials.

INTRODUCTION:

Heterostructures containing Two Dimensional Electron Gas (2DEG) are important in industrial applications. The parameter of

greatest interest in such samples is the mobility of 2DEG. Photorefectance (PR) and Differential Photorefectance (DPR) are two nonintrusive methods for detection of 2DEG at room temperature.¹⁻⁴ However, PR and to some extent the DPR are both difficult to quantify because they perturb or modulate more than just the 2DEG region of the sample.^{5,6} Since the characteristic property of high quality heterojunctions is the very high mobility and persistent confinement of 2DEG, one may be able to use these properties in exciting modulation of the electron gas outside of the monitored region of the sample, say outside of the illuminated spot in a reflectance measurement. We observe indirect PR by laser modulating the sample slightly off the probe illumination, in an otherwise standard Photorefectance setup.⁷ The resulting signal from our best High Electron Mobility Transistors (HEMT) shows an enhancement of a signature attributed to 2DEG.¹ We observe similar enhancement in the DPR⁸ for these samples when we selectively modulate their 2DEG potential wells.

We simulate the 2DEG DPR in terms of a numerical model proposed by Snow, Glembocki, and Shanabrook.⁹ The details of the numerical model are being presented separately. Here we use the model to discuss the origin of the 1.45 eV signal which characterizes the DPR from HEMT showing Cyclotron Resonance determined mobilities of 10^5 cm²/Vs or better.

DISCUSSION OF METHOD:

The samples investigated here were typical HEMT whose representative structure and characteristic PR spectra are shown in Fig. 1. The broad PR response in Fig. 1, differentiating the two samples, appears to depend the unintentional doping of the channel layer and presence extraneous layers such as the protective cap, its doping, and the structure of the buffer which isolates the HEMT from the substrate.^{5,6} For instance, the oscillatory signal at ~ 1.58 eV comes from ten 30×30 isolation quantum wells comprising the buffer. The amplitude and the shape of the broad signal is ubiquitous and does not appear to have much to do with the samples' 2DEG quality. Both samples in Fig. 1 are excellent. The broad signal is influenced by the removal of the protective cap,⁵ and according to our numerical results, verified by DPR measurements, can also be associated with the unintentional doping of the channel layer. The broad signal when excessive distorts the entire spectrum, especially the sharp oscillatory signal at the 1.42 eV GaAs band-edge. The band-edge signal comes from the 2DEG potential well and the remainder of the undoped GaAs layer to which we simply refer to as the channel layer. see the insert in Fig. 1. The sharp band edge signals shown in Fig. 1 are typical of all HEMT regardless of their 2DEG quality. Poor HEMT ($\sim 10^4$ cm²/Vs) usually exhibit somewhat broader band-edge oscillations⁵ than the ones shown in Fig.1. However, the band edge signal is always there and its sharpness and magnitude has no apparent relationship to the sample's 2DEG concentration or mobility.^{1,2,5,6} None the less, in HEMT with high 2DEG nobility Glembocki et al.¹, and Snow, Glembocki, and

Shanabrook (SGS)⁹ show the band-edge PR is a pseudo composite of two signals which seem to phase shift at low temperature.^{1,9} Glembocki et al.¹ show that most of the band edge signal at 1.42 eV comprising the leading peak at ~ 1.418 eV and the subsequent large oscillation comes from undoped GaAs and constitutes the low electric field PR typical of the epitaxial GaAs. Only the high energy tail of the band-edge PR in Fig. 1 may come from the changes in the absorption due to the optical transitions within the 2DEG triangular potential well.⁹ Thus, the signal specific to and indicative of room temperature 2DEG is obscured, and is often manifested only as an extra small oscillation or a kink at the tail of the band-edge PR.¹ The 2DEG signal can not be isolated from the main PR from the channel layer by using ordinary PR techniques which modulate all depths of the sample. To establish the shape of the signal due to the optical transitions within the 2DEG potential well, it is necessary suppress the modulation within the channel layer. This can be done by using a DPR technique,⁸ or by preferential modulation of 2DEG through indirect means as we attempted here. Both the indirectly modulated PR and the DPR show an enhancement of the high energy tail attributed to the 2DEG.^{1,9} This is shown in Fig. 2. In the DPR of Fig. 2, the modulation of the channel layer was suppressed by illuminating the sample with two superimposed alternately chopped laser beams (633 nm and 544 nm) whose intensities were matched at the depth of buffer's quantum wells (see the insert in Fig. 1). When pump intensities were matched at the quantum wells, the quantum well PR at 1.58 eV in Fig. 1 disappeared, as did most of the ~ 1.42 eV band edge PR from the channel. However the laser pumps

had different wavelengths and their absorption in the intervening layers was different. Thus matched pump intensities at the quantum wells left the 2DEG region of the HEMT weakly modulated, resulting in a small (10^{-5}) oscillatory signal above 1.42 eV, which we believe comes from the 2DEG. The DPR from 2DEG has a shape which is similar to the large PR signal. The 2DEG is slightly shifted and the leading band edge peak is nearly absent. Notice also a more pronounced tail oscillation in the DPR signal in Fig. 2. The enhancement of the ~ 1.45 eV oscillation is also seen in the indirect PR for this sample as shown in Fig. 3. The indirect PR was obtained by using a single chopped 633 nm laser pump which modulated an area ~ 1 mm off the probe illumination .

In general, the very high mobility HEMT, those with excess of $60000 \text{ cm}^2/\text{Vs}$ at 80 K, show a well defined DPR oscillatory structures at ~ 1.432 and ~ 1.45 eV. Sometimes an additional low structure also appears at ~ 1.47 eV.² The exact shape and phase of the DPR at 1.432 and 1.45 eV depends on modulation.² Since the 2DEG signal had a character similar to the DPR we observed from the buffer quantum wells, we initially determined the energies of the 2DEG by fitting its signal with derivatives of Gaussian line-shapes.¹⁰ The portion of 2DEG DPR signal around 1.432 eV appears to be common in varying degree to most HEMT. The oscillation at 1.45 eV was present only in the very high mobility HEMT, those with Cyclotron Resonance (CR) mobility of $\sim 10^5 \text{ cm}^2/\text{Vs}$ (6K) or better. Cyclotron Resonance¹¹ showed mobilities of $\sim 2 \times 10^5 \text{ cm}^2/\text{Vs}$ for several samples. In HEMT with $\sim 10^5 \text{ cm}^2/\text{Vs}$ 6 K mobility, the ratio of the amplitudes of the 1.45 eV to the 1.432 eV DPR structures is

~0.25. To unravel the origin of the DPR and the significance of the 1.45 eV signal in the highest mobility HEMT, we modeled the 2DEG absorption process and the 2DEG DPR.¹²

Our model¹² followed the method of SGS.⁹ We included the density of states in our calculations, and limited the summation of the transitions from the unconfined valence states to the confined conduction subbands to the first two subbands (E_0 and E_1). This procedure simulates the DPR modulation. In our model, the higher order confined states contributed mainly to the band-edge PR which the DPR suppresses.

For low 2DEG modulation (~1%), our model predicts a narrow oscillatory DPR in the 40 meV energy region above the GaAs band gap energy. Our numerical results resemble the low temperature 2DEG PR data shown by SGS,⁹ and simulate the 2DEG DPR which we observed here, as shown in Fig. 4. The model did not include temperature broadening, thus the simulated signal in Fig. 4 is narrower than the room temperature DPR. However, for any given modulation the breadth of the signal also depends on the level of the unintentional doping of the channel layer. This parameter is poorly defined and understood, and may well be measurable using the DPR in conjunction with the numerical results. 2DEG modulations of few percent, SGS took ~ 30%, produced in our model a broad response, like the one obtained by SGS in their model.⁹

Outside of predicting a narrow 2DEG DPR response which resembles the data, the most interesting result of our model, germane to the discussions here, is the identification of the ~1.432

eV structure and the secondary ~ 1.45 eV part of the 2DEG DPR associated with highest mobility samples. The 1.45 eV signal and part of the 1.432 eV signal in Fig 4 appears to come from the overlap of the first excited subband (E_1) wavefunction with the unconfined hole wavefunctions in the outer region of 2DEG potential well. Transitions to the subbands' ground state (E_0) also contribute to the DPR structures at 1.43 eV, and at 1.47 eV.² It would appear then that highest samples showing the 1.45 eV DPR structures, should have 2DEG concentrations which fill E_0 and provide a relatively empty E_1 for a preponderance of transitions to E_1 . These results appear in keeping with the shape of the DPR for samples shown in Fig. 5, and parallel the results of Shubnikov-de Haas measurements.¹³ However the DPR reflects the room temperature conditions. Both the ground and the first excited state also contribute weakly to the DPR at the band gap energy, thus the band edge signal is not entirely eliminated in the DPR. Actually 2DEG contributions to the DPR begin slightly below the GaAs band gap energy as was pointed out by SGS.⁹

CONCLUSIONS:

The character of the indirectly modulated PR signal from the best HEMT appears to change at large modulation distances. The portion of the 2DEG signal at 1.45 eV persists in some samples for modulations up to ~ 1.5 mm away from the reflectance spot. However the best indirect PR sample did not appear to have the best CR determined mobility. The reason for this discrepancy may come from the fact that indirect PR may be subject to sample structure, internal reflections, and scattering effects. Although one could expect

a relationship between the electron mobility and electron diffusion according to Einstein relation,¹⁴ it is not clear at this time that indirect PR is related to diffusion. Although there are noticeable sample dependent variations in the amplitude and phase of the indirectly modulated PR even at 400 Hz chopper frequency, the large distances involved rule out unaided electron transport. Scattering, and internal reflection are more likely. SUMMARY:

As seen in Fig. 3 the indirect PR appears to accentuate the 2DEG signal at 1.45 eV. Since the 1.45 eV 2DEG signal appears associated our best samples the technique may serve as a room temperature indicator of material quality. The results need further testing and repetition at low temperature

REFERENCES

1. Glembocki O. J., B. V. Shanabrook, N. Bottka, W. T. Beard, and J. Comas. Appl. Phys. Lett. 46, 970 (1985)6 ; SPIE 524, 86 (1985)
2. Sydor M., Ali Badakhshan. J. Appl. Phys. Aug. 8, 1991
3. Pollak Fred H., and H. Shen. Journal of Electronic Materials 19, 399 (1990)
4. Tang Y.S., Y.W. Xu, D.S. Jiang, W.H. Zhuang, and M.Y. Kong, Superlattices and Microstructures, 6, 391, (1989)
5. Sydor M., Neal Jahren, W.C. Mitchel, W.V. Lampert, T.W. Haas, M.Y. Yen, S.M. Mudare, and D.H. Tomich, J. Appl. Phys. 67 (12), 7423, (1990)
6. Pan N., X. L. Zheng, H. Hendriks, and J. Carter J. Appl. Phys 68, 2355 (1990)
7. Wang E. Y., W. A. Albers and C. E. Bleil, in Proc. Intern. Conf. on II-VI Semiconducting Compounds, Providence, 1967, edited by D. G. Thomas (Benjamin, New York 1967), p. 1368.
8. Sydor M. Ali Badakhshan, J.R. Engholm, and D.A. Dale. Appl. Phys. Lett. 58, 948 (1991)
9. Snow E.E., O.J. Glembocki, and B.V. Shanabrook, Phys. Rev. B, 38, 12 484, (1988)
10. Shanabrook B. V., O. J. Glembocki, W. T. Beard. Phys. Rev. B 35, 2540 (1987)
11. Manasreh M. O., D. W. Fischer, K. R. Evans, and C.E. Stutz. Phys. Rev. B 43, 9772 (1991-II)

12. Engholm J. R., M. Sydor, F.Szmulowicz, and T. Vaughan submitted with above manuscript.
13. Ikai Lo, W. C. Mitchel, R. E. Perrin, R. L. Messham, and M.Y. Yen.
Phys. Rev. B 43, 11 787 , (May 1991-1)
14. Christman J. R. Fundamentals of Solid State Physics p 468, John Wiley & Sons New York, 1988

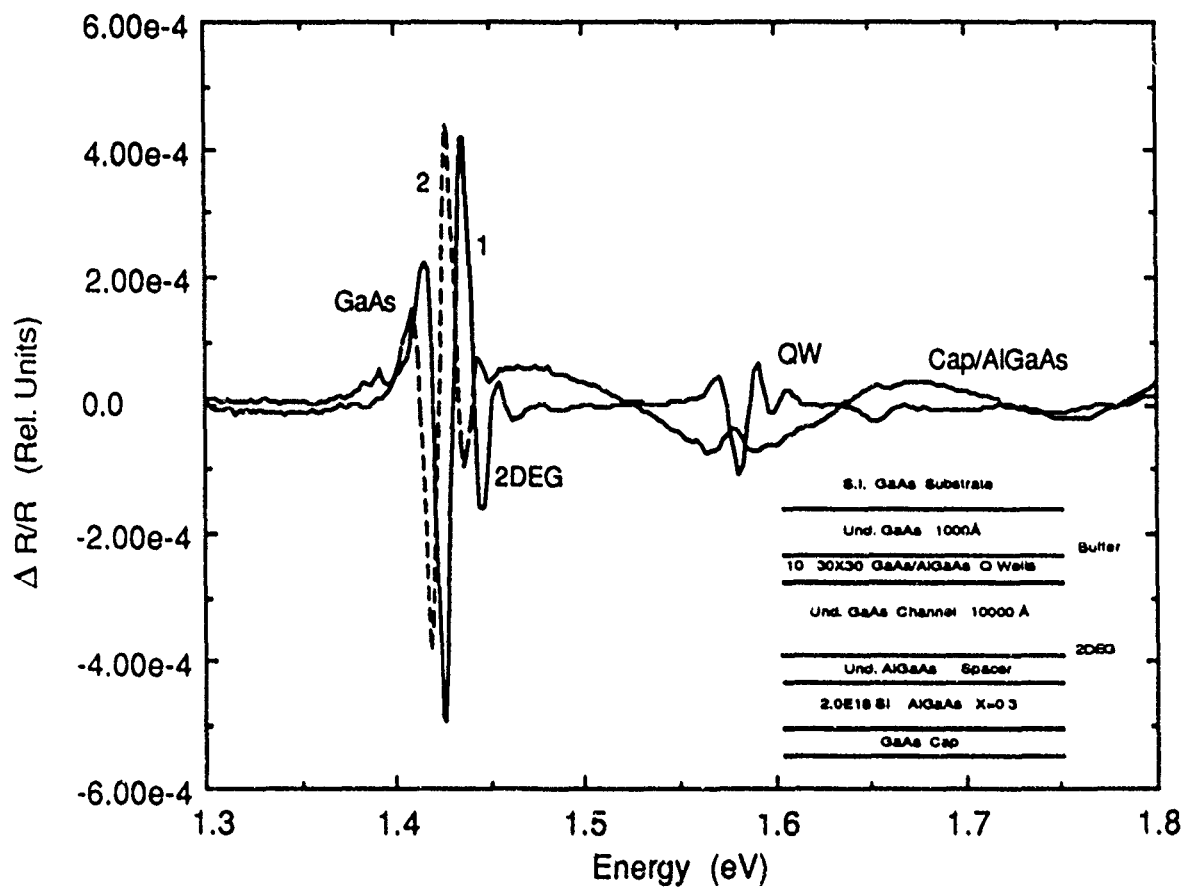


Fig. 1

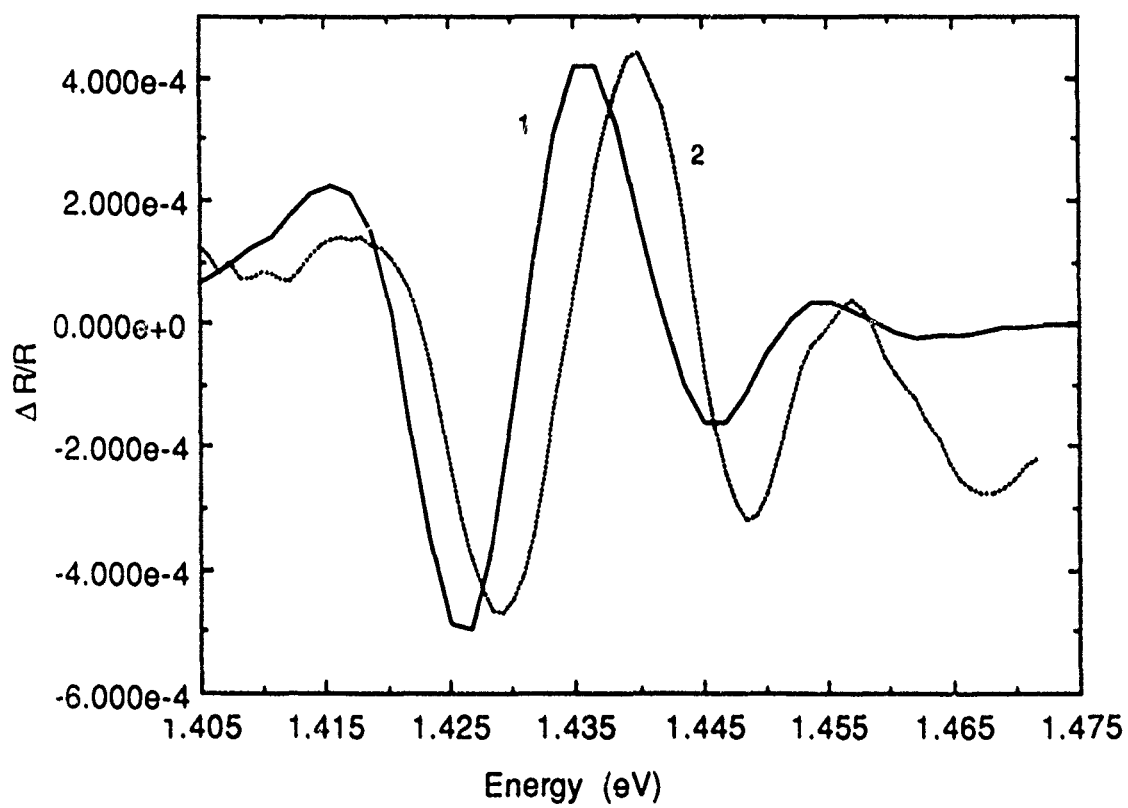


Fig. 2

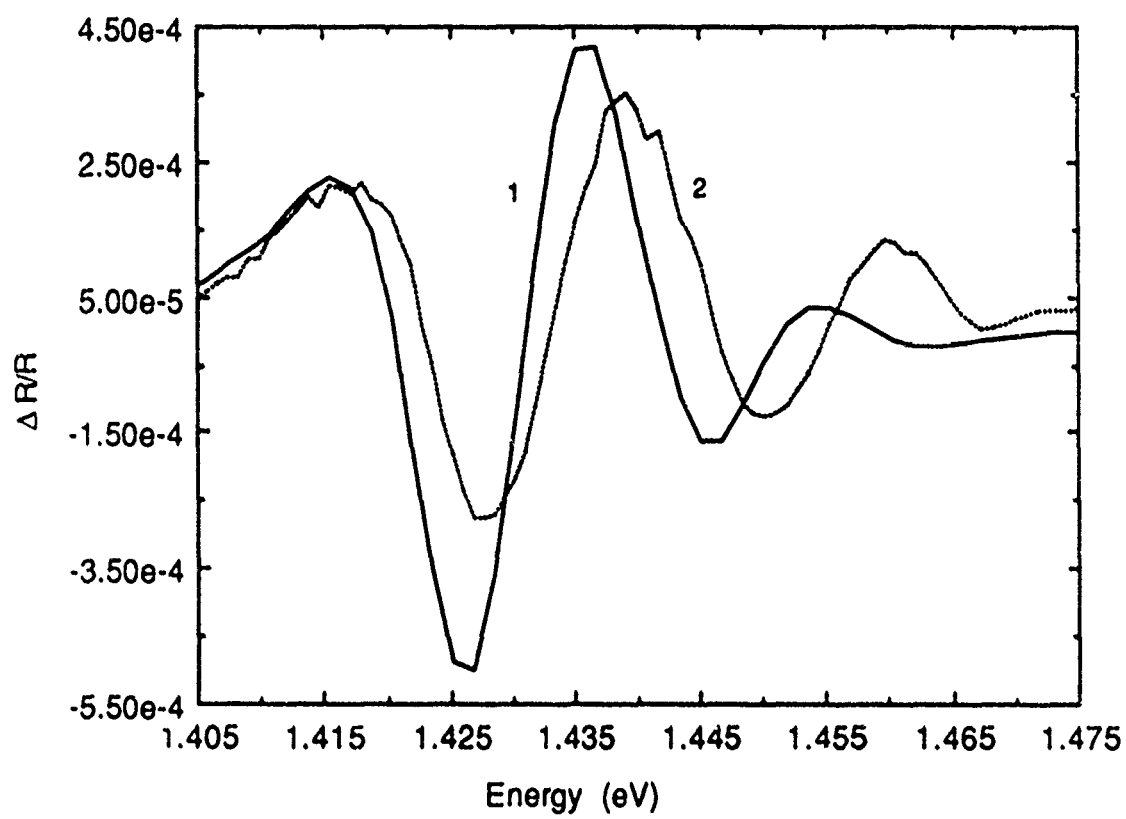
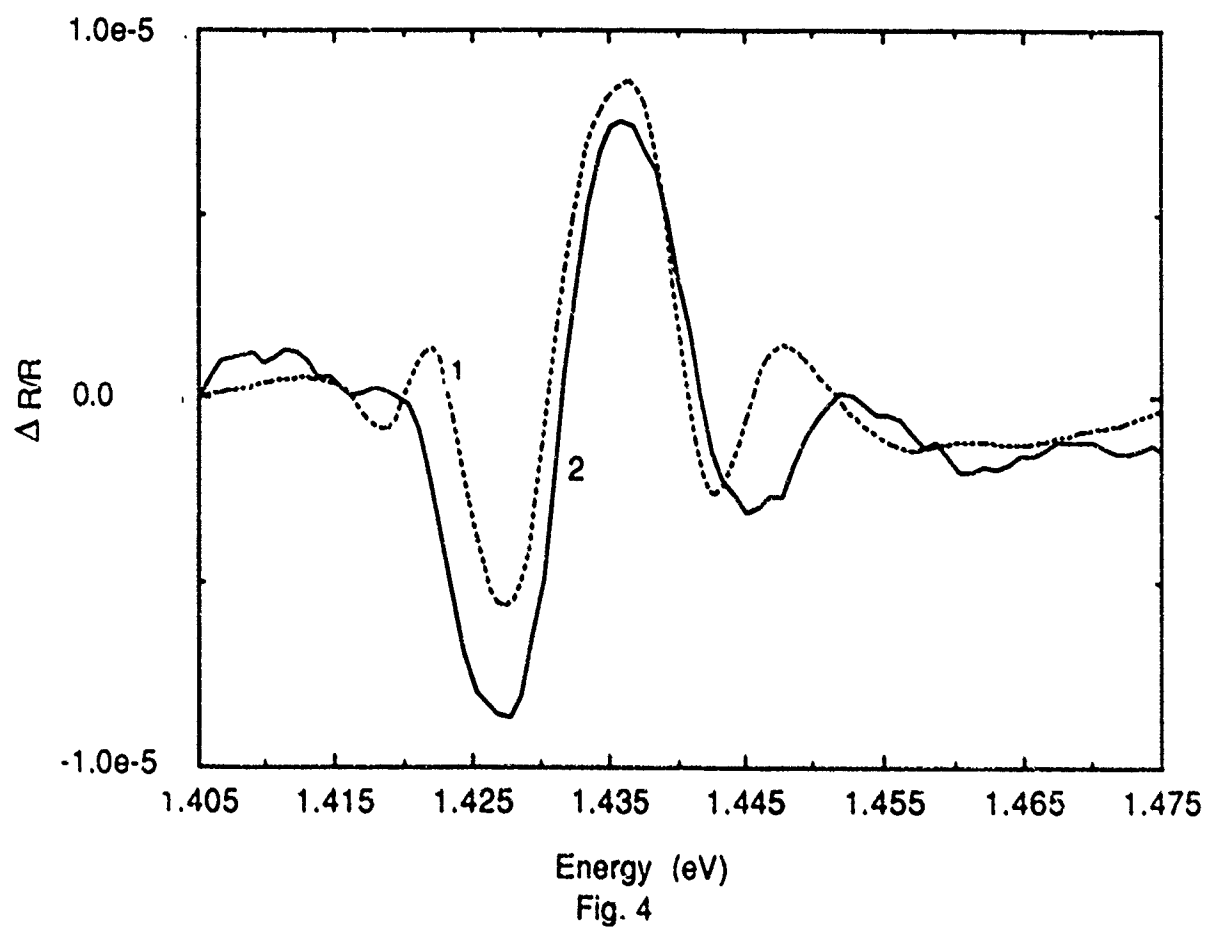


Fig. 3



CREEP BEHAVIOR OF A FINE-GRAINED $\text{Y}_3\text{Al}_5\text{O}_{12}+\text{YAlO}_3$ (18 Vol.%) MATERIAL

Jeff Wolfenstine

Assistant Professor

University of California, Irvine

Department of Mechanical and Aerospace Engineering

Irvine, CA 92717

Abstract

The creep behavior of a fine-grained two-phase $\text{Y}_3\text{Al}_5\text{O}_{12}+\text{YAlO}_3$ (18 vol.%) material prepared from mixed alkoxides powders was investigated in a temperature range between 1600 to 1680°C. It was observed that at strain rates less than 10^{-3} s^{-1} the two-phase material deforms by a Nabarro-Herring diffusional creep mechanism controlled by cation lattice diffusion. In the diffusional creep regime the two-phase material can be deformed to true strains between 40 to 50% without microcracking or void formation. At strain rates above 10^{-3} s^{-1} severe microcracking and void formation occurred which caused the stress exponent to be greater than unity and limited the strain-to-failure.

Introduction

In recent years there has been a recognition of the potential of structural ceramics for use in advanced heat engines (both turbine and reciprocating) and heat exchangers [1]. Compared to metals ceramics have higher operating temperatures, lower density, superior wear resistance and chemical stability. Unfortunately, ceramics also have low fracture toughness, resulting in brittle failure. One method of providing increased fracture toughness is to incorporate the ceramics in composite structures. In order for the ceramic composites to be used at elevated temperature the creep behavior of both the matrix and the fiber must be characterized. One of the most promising matrix materials under

CREEP BEHAVIOR OF A FINE-GRAINED $\text{Y}_3\text{Al}_5\text{O}_{12}+\text{YAlO}_3$ (18 Vol.%) MATERIAL

Jeff Wolfenstine

Assistant Professor

University of California, Irvine

Department of Mechanical and Aerospace Engineering

Irvine, CA 92717

Abstract

The creep behavior of a fine-grained two-phase $\text{Y}_3\text{Al}_5\text{O}_{12}+\text{YAlO}_3$ (18 vol.%) material prepared from mixed alkoxides powders was investigated in a temperature range between 1600 to 1680°C. It was observed that at strain rates less than 10^{-3} s^{-1} the two-phase material deforms by a Nabarro-Herring diffusional creep mechanism controlled by cation lattice diffusion. In the diffusional creep regime the two-phase material can be deformed to true strains between 40 to 50% without microcracking or void formation. At strain rates above 10^{-3} s^{-1} severe microcracking and void formation occurred which caused the stress exponent to be greater than unity and limited the strain-to-failure.

Introduction

In recent years there has been a recognition of the potential of structural ceramics for use in advanced heat engines (both turbine and reciprocating) and heat exchangers [1]. Compared to metals ceramics have higher operating temperatures, lower density, superior wear resistance and chemical stability. Unfortunately, ceramics also have low fracture toughness, resulting in brittle failure. One method of providing increased fracture toughness is to incorporate the ceramics in composite structures. In order for the ceramic composites to be used at elevated temperature the creep behavior of both the matrix and the fiber must be characterized. One of the most promising matrix materials under

consideration for use in oxide/oxide composites at temperatures greater than 1400°C is $\text{Y}_3\text{Al}_5\text{O}_{12}$ (YAG). As a consequence understanding the creep behavior of polycrystalline YAG is of great importance. It is the purpose of this paper to report on the creep behavior of a fine-grained two-phase material consisting of a YAG matrix with about 18 volume percent of a YAlO_3 (YAP) second phase at temperatures between 1600 to 1680°C.

Experimental

(1) Sample Preparation

Powders of a two-phase material consisting of a YAG matrix and about 18 volume percent of a YAP second phase were prepared using a mixed alkoxide method. The resultant hydroxide powders were air dried at room temperature and then calcined at 1000°C for 10 h. The calcined powders were then consolidated by uniaxial hot-pressing in a graphite die lined with graphite at 1640°C with a stress of 7 MPa for 1 to 1.5 h under an argon atmosphere. After hot-pressing the densified material was annealed at 1400°C for 10 h in air. X-ray diffraction after the annealing treatment revealed the presence of only two phases, YAG and YAP. The microstructure of the hot-pressed material is shown in Fig. 1. Figure 1 is a backscattered electron image of the two-phase material. From Fig. 1 several important points are noted. First, the YAP (bright) phase is uniformly distributed throughout the YAG (dark) matrix. Second, the volume fraction of the YAP determined using image analysis and density measurements is about 18%. Third, the dark spots within the YAG matrix are pores. The volume fraction of porosity was determined using a linear intercept method. The density of the samples was about 98% of the theoretical density. Figure 2 is the microstructure of the hot-pressed material after thermal etching at 1600°C for 4 h. Fig. 2 reveals that the material after hot-pressing exhibits a very equiaxed grain structure. The average linear intercept grain size for the sample is about 3.1 μm . From Fig. 2 it is observed that several grains have linear intercept grain sizes of less than 1 μm and a few grains are greater than 5 μm . Backscattered electron images of the etched samples revealed that the YAG matrix had a linear intercept grain of about 2.7 μm while the YAP phase had an linear intercept grain size of approximately 4.2 μm . No YAG grains were greater than 5 μm . Grains less than 1 μm were typically YAG. It can also be seen

from Fig. 2 that the pores are primarily located at grain boundary triple junctions. There is no intragranular porosity.

(2) Deformation Experiments

Deformation samples were prepared by cutting and grinding the hot-pressed material into rectangular parallelepipeds. The ratio of the height to the width of the samples was approximately 2:1 with dimensions of a typical sample being 2 x 2 x 4 mm.

Two types of mechanical tests were used. In the first type of test the samples were deformed under compression at a constant displacement rate. This type of test was used to determine the strain-to-failure as well as to provide an indication of any microstructural changes that occur as a result of the deformation. The second type of test involved compression strain-rate-change tests. These tests were used to determine the flow stress-strain rate relations as well as the strain-rate-sensitivity exponent, n . The mechanical tests were carried out over a temperature range 1600 to 1680°C in a vacuum ($\approx 10^{-4}$ torr) at true strain rates between 10^{-5} to 10^{-2} s $^{-1}$. After the creep experiments the samples were sectioned parallel to the applied stress axis for microstructural examination. The sections were polished and thermally etched at 1600°C for 4 h.

Results and Discussion

The results of the strain-rate-change tests at the various temperatures are shown in Fig. 3. Figure 3 is a plot of logarithm of the strain rate, $\dot{\epsilon}$, versus logarithm of the flow stress, σ . The slope of the curves yields the stress exponent. Also included in Fig. 3 is the result from two constant displacement rate tests. From Fig. 3 it is observed that there is excellent agreement between the two different testing methods used in this study. Either test is valid for determining the flow stress-strain rate relationships. It is also observed from Fig. 3 that two different stress exponent regions are exhibited as a function of the strain rate. At low strain rates ($\dot{\epsilon} < 10^{-3}$ s $^{-1}$) the stress exponent is about equal to unity. In this region diffusional creep is believed to be the dominant deformation mechanism [2-4].

At high values of the strain rate ($\dot{\epsilon} > 10^{-3} \text{ s}^{-1}$) the stress exponent increases to between 5 to 8. In this region the increase in the value of the stress exponent could possibly be associated with the onset of a region where the creep behavior is controlled by intragranular dislocation motion. If indeed the high stress exponent region shown in Fig. 3 is a result of intragranular dislocation motion then, strain rates recorded in this region for the fine-grained two-phase material with a YAG matrix should be very similar to those observed for single crystalline YAG deformed at equivalent temperatures and stresses. A comparison of the creep rates for the two-phase material with a YAG matrix with those for single crystalline YAG revealed that the creep rate of the polycrystalline two-phase material was between 1,000-10,000 times faster than that predicted based on YAG single crystal behavior. A possible explanation for the difference in the creep rates between the polycrystalline sample and single crystalline material may be a result of the added contribution of a boundary deformation mechanism such as grain boundary sliding which can be operative in a polycrystalline sample but can not occur in a single crystal. However, this explanation can not account for the large experimental difference observed in Fig. 3. An other possible reason for the variation in creep rates may be due to differences in aliovalent impurity levels between the polycrystalline and single crystalline samples. A comparison of the impurity concentrations between the polycrystalline and single crystalline samples revealed that such a suggestion was not possible. It is more likely that the increase in the stress exponent observed in Fig. 3 is associated with onset of severe microcracking and void formation. Microstructural examination of samples deformed in the high stress exponent region ($n \approx 5$ to 8) revealed extensive microcracking and void formation along grain boundaries that were parallel to the applied compressive stress direction. In contrast, samples that were deformed in the low stress exponent region ($n \approx 1$) to true strains as large as 40% exhibited almost no microcracking and void formation. These observations suggest that at strain rates above 10^{-3} s^{-1} severe microcracking and void formation occurred which caused the stress exponent to be greater than unity.

The results of the constant displacement rate tests for samples deformed in the low stress region ($n \approx 1$) at the lowest and highest temperatures investigated in this study are shown in

Fig. 4. The data in Fig. 4 are plotted as true stress versus true plastic strain. Figure 4 reveals two important points. First, it can be seen that the fine-grained two-phase YAG and YAP material can be deformed to true strains of at least 40%. Second, the flow stress does not change with strain for the sample deformed at 1600°C. In contrast, the flow stress for the sample deformed at 1680°C increases with strain up to about 20% after, which very little change with strain is observed. The flow stress almost doubles during the first 20% strain. The increase in the flow stress shown in Fig. 4 can be related to microstructural changes that occur during deformation. Microstructural examination of the sample deformed at 1600°C to a true strain of about 40% revealed that grains retain an equiaxed structure with no grain growth. In addition no significant microcracking and void formation was observed. Microstructural analysis of the sample deformed at 1680°C to a true strain of about 40% also revealed that the grains remained equiaxed with no significant microcracking and void formation. However, grain growth had occurred in this sample. The linear intercept grain size after deformation was about 4.2 μm compared to 3.1 μm in the undeformed sample. For diffusional creep mechanism the creep rate varies inversely with grain size [2-4]. Thus, in the case of sample deformed in a diffusional creep regime at a constant creep rate (=constant displacement rate) where grain growth occurs, an increase in the flow stress is expected. However, if the grain size stays constant with strain the flow stress should also remain constant with strain. Such a prediction is in agreement with the results shown in Fig. 4. At 1600°C no grain growth occurred hence, the flow stress does not change with strain. At 1680°C grain growth occurred consequently, an increase in flow stress is observed. The data in Fig. 4 at 1680°C suggests that most of the grain growth occurs during the first 20% strain. After a strain of about 20% the flow stress remains relatively constant suggesting very little grain growth occurs past this stage.

The diffusional creep behavior of the two-phase YAG and YAP material can be controlled by either a Nabarro-Herring creep [2,3] or Coble creep [4] mechanism. Nabarro-Herring creep is controlled by lattice diffusion of the slowest moving ion. The Nabarro-Herring creep rate is given by the following equation [2,3]:

$$\dot{\epsilon} = A_{\text{NH}} \sigma / L^2 \exp(-Q_L/RT) \quad (1)$$

where A_{NH} is constant, L is the linear intercept grain size, Q_L is the activation energy for lattice diffusion of the slowest moving ion, T is the absolute temperature and R is the gas constant. Coble creep is controlled by grain boundary diffusion of the slowest moving ion. The Coble creep rate is given by the following equation [4]:

$$\dot{\epsilon} = A_C \sigma / L^3 \exp(-Q_{GB}/RT) \quad (2)$$

where A_C is constant and Q_{GB} is the activation energy for grain boundary diffusion of the slowest moving ion. The major difference between the Nabarro-Herring and Coble creep mechanisms is in the dependence of the creep rate on grain size and temperature. Thus, it is possible to decide whether the diffusional creep of the two-phase YAG and YAP material is controlled by either a Nabarro-Herring or Coble creep mechanism by comparing the experimental dependence of the creep rate on grain size and temperature to the theoretical predictions given in Equations 1 and 2.

From the data shown in Fig. 4 and knowing the final grain size and assuming that all the hardening observed in Fig. 4 at 1680°C is a result of grain growth it can be shown that the creep rate of the two-phase YAG and YAP material is inversely proportional to the grain size raised to the -2.2 power ($\dot{\epsilon} \propto 1/L^{2.2}$). A comparison of this result to Equations 2 and 3 suggests that the deformation behavior of the two-phase YAG and YAP material is controlled a Nabarro-Herring diffusional creep mechanism. For the case of the two-phase YAG and YAP material where YAG is the matrix phase the Nabarro-Herring creep rate of the material is likely controlled by lattice diffusion of either yttrium or aluminum or oxygen in the YAG phase. A comparison of the activation energy for creep to the activation energies for lattice self-diffusion of yttrium and aluminum and oxygen in YAG can be used to determine which one of the three ions is the rate-controlling ion in the two-phase YAG and YAP material. The activation energy for creep for the two-phase YAG and YAP material can be determined from a plot of logarithm strain rate versus inverse temperature at a fixed value of the stress and grain size. Figure 5 is such a plot for the two-phase YAG and YAP material at stress equal to 18 MPa ($n \approx 1$) and a grain size equal to 3.1 μm . The activation energy for creep of the two-phase YAG and YAP material is about equal to 580 kJ/mole. No data is available for lattice diffusion of either cation (Al or Y) in YAG.

However, data is available for oxygen lattice diffusion in YAG. The activation energy for lattice diffusion of oxygen in single crystalline YAG is about 325 kJ/mole [5]. The predicted Nabarro-Herring creep rate (Equation 1) using a value of 325 kJ/mole for the activation energy for oxygen lattice diffusion yields predicted creep rates that are 10 to 100 times faster than the experimentally observed creep rates. As a result of the large difference between the theoretical and experimental creep rates and activation energy for creep compared to the activation energy for oxygen lattice diffusion it is unlikely that the creep rate of the two-phase YAG and YAP material is controlled by oxygen lattice diffusion. Thus, it is more likely that the diffusional creep rate of the two-phase YAG and YAP material is controlled by cation lattice diffusion. However, based on the currently available diffusion data it is impossible to determine whether yttrium or aluminum is the rate-controlling ion.

Conclusions

1. A dense fine-grained ($L \approx 3 \mu\text{m}$) two-phase $\text{Y}_3\text{Al}_5\text{O}_{12} + \text{YAlO}_3$ (18 vol.%) material can be prepared from mixed alkoxides powders.
2. At strain rates less than 10^{-3} s^{-1} in the temperature range between 1600 to 1680°C the two-phase YAG and YAP material deforms by a Nabarro-Herring diffusional creep mechanism controlled by cation lattice diffusion. The activation energy for creep for the two-phase material is about equal to 580 kJ/mole.
3. In the diffusional creep regime the two-phase YAG and YAP material can be deformed to true strains between 40 to 50% without microcracking or void formation.
4. At strain rates above 10^{-3} s^{-1} severe microcracking and void formation occurs which causes the stress exponent to be greater than unity and reduces the strain-to-failure.

Acknowledgements

The author would like to thank Doug Barlage and Dr. T. A. Parthasarathy for their help and suggestions.

References

1. G. S. Corman, "Creep of Oxide Single Crystals", Final Technical Report, WRDC-TR-4059, 1990.
2. F. R. N. Nabarro, "Deformation of Crystals by the Motion of Single Ions"; pp. 75-90 in Report of Conference on Strength of Solids, Vol. 75. Physical Society of London, England, 1948.
3. C. Herring, "Diffusional Viscosity of a Polycrystalline Solid," J. Appl. Phys., 21, 437-445 (1950).
4. R. L. Coble, "A Model for Boundary Diffusion Controlled Creep in Polycrystalline Materials," J. Appl. Phys., 34 [6], 1679-1682 (1963).
5. H. Haneda, Y. Miyazawa, and S. Shiraski, "Oxygen Diffusion In Single Crystal Yttrium Aluminum Garnet," J. Crystal Growth, 68, 581-588 (1984).

List of Figures

Fig. 1. Backscattered electron image of the two-phase $\text{Y}_3\text{Al}_5\text{O}_{12}+\text{YAlO}_3$ (18 vol.%) material after hot-pressing. The bright phase is YAlO_3 .

Fig. 2. An SEM micrograph of the etched two-phase $\text{Y}_3\text{Al}_5\text{O}_{12}+\text{YAlO}_3$ (18 vol.%) material prior to deformation.

Fig. 3. Steady-state strain rate versus flow stress for the $\text{Y}_3\text{Al}_5\text{O}_{12}+\text{YAlO}_3$ (18 vol.%) material at several temperatures.

Fig. 4. True stress versus true strain curves for the $\text{Y}_3\text{Al}_5\text{O}_{12}+\text{YAlO}_3$ (18 vol.%) material deformed in the diffusional creep regime at 1680°C and 1600°C.

Fig. 5. Steady-state strain rate versus inverse temperature for the $\text{Y}_3\text{Al}_5\text{O}_{12}+\text{YAlO}_3$ (18 vol.%) material.

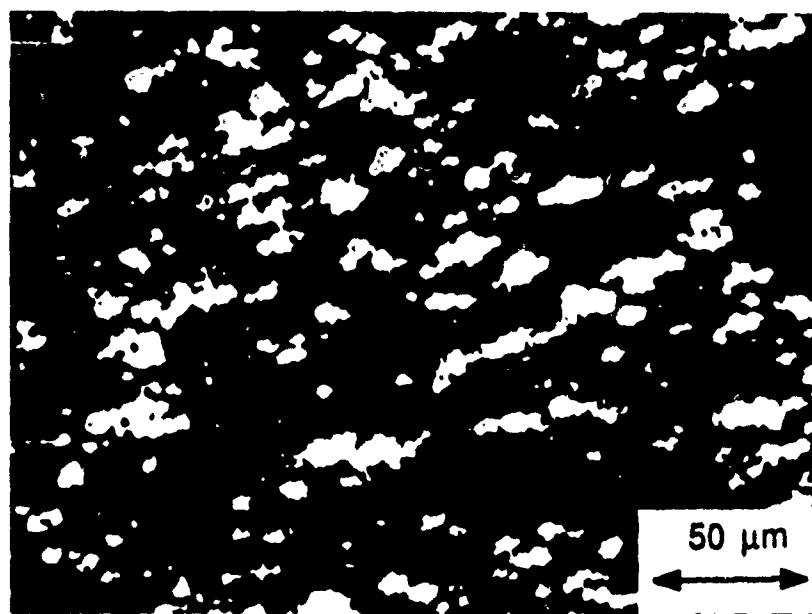


Fig. 1. Backscattered electron image of the two-phase $\text{Y}_3\text{Al}_5\text{O}_{12} + \text{YAlO}_3$ (18 vol.%) material after hot-pressing. The bright phase is YAlO_3 .

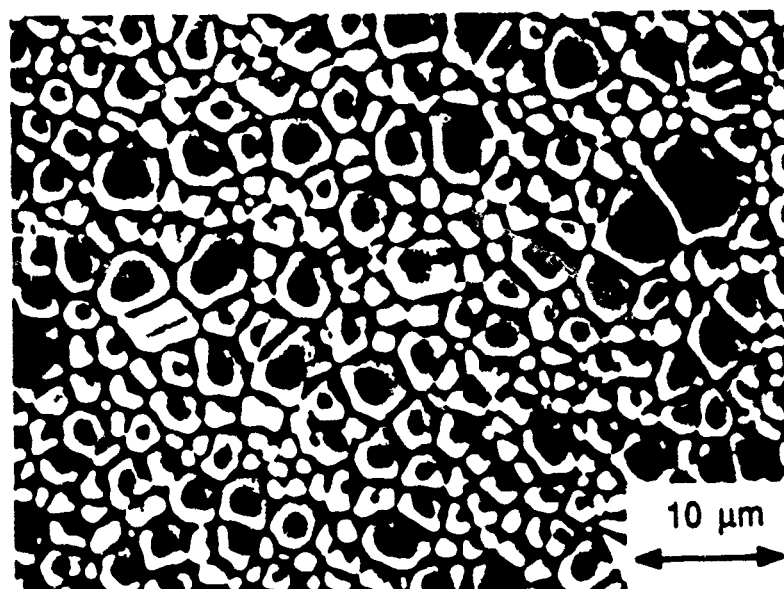


Fig. 2. An SEM micrograph of the etched two-phase $Y_3Al_5O_{12}+YAlO_3$ (18 vol.%) material prior to deformation.

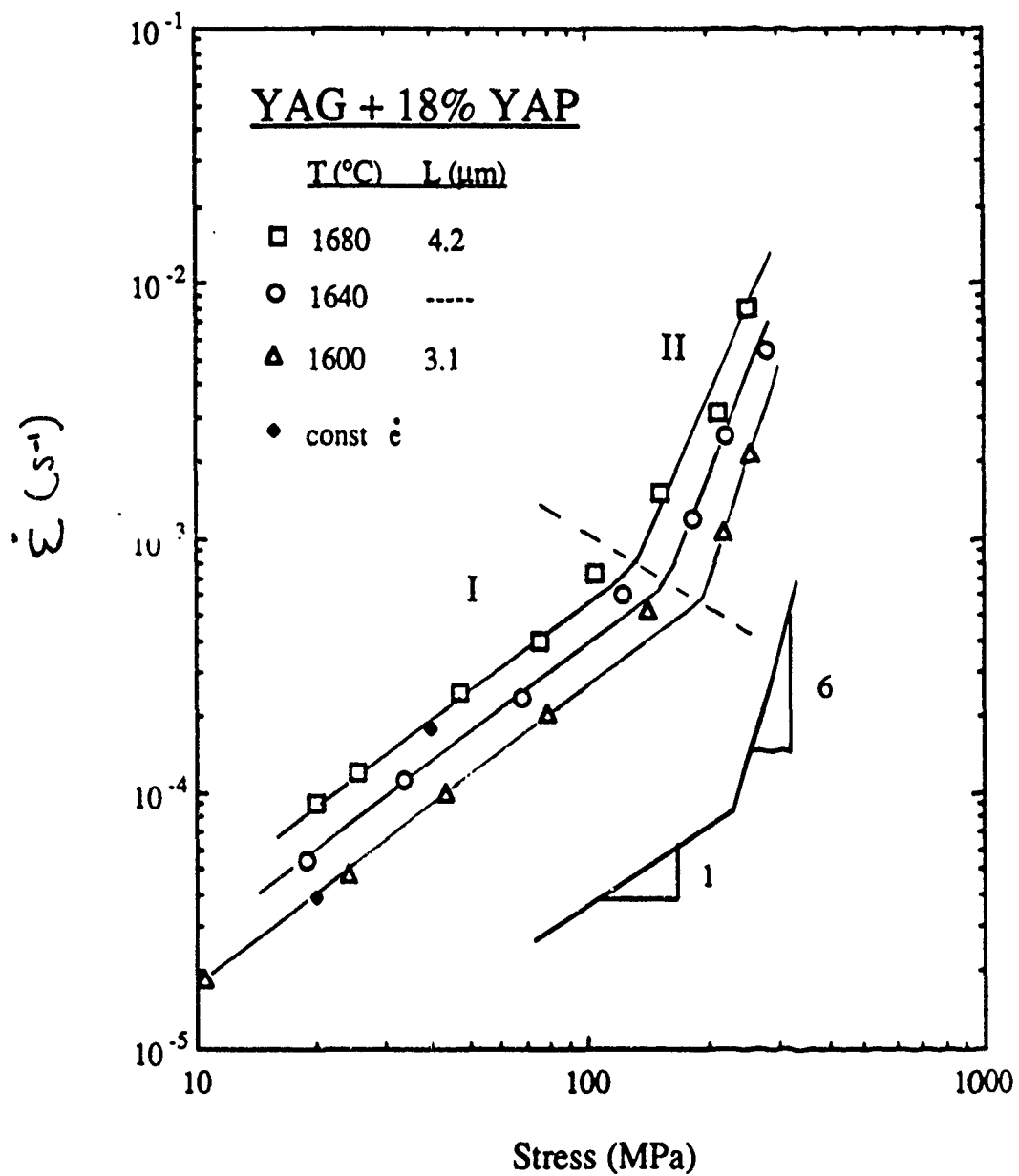


Fig. 3. Steady-state strain rate versus flow stress for the $Y_3Al_5O_{12} + YAlO_3$ (18 vol.%) material at several temperatures.

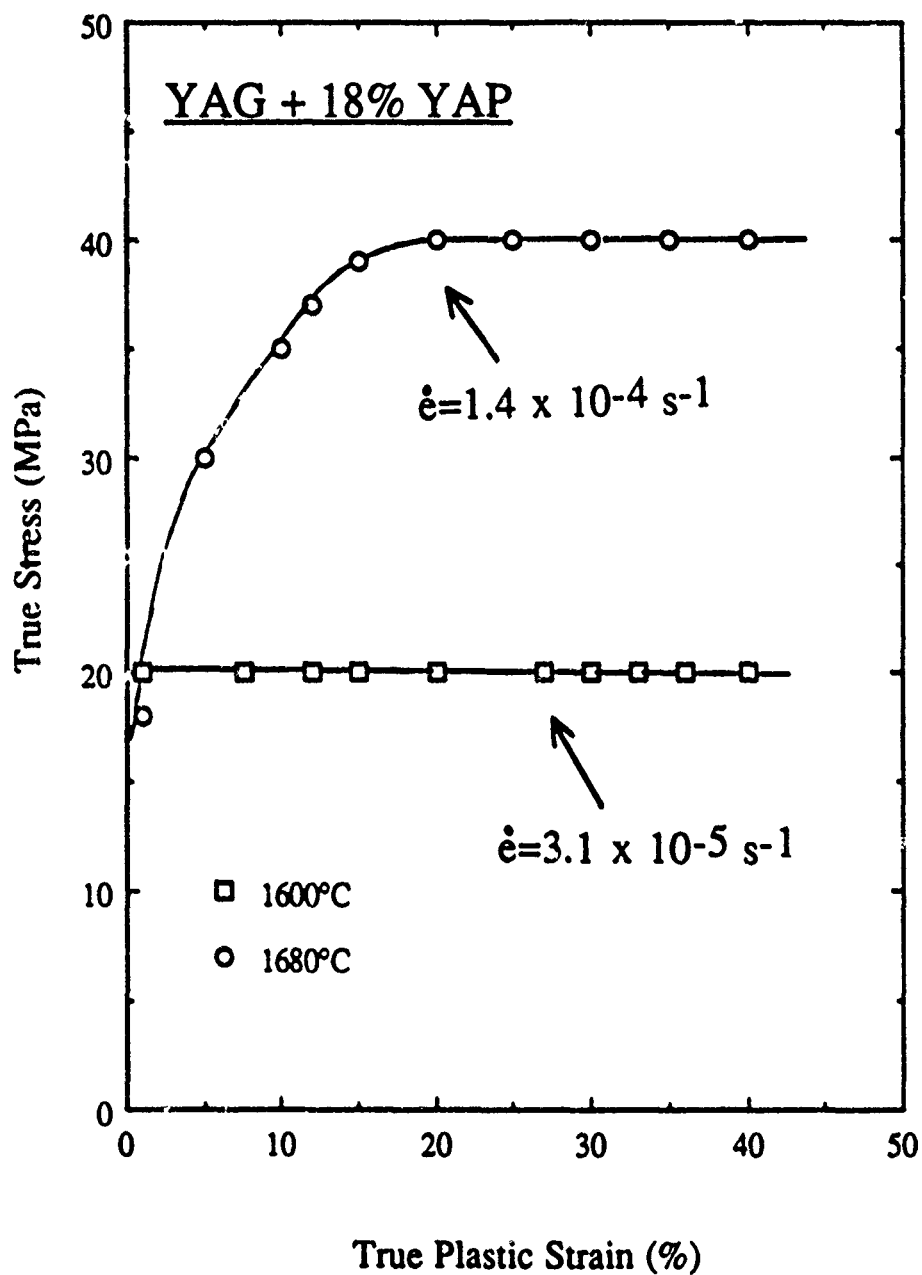


Fig. 4. True stress versus true strain curves for the $\text{Y}_3\text{Al}_5\text{O}_{12} + \text{YAlO}_3$ (18 vol.%) material deformed in the diffusional creep regime at 1680°C and 1600°C.

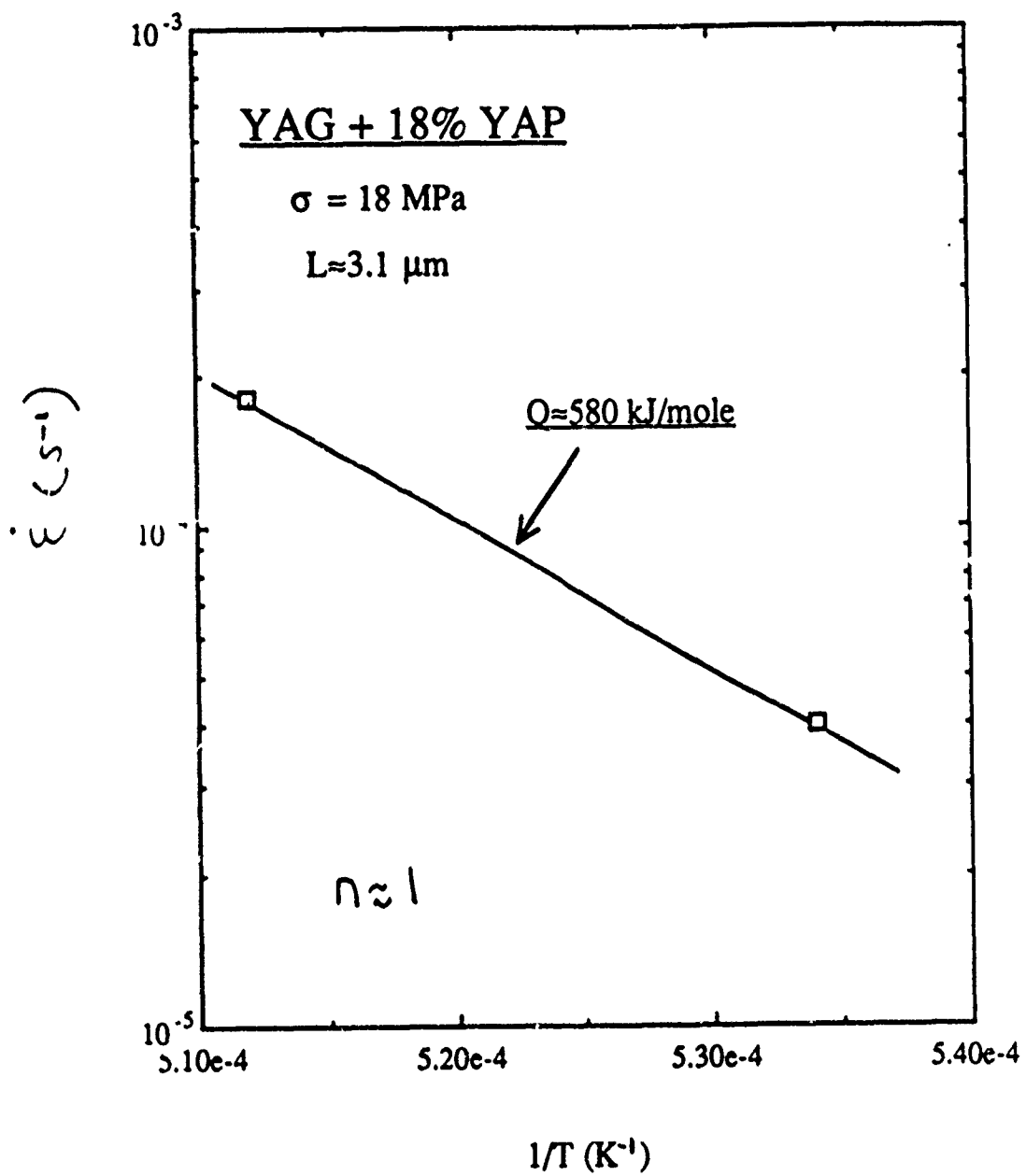


Fig. 5. Steady-state strain rate versus inverse temperature for the $\text{Y}_3\text{Al}_5\text{O}_{12} + \text{YAlO}_3$ (18 vol.%) material.

**ELASTIC MODULI OF FIBER REINFORCED BRITTLE MATRIX
COMPOSITES WITH INTERFACIAL DEBONDING**

FINAL REPORT

Prepared by

**Fuh-Gwo Yuan
Assistant Professor
Department of Mechanical and Aerospace Engineering
North Carolina State University**

For

**The Air Force Office of Scientific Research (AFOSR)
Summer Research Program**

August 1991

ELASTIC MODULI OF FIBER REINFORCED BRITTLE MATRIX COMPOSITES WITH INTERFACIAL DEBONDING

Fuh-Gwo Yuan
Assistant Professor
Department of Mechanical and Aerospace Engineering
North Carolina State University

ABSTRACT

A theoretical analysis using finite element methods has been applied to fiber reinforced brittle matrix composites in order to predict the influence of the debonded interface on "effective" elastic moduli of the composites. Two types of geometry layout of the composites (a) composite cylinder model, (b) periodic square array model are considered in the analysis. The prescribed displacement boundary conditions and constraints equations are imposed for different deformation modes in order to maintain the geometric compatibility between neighboring RVE. The results show that the elastic constants obtained from composite cylinder model give much less degree of the unsymmetry than those of periodic square array model. Furthermore, some discrepancies about transverse moduli prevail between finite element analyses and the approximate model proposed by Pagano and Tandon(1990).

1. INTRODUCTION

The mechanical properties of fiber-reinforced composites are significantly affected by the bond between the various constituents materials at the microscale level, such as the interface between fiber-interphase or interface-matrix. In polymer matrix composites, the composite systems consist of brittle fibers such as graphite and boron in a relatively soft matrix materials such as epoxy, a strong fiber/matrix bond is desired. However, in certain

brittle matrix composites, the constituents are both brittle in nature, the fibers are loosely bonded to the matrix. Although this loose bond is detrimental to compressive and transverse strength properties, it is believed to be the most important source of enhancing strength and fracture toughness in these composite systems. Recent experimental studies; Prewo et. al.(1980), Rice(1981), Grande et. al.(1988), on brittle matrix composites have also shown that the nature and degree of bonding between the fiber and the matrix dominant their mechanical properties and associated failure modes. In order to achieve optimal performance between strength and stiffness for composite development, the effect of weak bond or debonded interface condition on the mechanical properties of composite materials needs to be fully understood.

The prediction of the overall mechanical properties of composite materials can be approached in many ways. Perhaps the most acceptable approach for many engineering applications is based on a theory which replaces the actual heterogeneous medium by an equivalent but anisotropically homogeneous continuum if the scale of the deformation is sufficiently larger than the characteristic length of the microstructure. By further assuming the periodicity of the microstructure, the effective elastic moduli of the composite are determined by the elastic properties of the constituents and internal geometry of the representative volume element (R V E). Since the early 1960's many analytical and numerical studies have been carried out on the determination of the elastic properties of composite materials with perfect bonded interface. In general, concentric cylinders, square array, hexagonal array are assumed for mathematical models. Hashin and Rosen(1964) provided the lower and upper bounds of elastic moduli based on variational principles. Semi-analytical approaches has been treated by Chen and Cheng(1967), Chen(1970, 1971) to evaluate elastic moduli of the composite. Fourier method and least square method have been utilized to match the continuity of the interface. Application of finite difference and

finite element method to this class of the problem has been made by Adams and Doner(1967a,b) and Foye(1966), While closed form solutions such as the composite cylinder assemblage (CGA) model or generalized self-consistent scheme (GSCS) have been made by Hashin and Rosen(1964) and Christensen and Lo(1979).

The effect of weak bond or debonded interface on the mechanical properties has been recently studied by several investigators. Some simplified models have been proposed to simulate the imperfect interface condition. Pagano and Tandon(1990) developed an approximate model by assuming various interfacial condition with different values in an fictitious coating region. Several definitions of composite strain were used in the determination of effective moduli. They also showed the effective stiffness constants become unsymmetric under certain interfacial conditions. Benveniste (1984,1985) simulated the interface by imposing the continuity of normal displacements and tractions at the interface while allowing a jump in the tangential displacement. Takahashi and Chou(1988) used Eshelby's equivalent inclusion method in conjunction with the Mori-Tanaka theorem to predict transverse moduli of the perfect and complete debonding of the composite. Zashin(1990) simulated the interface condition by linear relations between interface tractions and displacement jumps and used GSCS model to predict the effective moduli of the composite. Shimansky et. al. (1989) used a finite element method to predict transverse moduli of the debonded interface in a ceramic matrix composite.

In this report, R V E model of concentric cylinder and periodic square arrays are discretized and analysed by the finite element method. The boundary conditions and constraint equations are imposed to maintain geometric compatibility inherent to the periodic configuration. The debonded interface is assumed to be completely separated. The model has been devised to study specific fiber/matrix debonded conditions and to determine the dependence of effective moduli on the degree of the debonding.

2. FORMULATION OF THE PROBLEM

Consider a two phase macroscopically homogeneous elastic composite, whose each phase is linearly elastic and isotropic. Let a large composite specimen of volume V and surface S , be subjected to the homogeneous boundary conditions

$$u_i(S) = \epsilon_{ij}^0 x_j \quad (i, j = 1, 2, 3)$$

In the case of perfect interface conditions, ϵ_{ij}^0 are the volume average strain, $\bar{\epsilon}_{ij}$, in the composite. However, in the case of debonding on the interface where the interface displacement continuity is not satisfied, the average strain theorem gives

$$\epsilon_{ij}^0 = \bar{\epsilon}_{ij} + \frac{1}{2V} \int_{S_{12}} ([u_i]n_j + [u_j]n_i) ds$$

It follows from the linear theory of elasticity that the average stresses are linearly related to the average strains by

$$\bar{\sigma}_{ij} = C_{ijkl}^* \epsilon_{kl}^0$$

where C_{ijkl}^* are defined as the effective elastic moduli.

Suppose that the composite is macroscopically orthotropic. Then the effective constitutive relations must be macroscopically orthotropic and therefore has the form

$$\bar{\sigma}_x = C_{11}^* \bar{\epsilon}_x + C_{12}^* \bar{\epsilon}_y + C_{13}^* \bar{\epsilon}_z$$

$$\bar{\sigma}_y = C_{21}^* \bar{\epsilon}_x + C_{22}^* \bar{\epsilon}_y + C_{23}^* \bar{\epsilon}_z$$

$$\bar{\sigma}_z = C_{31}^* \bar{\epsilon}_x + C_{32}^* \bar{\epsilon}_y + C_{33}^* \bar{\epsilon}_z$$

$$\bar{\tau}_{yz} = C_{44}^* \bar{\gamma}_{yz}$$

$$\bar{\tau}_{xz} = C_{55}^* \bar{\gamma}_{xz}$$

$$\bar{\tau}_{xy} = C_{66}^* \bar{\gamma}_{xy}$$

For purpose of analysis one considers two models which have been often used in analyzing the material properties of fiber composites.

2.1 Concentric Cylinder Model

A. Determination of C_{ij}^* ($i, j = 1, 2, 3$)

The concentric cylinder representative element of unidirectional composites under the applied displacement boundary conditions is given by

$$u_i(\mathbf{S}) = \epsilon_{ij}^0 x_j \quad (i, j = 1, 2, 3)$$

where displacements in ϵ_{ij}^0 are constants. Due to the geometrical symmetry, only one quadrant of the R V E. is needed to model the deformation. The boundary conditions along the symmetry axes are

$$u_1 = 0, \text{ along } x_1 = 0$$

$$u_2 = 0, \text{ along } x_2 = 0$$

There are three deformation states which are required to obtain these elastic constants. The deformation states ($I = 1, 2$) are plane strain states with strain components $\epsilon_z = 0$, whereas the deformation state ($I = 3$) corresponds to generalized plane strain conditions with $\epsilon_z = 1$ and $u_1(\mathbf{S}) = u_2(\mathbf{S}) = 0$. The associated stress and strain components are independent of x_3 . After solving the problem by the finite element method, the average

stresses ($\bar{\sigma}_x, \bar{\sigma}_y$) are determined by calculating the stresses along the boundary of the cylinder, whereas the average stress $\bar{\sigma}_z$ is calculated over the cross section of the representative element.

B. Determination of C_{66}^*

The transverse shear modulus $C_{66}^* = G_{12}$ may be obtained from the following displacement boundary conditions on the outer surface of the cylinder:

$$u_1(S) = \epsilon_{12}^0 x_2, \quad u_2(S) = \epsilon_{12}^0 x_1, \quad u_3(S) = 0.$$

From antisymmetric conditions, the boundary conditions on the two sides of the first quadrant of the fundamental region are:

$$u_2 = 0, \text{ along } x_1 = 0$$

$$u_1 = 0, \text{ along } x_2 = 0$$

The average stress $\bar{\tau}_{xy}$ is calculated from the following relation:

$$\bar{\tau}_{xy} = \frac{4}{\pi} \int_0^{\frac{\pi}{2}} (\sigma_x \sin \theta \cos \theta + \tau_{xy} \sin^2 \theta) d\theta$$

C. Determination of C_{44}^*, C_{55}^*

The boundary value problem of determining longitudinal shear moduli C_{44}^* and C_{55}^* is associated with the following displacement field:

$$u_1 = u_2 = 0, \quad w = w(x_1, x_2)$$

The equilibrium equation for w is given by the Laplace equation.

$$\nabla^2 w = 0 \quad \nabla^2 = \frac{\partial^2}{\partial x_1^2} + \frac{\partial^2}{\partial x_2^2}$$

In order to solve the modulus C_{55}^* , the displacement along the outer surface of the cylinder is of the form:

$$w(S) = \epsilon_{31}^0 x_1$$

From symmetric conditions, the boundary conditions are written as

$$\frac{\partial w}{\partial x_2} = 0 \quad \text{along } x_2 = 0$$

$$w = 0 \quad \text{along } x_1 = 0$$

The average stress $\bar{\tau}_{xz}$ is calculated from the following relation:

$$\bar{\tau}_{xz} = \frac{4}{\pi} \int_0^{\frac{\pi}{2}} (\tau_{xz} \cos^2 \theta + \tau_{yz} \sin \theta \cos \theta) d\theta$$

Similar procedure can be applied to obtain the modulus C_{44}^* with specified displacement $w(S) = \epsilon_{32}^0 x_2$ and boundary conditions $\frac{\partial w}{\partial x_1} = 0$ along $x_1 = 0$, and $w = 0$ along $x_2 = 0$.

2.2 Square Array Model

A. Determination of C_{ij}^* ($i = 1, 2, 3$)

As with the R V E of square array in Fig. 1.b, the boundary must deform in such a pattern that the repeating elements match without generating cracks or penetrations. It is required, under normal loadings, that the boundary of the R V E. remain straight and parallel to each other. Boundary displacements associated with three deformation states for the quarter of the R V E. are listed as follows:

$$(I) \quad u_1(S) = \epsilon_{11}^0 x_1$$

$$u_2(S) = 0$$

$$u_3(S) = 0$$

$$(II) \quad u_2(S) = \epsilon_{22}^0 x_2$$

$$u_1(S) = 0$$

$$u_3(S) = 0$$

$$(III) \quad u_3(S) = \epsilon_{33}^0 x_3$$

$$u_1(S) = 0$$

$$u_2(S) = 0$$

B. Determination of C_{66}^*

The displacement boundary conditions for the R.V.E. under transverse shear loading is unlikely to be determined beforehand. Linear constraint equations for the R V E are then used to insure that the deformed repeating element maintains in a periodic manner,

$$u_1(x_1, a) = u_1(x_1, -a) + 2a \epsilon_{12}^0$$

$$u_2(a, x_2) = u_2(-a, x_2) + 2a \epsilon_{12}^0$$

$$u_1(a, x_2) = u_1(-a, x_2)$$

$$u_2(x_1, a) = u_2(x_1, -a)$$

C. Determination of C_{44}^* , C_{55}^*

The longitudinal shear moduli may be determined by applying the following linear constraint equations along the boundary of the R V E.

$$w(x_1, a) = w(x_1, -a) + 2a \epsilon_{31}^0$$

$$w(a, x_2) = w(-a, x_2) + 2a \epsilon_{31}^0$$

for C_{55} and

$$w(x_1, a) = w(x_1, -a) + 2a \epsilon_{32}^0$$

$$w(a, x_2) = w(-a, x_2)$$

for C_{44} .

3. RESULTS AND DISCUSSIONS

The COSMOS finite element package is selected to generate the RVE of concentric cylinder model and periodic square model shown in Fig.1. Displacement boundary conditions and constraint equations associated six different deformation modes are imposed to obtain the composite effective moduli. The fiber is perfectly bonded to the matrix except

over the interface region $|\theta| \leq \theta^*$ and $|\pi - \theta| \leq \theta^*$. The debonded interface is assumed to be completely separated without slippage. The volume fraction of the model is taken to be 0.4 and the fiber and matrix material properties are listed as follows:

Material	E(GPa)	G(GPa)
Nicalon	200.0	77.0
1723 Glass	88.0	36.0

After the stiffness coefficients are obtained, the effective engineering constants are calculated by

$$E_{33} = C_{33}^* - \frac{2C_{31}^*C_{13}^*}{C_{11}^* + C_{12}^*},$$

$$\nu_{31} = \frac{C_{13}^*}{C_{11}^* + C_{12}^*}$$

$$K_{12} = \frac{1}{2}(C_{11}^* + C_{12}^*),$$

$$G_{31}^* = C_{55}^*$$

$$E_{11} = C_{11}^* + \frac{\{C_{31}^*C_{13}^*(-C_{11}^* + C_{12}^*) + C_{12}^*(-C_{33}^*C_{12}^* + C_{31}^*C_{13}^*)\}}{C_{33}^*C_{11}^* - C_{31}^*C_{13}^*}$$

For the concentric cylinder model, Fig.2 illustrates the effect of debonding on ten effective stiffness const C_{ij}^* (except longitudinal shear constants C_{44}^*, C_{55}^*). In the extreme cases of perfect bonding and totally debonding, the numerical results coincide with the exact solution obtained by Hashin (1964). In contrast to the approximate model developed by Pagano and Tandon (1990), An insignificant unsymmetric effective stiffness constants are exhibited. Fig.3 depicts the five engineering constants $E_{33}, \nu_{31}, E_{11}, G_{12}$, and K_{12} with different degree of debonding. The effective axial modulus has a little effect

on the debonded interface conditions. However, the debonded interface may have significant effect on transverse Young's moduli, Transverse shear moduli, longitudinal Poisson's ratio, and plane strain bulk moduli. For periodic square model. Fig. 4 shows the effect of debonding on eight effective stiffness constants. The unsymmetric nature of the effective constants are observed in the figure.

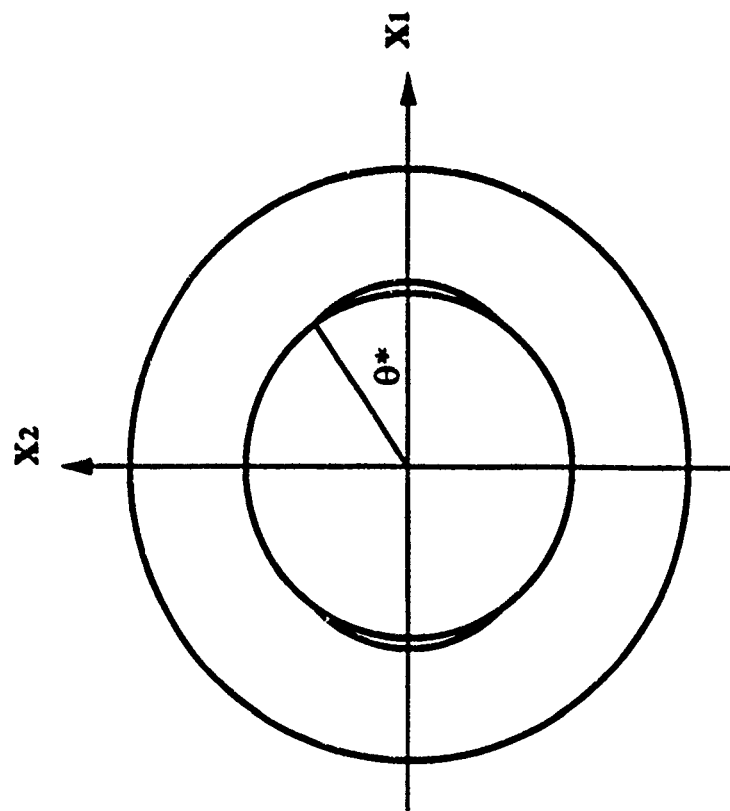
4. Acknowledgements

The research was supported by the Air Force Office of Scientific Research (AFOSR) Summer Research Program. The author is grateful to Dr. N. J. Pagano and Dr. J. Whitney of Nonmetallic Laboratory at Wright-Patterson AFB for their guidance and encouragement.

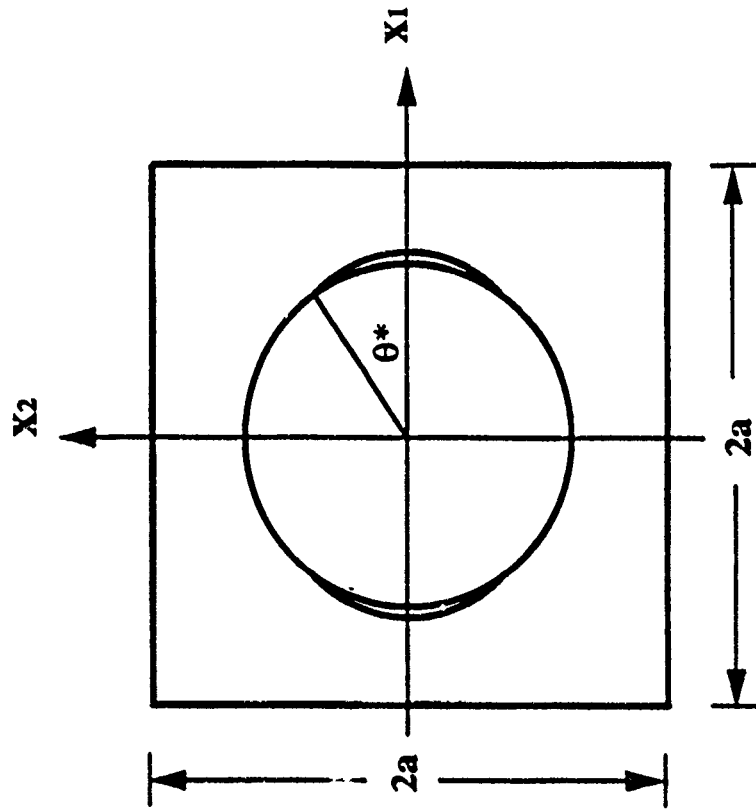
5. REFERENCES

1. Z. Hashin and B. W. Rosen, "The Elastic Moduli of Fiber Reinforced Materials," *ASME Journal of Applied Mechanics*, Vol.31, pp. 223-232, 1964.
2. R. L. Foye, "An Evaluation of Various Engineering Estimates of the Transverse Properties of Unidirectional Composites", *Proceedings of the 10th National Symposium - Advanced Fibrous Reinforced Composites*, San Diego, pp. C31-42, Nov. 9-11, 1966.
3. D. F. Adams and D. R. Doner, "Longitudinal Shear Loading of a Unidirectional Composite", *Journal of Composite Materials*, Vol. 1, pp. 4-17, 1967.
4. D. F. Adams and D. R. Doner, "Transverse Normal Loading of a Unidirectional Composite", *Journal of Composite Materials*, Vol. 1, pp. 152-164, 1967.
5. C. H. Chen and S. Cheng, "Mechanical Properties of Fiber Reinforced Composites," *Journal of Composite Materials*, Vol. 1, pp. 30-40, 1967.
6. C. H. Chen, "Fiber-Reinforced Composites under Longitudinal Shear Loading", *ASME Journal of Applied Mechanics*, Vol. 37, pp. 198-201, 1970.
7. C. H. Chen, "Rectangular or Square Array Fibrous Composite with Anisotropic or Isotropic Filament," *ASME Journal of Applied Mechanics*, Vol. 38, 710-712, 1971.

8. R. M. Christensen and K. M. Lo, "Solutions for Effective Shear Properties of Three-Phase Sphere and Cylinders", *Journal of the Mechanics and Physics of Solids*, Vol.37, pp.315-330, 1979.
9. K. M. Prewo and J. J. Brennan, "High-Strength Silicon Carbide Fiber-Reinforced Glass Matrix Composites", *Journal of Materials Science*, Vol.15, No.2, pp.463-468, 1980.
10. R. W. Rice, "Mechanisms of Toughening in Ceramic Matrix Composites", *Ceramic Engineering and Science Proceedings*, Vol.2, pp.661-701, 1981.
11. Y. Benveniste, "On the Effect of Debonding on the Overall Behavior of Composite Materials," *Mechanics of Materials*, Vol. 3, pp. 349-358, 1984.
12. Y. Benveniste, "The Effective Mechanical Behavior of Composite Materials with Imperfect Contact between the Constituents," *Mechanics of Materials*, Vol. 4, pp. 197-208, 1985.
13. G. P. Tandon and N. J. Pagano, "A Study of Fiber-matrix Interfacial Modeling," *Proceedings of 4th Japan-U.S. Conference on Composite Materials*, Technomic Publishing Co. Inc., pp. 191-200, 1988.
14. K. Takahashi and T.-W. Chou, "Transverse Elastic Moduli of Unidirectional Fiber Composites with Interfacial Debonding," *Metallurgical Transactions A*, Vol. 19A, pp. 129-135, 1988.
15. D. H. Grande, J. F. Mandell and K. C. C. Hong, "Fiber-matrix Bond Strength Studies of Glass, Ceramic, and Metal Matrix Composites", *Journal of Materials Science*, Vol.23, pp.311-323, 1988.
16. R. A. Shimansky, H. T. Hahn and N. J. Salamon, "The Effect of Weak Interface on Transverse Properties of a Ceramic Matrix Composite", *Interfaces in Composites, Materials Research Society Symposium Proceedings*, C. C. Pantano and Eric J. H. Chen, Eds., Vol. 170, pp. 193-204, Boston, 1989.
17. N. J. Pagano and G. P. Tandon, "Modeling of Imperfect Bonding in Fiber Reinforced Brittle Matrix Composites," *Mechanics of Materials*, Vol. 9, pp. 49-64, 1990.
18. N. J. Pagano and G. P. Tandon, "Thermo-elastic Model for Multidirectional Coated-Fiber Composites: Traction Formulation," *Composites Science and Technology*, Vol.38, pp. 247-269, 1990.
19. Z. Hashin, "Thermoelastic Properties of Fiber Composites with Imperfect Interface", *Mechanics of Materials*, Vol.8, pp.333-348,1990.



(a) Concentric Cylinder Model



(b) Square Array Model

Fig. 1 Representative volume element with debonding

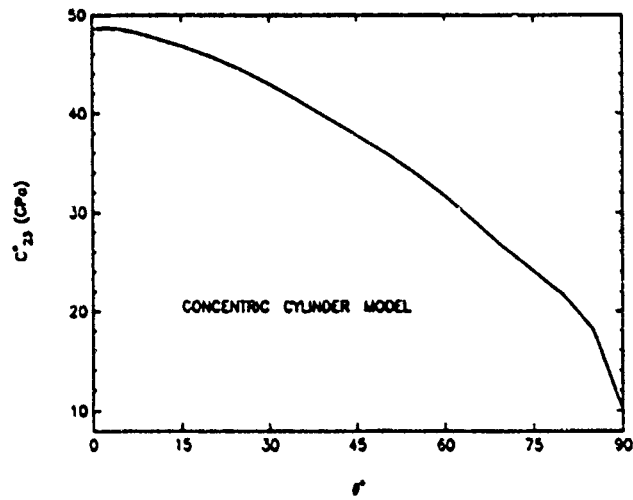
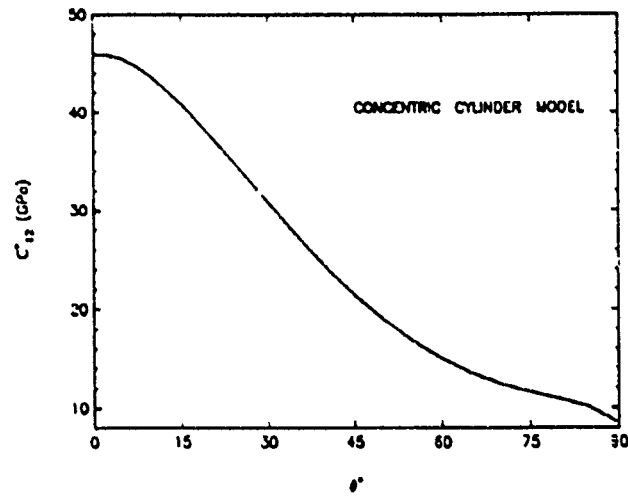
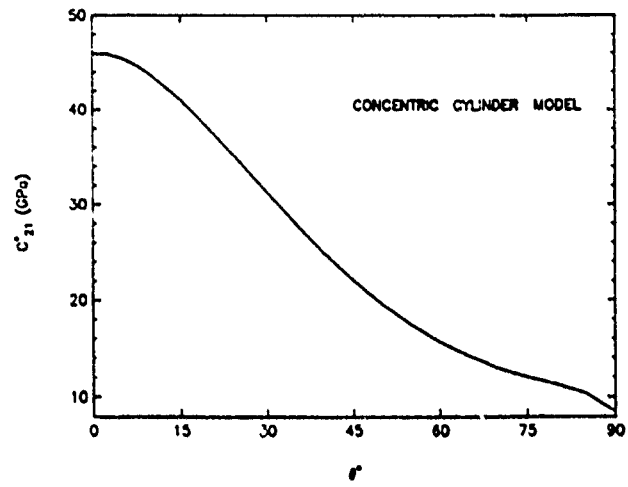


Fig. 2 Effective stiffness constants for concentric cylinder model

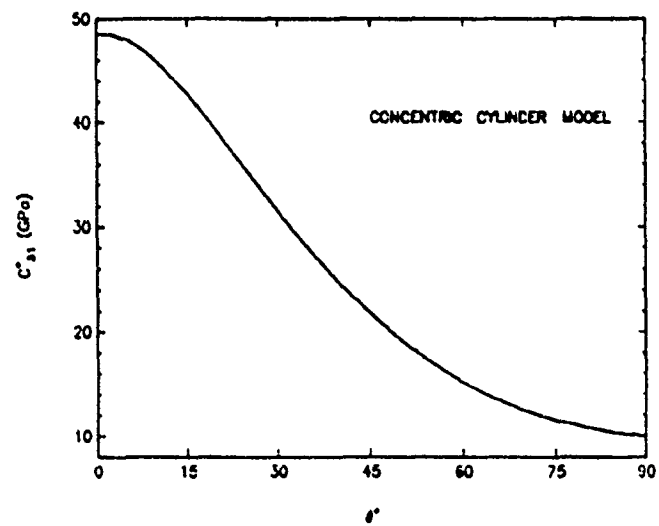
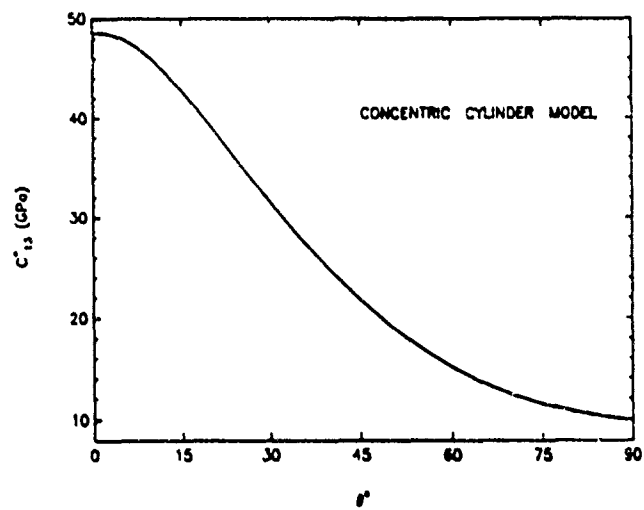
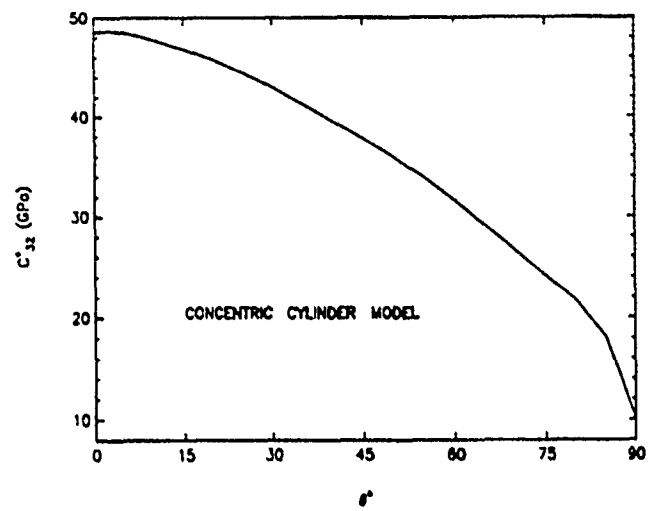


Fig. 2 (cont.) Effective stiffness constants for concentric cylinder model

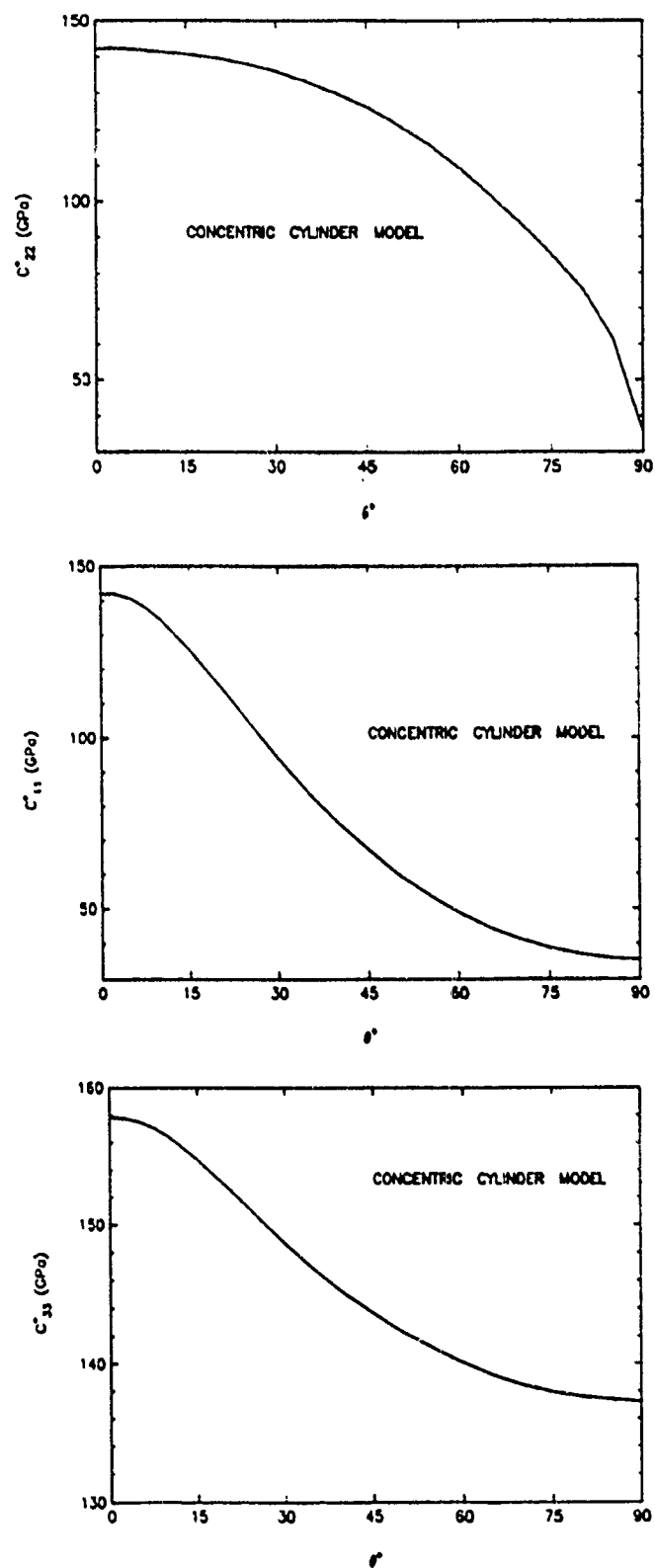


Fig. 2 (cont.) Effective stiffness constants for concentric cylinder model

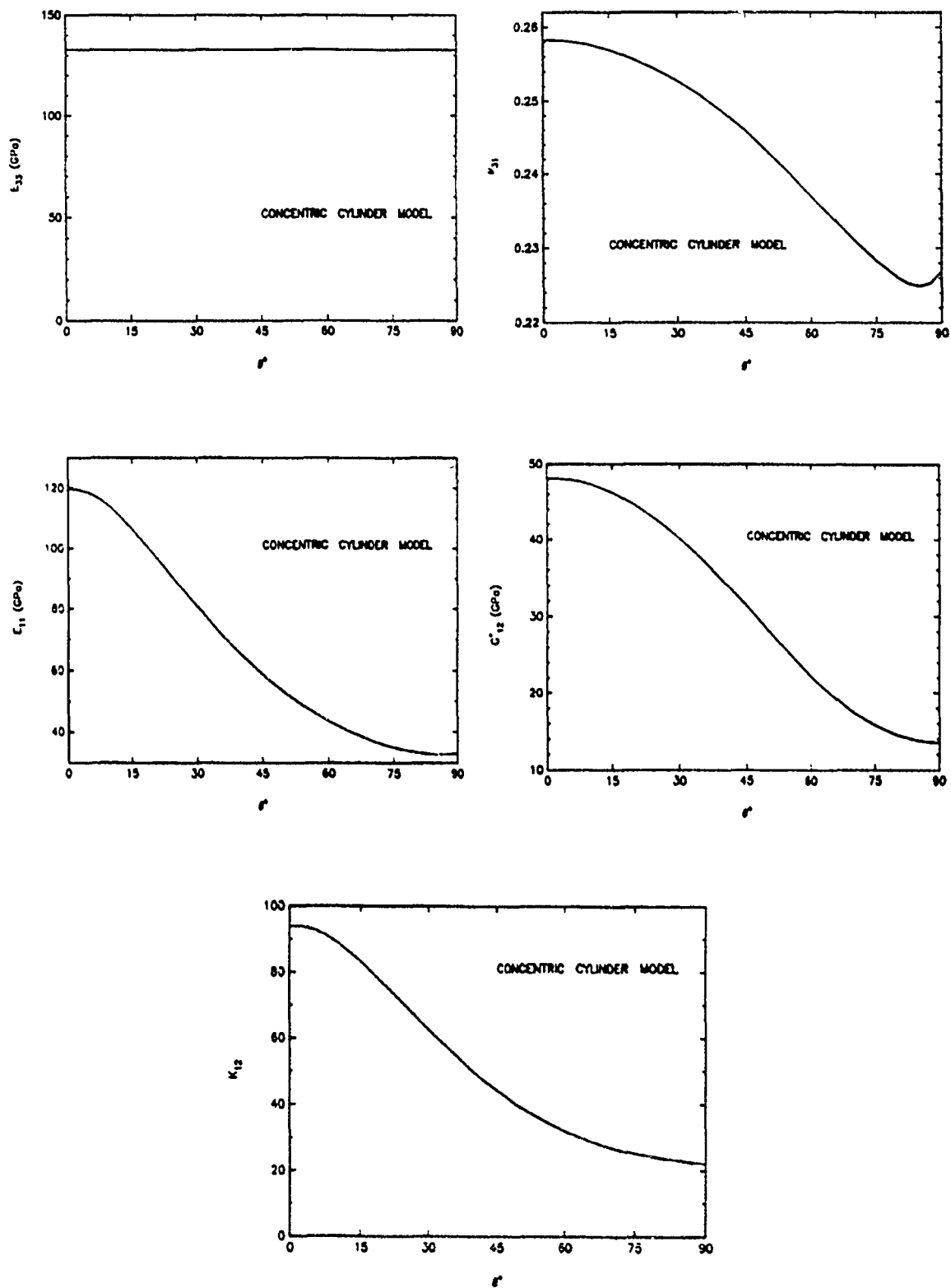


Fig. 3 Effective engineering constants for concentric cylinder model

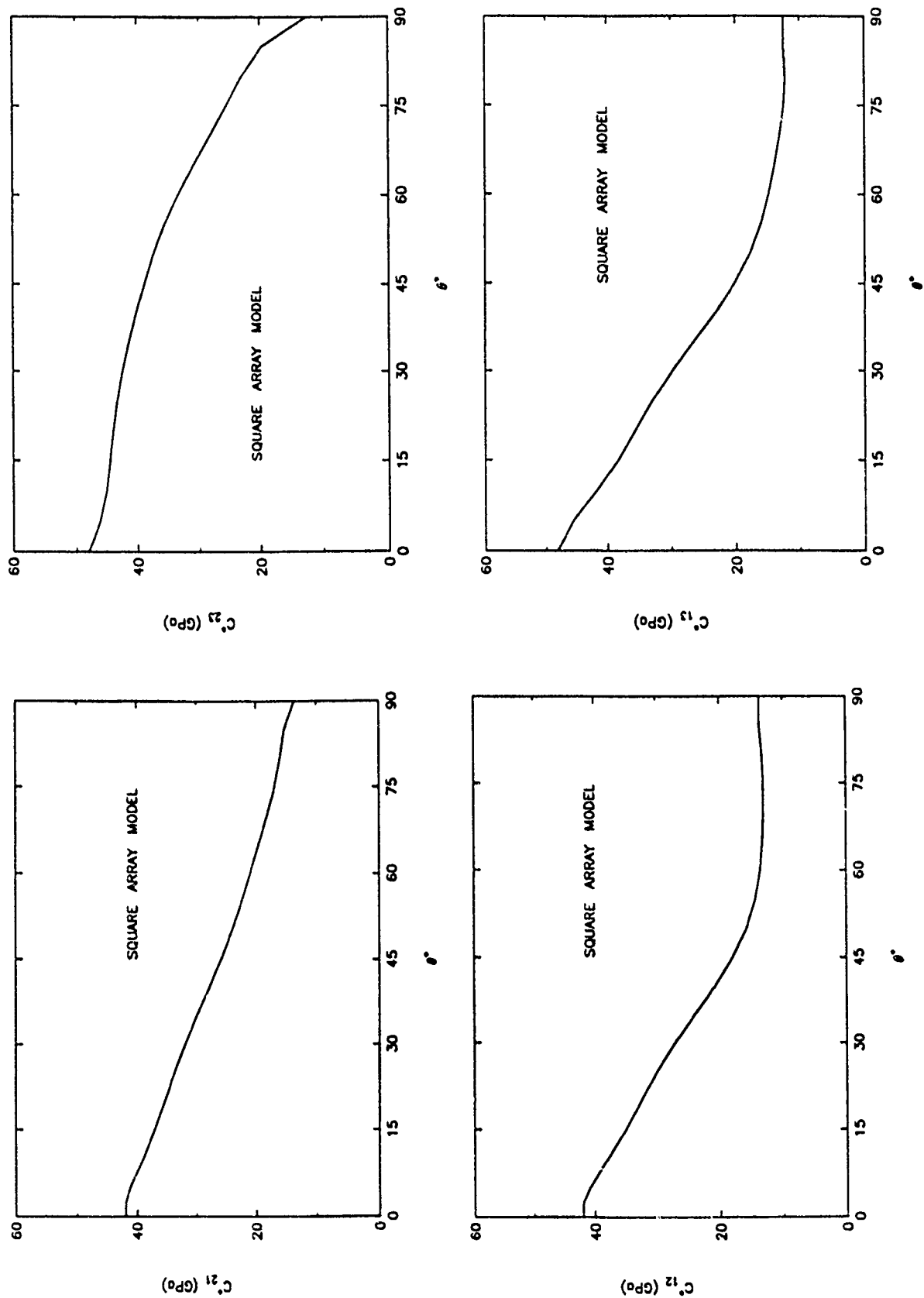


Fig. 4 Effective stiffness constants for square array model

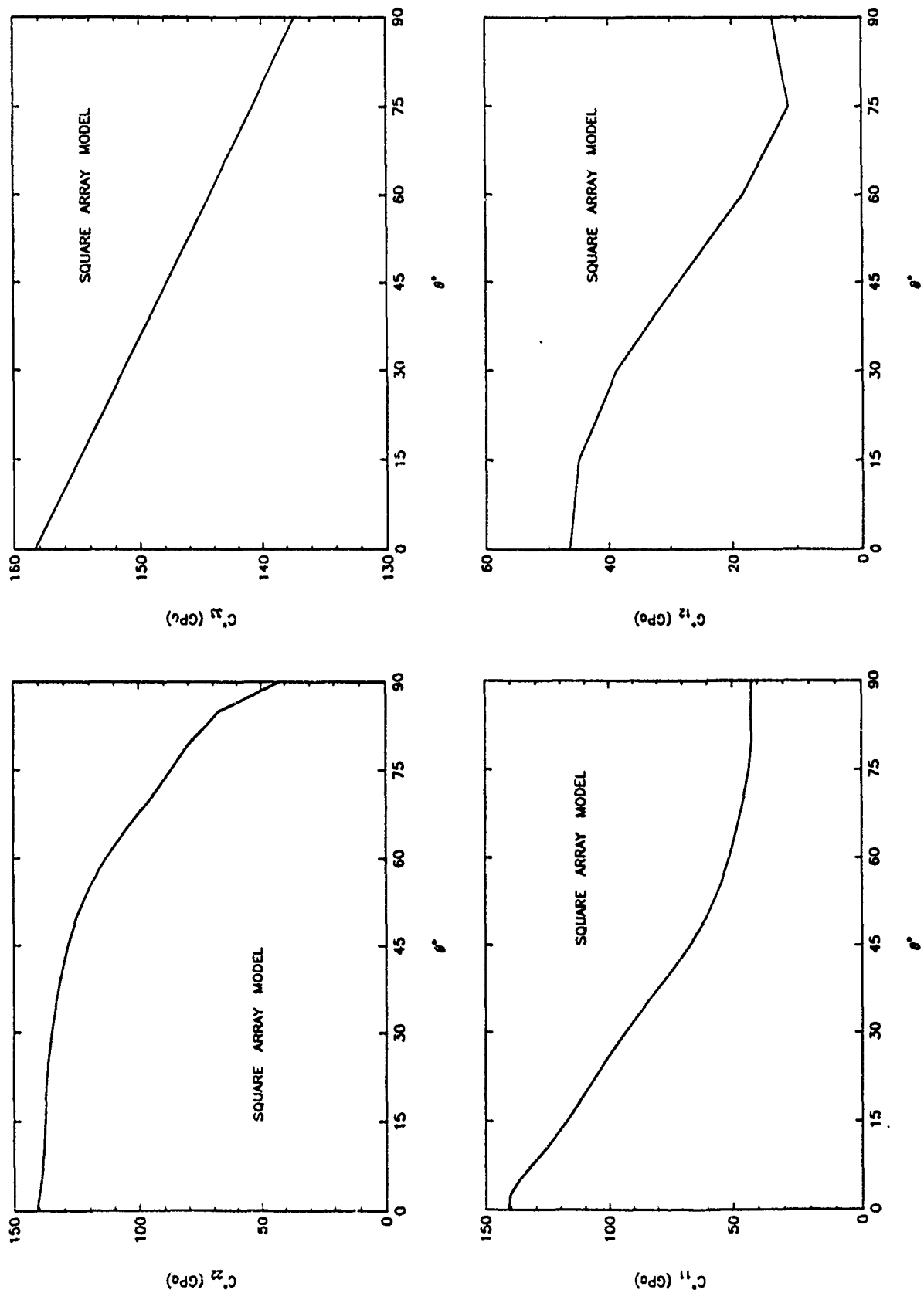


Fig. 4 (cont.) Effective stiffness constants for square array model